Hydrothermal Fe-Carbonate Alteration Associated with Volcanogenic Massive Sulfide (VMS) Deposits in Cycle IV of the Noranda Mining Camp, Rouyn-Noranda, Quebec

Ryan Wilson

A thesis submitted to the

Faculty of Graduate and Postdoctoral Studies

In partial fulfillment of the requirements for the

Master of Science Degree in Earth Sciences

Department of Earth Sciences

Faculty of Science

University of Ottawa

© Ryan Wilson, Ottawa, Canada, 2012

ABSTRACT

Massive sulfide deposits in the Noranda mining camp, northwestern Québec, are mainly associated with extensive footwall alteration defined by intense chloritization and sericitization. However, Fe-carbonate alteration also occurs in proximity to some deposits. To test the exploration significance of carbonate alteration in the camp, two areas of intense carbonate alteration were examined, around the small Delbridge deposit and near the new Pinkos occurrence in the Cyprus Rhyolite. Between 1969 and 1971, the Delbridge deposit produced 370,000 t of ore grading 9.6% Zn, 0.61% Cu, 110 g/t Ag, and 2.1 g/t Au. Recent drilling at the new Pinkos occurrence intersected 2.64 m of massive to semi-massive sulfides grading 8.1% Zn and 18.2 g/t Ag. Alteration mapping has shown that the distribution of Fe-carbonates can be used to identify vertically extensive zones of hydrothermal upflow at both properties. At Delbridge, intense Fe-carbonate alteration in brecciated rhyolite defines a pipe-like upflow zone that extends vertically for up to 300 m within the stratigraphic footwall of the massive sulfides and 100 m into the hanging wall. The location of known massive sulfide mineralization coincides with the intersection of the alteration pipe and a favorable horizon marked by the occurrence of fine-grained volcaniclastic rocks. At Pinkos, a similar zone of Fe-carbonate alteration occurs in outcrops of coherent rhyolite. Fe-carbonate alteration is most intensely developed along polygonal cooling fractures in massive rhyolite and decreases in intensity towards the centers of the columns. Fe-carbonate stringers and locally abundant matrix carbonate occur in fragmental rocks at the stratigraphic top of the coherent rhyolite flows and are most intense at the location of sulfide-bearing outcrops that mark the known mineralized horizon.

Whereas Fe-carbonate alteration defines the central part of the hydrothermal upflow zones at both properties, disseminated pyrite occurs at the margins and is widespread outside the main upflow zones. This may indicate that Fe-carbonate in the main upflow zones formed at the expense of earlier disseminated sulfides. Replacement of pyrite by synvolcanic Fe-carbonate alteration at Delbridge and Pinkos can probably be attributed to a relatively high concentration of dissolved CO_2, possibly of magmatic origin, in the main-stage ore-forming fluids.

TABLE OF CONTENTS

Abstract……II

Table of Contents……IV

List of Tables……VIII

List of Figures……...X

Acknowledgments……...XVII

1.0 Introduction...……...1

2.0 Regional Geology of the Noranda Camp……5

3.0 Geology of the Delbridge and Pinkos Properties……7

3.1 Delbridge ……7

Hydrothermal Alteration and Mineralization……. 8

3.2 Pinkos……11

Hydrothermal Alteration and Mineralization …..…….....12

4.0 Petrology of the Delbridge Rhyolite……..25

Spherulitic QP Rhyolite……25

Host Rhyolite Breccia……...26

QP Rhyolite Lobes……27

Hanging-wall Mafic Volcaniclastic Rocks……27

Hanging-wall FP and QFP Rhyolite……..28

Alteration and Mineralization……...28

Silicification……...28

Sericite Alteration……..29

Chlorite Alteration……31

Carbonate Alteration……..32

Disseminated and Stringer Sulfides……...35

Oxides……...38

5.0 Petrology of the Pinkos Rhyolite……...53

Coherent Rhyolite……..53

Fractured Rhyolite…….54

Fragmental Rhyolite……..54

Intrusive Mafic Rocks……...55

Alteration and Mineralization……...56

Silicification……...56

Sericite Alteration……..58

Chlorite Alteration…….59

Carbonate Alteration……..60

Epidote and Albite……63

Disseminated and Stringer Sulfides……...63

Oxides……...66

6.0 Lithogeochemistry of the Delbridge Rhyolite……...84

6.1 Geochemistry of Different Lithofacies……..85

6.2 Geochemistry of Alteration and Mineralization Types…….87

Major Element Correlations……89

Trace Element Correlations……90

Identification of Least-Altered Rhyolite Compositions……92

Incompatible Elements……...93

Compatible Elements……..94
Mass Gains and Losses Due to Alteration……..95
Rare-Earth Elements……...97
Alteration Intensity…….99
Ishikawa Alteration Index…….99
Chlorite-Carbonate-Pyrite Index…….100
Alteration Box Plot……..101
Carbonate Index……...102
Manganese Carbonate Index……103
Normative Alteration Mineralogy……...103
6.3 Geochemistry of Stringer and Disseminated Sulfides…….107
7.0 Lithogeochemistry of the Pinkos Rhyolite……..163
7.1 Geochemistry of Different Lithofacies…….163
7.2 Geochemistry of Alteration and Mineralization Types……165
Major Element Correlations……..167
Trace Element Correlations……..169
Identification of Least-Altered Rhyolite Composition…….170
Incompatible Elements……..171
Compatible Elements……171
Mass Gains and Losses Due to Alteration……172
Rare-Earth Elements…….174
Alteration Intensity……175
Ishikawa Alteration Index……175

Chlorite-Carbonate-Pyrite Index……176

Alteration Box Plot……..176

Carbonate Index……...177

Manganese Carbonate Index……177

Normative Alteration Mineralogy……...178

7.3 Geochemistry of Stringer and Disseminated Sulfides……180

8.0 Alteration Mineralogy and Mineral Chemistry……248

8.1 Short-wave Infrared Spectroscopy (SWIR)……248

8.2 Alteration Mineral Chemistry……..252

8.2.1 Delbridge……252

Muscovite……252

Chlorite……253

Carbonate……253

8.2.2 Pinkos……254

Muscovite……255

Chlorite……255

Carbonate……256

9.0 Summary and Conclusions……..286

Major Controls on Alteration and Mineralization……...286

Comparisons with Other VMS Deposits……290

Genetic Significance of Carbonate Alteration……293

10.0 References……298

LIST OF TABLES

Table 4.1 Delbridge Modal Mineralogy……52

Table 5.1 Pinkos Modal Mineralogy……83

Table 6.1a Delbridge Major Element Oxide Data……139

Table 6.1b Delbridge Trace Element Data……141

Table 6.1c Delbridge Rare-Earth Element Data……...145

Table 6.2a Delbridge Rhyolite Correlation Matrix……147

Table 6.2b Delbridge Mafic Volcaniclastic Unit Correlation Matrix……149

Table 6.3 Delbridge Least-Altered Footwall and Hanging-Wall Criteria……...151

Table 6.4 Delbridge Immobile Element Concentrations and Magmatic Affinities…152

Table 6.5 Delbridge Rhyolite Mass Balance Data……...154

Table 6.6a Delbridge Footwall Rhyolite Mass Balance Correlation Matrix……155

Table 6.6b Delbridge Hanging-Wall Rhyolite Mass Balance Correlation Matrix……155

Table 6.7 Delbridge Chondrite-Normalized Rare-Earth Element Compositions…...156

Table 6.8 Delbridge Alteration Intensity Calculations……157

Table 6.9 Delbridge Normative Mineral Abundance Estimates……158

Table 6.10 Delbridge Wallrock Pyrite Analytical Data……159

Table 6.11 Delbridge Pyrite Trace Element Correlation Matrix……...161

Table 7.1a Pinkos Major Element Oxide Data……...215

Table 7.1b Pinkos Trace Element Data……..218

Table 7.1c Pinkos Rare-Earth Element Data…….....224

Table 7.2a Pinkos Rhyolite Correlation Matrix……227

Table 7.2b Pinkos Mafic Volcaniclastic Unit Correlation Matrix……229

Table 7.3 Pinkos Least-Altered Footwall and Hanging-Wall Criteria …….....231

Table 7.4 Pinkos Immobile Element Concentrations and Magmatic Affinities …….232

Table 7.5 Pinkos Rhyolite Mass Balance Data…….....235

Table 7.6 Pinkos Footwall Rhyolite Mass Balance Correlation Matrix …….237

Table 7.7 Pinkos Chondrite-Normalized Rare-Earth Element Compositions ….....238

Table 7.8 Pinkos Alteration Intensity Calculations…….240

Table 7.9 Pinkos Normative Mineral Abundance Estimates……...242

Table 7.10 Pinkos Wallrock Pyrite Analytical Data……..244

Table 7.11 Pinkos Pyrite Trace Element Correlation Matrix …….....246

Table 8.1 Dominant Delbridge Alteration from Short-Wave Infrared Analyses……276

Table 8.2 Dominant Pinkos Alteration from Short-Wave Infrared Analyses…….277

Table 8.3 Microprobe Analyses of Sericite at Delbridge and Pinkos…….279

Table 8.4 Microprobe Analyses of Chlorite at Delbridge……280

Table 8.5 Microprobe Analyses of Carbonate at Delbridge……281

Table 8.6 Microprobe Analyses of Chlorite at Pinkos…….283

Table 8.7 Microprobe Analyses of Carbonate at Pinkos…….284

LIST OF FIGURES

Figure 1.1 Regional Geology Map of the Noranda Camp……3

Figure 1.2 Location Map of the Delbridge and Pinkos Properties……4

Figure 3.1 Local Geology Map of the Delbridge VMS Deposit…….16

Figure 3.2 Map of Carbonate Alteration Intensity at Delbridge…….17

Figure 3.3 Styles of Alteration and Mineralization at Delbridge……18

Figure 3.4 Map of Sulfide Intensity at Delbridge……...19

Figure 3.5 Local Geology Map of the Pinkos VMS Occurrence……20

Figure 3.6 Map of Carbonate Alteration Intensity at Pinkos……..21

Figure 3.7 Map of Sulfide Intensity at Pinkos…….22

Figure 3.8 Styles of Alteration and Mineralization at Pinkos…….23

Figure 3.9 Schematic Illustration of Paragenetic Sequence at Pinkos……24

Figure 4.1 Photomicrographs of Primary Volcanic Textures in Spherulitic QP Rhyolite at Delbridge ……..39

Figure 4.2 Photomicrographs of Primary Volcanic Textures in Rhyolite Breccia and Felsic Lapilli Tuff at Delbridge……...40

Figure 4.3 Photomicrographs of Primary Volcanic Textures in QP Rhyolite Lobes, Mafic Volcaniclastic Rocks, and FP and QFP Rhyolite at Delbridge……..41

Figure 4.4 Photomicrographs of Hydrothermal Quartz Textures at Delbridge……..42

Figure 4.5 Photomicrographs of Hydrothermal Muscovite Textures at Delbridge……43

Figure 4.6 Photomicrographs of Hydrothermal Chlorite Textures at Delbridge…..... ..44

Figure 4.7 Photomicrographs of Hydrothermal Carbonate Textures at Delbridge……45

Figure 4.8 Photomicrographs of Carbonate Replacing Sulfide at Delbridge ……...47

Figure 4.9 Photomicrographs of Disseminated and Fracture-Controlled Pyrite in Altered Wallrock at Delbridge …….....49

Figure 4.10 Back-Scattered Secondary Electron Images of Selected Pyrite Grains at Delbridge…….....50

Figure 4.11 Photomicrographs of Sphalerite, Chalcopyrite, and Rutile at Delbridge……51

Figure 5.1 Photomicrographs of Primary Volcanic Textures in Coherent QP Rhyolite at Pinkos……..67

Figure 5.2 Photomicrographs of Primary Volcanic Textures in Fractured QP Rhyolite at Pinkos……..68

Figure 5.3 Photomicrographs of Primary Volcanic Textures in Fragmental Rhyolite and Mafic Intrusive Rocks at Pinkos……..69

Figure 5.4 Photomicrographs of Hydrothermal Quartz Textures at Pinkos……...70

Figure 5.5 Photomicrographs of Hydrothermal Muscovite Textures at Pinkos…….71

Figure 5.6 Photomicrographs of Hydrothermal Chlorite Textures at Pinkos…….72

Figure 5.7 Photomicrographs of Hydrothermal Carbonate Textures at Pinkos …….73

Figure 5.8 Photomicrograhs of Carbonate Replacing Sulfide at Pinkos……75

Figure 5.9 Photomicrographs of Epidote Alteration at Pinkos……...77

Figure 5.10 Photomicrographs of Hydrothermal Sulfide and Replacement Textures in Stringers and Stockwork at Pinkos……....78

Figure 5.11 Photomicrographs of Hydrothermal Sulfide and Replacement Textures in Columnar-Jointed and Distal Coherent Rhyolite at Pinkos……..79

Figure 5.12 Photomicrographs of Hydrothermal Sulfide and Replacement Textures in Fragmental Rhyolite and Mafic Intrusive Rocks at Pinkos……..80

Figure 5.13 Back-Scattered Secondary Electron Images of Selected Pyrite Grains at Pinkos……81

Figure 5.14 Photomicrographs of Oxides at Pinkos……..82

Figure 6.1 Contoured Distribution Maps of Total Fe_2O_3 and CO_2 at Delbridge …….110

Figure 6.2 Contoured Distribution Map of Total S at Delbridge……..111

Figure 6.3 Contoured Distribution Maps of Na_2O and K_2O at Delbridge……112

Figure 6.4 Contoured Distribution Maps of CaO and MgO at Delbridge……113

Figure 6.5 Contoured Distribution Maps of Al_2O_3 and Li at Delbridge……...114

Figure 6.6 Contoured Distribution Maps of Ba and Sr at Delbridge……115

Figure 6.7 Contoured Distribution Maps of SiO_2 and Mn at Delbridge ……..116

Figure 6.8 Contoured Distribution Map of Total REE at Delbridge……117

Figure 6.9 Contoured Distribution Maps of Cu and Zn at Delbridge……...118

Figure 6.10 Contoured Distribution Map of Pb at Delbridge…….119

Figure 6.11 Bivariate Plots of Potentially Immobile Elements in Rhyolite at Delbridge……..120

Figure 6.12 Y-Zr Magmatic Affinity Plot for the Delbridge Sample Suite……121

Figure 6.13 Zr-Ti vs. Nb-Y and TiO_2-Zr Plots for the Delbridge Sample Suite……122

Figure 6.14 Ta-Zr and Nb-Zr Plots for the Delbridge Sample Suite……..123

Figure 6.15 Mass Balance Change Histograms for Footwall and Hanging-Wall Rhyolites at Delbridge…….124

Figure 6.16 REE Correlation Matrix and Representative Profiles at Delbridge……125

Figure 6.17 Contoured Maps of Ishikawa Alteration and Chlorite-Carbonate-Pyrite Indices at Delbridge……...126

Figure 6.18 Ishikawa Alteration and Chlorite-Carbonate-Pyrite Traverse Maps of the Delbridge Stratigraphic Footwall……..127

Figure 6.19 Delbridge Alteration Box Plot…….128

Figure 6.20 Contoured Maps of Carbonate Intensity and Mn-Carbonate Indices at Delbridge……..129

Figure 6.21 Abundance and Distribution Map of Normative White Mica at Delbridge ….....130

Figure 6.22 Abundance and Distribution Map of Normative Chlorite at Delbridge……..131

Figure 6.23 Abundance and Distribution Map of Normative Carbonate at Delbridge……..132

Figure 6.24 Contoured Distribution Maps of Cu and Zn Concentrations in Disseminated Sulfides at Delbridge…….133

Figure 6.25 Contoured Distribution Maps of Pb and Cd Concentrations in Disseminated Sulfides at Delbridge…….134

Figure 6.26 Contoured Distribution Maps of Au and Ag Concentrations in Disseminated Sulfides at Delbridge…….135

Figure 6.27 Contoured Distribution Maps of As and Sb Concentrations in Disseminated Sulfides at Delbridge…….136

Figure 6.28 Contoured Distribution Map of Tl Concentrations in Disseminated Sulfides at Delbridge……...137

Figure 6.29 Contoured Distribution Maps of Co and Ni Concentrations in Disseminated Sulfides at Delbridge…….138

Figure 7.1 Contoured Distribution Maps of Total Fe_2O_3 and CO_2 at Pinkos……...183

Figure 7.2 Contoured Distribution Map of Total S at Pinkos……...184

Figure 7.3 Contoured Distribution Maps of Na_2O and K_2O at Pinkos……185

Figure 7.4 Contoured Distribution Maps of CaO and MgO at Pinkos…….....186

Figure 7.5 Contoured Distribution Maps of Al_2O_3 and Li at Pinkos …….....187

Figure 7.6 Contoured Distribution Maps of Ba and Sr at Pinkos…….188

Figure 7.7 Contoured Distribution Maps of SiO_2 and Mn at Pinkos……189

Figure 7.8 Contoured Distribution Map of Total REE at Pinkos…….190

Figure 7.9 Contoured Distribution Maps of Cu and Zn at Pinkos …….....191

Figure 7.10 Contoured Distribution Map of Pb at Pinkos……..192

Figure 7.11 Bivariate Plots of Potentially Immobile Elements in Rhyolite at Pinkos……...193

Figure 7.12 Y-Zr Magmatic Affinity Plot for the Pinkos Sample Suite……194

Figure 7.13 Zr-Ti vs. Nb-Y and TiO_2-Zr Plots for the Pinkos Sample Suite…….195

Figure 7.14 Ta-Zr and Nb-Zr Plots for the Pinkos Sample Suite……196

Figure 7.15 Mass Balance Change Histograms for Footwall QP Rhyolite at Pinkos……...197

Figure 7.16 REE Correlation Matrix and Representative Profiles at Pinkos…….198

Figure 7.17 Contoured Maps of Ishikawa Alteration and Chlorite-Carbonate-Pyrite Indices at Pinkos…….....199

Figure 7.18 Ishikawa Alteration and Chlorite-Carbonate-Pyrite Traverse Maps of the Pinkos Stratigraphic Footwall……200

Figure 7.19 Pinkos Alteration Box Plot……..201

Figure 7.20 Contoured Maps of Carbonate Intensity and Mn-Carbonate Indices at Pinkos……...202

Figure 7.21 Abundance and Distribution Map of Normative White Mica at Pinkos ….....203

Figure 7.22 Abundance and Distribution Map of Normative Chlorite at Pinkos……...205

Figure 7.23 Abundance and Distribution Map of Normative Carbonate at Pinkos……...207

Figure 7.24 Contoured Distribution Maps of Cu and Zn Concentrations in Disseminated Sulfides at Pinkos……..209

Figure 7.25 Contoured Distribution Maps of Pb and Cd Concentrations in Disseminated Sulfides at Pinkos……..210

Figure 7.26 Contoured Distribution Maps of Au and Ag Concentrations in Disseminated Sulfides at Pinkos……..211

Figure 7.27 Contoured Distribution Maps of As and Sb Concentrations in Disseminated Sulfides at Pinkos……..212

Figure 7.28 Contoured Distribution Map of Tl Concentrations in Disseminated Sulfides at Pinkos…….....213

Figure 7.29 Contoured Distribution Maps of Co and Ni Concentrations in Disseminated Sulfides at Pinkos……..214

Figure 8.1 Representative SWIR Profiles for Alteration Assemblages at Delbridge and Pinkos……...258

Figure 8.2 Distribution Map of Dominant Alteration Minerals Identified by SWIR at Delbridge……...259

Figure 8.3 Distribution Map of Dominant Alteration Minerals Identified by SWIR at Pinkos…….....260

Figure 8.4 Chlorite Composition (Hey) Diagram at Delbridge …….....261

Figure 8.5 Map of Chlorite Compositional Variation at Delbridge……..262

Figure 8.6 Carbonate Cation Ternary Diagram at Delbridge……...263

Figure 8.7 Map of Carbonate Chemical Variability at Delbridge……264

Figure 8.8 Scanning Electron Microscope Images of Chlorite and Carbonate at Delbridge……..265

Figure 8.9 Distribution Map of Manganese Content in Carbonate at Delbridge …….266

Figure 8.10 White Mica Ternary Diagram at Delbridge and Pinkos……..267

Figure 8.11 Chlorite Composition (Hey) Diagram at Pinkos…….268

Figure 8.12 Map of Chlorite Compositional Variation at Pinkos……...269

Figure 8.13 Comparison of Delbridge and Pinkos Chlorite Compositions to Other VMS Deposits of the Noranda Camp……270

Figure 8.14 Carbonate Cation Ternary Diagram at Pinkos…….271

Figure 8.15 Map of Carbonate Chemical Variability at Pinkos……..272

Figure 8.16 Scanning Electron Microscope Images of Carbonate at Pinkos …….273

Figure 8.17 Distribution Map of Manganese Content in Carbonate at Pinkos ……..275

Figure 9.1 Schematic Illustrations of Noranda-type vs. Delbridge and Pinkos VMS Deposits……..297

ACKNOWLEDGMENTS

There are many people who provided much support and guidance throughout the lengthy course of this thesis to whom I am thankful. I would like to express my sincere gratitude to Mark Hannington for suggesting and supervising this project but most of all for not giving up on me. Mark's limitless encouragement to see this study through to completion after a relatively tortuous path will never be lost on me. Professionalism, integrity, and a constantly open door are but a few qualities that complement Mark's nature as an ideal supervisor. His vast expertise, many useful comments and suggestions, and relentless desire to mentor truly made this project an enjoyable and fulfilling experience.

This study was funded by a number of different parties who deserve a great many thanks. This research was initiated and supported in a joint effort between the mining industry, the University of Ottawa, and the Geological Survey of Canada. Geological information, funding, and employment opportunities were kindly provided by Xstrata Copper Canada Ltd. and Alexis Minerals Corporation. I would also like to thank the TGI-3 (Targeted Geoscience Initiative - 3) Abitibi program led by Benoit Dube from the Geological Survey of Canada for their financial support (Research Affiliate Program, RAP) and scientific contributions. I am also thankful for a PGS-M research grant awarded to the author by NSERC in the early stages of this project.

I am indebted to Thomas Monecke and Harold Gibson for many hours spent in the field developing and documenting a firm understanding of the regional Noranda camp

and local geology associated with the Delbridge and Pinkos deposits. Ian Jonasson played a crucial role in sample preparation, analytical techniques, and the direction of this project. Jeanne Percival kindly offered her time and expertise with respect to sample preparation when X-ray diffraction analyses were considered. I must express my sincere gratitude towards Howard Poulsen for steering me into the field of geology and providing constant support towards my research interests as well as acting as both a professional and personal mentor.

I owe many thanks to Sandy Sheperd for countless hours of emotional support and friendly banter above and beyond all of the technical and administrative assistance she kindly offered over the years.

I would like to thank my family and close friends for their unwavering support and encouragement, providing a multitude of welcome distractions, and always welcoming me with open arms. Last but certainly not least, I would like to thank Robyn Diver to whom I am ever grateful for her relentless support, companionship, and most importantly her patience. Robyn's astounding strength as well as her kind and caring nature helped me find myself in a time of great need as she stood by my side right through to the end.

1. INTRODUCTION

Volcanogenic massive sulfide (VMS) deposits of the Noranda camp are hosted by the Noranda Volcanic Complex (NVC) of the Archean Blake River Group, Abitibi Subprovince. Most deposits occur within or along the margins of a structurally-controlled asymmetric volcanic depression, known as the Noranda Cauldron, which is filled with basalt and basaltic andesite flows and subordinate rhyolite flow and dome complexes (Gibson and Galley, 2007). VMS deposits within the Noranda camp are interpreted to have formed during two main cycles of cauldron subsidence (Cycles III and IV) that were accommodated by synvolcanic faulting (Gibson and Watkinson, 1990). Multiphase subvolcanic intrusive complexes are represented by the Flavrian and Powell plutons, which are considered to have been the heat sources responsible for the VMS deposits (Gibson, 1990; Mortensen, 1993; 1987). Subsidence of the Noranda Cauldron is interpreted to have been influenced by the partial evacuation of the underlying magma chambers (Gibson and Galley, 2007). Cycle III volcanic rocks, referred to as the Mine Sequence, host 17 VMS deposits. The Delbridge and Pinkos occurrences are located in Cycle IV volcanic rocks along the eastern margins of the NVC (Figure 1.1). Delbridge is ~4 km east-northeast of the city of Rouyn-Noranda, Québec; Pinkos is located ~8.5 km northeast.

Exploration at the Delbridge property began in the 1920s. Deldona (No. 1) (Figure 1.2) was found in 1947, and the exploration team at Falconbridge Nickel Mines Ltd. discovered the Delbridge (No. 2) deposit in 1965. Between 1969 and 1971, the Delbridge deposit produced 370,000 t of ore grading 9.6% Zn, 0.61% Cu, 110 g/t Ag, and

2.1 g/t Au (Barrett et al, 1993; Boldy, 1979). Boldy (1968, 1979), and more recently Barrett et al (1993), described the geology of Delbridge. The Pinkos VMS occurrence was discovered in 2007 by a joint venture between Xstrata Canada Corporation and Alexis Minerals (Alexis Minerals Press Release, January 9, 2007). Drilling at Pinkos in 2006 intersected 2.64 m of massive to semi-massive sulfides grading 8.1% Zn and 18.2 g/t Ag. This paper is the first description of the geology and alteration at the Pinkos property.

Most VMS deposits of the Noranda camp are characterized by vertically extensive chlorite-sericite footwall alteration in dominantly coherent volcanic rocks, typical of many Archean Cu-Zn deposits worldwide. Morton and Franklin (1987) identified this alteration as Noranda-type. Another style of alteration with abundant Fe-carbonate in the footwall is found at Delbridge and Pinkos. Mueller et al (2009) describe similar alteration at Normetal and elsewhere in the Blake River Group. However, Gibson and Galley (2007) noted that the relationship between hydrothermal carbonate alteration and VMS mineralization in Noranda was unclear. Two areas of intense carbonate alteration were studied at Delbridge and Pinkos to evaluate the exploration significance of carbonate alteration in the Noranda camp. The distribution of hydrothermal alteration was mapped to determine the spatial relationship to VMS mineralization. The alteration mineralogy, textural relationships, and compositional variations have been determined through field mapping, petrography, short-wave infrared (SWIR) spectroscopy, and mineral chemistry.

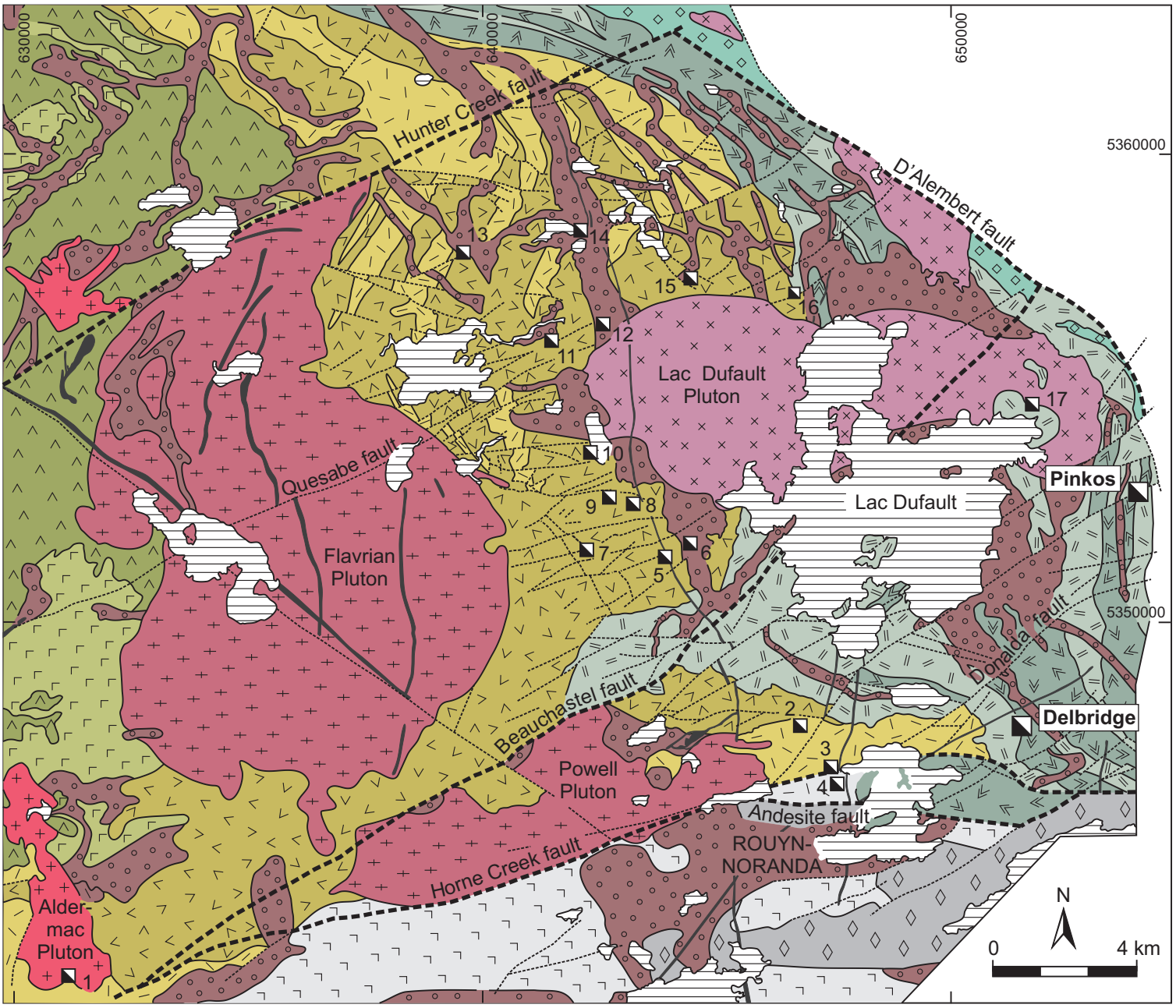

VMS deposits: 1=Aldermac, 2=Joliet, 3=Quemont, 4=Horne, 5=D68, 6=Millenbach, 7=Corbet, 8=Amulet A, 9=Amulet C, 10=Amulet F, 11=Old Waite, 12=East Waite, 13=Ansil, 14=Vauze, 15=Norbec, 16=Newbec, and 17=Gallen

ARCHEAN EXTRUSIVE ROCKS

Undifferentiated
- Rhyolite
- Basalt/andesite

Cycle 1+2
- Rhyolite
- Basalt/andesite

Cycle 3
- Rhyolite
- Basalt/andesite

Cycle 4
- Rhyolite
- Basalt/andesite

Cycle 5
- Basalt/andesite

ARCHEAN INTRUSIVE ROCKS
- Syenite
- Granodiorite
- Trondhjemite, tonalite
- Gabbro, quartz diorite

PROTEROZOIC INTRUSIVE ROCKS
- Diabase

- Major fault
- Minor fault
- VMS deposit

Figure 1.1. Generalized geological map of the Noranda Camp, showing the regional geology and major structural elements, as well as the distribution of extrusive and intrusive rocks. The locations of the Delbridge and Pinkos VMS occurrences are identified in bold along the eastern margin of the Noranda cauldron. The distribution of main camp VMS deposits is also included (modified after Monecke et al, 2008).

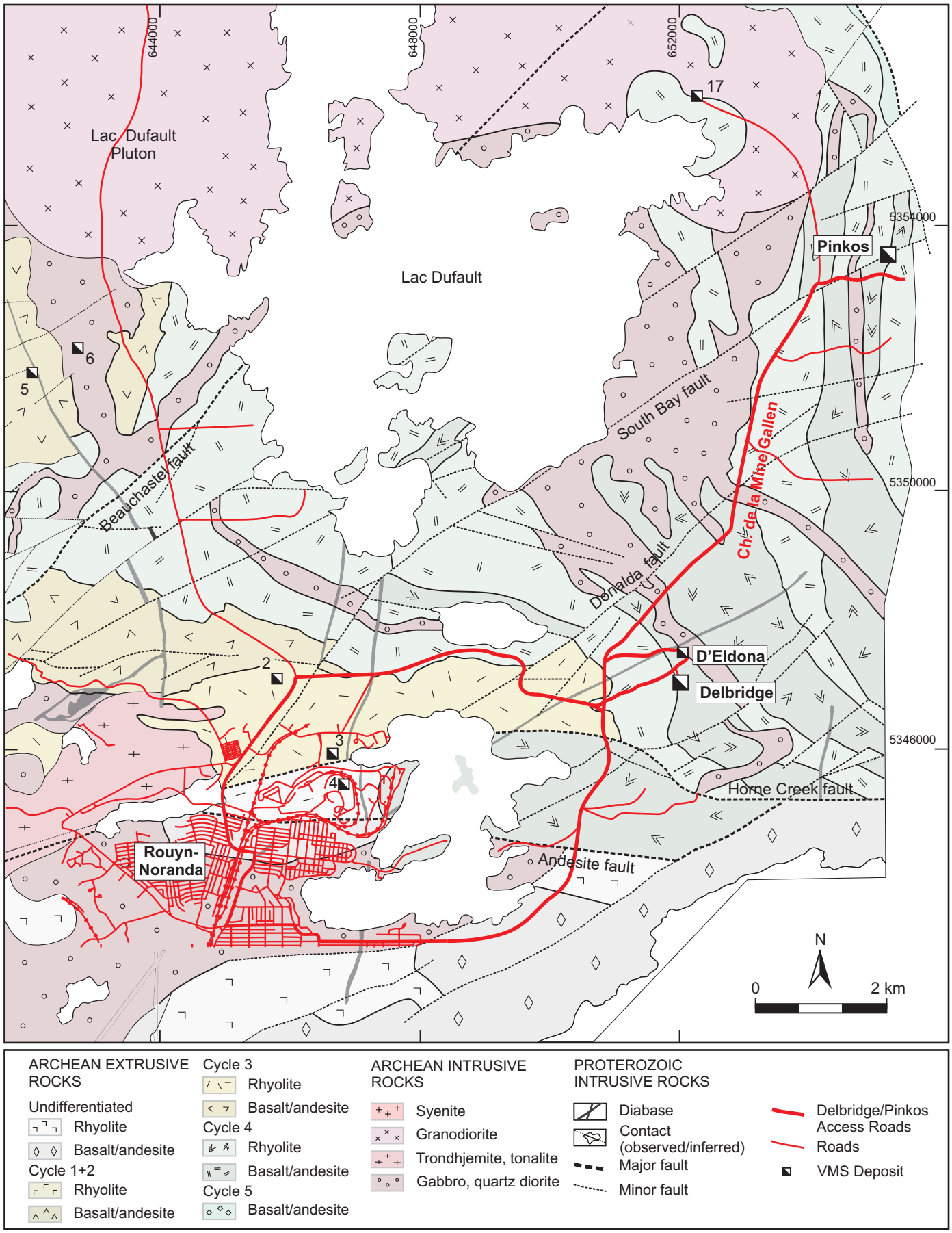

Figure 1.2. Generalized geological map of the eastern part of the Noranda Camp, showing the distribution of extrusive and intrusive rocks. Access roads to both Delbridge and Pinkos properties are highlighted in bold red (modified after Monecke et al, 2008).

2. REGIONAL GEOLOGY

The Noranda Volcanic Complex (NVC) is composed of predominantly tholeiitic bimodal volcanic strata, including basaltic, andesitic and rhyolitic units (Gibson and Watkinson, 1990). The 7.5 to 9 km-thick volcanic succession has traditionally been subdivided into five cycles, each represented by lower basaltic to andesitic units overlain by alternating basaltic, andesitic and rhyolitic upper units (Gibson, 1990). Synvolcanic diorite dikes are observed to cross-cut these volcanic units. This classification is under review after recent detailed dating of the Blake River Group. Goutier et al (2009) currently identify four volcanic episodes in the temporal evolution of the Blake River Group with the following U-Pb zircon ages: 2704 to 2707.8 Ma for Episode 1, 2701.8 to 2699.3 Ma for Episode 2, 2699.3 to 2696.7 Ma for Episode 3, and 2696.7 to 2695 Ma for Episode 4. This dating indicates a relatively short period during which the entire NVC volcanic stratigraphy of the Blake River Group accumulated.

The NVC is intruded by the Flavrian and Powell synvolcanic intrusions which consist of sill-like bodies with shallow dips and generally conformable contacts with the overlying volcanic succession (Galley, 2003). The Lac Dufault pluton, a smaller intrusive complex in the eastern part of the NVC, cross-cuts the surrounding volcanic stratigraphy and is interpreted to post date Cycle III and Cycle IV (or Episode 3) volcanic rocks (Mortensen, 1993).

A number of structural blocks delimited by major faults subdivide the NVC into the Hunter Creek block north of the Hunter Creek fault, the Flavrian block between the

Hunter Creek and Beauchastel faults, the Powell block between the Beauchastel and Horne Creek faults, and the Horne block between the Horne Creek and Andesite faults (Figure 1.1: Monecke et al, 2008). Delbridge and Pinkos are located within Cycle IV volcanic rocks of the Powell structural block along the eastern margin of the NVC. The Delbridge deposit occurs in volcanic rocks dominated by quartz- and feldspar-porphyritic (± spherulitic) to aphyric massive rhyolite, coarse rhyolite breccias, and graded felsic lapilli tuff lithofacies. Pinkos occurs in coherent, quartz- and feldspar-porphyritic (± spherulitic) rhyolite with lesser volcaniclastic deposits. Volcaniclastic rocks are notably abundant at Delbridge and Pinkos compared to deposits of the Central Mine Sequence (Cycle III), which occur in predominantly coherent volcanic flows intercalated with lesser amounts (<5%) of volcaniclastic rocks (Monecke et al, 2008; Spence and de Rosen-Spence, 1975; Kerr and Gibson, 1993).

The Archean supracrustal rocks of the NVC have been metamorphosed to prehnite-pumpellyite or lower greenschist facies (Powell et al, 1995). This regional metamorphism has overprinted the synvolcanic hydrothermal alteration.

3. GEOLOGY OF THE DELBRIDGE AND PINKOS PROPERTIES

3.1 DELBRIDGE

The main rock types associated with the Delbridge deposit are quartz- and feldspar-porphyritic to aphyric massive rhyolite and rhyolite breccia (Figure 3.1). A thick unit, approximately 300 m, of spherulitic quartz-porphyritic rhyolite occurs at the base of the mapped section (Figure 3.1). This locally flow-banded unit is defined by its relatively high abundance of feldspathic spherulites. Flow-banding is exhibited by the alignment of fine tabular plagioclase crystals and subrounded quartz eyes.

Coarse rhyolite breccia and graded felsic lapilli tuff facies immediately overlie the spherulitic rhyolite (Figure 3.1). A moderately east-dipping coarse breccia pile, ~300 m thick, dominates this part of the stratigraphy. It comprises framework-supported quartz-porphyritic and some aphyric intrusive rhyolite clasts. Poorly sorted blocky and curviplanar rhyolite clasts dominate the volcaniclastic material. The rhyolite breccia pile is stratified with an upper, normally graded felsic lapilli tuff facies. Meter-scale beds (S_0) dip subvertically along a trend of ~340°. The breccia pile is delimited to the north by intrusive rhyolite that extends to and separates the Delbridge and Deldona deposits, which occur along the same ore horizon. This unit is interpreted as the feeder for the aphyric rhyolite above the ore horizon (Boldy, 1968; O'Dowd, 1990). To the south, the breccia pile is bounded by quartz-porphyritic rhyolite lobes, with locally peperitic margins, and mafic volcaniclastic units.

The sulfide deposit occurs near the top of the rhyolite breccia pile, and the ore

horizon is marked by a finely-laminated chert bed that is interpreted to have been deposited during a period of quiescence in volcaniclastic deposition. The sulfides are developed in felsic fragmental rocks that are overlain by a thick (~100 m) unit of fine-grained mafic volcaniclastic rocks (Figure 3.1). The mafic volcaniclastic rocks are composed chiefly of chloritic and feldspathic grains that are moderately packed and sorted. Bedding is defined by the alignment of subangular and platy grains and strikes ~350° with a subvertical dip. The mafic volcaniclastic rocks appear to onlap the underlying felsic sequence from a separate, distal source to the south.

The hanging wall is dominated by more coherent units of feldspar-porphyritic (FP) and quartz-feldspar-porphyritic (QFP) rhyolite (Figure 3.1). The FP rhyolite is defined by its lath-shaped feldspar phenocrysts that are notable in hand specimen. The aphyric rhyolite that overlies the FP, QFP and intrusive rhyolite bodies was not mapped.

A series of both felsic and mafic dikes are present in the map area, including a Proterozoic diabase dike that strikes approximately 060° from the Horne mine. Figure 3.1 also identifies two possible synvolcanic faults that were previously identified in Cattalani et al (1993) and Boldy (1968).

HYDROTHERMAL ALTERATION AND MINERALIZATION

Moderate to strong sericite alteration occurs both within fractures and disseminated in massive coherent rhyolite and is associated locally with fracture-controlled chlorite. The coherent rhyolite lacks carbonate at the base of the section but is

weakly carbonatized within 100 m of the upper contact; abundant Fe-carbonate occurs locally in the brecciated margins of the flows. Both silica alteration and disseminated and fracture-controlled pyrite are present throughout the unit. Coarse rhyolite breccias are strongly carbonatized, with Fe-carbonate flooding the lapilli tuff matrix. Fe-carbonate also occurs within foliation planes and as disseminations in coherent clasts. Lesser sericite, chlorite and silicification are also observed within the matrix and fractures. The coherent intrusive rhyolite is strongly sericitized, with white mica occurring pervasively both within fractures and as disseminations. Moderate to strong silicification and chlorite alteration also occur locally. Alteration of the mafic volcaniclastic unit includes mainly calcite and chlorite along bedding planes, together with minor pyrite and trace chalcopyrite. Alteration of the feldspar-porphyritic rhyolite in the hanging-wall position includes moderate chloritization ($\pm$ sericitization) within fracture networks together with weakly disseminated pyrite. Weak to moderate silicification is evident in the groundmass. Quartz-feldspar-porphyritic rhyolite in the hanging wall shows pervasive silicification of the groundmass and fracture-controlled sericite ($\pm$ chlorite) and pyrite. Very minor calcite is also observed in the hanging-wall QFP rhyolite.

Carbonate and muscovite are the main hydrothermal alteration minerals observed at Delbridge. The most abundant carbonate occurs at and immediately surrounding the surface projection of the Delbridge deposit. The intensity of carbonate alteration was mapped on a relative scale from 1 to 10 based on abundance of observed carbonate and response to 3% and 10% HCl. Carbonate abundance ranges from <1 vol.% (disseminated, fracture-controlled) to more than 10 vol.% (spotty to pervasive). The field

data have been plotted and contoured using inverse-distance weighting (Figure 3.2). The presence of Fe-carbonate is indicated by the deep red-brown colour in outcrop. Proximal to the deposit (within ~200 m), Fe-carbonate occurs in highly sericitized fragmental rhyolite as disseminations and in fractures (Figure 3.3a). More abundant Fe-carbonate occurs in the matrix of rhyolite breccias (Figure 3.3b) and in stringers and stockwork (Figure 3.3c). The stockwork defines a proximal upflow zone, approximately 100 m in width, beneath the deposit and appears to be closely spatially associated with two inferred synvolcanic faults shown in Figure 3.1. Intense Fe-carbonate also appears to follow a broadly concordant zone of strongly sericitized fragmental rhyolite at and below the ore horizon. This alteration has been mapped to the north north-west for a distance of more than 300 m and is notable in the field by the red-brown staining characteristic of Fe-carbonate, as well as the development of a strong cleavage due to the abundant sericite alteration. The carbonate abundance decreases rapidly about 175 m stratigraphiclly below the ore horizon, where the permeability of the host rhyolite diminishes. Moderate carbonate alteration also extends stratigraphically above the ore horizon within the hanging-wall quartz-feldspar- and feldspar-porphyritic rhyolite. Local chloritization and silicification are also observed within the hanging-wall rhyolite and mafic volcaniclastic rocks.

The abundance of disseminated sulfides in the altered wall rock was also mapped using a similar relative scale (Figure 3.4). Sulfide abundance at surface ranges from trace to about 5 vol.%. Disseminated and stringer sulfides occur at the margins of the most intense zone of Fe-carbonate alteration (Figure 3.3d). Centimeter-scale patches of

disseminated subhedral pyrite, as well as mm-scale fracture-controlled pyrite are locally abundant in the footwall spherulitic rhyolite and silicified quartz-porphyritic rhyolite. Near the ore horizon pyrite occurs as coarse-grained disseminated subhedral to euhedral grains, cm-scale stringers together with sphalerite, and in local gossanous patches in the quartz-porphyritic rhyolite breccia. Weakly disseminated fine-grained anhedral pyrite grains also occur in the hanging-wall quartz-feldspar- and feldspar-porphyritic rhyolite. However, sulfides are notably almost absent in the zone of most intense Fe-carbonate alteration (Figures 3.2, 3.4).

3.2 PINKOS

The volcanic stratigraphy at the Pinkos VMS occurrence is dominated by ~1 km of felsic to intermediate volcanic rocks belonging to the Cyprus Rhyolite. The Cyprus Rhyolite is a regional stratigraphic unit that is truncated to the east by the d'Alembert shear (Figure 3.5). The units are steeply dipping and east-facing. The map area is dominated by coherent, quartz- and feldspar-porphyritic (+/- spherulitic) rhyolite, with lesser overlying volcaniclastic deposits. Primary volcanic structures observed include flow alignment banding and a variety of spectacular cooling features (i.e., polygonal, planar, and tortoise-shell styles of columnar jointing). A weakly altered intermediate extrusive also occurs at the base of the mapped section.

Semimassive to massive sulfide mineralization at the Pinkos property occurs at the top of the Cyprus Rhyolite. The main host for mineralization is a relatively thin (< 50 m) lens of intensely sericitized fragmental rhyolite overlying massive coherent to lobate

rhyolite flows. Drill hole PNK-06-02 intersected 2.64 m of massive to semimassive pyrite and sphalerite in the fragmental unit at the top of the Cyprus Rhyolite, as well as 3 m of semimassive pyrite containing chalcopyrite stringers. Several zones of disseminated sulfides occur at surface in the intensely sericitized quartz-porphyritic fragmental rhyolite unit. They are characterized by weakly to moderately gossanous outcrops with fracture-controlled, mm-scale sulfide veins.

A metre-scale medium-grained gabbroic dike cuts the basal intermediate unit in the southern portion of the study area and may represent the feeder plug for a thin gabbroic intrusion that occurs 100-200 m higher in the stratigraphy and is broadly conformable with the thick rhyolite package (Figure 3.5). The gabbro is characterized by medium-grained feldspar (plagioclase) and (clino-) pyroxene phenocrysts and is altered dominantly to chlorite and epidote. An ENE-trending synvolcanic fault has been inferred to occur north of the access road to the Lamothe Pit (South Bay Fault in Figure 3.5; SIGÉOM Geological Compilation Map CG-4, 2000), terminating stratigraphically below the massive, coherent rhyolite flows.

HYDROTHERMAL ALTERATION AND MINERALIZATION

Primary features such as cooling fractures, amygdules, and flow banding appear to have been the main control on hydrothermal alteration of the massive rhyolite. This contrasts with Delbridge, where hydrothermal alteration is localized mainly within coarse rhyolite breccias. Quartz, carbonate, and muscovite are the dominant alteration. Similar to Delbridge, the carbonate ranges from Fe-poor to Fe-rich, the latter indicated by deep

red-brown to orange-brown colour in outcrop. Dark chlorite occurs locally within amygdules and fractures and also as wispy cm-scale disseminations in the coherent facies of the rhyolite.

Carbonate abundance ranges from <1 vol.% (disseminated, fracture-controlled) to more than 10 vol.% (spotty and pervasive). Two discordant zones of Fe-carbonate alteration occur in the map area (Figure 3.6): along the Lamothe pit road and near drill-hole PNK-06-02 which intersected the massive sulfide body. The most intense Fe-carbonate alteration occurs in a broadly discordant zone along the access road. This zone is ~100 m wide and extends several hundred meters into the footwall.

Disseminated and stringer sulfides in the altered wall rock (Figure 3.7) overlie the zone of most intense Fe-carbonate alteration and also occur at the margins of the discordant Fe-carbonate alteration zone. The thick succession of massive coherent rhyolite in the central part of the map area lacks carbonate and sulfide alteration, suggesting that these rocks were relatively impermeable to hydrothermal upflow. They are characterized by less well-developed columnar jointing, fewer amygdules and more intense silicification (Figures 3.8a, 3.8b).

Columnar jointing in the massive rhyolite was a focus for fluid flow, with distinctive zonation of sericite and Fe-carbonate minerals adjacent to cooling fractures and in nearby amygdules (Figures 3.8c, 3.8d). Early silicification is pervasive within the groundmass of coherent rhyolite, with many primary volcanic textures such as

spherulites, flow banding, and perlitic fractures still preserved. Quartz rims most amygdules and lines many cooling fractures. This early silicification is followed by sericitization and eventually replacement along fractures by Fe-carbonate. Clear zonation from quartz to sericite to red-weathering Fe-carbonate is observed in rims around amygdules and adjacent to the cooling fractures of columnar joints. This sequence is illustrated schematically in Figure 3.9. A late stage of sericite commonly lines the fractures. Zones of spotted to pervasive carbonate occur locally which nearly replace all sericite except along joints (Figure 3.8e). Veins of Fe-carbonate and pervasive replacement of flow bands occur in coherent rhyolite (Figures 3.8f, 3.8g). In the pervasively altered fragmental unit at the top of the massive rhyolite, Fe-carbonate and chlorite also clearly overprint sericite and sulfides are locally abundant.

All of these features are cut by shallowly-dipping en echelon quartz veins (Figure 3.8h) that increase in abundance with proximity to the d'Alembert shear. These barren quartz veins are interpreted to be the result of extensional fracture infill related to the later deformational event that produced the d'Alembert shear. Importantly, the late fractures and flat veins do not show the same zoned Fe-carbonate alteration. The veins are filled by un-metamorphosed quartz. The flat veins strike between 230° and 345° and are filled with cloudy white and/or pinkish quartz and minor calcite. A subset of more steeply-dipping quartz veins, which is also observed cross-cutting primary volcanic features, is composed of crystalline quartz with little to no carbonate. The steeply-dipping veins strike at ~200° and dip at ~45-50°. Petrographic observations indicate quartz in these late veins is medium-grained (~0.25-0.5 mm) and subhedral to euhedral.

The notable discordance of the mapped alteration supports the interpretation of primary synvolcanic hydrothermal upflow related to the zinc mineralization at the top of the coherent rhyolite flows. The hydrothermal upflow zone is dominated by vertically extensive, fracture-controlled Fe-carbonate in the massive rhyolite and locally intense sulfide mineralization and sericitization of the overlying fragmental unit. The carbonate alteration dissipates outward within a few 100 m of the inferred upflow zone in the fractured coherent rhyolite. Abundant disseminated sulfides define a broadly conformable zone of hydrothermal infiltration or discharge at the top of the volcanic pile. However, sulfides appear to be mainly absent in the centre of the upflow, as observed at Delbridge.

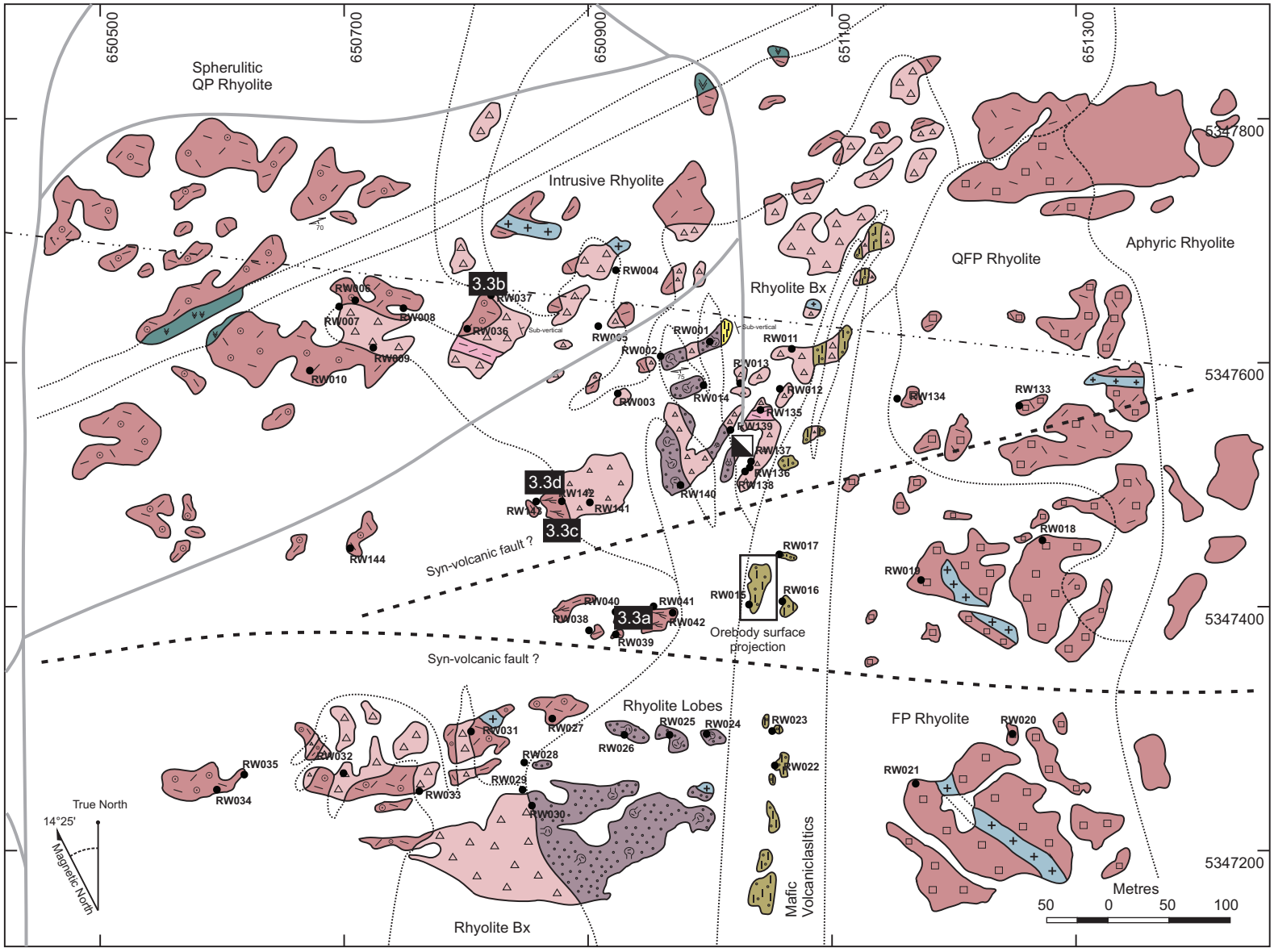

Figure 3.1. Geology of the Delbridge property, showing the surface projection of the orebody (box) between two possible synvolcanic faults. Locations of 54 surface samples collected to characterize hydrothermal alteration are shown. The locations of photographs shown in Figures 3.3a-d are also identified.

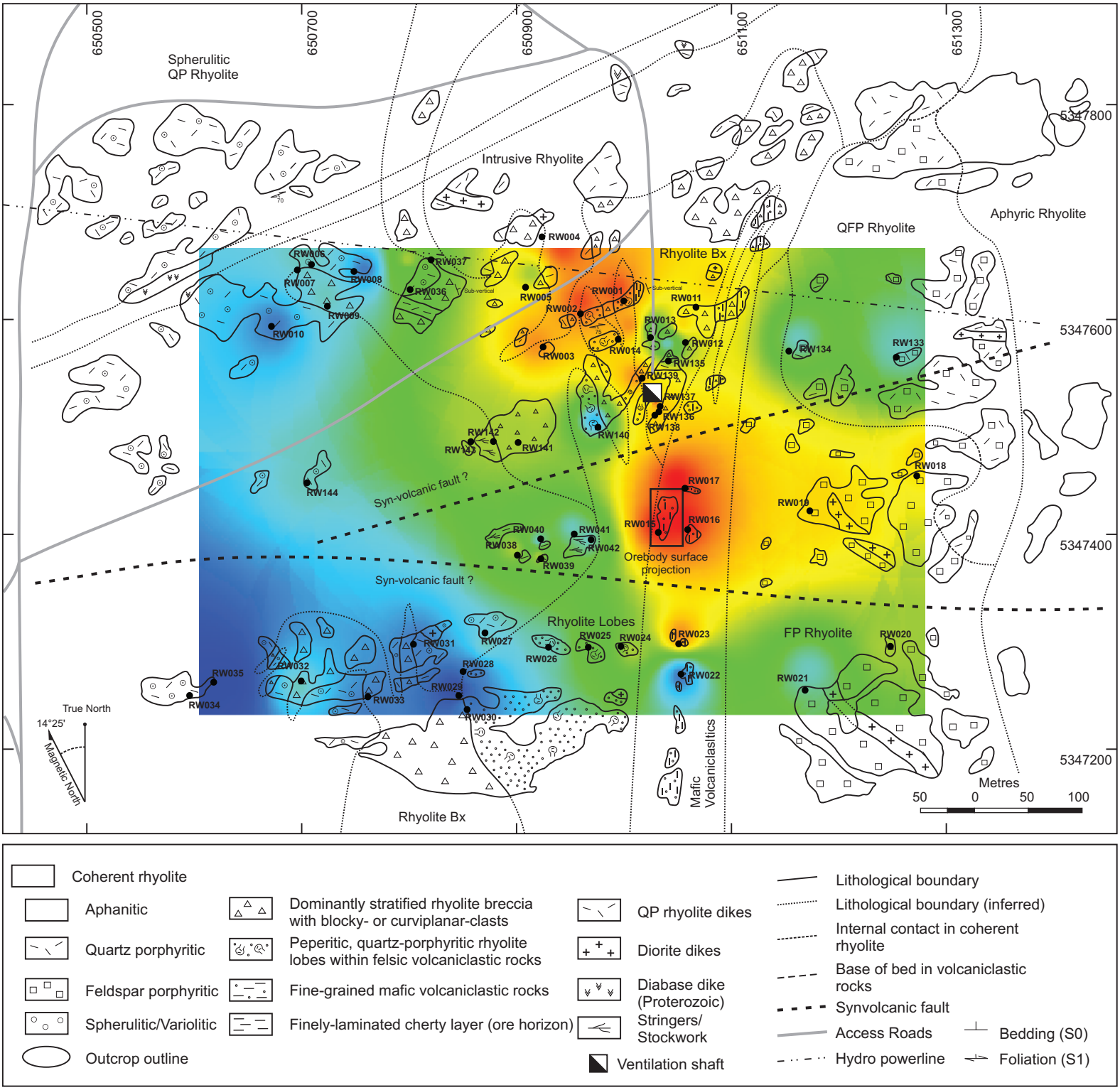

Coherent rhyolite
Aphanitic
Quartz porphyritic
Feldspar porphyritic
Spherulitic/Variolitic
Outcrop outline
Dominantly stratified rhyolite breccia with blocky- or curviplanar-clasts
Peperitic, quartz-porphyritic rhyolite lobes within felsic volcaniclastic rocks
Fine-grained mafic volcaniclastic rocks
Finely-laminated cherty layer (ore horizon)
QP rhyolite dikes
Diorite dikes
Diabase dike (Proterozoic)
Stringers/ Stockwork
Ventilation shaft
Lithological boundary
Lithological boundary (inferred)
Internal contact in coherent rhyolite
Base of bed in volcaniclastic rocks
Synvolcanic fault
Access Roads
Hydro powerline
Bedding (S0)
Foliation (S1)

Figure 3.2. Intensity of carbonate alteration at the Delbridge property. Plotted data are based on semi-quantitative field estimates and contoured using inverse-distance weighting (IDW). Blue = absent; red = abundant (see text for discussion). Refer to Figure 3.4 for comparison with the abundance of distal disseminated and fracture-controlled sulfides.

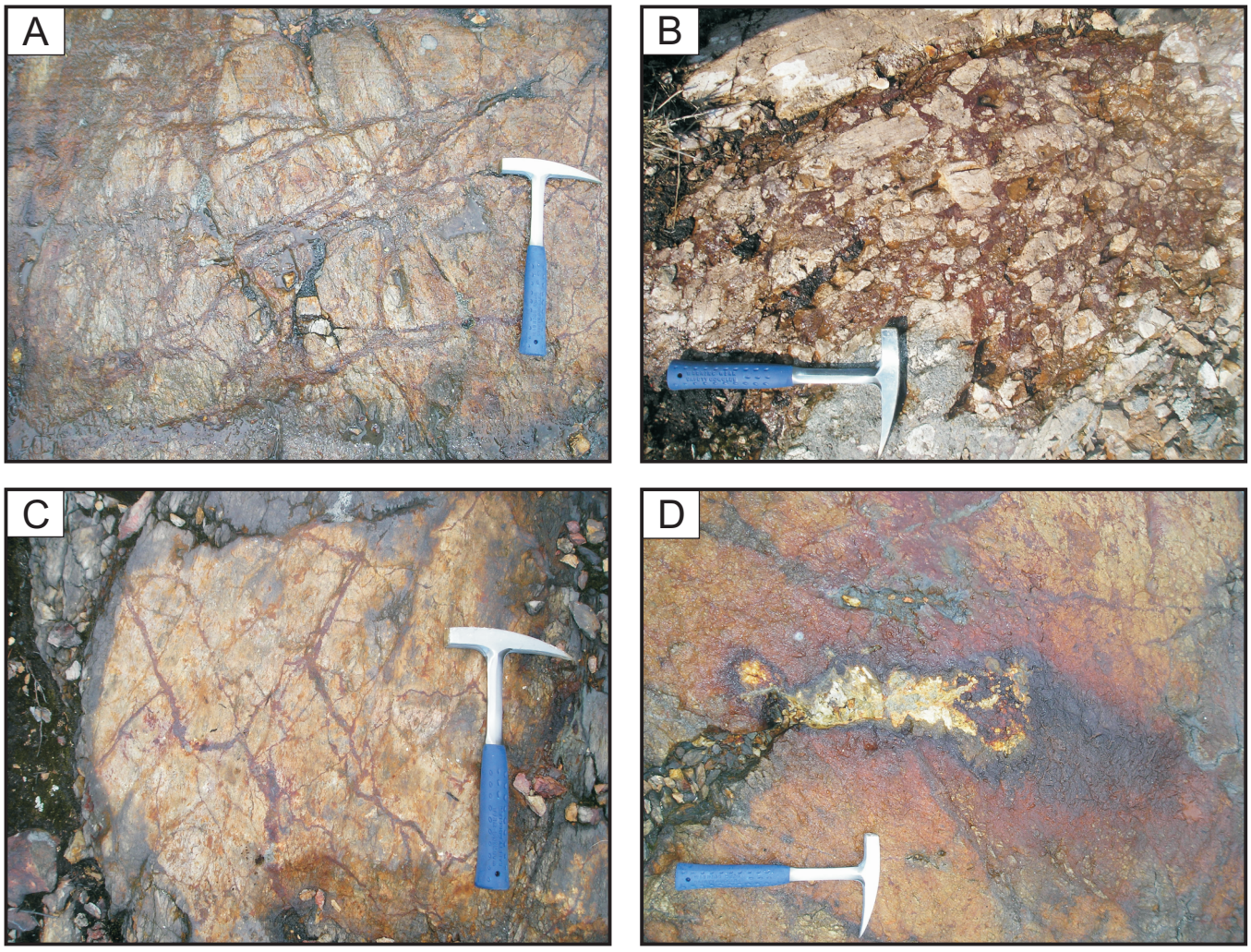

Figure 3.3. Documentation of different alteration styles at Delbridge: a) Disseminated and fracture-controlled Fe-carbonate in highly sericitized fragmental quartz-phyric rhyolite; b) Matrix-controlled Fe-carbonate in rhyolite breccia; c) Fe-carbonate stringers and stockwork in the interpreted hydrothermal upflow zone; and d) Stringer sulfides in footwall quartz-phyric rhyolite along the margins of same upflow zone.

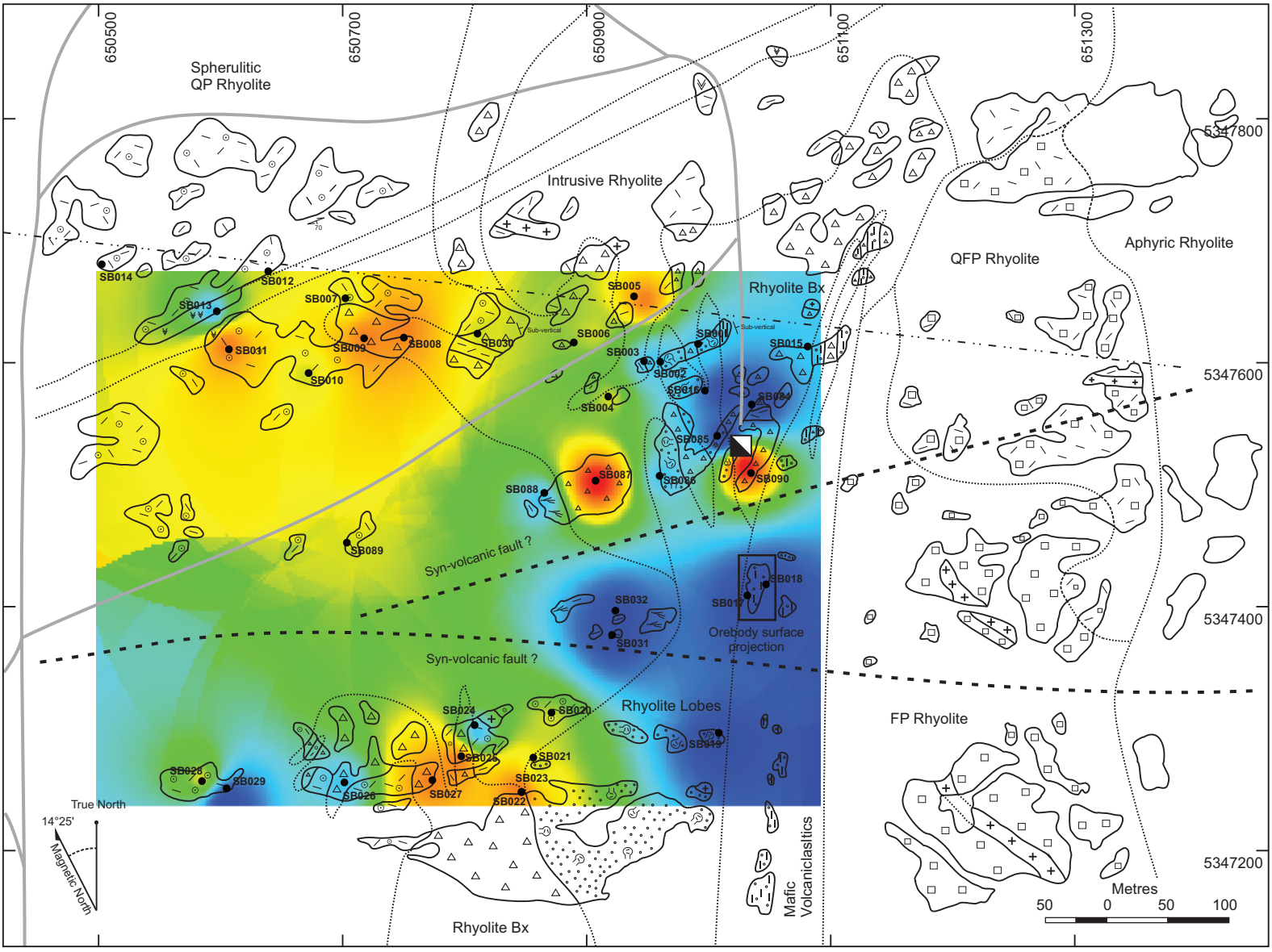

Coherent rhyolite
Aphanitic
Quartz porphyritic
Feldspar porphyritic
Spherulitic/Variolitic
Outcrop outline
Dominantly stratified rhyolite breccia with blocky- or curviplanar-clasts
Peperitic, quartz-porphyritic rhyolite lobes within felsic volcaniclastic rocks
Fine-grained mafic volcaniclastic rocks
Finely-laminated cherty layer (ore horizon)
QP rhyolite dikes
Diorite dikes
Diabase dike (Proterozoic)
Stringers/ Stockwork
Ventilation shaft
Lithological boundary
Lithological boundary (inferred)
Internal contact in coherent rhyolite
Base of bed in volcaniclastic rocks
Synvolcanic fault
Access Roads
Hydro powerline
Bedding (S0)
Foliation (S1)

Figure 3.4. Abundance of disseminated and fracture-controlled sulfide mineralization at the Delbridge property. Plotted data are based on semi-quantitative field estimates and contoured using inverse-distance weighting (IDW). Blue = absent; red = abundant (see text for discussion). Note that the area of most intense Fe-carbonate alteration between the synvolcanic faults contains little or no disseminated sulfides.

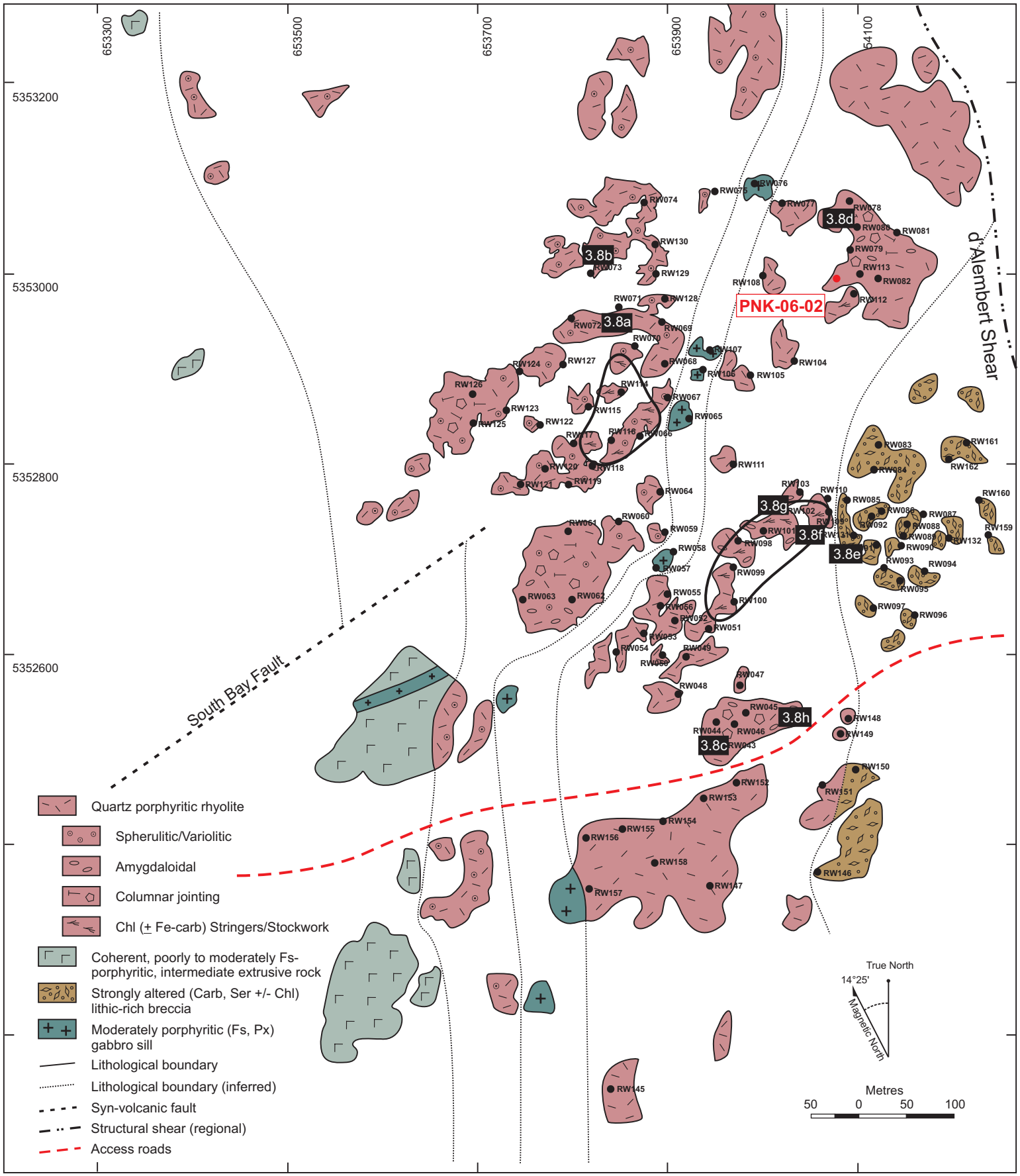

Figure 3.5. Geology of the Pinkos property, showing the location of newly discovered mineralization in drill-hole PNK-06-02, which is along trend of the South Bay Fault. Two zones of stringers/stockwork are indicated as well as localized zones of enhanced primary porosity such amygdules and a variety of cooling fractures. Alteration intensity is strongly spatially associated with these zones. The locations of 108 surface samples collected to characterize hydrothermal alteration are plotted. The locations of photographs shown in Figures 4.4a-h are also identified.

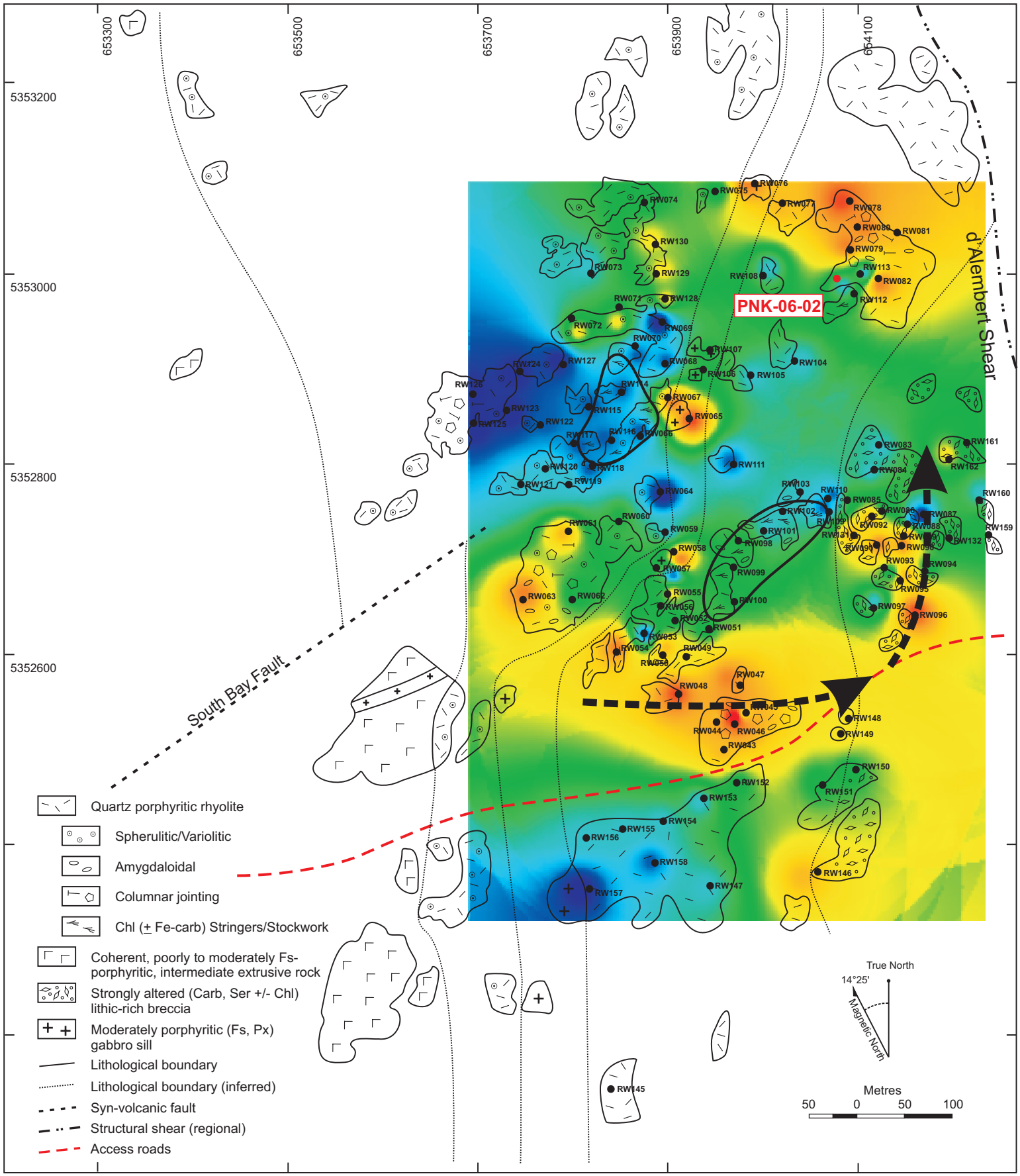

Figure 3.6. Intensity of carbonate alteration at the Pinkos property. Plotted data are based on semi-quantitative field estimates and contoured using inverse-distance weighting (IDW). Blue = absent; red = abundant (see text for discussion). The arrows indicate the inferred path of hydrothermal upflow related to intense carbonate alteration and mineralization in the lithic breccias at the stratigraphic top of the succession.

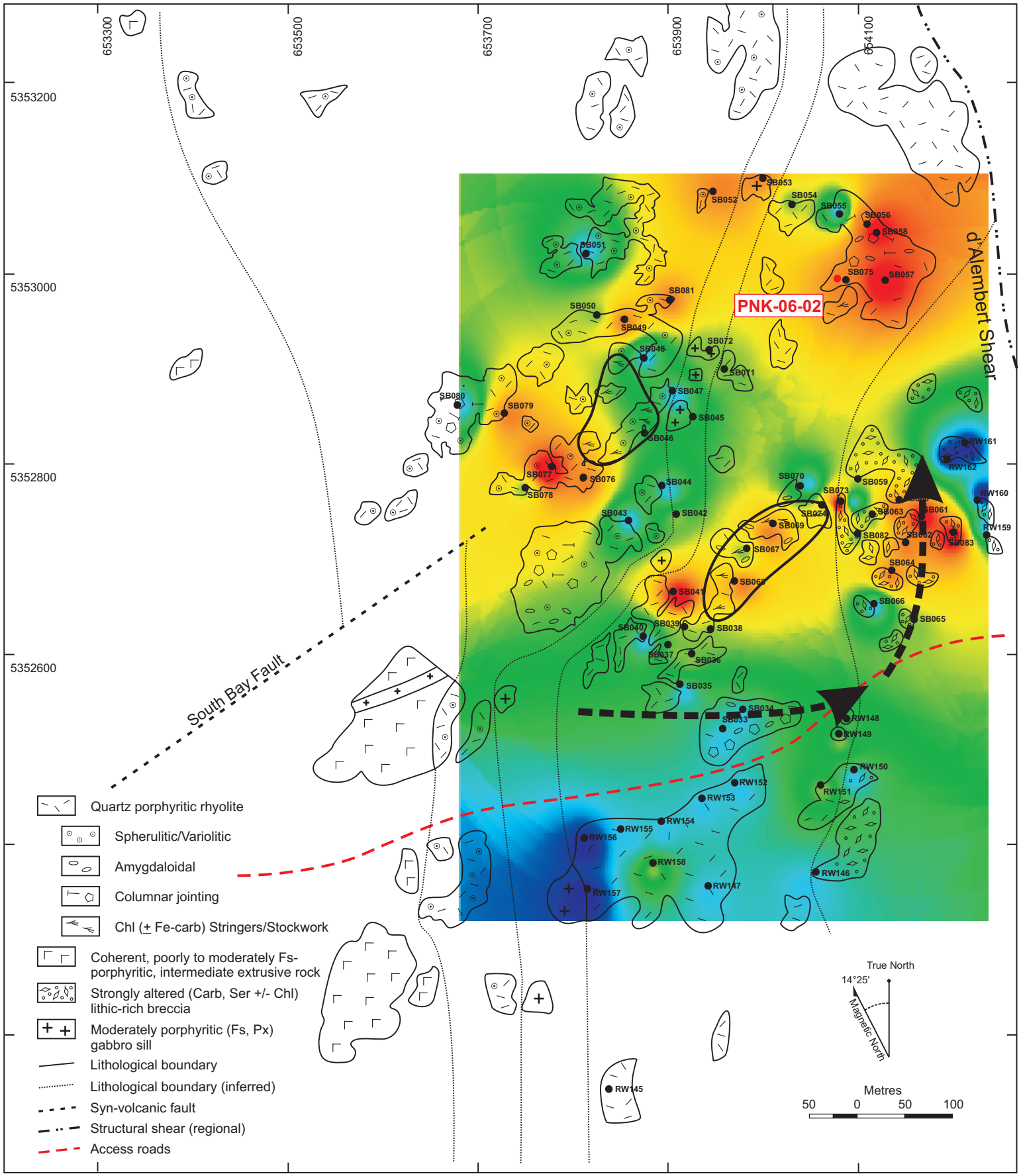

Figure 3.7. Abundance of disseminated and fracture-controlled sulfide mineralization at the Pinkos property. Plotted data are based on semi-quantitative field estimates and contoured using inverse-distance weighting (IDW). Blue = absent; red = abundant (see text for discussion). The arrows indicate the inferred path of hydrothermal upflow related to intense carbonate alteration and mineralization in the lithic breccias at the stratigraphic top of the succession.

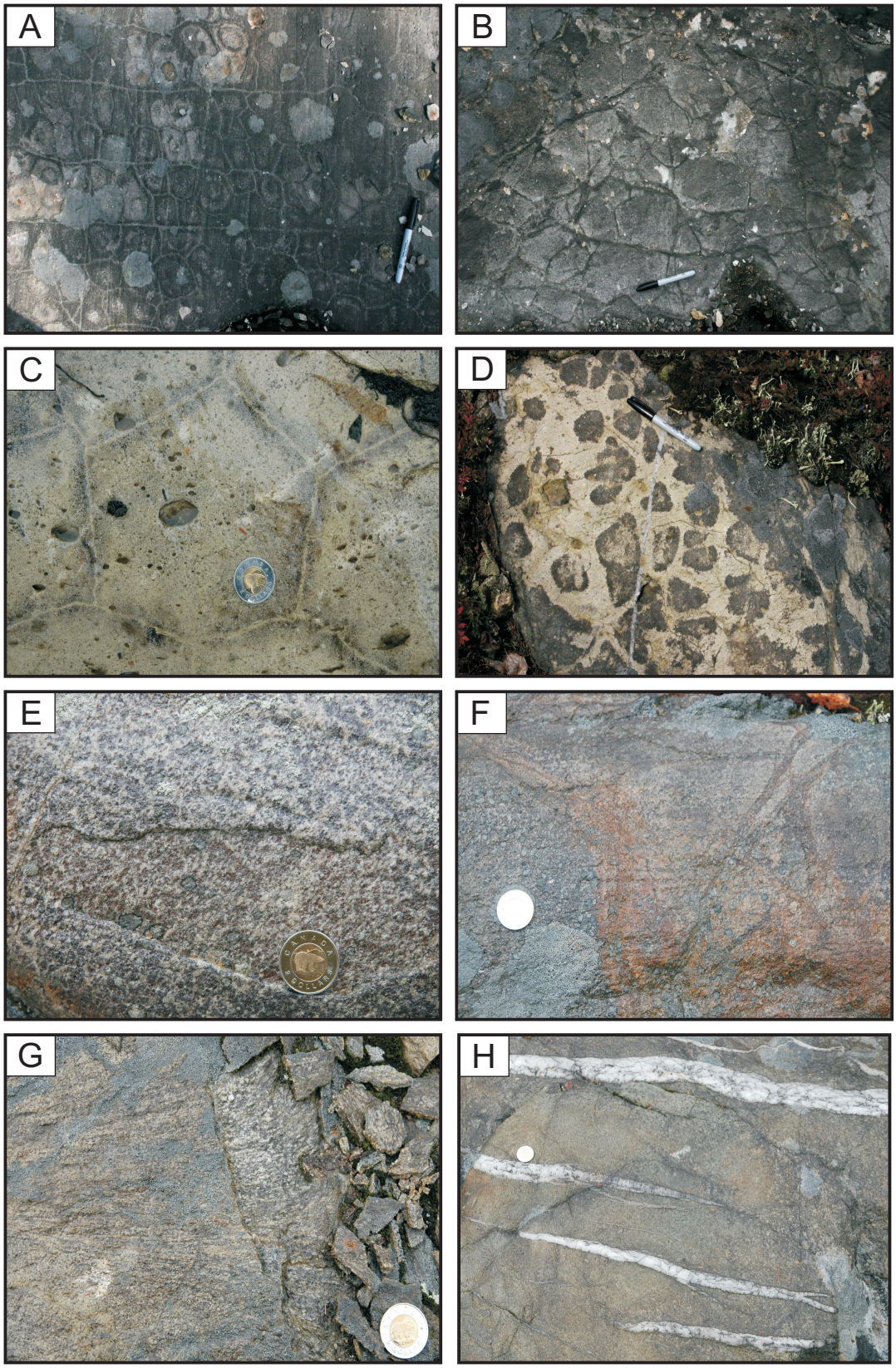

Figure 3.8. Documentation of different alteration styles at Pinkos. a) Tortoise-shell cooling fractures manifested by several parallel master joints with perpendicular internal joints. Polygons are defined by competent, siliceous alteration with positive relief; b) Poorly-developed cooling fractures are less altered, showing that footwall permeability is a major control on hydrothermal alteration and mineralization; c) Infill of amygdules and well-developed polygonal columnar joints by Fe-carbonate and sericite demonstrates early timing of fluids; d) Similar Fe-carbonate and sericite zonation of columnar joints as in (c) but with significantly less early sericite in their cores; e) Zones of spotted to pervasive carbonate occur locally and nearly replace all sericite except along joints; f) Veins of Fe-carbonate in stockwork-altered rhyolite near the top of the succession; g) Intense replacement of flow bands also occurs in coherent rhyolite at the top of the sequence; and h) Shallowly-dipping en echelon quartz veins cross-cut all earlier alteration and are interpreted as the result of extensional fracture infill associated with the d'Alembert shear, a regional deformation structure.

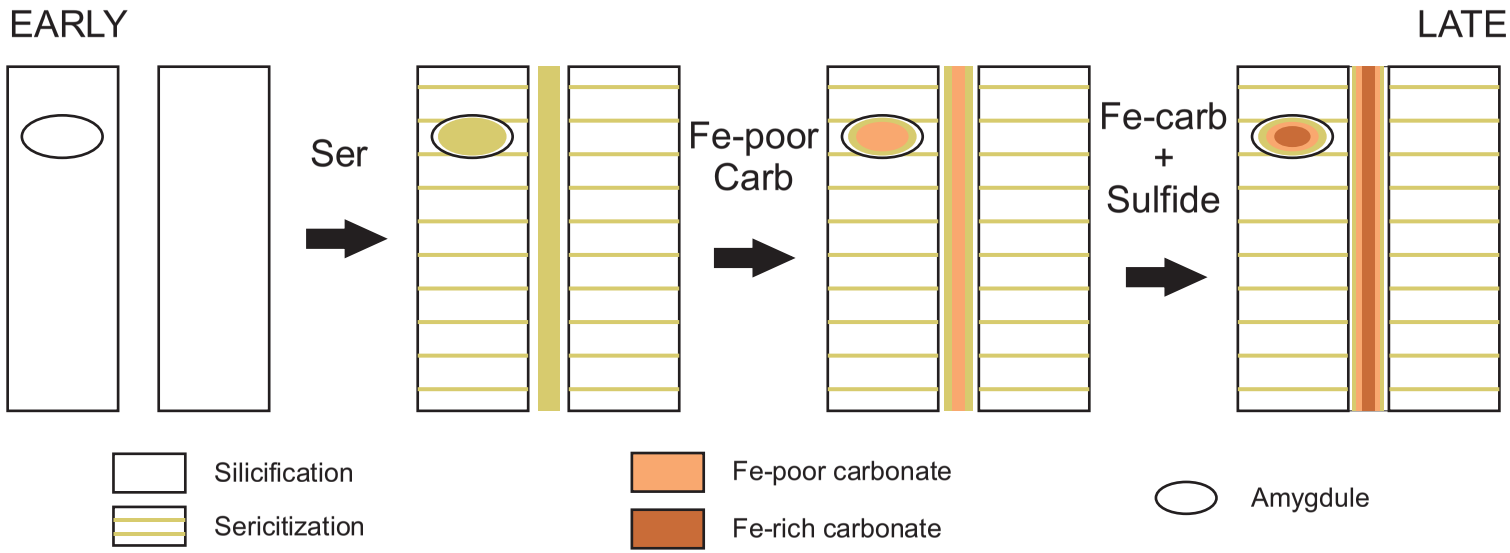

Figure 3.9. Schematic illustration of alteration adjacent to columnar joints in QP rhyolite based on relationships in outcrop and thin section. Early silicification is followed by sericitization and eventually replacement by Fe-carbonate. A clear zonation from quartz to sericite to Fe-carbonate in rims around amygdules mimics that seen in cooling fractures of columnar joints. Late stage sericite commonly fills the fractures (not shown).

4. PETROLOGY OF THE DELBRIDGE RHYOLITE

SPHERULITIC QP RHYOLITE

In the spherulitic QP rhyolite, phenocrysts are sub-spherical to cubic in shape (Figure 4.1a) and account for ~5% of the rock by volume. Ranging in size from 0.5-1.5 mm, these quartz phenocrysts are frequently deeply embayed (Figure 4.1b), which suggests rapid growth prior to the extrusion of the rhyolite lava (Barrett et al, 1993). In some samples collected within this basal unit finely crystalline quartz dendrites are observed rimming quartz phenocrysts in optical continuity, creating a sieve-like texture (Figure 4.1c). Barrett et al (1993) interpreted these overgrowths as "a quench product, in which silica in the supercooled rhyolite lava nucleated and grew as dendritic quartz crystals in crystallographic continuity with the quartz phenocrysts". Highly abundant and variably altered plagioclase spherulites range in size from 0.1-0.5 mm and define the unit (Figures 4.1d, e). Lath-shaped and tabular plagioclase crystals are noted locally and in some cases display oscillatory zoning (Figure 4.1f). Flow banding is indicated locally by the alignment of these albite-twinned crystals with interstitial quartz and chlorite (Figures 4.1g, h). Vermicular quartz and feldspar intergrowths are also observed in myrmekitic-type textures (Figure 4.1i). It is uncertain whether these textural relationships are the result of metasomatic processes.

A very weak foliation (S_1) is defined by the development of pressure shadows (growth fringes containing mainly feldspar, quartz and chlorite) and locally by the alignment of secondary muscovite within weak cleavage domains. Fractures in quartz phenocrysts are perpendicular to these micas, helping to define S_1. Minor

recrystallization textures (annealing) are also observed within quartz phenocrysts and are further evidence of the weak deformation.

HOST RHYOLITE BRECCIA

QP rhyolite clasts within the coarse breccia pile are weakly spherulitic (Figures 4.2a, b) and contain quartz phenocrysts similar to the underlying coherent unit (Figure 4.2c). Finely crystalline quartz dendrites also rim quartz phenocrysts in optical continuity to form a sieve-like texture (Figure 4.2d). Relict fine-grained (0.1-0.5 mm) spherulites are largely replaced by sericite, likely a function of greater permeability in this fragmental unit. Subhedral lath-shaped and tabular plagioclase crystals are noted locally and in some cases exhibit oscillatory zoning (Figure 4.2e). Quartz phenocrysts and grains in this unit display stronger recrystallization textures and undulose extinction than in coherent rhyolite facies. Foliation (S_1) is defined by the alignment of elongated and platy minerals within cleavage domains. Sinistral rotation noted in a few quartz porphyroclasts may indicate a weak crenulation cleavage (S_2).

The felsic lapilli tuff facies that is intermixed with the coarse breccia pile appears relatively immature as it contains poorly sorted and loosely packed sub-angular to sub-rounded grains (Figures 4.2f-h). Quartz grains are ~0.5-2 mm in size, and some are broken. Feldspar grains are roughly half the size of quartz grains, and albite-twinning indicates plagioclase composition. Spherulites are present and are largely replaced by sericite.

QP RHYOLITE LOBES

The QP rhyolite lobes that are partly intrusive into fine-grained felsic volcaniclastic rocks display variably embayed subhedral quartz phenocrysts that are roughly 1-2 mm in diameter (~5 vol.%; Figures 4.3a, b). Finer-grained (~0.25-0.5 mm) feldspathic spherulites are variably replaced by sericite (Figure 4.3c). Albite twinning indicates that the feldspar phenocrysts are of plagioclase composition. Foliation (S_1) is weakly defined by the alignment and wrapping of secondary muscovite around quartz phenocrysts, as well as the development of quartz growth fringes within pressure shadows of euhedral pyrite crystals.

HANGING-WALL MAFIC VOLCANICLASTIC ROCKS

The fine-grained mafic volcaniclastic unit that constitutes the immediate hanging wall of the ore horizon was sampled proximal to the two interpreted confining syn-volcanic faults over a strike length of ~200 m. This mafic unit is composed of volcaniclastic material with broken grains defining bedding and a lack of primary volcanic textures (Figures 4.3d, e). The mineralogy consists mainly of chlorite, plagioclase and clinopyroxene with a few relict spherulitic clasts. Though previously described in the literature as a mafic debris flow (O'Dowd, 1990; Barrett et al, 1993), at surface this unit displays moderate sorting and packing of grains in thin section. Bedding is well defined by the alignment of platy chlorite and lath-shaped to tabular albite-twinned plagioclase grains (Figure 4.3f). A weak crenulation cleavage is defined locally by chlorite wrapping around plagioclase and clinopyroxene grains.

HANGING-WALL FP AND QFP RHYOLITE

The FP rhyolite that overlies the mafic volcaniclastic unit is defined by medium to coarsely crystalline (up to 4 mm in penetration twins) albite phenocrysts (~5-10 vol.%; Figures 4.3g, h). Fine-grained spherulites are rarely identified. This coherent unit exhibits a weak foliation defined by the alignment of both muscovite and chlorite. The QFP rhyolite, which overlies the tongue of mafic volcaniclastic material to the north, contains ~5 vol.% each of quartz and albite phenocrysts that are ~1-2 mm in size (Figure 4.3i). Unlike the footwall QP rhyolite, dendritic quartz overgrowths are not observed in the hanging-wall FP and QFP rhyolite.

ALTERATION AND MINERALIZATION

A summary of the alteration mineralogy in the Delbridge rhyolite is given in Table 4.1.

Silicification

Quartz is the dominant mineral observed replacing primary material (e.g., glass) in volcanic groundmass. It is cut or overprinted by all other alteration minerals and is therefore interpreted as the earliest phase in the alteration paragenesis. Quartz is the main mineral filling amygdules and the first to rim amygdules (Figures 4.4a-e).

The most common style of silicification is patchy to pervasive microcrystalline quartz in the groundmass of coherent and fractured rhyolite (Figures 4.4f and g). This

alteration is most obvious towards the margins of the interpreted upflow in the footwall of the Delbridge ore horizon as well as in the hanging wall. In these distal zones, quartz also lines fractures as medium- to coarse-grained (~0.25-0.75 mm) subhedral crystals with sericite, Mg-chlorite, and Ca-carbonate (Figure 4.4h). Notably however, a small core zone of silicification cut by later sericite, chlorite, and carbonate also occurs in the fractured rhyolite immediately beneath the orebody. Minor quartz appears associated with sulfide mineralization in fractures here (Figure 4.4i and j).

Microcrystalline to fine-grained subhedral quartz is also abundant in the matrix of felsic volcaniclastic facies (Figures 4.4k and l). In general, quartz is more abundant in distal felsic lapilli tuff than in proximal coarse rhyolite breccia samples.

Sericite Alteration

Fine-grained muscovite is the most abundant alteration mineral at Delbridge and occurs in all of the alteration assemblages. However, it is most abundant in association with quartz (silicification), Mg-chlorite, and Ca-carbonate along the margins of interpreted hydrothermal upflow and in the hanging wall. The most intense sericitization, up to ~25-35 vol.%, is observed in rhyolite breccia and felsic lapilli tuff facies outside the main upflow zone. Coherent and fractured rhyolite contains the least abundant sericite (trace to ~15 vol.%).

The stockwork-altered QP rhyolite contains moderately abundant sericite (~10-15 vol.%) mainly as fine-grained (<0.25 mm) platy to ultrafine grains that concentrate in

fracture networks and along foliation with chlorite (Figures 4.5a, b). Fine-grained muscovite also replaces relict feldspar phenocrysts and spherulites. In coherent QP rhyolite, fine-grained muscovite is commonly disseminated, distributed along foliation, and wrapping phenocrysts (Figure 4.5c). Locally, sericite occurs in veins with quartz and Ca-rich carbonate (Figures 4.5d, e).

The coarse rhyolite breccia and felsic lapilli tuff facies contain abundant matrix-controlled sericite together with quartz and carbonate (Figures 4.5f, g). Although it is abundant in the matrix of breccias proximal to the main upflow zone (~10-20 vol.%), sericite is most abundant in distal samples where it generally accounts for ~20-30 vol.% of the rock (Figure 4.5h). These rocks commonly have the strongest cleavage development.

Volcanic rocks in the hanging wall typically contain only trace to <5 vol.% sericite, occurring mainly along fine fractures, at phenocryst grain boundaries, and in foliation planes with chlorite (Figure 4.5i). The local presence of amygdules filled with sericite, quartz, and carbonate (Figure 4.5j) suggests early synvolcanic precipitation.

Fine-grained muscovite commonly defines the weak foliation at Delbridge by wrapping around phenocrysts and grains in coherent rhyolite. Locally, sericite is developed in pressure shadows, cleavage domains and micro-shears (Figures 4.5k, l), which may suggest at least partial re-mobilization.

Chlorite Alteration

Chlorite abundance ranges from absent to minor (<5 vol.%) in altered rhyolite at Delbridge. It is most abundant in samples collected along the southern margin of the interpreted upflow zone and not in the stringer/stockwork zone immediately beneath the surface projection of the orebody. However, a distinct zonation from Mg-rich chlorite (light greenish-brown in XPL) to Fe-rich chlorite (berlin blue) in the core of the upflow zone and in proximal rhyolite breccia is evident in thin section. Minor chlorite (<5 vol.%) in the stockwork generally occurs as fine platy crystals (~0.1-0.2 mm) and finer-grained anhedral masses (up to 0.5 mm). This chlorite is dominantly fracture-controlled and associated with sulfide (± carbonate) mineralization (Figure 4.6a) and has distinctive berlin blue colours in XPL (Figure 4.6b).

The fine-grained felsic volcaniclastic rocks typically contain trace to minor disseminated chlorite in the matrix, and it is almost always associated with sulfide (Figures 4.6c, d). Chlorite is mainly absent to weakly disseminated in coarse rhyolite clasts. Mg-chlorite (greenish-brown in XPL) occurs locally in vein material with quartz and Ca-rich carbonate (Figure 4.6e).

In coherent footwall rhyolite, chlorite (~5-15 vol.%) is weakly disseminated and fracture-controlled (Figure 4.6f); disseminated chlorite crystals are small and platy (~0.1-0.2 mm), whereas fracture-controlled chlorite typically occurs as finer-grained anhedral masses (up to 0.5 mm). Locally, chlorite is also aligned within flow-banding (Figure 4.6g) or occurs in amygdules (Figure 4.6h), which suggests early (synvolcanic)

precipitation, also associated with sulfide mineralization. Chlorite in the footwall rhyolite is dominantly Mg-rich (greenish-brown in XPL), but purple and blue interference colours (Figure 4.6i) are found locally.

More intense spotted to pervasive chloritization (~10 to >30 vol.%) is restricted to the mafic volcaniclastic rocks in the immediate hanging wall of the ore horizon (Figure 4.6j). Fine- to medium-grained (~0.1-0.5 mm) chlorite in the matrix is Fe-rich (berlin blue in XPL), likely a result of the Fe-rich nature of the precursor mafic rocks. Minor Fe-rich chlorite (up to ~2-3 vol.%) is also found locally in fracture networks in the mafic rocks, where it is associated with pyrite mineralization (Figure 4.6k).

Like muscovite, remobilized chlorite commonly defines a weak foliation occurring with quartz in growth fringes and in pressure shadows along crystal edges, often in the shadow of pyrite grains (Figure 4.6l).

Scanning electron microscope (SEM) images of footwall felsic lapilli tuff and hanging-wall FP rhyolite show bladed and radial chlorite as inclusions in evidently later phase carbonate (see Chapter 8; Figure 8.8), which supports the paragenetic sequence interpreted from field mapping and transmitted/reflected light petrography.

Carbonate Alteration

Where it is abundant, carbonate occurs mainly within fractures and as disseminations in coherent rhyolite and as matrix in rhyolite breccia (Figure 4.7a). In the

interpreted hydrothermal upflow zone, carbonate abundance is ~5 to >20 vol.% as medium-grained (~0.25-0.75 mm) anhedral grains to subhedral crystals dominantly in mm- to cm-scale veins and along foliations within fractured QP rhyolite (Figure 4.7b). Carbonate in samples from the main upflow zone is Fe-rich, indicated by orange-brown turbidity common to the crystals in plane-polarized light (PPL) and high birefringence in cross-polarized light (XPL). Fe-poor carbonate occurs as fine-grained (<0.25 mm) clear and colourless to mildly turbid crystals (Figure 4.7c). Fe-rich carbonate is also observed in amygdules; however, it appears to have been precipitated mainly after quartz and muscovite, which occur as inclusions in carbonate (Figures 4.7d, e).

In proximal rhyolite breccia, matrix-controlled carbonate is patchy to pervasive (~5-20 vol.%) and occurs mainly as medium-grained (~0.25-0.75 mm) subhedral to euhedral rhombohedra with lesser fine-grained anhedral masses (Figure 4.7f). Coarse rhyolite clasts and rhyolite lobes, which are typically highly fractured, also contain abundant fracture-controlled and matrix carbonate (Figure 4.7g). Fe-rich carbonate is dominant with calcite mainly identified outside the interpreted upflow. Distal rhyolite breccia and felsic lapilli tuff appear to contain mainly Ca-rich carbonate with minor Fe-rich carbonate (~5-10 vol.%; Figure 4.7h).

Overall carbonate abundance is significantly reduced at the margins of the inferred upflow zone (<7-8 vol.%), with the QP rhyolite facies containing mainly calcite with characteristic calcite-twinning identified in XPL (Figures 4.7i, j). The calcite commonly occurs as fine-grained (<0.25 mm) disseminations of clear and colourless

rhombohedra in the groundmass. Within fractures and along foliations, medium-grained (~0.25-0.5 mm) subhedral calcite can occur with more Fe-rich carbonate (Figure 4.7k). Locally carbonate and muscovite also occur in the pressure shadows of pyrite grains (Figure 4.7l, m).

Calcite is dominant in the hanging-wall lithologies. It is patchy to pervasive in mafic volcaniclastic rocks up to ~50 m into the hanging wall where it occurs as fine- to medium-grained (~0.1-0.75 mm) subhedral grains to rhombohedra (Figure 4.7n). Fluids appear to have migrated along bedding planes in this unit. In coherent hanging-wall FP rhyolite, calcite is absent or minor and occurs mainly as fine-grained (0.1-0.25 mm) disseminations (Figure 4.7o).

A complex paragenetic relationship is observed between sulfides and Fe-carbonate in the Delbridge rhyolite. In sulfide-bearing samples close to the ore zone, Fe-rich carbonate commonly envelopes, penetrates, and overprints sulfide crystals or grains (Figures 4.8a-f). However, sulfides are nearly absent in zones of the most intensely carbonatized rocks, suggesting replacement by carbonate. Carbonate is also observed replacing sulfide locally in samples collected along the margins of the upflow zone and in the hanging wall (Figures 4.8g-j). Though pyrite and sphalerite are the most common sulfide minerals replaced by carbonate, galena and chalcopyrite are also locally overgrown and partly replaced by carbonate (Figures 4.8k and l). The progressive replacement of sulfide by carbonate can be seen in the series of photomicrographs depicted in Figures 4.8m-o. Inclusions of chlorite and sulfide identified by SEM images

in footwall felsic lapilli tuff and hanging-wall FP rhyolite (see Chapter 8; Figure 8.8) support that carbonate post-dated the earliest hydrothermal alteration. Strong etching at the surface of pyrite grains, possibly caused by CO_2-rich fluids, is also evident in SEM images (see below; Figure 4.10).

Disseminated and Stringer Sulfides

Disseminated and stringer sulfides account for <1 vol.% of the alteration of the Delbridge rhyolite. Sulfides are locally abundant with Fe-rich carbonate in the stockwork zone immediately below the ore horizon; however, an inverse relationship with carbonate abundance is evident as noted above within or proximal to the interpreted upflow zone. These rocks have significant carbonate but are notably sulfide-poor. In contrast, samples along the margins of the upflow zone contain abundant disseminated sulfide (~1-5 vol.%) and significantly less carbonate (trace to minor). Somewhat elevated sulfide abundance (~1-2 vol.%) is observed in ore-hosting rhyolite breccia where the permeability was greatest. Minor amounts of disseminated pyrite are also present in the hanging wall, mainly distributed along foliation (<2-3 vol.%).

Pyrite is the dominant sulfide phase in the altered rhyolite at surface. Very fine- to coarse-grained (~0.1-2 mm) pyrite is mainly fracture-controlled with lesser disseminations (Figures 4.9a-f). Very rare pyrrhotite occurs as inclusions in pyrite (Figure 4.9c). Larger aggregates (~0.25-1 mm) of fine-grained pyrite are also common within fine fractures and along foliation (Figure 4.9f). Sphalerite $\pm$ chalcopyrite also occur locally as inclusions. In the stockwork veins Fe-rich chlorite, Fe-rich carbonate,

and sometimes quartz are the most commonly associated gangue minerals. Fine-grained anhedral masses of chlorite tend to concentrate around sulfide grains and bladed chlorite crystals are often developed perpendicular to grain boundaries within pressure shadows. The pyrite is variably hematized and overprinted or replaced by carbonate, as noted above. Outside the stockwork zone typical gangue mineral associations include Mg-chlorite, Ca-carbonate, and sometimes quartz within vein material.

As part of a B.Sc. honours thesis, Boucher (2007) examined pyrite grains from altered rhyolite in the upflow zone. Disseminated pyrite grains were obtained by crushing and sieving the rock samples into sizes ranging from 100-150 mesh, 150-200 mesh, and greater than 250 mesh. These splits were then super-panned into sulfide separates from which representative grains were selected for SEM imaging (Figure 4.10). A sequence of representative grains shows progressive etching and pitting of the euhedral pyrite crystals, which is interpreted to reflect the progressive replacement by Fe-carbonate noted in Figure 4.9. The etching of pyrite grains is most intense in more proximal and strongly carbonate-altered zones (Figures 4.10a, b) compared to samples from outside the main upflow zone (Figure 4.10c).

Traces of sphalerite (~1-2 vol.%) are also present in the altered Delbridge rhyolite. Notably, the greatest sphalerite abundances tend to occur in more distal samples that are weakly carbonate-altered. It occurs as fine- to medium-grained (~0.1-0.4 mm) subhedral disseminations with yellow-brown internal reflections (Figure 4.11a). For the most part, sphalerite is weakly disseminated and fracture-controlled (Figure 4.11b). The

most abundant sphalerite occurs in proximal coarse rhyolite breccia and the felsic lapilli tuff facies (Figure 4.11c). No sphalerite was identified in the stratigraphic hanging wall. Sphalerite inclusions in pyrite are relatively common (Figure 4.11d) but inclusions of chalcopyrite (± pyrite) are generally restricted to larger sphalerite grains (Figure 4.11e). The most common gangue minerals associated with sphalerite include Fe-chlorite, Fe-carbonate, and sometimes quartz.

Traces of chalcopyrite (~1-2 vol.%) occur in proximal rhyolite breccia as disseminated blebs (Figure 4.11f) and as inclusions in pyrite, sphalerite, and oxides (Figure 4.11g). Trace inclusions of chalcopyrite also occur in pyrite, sphalerite, and hematite in the footwall stockwork below the ore horizon (Figure 4.11h). Fracture-controlled chalcopyrite was only rarely observed in distal coherent rhyolite (Figure 4.11i). Traces of chalcopyrite were also identified consistently throughout the hanging wall at Delbridge, including in the mafic rocks. Chalcopyrite here is mainly disseminated in coherent rock (Figure 4.11j), but also occurs in fine fractures and along foliations.

Pyrite, sphalerite, and chalcopyrite at are all variably oxidized to Fe-oxides (± hydroxides) such as hematite (Figure 4.11h) and goethite. Sulfide oxidation at Delbridge appears most intense in footwall rhyolite breccia and in hanging-wall mafic volcaniclastic rocks where stratal permeabilities are greatest.

Rare galena was identified in three samples collected in rhyolite breccia.

Oxides

Accessory rutile occurs as fine to medium (~0.1-0.5 mm) aggregates of anhedral to lath-shaped grains exhibiting white to light yellow-brown internal reflections (Figure 4.11k). Though mainly disseminated (<0.5 vol.%) in coherent rhyolite and rhyolite breccia (Figure 4.11l), wispy concentrations of fine-grained rutile were also identified along fine fractures and foliations. Rutile is most abundant (~1-2 vol.%) in the mafic volcaniclastic unit.

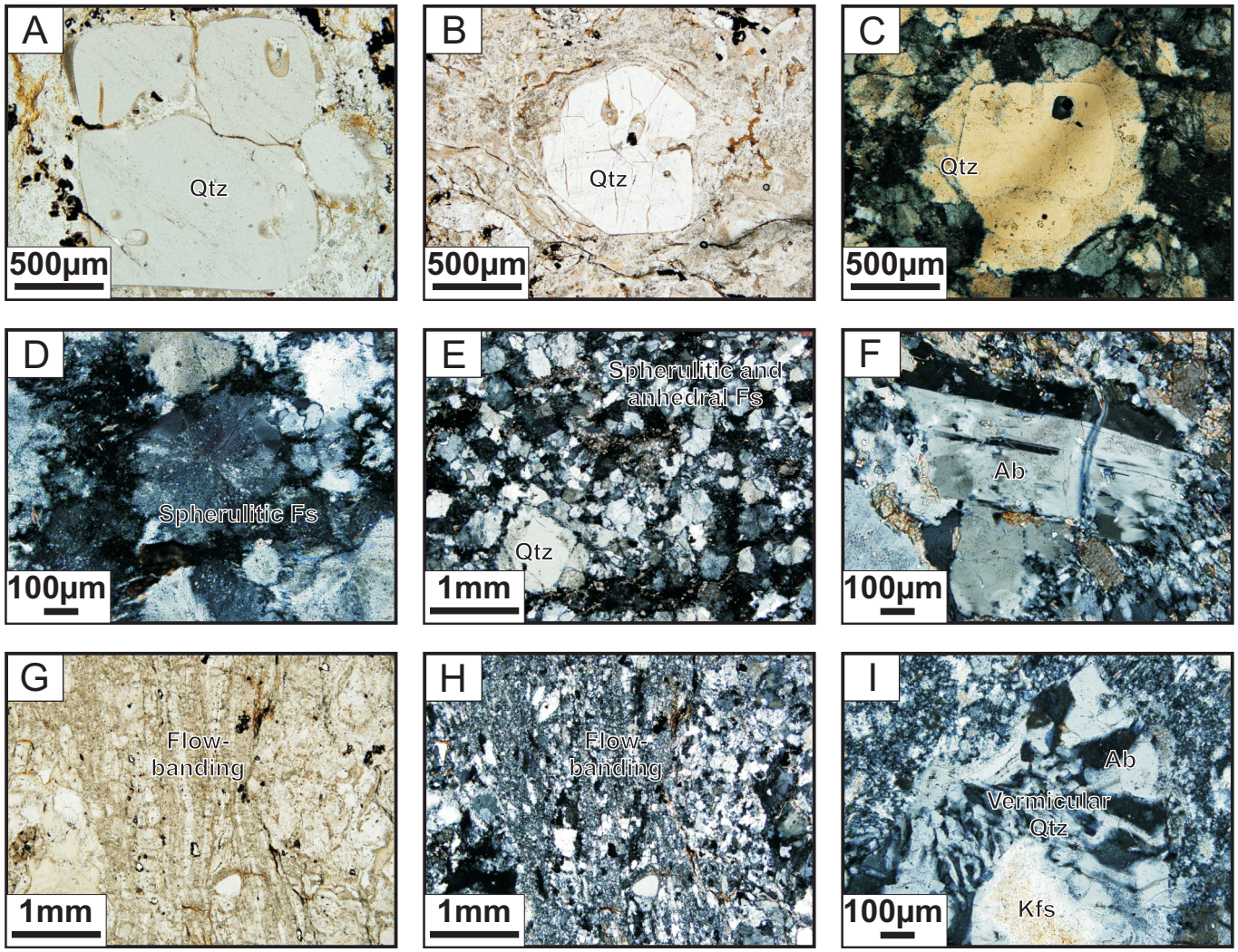

Figure 4.1. Photomicrographs of primary volcanic textures in spherulitic QP rhyolite at Delbridge. a) Sub-rounded cubic quartz phenocryst in basal spherulitic QP rhyolite (10x, PPL) - RW006; b) Quartz phenocrysts in distal coherent rhyolite are commonly deeply embayed, suggesting rapid growth (10x, PPL) - RW008; c) Finely crystalline quartz dendrites rim phenocrysts in optical continuity, creating a sieve-like texture (10x, XPL) - RW035; d) Radial extinction exhibited by spherulitic feldspar in basal coherent rhyolite (20x, XPL) - RW035; e) Highly abundant and variably altered spherulites define the basal rhyolite unit at Delbridge (5x, XPL) - RW035; f) Albite-twinned tabular plagioclase crystals are identifed locally in spherulitic QP rhyolite (20x, XPL) - RW006; g) Flow-banding is defined locally by the alignment of primary quartz and feldspar with interstitial quartz and chlorite alteration (5x, PPL) - RW010; h) Same as (g), except shown in XPL (5x) - RW010; i) Vermicular quartz and feldspar are intergrown in myrmekitic-type textures (20x, XPL) - RW034.

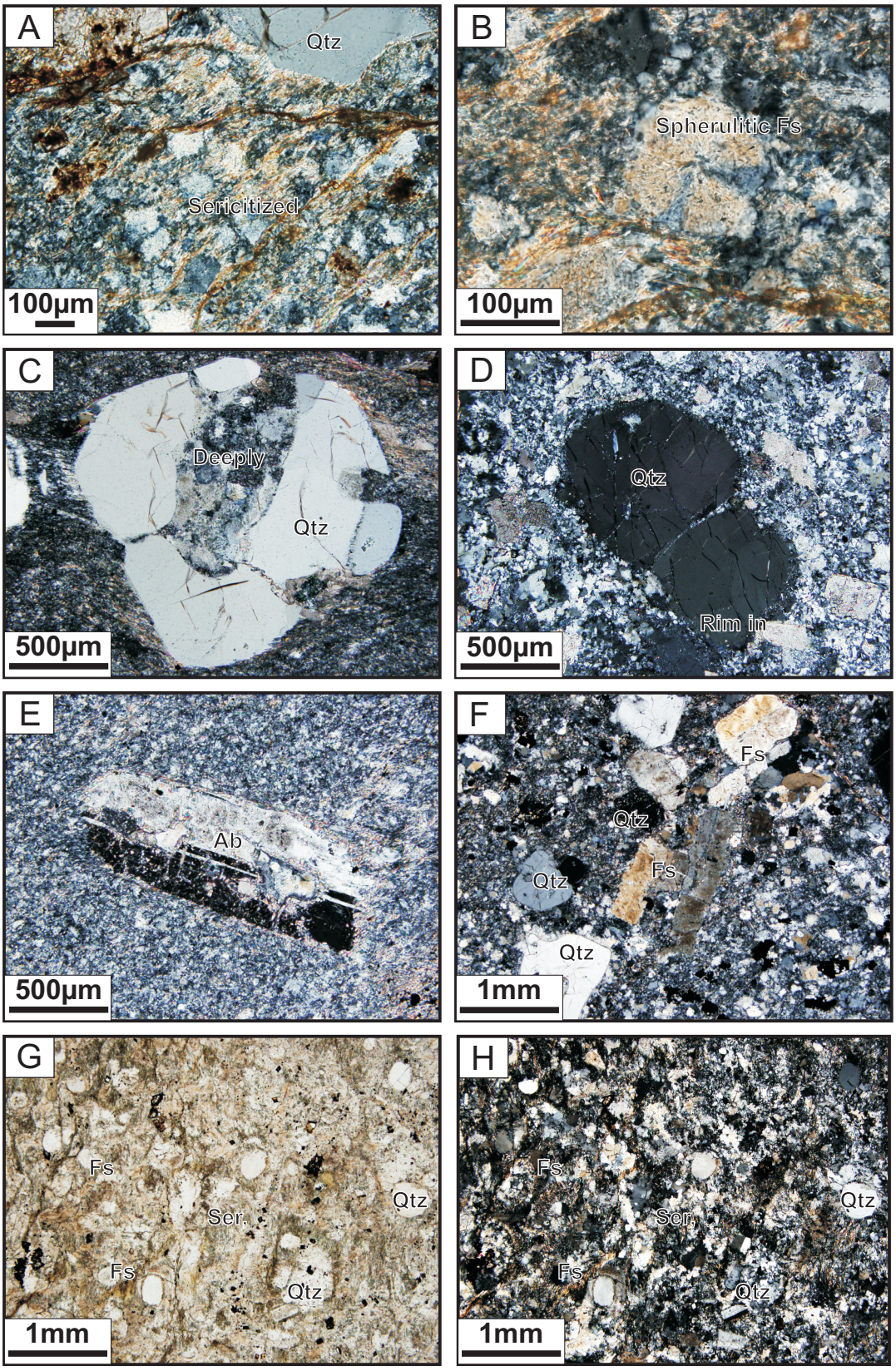

Figure 4.2. Photomicrographs of primary volcanic textures in host rhyolite breccia and felsic lapilli tuff facies at Delbridge. a) Weakly abundant spherulitic feldspar is commonly replaced by sericite in rhyolite breccia clasts (20x, XPL) - RW037; b) Close-up of spherulite showing sweeping radial extinction in coarse rhyolite breccia clast (50x, XPL) - RW037; c) Variably embayed quartz phenocrysts in rhyolite breccia clasts are similar to the underlying coherent rhyolite unit (10x, XPL) - RW011; d) Finely crystalline quartz dendrites rim phenocrysts in optical continuity, creating a sieve-like texture (10x, XPL) - RW014; e) Albite-twinned plagioclase crystals are identified locally in rhyolite clasts (10x, XPL) - RW011; f) Distal felsic lapilli tuff is relatively immature with poorly sorted and loosely packed sub-angular to sub-rounded quartz and feldspar grains (5x, XPL) - RW004; g) Poorly sorted and loosely packed rounded to sub-rounded quartz grains with interstitial matrix-controlled quartz-sericite-chlorite (5x, PPL) - RW033; h) Same as (g), except shown in XPL (5x) - RW033.

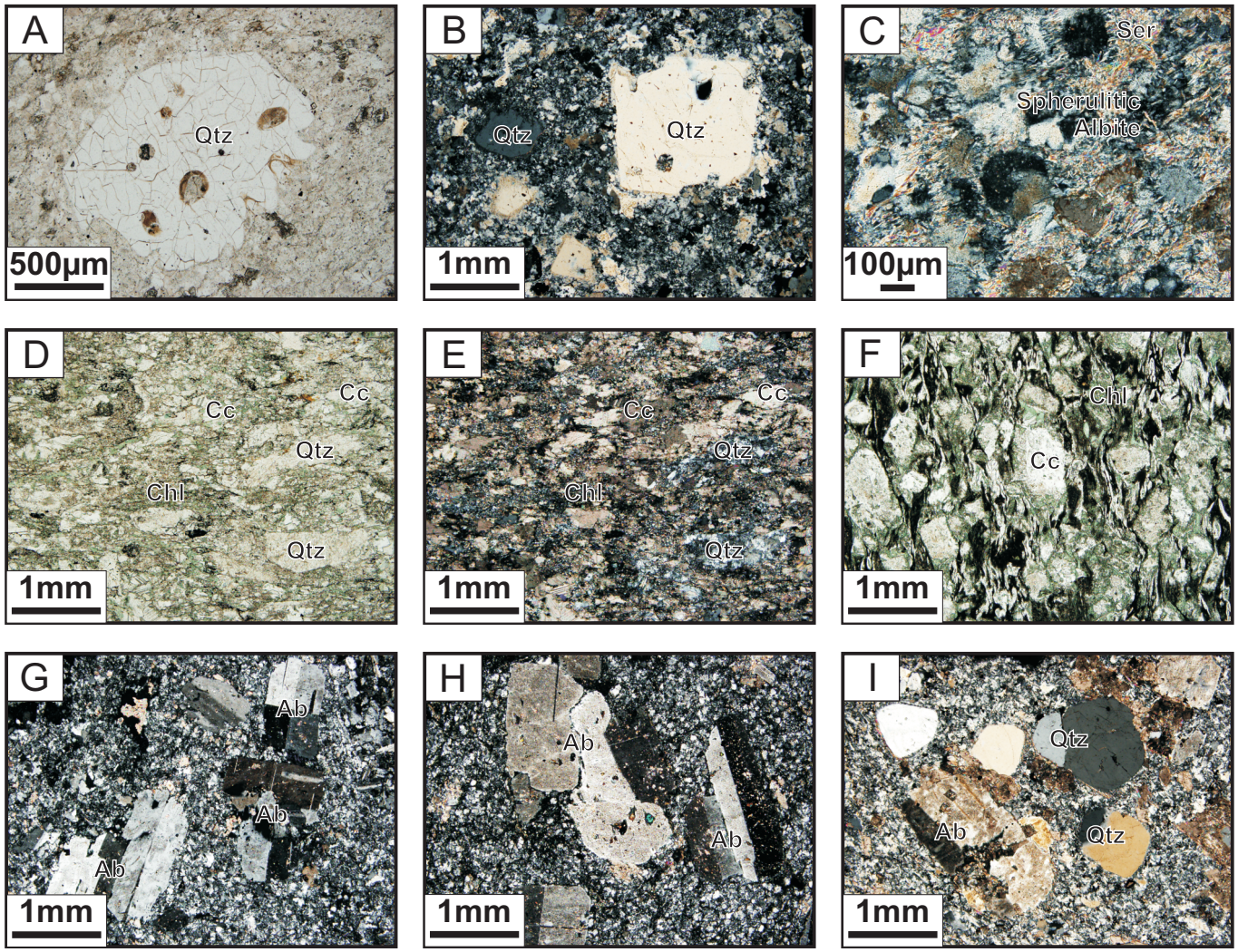

Figure 4.3. Photomicrographs of primary volcanic textures in QP rhyolite lobes, mafic volcaniclastic rocks, and FP and QFP rhyolite at Delbridge. a) Subhedral isometric quartz phenocrysts are variably embayed in lobate QP rhyolite (10x, PPL) - RW001; b) Subhedral cubic to sub-rounded quartz phenocrysts are rimmed by dendritic quartz in optical continuity in lobate QP rhyolite (5x, XPL) - RW140; c) Fine-grained spherulitic feldspar is variably replaced by sericite in lobate QP rhyolite (20x, XPL) - RW002; d) Primary pyroxene and plagioclase mineralogy is intensely replaced by chlorite and Ca-rich carbonate in hanging-wall mafic volcaniclastic rocks. Alignment of tabular and elongate grains indicates moderately defined bedding (5x, PPL) - RW015; e) Same as in (d), but shown in XPL (5x) - RW015; f) Bedding in mafic volcaniclastic rocks is often well-defined by the alignment of more elongate grains and a weak crenulation cleavage is denoted by platy chlorite wrapping phenocrysts (5x, PPL) - RW022; g) Medium- to coarse-grained tabular albite phenocrysts are commonly identified as penetration twins in hanging-wall FP rhyolite (5x, XPL) - RW018; h) Coarse-grained tabular albite phenocrysts are the defining characteristic of hanging-wall FP rhyolite (5x, XPL) - RW021; i) Subhedral tabular albite and subrounded quartz phenocrysts are equally abundant and evenly distributed in hanging-wall QFP rhyolite (5x, XPL) - RW133.

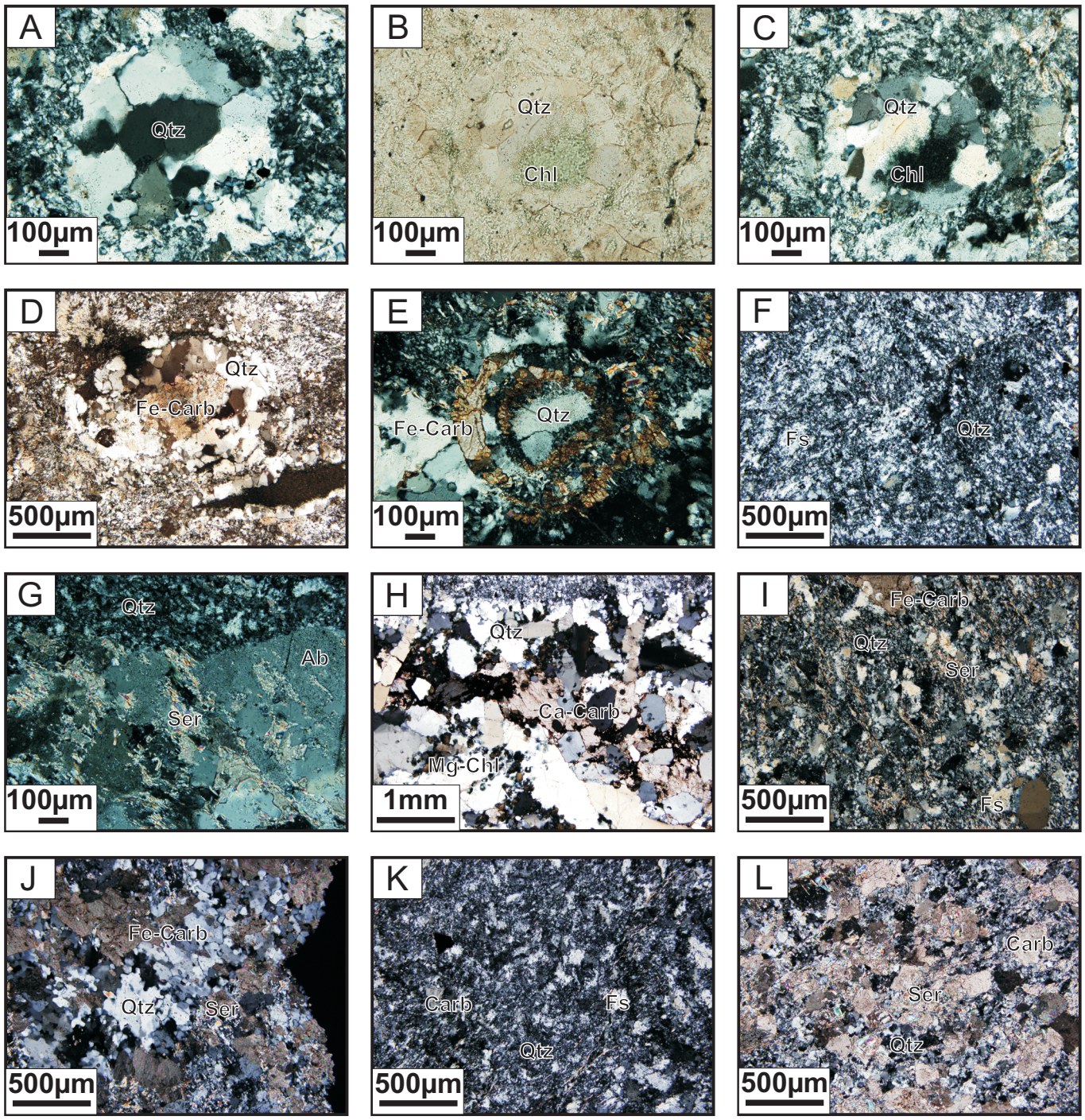

Figure 4.4. Photomicrographs of hydrothermal quartz textures at Delbridge. a) Amygdaloidal quartz in stockwork-altered rhyolite (20x, XPL) - RW140; b) Amygdaloidal quartz with later chlorite in distal coherent rhyolite (20x, PPL) - RW027; c) Same as (b), but in XPL (20x) - RW027; d) Amygdaloidal quartz with later carbonate in distal coherent rhyolite (10x, XPL) - RW027; e) Amygdule filled with zoned quartz and carbonate in distal rhyolite (20x, XPL) - RW006; f) Pervasive quartz replacement of groundmass in distal coherent rhyolite (10x, XPL) - RW034; g) Intense quartz replacement of groundmass in hanging-wall rhyolite (20x, XPL) - RW020; h) Quartz vein (mm-scale) containing minor Mg-chlorite and Ca-carbonate (5x, XPL) - RW032; i) Significant early quartz cross-cut by sericite and carbonate in silicified pod-like core immediately beneath mineralization (10x, XPL) - RW038; j) Quartz-carbonate vein containing minor sericite and sulfide (10x, XPL) - RW038; k) Pervasive matrix-controlled quartz in distal felsic lapilli tuff facies (10x, XPL) - RW032; l) Weak matrix-controlled quartz in proximal coarse rhyolite breccia (10x, XPL) - RW003.

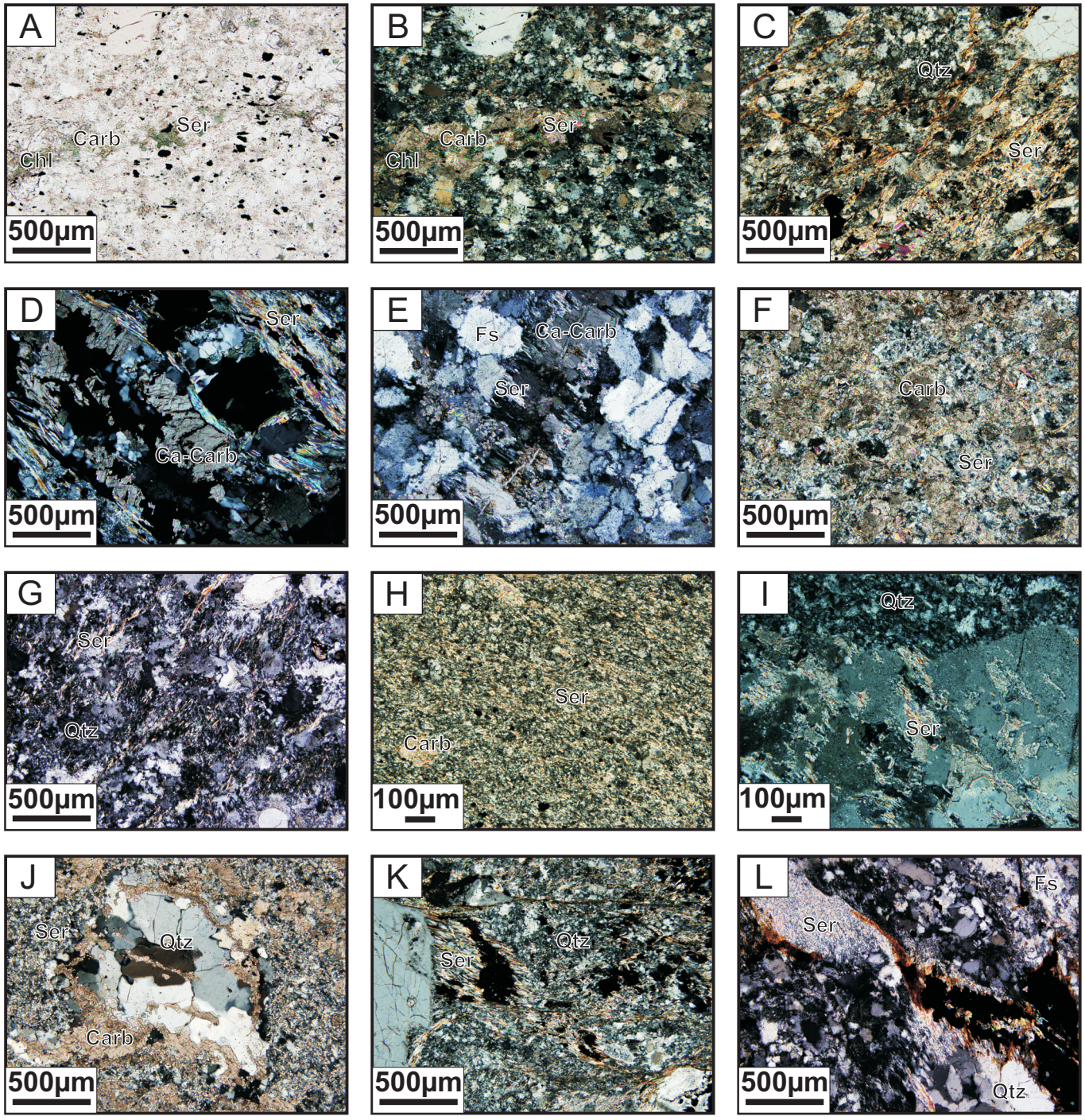

Figure 4.5. Photomicrographs of hydrothermal muscovite at Delbridge. a) Fracture-controlled fine-grained sericite with chlorite and carbonate in stockwork-altered QP rhyolite (10x, PPL) - RW042; b) Same as (a), but shown in XPL (10x) - RW042; c) Moderate sericite in distal coherent rhyolite is disseminated, distributed along foliation and wrapping primary material (10x, XPL) - RW001; d) Quartz vein (mm-scale) containing well-developed medium-grained sericite with Ca-carbonate (± sulfide) in distal rhyolite (10x, XPL) - RW008; e) Fracture-controlled sericite with chlorite and filamentous carbonate in distal rhyolite (10x, XPL) - RW035; f) Highly abundant fine-grained sericite is matrix-controlled with Fe-carbonate and quartz in proximal rhyolite breccia (10x, XPL) - RW003; g) Matrix-controlled sericite and quartz are dominant alteration minerals in distal felsic lapilli tuff (10x, XPL) - RW033; h) Pervasive matrix-controlled sericite (clay fraction) with minor carbonate identified locally in distal felsic volcaniclastic rocks (20x, XPL) - RW011; i) Weak sericite in the hanging-wall occurs mainly along foliation and in fine fractures (20x, XPL) - RW020; j) Amygdaloidal sericite with quartz and carbonate in hanging-wall QFP rhyolite (10x, XPL) - RW134; k) Development of cleavage domain in pressure shadow of quartz phenocryst suggests early sericite precipitation and subsequent re-mobilization (10x, XPL - RW013; l) Sericitic cleavage domains again suggest early emplacement and subsequent re-mobilization (10x, XPL) - RW010.

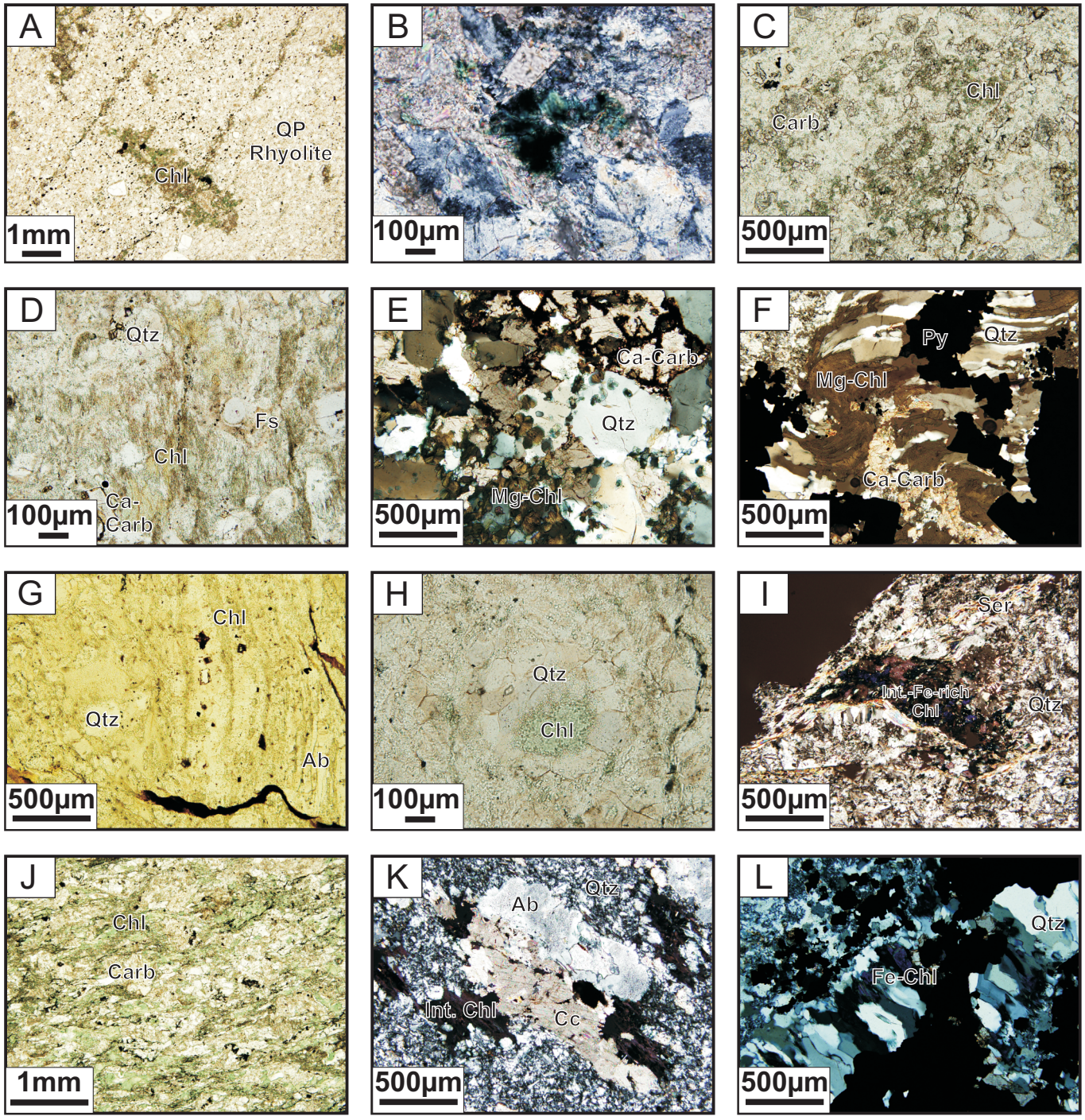

Figure 4.6. Photomicrographs of hydrothermal chlorite at Delbridge. a) Chlorite in the altered stockwork zone is dominantly fracture-controlled, weakly disseminated, and associated with sulfide (± carbonate) (2.5x PPL - RW042; b) Chlorite speciation in stockwork-altered rhyolite is dominantly intermediate to Fe-rich (20x, XPL) - RW041; c) Proximal rhyolite breccia contains minor matrix-controlled chlorite with sericite and carbonate (10x, PPL) - RW003; d) Distal felsic lapilli tuff contains trace matrix chlorite mixed with sericite, quartz, and Ca-carbonate (20x, PPL) - RW033; e) Quartz vein containing fine-grained anhedral Mg-chlorite and Ca-carbonate in distal felsic volcaniclastic rocks (10x, XPL) - RW032; f) Fracture-controlled Mg-chlorite associated with quartz and sulfide (± carbonate) in distal coherent footwall rhyolite. Strained chlorite and quartz crystals evidence precipitation prior to deformation (10x, XPL) - RW008; g) Chlorite is distributed along flow-banding locally in basal QP rhyolite, suggesting syn-volcanic precipitation (10x, PPL) - RW010; h) Chlorite filling amygdule after earlier quartz rim in footwall rhyolite, which further suggests syn-volcanic timing for these alteration fluids (20x, PPL) - RW027; i) Purple and blue interference colours indicate the presence of at least some intermediate to Fe-rich chlorite in distal zones (10x, XPL) - RW026; j) Spotted to pervasive chlorite occurs locally in haning-wall mafic volcaniclastic rocks (5x, PPL) - RW016; k) Notably, intermediate to Fe-rich chlorite also occurs higher in the stratigraphic hanging-wall in FP rhyolite and associated with sulfide (± carbonate) (10x, XPL) - RW020; l) Fe-chlorite occurs as a growth fringe along pyrite grain boundary in pressure shadow, supporting re-mobilization (10x, XPL) - RW006.

Figure 4.7. Photomicrographs of hydrothermal carbonate at Delbridge. a) Abundant fracture-controlled Fe-carbonate in stockwork-altered QP rhyolite (2.5x, PPL) - RW038; b) Medium-grained subhedral Fe-carbonate occurs with quartz and sericite (± sulfide) in stringer veins (10x, XPL) - RW038; c) Fe-carbonate is also paired with minor Ca-rich to intermediate members in stockwork rhyolite (10x, XPL) - RW140; d) Fe-carbonate filling an amygdule after quartz in footwall rhyolite (10x, XPL) - RW039; e) Fe-carbonate in minor amygdules indicates syn-volcanic precipitation at Delbridge (10x, XPL) - RW042; f) Matrix-controlled Fe-carbonate is spotted to pervasive in proximal coarse rhyolite breccia (10x, PPL) - RW003; g) Fracture- and matrix-controlled carbonate in coarse rhyolite clasts is dominantly Fe-rich (10x, PPL) - RW014; h) Gradation towards more Ca-rich and intermediate carbonate in distal felsic lapilli tuff (10x, PPL) - RW004; i) Ample calcite-twinning identified in distal coherent rhyolite indicates Ca-rich carbonate members are dominant (5x, PPL) - RW008; j) Medium-grained subhedral calcite (twinning) identified in quartz vein in distal fine-grained felsic volcaniclastic rocks (5x, XPL) - RW032; k) Mixed Fe- and Ca-rich carbonate occurs in fine fractures in distal lobate footwall rhyolite (5x, PPL) - RW001; l) Interesting filamentous carbonate extending outward from fine fractures in basal and distal coherent rhyolite (10x, XPL) - RW035; m) Filamentous carbonate developed along relict twinned pyrite grain boundaries in basal rhyolite breccia (10x, XPL) - RW007; n) Spotted to pervasive carbonate in mafic volcaniclastic rocks of the immediate hanging wall exhibits abundant twinning and turbidity, suggesting Ca- to Mg-rich members (20x, XPL) - RW015; o) Weak carbonate deep into hanging-wall FP rhyolite is clearly Ca-rich and mainly disseminated (20x, XPL) - RW020.

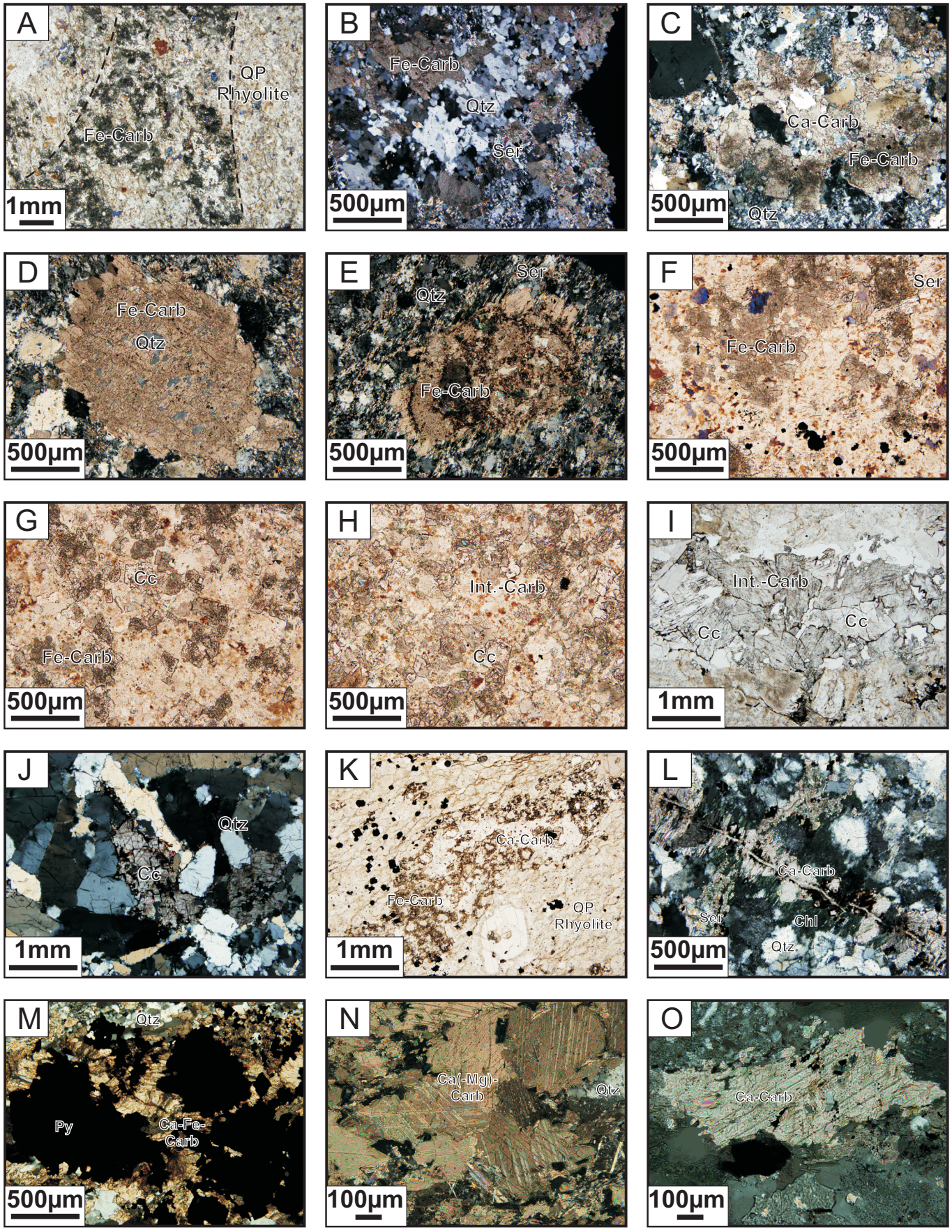
A
QP
Rhyolite
Fe-Carb
1mm
B
Fe-Carb
Qtz
Ser
500µm
C
Ca-Carb
Fe-Carb
500µm
Qtz
D
Fe-Carb
Qtz
500µm
E
Ser
Qtz
Fe-Carb
500µm
F
Ser
Fe-Carb
500µm
G
Cc
Fe-Carb
500µm
H
Int.-Carb
Cc
500µm
I
Int.-Carb
Cc
Cc
1mm
J
Qtz
Cc
1mm
K
Ca-Carb
Fe-Carb
QP
Rhyolite
1mm
L
Ca-Carb
Ser
Chl
Qtz
500µm
M
Qtz
Py
Ca-Fe-
Carb
500µm
N
Ca(-Mg)-
Carb
Qtz
100µm
O
Ca-Carb
100µm

Figure 4.8. Photomicrographs of hydrothermal carbonate-sulfide replacement textures at Delbridge. a) Fe-carbonate clearly cross-cutting and overprinting pyrite grains in stockwork rhyolite (10x, XPL/RL) - RW039; b) Fe-carbonate surrounding and penetrating pyrite grains in same stringer zone (20x, XPL/RL) - RW042; c) Nanoscopic sphalerite aggregate is completely enveloped and partially replaced by carbonate in distal rhyolite breccia (20x, XPL) - RW011; d) Same as in (c), but shown in RL (20x) - RW011; e) Subhedral sphalerite and pyrite appear partially replaced by Fe-carbonate in proximal lobate rhyolite (20x, XPL) - RW140; f) Same as in (e), except shown in RL (20x) - RW140; g) Ca-rich to intermediate carbonate surrounding and overprinting apparently etched pyrite grains in distal zones. Growth fringes may indicate re-crystallization (10x, XPL) - RW007; h) Ca-rich to intermediate carbonate clearly cross-cutting and replacing anhedral pyrite in distal coherent rhyolite (20x, XPL) - RW031; i) Ca-rich carbonate appears closely linked to pyrite grain boundary irregularities (cf. quartz; 10x, XPL) - RW006; j) Calcite (twinning) cross-cuts and replaces fracture-controlled pyrite even in the hanging-wall (10x, XPL) - RW020; k) Ca-rich to intermediate carbonate envelops, penetrates, and replaces blebby galena locally in basal footwall (20x, XPL/RL) - RW007; l) Anhedral chalcopyrite bleb surrounded and overprinted by Ca-rich to intermediate carbonate in distal footwall breccia (20x, XPL) - RW037; m) Anhedral pyrite appears strongly etched and replaced by Fe-carbonate in footwall QP rhyolite (20x, XPL/RL) - SB025; n) Subhedral pyrite completely surrounded and partially replaced by Fe-carbonate in QP rhyolite (20x, XPL/RL) - SB057; o) Anhedral pyrite surrounded, intruded, and included in Fe-carbonate (20x, XPL/RL) - SB069.

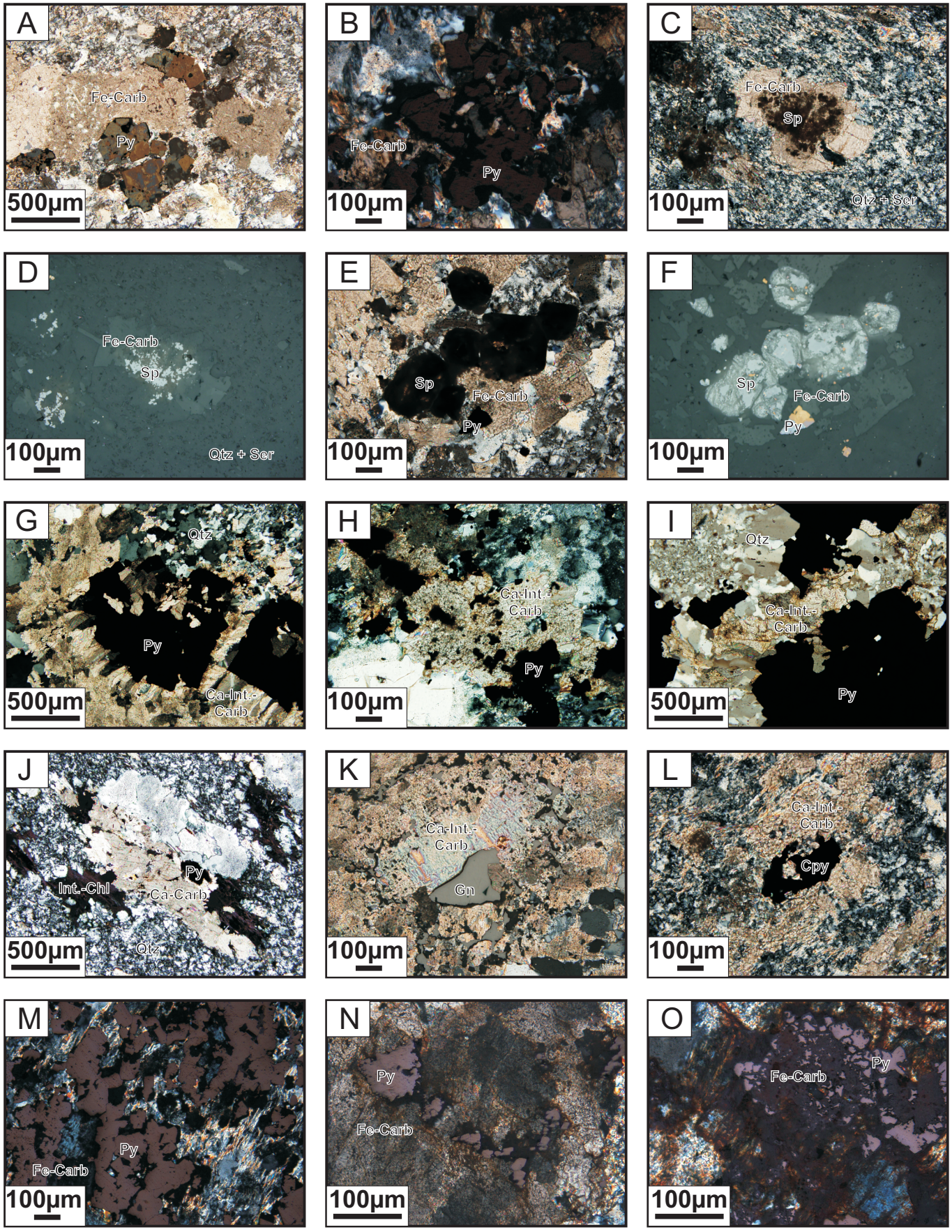
A
Fe-Carb
Py
500µm
B
Fe-Carb
Py
100µm
C
Fe-Carb
Sp
Qtz + Ser
100µm
D
Fe-Carb
Sp
Qtz + Ser
100µm
E
Sp
Fe-Carb
Py
100µm
F
Sp
Fe-Carb
Py
100µm
G
Qtz
Py
Ca-Int.-Carb
500µm
H
Ca-Int.-Carb
Py
100µm
I
Qtz
Ca-Int.-Carb
Py
500µm
J
Py
Int.-Chl
Ca-Carb
Qtz
500µm
K
Ca-Int.-Carb
Gn
100µm
L
Ca-Int.-Carb
Cpy
100µm
M
Py
Fe-Carb
100µm
N
Py
Fe-Carb
100µm
O
Fe-Carb
Py
100µm

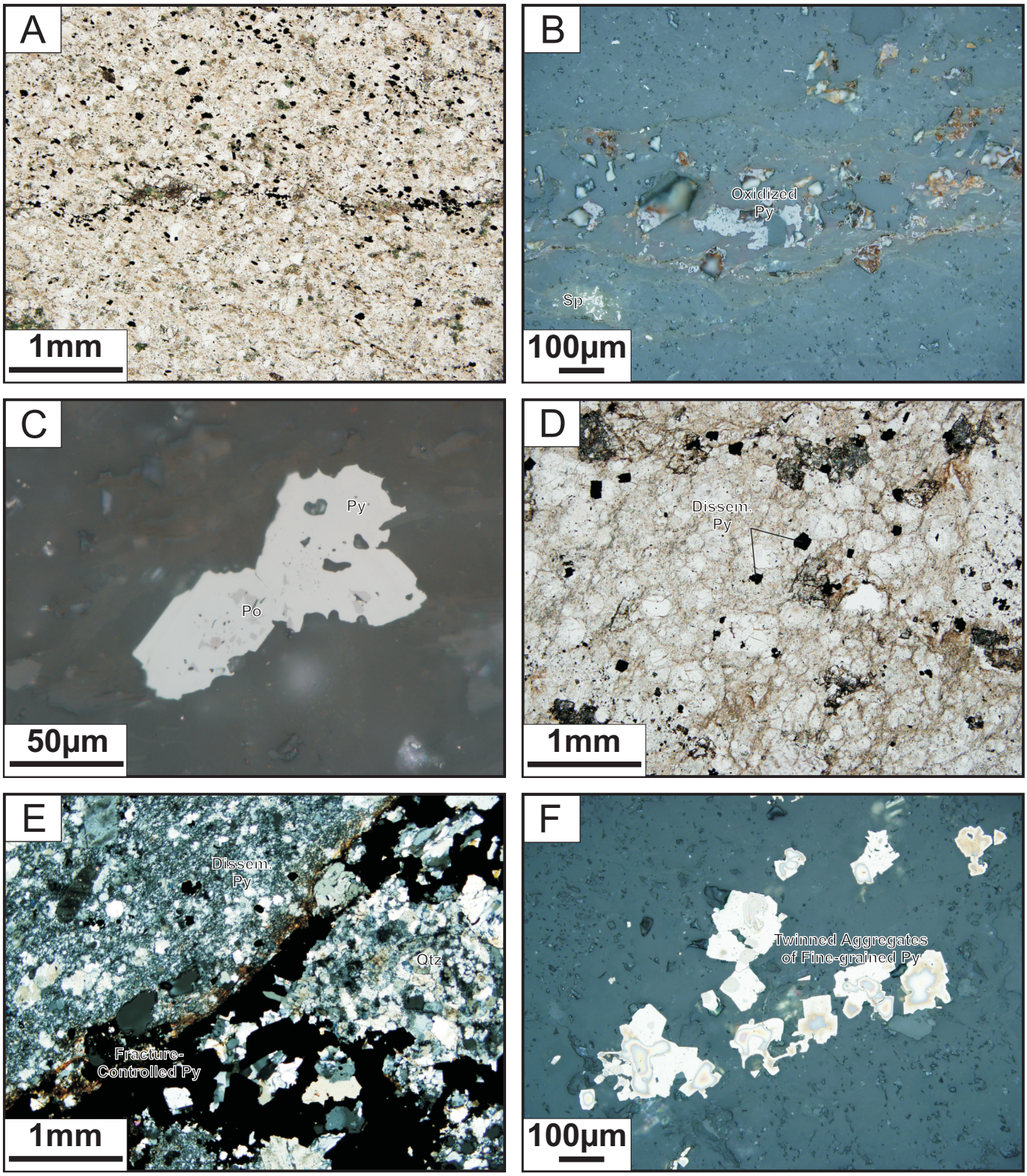

Figure 4.9. Photomicrographs of disseminated and fracture-controlled pyrite in altered wallrock at Delbridge. a) Fracture-controlled and disseminated fine-grained pyrite appears strongly associated with chlorite in stockwork (5x, PPL) - RW042; b) Pyrite (oxidized) and sphalerite are the dominant sulfide minerals in stringers and stockwork (20x, RL) - RW143; c) Pyrrhotite inclusions in pyrite occur locally in fractured rhyolite immediately beneath mineralization (100x, RL) - RW042; d) Matrix-controlled anhedral pyrite grains are mainly disseminated in coarse rhyolite breccia (5x, PPL) - RW003; e) Pyrite is both disseminated and fracture-controlled in distal felsic lapilli tuff facies (5x, XPL) - RW004; f) Larger aggregates of twinned fine-grained pyrite are also identified in fractures in distal footwall rhyolite (20x, RL) - RW036.

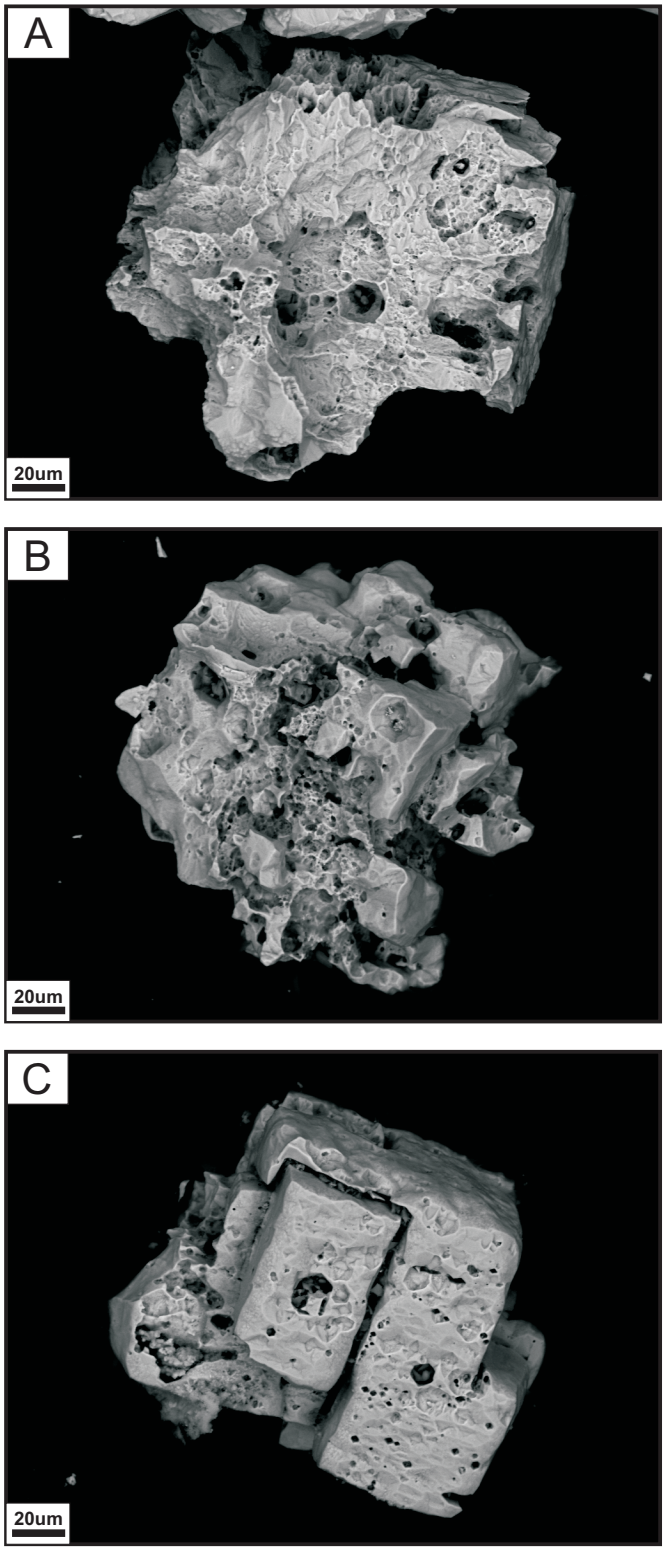

Figure 4.10. Back-scattered secondary electron (BSE) images of selected pyrite grains from sulfide-rich samples collected at Delbridge taken with an EVO Zeiss scanning electron microprobe (SEM) instrument at the Geological Survey of Canada. The EVO Zeiss microscope has a 20 kV accelerating voltage and 500 pA beam current. Grain surfaces appear etched, possibly by a combination of CO_2-rich fluids and microbial activity. Degree of etching appears greater in more proximal and strongly carbonatized zones (a, b) relative to distal samples (c) containing weakly abundant carbonate. Euhedral rhombic represent etching on the (100) and (110) crystal surfaces and triangular pits occur on the (111) surface. a) SB011; b) SB020; c) SB028.

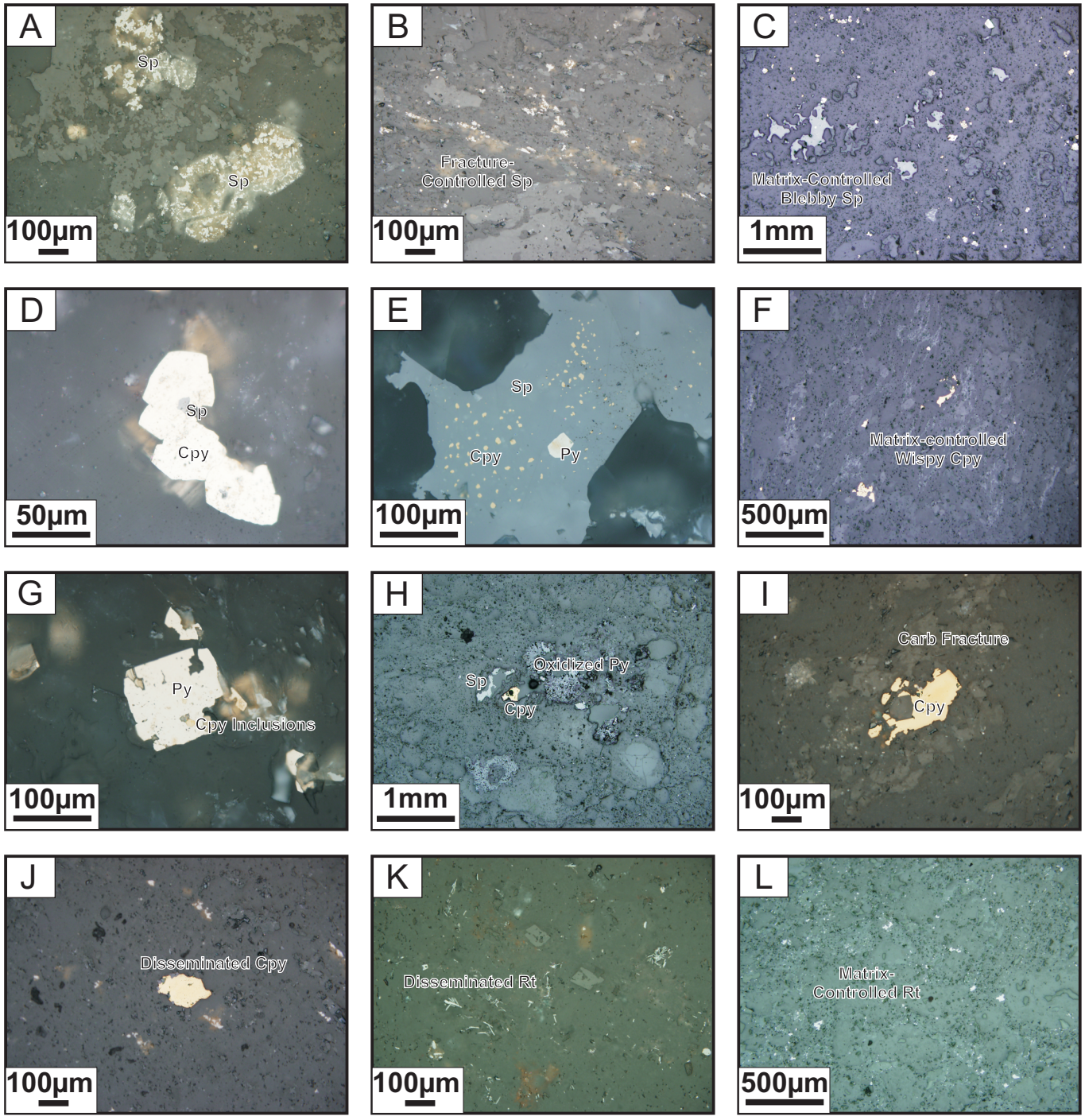

Figure 4.11. Photomicrographs of other disseminated sulfides in altered rhyolite at Delbridge. a) Sphalerite at Delbridge commonly occurs as fine- to medium-grained subhedral rhombic masses of nanoscopic grains exhibiting yellow-brown internal reflections (20x, RL) - RW034; b) Trace micron-sized grains of anhedral sphalerite is primarily disseminated and lines fine fractures locally in distal coherent rhyolite (20x, RL) - RW036; c) Relatively abundant fine- to medium-grained anhedral sphalerite in proximal rhyolite breccia and distal felsic lapilli tuff (5x, RL) - RW005; d) Sphalerite inclusion identified in pyrite in rhyolite breccia (100x, RL) - RW005; e) Chalcopyrite and pyrite inclusions generally restricted to larger anhedral sphalerite grains (50x, RL) - RW005; f) Minor fine-grained anhedral blebs of chalcopyrite is matrix-controlled in proximal coarse rhyolite breccia (10x, RL) - RW141; g) Chalcopyrite inclusions in euhedral pyrite grain (50x, RL) - RW005; h) Trace chalcopyrite with pyrite and sphalerite in stockwork-altered rhyolite (5x, PPL) - RW142; i) Rare anhedral chalcopyrite identified in carbonate-rich fracture in distal coherent rhyolite (20x, RL) - RW037; j) Fine-grained blebby to subhedral chalcopyrite in hanging-wall rhyolite is typically disseminated (20x, RL) - RW019; k) Fine- to medium-grained aggregates of anhedral to lath-shaped rutile exhibit white to light yellow-brown internal reflections (20x, RL) - RW133; l) Abundant matrix-controlled rutile in hanging-wall mafic volcaniclastic rocks (10x, RL) - RW017.

Table 4.1. Abundance* of alteration minerals in different units of the Delbridge property

Alteration Facies	Phenocrysts/ Components	Abundances (vol.%) and Alteration Styles				
		Quartz	**Sericite**	**Chlorite**	**Carbonate**	**Sulfide**
Stringers and Stockwork	5% Qtz phenocrysts; 15-25% Fs	40-55% Fractures, amygdules, groundmass	10-15% Fractures, disseminated	<5% *Fe-rich* Fractures, amygdules, disseminated	5-20% *Fe-rich to Int.* Fractures, amygdules, disseminated	Typically <1% *Py, Sp (± Cpy)* Fractures, disseminated
Distal Coherent QP Rhyolite	5% Qtz phenocrysts; 20-30% Fs	50-60% Groundmass, fractures/veins	15-25% Disseminated, foliation, (± veins)	5-15% *Mg-rich to Int. (± Fe)* Fractures, disseminated (± flow-bands, amygdules)	<7-8% *Ca-rich to Int. (± Fe)* Disseminated, fractures/foliation	Tr.-5% *Py, Sp (± Cpy, Gn)* Disseminated, fractures (± foliation)
Proximal Rhyolite Breccia	20-30% volcaniclastic fragments	35-60% Matrix, fractures/ groundmass (clasts)	10-20% Matrix, fractures/ disseminated (clasts)	Abs.-5% *Indiscernible* Matrix, disseminated (clasts)	5-20% *Fe-rich to Int.* Matrix, fractures/ disseminated (clasts)	1-2% *Py, Sp, Cpy* Matrix, fractures/ dissem. (clasts)
Distal Felsic Lapilli Tuff	10-20% volcaniclastic fragments	40-65% Matrix, veinlets (locally)	20-30% Matrix, foliation	Abs.-10% *Mg-rich* Matrix, foliation, veinlets (locally)	5-10% *Ca-rich to Int.* Matrix, veinlets (locally)	2-5% *Py, Sp (± Cpy)* Matrix, fractures (locally)
H-W Mafic Volcaniclastic Rocks	25-60% Fs, Px	Tr.-10% Disseminated	Abs.-5% Disseminated, foliation	10-30% *Fe-rich* Matrix, foliation	10-25% *Ca(±Mg)-rich* Matrix, fractures (clasts)	Absent to 2-3% *Py (± Cpy)* Disseminated (± foliation)
H-W FP and QFP Rhyolite	0-5% Qtz and 5-10% Fs phenocrysts; 30-40% Fs	25-40% Groundmass, fractures, (± amygdules)	Typically <5% Disseminated, foliation, (± amygdules)	<5% *Int. to Fe-rich* Fractures, foliation	FP <5%; QFP 10-15% *Ca-rich* Disseminated, (± fractures, amygdules)	Abs.-Tr. *Py (+ Cpy)* Disseminated, (± foliation)

* Based on petrography.

5. PETROLOGY OF THE PINKOS RHYOLITE

CYPRUS RHYOLITE

Petrographic observations support the field interpretation of a thick and relatively homogeneous rhyolite succession occurring at Pinkos. The three distinct facies that are easily discriminated in the field have consistent textural characteristics and phenocryst distributions suggesting a single magmatic precursor for all of the mapped rhyolitic rocks.

Coherent Rhyolite

Highly spherulitic and dominantly quartz-porphyritic rhyolite in the basal portions of the stratigraphy mapped at Pinkos is massive to flow-banded. Quartz phenocrysts (~5 vol.%) are subrounded to subangular with cubic to hexagonal habits, range in size from ~0.5 to 2 mm, and are sometimes deeply embayed (Figure 5.1a). Similar to Delbridge, finely crystalline quartz dendrites commonly rim and overgrow phenocrysts in optical continuity, producing sieve-like textures (Figure 5.1b). Weakly abundant lath-shaped to tabular albite phenocrysts are generally ~1-2 mm in size (Figure 5.1c) and their alignment causes flow banding locally. Fine- to medium-grained (~0.1-0.5 mm) subspherical to spherulitic primary feldspar appears mainly albitic (only up to ~5 vol.% K-feldspar) and constitutes a significant portion of the groundmass (~15-25 vol.%) with quartz (Figure 5.1d). Primary porosity in the form of amygdules (~0.5-1 mm) is trace to minor (<5 vol.%) in this part of the map area (Figure 5.1e). Vermicular quartz and feldspar intergrowths are also observed in myrmekitic-type textures (Figure 5.1f).

In this basal coherent facies, a weak foliation (S_1) is defined by the alignment and wrapping of micas and clays around phenocrysts and amygdules. Recrystallization textures (annealing) and fractures perpendicular to the interpreted foliation in phenocrysts and quartz-filled amygdules are sometimes observed. Very weakly developed crenulations (S_2) occur locally within phyllosilicate-rich cleavage domains.

Fractured Rhyolite

Increased primary porosity is a defining characteristic of the fractured rhyolite facies that dominates the central portion of the Pinkos study area. This porosity includes abundant (~5-10 vol.%) and large (~1-3 mm) amygdules (Figures 5.2a, b) and a variety of fine mm-scale cooling fractures (Figures 5.2c, d). The two off-set zones of discordant stockwork alteration occur in highly fractured to brecciated rhyolite with abundant mm-scale fracture networks (Figures 5.2e, f) contributing to increased early porosity (up to 10 vol.%). Phenocryst types, abundance, and distribution in fractured rhyolite are identical to underlying and distal coherent facies (Figures 5.2g, h). Spherulites appear less prominent at the micro scale, possibly due to increased alteration as a result of greater permeability for transport of mineralizing fluids (Figures 5.2i, j). This facies also commonly contains relatively minor (~5-10 vol.%) fine- to medium-grained (0.1-0.5 mm) anhedral K-feldspar and rare coarse (1-2 mm) tabular sanidine (Figure 5.2k). Myrmekite (Figures 5.2l) and flow banding are identified locally in fractured rhyolite.

Fragmental Rhyolite

Fragmental rhyolite occurs at the top of the Pinkos stratigraphy and is

characterized by extreme alteration; the majority of primary minerals have been replaced and their textures destroyed. Distant from the main upflow zone, samples are less fragmented and altered and indicate a protolith of quartz-porphyritic rhyolite (Figure 5.3a), likely identical to the two underlying rhyolite facies based on phenocryst types and distribution (Figures 5.3b, c) and textural similarities (i.e., presence of myrmekite ± spherulites). Porosity is dominated by large (~2-4 mm), subspherical to elliptical amygdules (~10-15 vol.%) and concentrations of complex fracture networks, possibly indicating in situ fragmentation. Feldspar abundance is highly variable in the fragmental rhyolite (~10-40 vol.%); they occur as fine- to medium-grained (~0.1-0.5 mm) anhedral and coarse (~1-3 mm) tabular crystals (Figure 5.3d). The greatest amounts of K-feldspar (~10-15 vol.%) are identified in this facies. The most intensely altered samples clearly show separation into anastomosing domains of different mineralogy. The matrix consists of very fine-grained (<0.1 mm) to clay-sized fractions of sericite with lesser microcrystalline subspherical quartz (Figure 5.3e). Fragments comprise dominantly fracture-controlled and amygdaloidal quartz-sericite-carbonate alteration with variable quantities of primary quartz and feldspar (Figures 5.3f, g). The complex nature of the fracture networks and inherent alteration obscures the identification of structure in the fragmental rhyolite.

INTRUSIVE MAFIC ROCKS

Located in the central part of the map area, the intrusive mafic rocks at Pinkos are characterized by medium-grained (~0.5 mm) pyroxene interstitial to coarser (~1 mm) plagioclase laths. Parallel extinction in cross-polarized light indicates that the pyroxene

is orthorhombic. Aphyric textures are identified locally in the north. It is difficult to identify primary mineralogy and textures due to pervasive alteration (Figures 5.3h, i). Silicification is relatively weak (~10-20 vol.%) in the mafic intrusive rocks and occurs as disseminated fine (<0.2 mm) to microcrystalline quartz grains. Weak sericite alteration (<5 vol.%) occurs as disseminations and along foliation (Figure 5.5l). Spotty to pervasive chloritization (~25-40 vol.%) only occurs locally in mafic intrusive rocks (Figure 5.6l) in the central part of the map area. Purple and blue anisotropies indicate intermediate to Fe-rich compositions for this fine- to medium-grained (~0.1-0.5 mm) chlorite, likely a result of the ferromagnesian character of the host rocks. Similar to Delbridge, carbonate is highly abundant (~5-20 vol.%) in mafic rocks at Pinkos. Compositional variation is similar to the surrounding felsic stratigraphy with intermediate carbonate dominant in proximal samples and Ca-rich to intermediate members more distally (Figures 5.7n, o). Relatively abundant sulfide (~1-5 vol.%) is consistently observed in mafic intrusive rocks as uniformly disseminated and variably oxidized fine-grained pyrite with trace to minor sphalerite and chalcopyrite locally (Figures 5.12j-l). The unit is predominantly massive to weakly foliated (S_1). Kink bands in larger micas within phyllosilicate-rich domains may indicate a weak crenulation cleavage (S_2).

ALTERATION AND MINERALIZATION

A summary of the alteration mineralogy in the Cyprus rhyolite is provided in Table 5.1.

Silicification

Silicification is the earliest hydrothermal alteration in the paragenetic sequence because it is cut, overprinted, and rimmed by all other alteration minerals. Silicification is most obvious in a discontinuous zone surrounding the interpreted core of hydrothermal upflow towards the margins of the map area. Unlike at Delbridge, silicification is the least intense in the two off-set stockwork zones and there is no silicified pod-like core beneath known mineralization. However, quartz (<5 vol.%) does occur locally in fine fracture networks within stockwork-altered rhyolite (Figure 5.4g).

In coherent rhyolite, quartz is dominantly subspherical and microcrystalline, replacing glass and spherulites in volcanic groundmass (Figures 5.4a, b). Fine- to medium-grained (~0.1-0.25 mm) anhedral quartz commonly fills and rims amygdules in columnar-jointed rhyolite and in the stockwork (Figures 5.4c, d) together with sericite, carbonate, and sometimes chlorite and sulfide. Annealed textures in this quartz are not uncommon, suggesting recrystallization during later deformation. Quartz is also observed rimming preserved primary textures such as phenocrysts and spherulites. Fracture-controlled subhedral quartz (~0.25-0.75 mm) is primarily observed in marginal rhyolite facies (Figures 5.4e, f) together with sericite, Mg-chlorite, and Ca-carbonate.

In fragmental rhyolite at the top of the succession, hydrothermal quartz occurs mainly in fractures and amygdules of rhyolitic fragments (Figures 5.4h, i) as fine-to medium-grained subhedral crystals with sericite and carbonate ($\pm$ chlorite, sulfide). Microcrystalline quartz is also a minor matrix constituent with abundant sericite (Figure 5.4j).

Sericite Alteration

All rhyolitic rocks at Pinkos are intensely sericitized with modal abundances from ~5 to 40 vol.%. In coherent and fractured rhyolite, sericite alteration is typically only dominant (~15-30 vol.%) in distal samples collected along the interpreted margins of the system. Stockwork-altered rhyolite in the core of hydrothermal upflow and in columnar-jointed rhyolite contain slightly less sericite (~10-20 vol.%). The most intense sericite alteration (~20-40 vol.%) is observed in fragmental rhyolite near the mineralized horizon.

In coherent and fractured facies, sericite is clay-sized to fine-grained (<0.25 mm) and occurs mainly within fine fracture networks (Figures 5.5a, b), along foliation planes (Figure 5.5c), and filling amygdules (Figures 5.5d, e). Cooling fractures in columnar-jointed rhyolite are commonly lined by sericite, which also occurs in the adjacent rhyolite (Figure 5.2c). Sericite is associated with Fe-chlorite and Fe-carbonate in stockwork veins and in columnar-jointed rhyolite (Figure 5.5f) and with quartz, Mg-chlorite, and Ca-carbonate in distal coherent rhyolite. Disseminated sericite has replaced relict feldspar phenocrysts and spherulites in coherent rhyolite (Figure 5.5g), often forming pseudomorphs. Sericite is the most common alteration mineral rimming quartz in amygdules and where quartz replaces spherulites and phenocrysts, suggesting that sericitization post-dates or was contemporaneous with early silicification. SEM images indicate that sericite is closely associated with and immediately succeeds quartz in the paragenetic sequence (see Chapter 8; Figure 8.16). However, sericite also overprints Fe-rich chlorite and carbonate locally (Figures 5.5h, i), which indicates a later stage of

sericitization. Late sericite overprinting carbonate in cooling fractures of columnar-jointed rhyolite supports this interpretation. Sericite occurring along foliation, within stress fractures, and as growth fringes may reflect remobilization during later deformation.

In fragmental rhyolite, sericite alteration is typically spotty to pervasive. It is the primary matrix constituent with lesser quartz (Figure 5.5j). Fracture-controlled and amygdaloidal sericite also occur in the intensely altered rhyolite fragments (Figure 5.5k).

Chlorite Alteration

Chlorite is generally less abundant at Pinkos than at Delbridge. The greatest chlorite abundances (~10-25 vol.%) occur in the two off-set stockwork zones of interpreted hydrothermal upflow.

In stockwork-altered rhyolite, abundant chlorite is dominantly fracture-controlled and appears strongly associated with weak sulfide mineralization (Figures 5.6a, b). Chlorite less commonly rims and fills (Figure 5.6c) or replaces (Figure 5.6d) primary volcanic structures (i.e., amygdules, spherulites, and phenocrysts). The chlorite is generally fine-grained (~0.1-0.2 mm) platy crystals and finer-grained anhedral masses (up to 0.5 mm). Mg-rich and Fe-rich chlorite members are present based on distinctive green-brown and berlin blue anisotropies in XPL, respectively. Purple anisotropic colours indicate that intermediate chlorite is also present. Chlorite in the stringer zone located to the northwest appears to be a mixture of Mg-rich and intermediate

compositions, whereas the stockwork to the southeast contains dominantly intermediate to Fe-rich chlorite.

In columnar-jointed rhyolite, chlorite is typically absent or occurs in fine fracture networks and as disseminations (~1-2 vol.%; Figure 5.6e). Mineralogical zonation from quartz to sericite to chlorite (± sulfide) is observed in amygdules (Figure 5.6f), indicating chlorite followed quartz and sericite in the paragenetic sequence. SEM images confirm this zonation in amygdules and chloritic inclusions in later phase carbonate support the interpreted paragenetic history (see Chapter 8; Figure 8.16). Locally, chlorite is overprinted by a second stage of sericite. Columnar-jointed rhyolite immediately beneath mineralized fragmental rocks contains Fe-rich chlorite, whereas more distal samples of the same facies have apparently Mg-rich to intermediate chlorite compositions. In fragmental rhyolite, Fe-chlorite occurs locally as disseminations and filling amygdules (Figures 5.6g, h) mainly in rhyolite fragments (± matrix).

Distal coherent rhyolite generally contains trace Mg-chlorite that is disseminated (Figure 5.6i), fills amygdules (Figures 5.6j, k), and is distributed along foliation.

Fine-grained (~0.1-0.2 mm) anhedral to platy chlorite is identified locally along foliation, in stress fractures, and as growth fringes, suggesting remobilization during subsequent deformation/metamorphism.

Carbonate Alteration

Carbonate is most abundant (up to ~10 vol.%) in columnar-jointed rhyolite and in the overlying fragmental rhyolite. There is also an apparent marked zonation from proximal brown Fe-rich carbonate to distal calcite.

Significant carbonate alteration (~5-10 vol.%) is mainly observed in diffuse selvages along fine cooling fracture networks in columnar-jointed rhyolite (Figure 5.2d), filling and rimming amygdules (Figure 5.7a), and sometimes within larger mm-scale veinlets (Figure 5.7b). Spotted to pervasive carbonate is identified locally and replaces nearly all sericite except along cooling fractures and amygdule rims (Figure 5.7c). Filling of cooling fractures and amygdules suggests a syn-volcanic timing for carbonate precipitation. Notably, these conspicuous zones of carbonate flank stringer and stockwork alteration to the north and south and both occur immediately beneath fragmental rhyolite at the mineralized horizon. In these zones carbonate is medium-grained (~0.25-0.75 mm), anhedral to subhedral, and closely associated with sulfide mineralization. Coarser (~0.5-1.5 mm) subhedral to euhedral rhombs are commonly identified in larger (~2-3 mm) amygdules. Fe-rich carbonate is identified in thin section by its dark orange-brown turbidity in PPL and high birefringence in XPL. Fine-grained (<0.25 mm) Ca-rich carbonate is also identified as clear and colourless, subhedral to euhedral rhombs, commonly with twinning in XPL.

The most abundant carbonate in both coherent and fragmental rhyolite is observed rimming and filling amygdules (Figure 5.7d), fine fractures (Figure 5.7e), and veinlets (Figure 5.7f). Mineralogical zonation from quartz to sericite to chlorite ($\pm$ sulfide) to

carbonate within and rimming amygdules indicates carbonate alteration post-dated quartz, sericite, and chlorite (± sulfide). SEM images confirm this zonation (see Chapter 8; Figure 8.16) and support the interpreted paragenetic sequence. Carbonate is also overprinted by a later sericite phase (Figure 5.7m) as noted above. Trace carbonate is also disseminated in the quartz-sericite matrix locally (Figure 5.7g). Again, carbonate is almost always associated with sulfide.

Carbonate is less abundant in the chlorite-rich stockwork zones (< 1 vol.% as disseminations; Figure 5.7h). Minor (<5 vol.%) carbonate is observed where chlorite is less abundant. In these zones, fine- to coarse-grained (~0.2-1 mm) subhedral carbonate is commonly fracture-controlled (Figure 5.7i) and amygdaloidal (Figure 5.7j) and strongly associated with sulfide. The stringer zone to the southeast, immediately beneath fragmental rhyolite, contains abundant brown Fe-rich carbonate, whereas the stringer zone to the northwest contains dominantly Ca-rich carbonate.

Samples of distal coherent rhyolite collected at the margins of the interpreted upflow contain trace to minor (<5 vol.%) carbonate that is mainly Ca-rich, fine-grained (<0.25 mm), and disseminated (Figure 5.7k). Fracture-controlled carbonate is only identified locally with quartz, sericite, and chlorite (Figure 5.7l). Locally carbonate also occurs as growth fringes within pressure shadows and stress fractures indicating remobilization during deformation.

Although carbonate is commonly associated with sulfide in thin section, Fe-rich

carbonate typically envelopes, penetrates, and overprints sulfide grains (Figures 5.8a-c), suggesting replacement similar to that observed at Delbridge. Carbonate pseudomorphs are commonly observed in relict sulfide structures (Figure 5.8d). Ca-rich carbonate also replaces and cross-cuts sulfide locally in distal coherent rhyolite (Figures 5.8e-h) along the margins of the interpreted upflow zone. Pyrite grains are mainly anhedral to subhedral where they are surrounded and penetrated by carbonate (Figures 5.8i-m). Chalcopyrite, sphalerite, and rare galena also appear to be locally replaced (Figures 5.8n, o).

Epidote and Albite

Trace to minor (~1-2 vol.%) disseminated fine-grained (~0.1-0.2 mm) epidote is observed in fragmental rhyolite (Figure 5.9a) and locally in underlying columnar-jointed rhyolite (Figure 5.9b) and intrusive mafic rocks (Figure 5.9c). Locally patchy albite alteration occurs as medium-grained (~0.25-0.5 mm) irregular to amoeboidal anhedral crystals that cross-cut and overprint carbonate (Figure 5.9d), possibly related to metamorphism.

Disseminated and Stringer Sulfides

Sulfide abundance in altered rhyolite at Pinkos is generally low (<1 vol.%). As observed at Delbridge, the abundance of disseminated sulfide is inversely related to carbonate alteration. Samples within or proximal to the interpreted upflow have <1 vol.% sulfide but significant carbonate (~5-10 vol.%). Sulfide is somewhat more abundant (~1-5 vol.%) in carbonate-poor samples collected in more distal rhyolite and

again in the fragmental rhyolite at the ore horizon.

In the stringers and stockwork, fine- to medium-grained (<0.5 mm) anhedral pyrite occurs in veins, fractures and amygdules (Figures 5.10a, b). Chalcopyrite and sphalerite occur with pyrite in the southeast stockwork zone beneath fragmental rhyolite (Figures 5.10c, d). These sulfides are associated with Fe-rich chlorite and carbonate (Figure 5.10e). Sphalerite also occurs as fine-grained anhedral masses lining fine fractures and amygdules and as inclusions in pyrite in the northwest stockwork (Figures 5.10f-h). Here, the sphalerite is associated with Mg-chlorite, Ca-carbonate, sericite, and quartz.

In proximal columnar-jointed rhyolite, trace to minor (<3 vol.%) fine-grained (<0.2 mm) and anhedral to subhedral pyrite-sphalerite (± chalcopyrite) mineralization is disseminated, lines fine fractures, and rims amygdules (Figures 5.11a-c). Larger pyrite grains (~0.5 mm) and anhedral masses of sphalerite are identified in amygdules and recrystallized veinlets (Figures 5.11d-f). Trace chalcopyrite occurs as inclusions in both pyrite and sphalerite locally. Rare fine-grained and blebby galena is also observed. These sulfides are associated with Fe-rich carbonate (± chlorite) and lesser quartz-sericite in the columnar-jointed rhyolite.

In distal coherent rhyolite, fine-grained (<0.2 mm) pyrite is subhedral to euhedral and mainly disseminated (± amygdaloidal; Figures 5.11g, h). Sphalerite and chalcopyrite occur locally with pyrite in amygdules and as inclusions (Figures 5.11i-l). Sulfide is

associated with quartz, sericite, Mg-chlorite, and Ca-rich carbonate in these zones of weakly altered rhyolite.

At the mineralized horizon, pyrite and sphalerite (± rare chalcopyrite, galena) occur mainly in fine fractures (Figures 5.12a-c) and amygdules (Figures 5.12d-f) of rhyolitic fragments and in matrix (Figures 5.12g-i). Associated alteration here includes sericite, intermediate to Fe-rich carbonate, and lesser quartz.

Pyrite, sphalerite, and chalcopyrite are all variably oxidized to Fe-oxides (± hydroxides) such as hematite and goethite (Figures 5.14e, f). Sulfide oxidation appears most intense in fragmental rhyolite where stratal permeability is greatest at Pinkos.

Selected pyrite grains from a subset of sulfide-rich samples at Pinkos were examined by Boucher (2007). Figure 5.13 provides SEM images of three representative pyrite grains from the Pinkos sample set. The abundance, size, morphology, and complexity of etch pits appears highly variable between the three grains. The etching of pyrite grains is most intense in more proximal and strongly carbonatized zones (Figures 5.13a, b) compared to samples distal to the interpreted upflow zone (Figure 5.13c), further suggesting a paragenetic sequence of carbonate replacing sulfide at Pinkos. Larger pits (~10-20 μm) and euhedral inverted triangular pits occur rarely. Smaller (~2 μm), irregularly-shaped pits are clearly the most abundant and reflect complex etching patterns.

Oxides

Fine- to medium-grained (~0.1-0.5 mm) anhedral rutile displaying white to light yellow-brown internal reflections is commonly disseminated (Figure 5.14a) at Pinkos with wispy aggregates lining fine fractures and foliation (Figures 5.14b-d). Felsic volcanic rocks typically contain trace rutile (absent to ~0.1 vol.%), but the uppermost fragmental and fractured rhyolite facies appear to be slightly enriched (up to ~0.5 vol.%). The greatest rutile abundances (~2-3 vol.%) occur in mafic intrusive rocks.

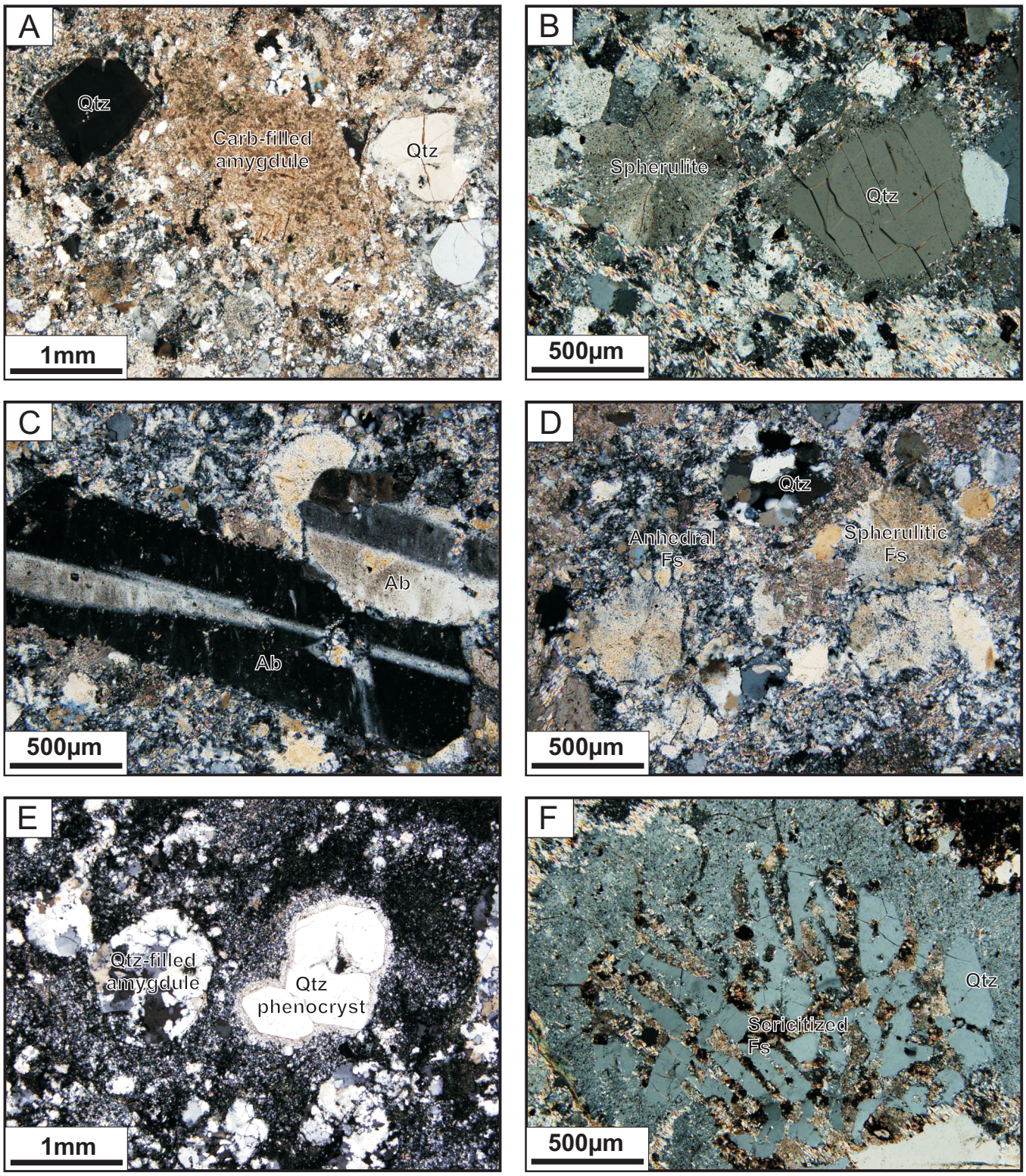

Figure 5.1. Photomicrographs of primary volcanic in basal and distal coherent QP rhyolite at Pinkos. a) Dendritic quartz rims in optical continuity with quartz phenocrysts and amygdaloidal carbonate (5x, XPL) - RW059; b) Quartz phenocryst with optically continuous quartz rim and spherulitic feldspar showing radial extinction (10x, PPL) - RW074; c) Coarse-grained tabular albite phenocrysts locally with typical fine-grained anhedral and spherulitic feldspar (10x, XPL) - RW059; d) Variably altered anhedral and spherulitic primary feldspar with re-crystallized quartz-filled amygdule (10x, XPL) - RW059; e) Quartz-filled amygdules and twinned quartz phenocrysts (5x, XPL) - RW073; f) Altered feldspar and vermicular quartz in myrmekitic texture (10x, XPL) - RW074.

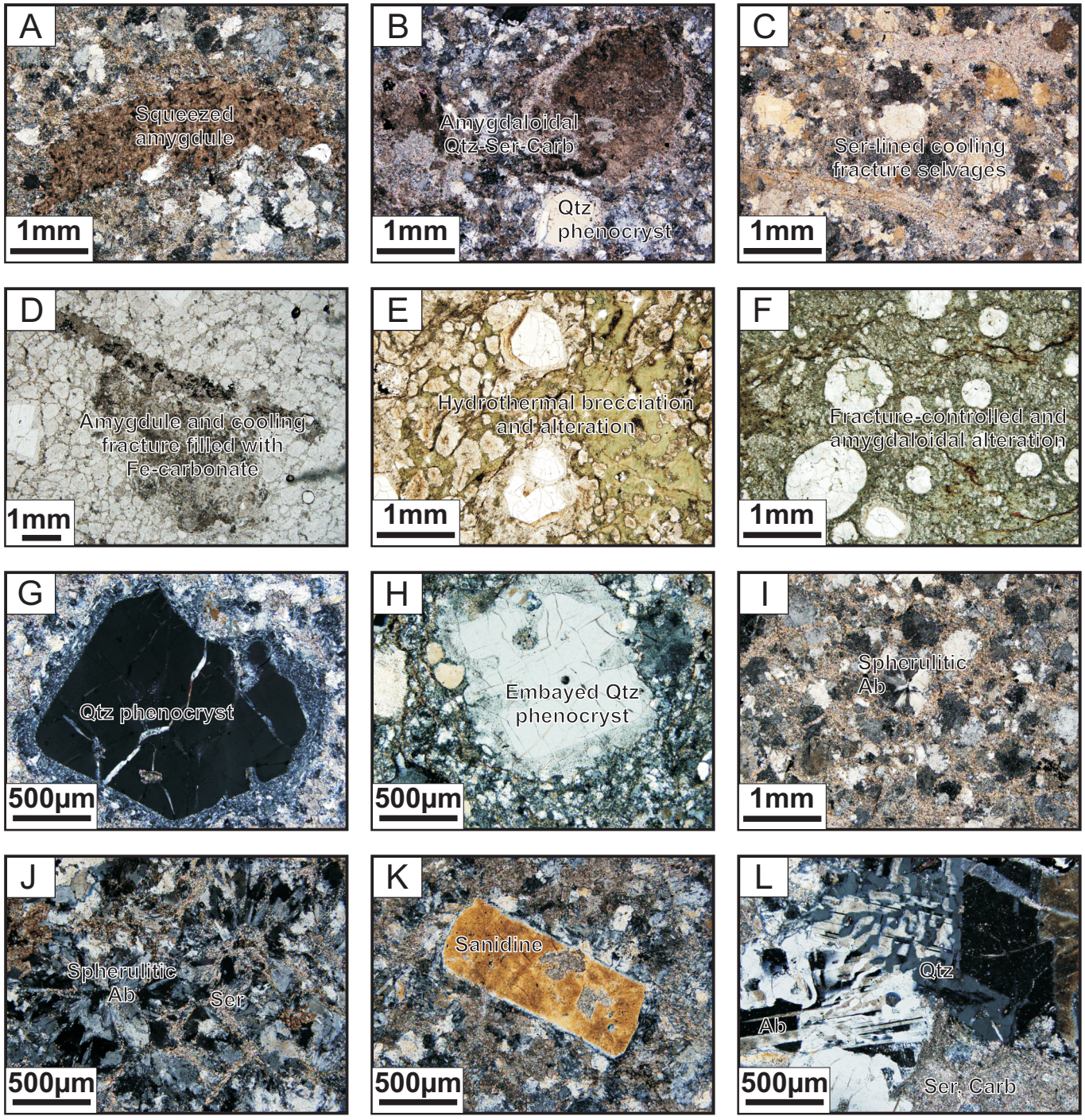

Figure 5.2. Photomicrographs of volcanic textures in fractured QP rhyolite facies at Pinkos. a) Amygdules are the most common form of primary porosity identified at Pinkos and are commonly filled with interpreted syn-volcanic alteration minerals (5x, XPL) - RW043; b) Abundant amygdules are one of the defining characteristics of fractured QP rhyolite facies (5x, XPL) - RW080; c) Cooling fractures filled with interpreted syn-volcanic alteration minerals define proximal columnar-jointed QP rhyolite (5x, XPL) - RW046; d) Cooling fracture adjacent to amygdule in proximal columnar-jointed rhyolite (2.5x, PPL) - RW112; e) Porosity in stringers and stockwork is dominated by fractures and interpreted hydrothermal brecciation (5x, PPL) - RW101; f) Micro-fracture networks and abundant sub-spherical amygdules in stringers and stockwork contributed to increased early permeability and associated intense alteration (5x, PPL) - RW117; g) Sub-angular quartz phenocryst with optically continuous quartz rim (10x, XPL) - RW078; h) Variably embayed quartz phenocryst with quartz rim in optical continuity (10x, XPL) - RW116; i) Spherulitic albite is strongly replaced in fractured QP rhyolite, likely due to increased early porosity and permeability (5x, XPL) - RW043; j) Variably altered spherulitic albite in proximal columnar-jointed rhyolite (10x, XPL) - RW079; k) Rare sanidine phenocrysts in fractured rhyolite are partially altered by sericite and carbonate (10x, XPL) - RW078; l) Vermicular quartz and albite in myrmekitic-type textures are identical to those examples in underlying coherent rhyolite (10x, XPL) - RW078.

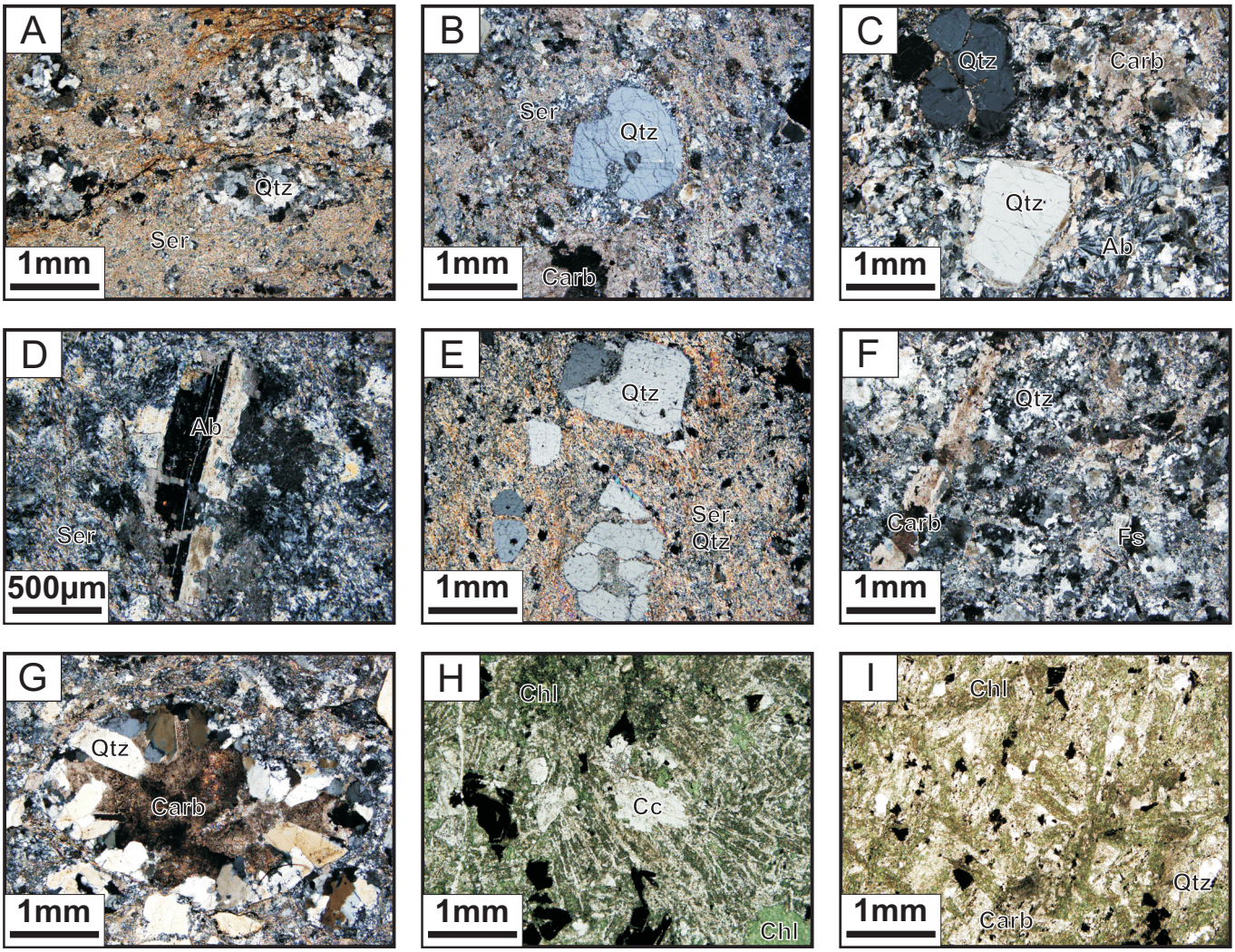

Figure 5.3. Photomicrographs of volcanic textures in fragmental rhyolite and mafic intrusive rocks at Pinkos. a) Distal fragmental rhyolite contains abundant amygdules and fracture networks, indicating highly porous protolith (5x, XPL) - RW083; b) Variably embayed quartz phenocrysts in fragmental rhyolite appear identical to underlying facies (5x, XPL) - RW083; c) Distribution of quartz phenocrysts and spherulitic albite in fragmental rhyolite appears identical to underlying facies (5x, XPL) - RW096; d) Variably altered fine-grained anhedral feldspar and weak coarse tabular albite crystals in fragmental rhyolite (10x, XPL) - RW097; e) Matrix in fragmental rhyolite consists of dominantly sericite and lesser microcrystalline quartz (5x, XPL) - RW089; f) Fracture-controlled carbonate cross-cutting earlier quartz-sericite alteration in rhyolite fragment (5x, XPL) - RW083; g) Amygdaloidal quartz-carbonate alteration in rhyolite fragment is further evidence of highly porous protolith (5x, XPL) - RW088; h) Mafic intrusive primary mineralogy largely replaced by chlorite and calcite alteration (5x, PPL) - RW057; i) Mafic intrusive mineralogy dominated by intense chlorite and carbonate alteration (5x, PPL) - RW076.

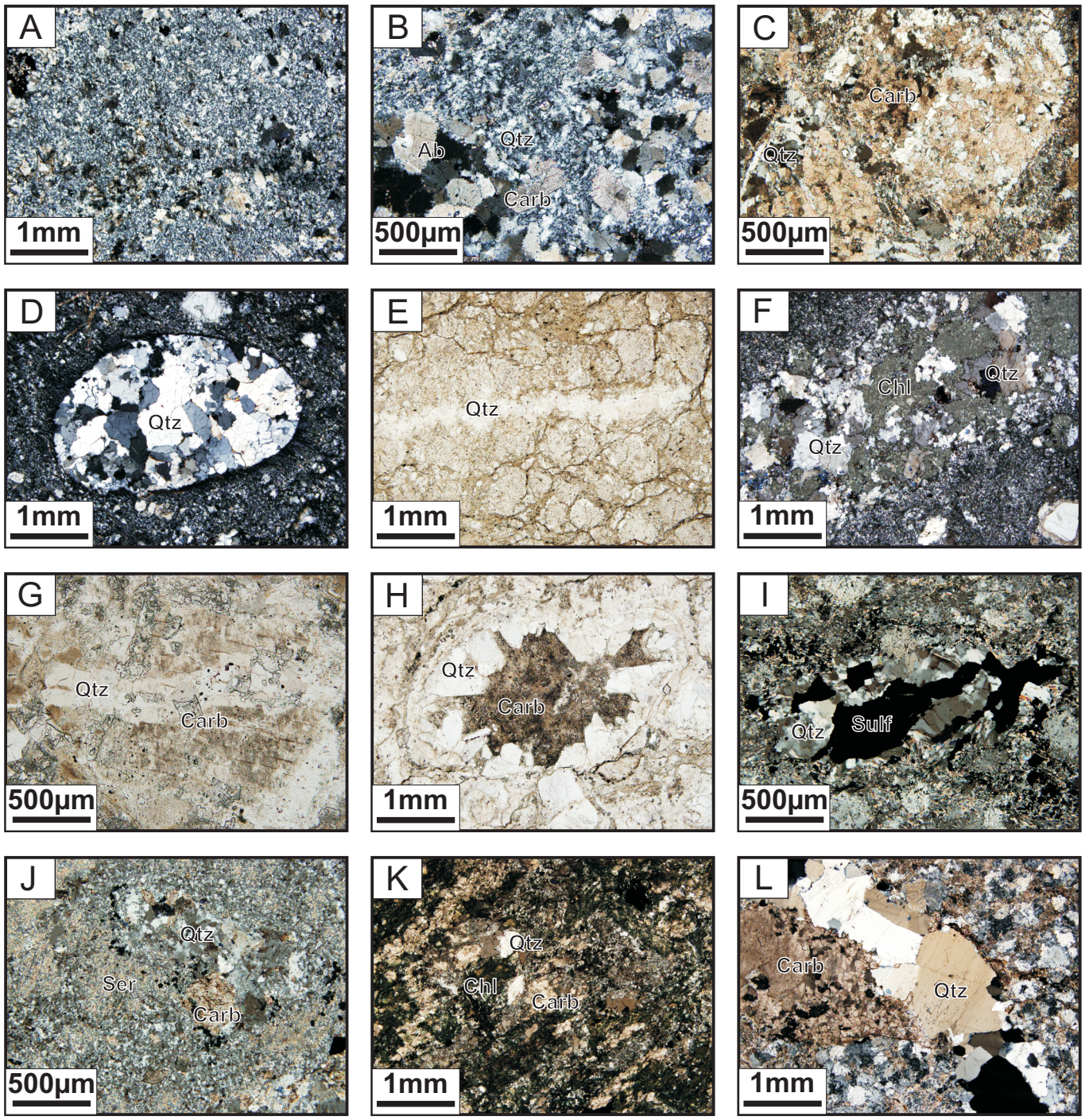

Figure 5.4. Photomicrographs of hydrothermal quartz textures at Pinkos. a) Pervasive groundmass replacement by microcrystalline quartz in basal coherent rhyolite (5x, XPL) - RW061; b) Spotted groundmass replacement by microcrystalline to anhedral quartz in proximal columnar-jointed rhyolite (10x, XPL) - RW047; c) Amygdaloidal quartz forms earliest rim with later sericite and carbonate in proximal columnar-jointed rhyolite (10x, XPL) - RW044; d) Amygdaloidal quartz at Pinkos is commonly annealed, indicating early precipitation and subsequent recrystallization during later deformation (5x, XPL) - RW117; e) Fracture-controlled quartz is cross-cut by chlorite in distal coherent rhyolite (5x, PPL) - RW069; f) Quartz-chlorite vein in distal coherent rhyolite (5x, XPL) - RW073; g) Fracture-controlled quartz (± carbonate) is identified locally in stockwork rhyolite and micro-scale displacement evidences early precipitation (10x, PPL) - RW099; h) Amygdaloidal quartz and Fe-carbonate in fragmental rhyolite (5x, PPL) - RW088; i) Amygdaloidal and fracture-controlled quartz in rhyolite fragment (10x, XPL) - RW093; j) Microcrystalline sub-spherical quartz is a minor matrix constituent with abundant sericite in fragmental rhyolite (10x, XPL) - RW087; k) Weak fine to microcrystalline quartz grains in mafic intrusive rocks are mainly disseminated (5x, XPL) - RW058; l) Late monomineralic quartz veins that cross-cut interpreted primary and syn-volcanic textures are likely related to the d'Alembert Shear (5x, XPL) - RW078.

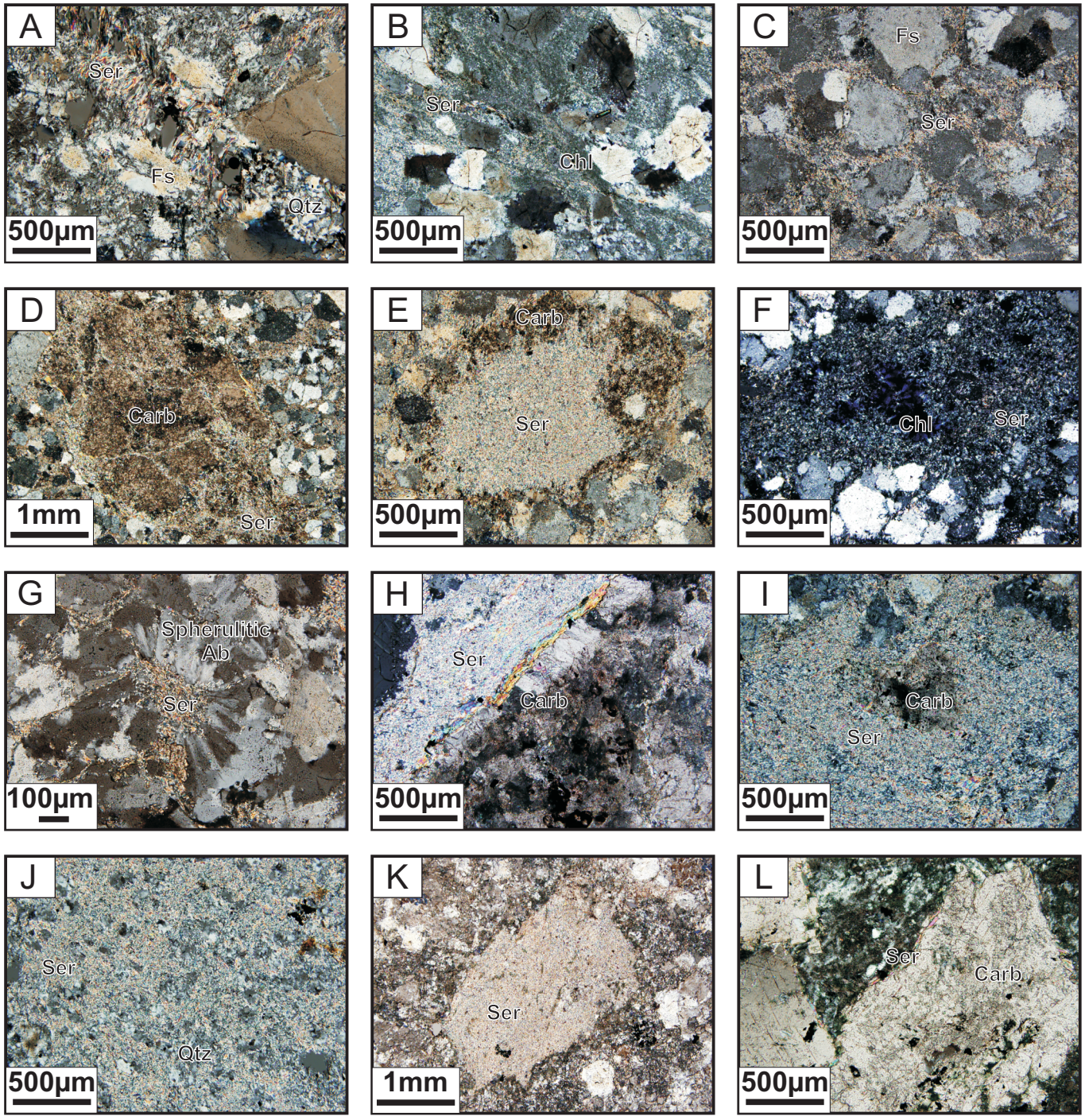

Figure 5.5. Photomicrographs of hydrothermal sericite at Pinkos. a) Fracture-controlled fine-grained platy sericite with quartz in basal coherent rhyolite (10x, XPL) - RW063; b) Sericitic clays are also intermixed with chlorite in fine fractures in basal coherent rhyolite (10x, XPL) - RW064; c) Moderate sericite in proximal columnar-jointed rhyolite is commonly distributed along foliation and wrapping primary material (10x, XPL) - RW043; d) Sericite commonly forms the earliest rim in amygdules with later carbonate infill in proximal columnar-jointed rhyolite at Pinkos. Minor fracture-controlled sericite cross-cutting carbonate appears re-mobilized (5x, XPL) - RW112; e) Amygdaloidal sericite and Fe-carbonate in proximal columnar-jointed rhyolite. Notably, sericite appears to fill amygdules after carbonate locally, suggesting a second sericite phase possibly formed during cooling of the hydrothermal system (10x, XPL) - RW044; f) Fracture-controlled sericite and Fe-chlorite in stockwork-altered rhyolite (10x, XPL) - RW118; g) Disseminated sericite replacing spherulitic albite in proximal columnar-jointed rhyolite (20x, XPL) - RW079; h) Fracture-controlled sericite lining interpreted earlier amygdaloidal Fe-carbonate in proximal columnar-jointed rhyolite (10x, XPL) - RW112; i) A second phase of sericite clearly enveloping earlier Fe-carbonate in proximal columnar-jointed rhyolite may have formed during cooling of the hydrothermal system (10x, XPL) - RW078; j) Sericite is the primary matrix constituent with lesser quartz in fragmental rhyolite (10x, XPL) - RW089; k) Intensely altered rhyolite fragments commonly contain abundant amygdaloidal sericite (5x, XPL) - RW097; l) Mafic intrusive samples contain weak sericite commonly distributed along foliation (10x, XPL) - RW057.

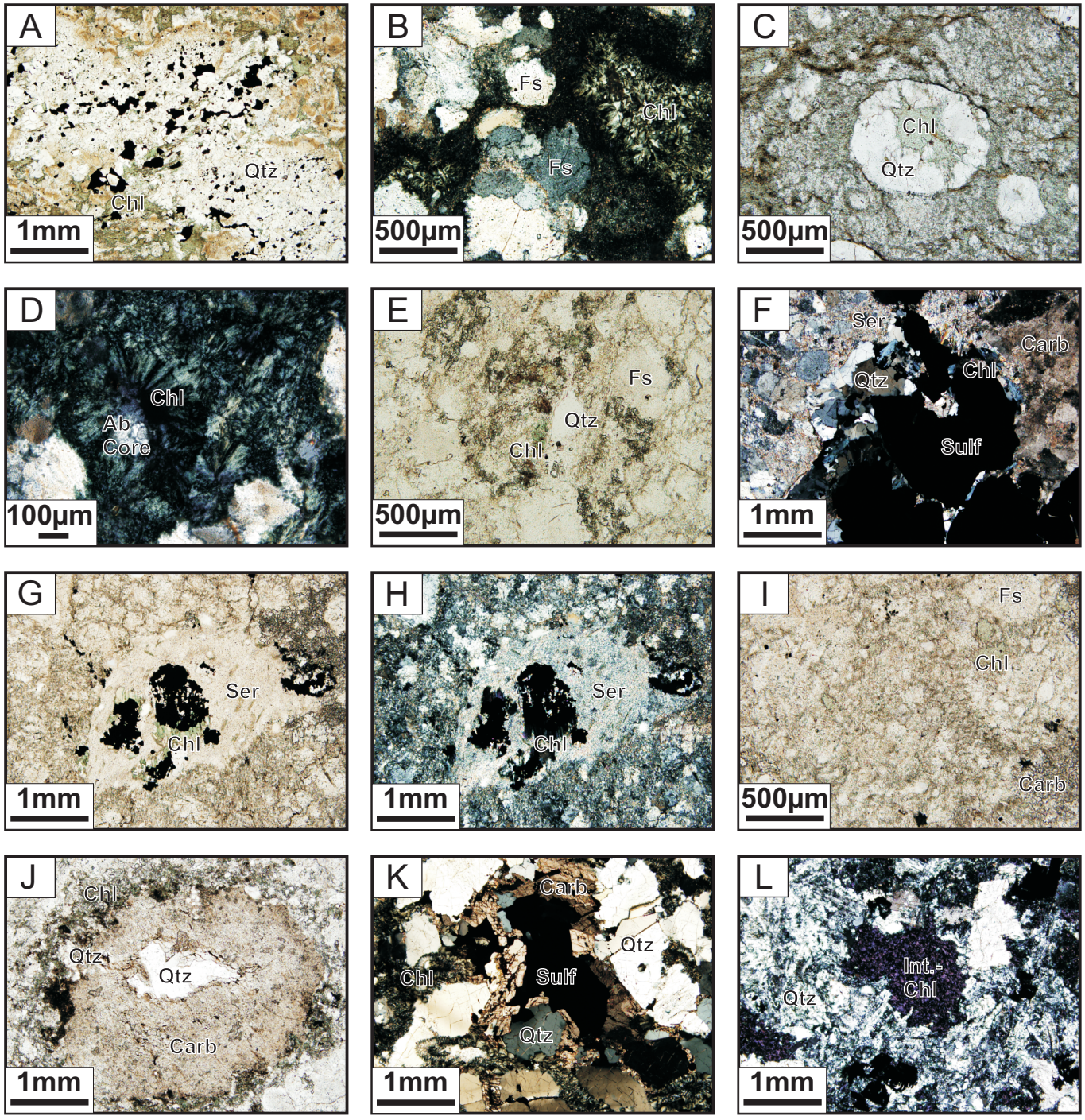

Figure 5.6. Photomicrographs of hydrothermal chlorite at Pinkos. a) Chlorite in the stockwork zone to the southeast at Pinkos is commonly associated with quartz, sericite, and sulfide (5x, PPL) - RW102; b) Radial crystals of Mg-chlorite are mainly fracture-controlled in the stockwork zone to the northwest (10x, XPL) - RW115; c) Weak amygdaloidal chlorite in stockwork-altered rhyolite is clearly later than quartz alteration (10x, PPL) - RW117; d) Radial Fe-chlorite replacing spherulites in stockwork (20x, XPL) - RW101; e) Chlorite typically occurs in fine fracture networks and as disseminations in columnar-jointed rhyolite (10x, PPL) - RW045; f) Mineralogical zonation in amygdules indicates chlorite (± sulfide) alteration succeeded quartz and sericite in the paragenetic sequence (5x, XPL) - RW112; g) Fragmental rhyolite contains weak amygdaloidal Fe-chlorite (5x, PPL) - RW097; h) Same as (g), but shown in XPL (5x) - RW097; i) Trace Mg-chlorite is mainly disseminated in distal coherent rhyolite (10x, PPL) - RW128; j) Amygdaloidal chlorite appears earlier than carbonate as it forms the immediate rim with sulfide, sericite, and quartz (5x, PPL) - RW062; k) Amygdaloidal and fracture-controlled radial Mg-chlorite is associated with sulfide and overprinted by Ca-rich to intermediate carbonate (5x, XPL) - RW125; l) Spotted to pervasive intermediate to Fe-rich chlorite alteration occurs locally in mafic intrusive rocks (5x, XPL) - RW057.

Figure 5.7. Photomicrographs of hydrothermal carbonate textures at Pinkos. a) Amygdule showing zonation from sericite to Fe-carbonate in proximal columnar-jointed rhyolite (5x, XPL) - RW043; b) Veinlet containing Ca-rich to intermediate carbonate and quartz in proximal columnar-jointed rhyolite (5x, XPL) - RW081; c) Spotted to pervasive Fe-carbonate replacing nearly all sericite in columnar-jointed rhyolite (10x, XPL) - RW080; d) Amygdaloidal zonation from quartz to Fe-carbonate identified in fragmental rhyolite (5x, XPL) - RW088; e) Ca-rich to intermediate carbonate lining fine fractures in altered rhyolite fragments (10x, XPL) - RW091; f) Veinlet containing intermediate to Fe-rich carbonate and minor quartz in rhyolitic fragment (10x, XPL) - RW083; g) Trace Fe-carbonate is disseminated in the matrix of fragmental rhyolite (5x, XPL) - RW089; h) Weak carbonate is commonly disseminated in stockwork rhyolite (10x, XPL) - RW114; i) Fracture-controlled carbonate alteration in stockwork rhyolite (5x, XPL) - RW099; j) Amygdaloidal Fe-carbonate with chlorite inclusions, indicating carbonate was later than chlorite in the paragenetic sequence (10x, XPL) - RW109; k) Ca-rich to intermediate carbonate is mainly disseminated in distal coherent rhyolite (10x, XPL) - RW129; l) Fracture-controlled Ca-rich to intermediate carbonate and quartz identified locally in distal coherent rhyolite (10x, XPL) - RW072; m) A second sericite phase is identified locally by the infill of amygdules after earlier carbonate (5x, XPL) - RW044; n) Mafic intrusive samples proximal to interpreted hydrothermal upflow contain intermediate to Fe-rich carbonate (5x, XPL) - RW058; o) Distal mafic intrusive samples contain dominantly Ca-rich carbonate based on abundant calcite-twinning (10x, PPL) - RW076.

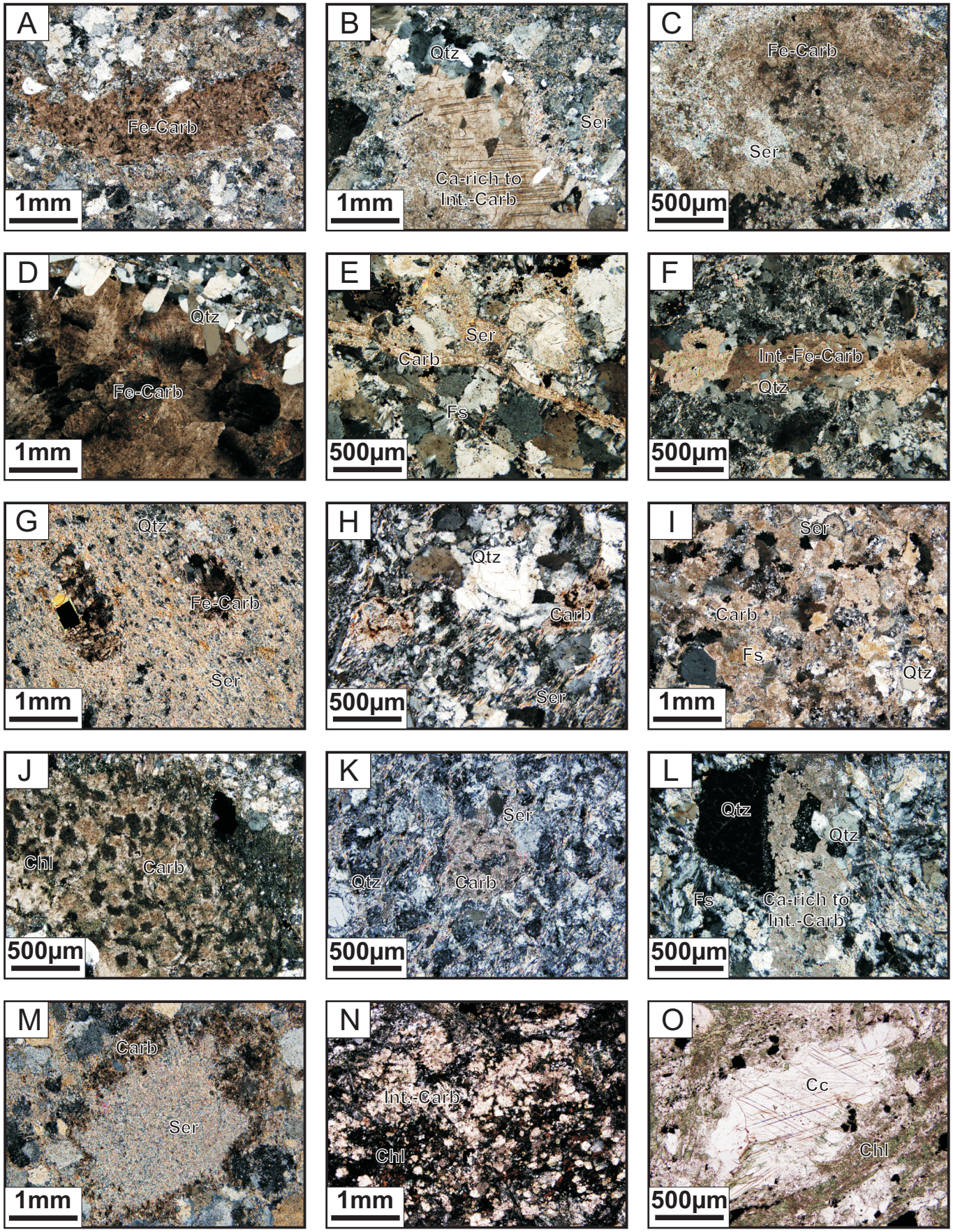
A
Fe-Carb
1mm
B
Qtz
Ser
Ca-rich to
Int.-Carb
1mm
C
Fe-Carb
Ser
500µm
D
Qtz
Fe-Carb
1mm
E
Ser
Carb
Fs
500µm
F
Int.-Fe-Carb
Qtz
500µm
G
Qtz
Fe-Carb
Ser
1mm
H
Qtz
Carb
Ser
500µm
I
Ser
Carb
Fs
Qtz
1mm
J
Chl
Carb
500µm
K
Ser
Qtz
Carb
500µm
L
Qtz
Qtz
Fs
Ca-rich to
Int.-Carb
500µm
M
Carb
Ser
1mm
N
Int.-Carb
Chl
1mm
O
Cc
Chl
500µm

Figure 5.8. Photomicrographs of hydrothermal sulfide-carbonate replacement textures at Pinkos. a) Strongly oxidized pyrite is clearly penetrated and replaced by intermediate carbonate in proximal mafic intrusive rocks (20x, XPL/RL) - RW057; b) Anhedral chalcopyrite is overprinted by translucent mineral in stockwork rhyolite (10x, RL) - RW109; c) Same image as (b), but transmitted light shows Fe-carbonate invading and overprinting both chalcopyrite and quartz gangue (10x, XPL) - RW109; d) Relict sphalerite overprinted, included, and replaced by later intermediate and Fe-rich carbonate in proximal columnar-jointed rhyolite (20x, XPL) - RW043; e) Partially hematized anhedral chalcopyrite clearly overprinted and replaced along grain boundaries (10x, RL) - RW125; f) Same image as (e), except transmitted light indicates Ca-rich to intermediate carbonate is the invading mineral along grain boundaries (10x, XPL) - RW125; g) Ca-rich to intermediate carbonate completely surrounding anhedral galena grain in basal coherent rhyolite (20x, XPL/RL) - RW048; h) Sphalerite grain is enveloped, included, and cross-cut by Ca-rich to intermediate carbonate in basal coherent rhyolite (20x, XPL) - RW048; i) Fine-grained anhedral pyrite appears largely replaced by and included later carbonate in proximal columnar-jointed rhyolite (20x, RL) - RW078; j) Cross-polarized light identifies the replacement mineral in (i) as intermediate to Fe-rich carbonate (20x, XPL) - RW078; k) Matrix-controlled subhedral pyrite overprinted by a later alteration mineral in fragmental rhyolite (10x, RL) - RW132; l) The same image as (k) shown in XPL indicates the later alteration as intermediate to Fe-rich carbonate (10x, XPL) - RW132; m) Amygdaloidal anhedral pyrite appears possibly etched and is clearly replaced by Ca-rich to intermediate carbonate in proximal coherent rhyolite (10x, XPL) - RW051; n) Anhedral sphalerite and pyrite ($\pm$ chalcopyrite inclusions) are evidently enveloped, penetrated, and overprinted by a translucent alteration mineral in proximal columnar-jointed rhyolite (10x, RL) - RW112; o) Same image as (n) shown in XPL identifies this replacement of sulfide by intermediate to Fe-rich carbonate (10x, XPL) - RW112.

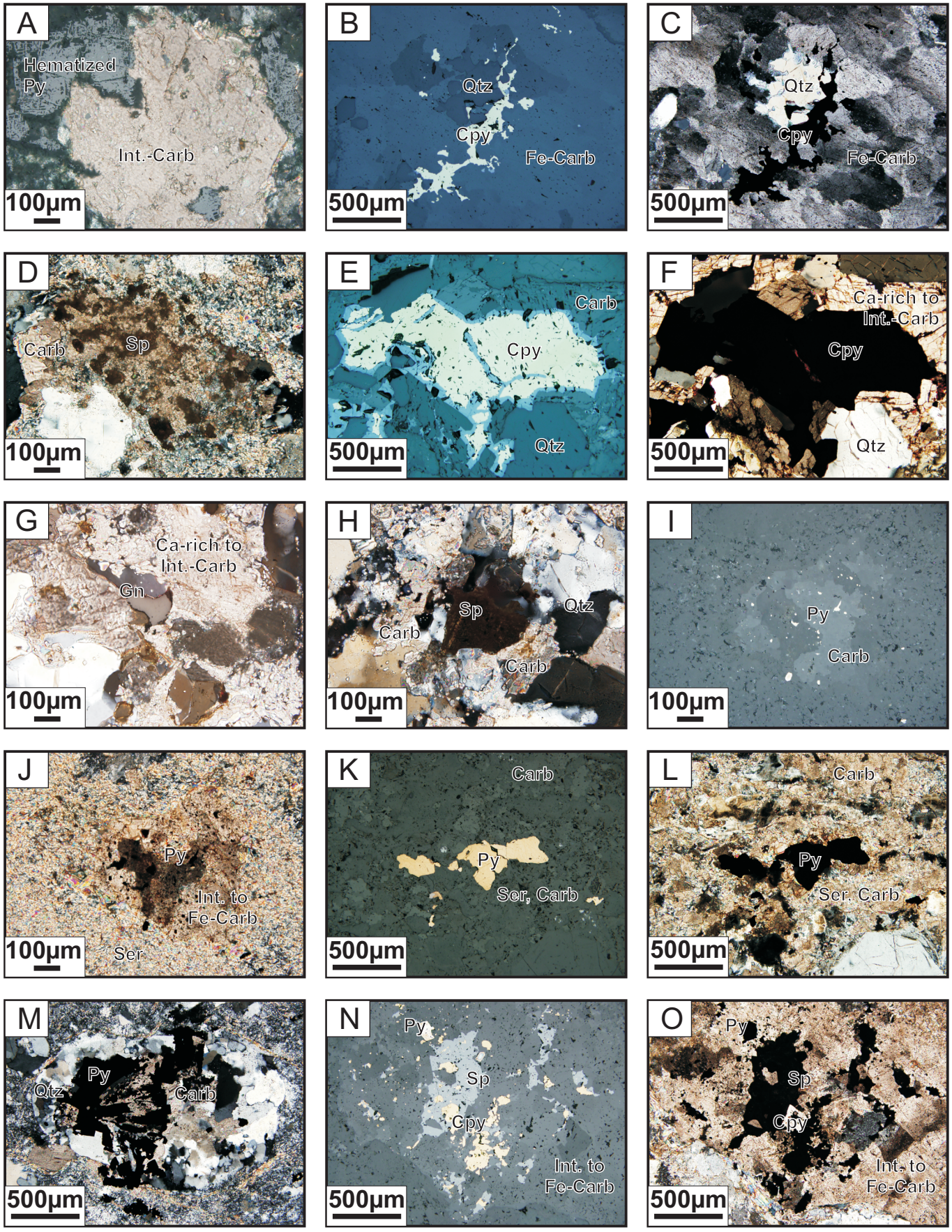
A
Hematized
Py
Int.-Carb
100µm
B
Qtz
Cpy
Fe-Carb
500µm
C
Qtz
Cpy
Fe-Carb
500µm
D
Carb
Sp
100µm
E
Carb
Cpy
Qtz
500µm
F
Ca-rich to
Int.-Carb
Cpy
Qtz
500µm
G
Ca-rich to
Int.-Carb
Gn
100µm
H
Sp
Qtz
Carb
Carb
100µm
I
Py
Carb
100µm
J
Py
Int. to
Fe-Carb
Ser
100µm
K
Carb
Py
Ser, Carb
500µm
L
Carb
Py
Ser, Carb
500µm
M
Py
Qtz
Carb
500µm
N
Py
Sp
Cpy
Int. to
Fe-Carb
500µm
O
Py
Sp
Cpy
Int. to
Fe-Carb
500µm

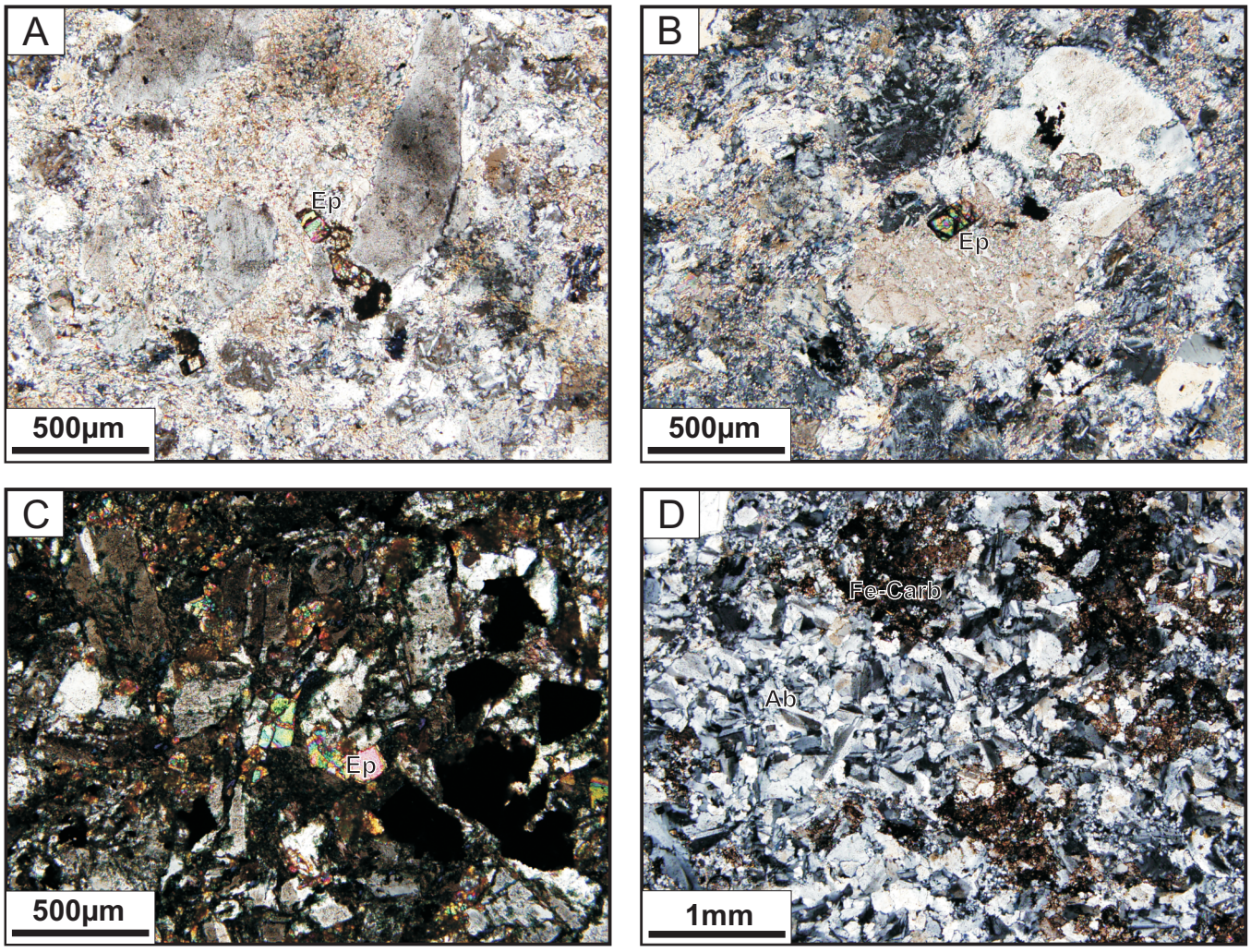

Figure 5.9. Photomicrographs of epidote alteration at Pinkos. a) Trace to minor fine-grained epidote disseminated in the matrix of fragmental rhyolite (10x, XPL) - RW086; b) Trace fine-grained epidote identifed locally in proximal columnar-jointed rhyolite (10x, XPL) - RW078; c) Minor disseminated epidote in mafic intrusive rocks (10x, XPL) - RW107; d) Irregular to amoeboidal albite alteration appears to cross-cut earlier turbid carbonate alteration locally, suggesting diagenetic precipitation (5x, XPL) - RW060.

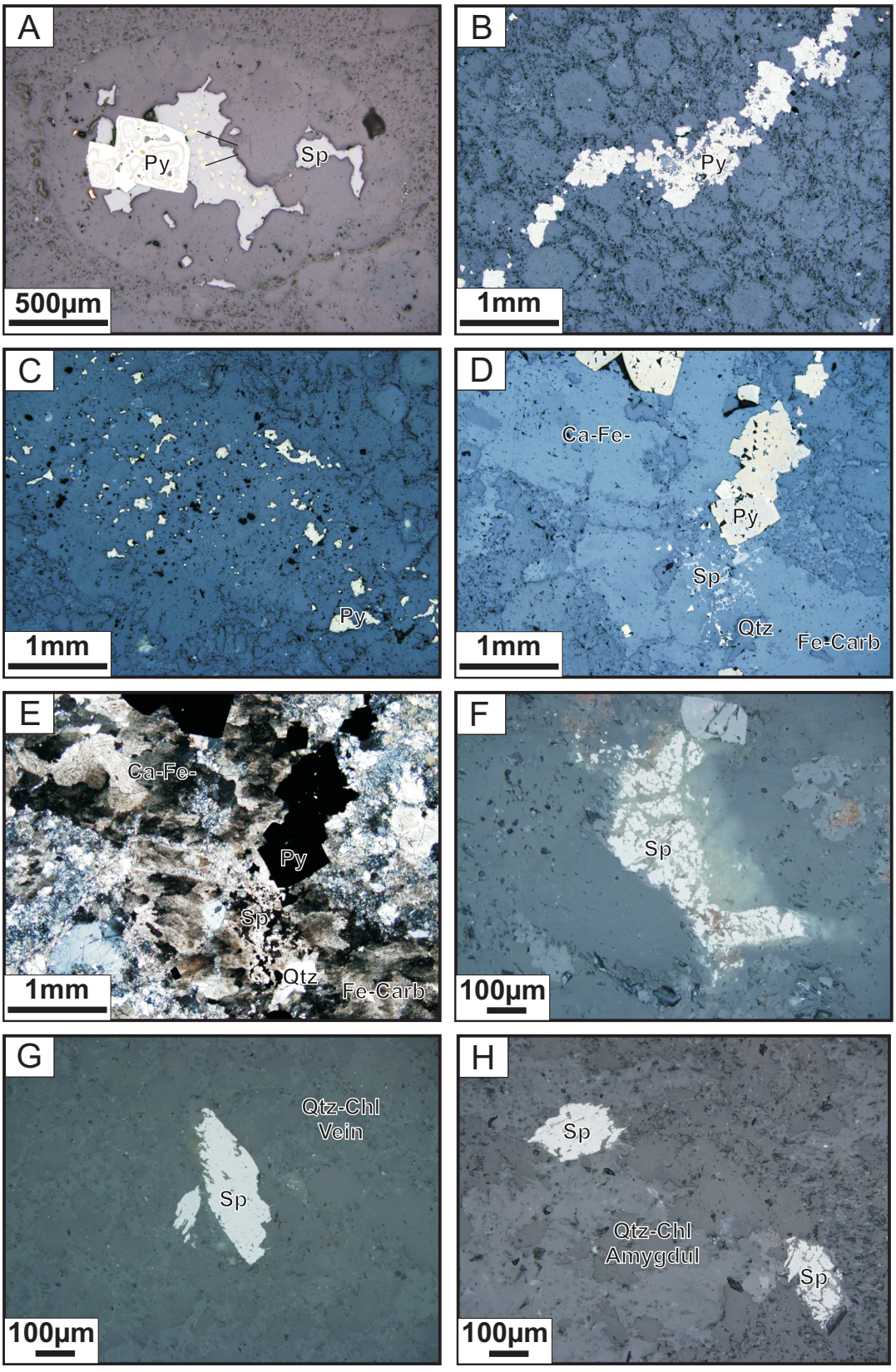

Figure 5.10. Photomicrographs of hydrothermal sulfide and replacement textures in stringers and stockwork at Pinkos. a) Pyrite is typically the dominant amygdaloidal sulfide with lesser sphalerite and chalcopyrite (10x, RL) - RW051; b) Fracture-controlled sulfides are also dominated by fine-grained anhedral pyrite (5x, RL) - RW109; c) Fine-grained blebby chalcopyrite with minor anhedral pyrite are fracture-controlled in stockwork to the southeast (5x, RL) - RW102; d) Coarse-grained subhedral pyrite with minor anhedral sphalerite mineralization occurs in vein material in the stockwork zone to the southeast (5x, RL) - RW109; e) Same image as (d), but XPL identifies Fe-carbonate as the veined gangue mineral (5x, XPL) - RW109; f) Partially replaced fracture-controlled sphalerite in stockwork to the northwest (20x, RL) - RW114; g) Trace anhedral sphalerite in quartz-chlorite vein in the northwest stockwork zone (20x, RL) - RW116; h) Minor anhedral sphalerite occurs with quartz and chlorite in amygdules in stockwork to the northwest (20x, RL) - RW117.

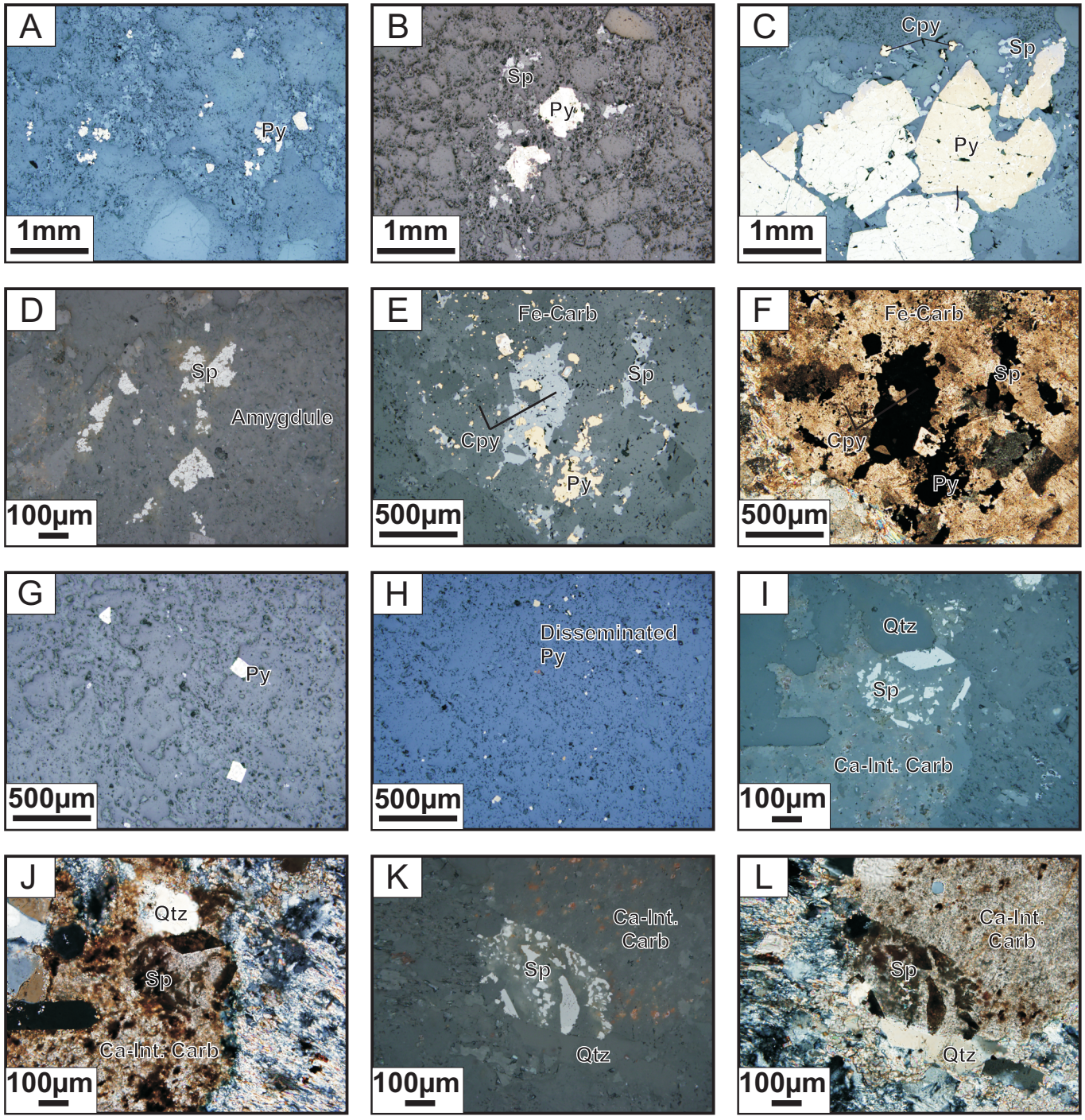

Figure 5.11. Photomicrographs of hydrothermal sulfide and replacement textures in proximal columnar-jointed (a-f) and distal coherent (g-l) rhyolite at Pinkos. a) Fine-grained anhedral to subhedral pyrite commonly distributed along fine fracture networks (5x, RL) - RW082; b) Disseminated subhedral pyrite (± sphalerite) in columnar-jointed rhyolite (5x, RL) - RW045; c) Amygdaloidal coarse-grained subhedral pyrite with minor blebby sphalerite and chalcopyrite (5x, RL) - RW112; d) Amygdaloidal anhedral to subhedral sphalerite is partially replaced in columnar-jointed rhyolite (20x, RL) - RW044; e) Amygdaloidal sphalerite and pyrite with micron-sized blebs of chalcopyrite appear partially replaced (10x, RL) - RW112; f) The same image as (e), but XPL clearly shows sulfide has been replaced by Fe-carbonate (10x, XPL) - RW112; g) Fine-grained subhedral to euhedral pyrite is dominantly disseminated in distal coherent rhyolite (10x, RL) - RW070; h) Disseminated micron-sized subhedral to euhedral pyrite (10x, RL) - RW128; i) Amygdaloidal sphalerite is evidently overprinted and replaced by a later alteration phase in distal coherent rhyolite (20x, RL) - RW108; j) The same image as (i) shown in XPL identifies replacement by Ca-rich to intermediate carbonate (20x, XPL) - RW108; k) Amygdaloidal sphalerite clearly overprinted and partially replaced by a later phase (20x, RL) - RW108; l) XPL identifies the later alteration replacing sphalerite in image (k) as Ca-rich to intermediate carbonate (20x, XPL) - RW108.

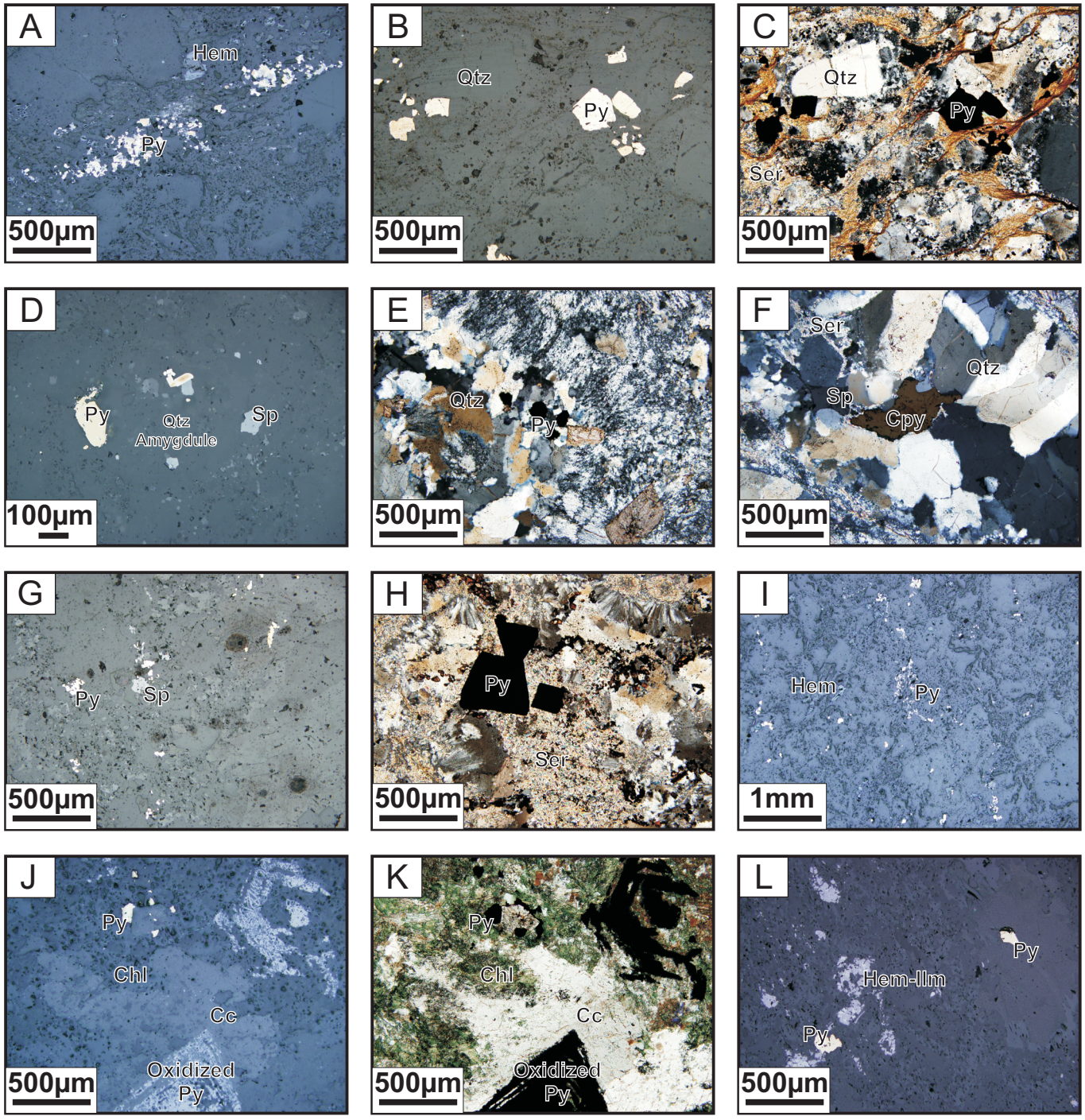

Figure 5.12. Photomicrographs of hydrothermal sulfide and replacement textures in fragmental rhyolite (a-h) and mafic intrusive rocks (j-l) at Pinkos. a) Fine-grained anhedral pyrite and hematite occur in fractures in rhyolitic fragments (10x, RL) - RW131; b) Fine-grained subhedral pyrite distributed along fine fractures and foliation in rhyolitic fragments (10x, RL) - RW087; c) Same image as (b), but shown in XPL (10x, XPL) - RW087; d) Amygdaloidal subhedral pyrite and anhedral sphalerite (20x, RL) - RW095; e) Quartz-filled amygdule with minor fine-grained subhedral pyrite (10x, XPL) - RW131; f) Squeezed quartz-filled amygdule with minor anhedral chalcopyrite and sphalerite (10x, XPL/RL) - RW088; g) Minor fine-grained anhedral pyrite and sphalerite are commonly matrix-controlled in fragmental rhyolite (10x, RL) - RW084; h) Medium-grained euhedral pyrite observed in sericite-rich matrix (10x, XPL) - RW091; i) Matrix-controlled fine-grained pyrite and hematite (± sphalerite) (5x, RL) - RW131; j) Partially replaced and strongly hematized coarse-grained pyrite in mafic intrusive rocks. Trace fine-grained anhedral pyrite and blebby chalcopyrite appear less oxidized (10x, RL) - RW057; k) Same image as (j) shown in XPL indicates carbonate replacement of the variably oxidized sulfides (10x, XPL) - RW057; l) Anhedral pyrite and exsolved hematite-ilmenite have been largely overprinted and replaced by later Ca-rich carbonate (10x, RL) - RW076.

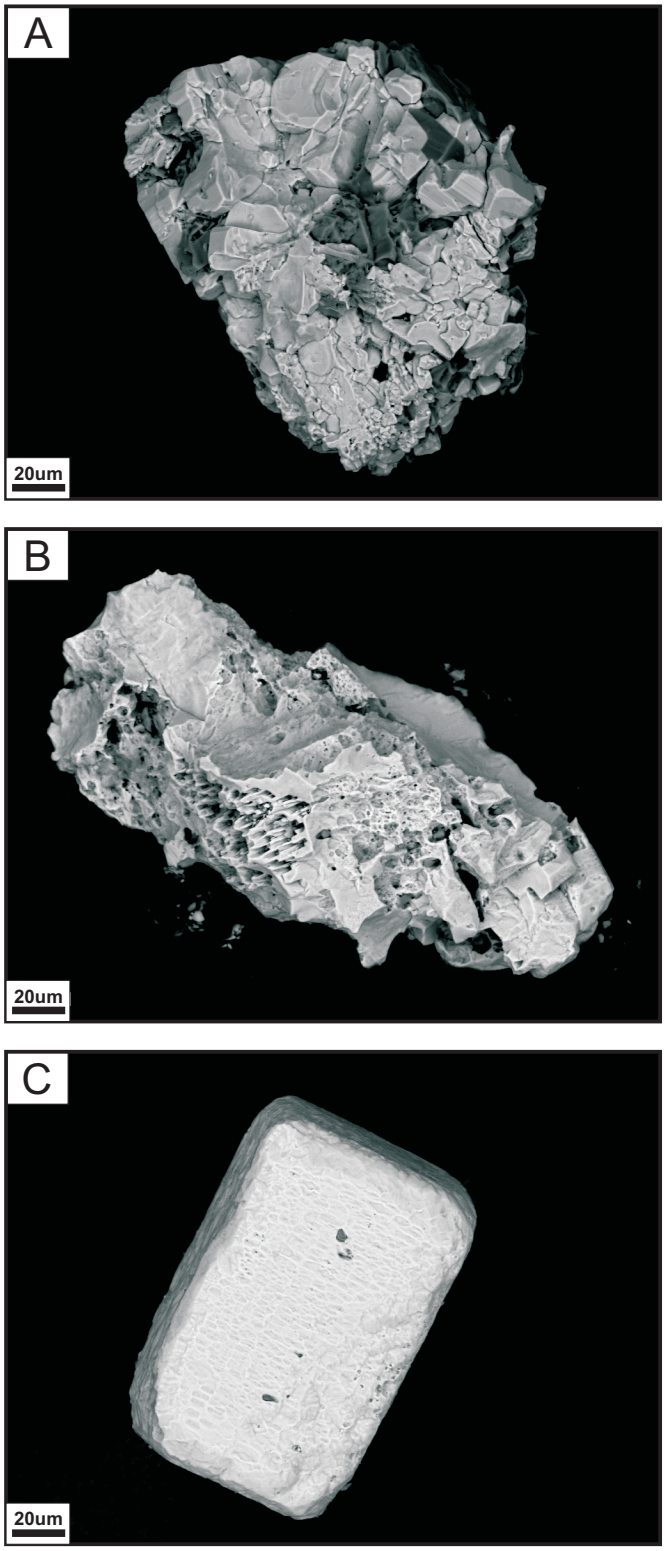

Figure 5.13. Back-scattered secondary electron (BSE) images of selected pyrite grains from sulfide-rich samples collected at Pinkos taken with an EVO Zeiss scanning electron microprobe (SEM) instruments at the Geological Survey of Canada. The EVO Zeiss microscope has a 20 kV accelerating voltage and 500 pA beam current. Grain surfaces appear etched, possibly by a combination of CO_2-rich fluids and microbial activity. Degree of etching appears greater in more proximal and strongly carbonatized zones (a, b) relative to distal samples (c) containing weakly abundant carbonate. Euhedral rhombic represent etching on the (100) and (110) crystal surfaces and triangular pits occur on the (111) surface. a) SB037; b) SB060; c) SB049.

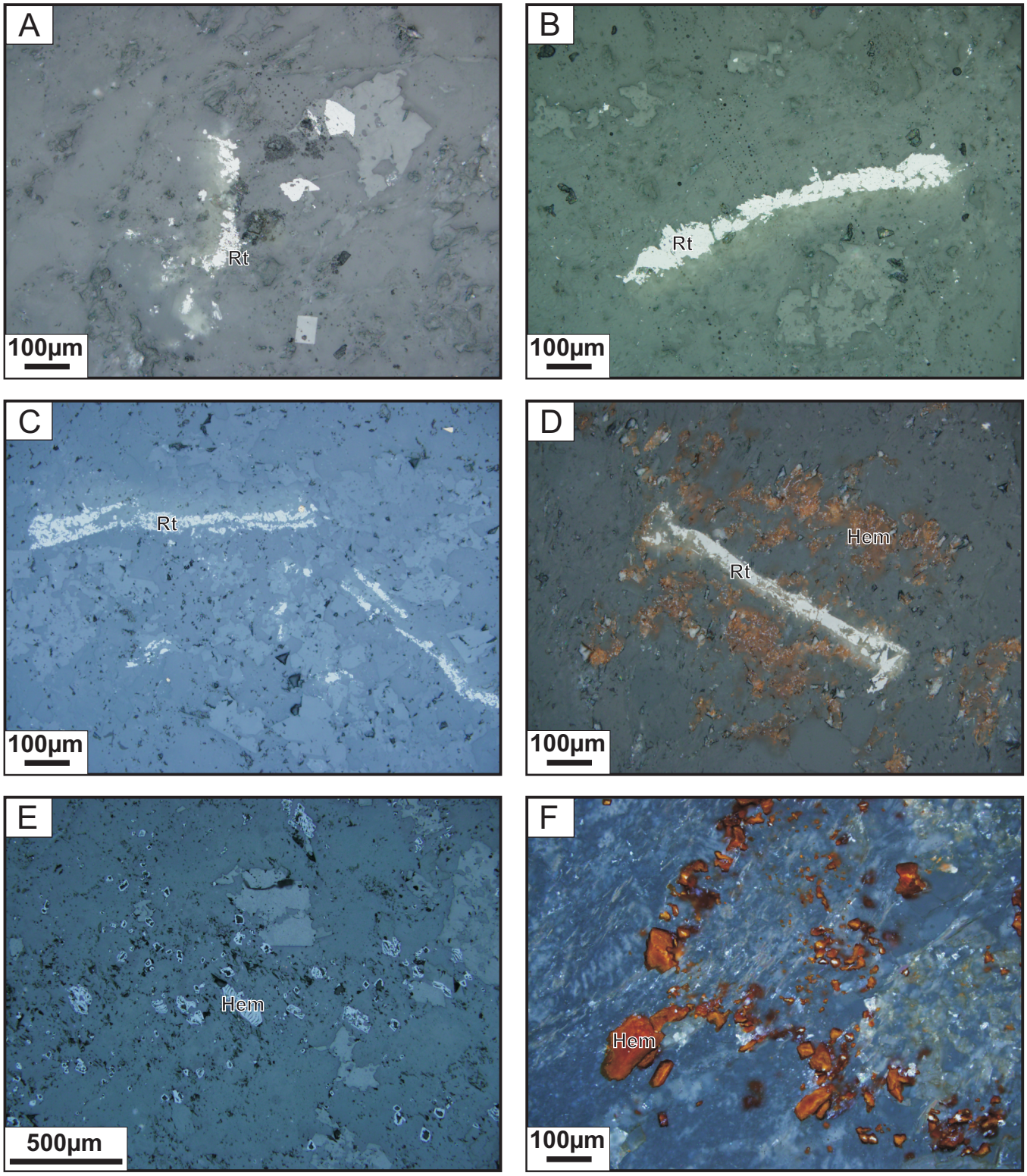

Figure 5.14. Photomicrographs of oxides at Pinkos. a) Disseminated fine-grained anhedral rutile displaying white to light yellow-brown internal reflections in distal coherent rhyolite (20x, RL) - RW072; b) Wispy rutile distributed along a fine fracture in the stockwork zone to the northwest (20x, RL) - RW067; c) Rutile also commonly occurs along foliation (20x, RL) - RW128; d) Wispy rutile within fine fracture or along foliation with surrounding hematite alteration in distal coherent rhyolite (20x, RL) - RW074; e) Fine-grained euhedral and coarser anhedral hematite alteration is typically matrix-controlled and distributed along foliation in fragmental rhyolite (10x, RL) - RW089; f) Matrix-controlled fine-grained anhedral hematite showing deep red-orange internal reflections in fragmental rhyolite (20x, RL) - RW131.

Table 5.1. Abundance* of alteration minerals in different units of the Pinkos property

Alteration Facies	Phenocrysts/ Components	Abundances (vol.%) and Alteration Styles				
		Quartz	Sericite	Chlorite	Carbonate	Sulfide
Stringers and Stockwork (Southeast)	5-10% Qtz phenocrysts; 0-20% Fs	45-55% Fractures, amygdules, groundmass	10-20% Fractures, amygdules, foliation, disseminated	10-25% *Fe-rich to Int.* Fractures, amygdules, foliation	Tr. (<1%) to 5% *Fe-rich (± Int.-Ca)* Fractures (± amygdules)	Absent to Tr. (<1%) *Py (± Cpy)* Fractures, amygdules
Stringers and Stockwork (Northwest)	5-10% Qtz phenocrysts; 0-20% Fs	45-55% Fractures, amygdules, groundmass	10-20% Fractures, amygdules, disseminated, foliation	10-25% *Mg-rich to Int.* Fractures, amygdules, foliation	Tr. (<1%) to 5% *Ca-rich to Int.* Fractures (± amygdules)	Absent to Tr. (<1%) *Py (± Sp)* Fractures, amygdules
Proximal Columnar-Jointed Rhyolite	5-10% Qtz phenocrysts; 5-15% Fs	50-60% Fractures, amygdules, groundmass	10-20% Fractures, amygdules, disseminated, foliation	Absent to 2-3% *Fe-rich to Int.* Fractures, amygdules (± disseminated)	5-10% *Fe-rich (± Int.-Ca)* Fractures, amygdules, disseminated	Tr. (<1%) to 2-3% *Py, Sp (± Cpy, Gn)* Fractures, amygdules
Basal/Distal Coherent Rhyolite	5-10% Qtz phenocrysts; 20-40% Fs	40-50% Fractures, groundmass (± amygdules)	15-30% Disseminated (± fractures), foliation	Absent to Tr. (<1%) *Mg-rich* Disseminated, foliation	Tr. (<1%) to 5% *Ca-rich to Int.* Disseminated (± fractures)	1-5% *Py (± Sp, Cpy)* Disseminated (± amygdules)
Fragmental Rhyolite	10-30% rhyolite fragments	30-50% Matrix, fractures, amygdules	20-40% Matrix, fractures, amygdules	Absent to Tr. (<1%) *Fe-rich* Disseminated (± matrix)	5-10% *Fe-rich (± Int.-Ca)* Fractures, amygdules (± matrix)	Tr. (<1%) to 2-3% *Py, Cpy (± Sp, Gn)* Fractures, amygdules (± matrix)
Mafic Intrusive Rocks	25-45% Fs, Px	10-20% Disseminated	<5% Disseminated, foliation	25-40% *Fe-rich to Int.* Spotted to pervasive, foliation	5-20% *Ca-rich to Int.* Strongly disseminated	1-5% *Py (± Sp, Cpy)* Disseminated

* Based on petrography.

6. LITHOGEOCHEMISTRY OF THE DELBRIDGE RHYOLITE

Table 6.1 contains major, trace, and rare-earth element geochemical data for 54 rock samples collected at Delbridge (Figure 3.1) and analyzed at Geoscience Laboratories (GeoLabs, Ontario Geological Survey) in Sudbury, Ontario. Major element oxide data were obtained by X-ray fluorescence (XRF) analysis of samples that were first run for loss-on-ignition (LOI; 100°C under nitrogen atmosphere, 1000°C under oxygen atmosphere until constant weight% is reached) and then fused with a borate flux to produce a glass bead. All iron oxide data are herein reported and manipulated as Fe_2O_3, however this does not suggest that all Fe in the system is oxidized (Fe^{3+}). Mineralogy indicates that most Fe at Delbridge occurs in its reduced (Fe^{2+}) state (e.g., carbonate, chlorite, sericite, pyrite). Minor and trace element analyses were conducted by ICP-MS (inductively coupled plasma – mass spectrometry) using a closed vessel multi-acid digestion (hydrofluoric, hydrochloric, nitric, and perchloric acids) to ensure total dissolution of rare earth elements (REE), high-field strength elements (HFSE), and large ion lithophile elements (LILE). Instrumentation was calibrated using a combination of synthetic multi-element solutions and certified reference materials. CO_2 and total S were analyzed by infrared absorption of oxidized samples combusted in an oxygen-rich environment.

Most samples are hydrothermally altered rocks. Table 6.1 classifies the samples according to four main types of alteration assemblages based on field observations, petrography, and SWIR spectroscopy (see Chapter 8). Samples of least-altered volcanic rocks have Na_2O contents in the ~3-5 wt.% range and contain minimal hydrothermal

alteration products (e.g., carbonate, chlorite, sericite, quartz, and sulfide). Lithogeochemical data were analyzed to characterize the lithofacies and quantify the chemical variability caused by hydrothermal alteration and mineralization.

6.1 GEOCHEMISTRY OF DIFFERENT LITHOFACIES

The quartz-porphyritic (QP) rhyolite facies show marked variation in SiO_2 content (60-83 wt.%) that appears to reflect the original porosity and permeability of the rock, as established from field relationships. Coherent and lobate QP rhyolite facies have Al_2O_3 contents of ~9-15 wt.%, whereas rhyolite breccias generally contain <10.5 wt.% Al_2O_3, reflecting dilution by silica. Uniformly low CaO concentrations are observed in QP rhyolite (generally <2 wt.%). All QP rhyolite facies (coherent, lobate, and breccia) have TiO_2 concentrations that are consistently less than ~0.3 wt.%. Coherent facies generally have lower loss on ignition (LOI) values than breccia. Field observations of increased carbonate alteration in felsic volcaniclastic material at or immediately beneath the interpreted paleo-seafloor are supported by CO_2 concentrations of up to nearly 10 wt.% for rhyolite breccia. Coherent and lobate QP rhyolite samples generally have <5 wt.% CO_2. HFSE concentrations are high in coherent QP rhyolite and lower in rhyolite breccia, again reflecting dilution by silica. Incompatible large ion lithophile elements (LILE; e.g., Ba, Cs, and Rb) are also high in the coherent QP rhyolite of the footwall but variable in breccia. Coherent QP rhyolite contains low base metals (e.g., Cu, Zn, and Pb) consistent with these being the least-altered rocks. Footwall QP rhyolite facies are enriched in REE, whereas hanging-wall rhyolite is relatively depleted.

The mafic volcaniclastic unit that marks the paleo-seafloor has the lowest SiO_2 content (~35-57 wt.%) and the highest Fe_2O_3 (~9-11.5 wt.%) and MgO (2.2-4.5 wt.%; up to 14.23 wt.%). This unit also contains high Al_2O_3 (~15-20 wt.%) and CaO (>4.5-18 wt.%), reflecting a combination of primary mineralogy (plagioclase, pyroxene) and alteration (chlorite, Ca-rich carbonate). Elevated Na_2O concentrations (up to ~7 wt.%) in some samples may indicate local albitization. TiO_2 is ~0.8-1.4 wt.% and P_2O_5 is >0.1 wt.%. High LOI values (4-17 wt.%) are likely caused by the abundance of hydrous phyllosilicates (i.e., chlorite alteration). Nearly all of the mafic samples contain at least 3.3 wt.% CO_2, supporting the plume of carbonate-rich alteration that was mapped up to ~100 m into the hanging wall. The mafic volcaniclastic rocks have low LILE and HFSE contents and high transition metal content (up to 53 ppm Cr, 40 ppm Sc, 300 ppm V, 32 ppm Co, and 28 ppm Ni). The unusually high Li (up to 53 ppm) corresponds to MgO and may represent Li-bearing chlorite from spilitization (Vilks, 1981). The mafic volcaniclastic rocks contain the lowest REE (both total and individual REE trends).

The feldspar-porphyritic (FP) and quartz-feldspar-porphyritic (QFP) rhyolite units that occur stratigraphically above the mafic volcaniclastic unit have the lowest SiO_2 contents of the felsic facies (~65-73 wt.%) and high Al_2O_3 (~11.4-14.2 wt.%), Na_2O (~4.9-5.8 wt.%), and CaO (~2.0-6.0 wt.%), consistent with the abundant plagioclase phenocrysts observed in thin section. TiO_2 and P_2O_5 are higher in the two feldspar-porphyritic units than in the QP rhyolite. The feldspar and quartz-feldspar porphyries have low CO_2 contents (~1-4 wt.%), consistent with the lack of alteration in these coherent flows. Incompatible HFSE concentrations are lower than in QP rhyolite, but Sc

and V are generally higher. Incompatible LILEs are also lower but concentrations of Sr are higher. Hanging-wall FP and QFP rhyolites are depleted in REE compared to footwall QP rhyolite.

6.2 GEOCHEMISTRY OF ALTERATION AND MINERALIZATION TYPES

There is generally very good agreement between both major and trace element geochemistry and alteration and mineralization identified by field mapping and petrography.

Fe-rich carbonate and chlorite alteration is clearly characterized by high CO_2 (>1 to nearly 10 wt.%) and low Fe_2O_3 (<4 wt.%) and Na_2O (mostly <3 wt.%). The presence of up to 6.5 wt.% CaO in assemblages dominated by Fe-rich alteration is consistent with the presence of abundant Fe-bearing carbonate observed in outcrop and in thin section. However, zones of intense Fe-rich carbonate alteration are overall depleted in total Fe, reflecting the destruction of Fe-sulfide in the main upflow zone (Figure 6.1a). Low Fe_2O_3 coupled with abundant CO_2 (Figure 6.1b) in these zones supports the replacement of sulfide by CO_2-rich fluids, as interpreted from field and petrographic relationships. The most abundant S in the footwall (~1-1.5 wt.% S) clearly occurs along the interpreted margins of the system (Figure 6.2), supporting observations of sulfide destruction. S is notably low in the stockwork zone immediately beneath the known orebody (Figure 6.2). The low S concentrations coincide with zones of high CO_2. The Na-depletion supports the interpretation of the alteration map pattern corresponding to the main hydrothermal upflow at Delbridge (Figure 6.3a). K_2O distribution is inversely related to Na_2O (Figure

6.3b), reflecting K-metasomatism coincident with destruction of primary plagioclase.

High CaO along the interpreted margins of hydrothermal upflow and in the hanging wall (Figure 6.4a) correlates with CO_2 (cf. Figure 6.1b), supporting the abundant Ca-rich carbonate mapped in these zones. Similarly, high MgO (~0.5-4.5 wt.%; Figure 6.4b) and Al_2O_3 (~9 to nearly 12 wt.%; Figure 6.5a) and relatively low CO_2 (~0.3 to <5 wt.%) clearly correspond to zones of intense Mg-rich chlorite ($\pm$ epidote) and sericite alteration outside of the interpreted main upflow and in the hanging wall. Li concentrations are consistently elevated (up to 41 ppm) in these chloritized marginal zones and in the mafic volcaniclastic rocks of the immediate hanging wall, possibly reflecting substitution in chlorite and/or sericite (Figure 6.5b). Aluminous Li-bearing chlorite has been documented in hydrothermal systems (Rozinova and Dubik, 1983; Bailey and Lister, 1989). Concentrations of Ba (~250-400 ppm; up to ~900 ppm) and Sr (~50-200 ppm) are generally higher in the immediate hanging wall and shallow footwall (Figure 6.6). The Ba is most likely in muscovite, whereas Sr may be substituting for Ca in carbonate. High MnO (~0.2-0.9 wt.%) corresponds to the interpreted main hydrothermal upflow in footwall stringers and stockwork and in hanging-wall mafic volcaniclastic rocks and FP rhyolite (Figure 6.7a). This distribution resembles both CaO and CO2 patterns (cf. Figures 6.4a and 6.1b), suggesting substitution of Mn^{2+} for Ca^{2+} in Fe-bearing carbonate.

Silicification is most intense in proximity to the interpreted paleo-seafloor, in the hanging wall, and in a pod-like zone immediately beneath the orebody surface projection;

however, these trends are not shown by the distribution of whole-rock SiO_2 data due to different rock types (Figure 6.7b). Hanging-wall FP and QFP rhyolites and mafic volcaniclastic rocks are depleted in REE compared to footwall QP rhyolite facies (Figure 6.8), possibly due to dilution by the addition of silica. In the hanging wall, elevated Na_2O (up to ~6-7 wt.%; Figure 6.3a) reflects the albite observed in thin section.

Cu concentrations are generally low (~5-80 ppm) in the footwall, except in and proximal to rhyolite breccia contacts (up to 225 ppm Cu; Figure 6.9a). Notably, samples from the stockwork zone contain very little Cu (<25 ppm). Cu content is consistently higher (~40-150 ppm) in the shallow hanging wall and proximal to the interpreted paleo-seafloor and the two inferred synvolcanic faults (Figure 6.9a). The highest Zn concentrations appear inversely related to Cu content with the highest Zn occurring stratigraphically below the stockwork (up to ~440 ppm Zn; Figure 6.9b) and more distally along rhyolite breccia contacts (up to nearly 900 ppm Zn). The same pattern is evident for Pb (Figure 6.10).

MAJOR ELEMENT CORRELATIONS

A Pearson correlation matrix of major, trace, and rare-earth elements in rhyolite at Delbridge is shown in Table 6.2a. SiO_2 is most highly correlated with K_2O, supporting the abundant quartz-sericite alteration identified towards the interpreted margins of hydrothermal upflow. Strong negative correlation with all other major components (especially carbonate) may indicate dilution by silica. The association of Al_2O_3 with Na_2O reflects the primary albite component. A clear inverse relationship between Na_2O

and K_2O confirms the Na-depletion and K-metasomatism mapped in the main upflow zone. CaO, MgO, and Fe_2O_3 correlate well with CO_2 and LOI, which reflects the major carbonate component and supports the presence of abundant Fe- and Mg-bearing carbonate (e.g., dolomite, ankerite) in the footwall at Delbridge. Strong correlation of Fe_2O_3 and MgO ($\pm$ Al_2O_3) also reflects the chlorite component. Co-enrichment of CaO, CO_2, and MnO suggests the substitution of Mn^{2+} in calcite. Association with P_2O_5 (phosphate) and TiO_2 (rutile) is also characteristic of the carbonate components.

A Pearson correlation matrix of major, trace, and rare-earth elements in hanging-wall mafic volcaniclastic rocks at Delbridge is shown in Table 6.2b. Co-enrichment of SiO_2, Al_2O_3, Na_2O, and MgO reflects primary clinopyroxene, albite (spilitization?), and Mg-rich chlorite and epidote alteration. Strong negative correlation of Na_2O and K_2O supports the mapped hydrothermal plume extending into the hanging wall. Extreme co-enrichment of CaO, CO_2, and MnO confirms the highly abundant calcite identified in thin section and suggests the substitution of trace Mn^{2+}. Weak positive and strong negative correlation of CO_2 with Fe_2O_3 and MgO, respectively, affirms the absence of Fe- and Mg-bearing carbonate in the hanging wall. TiO_2 (rutile) and phosphate (P_2O_5) also appear associated with ferromagnesian components (i.e., Fe_2O_3, MgO, Al_2O_3) in mafic volcaniclastic rocks.

TRACE ELEMENT CORRELATIONS

At Delbridge, SiO_2 is strongly correlated with both high-field strength elements (HFSE; Zr, Hf, Ta, Y, Nb, U, and Th) and rare-earth elements (REE), typical of felsic

volcanic rocks (Table 6.2a). A stronger correlation with heavier REE is apparent, possibly indicating mobility of the LREE related to SiO_2 gains and losses, especially in the silicified pod-like zone mapped in stringers and stockwork immediately beneath the orebody surface projection. K_2O is strongly correlated with Ba, Rb, Cs, Be, Tl, Ga, In, and REE, reflecting the muscovite component. Trace alkali and alkali earth metals are likely substituted for K^+ in muscovite. Notable co-enrichment of the trace elements Li, Sr, Sc, V, Cr, Cu, Co, Ni, Ti, P, and Sb with MgO and Fe_2O_3 ($\pm$ Al_2O_3) reflect the chlorite component. Correlation of Li, Sr, Cr, Sc, and V with CO_2, CaO, Fe_2O_3, and MgO is also characteristic of the carbonate component. Correlation of Na_2O, Al_2O_3, Sr, and Eu likely indicates the albite component. Trace phosphate (P_2O_5) and rutile (TiO_2) are most strongly associated with Li, Sr, Cr, Sc, and V. Pyrite component (Fe_2O_3) indicates co-enrichment of Cu, Zn, Co, and Ni ($\pm$ Pb, Sb, Bi, Ga, and In). Base metals (Cu, Zn, Pb) show negative correlation with CO_2, supporting sulfide destruction and carbonate replacement. Cu appears most strongly associated with the chlorite component (Fe_2O_3 $\pm$ MgO, Al_2O_3, TiO_2, P_2O_5, Sc, and V), Bi, In, and Sn. Zn is more closely associated with SiO_2, K_2O, HFSE, Ba, Cs, Li, Rb, Pb, Cd, Ga, In, Sn, and W. Traces of Cd (<2.4 ppm) appear to correlate well with both Zn and Pb. Sb is only very slightly anomalous (~1-2 ppm) immediately beneath and proximal to the paleoseafloor.

Unlike the felsic stratigraphy, HFSE and REE are not correlated with SiO_2 in mafic volcaniclastic rocks at Delbridge (Table 6.2b). Fe_2O_3 and MgO ($\pm$ SiO_2), Cr, Sc, and V are strongly correlated, typical of mafic rocks and chlorite ($\pm$ epidote) alteration. Cs, Li, Rb, Sr, Pb, Tl, and Ni are associated with carbonate components in altered mafic

volcaniclastic rocks. Phosphate (P_2O_5) and rutile (TiO_2) appear associated with ferromagnesian ($\pm$ chlorite) components (i.e., Fe_2O_3, MgO, Al_2O_3), HFSE, and REE in mafic volcaniclastic rocks. Base metals (Cu, Zn, Pb) appear most strongly correlated to SiO_2, Al_2O_3, and Na_2O in less altered mafic rocks.

IDENTIFICATION OF LEAST-ALTERED RHYOLITE COMPOSITIONS

Quantifying the chemical changes typically caused by hydrothermal alteration and metamorphism requires the identification of a least-altered rock composition. Due to the intense alteration at Delbridge, it is highly unlikely that true protolith compositions for either footwall or hanging-wall rhyolites still exist. Least-altered compositions may however be estimated by comparison with typical fresh-rock compositions for high silica rhyolites elsewhere in the Abitibi subprovince and by consideration of a number of geochemical criteria listed in Table 6.3 (e.g., Barrett et al, 1993; Koopman et al, 1999; Prior et al, 1999a, b). All samples collected within fragmental facies were excluded as candidates due to possible mixed provenance. Three QP rhyolite samples (RW001, RW006, and RW026) were selected to represent least-altered compositions in the footwall and are identified in each of the relevant lithogeochemical tables. The average of these three analyses gives a reasonable estimation of the least-altered composition for footwall QP rhyolite. One sample (RW021), which satisfies the geochemical criteria shown in Table 6.3, is selected as the representative least-altered composition for hanging-wall feldspar porphyritic rhyolites.

Comparison of analytical data for altered samples with estimated protolith

compositions using elements that have remained immobile can provide useful quantitative information with respect to the hydrothermal activity proximal to ore deposits (MacLean and Kranidiotis, 1987; Barrett et al, 1993; MacLean and Barrett, 1993; Skirrow and Franklin, 1994). Though the concentrations of immobile elements may be affected from net mass changes in the system due to alteration, their inter-element ratios theoretically remain the same. Elements that have been shown to remain essentially immobile during alteration of VMS deposits include Al, Ti, Zr, Nb, Y, heavy REE (Lu, Yb), Hf, and Ta (MacLean and Kranidiotis, 1987; MacLean and Barrett, 1993; Gifkins et al, 2005).

For the Delbridge sample suite, the elements Zr, Y, Nb, Hf, Ta, Ti, Al, Th, Yb, and Lu were all tested for immobility. Following the procedures of MacLean and Kranidiotis (1987) for a single precursor, immobile element pairs will produce highly correlated ($r > 0.85$) linear trends that project from the origin on x-y bivariate plots (Figure 6.11). Zr, Nb, Hf, Ta, Yb, and Lu all have highly correlated linear trends with other variables. However, Zr is selected as the immobile monitor component for mass balance calculations because of its high correlation coefficients and its much greater abundance, which reduces the likelihood of analytical errors affecting the calculations.

Incompatible Elements

Highly incompatible trace elements, which tend to be excluded from mineral lattices in crystallizing magmas and are partitioned into the melt, are used to monitor fractionation. The high-field strength elements (HFSE) Zr, Y, and Nb are generally

incompatible except in some calc-alkaline suites (Gifkins et al, 2005). Samples from different magmatic suites produce separate linear trends of magmatic enrichment on incompatible-incompatible immobile element plots (MacLean and Barrett, 1993; Gifkins et al, 2005). Some HFSE ratios change with magmatic affinity, providing reliable discriminants unaffected by alteration. Zr/Y ratios with ranges of ~3 to 5 are tholeiitic, ~5 to 7 are transitional, and ~7 to 30 are calc-alkaline suites (MacLean and Barrett, 1993). At Delbridge, the vast majority of collected samples fall within the tholeiitic range of an incompatible-incompatible Y-Zr plot (Figure 6.12). A small subset of samples collected in the stratigraphic hanging wall plots within the transitional to mildly calc-alkaline series. These magmatic affinities are consistent with La/Yb and Zr/Yb ratios (Table 6.4) and lithogeochemical trends previously identified at Delbridge by Barrett et al (1993). Figure 6.13a is a plot of Zr/Ti and Nb/Y immobile element ratios on the discrimination diagram of Winchester and Floyd (1977). The small number of samples that plot in the andesitic and sub-alkalic fields correspond to hanging-wall mafic volcaniclastic rocks and FP/QFP rhyolite, respectively.

Compatible Elements

Compatible elements are preferentially incorporated into minerals of crystallizing magmas (e.g., Al, Ti, Cr, Sc, and V) and are generally considered immobile during alteration (Gifkins et al, 2005). Bivariate plots of immobile compatible-incompatible element pairs (e.g., TiO_2-Zr) should produce negative fractionation trends (Figure 6.13b). On such diagrams, net mass changes caused by alteration will yield separate alteration lines for each chemically distinct rock unit (MacLean and Barrett, 1993; Barrett et al,

1993). A single fractionation curve has not been estimated because of an insufficient number of samples. However, two separate alteration lines projected from the origin and corresponding to two compositionally distinct precursor rhyolites are evident. These are referred to as rhyolites A and B to remain consistent with terminology used in previous studies at Delbridge (Barrett et al, 1993). Samples falling within the andesitic compositional range are those collected from the fine-grained hanging-wall mafic volcaniclastic unit. Samples falling along the rhyolite A trend (Figure 6.13b) correspond to coherent QP rhyolite (± spherulitic), peperitic QP rhyolite lobes, and rhyolite breccia in the stratigraphic footwall. The large spread of samples along the rhyolite A trend is consistent with the significant alteration within the felsic footwall. Samples that lie along the rhyolite B trend (Figure 6.13b) correspond to the FP and QFP rhyolites in the hanging wall that are significantly less altered.

Bivariate plots of Ta vs. Zr and Nb vs. Zr (Figures 6.14a, b) confirm the consistent separation into two rhyolite types with the mildly calc-alkaline samples, rhyolite B, displaying a somewhat lower slope than rhyolite A. Plots of the heavy REE vs. Zr (not shown) support the relationships established in the TiO_2-Zr diagram.

Mass Gains and Losses due to Alteration

Mass balance techniques are used to quantify the amounts of individual elements added to or removed from the rock as a result of alteration (Gifkins et al, 2005; Barrett and MacLean, 1994). Gains and losses of each mobile element are based on the concentration or dilution of an immobile element monitor. The absolute mass change for

each component is calculated using the following formula:

$$\Delta^a = [Z^o / Z^a \cdot C^a] - C^o$$

where Δ^a is absolute mass change expressed in g/100 g, C^a is the wt.% proportion of component in altered rock, C^o is the wt.% proportion of component in precursor rock, Z^a is the proportion of immobile element in altered rock, and Z^o is the proportion of immobile element in precursor rock (MacLean and Kranidiotis, 1987; MacLean and Barrett, 1993; Gifkins et al, 2005). This approach assumes no change in volume during alteration. However, substantial volume increases for many of the alteration types are evident from the extensive brecciation and fracturing. Therefore, the estimated mass changes are minimum values. Because two compositionally distinct rhyolite precursors have been identified, the mass change calculations for samples falling along rhyolite A and rhyolite B alteration lines were determined relative to their corresponding precursor compositions. Precursor compositions for respective rhyolite types shown in Table 6.5 represent the calculated averages of least-altered samples. As stated above, Zr is chosen as the most suitable immobile monitor for mass balance calculations at Delbridge.

Average mass changes for individual elements in different alteration types have been plotted on histograms in Figures 6.15a and 6.15b. In the stratigraphic footwall at Delbridge, large positive net mass changes are mainly due to SiO_2 addition, with smaller additions of Al_2O_3, CaO, Fe_2O_3, MgO, and CO_2, associated with carbonate, chlorite, and sericite alteration. The largest addition of CO_2 occurred in Fe- and Ca-rich assemblages; MgO addition was mainly as Mg-chlorite. The hanging wall experienced much less net mass change due to alteration (e.g., up to 20 g/100 g versus 50 g/100 g in the footwall).

Pearson correlation matrices of major element mass changes in both footwall and hanging-wall rhyolite are shown in Tables 6.6a and 6.6b. Strong negative correlation supports addition of K_2O coincident with loss of Na_2O in most alteration types. CO_2 addition is most closely associated with CaO, MgO, and Fe_2O_3, confirming the abundant Fe- and Mg-bearing carbonate identified in thin section. Minor MnO input is also clearly linked to CO_2. Co-enrichment of Na_2O, Al_2O_3, SiO_2, CaO ($\pm$ Fe_2O_3, MgO), MnO, and CO_2 in zones of Fe-rich carbonate alteration (Figure 6.15) may reflect the co-precipitation of ankerite ($\pm$ chlorite) and paragonite (see Normative Alteration Mineralogy below and Chapter 8.2: Mineral Chemistry). CO_2 addition is weakly correlated with loss of S in the footwall, which may support sulfide destruction coincident with carbonate replacement. In the hanging wall, very minor S addition (Table 6.5) is strongly associated with significant CO_2 input (Table 6.6b), possibly confirming CO_2-rich mineralizing fluids. Co-enrichment of S, K_2O, and Al_2O_3 in the hanging wall may reflect the remobilization of chalcopyrite and muscovite into cleavage domains commonly identified in thin section.

Rare-Earth Elements (REE)

Chondrite-normalized rare-earth element analytical data for Delbridge are presented along with La/Yb ratios in Table 6.7. As noted previously, all of the QP rhyolite facies in the footwall have La/Yb ratios of ~1.7-2.6, falling in the range of tholeiitic rhyolite (MacLean and Kranidiotis, 1987), whereas the hanging-wall FP and QFP rhyolites are in the mildly calc-alkaline range with La/Yb ratios of ~2.7-3.8.

Chondrite-normalized REE profiles for footwall QP rhyolite facies are flatter than those for hanging-wall FP and QFP rhyolite units (Figure 6.16b). These results are consistent with earlier findings by Barrett et al (1993).

Rare-earth elements (except Eu) are typically incompatible during igneous fractionation and only the heavy REE (Lu and Yb) are essentially immobile during hydrothermal alteration (MacLean and Barrett, 1993; Gifkins et al, 2005). Data for the light REE (particularly La) commonly show some degree of mobility. Incremental decreases in mobility from the light to the heavy REE are reflected in the slopes of chondrite-normalized REE profiles (MacLean and Barrett, 1993; Gifkins et al, 2005). This is evident in the Delbridge footwall where chondrite-normalized REE profiles have different slopes that converge towards heaviest REE (Figure 6.16c). This fan-shaped array of REE profiles is common in proximal alteration zones associated with VMS deposits (MacLean and Barrett, 1993). Some samples in the Delbridge suite show no differences in the REE behaviour as evidenced by sub-parallel chondrite-normalized profiles (Figure 6.16d). However, net mass changes in the system associated with alteration can produce significant vertical shifts of these profiles (MacLean and Barrett, 1993; Gifkins et al, 2005). Figure 6.16d shows these shifts in samples representative of different alteration types compared to least-altered rhyolite samples. Fe-carbonate ($\pm$ chlorite) alteration causes an upward shift of the profiles indicating net addition of REE by leaching (mass loss) and residual concentration. Strongly silicified samples are shifted downward as a result of net mass gain and dilution of REE. The REE profiles for Ca-rich carbonate samples have a large negative Eu anomaly relative to Fe-rich samples. This

may indicate slight positive enrichment of Eu^{2+} in reduced hydrothermal fluids responsible for Fe-carbonate precipitation.

Alteration Intensity

Simple, multi-component, or normalized ratios of major elements that are mobile during hydrothermal alteration can be used to determine alteration styles, quantify alteration intensity, and define exploration vectors (Gifkins et al, 2005). Alteration indices typically use proportions gained during alteration in the numerator and those lost in the denominator, which yields the greatest values for the most strongly altered rocks.

Ishikawa Alteration Index (AI)

The classic example commonly used in VMS systems is the Alteration Index (AI) of Ishikawa et al (1976):

$$AI = [100 (MgO + K_2O)] / [MgO + K_2O + CaO + Na_2O]$$

expressed as weight percentages (wt.%) and conveniently producing a potential range from zero to one hundred. The AI was originally devised as a measure of sericite and chlorite intensity associated with footwall alteration of the Kuroko-style VMS deposits. The key reactions measured by the AI are the breakdown of sodic plagioclase and volcanic glass and the subsequent replacement by sericite and chlorite (Ishikawa et al, 1976; Large et al, 2001). Values in unaltered rhyolite range from 20 to 60; values in altered rocks are typically from 50 to 100, with an AI of 100 indicating complete replacement of feldspars and glass (Ishikawa et al, 1976; Large et al, 2001). AI values

tend to increase to maximum values in the proximal hydrothermal alteration beneath massive sulfide lenses (Gifkins et al, 2005; Saeki and Date, 1980). Since loss of Na is generally the major chemical change in the breakdown of plagioclase, there is a strong inverse relationship between AI and Na concentration (e.g., Date et al, 1983; Large et al, 2001).

At Delbridge, Ishikawa AI values range from 10 to 95, with the majority (~90%) of the samples having values less than 60 (Table 6.8). The three highest AI values (>90) correspond to samples collected in zones of stringer and matrix-controlled sulfide and carbonate alteration within the interpreted hydrothermal upflow beneath the known massive sulfide orebody (Figures 6.17a, 6.18a). Low values (~10-35) in basal coherent rhyolite, proximal rhyolite lobes, and the hanging wall support host-rock permeability as the main control on alteration and mineralization at Delbridge.

Chlorite-Carbonate-Pyrite Index (CCPI)

Two major limitations of the Ishikawa AI are that it does not account for carbonate and that it cannot distinguish between chlorite- and sericite-rich alteration. Another ratio, the chlorite-carbonate-pyrite index (CCPI), has been devised to complement the AI and overcome these limitations:

$$CCPI = [100\ (MgO + FeO)] / [MgO + FeO + Na_2O + K_2O]$$

where FeO is the total ($FeO + Fe_2O_3$) content of the rock and the components are expressed as weight percentages (wt.%). The CCPI was designed to highlight the

prominence of Mg-Fe chlorite or carbonate, pyrite, and Fe-oxide common to the proximal alteration zones of many VMS deposits (Large et al, 2001). High CCPI values correspond to high FeO and MgO contents and suggest intense hydrothermal alteration. Because the CCPI of least-altered rocks is strongly dependent on primary composition, this index is not suitable for comparison of altered felsic and mafic rocks (Large et al, 2001).

CCPI values in the Delbridge suite range from roughly 30 to 95, with the majority (nearly 70%) of the samples having values less than 60 (Table 6.8). The highest CCPI values correspond to samples collected in rhyolite breccia, along breccia contacts, and in fractured facies proximal and beneath known mineralization (Figures 6.17b, 6.18b). Similar to the Ishikawa AI, low CCPI values in basal coherent rhyolite, proximal rhyolite lobes, and the hanging wall confirm the significance of host-rock porosity and permeability on hydrothermal fluid flow at Delbridge.

The Alteration Box Plot

A bivariate plot with the Ishikawa AI on the horizontal axis and the CCPI on the vertical axis, termed the *alteration box plot* by Large et al (2001), provides a useful illustration of the intensity of alteration (Figure 6.19). Least-altered volcanic rocks plot towards the center of the diagram and hydrothermally altered rocks plot towards the dominant mineral phases. Mineral end-members (albite, K-feldspar, sericite, chlorite, pyrite, dolomite, ankerite, and epidote) plot along the boundaries of the diagram. Large et al (2001) explain that the common diagenetic minerals (albite, K-feldspar, calcite, and

epidote) plot on the left-hand CCPI axis or the lower AI axis, whereas proximal hydrothermal minerals (sericite, chlorite, pyrite, dolomite, and ankerite) plot on the right-hand CCPI axis and the upper AI axis. Thus the diagonal line joining epidote and K-feldspar (Figure 6.19) separates the field of hydrothermal alteration in the upper right from the field of unaltered or diagenetic effects in the lower left. Large et al (2001) have identified common trend lines associated with specific hydrothermal and diagenetic alteration styles.

Least-altered footwall and hanging-wall rhyolite samples at Delbridge plot within the box bounded by an AI of ~10 to 30 and a CCPI of ~30 to 55 (Figure 6.19). Variably altered samples are subdivided into two clearly separated alteration fields that both plot within the hydrothermal alteration field. Field 1 includes strong sericite-chlorite-pyrite alteration of samples collected in the interpreted hydrothermal upflow zone beneath the known mineralization. Large et al (2001) typify this trend as the intense proximal footwall alteration of a VMS system. Samples that fall within Field 2 exhibit variable carbonate and chlorite with generally moderate sericite alteration. Samples dominated by carbonate and chlorite alteration are typically developed immediately adjacent to the massive sulfide mineralization within proximal footwall rhyolite breccia. Abundant carbonate and weaker sericite alteration also occur in proximal rhyolite breccia, as well as in the immediate hanging wall.

Carbonate Index

Intensity of carbonate alteration can be measured using molar proportions of the

components CO_2, CaO, FeO, and MgO in the following equation:

$$\text{Carbonate Index} = CO_2 / (CaO + FeO + MgO)$$

where FeO is the total ($FeO + Fe_2O_3$) content of the rock and the components are expressed in molar concentrations. This produces a potential range from zero to one. Carbonate index values at Delbridge are highly variable, ranging from 0.1 to 0.98 molar units (Table 6.8). The distribution of these normalized indices indicates that the intensity of carbonate alteration is highest in stringers and stockwork within the interpreted hydrothermal upflow, in the adjacent rhyolite breccia pile, and in the hanging wall in proximity to the more northerly of the two inferred synvolcanic faults (Figure 6.20a). This is consistent with earlier observations of total CO_2 concentrations (cf. Figure 6.1b).

Manganese Carbonate Index

Manganese carbonate alteration in a rock can be estimated from molar proportions of the components MnO and CO_2 in the following equation:

$$\text{Mn-carbonate index} = MnO / CO_2$$

where the components are expressed in molar concentrations, producing a range of values from zero to one. Weakly anomalous Mn-rich carbonate values (<0.26) occur mostly in footwall stockwork and overlying rhyolite breccia proximal to the inferred synvolcanic faults (Table 6.8; Figure 6.20b).

Normative Alteration Mineralogy

An estimate of the modal proportions of alteration minerals in a rock sample can be made by calculating normative abundances from whole-rock geochemical data (MacLean and Barrett, 1993). Mineral abundances can be calculated from bulk-rock data using the least-squares method described by Herrmann and Berry (MINSQ; 2002). Unlike earlier normative calculation procedures (e.g., GENMIX, Le Maitre, 1981; SEDNORM, Cohen and Ward, 1991), MINSQ does not incrementally partition components in a strict mineral hierarchy. Instead, MINSQ calculates a best-fit solution to the compositional data using the *Solver* analysis tool in Microsoft Excel™ to iteratively adjust the proportions of all specified phases (Herrmann and Berry, 2002).

The *Solver* tool minimizes the sum of squared (SSQ) residuals by varying its estimated proportions of minerals in an assemblage selected by the user. Residuals reflect differences between actual and calculated proportions (wt.%) of the input major element geochemical data and residual SSQ values of less than 0.5 typically indicate acceptable estimation of the mineral assemblage (Herrmann and Berry, 2002). A residual SSQ value of greater than 0.5 requires further inspection of the individual residuals to determine which chemical components are causing the most error and the suitability of the hypothetical assemblage. It is thus ideal for the user to have fundamental geological and mineralogical knowledge of the analyzed samples. Normative mineral compositions are input by the user and are derived from either ideal stoichiometric mineral formulae or directly from electron microprobe analyses of samples in the same area. MINSQ varies the estimated proportions of specified minerals to a sum of $\leq$ 100 wt.% to avoid unrealistic negative or overestimated totals (Herrmann and Berry, 2002). MINSQ can

also estimate the composition of a stoichiometrically variable mineral by using multiple ideal end-member compositions in the calculation. The average composition is weighted by the MINSQ proportions of the end-members, providing an estimate of the mineral composition (Herrmann and Berry, 2002).

Mineral estimates of quartz, albite, muscovite, chlorite, carbonate, epidote, and rutile were made for each sample and are presented in Table 6.9. Multiple compositional end-members were included in the calculations for muscovite, chlorite, and carbonate. The presence of different members of these series is supported by SWIR and microprobe data (see Chapter 8).

Least-altered samples towards the margins of the hydrothermal system have an average normative composition of ~50% quartz, 30% albite, 10% sericite, and 5% each of chlorite and carbonate. This correlates well with modal mineralogy established during petrographic studies (Table 4.1). Quartz abundance is generally higher in the alteration zone (up to 70 wt.%) and to a lesser extent in the quartz-sericite-chlorite assemblages. The highest quartz values clearly occur along the margins of the hydrothermal upflow and in the upper parts of the alteration pipe within stockwork. The lowest quartz contents are observed in the hanging wall and in carbonate-rich footwall samples.

White mica abundance is greatest (up to nearly 30 wt.%) in proximal footwall rhyolite breccia and in the stockwork beneath the orebody (Figure 6.21). Generally very little white mica is estimated in hanging-wall samples. Paragonite [$NaAl_2(AlSi_3)O_{10}(OH)_2$] is the dominant compositional end-member of normative white

mica calculated in the Delbridge sample suite but this likely reflects underestimation of primary albite. However, Franklin (1997) noted that paragonite, while generally not the most abundant mica species in alteration pipes, is common even in Na-depleted rocks. Phengite [$KAl_2(AlSi_3O_{10})(OH)_2$-$K(Mg,Fe^{2+})Fe^{3+}(Si_4O_{10})(OH)_2$] appears to occur most commonly towards the interpreted margins of the upflow zone and in the hanging wall (Figure 6.21), reflecting substitution of Mg^{2+} for Al^{3+} and sometimes increased silica in potassic white micas. Significant muscovite [$KAl_2(AlSi_3O_{10})(OH)_2$] abundance is only estimated in a few stockwork and coarse rhyolite breccia samples collected within the interpreted hydrothermal upflow (Figure 6.21). The compositional variation in normative white mica from potassic members proximal to the main upflow to more sodic members distally is interpreted to indicate Na-depletion and K-metasomatism typical of VMS-related hydrothermal alteration.

Fe-chlorite [$Fe_5Al)(AlSi_3)O_{10}(OH)_8$] is relatively localized with up to >15 wt.% in proximity to the two inferred faults bounding the hydrothermal upflow and at rhyolite breccia contacts (Figure 6.22). Notably, some of the higher Fe-chlorite values appear to occur in carbonate-poor samples. Normative Mg-chlorite [$Mg_5Al)(AlSi_3)O_{10}(OH)_8$] is most abundant (up to ~10 wt.%) in the shallow footwall and the immediate hanging wall (Figure 6.22). Increased Mg-chlorite is also observed along the margins of the interpreted upflow.

Normative carbonate (up to ~30 wt.%) occurs throughout the Delbridge rhyolites, but is clearly most abundant beneath the known mineralization and in adjacent rhyolite

breccia (Figure 6.23). The normative carbonate in the footwall is dominated by ankerite [$Ca(Fe,Mg,Mn)(CO_3)_2$], lesser siderite ($FeCO_3$), and trace dolomite [$CaMg(CO_3)_2$]. Normative siderite is clearly most abundant in stringers and stockwork within the interpreted core of upflow and in adjacent rhyolite breccia (Figure 6.23). Ca- and Mg-rich carbonate members are more abundant at the margins of the system (e.g., calcite, dolomite, and ankerite). Calcite ($CaCO_3$) abundance increases dramatically in the hanging wall where there is no significant Fe-rich carbonate. A few samples collected in the stockwork immediately beneath the surface projection of the orebody are predicted to contain trace to minor normative rhodocrosite (Figure 6.23) although none was identified in the studied samples.

Epidote is only estimated in ten samples (up to 15 wt.% in mafics; <10 wt.% in felsics) collected in the shallow footwall and immediate hanging wall.

6.3 GEOCHEMISTRY OF STRINGER AND DISSEMINATED SULFIDES

Systematic surface sampling of distal disseminated, fracture-, and matrix-controlled sulfides was done within an area of ~1 km^2 and at a spacing of approximately 50 to 100 m at Delbridge. Sulfide grains were obtained by crushing and sieving the rock sample into grain sizes ranging from 100-150 mesh, 150-200 mesh, and greater than 200 mesh. These grains were then super-panned into sulfide separates for chemical analyses. Analytical data, obtained by inductively coupled plasma (ICP) atomic emission spectrometry (AES) and mass spectrometry (MS) in the chemistry department at the University of Ottawa and by instrumental neutron activation analysis (INAA) at

Activation Laboratories Ltd. in Ancaster, Ontario, are summarized in Table 6.10. It should be noted that the sulfide separates were not necessarily entirely pure (e.g., some samples contain < 30-40 wt.% Fe as opposed to 46.5 wt.% for a good pyrite analysis).

Distribution plots of selected trace elements in pyrite are shown in Figures 6.24-6.29 and a correlation matrix identifies the main groups of elements (Table 6.11).

The co-enrichment of a consistent suite of trace elements in Zn-rich samples (Zn, Cd, Au, $\pm$Pb, $\pm$Ag, $\pm$Sb, $\pm$Bi, and $\pm$Hg) is characteristic of polymetallic sulfides in other volcanic-hosted massive sulphide deposits (e.g., Tanimura et al, 1983). The positive correlation of Cd and Pb with Zn in footwall rhyolite breccia ($\pm$ stringers and stockwork) and in the immediate hanging wall is similar to that documented in other Archean Cu-Zn deposits (e.g., Hannington et al, 1999; Table 6.11 and Figures 6.24b, 6.25). This shows that the pyrite being replaced is part of the hydrothermal system and not simply diagenetic or metamorphic in origin. Disseminated sulfides in these samples are notably enriched in Au ($\pm$Ag, $\pm$Bi, and $\pm$As; Table 6.11 and Figure 6.26) and show strong co-enrichment of As, Hg and Bi $\pm$ Sb, Tl (Figures 6.27b, 6.28). No minerals containing these elements were identified, suggesting the presence of unidentified trace minerals or inclusions in pyrite. Enrichment of REE most likely reflects concentration of heavy monazite and xenotime during superpanning; these are the likely source of REE enrichment in the altered wallrock.

High concentrations of Co and Ni (up to ~350 and 215 ppm, respectively) in Cu-

rich (up to ~0.2 wt.%) samples occur in stringers and stockwork within the interpreted hydrothermal upflow and stratigraphically below the mineralized horizon (Figures 6.24a, 6.29). Co and Ni show the strongest correlations with Cu (Table 6.11); however, discrete minerals containing Co and Ni were not identified. Strong correlation of Ni with As (Table 6.11; Figures 6.29b, 6.27a) and Te may indicate the presence of trace Ni-rich tellurides and arsenides, although none were observed. Slight co-enrichments of Eu and Cu as well as LREE and Sc are observed (Table 6.11).

A. Total Fe_2O_3

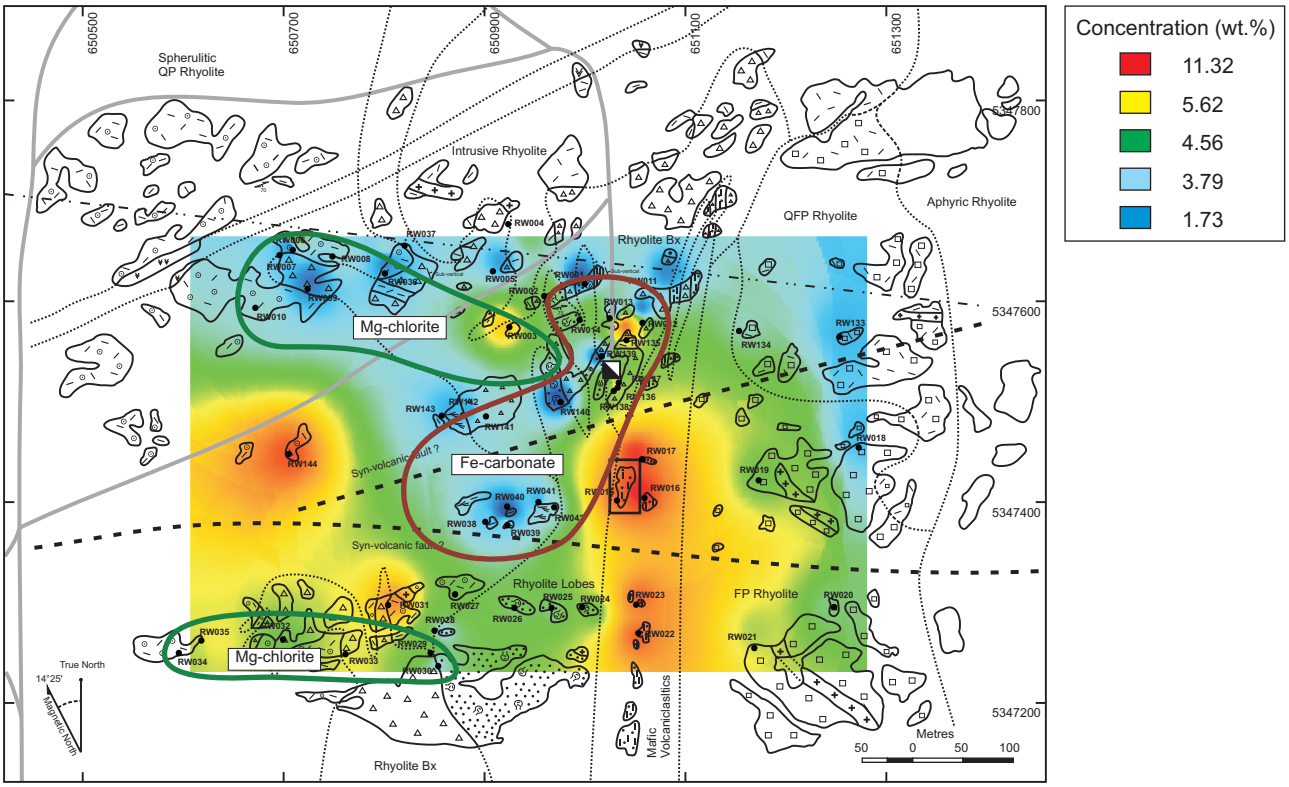

B. CO_2

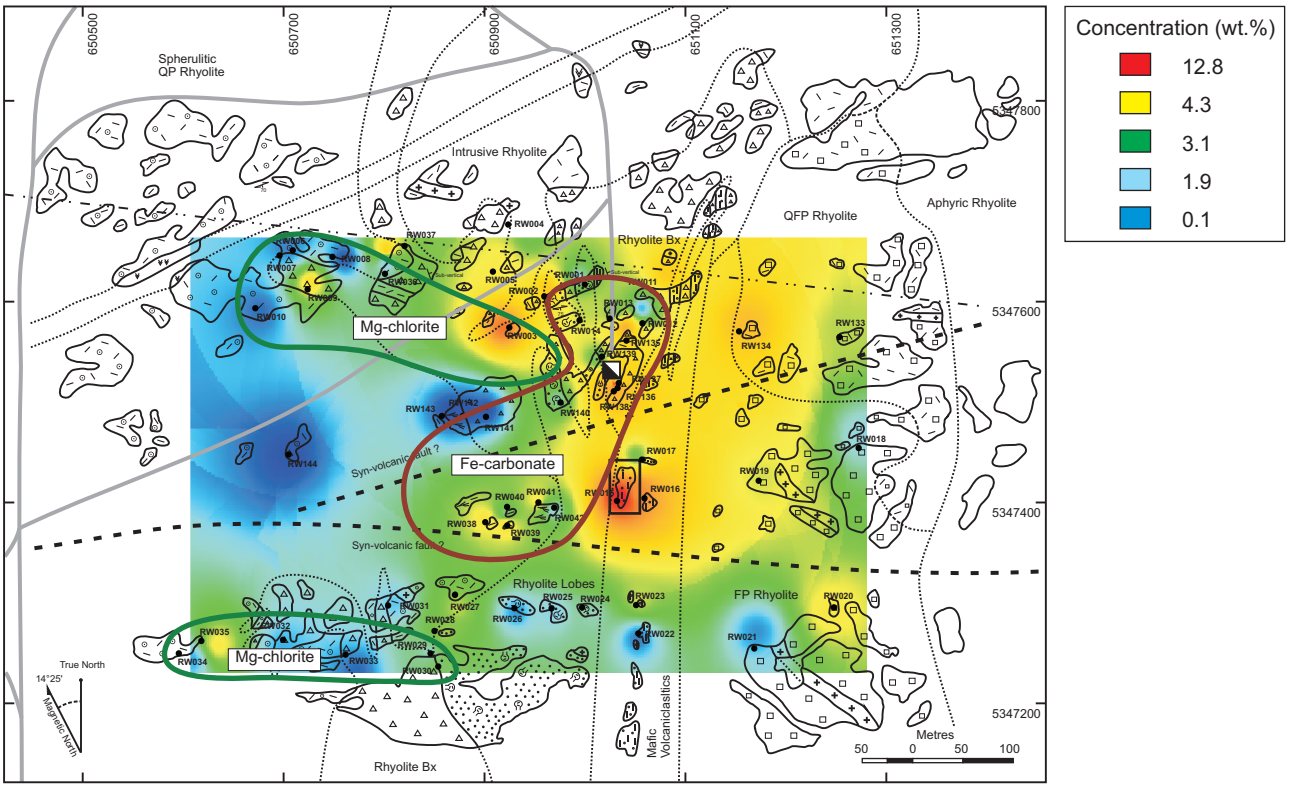

Figure 6.1. Concentrations (wt.%) of total Fe and CO_2 at Delbridge shown with respect to lithofacies and mapped alteration types. a) Total Fe as Fe_2O_3 corresponds to zones containing abundant distal disseminated sulfides along the interpreted margins of hydrothermal upflow and in the hanging wall. b) Abundant CO_2 clearly occurs in zones containing low total Fe, supporting replacement of sulfide by CO_2-rich fluids at Delbridge. All plotted data are based on quantitative whole-rock geochemistry and contoured using inverse-distance weighting (IDW).

Total S

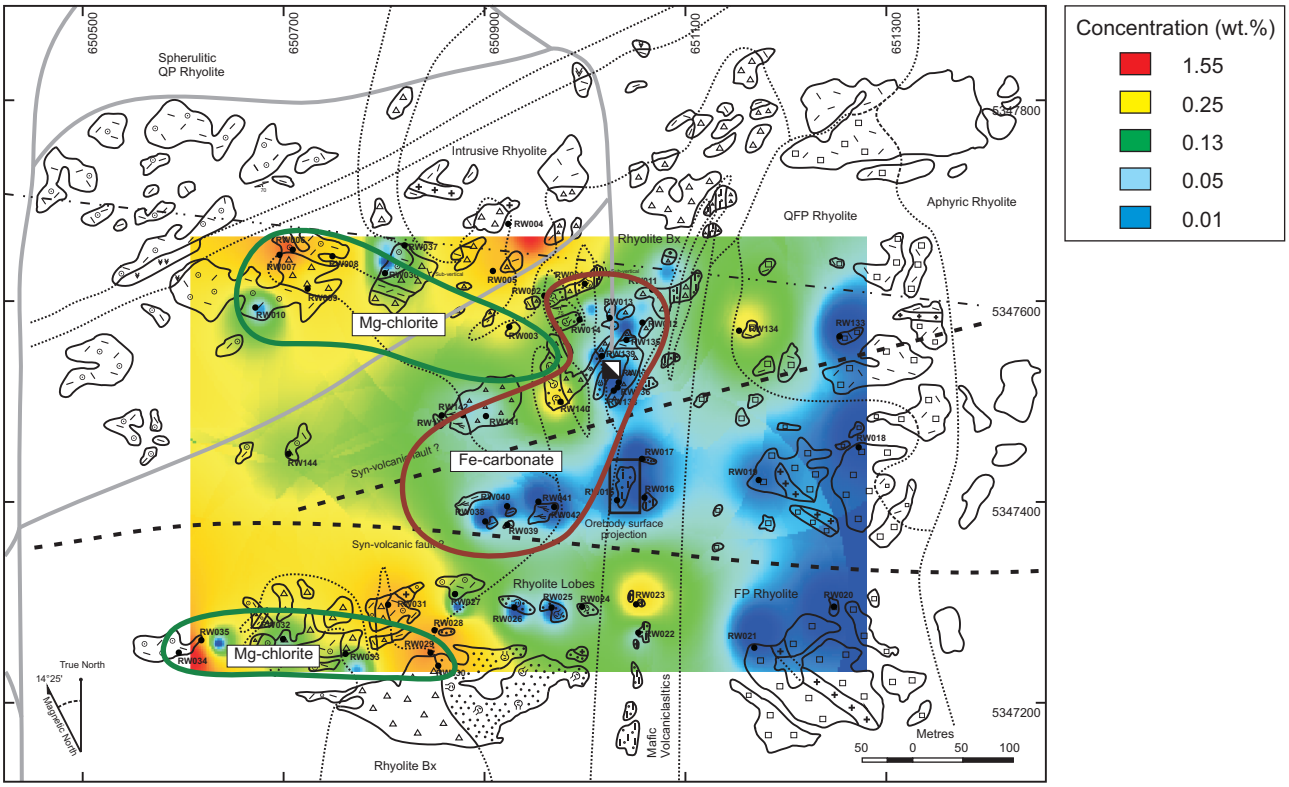

Figure 6.2. Concentrations of total S (wt.% S) at Delbridge shown with respect to lithofacies and mapped alteration types. The most abundant S in the footwall (~1-1.5 wt.%) clearly occurs along the interpreted margins of the system. S is notably absent in the stockwork zone located between the inferred synvolcanic faults and beneath the known orebody in zones of abundant carbonate alteration. All plotted values are based on quantitative whole-rock geochemical data and contoured using inverse-distance weighting (IDW).

A. Na_2O

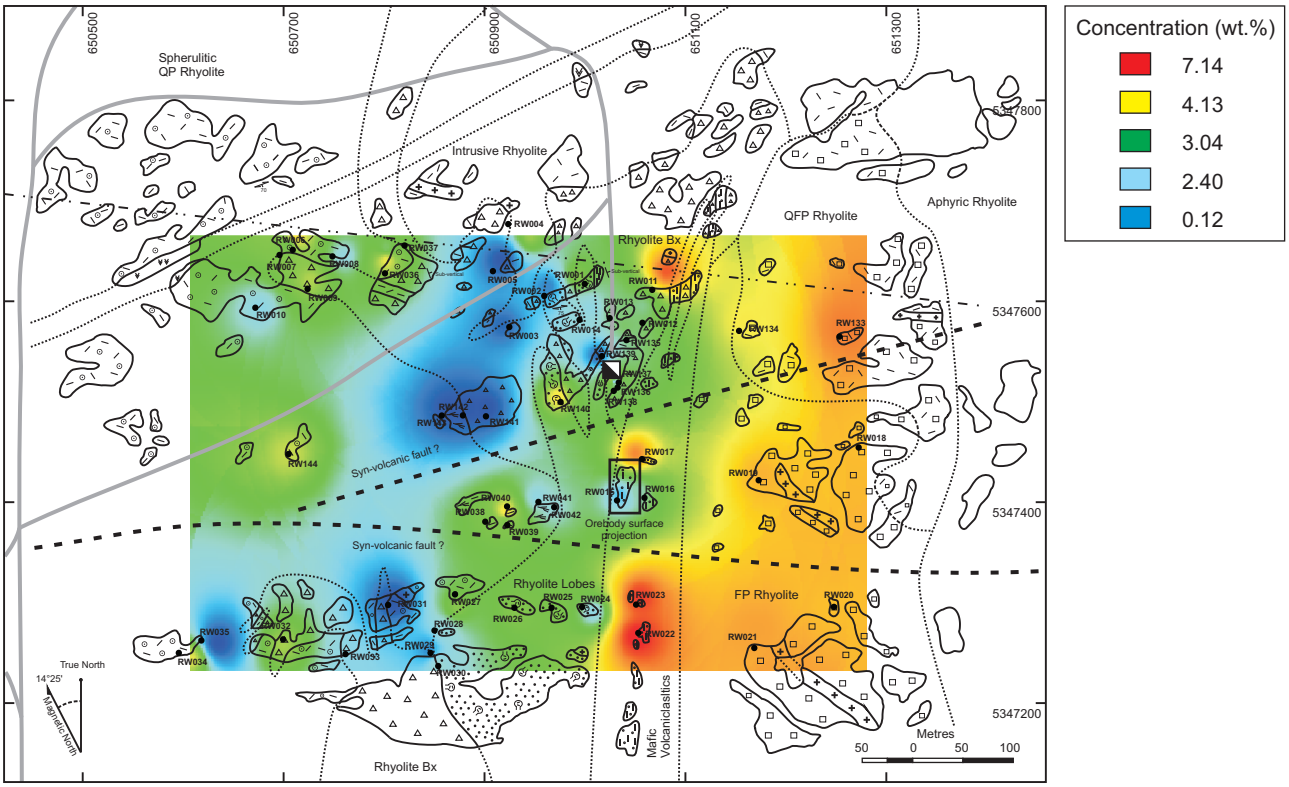

B. K_2O

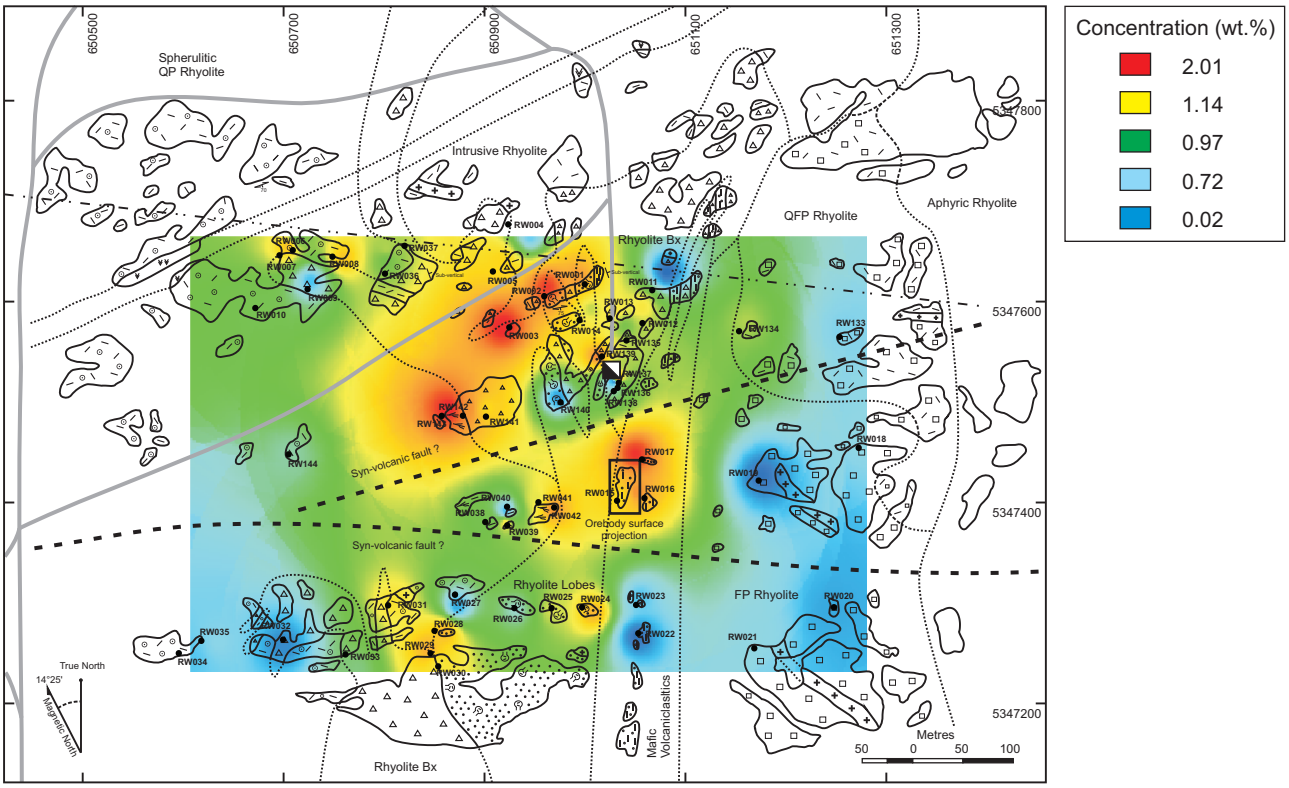

Figure 6.3. Concentrations (wt.%) of Na_2O and K_2O at Delbridge shown with respect to lithofacies. Plotted values are based on quantitative whole-rock geochemical data and contoured using inverse-distance weighting (IDW). a) Na_2O depletion is evident in the footwall with a sharp change to enriched values in the hanging-wall immediately above the mapped cherty ore horizon. b) K_2O concentrations are clearly inversely related to Na_2O with elevated values at the surface projection of known mineralization, in underlying stockwork, and in adjacent rhyolite breccia. Na depletion and associated K-metasomatism are characteristic vectors to mineralization in VMS systems.

A. CaO

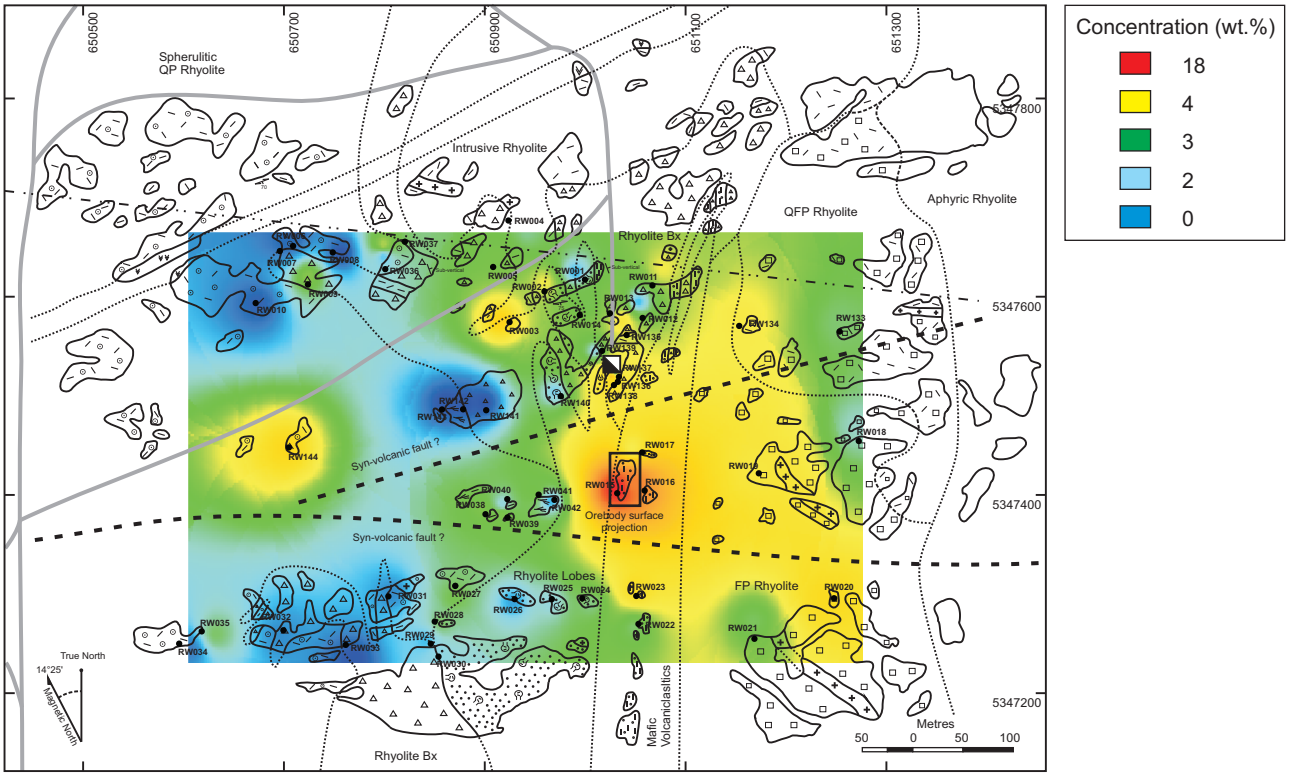

B. MgO

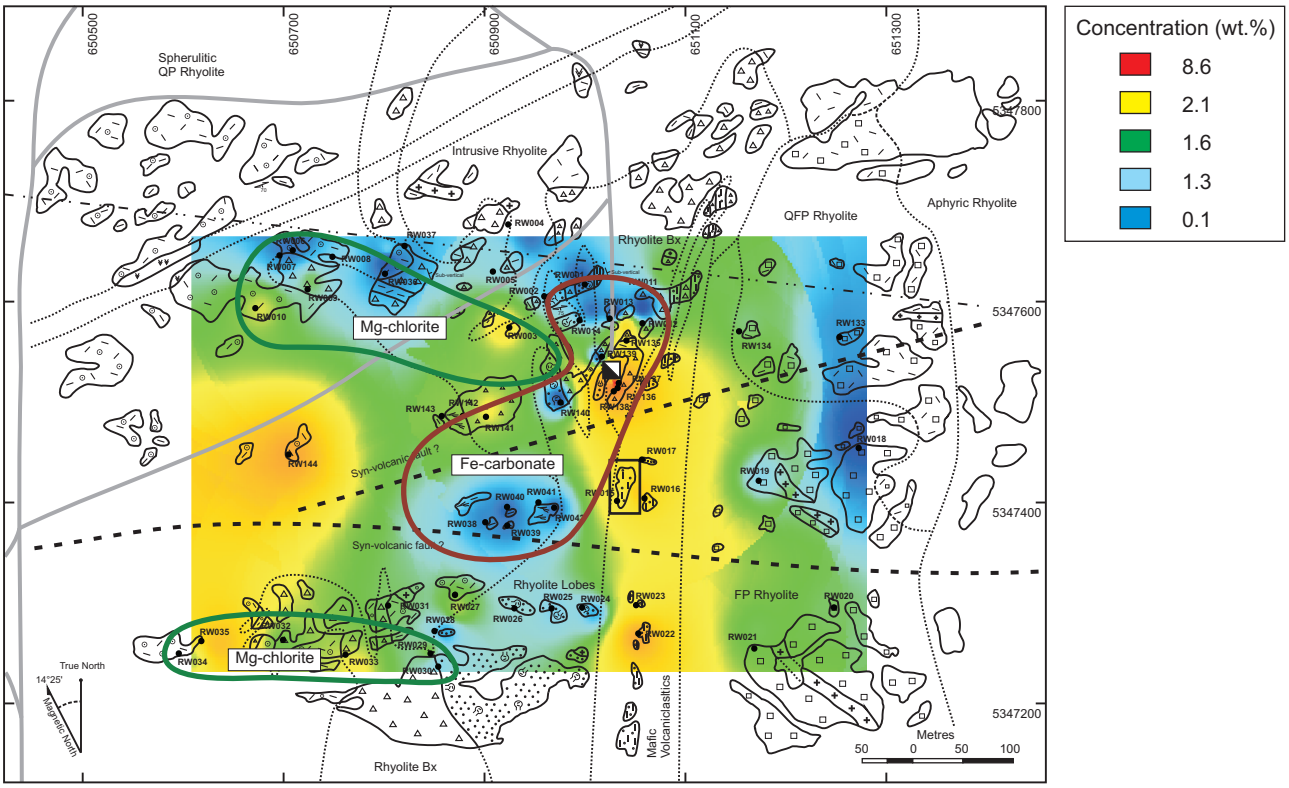

Figure 6.4. Concentrations (wt.%) of CaO and MgO at Delbridge shown with respect to lithofacies and mapped alteration types. All plotted data are based on quantitative whole-rock geochemistry and contoured using inverse-distance weighting (IDW). a) High CaO correlates with CO_2 (cf. Figure 6.1b), supporting abundant Ca-rich carbonate mapped along the interpreted margins of hydrothermal upflow and in the hanging wall. b) Similarly, high MgO clearly corresponds to mapped zones of intense Mg-rich chlorite (± epidote) outside of the interpreted main upflow and in the hanging wall.

A. Al_2O_3

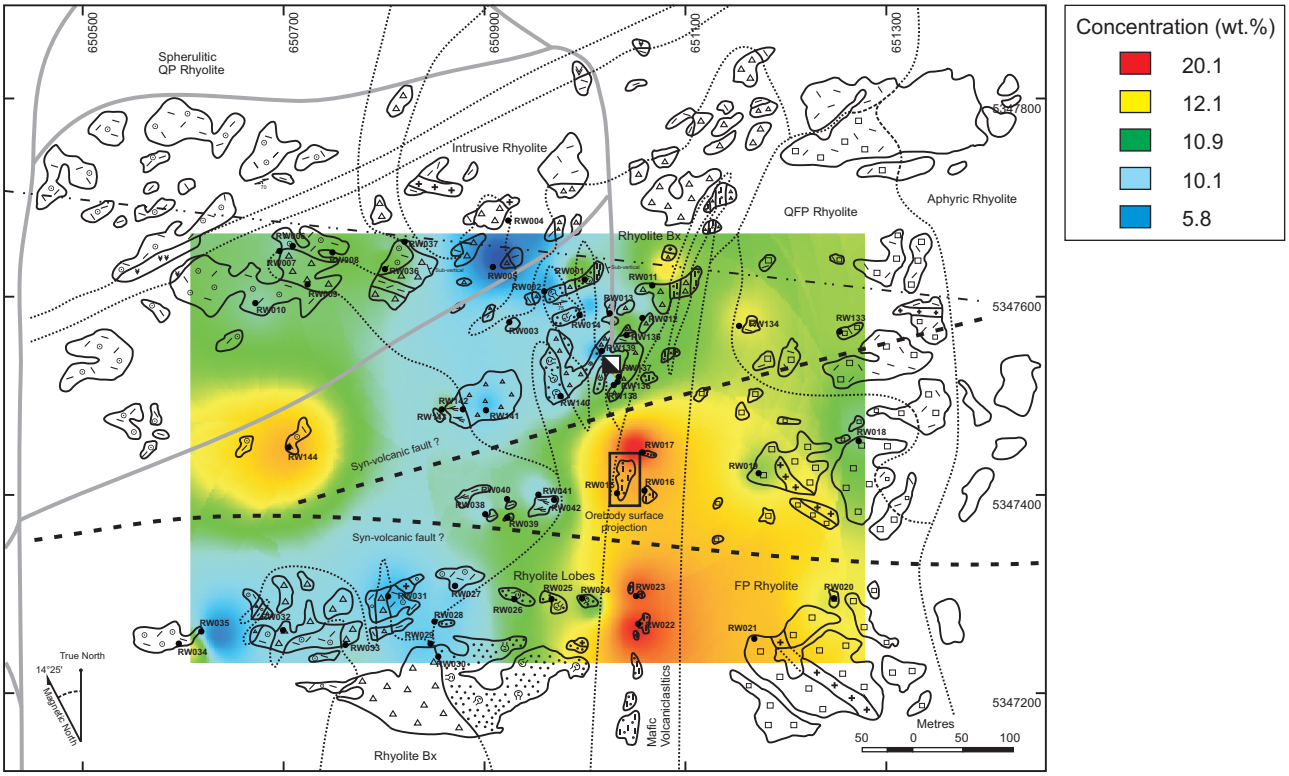

B. Li

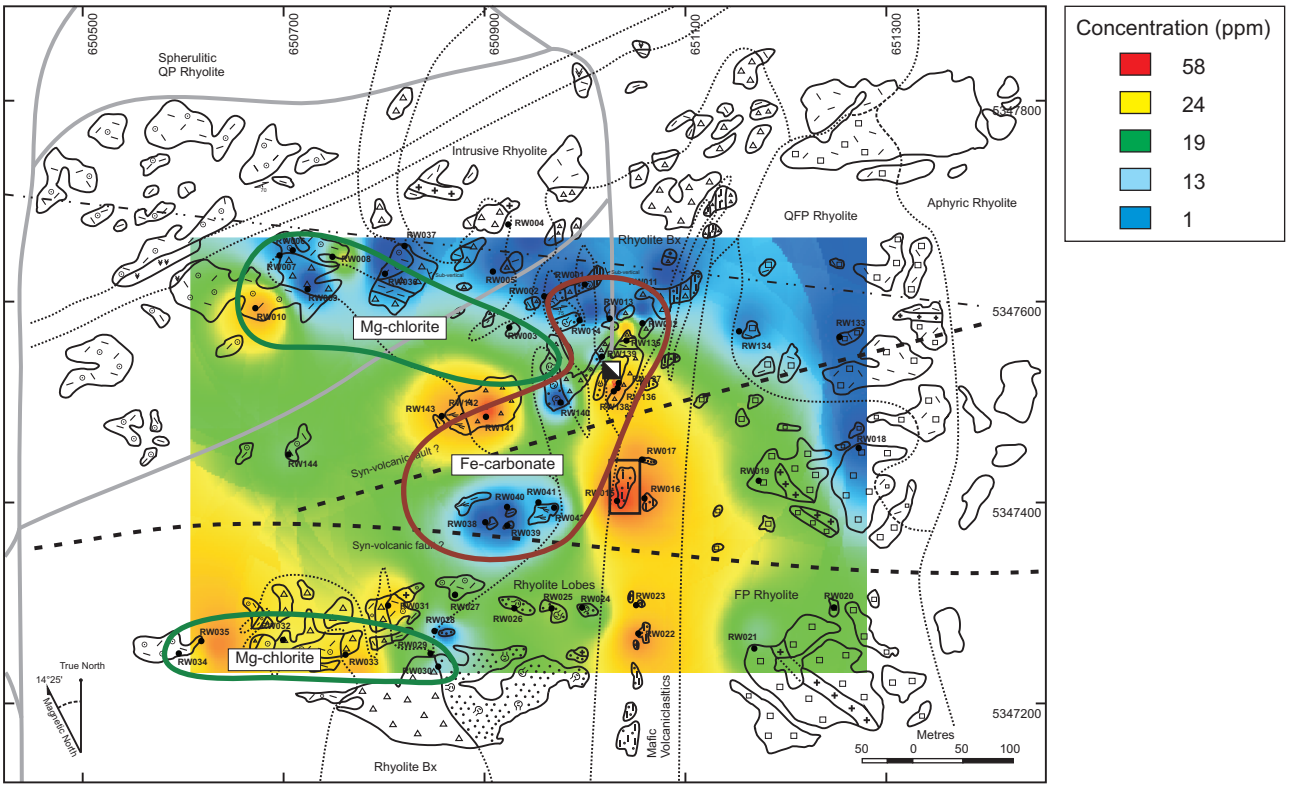

Figure 6.5. Concentrations of Al_2O_3 (wt.%) and Li (ppm) at Delbridge shown with respect to lithofacies. All plotted data are based on quantitative whole-rock geochemical analyses and contoured using inverse-distance weighting (IDW). a) High Al_2O_3 in the hanging wall corresponds to abundant chlorite (± sericite, epidote) in mafic volcaniclastic rocks and significant sericite (± primary feldspar) in FP and QFP rhyolite. b) Li concentrations clearly correlate with MgO (cf. Figure 6.4b), suggesting substitution of Li^+ for Mg^{2+} in mapped zones of intense chlorite alteration.

A. Ba

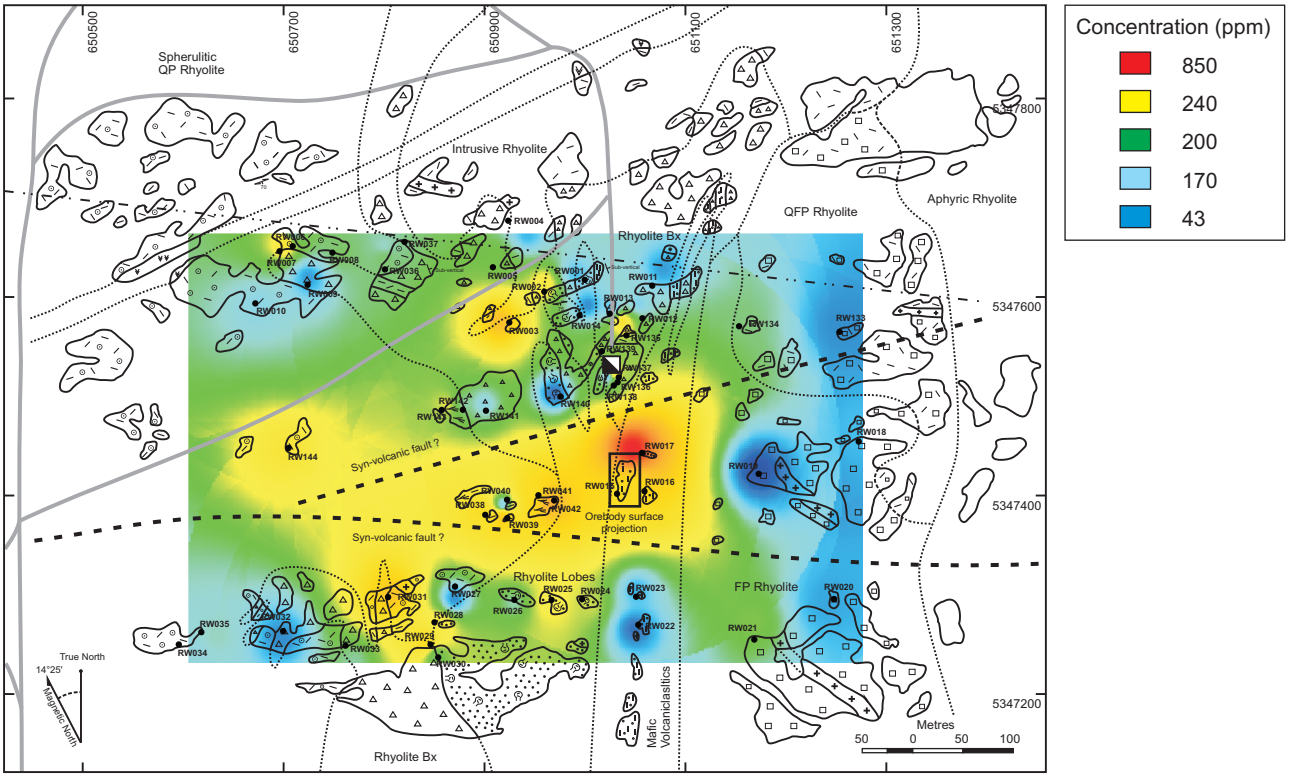

B. Sr

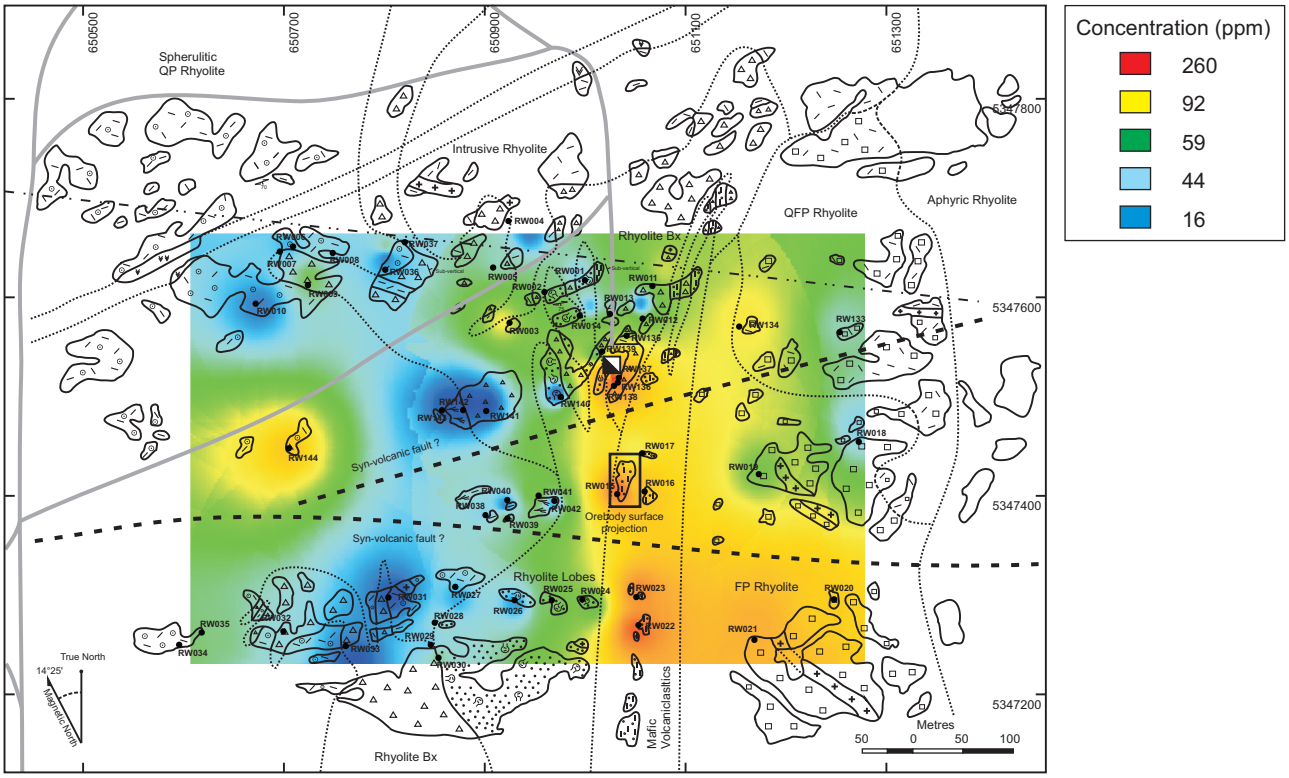

Figure 6.6. Concentrations (ppm) of Ba and Sr at Delbridge shown with respect to lithofacies. All plotted data are based on quantitative whole-rock geochemical analyses and contoured using inverse-distance weighting (IDW). a) Elevated Ba (250-400 ppm) occurs in the interpreted main hydrothermal upflow and is most likely contained in sericite. The highest concentrations at the paleo-seafloor may suggest interaction with seawater. b) Minor Sr enrichment (50-200 ppm) in the hanging wall clearly mirrors CaO distribution (cf. Figure 6.4a), suggesting substitution for Ca^{2+} in Ca-rich carbonate.

A. MnO

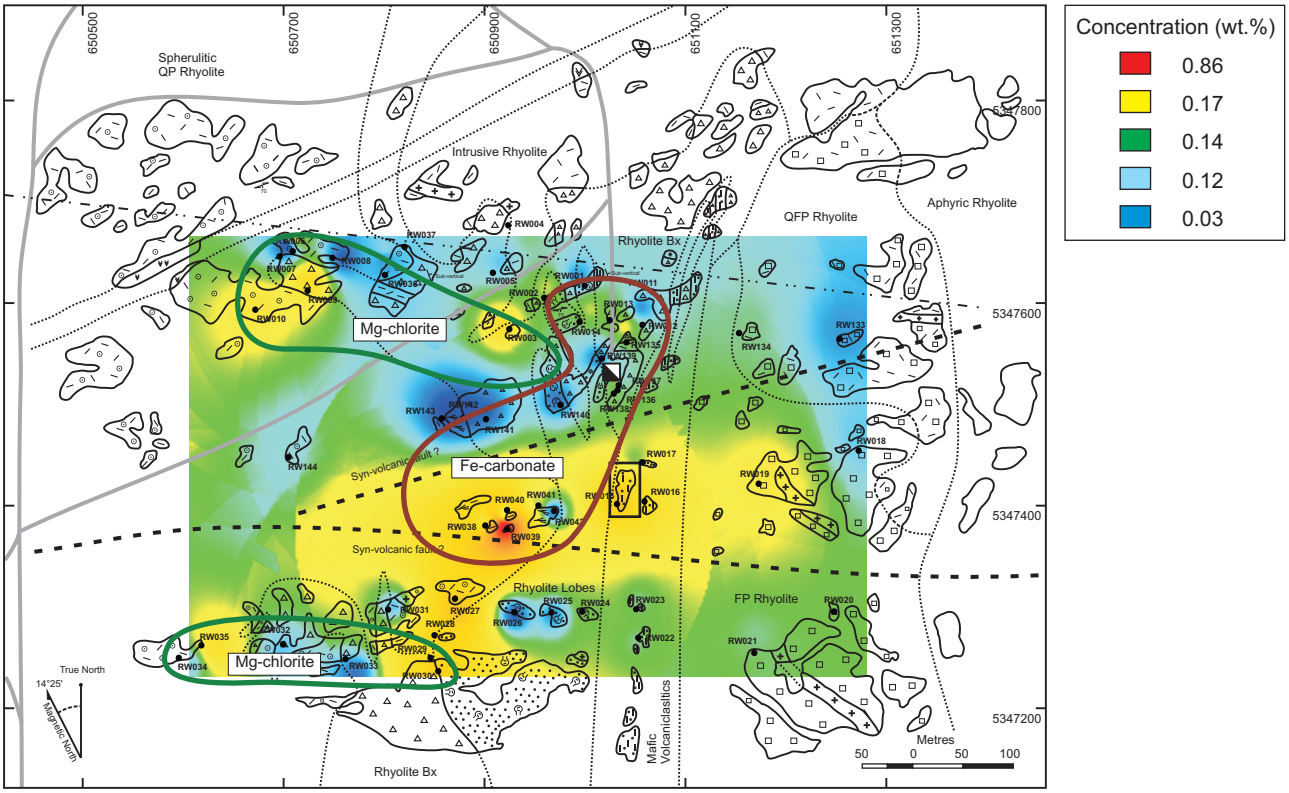

B. SiO_2

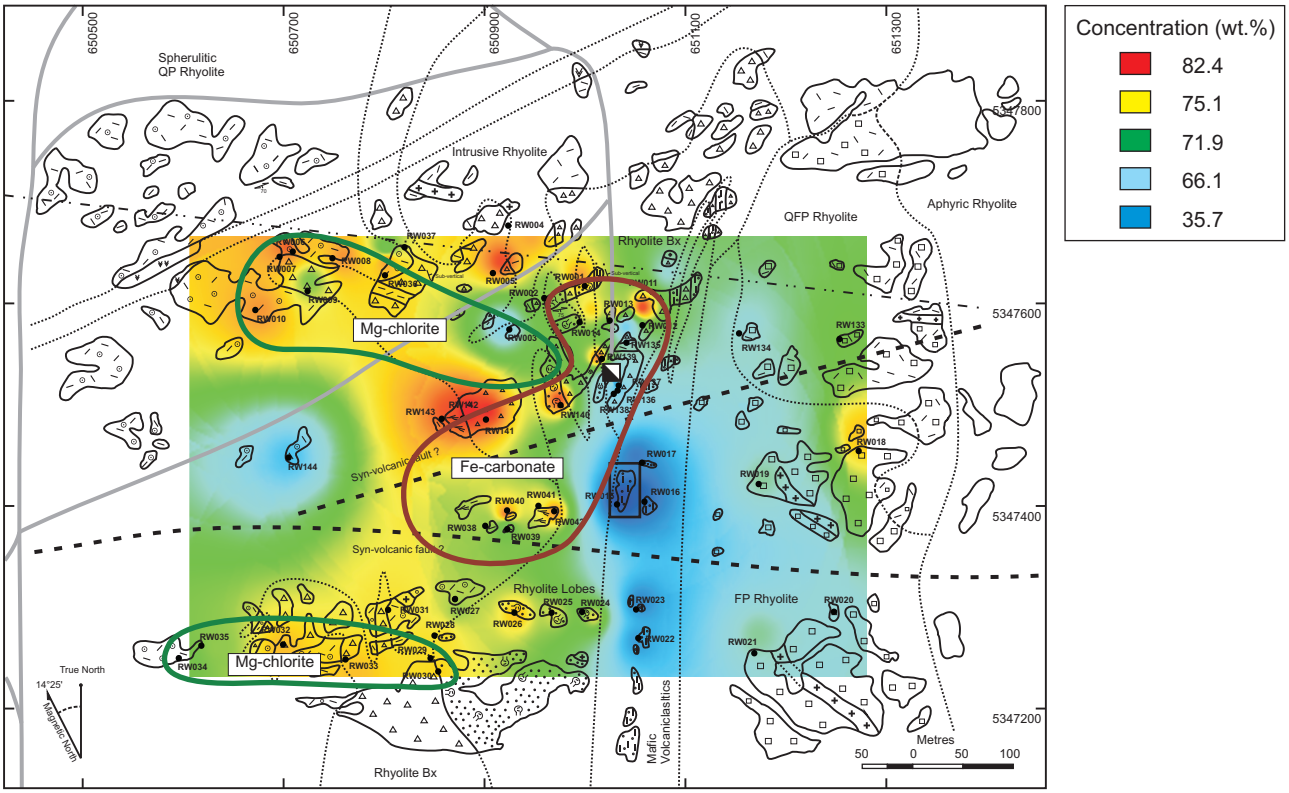

Figure 6.7. MnO and SiO_2 concentrations (wt.%) at Delbridge shown with respect to lithofacies. All plotted data are based on quantitative whole-rock geochemical analyses and contoured using inverse-distance weighting (IDW). a) High MnO (~0.2-0.9 wt.%) corresponds to the interpreted main hydrothermal upflow in footwall stringers and stockwork and hanging-wall mafic volcaniclastic rocks and FP rhyolite. This resembles both CaO and CO_2 patterns (cf. Figures 6.4a and 6.1b) and suggests substitution of Mn^{2+} in carbonate. b) Silicification is most intense in proximity to the interpreted paleo-seafloor, in the hanging wall, and in a pod-like zone immediately beneath the orebody surface projection; however, these trends are not shown by the distribution of whole-rock SiO2 data due to different rock types.

Total REE

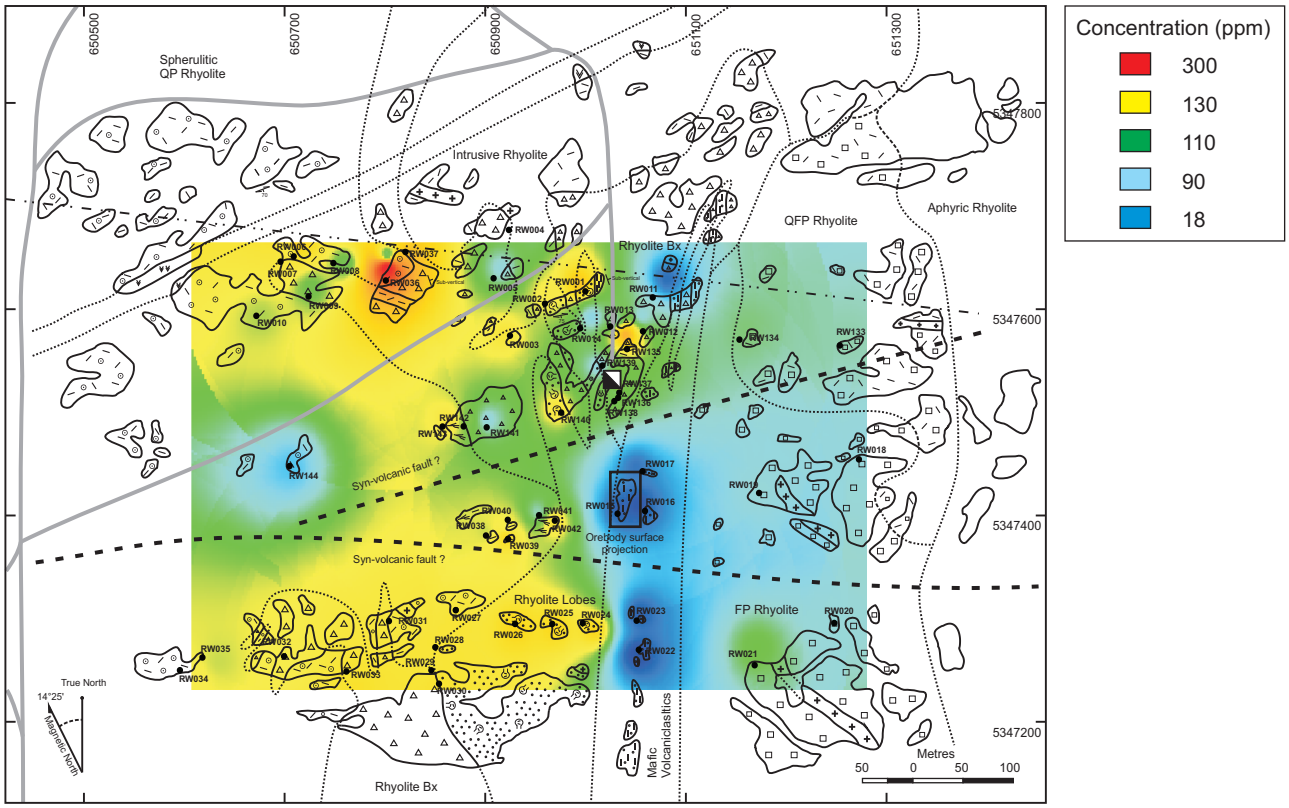

Figure 6.8. Rare-earth element (REE) concentrations (ppm) at Delbridge shown with respect to lithofacies. Plotted data are based on quantitative whole-rock geochemistry and contoured using inverse-distance weighting (IDW). Hanging-wall FP and QFP rhyolites and mafic volcaniclastic rocks are depleted in REE compared to footwall QP rhyolite facies.

A. Cu

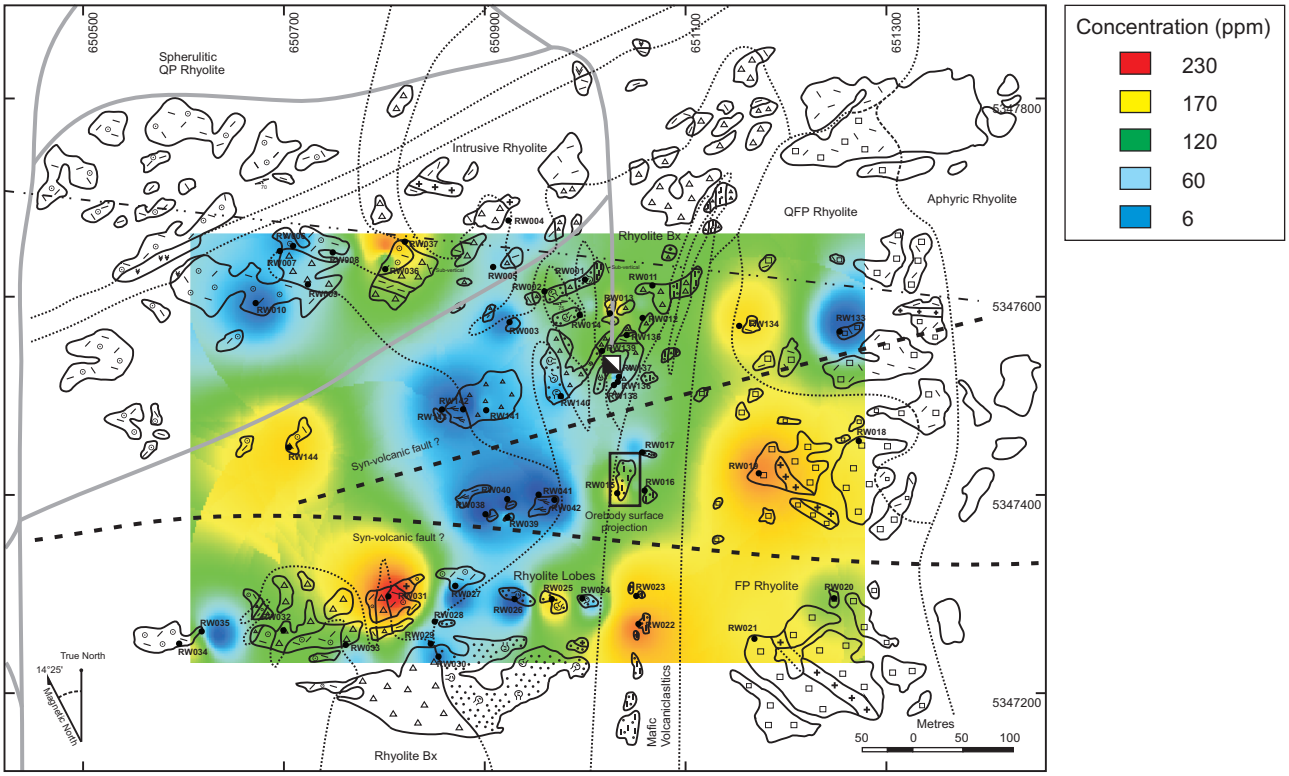

B. Zn

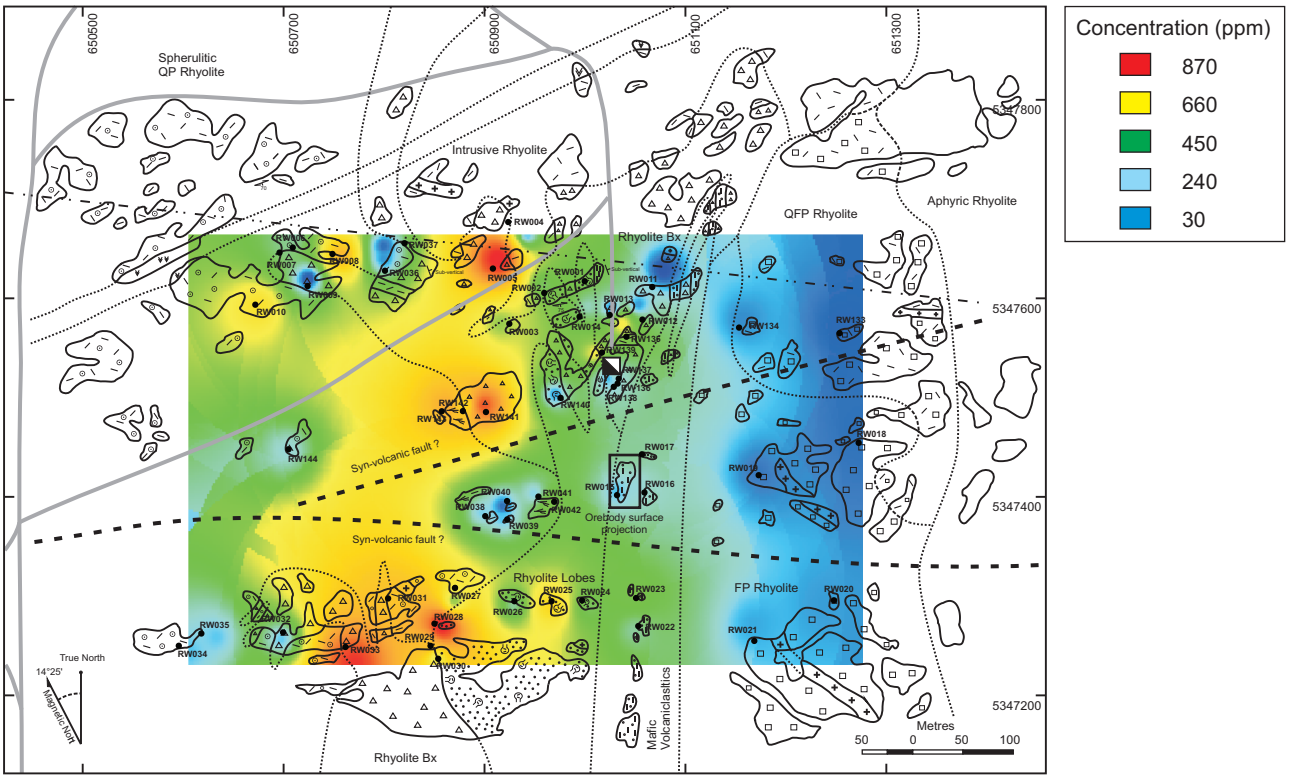

Figure 6.9. Cu and Zn concentrations (ppm) at Delbridge shown with respect to lithofacies. All plotted data are from quantitative whole-rock geochemical analyses and contoured using inverse-distance weighting (IDW). a) Cu concentrations are consistently higher (~40-150 ppm) in the hanging wall and proximal to the inferred synvolcanic faults. Cu is generally low (5-80 ppm) in the footwall and notably absent (<25 ppm) in stringers and stockwork. b) The highest Zn concentrations occur in the footwall in stringers and stockwork (up to 440 ppm) and more distally along rhyolite breccia contacts (up to 900 ppm). Notably, the most Zn-rich samples occur stratigraphically below those of Cu.

Pb

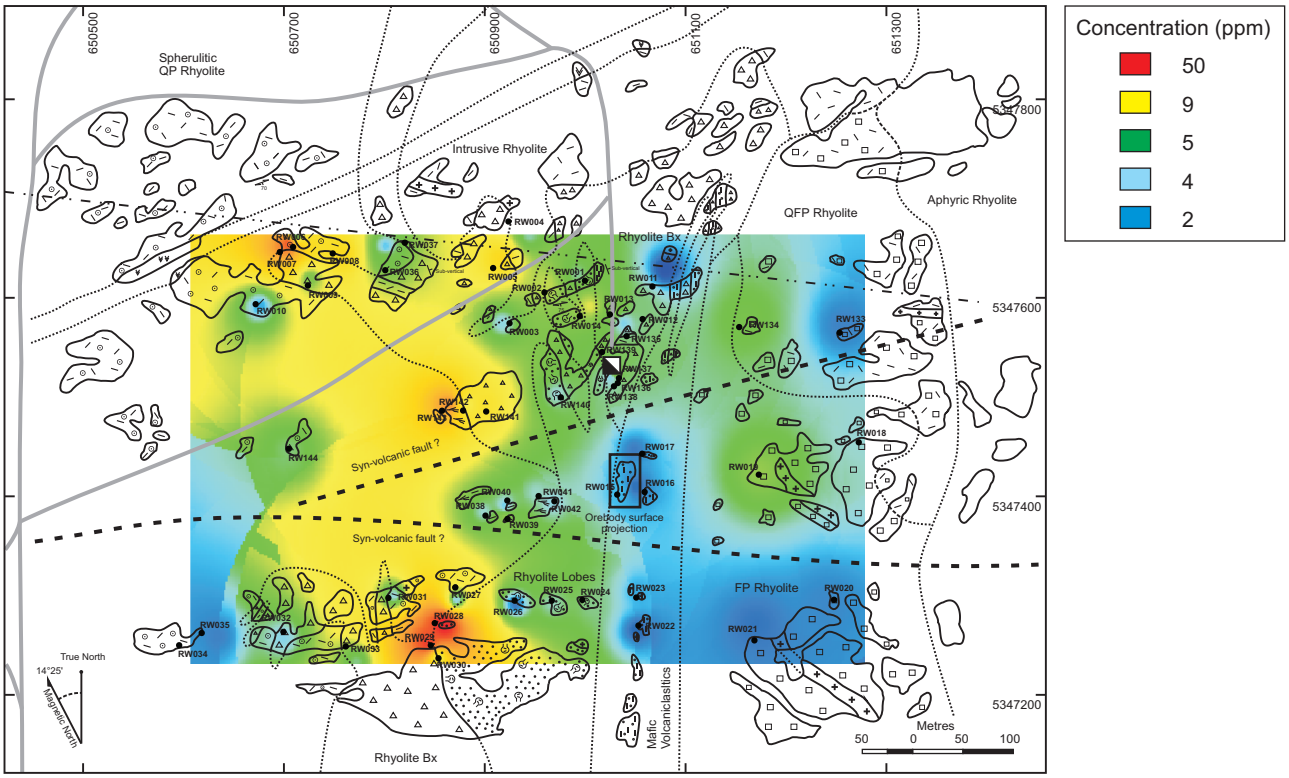

Figure 6.10. Pb concentrations (ppm) at Delbridge shown with respect to lithofacies. All plotted data are from quantitative whole-rock geochemical analyses and contoured using inverse-distance weighting (IDW). Pb clearly follows the same distribution pattern as Zn (cf. Figure 6.9b) with the highest concentrations (up to 50 ppm Pb) corresponding to stringers and stockwork and more distal footwall zones proximal to rhyolite breccia contacts.

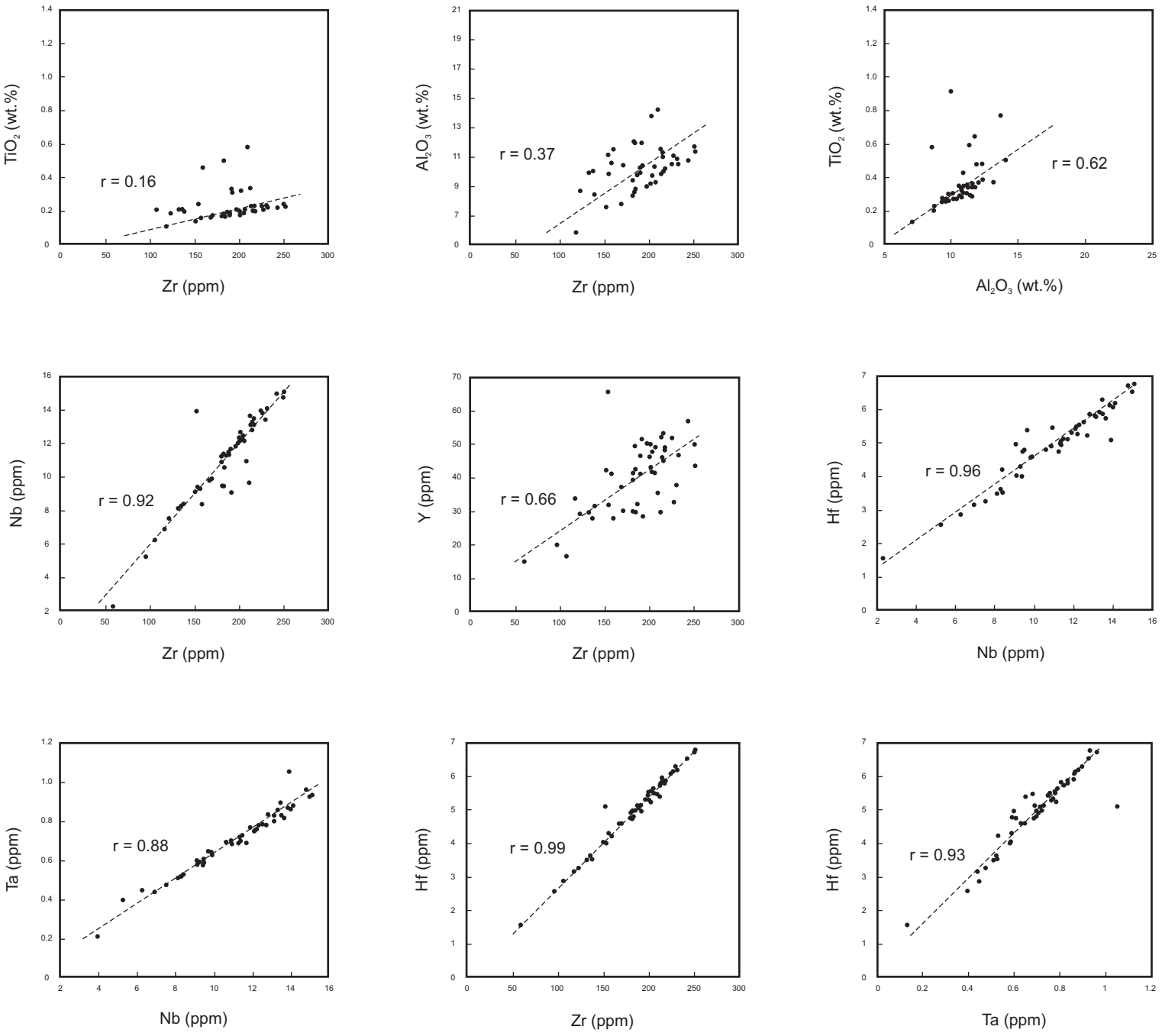

Figure 6.11. Representative x-y bivariate plots of potentially immobile elements in rhyolite at Delbridge. Zr is selected as the immobile monitor for mass balance calculations because it is highly correlated (r > 0.85) with other components. Zr abundance is also much greater than other immobile elements, which reduces the impact of analytical errors in subsequent calculations.

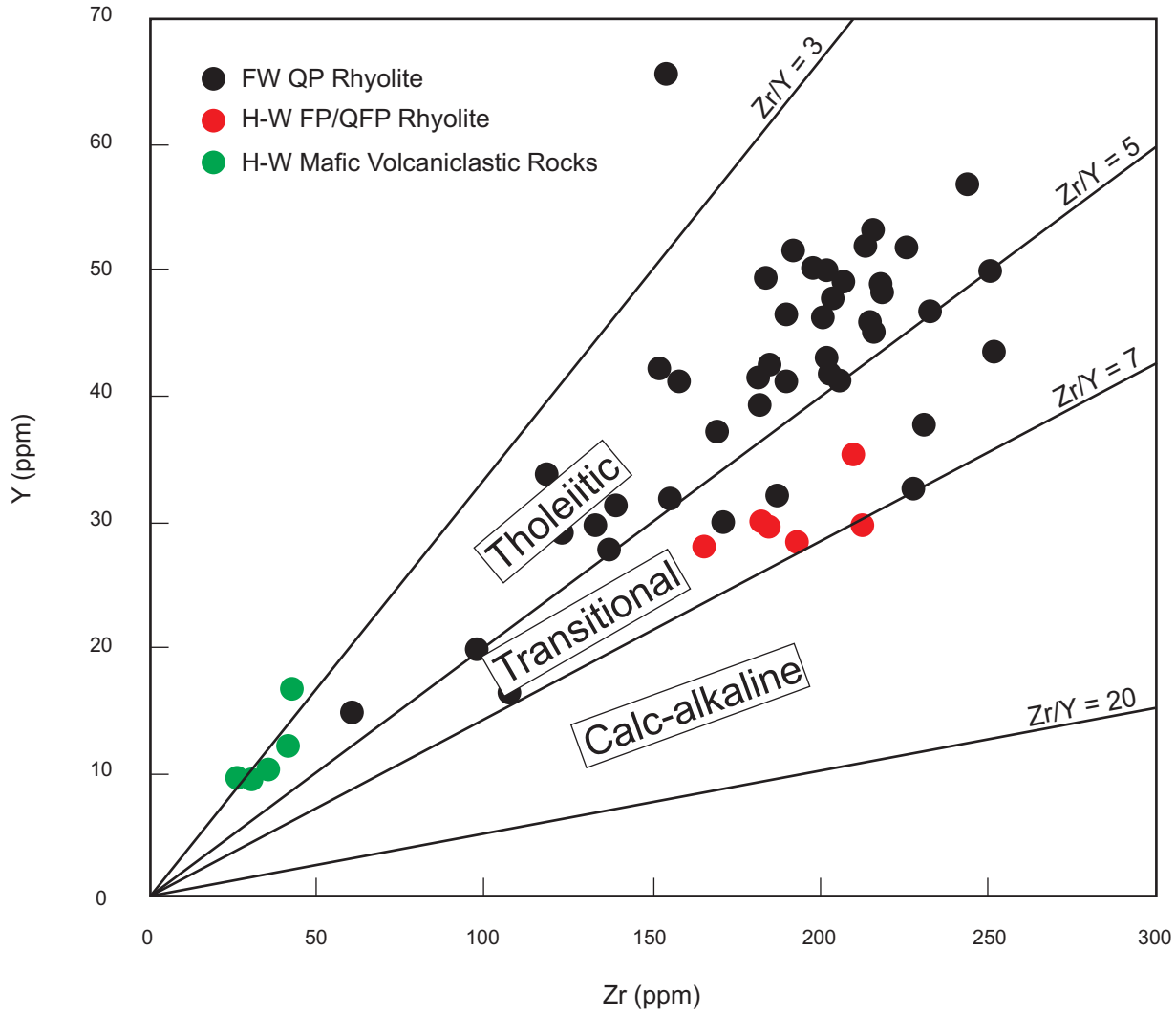

Figure 6.12. Plot of all Y-Zr data from Delbridge, indicating the spread of magmatic affinities in the sample suite. Footwall QP rhyolite samples are in the tholeiitic to transitional range and hanging-wall FP and QFP rhyolites fall in the transitional to mildly calc-alkaline range.

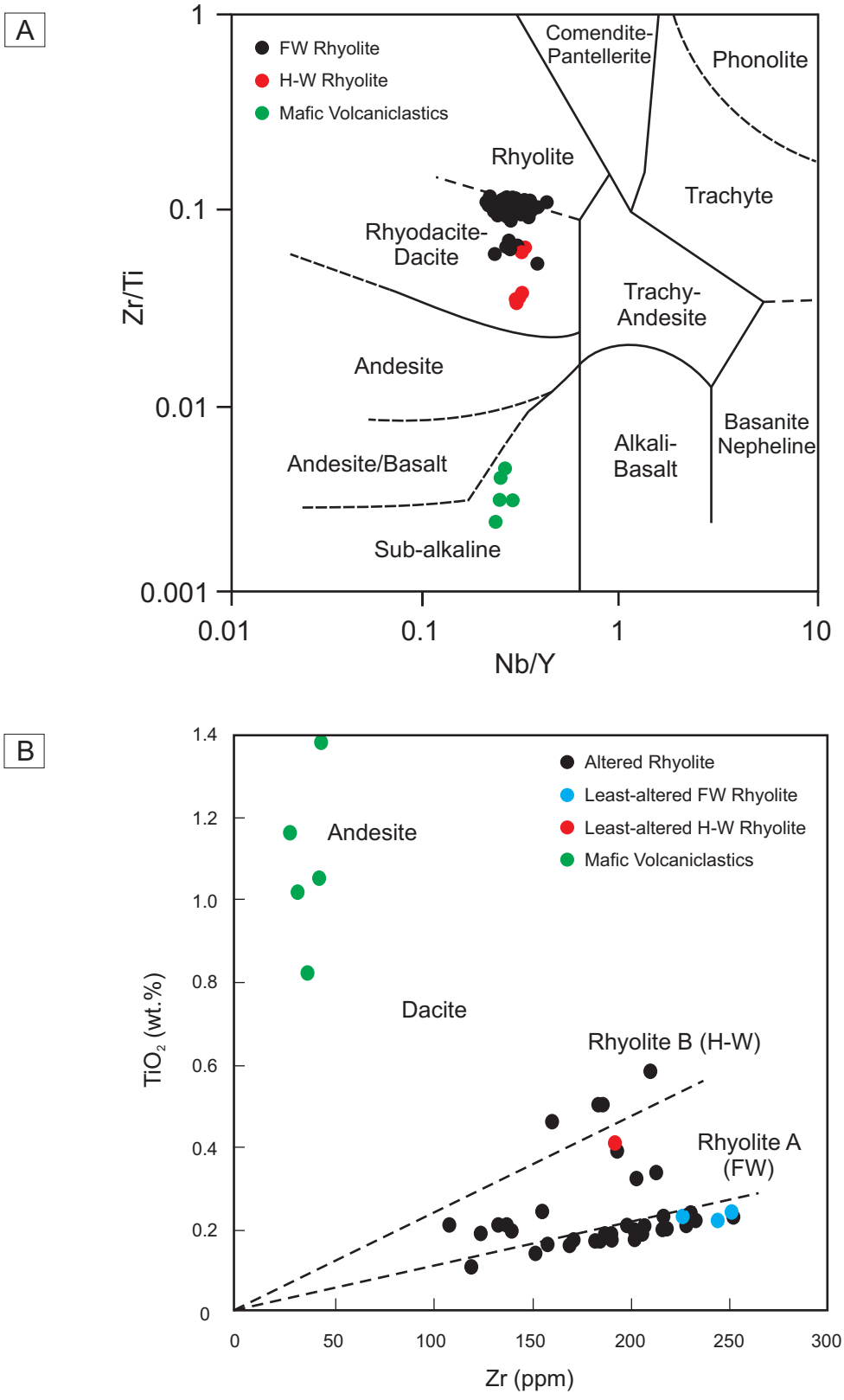

Figure 6.13. a) Zr/Ti vs. Nb/Y immobile element ratios indicate the vast majority of felsic samples at Delbridge are of rhyolite to rhyodacite composition (after Winchester and Floyd, 1977). The few samples that plot in the andesitic to sub-alkalic fields correspond to hanging-wall mafic volcaniclastic rocks and FP/QFP rhyolite. b) Plot of all TiO_2-Zr data, divided into altered and least-altered samples. Note two separate alteration lines extend from the origin, indicating separate magmatic sources for rhyolites A and B. Samples that plot along the rhyolite A trend were collected in footwall QP rhyolite and those that fall along the rhyolite B trend in hanging-wall FP and QFP rhyolite. The outliers are samples collected in the fine-grained mafic volcaniclastic unit. A single fractionation curve cannot be estimated due to lack of a sufficient number of samples.

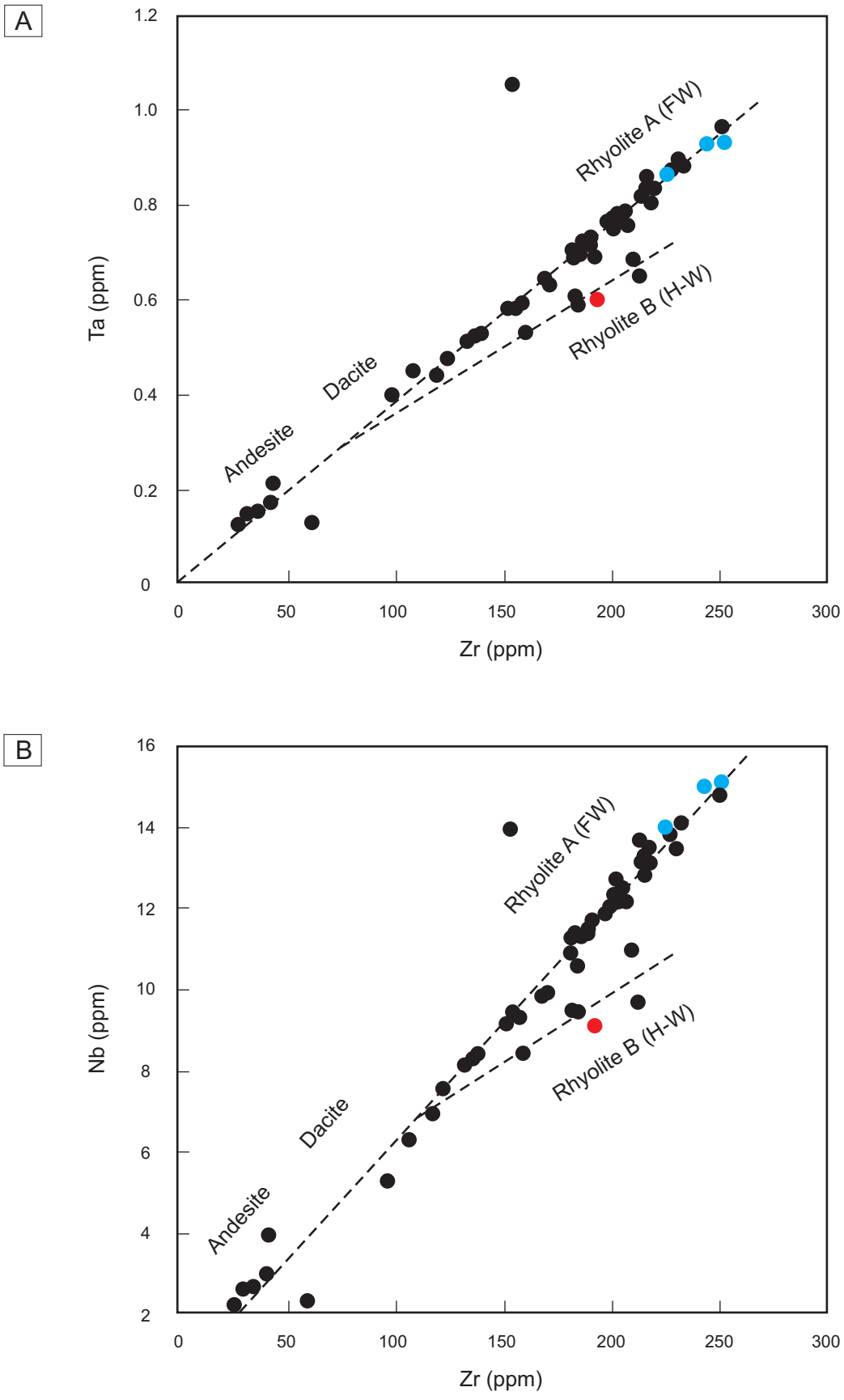

Figure 6.14. a) Plot of Ta versus Zr, indicating that the Delbridge volcanic rocks show consistent separation into two magmatic types with those of mildly calc-alkaline affinity having a lower slope than the tholeiitic-transitional series. b) Plot of Nb versus Zr, again showing the presence of two magmatic types. Samples that plot along the rhyolite A trend were collected in footwall QP rhyolite and those that fall along the rhyolite B trend in hanging-wall FP and QFP rhyolite. These observations are consistent with earlier findings by Barrett *et al* (1993). Samples in the andesitic range were collected in the fine-grained mafic volcaniclastic unit. Black symbols = altered samples; blue = least-altered footwall QP rhyolite compositions and; red = least-altered hanging-wall Fs-phyric rhyolite composition.

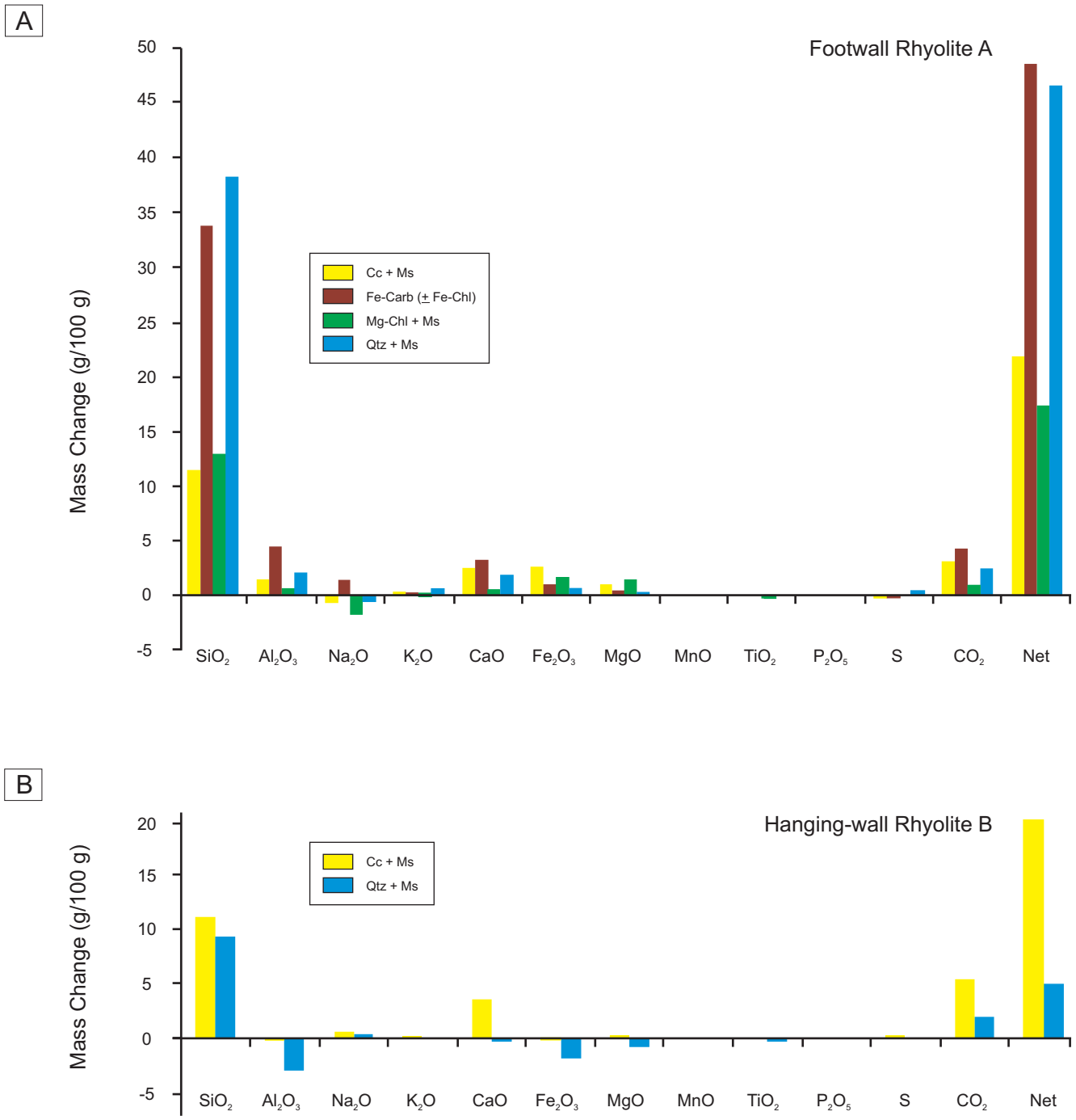

Figure 6.15. Visual comparison of system mass changes at Delbridge as a result of hydrothermal alteration. Each plotted value (in g/100 g) represents the average mass change of an individual chemical component for all samples in a given alteration assemblage. a) Histogram of major component mass changes in the footwall (rhyolite A). Major net gains in the system are evidently the result of major additions of silica. Other important enrichments include Al_2O_3, CaO, Fe_2O_3, MgO, and CO_2, likely caused by carbonate, chlorite, and sericite alteration. The greatest additions of CO_2 correspond to zones of Fe- and Ca-rich carbonate. Gains of MgO are highest in alteration dominated by Mg-chlorite. b) Histogram of major component mass changes in the hanging-wall (rhyolite B). Silica is clearly the dominant component contributing to net mass gains in the system. Zones of Ca-rich carbonate are characterized by important additions of CaO and CO_2. Quartz alteration only shows significant additions of SiO_2 with minor CO_2.

A

Pearson correlation matrix of potentially immobile REE in QP rhyolite at Delbridge

	La	Ce	Pr	Nd	Sm	Eu	Gd	Tb	Dy	Ho	Er	Tm	Yb	Lu
La	1													
Ce	0.982	1												
Pr	0.927	0.981	1											
Nd	0.852	0.933	0.984	1										
Sm	0.686	0.792	0.878	0.940	1									
Eu	0.504	0.611	0.702	0.763	0.816	1								
Gd	0.606	0.718	0.809	0.875	0.957	0.794	1							
Tb	0.514	0.631	0.727	0.795	0.893	0.744	0.982	1						
Dy	0.463	0.583	0.683	0.755	0.863	0.723	0.965	0.994	1					
Ho	0.463	0.582	0.680	0.751	0.854	0.718	0.956	0.987	0.997	1				
Er	0.482	0.599	0.695	0.762	0.859	0.725	0.951	0.979	0.990	0.996	1			
Tm	0.501	0.614	0.706	0.769	0.858	0.720	0.946	0.970	0.983	0.992	0.998	1		
Yb	0.498	0.613	0.707	0.771	0.855	0.724	0.937	0.960	0.974	0.986	0.995	0.998	1	
Lu	0.510	0.624	0.718	0.780	0.858	0.732	0.936	0.955	0.968	0.981	0.991	0.995	0.998	1

All values are different from zero with a significance level alpha = 0.05.

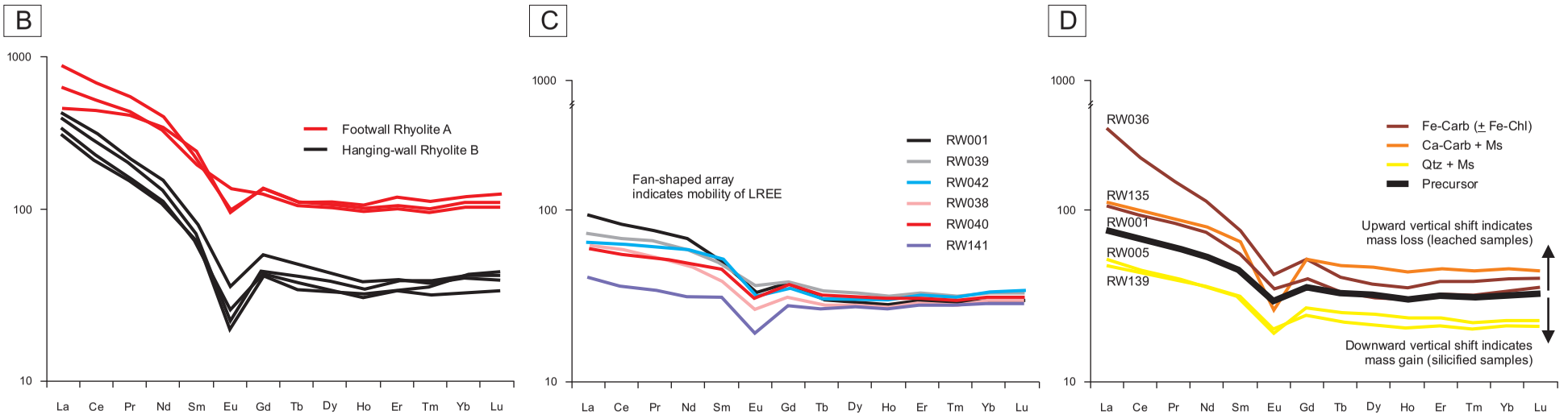

Figure 6.16. a) Pearson correlation matrix of rare-earth elements (REE) in the Delbridge volcanic rocks. Heavy REE show much stronger correlation than light REE indicating that they behaved coherently during alteration. b) Representative REE profiles for footwall rhyolite A are flatter than hanging-wall rhyolite B profiles. c) Fan-shaped array of REE profiles for proximal altered samples indicates partial mobility of LREE, which is common immediately beneath VMS mineralization. d) Sub-parallel REE profiles are vertically displaced both upward (net mass loss) and downward (net mass gain) from an average least-altered precursor composition, depending on alteration type.

A. Ishikawa Al Index

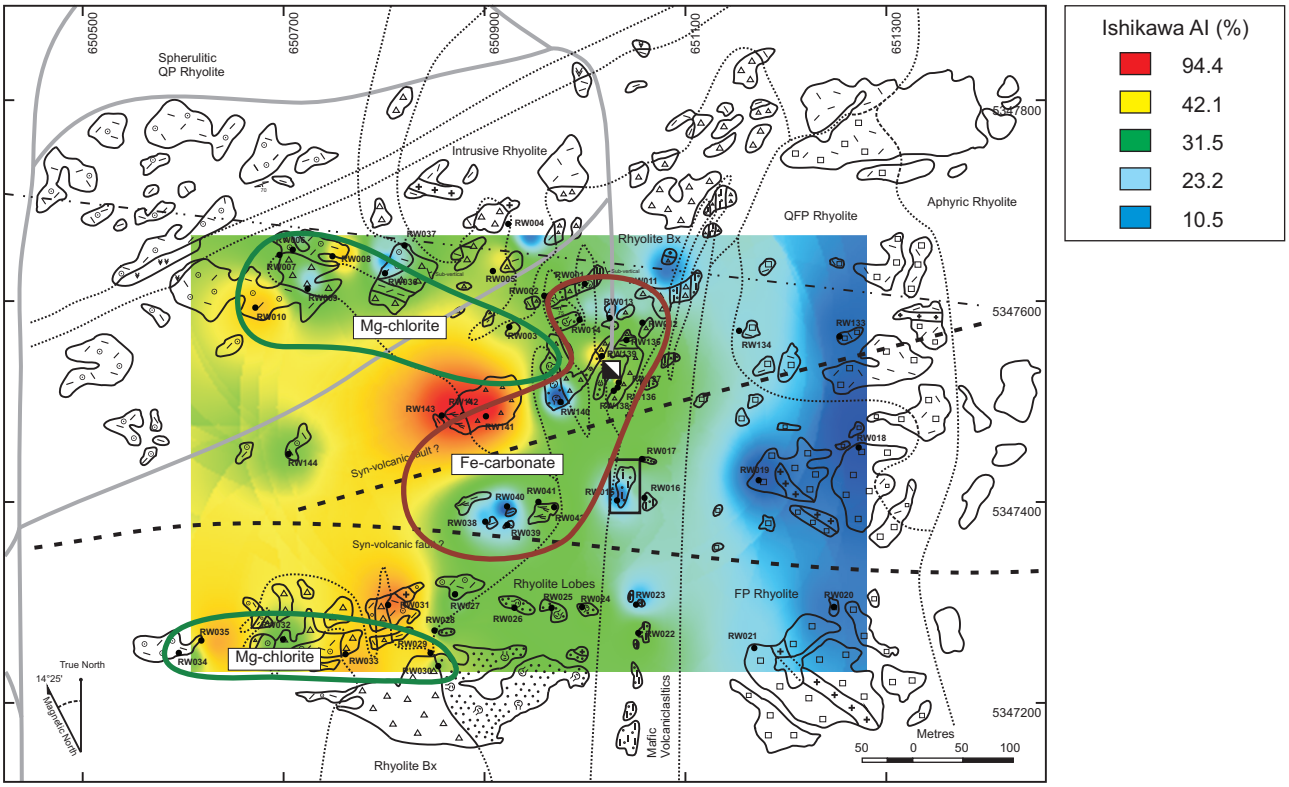

B. CCPI Index

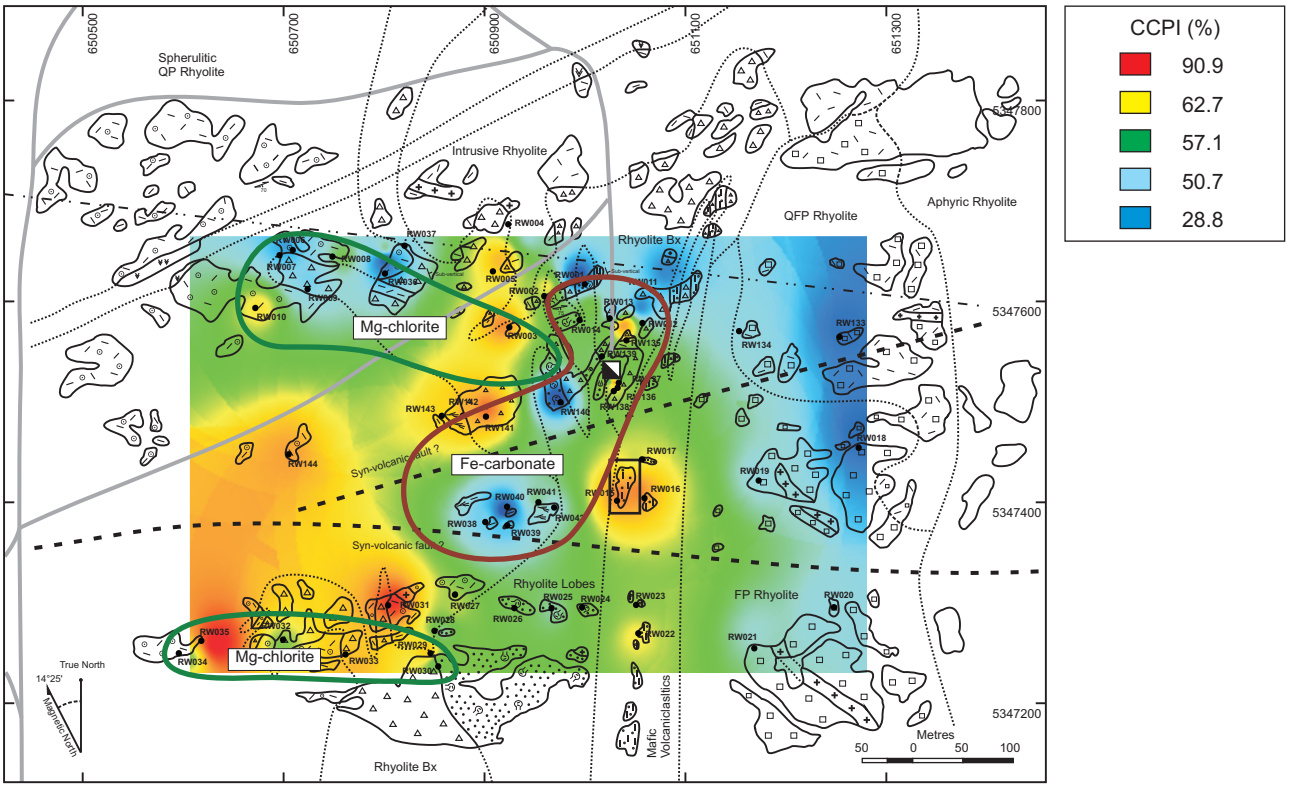

Figure 6.17. Alteration indices at Delbridge are estimated from whole-rock geochemical data and contoured using inverse-distance weighting (IDW). a) The highest Ishikawa Al values clearly occur in zones of stringer and matrix-controlled alteration within and proximal to the interpreted hydrothermal upflow beneath known massive sulfide mineralization; Al = [100(MgO+K_2O)] / [MgO+K_2O+CaO+Na_2O]. b) High CCPI values correspond to samples collected in rhyolite breccia, along breccia contacts, and in fractured facies proximal and beneath known mineralization, which supports host-rock permeability as the dominant control on fluid flow; CCPI = [100(MgO+FeO)] / [MgO+FeO+Na_2O+K_2O]. Both Al and CCPI correlate with K_2O, reflecting the processes of Na depletion and associated K-metasomatism common to VMS alteration systems.

A. Ishikawa AI

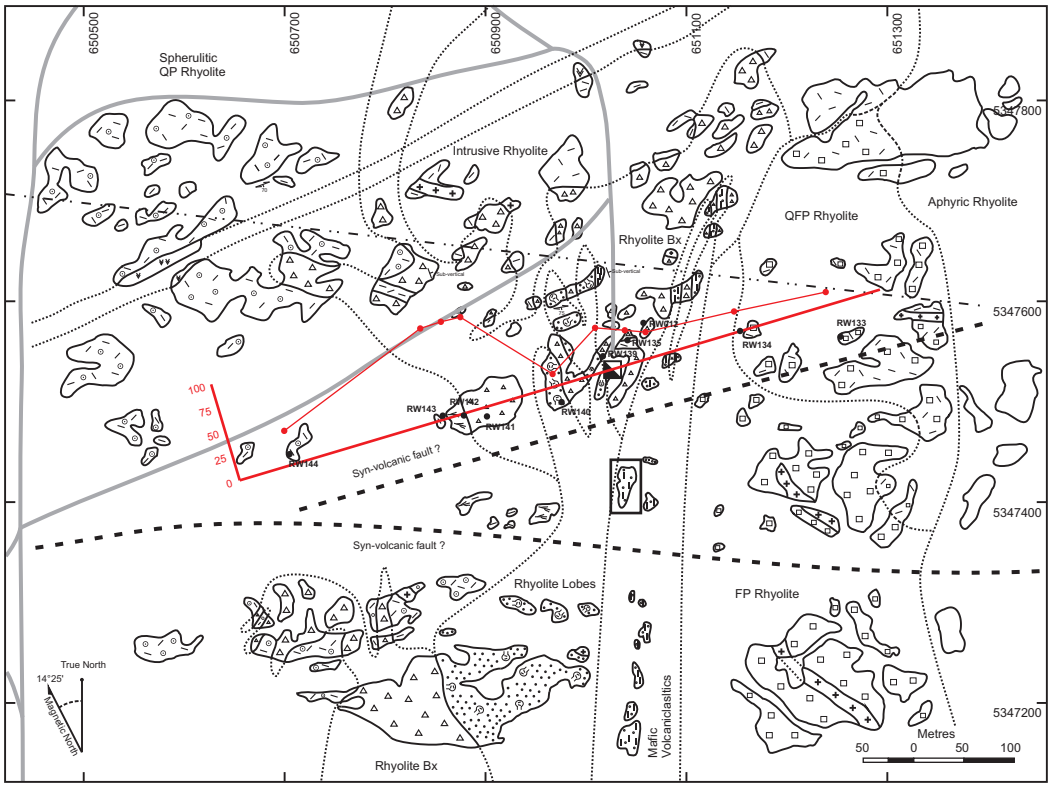

B. CCPI

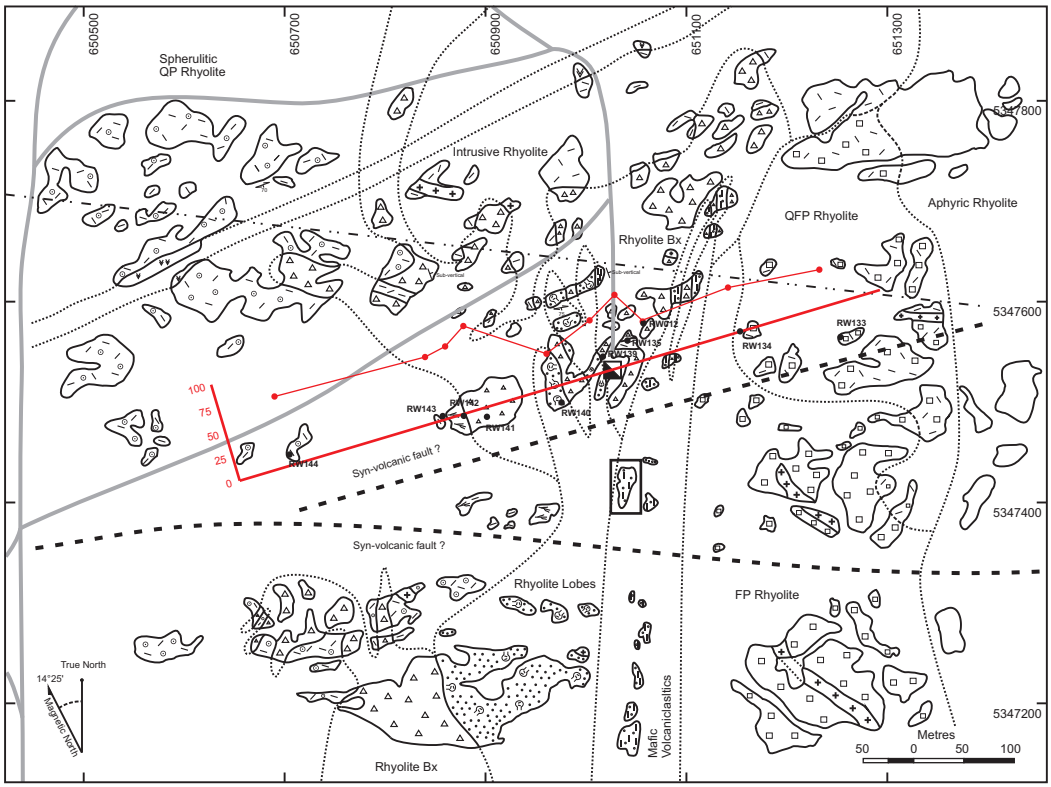

Figure 6.18. Ishikawa alteration indices (AI) and chlorite-carbonate-pyrite indices (CCPI) plotted on a traverse through the stratigraphic footwall, across the mineralized horizon, and into the hanging wall at Delbridge. Plotted values are shown in Table 6.7. a) The highest AI values (~90-95%) clearly occur in stockwork and rhyolite breccia in proximity to the mineralized horizon. This, coupled with low values (~10-35%) in basal coherent rhyolite, proximal rhyolite lobes, and the hanging wall, supports the main control of host-rock permeability on alteration and mineralization. b) The same trend shown in (a) is evident for CCPI values.

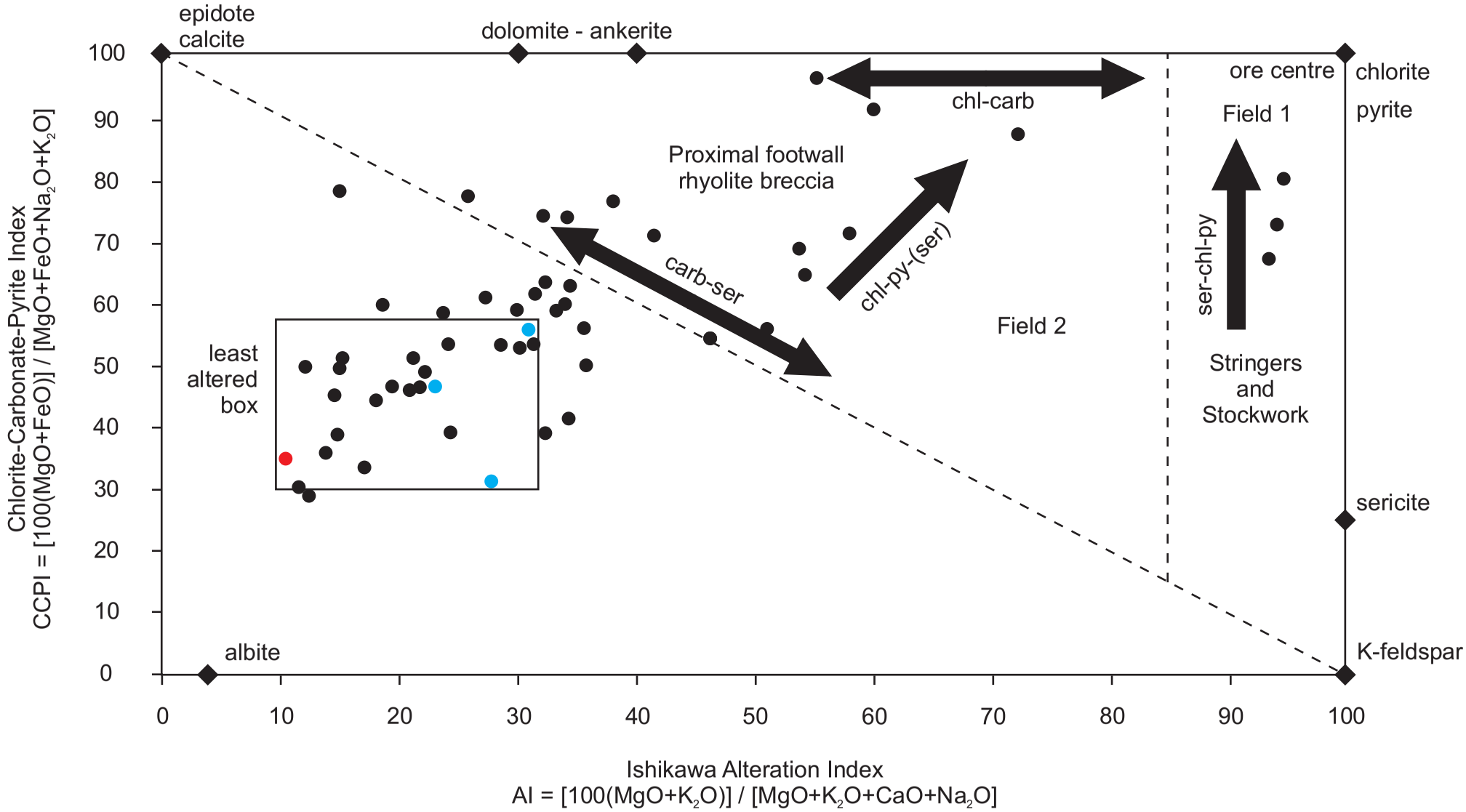

Figure 6.19. Alteration box plot for Delbridge VMS-style alteration and mineralization. Plotted indices (AI and CCPI) are derived from whole-rock geochemical data and divided into least-altered and hydrothermal alteration fields. Field 1 includes strong sericite-chlorite-pyrite alteration of 3 samples collected in stringers and stockwork beneath the surface projection of the orebody. Samples that fall within Field 2 show variable carbonate and chlorite with generally moderate sericite alteration. Alteration dominated by carbonate and chlorite is typically developed adjacent to the massive sulfide mineralization within proximal footwall rhyolite breccia. Black symbols = variably altered samples; blue = least-altered footwall QP rhyolite compositions and; red = least-altered hanging-wall Fs-phyric rhyolite composition.

A. Carbonate Intensity

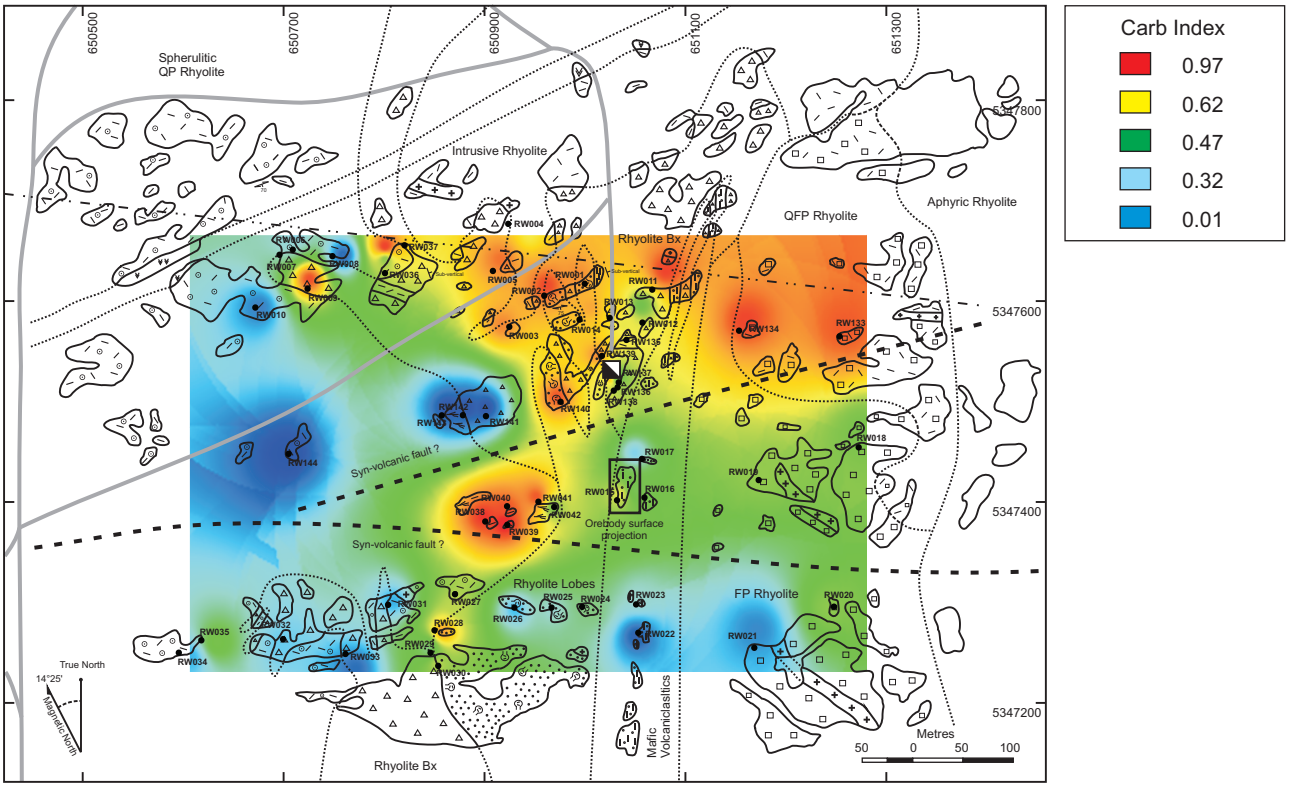

B. Mn-carbonate

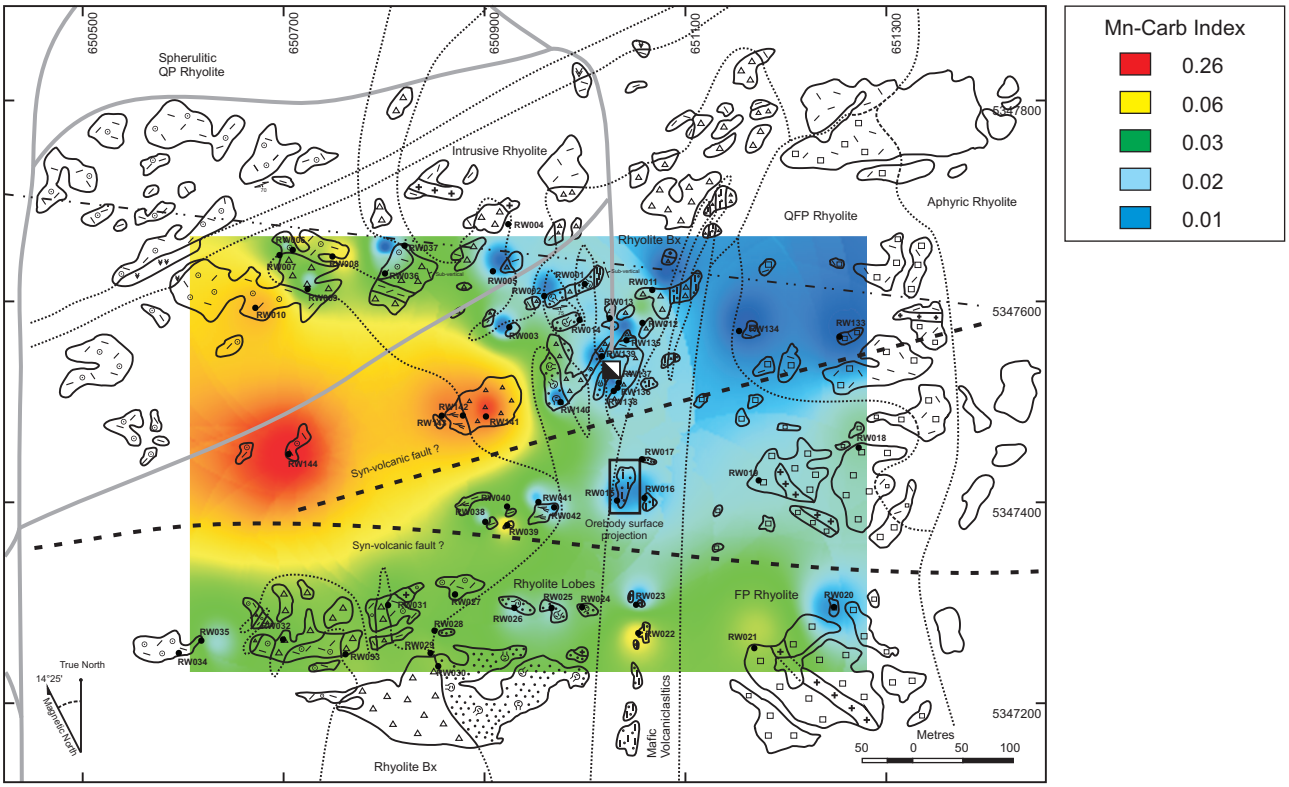

Figure 6.20. Intensity of carbonate alteration and associated Mn-substitution at Delbridge. Alteration indices are calculated from quantitative whole-rock geochemical data and contoured using inverse-distance weighting (IDW). a) Normalized carbonate indices (Carb Index = CO_2/CaO+FeO+MgO, molar proportions) indicate that the intensity of carbonate alteration is highest (up to 0.98 molar units) in stringers and stockwork within the interpreted hydrothermal upflow, in the adjacent rhyolite breccia pile, and in the hanging-wall in proximity to the more northerly of the two inferred synvolcanic faults. This supports earlier observations from the variation of total CO_2 concentrations (cf. Figure 6.1b). b) Weak Mn-rich carbonate (Mn-Carb Index = MnO/CO_2, molar proportions) occurs mainly in footwall stockwork and overlying rhyolite breccia proximal to the inferred synvolcanic faults.

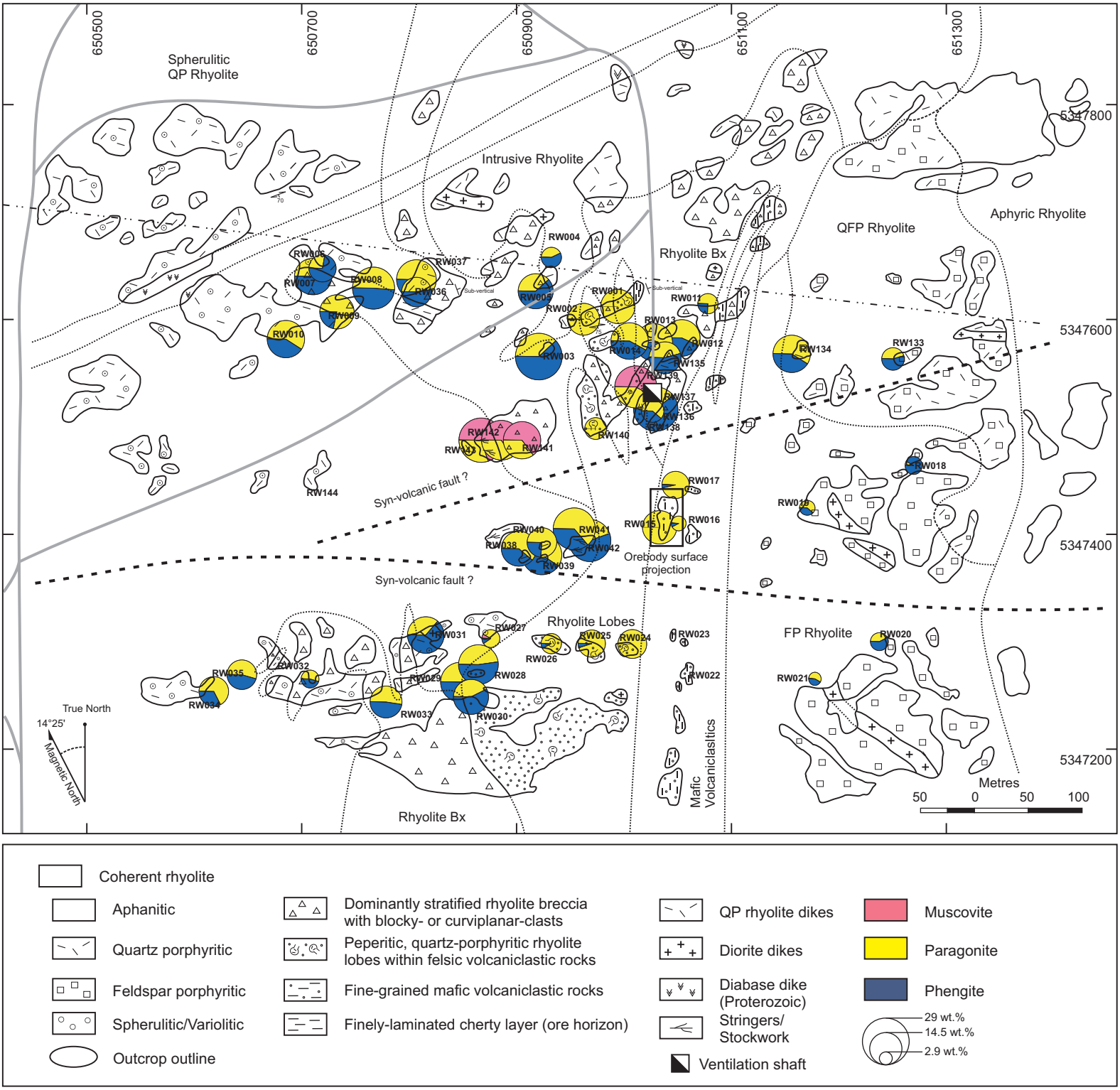

Figure 6.21. Abundance, distribution, and compositional variation of normative white mica at Delbridge calculated using the MINSQ method (Herrmann and Berry, 2002). Paragonite ($NaAl_2(Si_3Al)O_{10}(OH)_2$) is easily the most widespread white mica estimated despite evidence of Na-depletion and K-metasomatism in the footwall. Phengite ($K(AlMg)_2(OH)_2(SiAl)_4O_{10}$) is distributed mainly along the interpreted margins of the system and in the hanging-wall, supporting increased MgO in these zones and reflecting substitution of Mg^{2+} for Al^{3+} in potassic white micas. Significant muscovite ($KAl_2(AlSi_3O_{10})(OH)_2$) is only estimated in a few stockwork and coarse rhyolite breccia samples collected within and proximal to the interpreted hydrothermal upflow. Compositional variation of white micas calculated in each sample is expressed as normalized percentages in pie chart format. Symbol size is a function of the total white mica estimated in a given sample and varies proportionally to the sum of all components (i.e., total white mica abundance). A symbol diameter of 1 cm represents a maximum total abundance of 29 wt.% white mica. All smaller pie charts are scaled down by square root because the area of a circle varies by the square root of its radius.

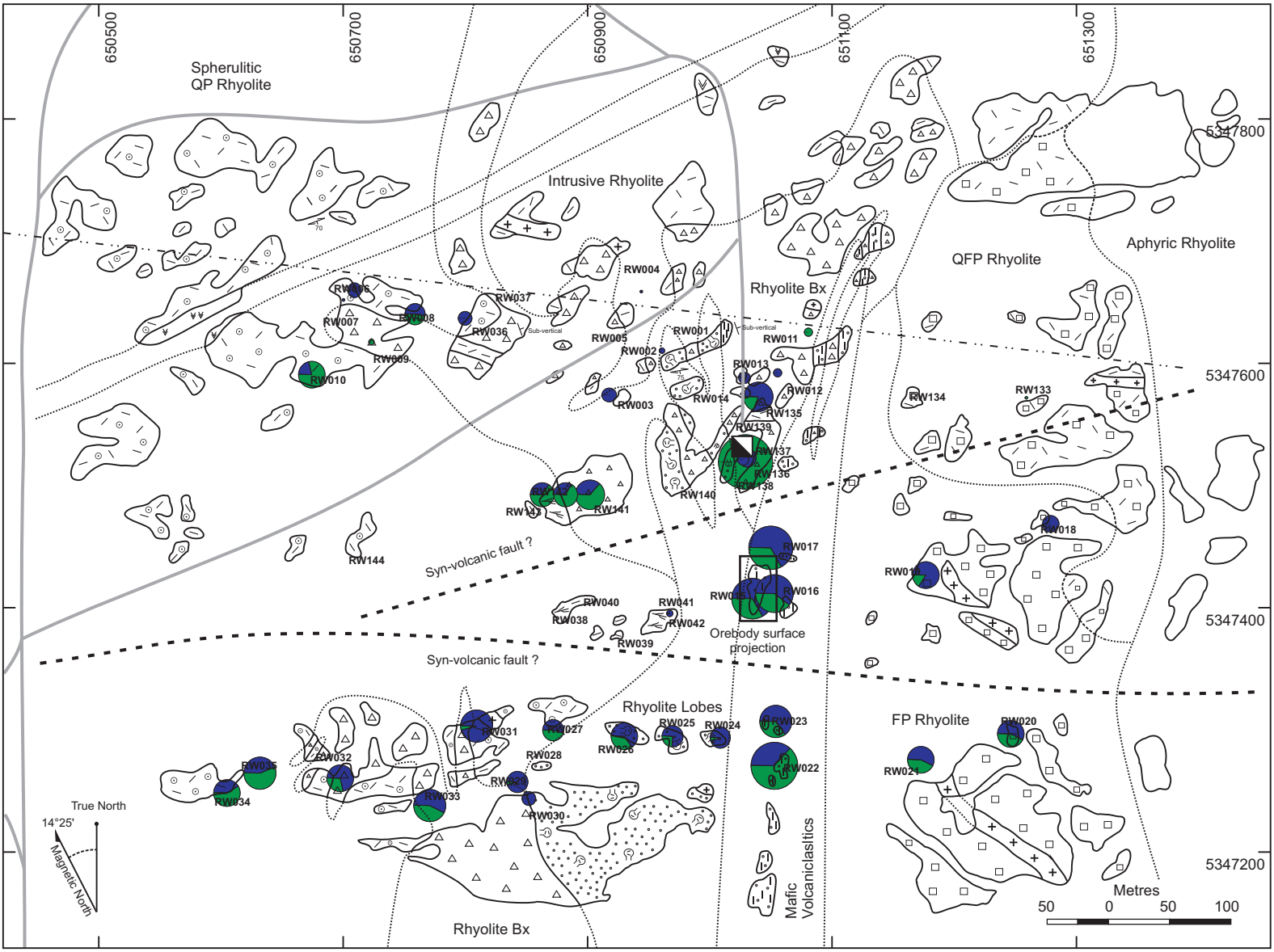

Coherent rhyolite

Aphanitic

Quartz porphyritic

Feldspar porphyritic

Spherulitic/Variolitic

Outcrop outline

Dominantly stratified rhyolite breccia with blocky- or curviplanar-clasts

Peperitic, quartz-porphyritic rhyolite lobes within felsic volcaniclastic rocks

Fine-grained mafic volcaniclastic rocks

Finely-laminated cherty layer (ore horizon)

QP rhyolite dikes

Diorite dikes

Diabase dike (Proterozoic)

Stringers/ Stockwork

Ventilation shaft

Mg-Chlorite

Fe-Chlorite

39 wt.%

19.5 wt.%

3.9 wt.%

Figure 6.22. Abundance, distribution, and compositional variation of normative chlorite at Delbridge calculated using the MINSQ method (Herrmann and Berry, 2002). Excluding mafic volcaniclastic rocks, Fe-chlorite is relatively localized at Delbridge with higher abundances (up to >15 wt.%) only found in proximity to the two inferred faults in the hydrothermal core and to rhyolite breccia contacts. Notably, some of the higher Fe-chlorite values coincide with carbonate-poor samples. Mg-chlorite abundance is elevated (up to 10 wt.%) in the shallow footwall and immediate hanging-wall probably due to interaction with seawater. Increased Mg-chlorite is also observed along the margins of the system where fluid temperatures were presumably reduced. Compositional variation of chlorite calculated in each sample is expressed as normalized percentages in pie chart format. Symbol size is a function of the total chlorite estimated in a given sample and varies proportionally to the sum of all components (i.e., total chlorite abundance). A symbol diameter of 1 cm represents a maximum total abundance of 39 wt.% chlorite. All smaller pie charts are scaled down by square root because the area of a circle varies by the square root of its radius.

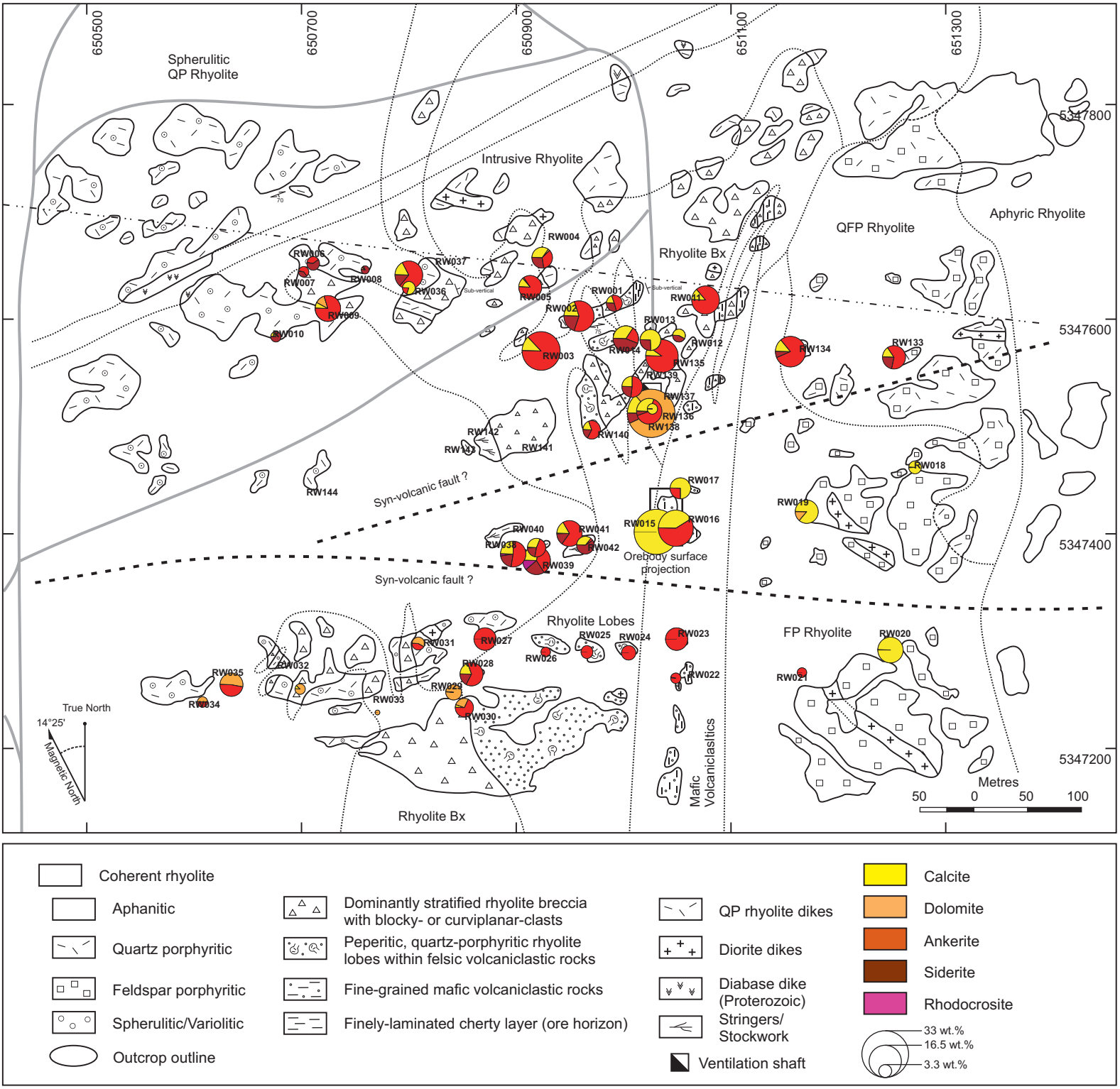

Figure 6.23. Abundance, distribution, and compositional variation of normative carbonate at Delbridge calculated using the MINSQ method (Herrmann and Berry, 2002). Carbonate is clearly most abundant in the core of the system beneath the known mineralization and in adjacent rhyolite breccia. Footwall compositional variation is dominated by ankerite ($Ca(Fe,Mg,Mn)(CO_3)_2$), lesser siderite ($FeCO_3$), and trace dolomite ($CaMg(CO_3)_2$). Normative siderite is most abundant in stringers and stockwork within the interpreted core of upflow and in adjacent rhyolite breccia. The margins of the system show chemical variation towards more Ca- and Mg-rich carbonate members. Calcite ($CaCO_3$) abundance increases dramatically in the hanging-wall where there is no significant Fe-rich carbonate. Trace to minor normative rhodocrosite is estimated in a few samples collected in the stockwork zone immediately beneath the surface projection of the orebody. Compositional variation of carbonate calculated in each sample is expressed as normalized percentages in pie chart format. Symbol size is a function of the total carbonate estimated in a given sample and varies proportionally to the sum of all components (i.e., total carbonate abundance). A symbol diameter of 1 cm represents a maximum total abundance of 33 wt.% carbonate. All smaller pie charts are scaled down by square root because the area of a circle varies by the square root of its radius.

A. Cu in disseminated sulfides

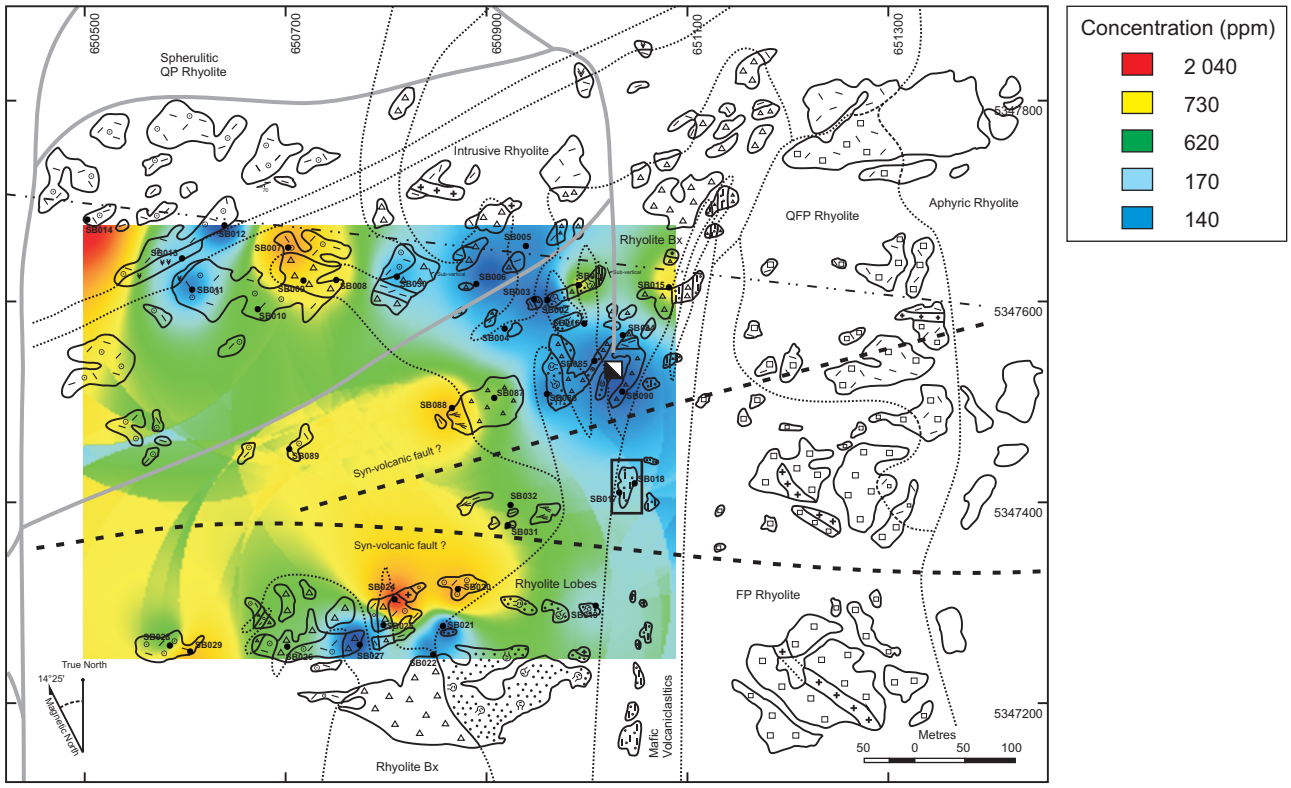

B. Zn in disseminated sulfides

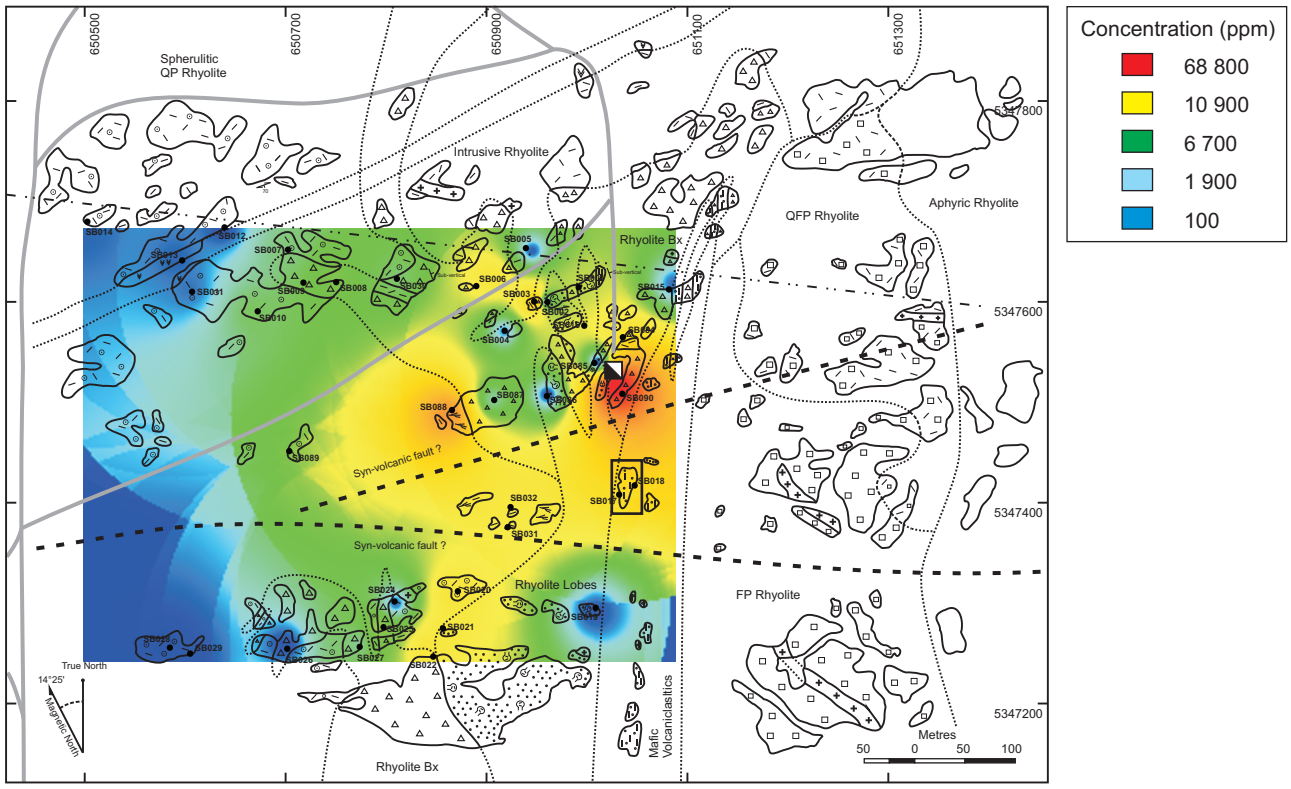

Figure 6.24. Concentrations (ppm) of Cu and Zn in disseminated and stringer sulfides at Delbridge. Plotted data are based on quantitative INAA, ICP-AES, and ICP-MS analyses and contoured using inverse-distance weighting. a) The highest Cu concentrations clearly occur in stringers and stockwork within the interpreted hydrothermal upflow. b) The highest Zn values occur in footwall rhyolite breccia (± stringers and stockwork) and in the immediate hanging wall.

A. Pb in disseminated sulfides

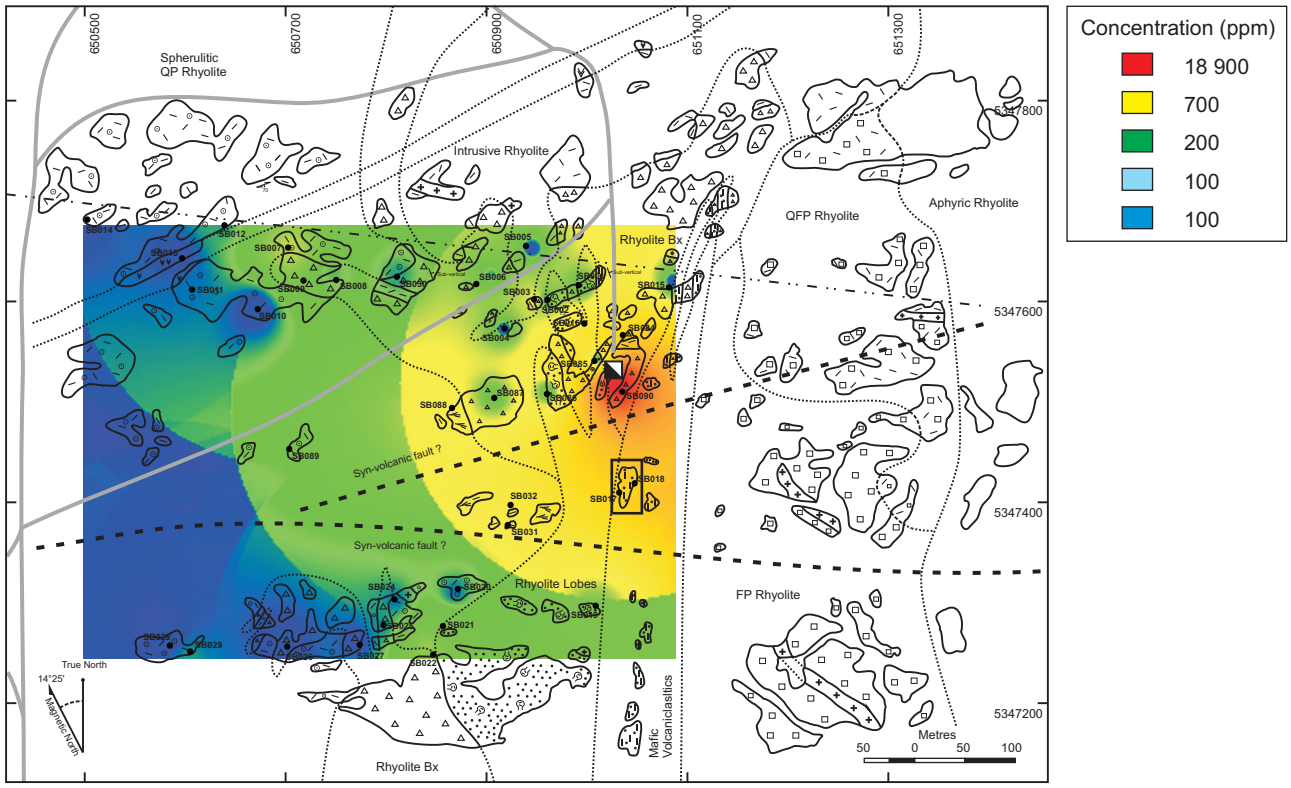

B. Cd in disseminated sulfides

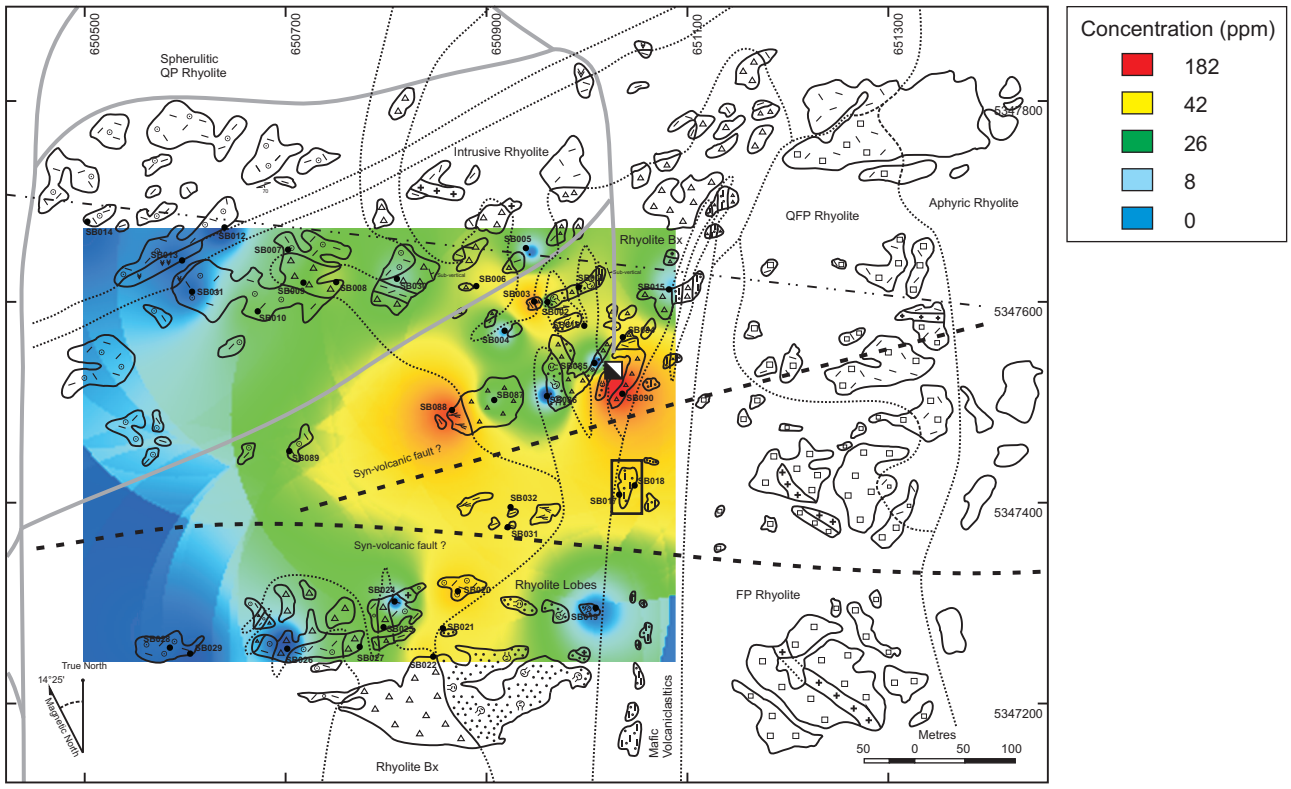

Figure 6.25. Concentrations (ppm) of Pb and Cd in disseminated and stringer sulfides at Delbridge. Plotted data are based on quantitative INAA, ICP-AES, and ICP-MS analyses and contoured using inverse-distance weighting. a) The most abundant Pb occurs in proximal footwall rhyolite breccia and the immediate hanging wall (± stringers and stockwork). b) Similar to Zn and Pb, high Cd occurs in footwall rhyolite breccia (± stringers and stockwork) and in the immediate hanging wall.

A. Au in disseminated sulfides

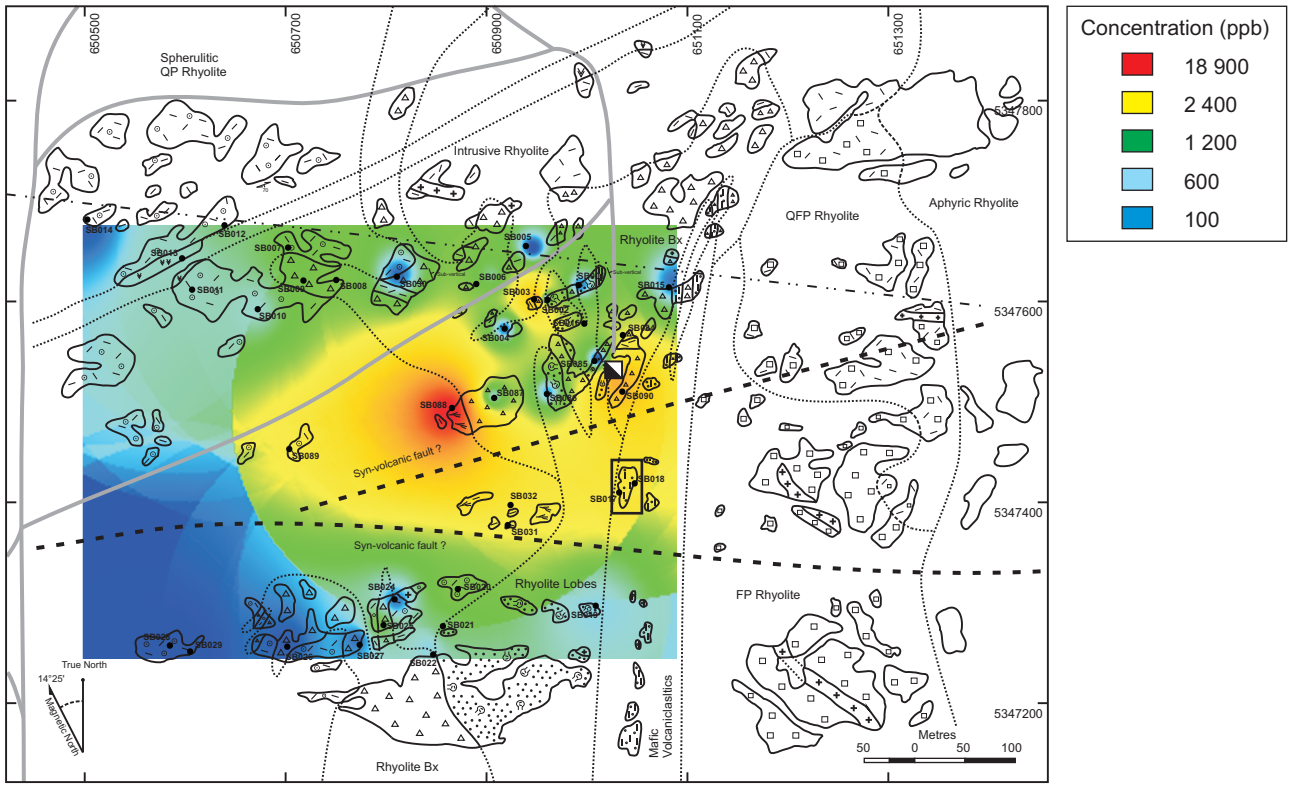

B. Ag in disseminated sulfides

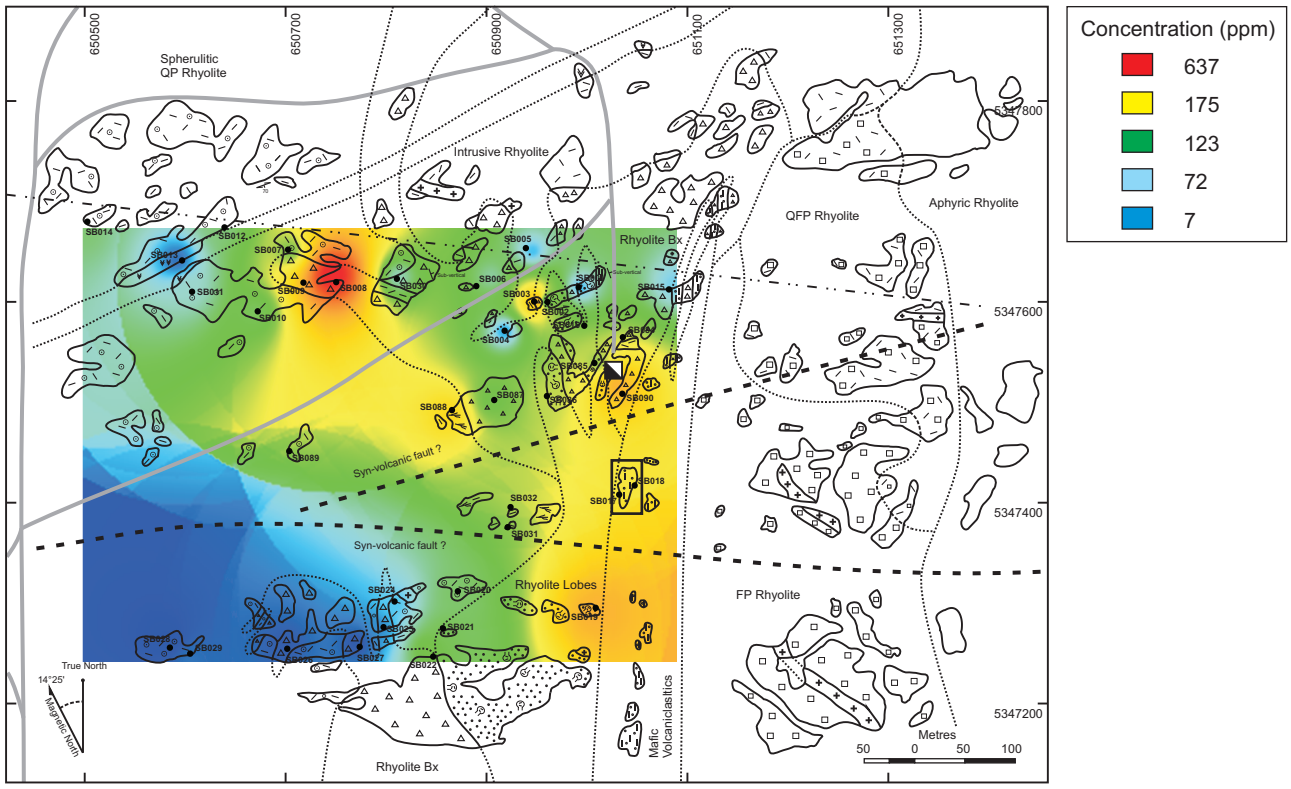

Figure 6.26. Concentrations of Au (ppb) and Ag (ppm) in disseminated and stringer sulfides at Delbridge. Plotted data are based on quantitative INAA, ICP-AES, and ICP-MS analyses and contoured using inverse-distance weighting (IDW). a) The highest Au concentrations are located in stringers and stockwork and proximal footwall rhyolite breccia. b) Abundant Ag occurs outside the interpreted main hydrothermal upflow in distal felsic volcaniclastic rocks and in the hanging wall.

A. As in disseminated sulfides

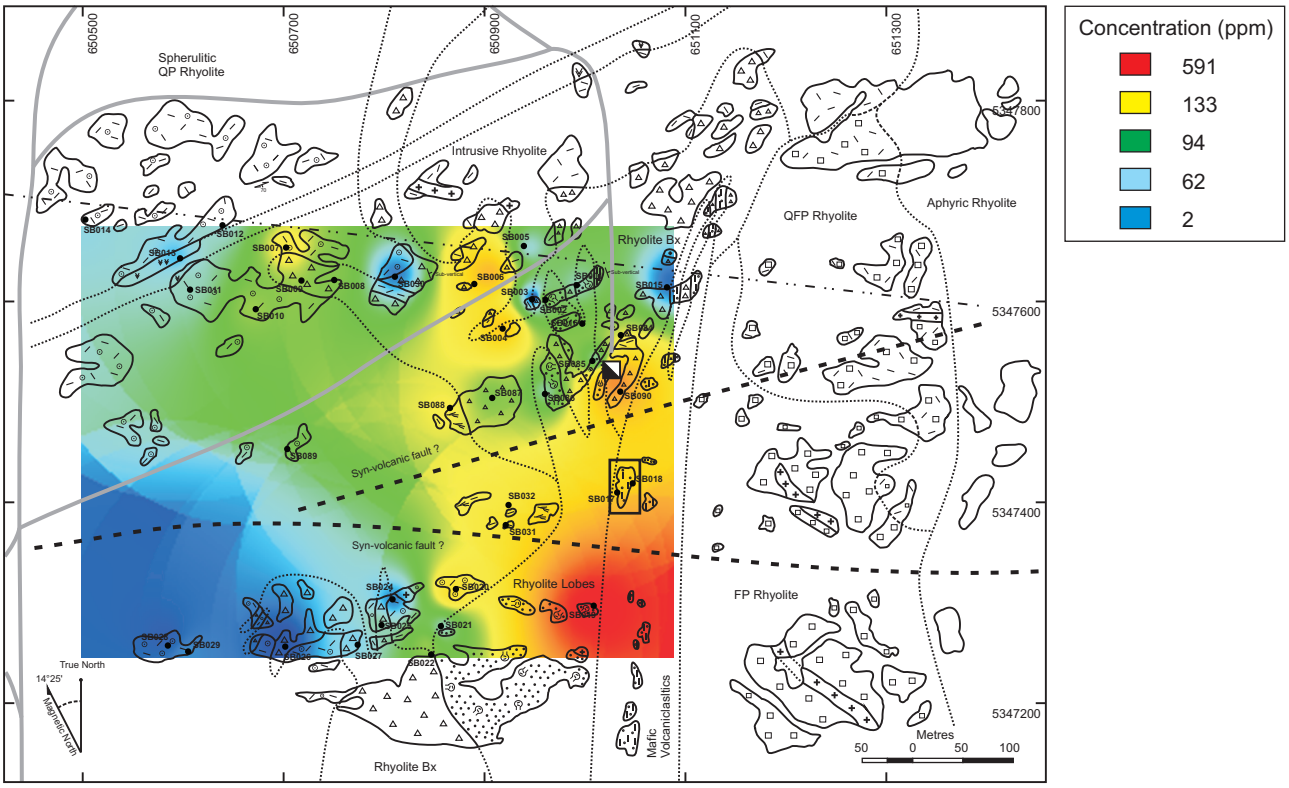

B. Sb in disseminated sulfides

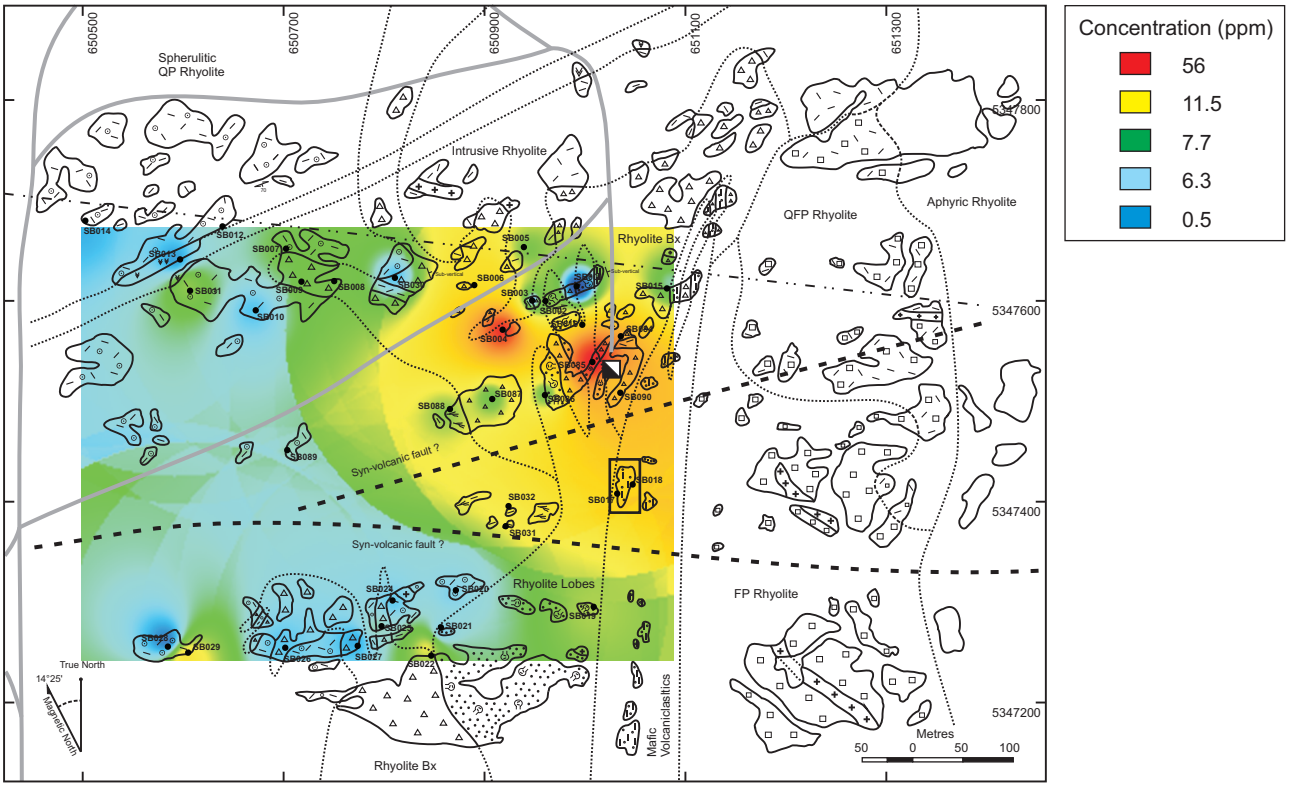

Figure 6.27. Concentrations (ppm) of As and Sb in disseminated sulfides at Delbridge. Plotted data are based on quantitative INAA, ICP-AES, and ICP-MS analyses and contoured using inverse-distance weighting (IDW). a) The highest As concentrations occur in hanging-wall mafic volcaniclastic rocks and in footwall coherent rhyolite (± rhyolite breccia). b) The highest Sb values are located in footwall coherent rhyolite and distal felsic volcaniclastic rocks.

Tl in disseminated sulfides

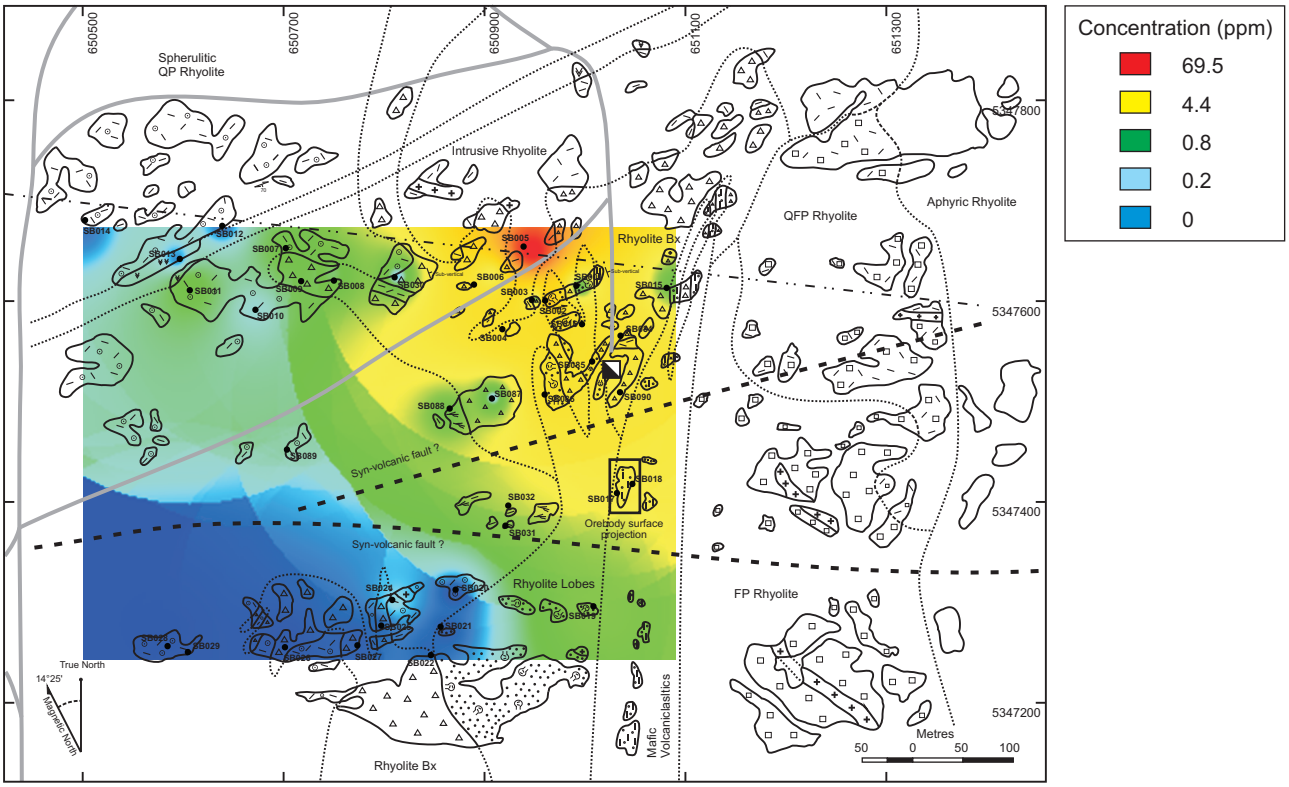

Figure 6.28. Tl concentrations (ppm) in disseminated sulfides at Delbridge. The highest Tl occurs towards the interpreted margins of the system in footwall coherent rhyolite and distal volcaniclastic rocks. Plotted data are based on quantitative trace element analyses and contoured using inverse-distance weighting (IDW).

A. Co in disseminated sulfides

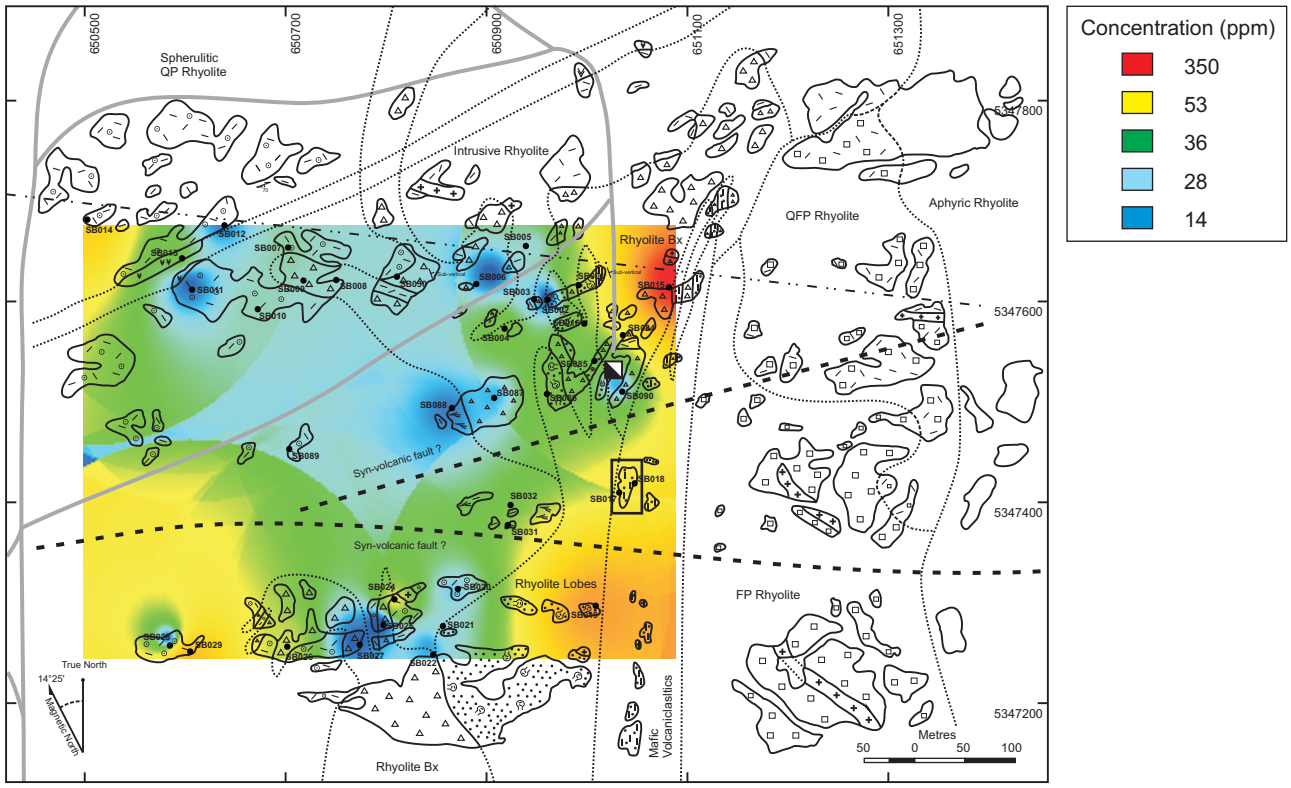

B. Ni in disseminated sulfides

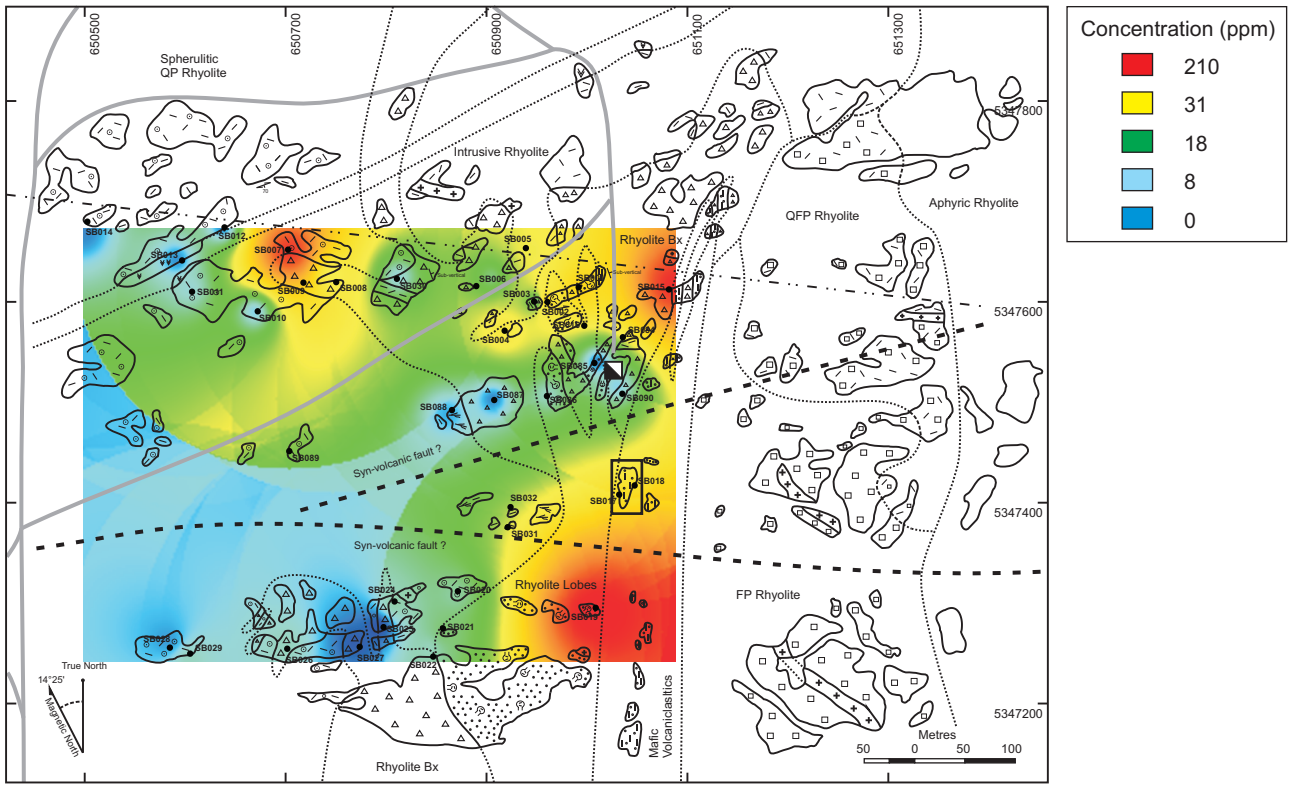

Figure 6.29. Concentrations (ppm) of Co and Ni in disseminated sulfides at Delbridge. Plotted data are based on quantitative INAA, ICP-AES, and ICP-MS analyses and contoured using inverse-distance weighting (IDW). a) High Co occurs in the hanging wall and in distal footwall coherent rhyolite. b) The highest Ni concentrations are located in the hanging wall and along the interpreted margins of the system.

Table 6.1a. Major element oxide data for Delbridge volcanic rocks

Sample Units	Strat. Pos.	Lithofacies	Alteration Type	SiO2 wt.%	TiO2 wt.%	Al2O3 wt.%	Fe2O3 wt.%	MnO wt.%	MgO wt.%	CaO wt.%	Na2O wt.%	K2O wt.%	P2O5 wt.%	LOI wt.%	Total wt.%	CO2 wt.%	S wt.%
RW001*	FW	Lobate QP Rhyo.	Fe-carb	78.02	0.23	11.37	2.01	0.08	0.30	1.31	3.37	1.51	0.03	2.93	101.16	1.94	0.35
RW002	FW	Lobate QP Rhyo.	Fe-carb	72.78	0.17	8.36	4.44	0.16	0.96	4.26	1.10	1.86	0.03	7.21	101.33	6.06	0.11
RW003	FW	Felsic Lapilli Tuff	Mg-Chl	61.13	0.23	9.87	6.77	0.23	2.44	6.59	0.65	2.01	0.04	11.15	101.11	9.22	0.25
RW004	FW	Felsic Lapilli Tuff	Qtz, Ser	77.74	0.16	7.74	4.22	0.13	0.52	2.40	3.59	0.56	0.03	3.90	100.99	3.00	1.43
RW005	FW	Felsic Lapilli Tuff	Qtz, Ser	80.55	0.11	5.80	2.88	0.10	1.20	3.20	0.29	1.28	0.02	5.42	100.85	4.46	0.59
RW006*	FW	Spherulitic QP Rhyo.	Mg-Chl	76.64	0.22	10.74	4.52	0.18	0.48	0.39	4.32	0.93	0.03	2.44	100.89	0.95	0.46
RW007	FW	Rhyo. Breccia	Qtz, Ser	79.78	0.20	10.22	2.87	0.04	0.50	0.48	3.08	1.36	0.03	2.63	101.19	0.81	1.13
RW008	FW	Spherulitic QP Rhyo.	Mg-Chl	78.36	0.21	11.03	3.76	0.05	1.12	0.10	2.25	1.34	0.03	2.35	100.60	0.30	0.42
RW009	FW	Rhyo. Breccia	Fe-carb	72.84	0.16	10.55	2.41	0.24	1.49	3.44	3.72	0.51	0.03	5.69	101.08	4.94	0.30
RW010	FW	Spherulitic QP Rhyo.	Mg-Chl	78.30	0.19	10.33	3.85	0.20	2.01	0.34	2.12	0.92	0.03	2.68	100.97	0.62	0.03
RW011	FW	Rhyo. Breccia	Fe-carb	66.11	0.21	12.44	2.67	0.12	1.63	4.27	6.18	0.21	0.04	6.66	100.54	5.93	0.03
RW012	FW	Rhyo. Breccia	Fe-carb	80.41	0.21	10.04	2.62	0.08	0.10	1.36	2.65	1.19	0.04	2.47	101.17	1.26	0.04
RW013	FW	Rhyo. Breccia	Fe-carb	75.81	0.21	9.87	3.26	0.14	0.18	3.45	2.72	1.19	0.05	4.38	101.26	3.14	0.03
RW014	FW	Lobate QP Rhyo.	Fe-carb	76.26	0.19	8.70	4.54	0.16	0.46	2.83	2.17	1.10	0.04	4.79	101.24	3.92	0.03
RW015	H-W	Mafic Volcaniclastic	Ca-carb, Ser	35.74	0.82	14.61	9.11	0.33	2.22	17.81	1.72	1.26	0.12	16.96	100.70	12.90	0.02
RW016	H-W	Mafic Volcaniclastic	Ca-carb, Ser	42.01	1.02	15.05	11.38	0.24	3.32	11.35	2.53	1.54	0.12	12.07	100.63	8.29	0.01
RW017	H-W	Mafic Volcaniclastic	Ca-carb, Ser	47.22	1.39	20.21	10.33	0.15	2.74	4.39	5.66	1.90	0.18	6.41	100.58	3.28	0.01
RW018	H-W	FP Rhyo.	Qtz, Ser	76.84	0.31	10.45	3.14	0.10	0.18	2.09	4.95	0.65	0.06	2.69	101.46	1.75	0.01
RW019	H-W	FP Rhyo.	Ca-carb, Ser	68.00	0.46	11.44	4.55	0.19	1.13	4.84	5.10	0.24	0.10	5.24	101.29	4.07	0.02
RW020	H-W	FP Rhyo.	Ca-carb, Ser	65.45	0.50	11.93	4.16	0.14	1.49	5.97	4.93	0.44	0.10	5.96	101.07	4.58	0.01
RW021*	H-W	FP Rhyo.	Ca-carb, Ser	68.11	0.58	14.18	5.21	0.13	1.53	2.70	5.32	0.65	0.12	2.65	101.18	1.02	0.01
RW022	H-W	Mafic Volcaniclastic	Ca-carb, Ser	52.66	1.16	19.38	9.21	0.13	4.45	2.60	7.15	0.23	0.08	3.73	100.78	0.79	0.06
RW023	H-W	Mafic Volcaniclastic	Ca-carb, Ser	49.87	1.05	17.52	9.09	0.13	2.34	5.77	6.64	0.52	0.09	6.15	99.17	4.00	0.40
RW024	FW	Lobate QP Rhyo.	Ca-carb, Ser	74.72	0.23	10.84	4.57	0.14	0.88	2.45	2.14	1.42	0.04	3.66	101.09	2.13	0.08
RW025	FW	Lobate QP Rhyo.	Ca-carb, Ser	74.56	0.24	11.69	4.16	0.08	1.08	1.87	3.20	1.12	0.03	3.33	101.36	1.62	0.01
RW026*	FW	Lobate QP Rhyo.	Ca-carb, Ser	76.79	0.23	10.51	4.26	0.05	1.29	1.15	3.37	0.74	0.04	2.60	101.03	1.06	0.01
RW027	FW	Spherulitic QP Rhyo.	Ca-carb, Ser	73.55	0.20	9.16	4.55	0.33	1.92	2.84	3.43	0.44	0.04	4.94	101.40	3.92	0.01
RW028	FW	Spherulitic QP Rhyo.	Mg-Chl	75.78	0.19	9.18	3.75	0.28	0.83	2.61	2.29	1.41	0.03	4.49	100.84	3.77	0.73
RW029	FW	Rhyo. Breccia	Mg-Chl	75.86	0.21	8.97	4.70	0.24	1.56	1.37	1.21	1.45	0.03	3.68	99.28	2.14	0.90
RW030	FW	Rhyo. Breccia	Mg-Chl	76.20	0.21	9.29	3.78	0.30	1.13	1.77	2.41	1.19	0.04	3.74	100.06	2.67	0.67
RW031	FW	Spherulitic QP Rhyo.	Ca-carb, Ser	75.62	0.18	8.62	8.30	0.10	1.49	0.92	0.12	1.22	0.03	3.75	100.35	1.45	0.69
RW032	FW	Felsic Lapilli Tuff	Mg-Chl	77.08	0.19	9.73	4.49	0.10	1.64	0.96	3.66	0.34	0.03	2.76	100.98	1.26	0.07
RW033	FW	Felsic Lapilli Tuff	Mg-Chl	77.01	0.23	10.19	5.58	0.06	2.15	0.07	2.09	0.84	0.04	3.05	101.31	0.53	0.03
RW034	FW	Spherulitic QP Rhyo.	Mg-Chl	71.95	0.33	11.98	5.25	0.11	1.93	0.76	4.01	0.53	0.08	3.58	100.51	1.20	1.56
RW035	FW	Spherulitic QP Rhyo.	Mg-Chl	73.28	0.14	7.58	5.60	0.22	3.71	2.62	0.25	0.62	0.02	6.95	100.99	4.49	0.01
RW036	FW	Spherulitic QP Rhyo.	Fe-carb	78.18	0.21	10.96	2.62	0.08	0.18	1.47	4.08	0.98	0.03	2.65	101.44	1.50	0.01
RW037	FW	Rhyo. Breccia	Fe-carb	71.06	0.17	10.41	3.71	0.11	1.04	3.82	2.79	1.08	0.03	6.64	100.86	5.58	0.04
RW038	FW	Stockwork QP Rhyo.	Fe-carb	73.63	0.18	9.90	3.29	0.21	0.65	3.28	3.26	0.93	0.03	5.71	101.07	4.70	0.01
RW039	FW	Stockwork QP Rhyo.	Fe-carb	70.31	0.23	11.26	3.53	0.89	0.56	3.26	3.27	1.18	0.04	6.01	100.54	5.00	0.06
RW040	FW	Stockwork QP Rhyo.	Fe-carb	78.94	0.19	10.26	1.73	0.16	0.37	1.86	4.27	0.50	0.04	3.11	101.43	2.46	0.01
RW041	FW	Stockwork QP Rhyo.	Fe-carb	75.26	0.19	9.76	3.09	0.16	0.96	3.02	2.17	1.13	0.03	5.68	101.45	4.40	0.01
RW042	FW	Stockwork QP Rhyo.	Fe-carb	78.23	0.20	9.99	3.73	0.07	0.50	1.30	2.34	1.54	0.04	3.46	101.40	1.88	0.01
RW133	H-W	QFP Rhyo.	Qtz, Ser	72.08	0.34	11.53	3.09	0.08	0.75	2.56	5.76	0.60	0.06	4.19	101.04	3.88	0.01
RW134	H-W	QFP Rhyo.	Ca-carb, Ser	65.93	0.50	12.03	3.92	0.13	1.45	4.63	4.19	1.08	0.11	7.01	100.98	6.60	0.26

Sample Units	Strat. Pos.	Lithofacies	Alteration Type	SiO2 wt.%	TiO2 wt.%	Al2O3 wt.%	Fe2O3 wt.%	MnO wt.%	MgO wt.%	CaO wt.%	Na2O wt.%	K2O wt.%	P2O5 wt.%	LOI wt.%	Total wt.%	CO2 wt.%	S wt.%
RW135	FW	QP Rhyo.	Ca-carb, Ser	59.84	0.80	11.13	8.75	0.17	2.72	5.04	2.79	1.00	0.08	8.78	101.10	7.12	0.01
RW136	FW	Rhyo. Breccia	Ca-carb, Ser	73.31	0.24	9.81	3.36	0.12	0.93	3.68	4.37	0.45	0.05	5.06	101.38	4.41	0.01
RW137	FW	Rhyo. Breccia	Mg-Chl	37.10	0.51	8.73	8.21	0.18	14.23	10.63	0.90	0.02	0.27	19.23	100.01	14.70	0.01
RW138	FW	Rhyo. Breccia	Qtz, Ser	73.29	0.32	13.77	3.52	0.09	0.48	1.56	3.68	2.04	0.06	2.65	101.46	1.35	0.02
RW139	FW	Lobate QP Rhyo.	Qtz, Ser	78.90	0.20	8.44	2.35	0.07	0.54	1.81	0.66	1.59	0.04	4.04	98.64	2.60	0.02
RW140	FW	Lobate QP Rhyo.	Qtz, Ser	80.01	0.17	9.42	1.84	0.06	0.36	1.59	4.26	0.41	0.03	2.34	100.49	2.28	0.36
RW141	FW	Rhyo. Breccia	Fe-carb	81.52	0.17	8.82	3.85	0.05	2.16	0.03	0.16	1.27	0.03	2.40	100.46	0.09	0.05
RW142	FW	Stockwork QP Rhyo.	Fe-carb	82.44	0.18	9.21	3.00	0.03	1.84	0.02	0.19	1.54	0.02	2.31	100.78	0.07	0.04
RW143	FW	Stockwork QP Rhyo.	Fe-carb	80.25	0.22	10.52	3.05	0.03	1.80	0.03	0.24	2.00	0.03	2.56	100.73	0.07	0.09
RW144	FW	Dike?	Fe-carb	57.34	1.26	14.75	9.51	0.12	4.43	6.15	3.86	0.79	0.11	2.45	100.77	0.18	0.19

* Denotes least-altered samples.

Table 6.1b. Trace element concentrations of Delbridge volcanic rocks

Sample	Strat.		Alteration	Zn	Cu	Pb	Ba	Cr	Sc	V	Cs	Li	Rb	Sr	Be	Cd	Sb	Tl	Co
Units	Pos.	Lithofacies	Type	ppm	ppm	ppm	ppm	ppm	ppm	ppm	ppm	ppm	ppm	ppm	ppm	ppm	ppm	ppm	ppm
RW001*	FW	Lobate QP Rhyo.	Fe-carb	125	32.6	4.4	132	37	12.5	3.4	0.901	2.3	31.9	39.5	1.18	0.469	0.50	0.242	1.10
RW002	FW	Lobate QP Rhyo.	Fe-carb	113	44.3	7.7	258	23	10.9	1.5	1.366	2.0	44.5	50.5	0.61	0.086	0.61	0.504	0.74
RW003	FW	Felsic Lapilli Tuff	Mg-Chl	169	16.0	3.7	402	11	14.6	2.3	1.588	14	53.7	92.2	1.07	0.210	0.44	0.560	1.18
RW004	FW	Felsic Lapilli Tuff	Qtz, Ser	67	25.0	4.3	125	34	9.40	1.7	0.450	1.1	11.7	27.2	0.40	0.181	0.62	1.236	0.74
RW005	FW	Felsic Lapilli Tuff	Qtz, Ser	873	27.8	14	205	19	5.90	1.5	0.961	2.9	24.8	46.4	0.56	2.335	0.42	0.352	0.95
RW006*	FW	Spherulitic QP Rhyo.	Mg-Chl	92	19.8	4.3	174	18	13.4	1.1	0.710	7.6	18.3	39.6	1.07	0.864	0.31	0.077	0.66
RW007	FW	Rhyo. Breccia	Qtz, Ser	101	19.8	37	278	14	12.0	1.1	0.899	6.3	25.5	34.6	1.03	0.190	0.45	0.093	0.58
RW008	FW	Spherulitic QP Rhyo.	Mg-Chl	407	32.7	15	190	14	8.70	1.0	1.237	24	26.2	39.2	1.24	0.701	0.45	0.113	0.55
RW009	FW	Rhyo. Breccia	Fe-carb	35	28.8	6.0	113	39	7.30	1.7	0.366	1.6	9.95	54.9	0.46	0.134	0.32	0.036	0.76
RW010	FW	Spherulitic QP Rhyo.	Mg-Chl	267	12.9	3.0	153	17	9.60	1.0	0.852	37	15.4	27.1	0.68	0.332	0.33	0.049	0.45
RW011	FW	Rhyo. Breccia	Fe-carb	30	43.0	1.5	112	22	4.70	16	0.258	1.0	4.66	83.6	0.21	0.149	0.68	0.023	6.71
RW012	FW	Rhyo. Breccia	Fe-carb	57	38.1	4.6	147	17	7.80	3.8	1.095	2.5	26.4	30.4	0.50	0.587	0.92	0.138	6.98
RW013	FW	Rhyo. Breccia	Fe-carb	51	76.6	5.9	132	19	7.80	3.0	0.970	1.1	26.0	44.5	0.54	0.188	1.05	0.145	4.53
RW014	FW	Lobate QP Rhyo.	Fe-carb	89	34.0	8.3	103	21	7.40	2.9	0.715	1.4	22.2	35.5	0.49	0.412	0.53	0.163	3.76
RW015	H-W	Mafic Volcaniclastic	Ca-carb, Ser	66	73.2	3.2	294	31	24.9	230	1.056	53	36.5	191	0.36	0.120	0.60	0.364	25.9
RW016	H-W	Mafic Volcaniclastic	Ca-carb, Ser	79	38.5	2.2	311	42	29.4	250	1.728	45	43.1	131	0.34	0.088	0.67	0.284	29.7
RW017	H-W	Mafic Volcaniclastic	Ca-carb, Ser	98	23.0	2.4	858	53	36.7	300	2.119	38	52.1	90.9	1.21	0.199	0.88	0.432	31.7
RW018	H-W	FP Rhyo.	Qtz, Ser	45	63.8	4.0	130	10	8.20	13	0.619	2.8	11.6	39.3	0.38	0.194	0.44	0.024	4.80
RW019	H-W	FP Rhyo.	Ca-carb, Ser	47	141	6.8	43.2	14	11.9	41	0.246	19	3.60	63.0	0.37	0.240	0.42	0.013	6.42
RW020	H-W	FP Rhyo.	Ca-carb, Ser	58	53.4	2.6	118	9	12.9	40	0.538	19	8.90	123	0.63	0.174	0.29	0.020	7.02
RW021*	H-W	FP Rhyo.	Ca-carb, Ser	61	67.3	2.3	211	11	16.0	52	0.815	16	11.6	148	0.67	0.028	0.23	0.018	8.33
RW022	H-W	Mafic Volcaniclastic	Ca-carb, Ser	97	152	2.1	81.2	37	37.7	290	0.380	41	5.70	197	0.31	0.037	0.59	0.023	27.6
RW023	H-W	Mafic Volcaniclastic	Ca-carb, Ser	141	92.3	3.0	125	33	32.2	240	0.601	31	13.9	174	0.27	0.183	0.60	0.058	31.0
RW024	FW	Lobate QP Rhyo.	Ca-carb, Ser	114	24.3	4.5	230	10	13.2	2.7	1.043	17	34.9	56.4	1.10	0.095	0.23	0.185	1.37
RW025	FW	Lobate QP Rhyo.	Ca-carb, Ser	300	81.5	4.2	245	11	14.9	2.0	1.064	22	30.8	53.4	0.93	0.491	0.23	0.136	0.94
RW026*	FW	Lobate QP Rhyo.	Ca-carb, Ser	97	5.80	2.3	177	12	12.6	3.2	0.723	21	20.1	31.7	0.75	0.074	0.29	0.080	2.57
RW027	FW	Spherulitic QP Rhyo.	Ca-carb, Ser	167	10.9	3.5	107	12	11.2	3.2	0.372	19	8.50	33.3	0.48	0.091	0.20	0.040	0.62
RW028	FW	Spherulitic QP Rhyo.	Mg-Chl	864	26.5	53	252	22	12.0	2.7	1.011	4.8	27.7	44.4	0.74	2.398	0.37	0.108	0.85
RW029	FW	Rhyo. Breccia	Mg-Chl	392	21.6	44	312	18	12.7	3.3	1.109	18	27.4	37.1	0.83	0.743	0.56	0.105	0.87
RW030	FW	Rhyo. Breccia	Mg-Chl	204	17.2	9.5	190	23	12.0	4.0	0.957	12	23.3	48.7	1.07	0.254	0.51	0.109	1.14
RW031	FW	Spherulitic QP Rhyo.	Ca-carb, Ser	376	225	3.8	380	17	10.4	1.3	0.811	31	21.3	17.8	0.76	0.349	0.29	0.069	0.84
RW032	FW	Felsic Lapilli Tuff	Mg-Chl	68	47.1	3.6	102	22	10.4	1.0	0.317	24	6.43	43.1	0.55	0.327	0.64	0.022	0.57
RW033	FW	Felsic Lapilli Tuff	Mg-Chl	776	26.4	4.5	179	16	11.2	3.5	0.775	35	14.8	18.6	0.63	2.187	0.43	0.049	0.48
RW034	FW	Spherulitic QP Rhyo.	Mg-Chl	67	62.0	2.8	160	19	14.3	4.0	0.444	26	9.17	52.7	0.80	0.247	0.80	0.029	2.62
RW035	FW	Spherulitic QP Rhyo.	Mg-Chl	68	11.3	2.5	174	14	10.2	1.3	0.601	41	10.9	50.9	0.72	0.307	0.36	0.033	0.93
RW036	FW	Spherulitic QP Rhyo.	Fe-carb	56	37.6	5.2	188	12	11.8	1.0	0.862	1.4	21.7	28.3	0.58	1.009	0.40	0.103	2.71
RW037	FW	Rhyo. Breccia	Fe-carb	43	148	3.3	172	21	7.30	1.3	0.836	1.0	24.1	48.1	0.59	0.059	0.39	0.104	3.16
RW038	FW	Stockwork QP Rhyo.	Fe-carb	71	5.90	4.0	304	16	9.40	1.5	0.762	1.9	18.8	39.2	0.64	0.050	0.30	0.161	0.65
RW039	FW	Stockwork QP Rhyo.	Fe-carb	67	25.1	6.6	365	12	12.2	4.2	1.008	2.8	24.6	50.0	1.00	0.048	0.53	0.236	1.51
RW040	FW	Stockwork QP Rhyo.	Fe-carb	43	6.40	3.4	146	30	9.60	3.4	0.442	1.3	10.7	28.8	0.64	0.108	0.35	0.129	0.71
RW041	FW	Stockwork QP Rhyo.	Fe-carb	73	7.20	4.1	308	23	11.6	3.7	1.237	8.8	26.8	62.1	0.91	0.131	0.32	0.369	0.63
RW042	FW	Stockwork QP Rhyo.	Fe-carb	150	5.90	3.7	444	12	11.8	1.9	1.458	7.1	36.0	34.4	0.83	0.085	0.39	0.493	0.83
RW133	H-W	QFP Rhyo.	Qtz, Ser	42	10.3	2.5	104	33	8.30	23	0.764	3.6	12.0	47.1	0.39	0.045	0.72	0.033	3.93
RW134	H-W	QFP Rhyo.	Ca-carb, Ser	54	82.8	5.6	185	11	14.1	50	0.916	6.2	21.7	99.1	0.88	0.248	0.52	0.076	8.17

Table 6.1b. Trace element concentrations of Delbridge volcanic rocks

Sample Units	Strat. Pos.	Lithofacies	Alteration Type	Ni ppm	Mo ppm	Ga ppm	In ppm	Sn ppm	W ppm
RW001*	FW	Lobate QP Rhyo.	Fe-carb	2.8	2.22	18.63	0.143	2.89	0.29
RW002	FW	Lobate QP Rhyo.	Fe-carb	2.8	1.44	13.92	0.088	5.07	0.29
RW003	FW	Felsic Lapilli Tuff	Mg-Chl	2.1	2.12	19.55	0.136	2.18	0.23
RW004	FW	Felsic Lapilli Tuff	Qtz, Ser	2.0	4.17	7.64	0.067	1.28	0.39
RW005	FW	Felsic Lapilli Tuff	Qtz, Ser	0.8	1.77	10.58	0.181	1.65	0.14
RW006*	FW	Spherulitic QP Rhyo.	Mg-Chl	0.8	2.33	17.79	0.102	2.43	0.25
RW007	FW	Rhyo. Breccia	Qtz, Ser	0.8	1.73	15.74	0.076	3.46	0.27
RW008	FW	Spherulitic QP Rhyo.	Mg-Chl	0.8	1.94	18.17	0.081	2.33	0.36
RW009	FW	Rhyo. Breccia	Fe-carb	0.8	2.30	9.51	0.059	2.99	0.26
RW010	FW	Spherulitic QP Rhyo.	Mg-Chl	0.8	1.76	16.01	0.049	1.85	0.23
RW011	FW	Rhyo. Breccia	Fe-carb	4.5	1.61	5.70	0.015	0.44	0.06
RW012	FW	Rhyo. Breccia	Fe-carb	7.3	1.14	11.95	0.048	1.22	0.13
RW013	FW	Rhyo. Breccia	Fe-carb	5.0	1.15	11.54	0.053	1.02	0.16
RW014	FW	Lobate QP Rhyo.	Fe-carb	5.3	1.71	10.07	0.054	1.10	0.21
RW015	H-W	Mafic Volcaniclastic	Ca-carb, Ser	25	0.16	14.37	0.036	0.62	0.05
RW016	H-W	Mafic Volcaniclastic	Ca-carb, Ser	26	0.13	14.49	0.038	0.51	0.07
RW017	H-W	Mafic Volcaniclastic	Ca-carb, Ser	28	0.15	22.43	0.062	1.54	0.23
RW018	H-W	FP Rhyo.	Qtz, Ser	1.7	0.96	9.45	0.031	2.81	0.17
RW019	H-W	FP Rhyo.	Ca-carb, Ser	3.1	1.64	11.49	0.037	5.13	0.16
RW020	H-W	FP Rhyo.	Ca-carb, Ser	3.2	0.57	13.47	0.040	1.62	0.23
RW021*	H-W	FP Rhyo.	Ca-carb, Ser	2.8	0.92	14.66	0.054	1.70	0.22
RW022	H-W	Mafic Volcaniclastic	Ca-carb, Ser	15	0.23	16.00	0.044	1.27	0.10
RW023	H-W	Mafic Volcaniclastic	Ca-carb, Ser	26	0.34	16.43	0.047	1.00	0.13
RW024	FW	Lobate QP Rhyo.	Ca-carb, Ser	4.7	0.84	18.51	0.112	3.22	0.16
RW025	FW	Lobate QP Rhyo.	Ca-carb, Ser	0.8	0.85	19.76	0.088	3.52	0.22
RW026*	FW	Lobate QP Rhyo.	Ca-carb, Ser	1.9	0.77	16.15	0.087	2.10	0.21
RW027	FW	Spherulitic QP Rhyo.	Ca-carb, Ser	0.8	1.45	13.51	0.057	1.75	0.26
RW028	FW	Spherulitic QP Rhyo.	Mg-Chl	0.8	2.58	14.75	0.170	3.00	0.29
RW029	FW	Rhyo. Breccia	Mg-Chl	0.8	1.24	16.24	0.167	3.40	0.29
RW030	FW	Rhyo. Breccia	Mg-Chl	0.8	2.87	15.59	0.149	3.93	0.26
RW031	FW	Spherulitic QP Rhyo.	Ca-carb, Ser	0.8	1.38	16.26	0.355	5.60	0.31
RW032	FW	Felsic Lapilli Tuff	Mg-Chl	0.8	1.93	15.30	0.039	1.66	0.25
RW033	FW	Felsic Lapilli Tuff	Mg-Chl	0.8	1.57	16.32	0.113	1.41	0.21
RW034	FW	Spherulitic QP Rhyo.	Mg-Chl	0.8	1.97	17.18	0.057	1.64	0.34
RW035	FW	Spherulitic QP Rhyo.	Mg-Chl	0.8	1.20	14.92	0.036	1.75	0.17
RW036	FW	Spherulitic QP Rhyo.	Fe-carb	0.8	5.71	15.94	0.032	2.06	0.36
RW037	FW	Rhyo. Breccia	Fe-carb	0.8	4.33	12.38	0.042	1.43	0.49
RW038	FW	Stockwork QP Rhyo.	Fe-carb	0.8	1.05	13.86	0.092	1.70	0.24
RW039	FW	Stockwork QP Rhyo.	Fe-carb	0.8	2.01	16.83	0.101	2.36	0.21
RW040	FW	Stockwork QP Rhyo.	Fe-carb	0.8	1.74	12.71	0.044	1.75	0.58
RW041	FW	Stockwork QP Rhyo.	Fe-carb	0.8	1.58	15.49	0.098	1.73	0.17
RW042	FW	Stockwork QP Rhyo.	Fe-carb	0.8	0.93	16.87	0.070	2.44	0.20
RW133	H-W	QFP Rhyo.	Qtz, Ser	4.0	3.94	12.95	0.034	2.21	0.23
RW134	H-W	QFP Rhyo.	Ca-carb, Ser	4.8	2.11	14.70	0.046	4.04	0.20

Table 6.1b. Trace element concentrations of Delbridge volcanic rocks

Sample Units	Strat. Pos.	Lithofacies	Alteration Type	Zn ppm	Cu ppm	Pb ppm	Ba ppm	Cr ppm	Sc ppm	V ppm	Cs ppm	Li ppm	Rb ppm	Sr ppm	Be ppm	Cd ppm	Sb ppm	Tl ppm	Co ppm
RW135	FW	QP Rhyo.	Ca-carb, Ser	228	54.3	3.5	281	10	25.3	190	1.063	33	25.6	71.6	0.62	0.350	1.78	0.172	24.2
RW136	FW	Rhyo. Breccia	Ca-carb, Ser	52	59.1	3.3	101	21	8.40	4.4	0.389	10	10.9	59.8	0.39	0.079	0.48	0.119	5.09
RW137	FW	Rhyo. Breccia	Mg-Chl	74	6.30	3.7	195	1174	27.9	160	0.143	93	0.46	397	0.90	0.133	2.18	0.003	53.8
RW138	FW	Rhyo. Breccia	Qtz, Ser	88	32.2	6.3	306	16	11.7	6.0	2.584	9.6	52.9	73.4	1.30	0.348	0.63	0.582	2.89
RW139	FW	Lobate QP Rhyo.	Qtz, Ser	214	51.4	5.1	218	9	8.80	3.2	1.074	9.0	38.4	49.4	0.83	1.035	0.58	0.334	2.11
RW140	FW	Lobate QP Rhyo.	Qtz, Ser	60	22.2	4.0	81.5	38	9.30	2.6	0.368	1.2	9.53	23.7	0.34	0.076	0.48	0.381	0.88
RW141	FW	Rhyo. Breccia	Fe-carb	661	23.4	12	154	19	10.7	1.4	1.048	49	27.0	15.9	0.61	1.290	1.83	0.640	0.33
RW142	FW	Stockwork QP Rhyo.	Fe-carb	315	9.90	9.2	178	17	10.7	1.6	1.145	37	32.2	16.5	0.59	0.394	0.52	0.679	0.25
RW143	FW	Stockwork QP Rhyo.	Fe-carb	441	12.5	28	234	8	14.2	1.1	1.462	37	39.4	18.7	0.67	0.620	0.42	0.676	0.27
RW144	FW	Dike?	Fe-carb	80	88.8	4.6	273	17	34.9	370	0.284	17	19.2	127	0.57	0.060	0.14	0.092	35.4

* Denotes least-altered samples.

Table 6.1b. Trace element concentrations of Delbridge volcanic rocks

Sample Units	Strat. Pos.	Lithofacies	Alteration Type	Ni ppm	Mo ppm	Ga ppm	In ppm	Sn ppm	W ppm
RW135	FW	QP Rhyo.	Ca-carb, Ser	17	0.83	18.21	0.093	2.80	0.44
RW136	FW	Rhyo. Breccia	Ca-carb, Ser	11	2.02	10.44	0.046	2.71	0.09
RW137	FW	Rhyo. Breccia	Mg-Chl	407	0.13	9.51	0.036	0.93	0.08
RW138	FW	Rhyo. Breccia	Qtz, Ser	4.1	1.33	22.10	0.081	1.92	0.23
RW139	FW	Lobate QP Rhyo.	Qtz, Ser	5.0	0.77	13.77	0.092	2.72	0.35
RW140	FW	Lobate QP Rhyo.	Qtz, Ser	1.7	3.84	11.59	0.072	2.43	0.20
RW141	FW	Rhyo. Breccia	Fe-carb	0.8	1.91	16.90	0.108	3.13	0.34
RW142	FW	Stockwork QP Rhyo.	Fe-carb	0.8	1.45	17.10	0.098	8.82	0.34
RW143	FW	Stockwork QP Rhyo.	Fe-carb	0.8	1.36	18.69	0.098	2.40	0.34
RW144	FW	Dike?	Fe-carb	16	1.50	16.86	0.057	3.53	0.24

* Denotes least-altered samples.

Table 6.1c. Rare-earth element composition of Delbridge volcanic rocks

Sample	Strat.		Alteration	La	Ce	Pr	Nd	Sm	Eu	Gd	Tb	Dy	Ho	Er	Tm	Yb	Lu	Total REE
Units	Pos.	Lithofacies	Type	ppm	ppm	ppm	ppm	ppm	ppm	ppm	ppm	ppm	ppm	ppm	ppm	ppm	ppm	ppm
RW001*	FW	Lobate QP Rhyo.	Fe-carb	25.2	57.3	7.85	33.9	8.2	1.9	7.7	1.2	7.5	1.6	5.16	0.79	5.41	0.87	165
RW002	FW	Lobate QP Rhyo.	Fe-carb	16.3	39.5	5.80	27.1	8.8	2.1	8.0	1.2	7.7	1.6	4.69	0.68	4.48	0.70	129
RW003	FW	Felsic Lapilli Tuff	Mg-Chl	16.3	39.3	5.55	26.2	8.6	2.2	9.2	1.5	9.5	2.0	5.97	0.89	5.84	0.90	134
RW004	FW	Felsic Lapilli Tuff	Qtz, Ser	14.8	33.8	4.57	19.8	5.4	1.5	5.8	1.0	6.4	1.4	4.20	0.63	4.36	0.66	104
RW005	FW	Felsic Lapilli Tuff	Qtz, Ser	12.1	27.3	3.75	16.3	4.6	1.1	5.3	0.9	6.0	1.3	3.74	0.55	3.61	0.55	87.0
RW006*	FW	Spherulitic QP Rhyo.	Mg-Chl	21.7	50.1	7.04	31.4	8.0	2.1	8.7	1.5	9.9	2.1	6.51	0.98	6.63	1.03	157
RW007	FW	Rhyo. Breccia	Qtz, Ser	17.5	41.0	5.63	25.1	7.0	1.5	7.3	1.2	8.0	1.8	5.53	0.84	5.73	0.89	129
RW008	FW	Spherulitic QP Rhyo.	Mg-Chl	14.8	34.2	4.74	21.2	5.8	1.3	5.7	0.9	6.0	1.3	3.95	0.62	4.21	0.66	105
RW009	FW	Rhyo. Breccia	Fe-carb	14.5	33.4	4.71	21.2	6.0	1.7	6.9	1.1	7.2	1.5	4.45	0.68	4.41	0.69	108
RW010	FW	Spherulitic QP Rhyo.	Mg-Chl	16.5	38.4	5.25	23.3	6.3	1.4	6.7	1.1	7.4	1.6	4.80	0.73	4.84	0.74	119
RW011	FW	Rhyo. Breccia	Fe-carb	4.4	11.0	1.58	7.2	2.2	0.7	2.4	0.4	2.7	0.6	1.92	0.29	2.01	0.30	37.5
RW012	FW	Rhyo. Breccia	Fe-carb	12.6	29.8	4.11	17.2	4.3	1.0	4.3	0.8	4.8	1.0	3.17	0.48	3.21	0.49	87.4
RW013	FW	Rhyo. Breccia	Fe-carb	13.9	32.1	4.35	18.8	4.6	1.1	4.8	0.8	5.1	1.1	3.34	0.51	3.37	0.52	94.4
RW014	FW	Lobate QP Rhyo.	Fe-carb	10.9	26.6	3.65	15.9	4.1	1.1	4.5	0.8	5.1	1.1	3.27	0.49	3.25	0.50	81.3
RW015	H-W	Mafic Volcaniclastic	Ca-carb, Ser	3.9	8.8	1.24	5.4	1.5	0.6	1.8	0.3	1.9	0.4	1.13	0.16	1.08	0.17	28.4
RW016	H-W	Mafic Volcaniclastic	Ca-carb, Ser	2.8	6.1	0.87	4.1	1.2	0.6	1.4	0.2	1.7	0.3	1.01	0.15	1.00	0.15	21.5
RW017	H-W	Mafic Volcaniclastic	Ca-carb, Ser	6.5	13.2	1.73	7.6	2.1	0.8	2.5	0.4	2.7	0.6	1.67	0.23	1.48	0.22	41.7
RW018	H-W	FP Rhyo.	Qtz, Ser	13.7	29.4	3.87	16.1	4.2	0.8	4.3	0.7	4.6	1.0	3.07	0.49	3.44	0.53	86.2
RW019	H-W	FP Rhyo.	Ca-carb, Ser	14.3	30.8	3.98	16.5	4.0	0.9	4.3	0.7	4.7	1.0	3.05	0.46	3.04	0.47	88.2
RW020	H-W	FP Rhyo.	Ca-carb, Ser	13.2	29.8	3.94	16.4	4.3	1.1	4.8	0.8	5.2	1.1	3.25	0.48	3.20	0.49	88.1
RW021*	H-W	FP Rhyo.	Ca-carb, Ser	17.3	37.7	4.96	20.7	5.1	1.1	5.5	0.9	6.2	1.3	3.98	0.60	4.10	0.65	110
RW022	H-W	Mafic Volcaniclastic	Ca-carb, Ser	1.8	4.4	0.63	3.1	1.1	0.5	1.4	0.3	1.7	0.4	1.09	0.16	1.06	0.16	17.7
RW023	H-W	Mafic Volcaniclastic	Ca-carb, Ser	4.3	9.6	1.32	5.8	1.6	0.7	1.9	0.3	2.1	0.5	1.35	0.19	1.31	0.19	31.2
RW024	FW	Lobate QP Rhyo.	Ca-carb, Ser	22.2	51.3	7.21	32.2	7.9	1.8	7.5	1.1	7.1	1.5	4.57	0.70	4.91	0.79	151
RW025	FW	Lobate QP Rhyo.	Ca-carb, Ser	21.3	49.3	6.74	29.6	7.7	2.2	8.1	1.3	8.6	1.9	5.69	0.87	5.92	0.92	150
RW026*	FW	Lobate QP Rhyo.	Ca-carb, Ser	22.2	50.8	6.92	29.6	7.3	1.9	7.7	1.3	8.8	1.9	5.91	0.89	5.98	0.94	152
RW027	FW	Spherulitic QP Rhyo.	Ca-carb, Ser	19.4	45.3	6.15	26.9	6.7	1.9	7.1	1.2	7.7	1.7	5.22	0.80	5.42	0.83	136
RW028	FW	Spherulitic QP Rhyo.	Mg-Chl	18.2	43.8	5.94	26.1	7.0	2.5	7.9	1.3	8.8	1.9	5.58	0.82	5.53	0.86	136
RW029	FW	Rhyo. Breccia	Mg-Chl	16.4	41.9	6.15	27.7	7.6	1.9	7.8	1.3	8.6	1.9	5.56	0.83	5.75	0.87	134
RW030	FW	Rhyo. Breccia	Mg-Chl	19.0	45.2	6.34	27.3	6.9	2.2	7.5	1.3	8.5	1.8	5.45	0.82	5.55	0.85	139
RW031	FW	Spherulitic QP Rhyo.	Ca-carb, Ser	19.1	42.4	5.84	25.4	6.5	1.0	7.7	1.3	8.7	1.8	5.28	0.79	5.20	0.80	132
RW032	FW	Felsic Lapilli Tuff	Mg-Chl	17.9	40.7	5.50	23.5	6.3	1.7	7.4	1.3	8.4	1.8	5.41	0.83	5.57	0.86	127
RW033	FW	Felsic Lapilli Tuff	Mg-Chl	19.3	45.5	6.27	27.7	7.3	1.6	7.9	1.3	8.6	1.9	5.52	0.83	5.69	0.88	140
RW034	FW	Spherulitic QP Rhyo.	Mg-Chl	16.0	39.5	5.60	25.2	6.9	1.5	8.0	1.3	8.9	1.9	5.47	0.81	5.37	0.85	127
RW035	FW	Spherulitic QP Rhyo.	Mg-Chl	17.2	40.3	5.46	24.3	6.5	0.9	7.0	1.1	7.1	1.5	4.39	0.65	4.31	0.66	121
RW036	FW	Spherulitic QP Rhyo.	Fe-carb	70.8	125	13.7	51.8	11.2	2.3	10.2	1.5	9.0	1.9	6.04	0.94	6.28	0.98	311
RW037	FW	Rhyo. Breccia	Fe-carb	14.2	32.4	4.51	20.6	5.7	1.2	5.3	0.8	5.3	1.1	3.58	0.55	3.66	0.56	99.4
RW038	FW	Stockwork QP Rhyo.	Fe-carb	16.8	39.8	5.51	24.0	6.2	1.6	6.6	1.1	7.2	1.5	4.77	0.73	4.99	0.76	121
RW039	FW	Stockwork QP Rhyo.	Fe-carb	19.4	47.2	6.66	29.8	7.8	2.2	8.0	1.3	8.6	1.8	5.44	0.83	5.57	0.86	145
RW040	FW	Stockwork QP Rhyo.	Fe-carb	15.7	38.0	5.41	24.9	7.3	1.8	7.7	1.2	8.1	1.7	5.31	0.81	5.42	0.82	124
RW041	FW	Stockwork QP Rhyo.	Fe-carb	12.5	29.8	4.09	18.4	5.3	1.3	5.4	0.9	5.8	1.3	3.88	0.60	4.06	0.63	93.9
RW042	FW	Stockwork QP Rhyo.	Fe-carb	17.0	43.1	6.25	29.7	8.4	1.9	7.5	1.2	8.0	1.8	5.47	0.84	5.78	0.90	138
RW133	H-W	QFP Rhyo.	Qtz, Ser	15.3	33.8	4.38	17.6	4.2	0.9	4.4	0.8	5.0	1.1	3.28	0.51	3.42	0.53	95.1
RW134	H-W	QFP Rhyo.	Ca-carb, Ser	15.8	35.6	4.53	19.0	4.6	1.1	4.9	0.8	5.3	1.1	3.32	0.50	3.36	0.51	100

Table 6.1c. Rare-earth element composition of Delbridge volcanic rocks

Sample Units	Strat. Pos.	Lithofacies	Alteration Type	La ppm	Ce ppm	Pr ppm	Nd ppm	Sm ppm	Eu ppm	Gd ppm	Tb ppm	Dy ppm	Ho ppm	Er ppm	Tm ppm	Yb ppm	Lu ppm	Total REE ppm
RW135	FW	QP Rhyo.	Ca-carb, Ser	26.3	60.7	8.20	36.1	9.5	1.5	10.1	1.7	11.3	2.4	7.18	1.09	7.17	1.08	184
RW136	FW	Rhyo. Breccia	Ca-carb, Ser	16.2	36.8	4.90	20.7	5.0	1.3	5.1	0.8	5.5	1.2	3.57	0.54	3.64	0.58	106
RW137	FW	Rhyo. Breccia	Mg-Chl	15.3	36.5	5.19	23.2	5.0	1.4	4.0	0.5	2.9	0.5	1.48	0.21	1.36	0.20	97.8
RW138	FW	Rhyo. Breccia	Qtz, Ser	18.3	42.7	5.68	24.1	5.8	1.5	6.3	1.1	7.1	1.5	4.67	0.71	4.78	0.74	125
RW139	FW	Lobate QP Rhyo.	Qtz, Ser	11.3	26.7	3.67	16.4	4.6	1.1	4.8	0.8	5.3	1.1	3.37	0.50	3.38	0.51	83.8
RW140	FW	Lobate QP Rhyo.	Qtz, Ser	17.8	43.9	6.12	27.6	7.6	1.9	7.6	1.2	7.8	1.6	4.69	0.70	4.69	0.71	134
RW141	FW	Rhyo. Breccia	Fe-carb	10.3	24.0	3.38	15.3	4.9	1.1	5.9	1.0	7.2	1.5	4.77	0.73	4.88	0.75	85.6
RW142	FW	Stockwork QP Rhyo.	Fe-carb	14.6	35.2	4.88	22.4	6.8	1.4	7.0	1.2	7.6	1.6	4.85	0.72	4.77	0.71	114
RW143	FW	Stockwork QP Rhyo.	Fe-carb	17.9	43.0	5.95	26.7	7.5	1.5	7.8	1.3	8.3	1.8	5.46	0.83	5.56	0.85	134
RW144	FW	Dike?	Fe-carb	11.8	25.1	3.15	12.9	3.1	0.9	3.4	0.5	3.6	0.7	2.14	0.31	2.10	0.32	70.0

* Denotes least-altered samples.

Table 6.2a. Pearson correlation matrix of major, trace, and rare-earth elements in rhyolite at Delbridge from whole-rock analytical data

	SiO2	*Al2O3*	*Na2O*	*K2O*	*CaO*	*Fe2O3*	*MgO*	*MnO*	*TiO2*	*P2O5*	*LOI*	*CO2*	*Zr*	*Hf*	*Ta*	*Y*	*Nb*	*U*	*Th*	*Cr*	*Sc*	*V*	*Ba*	*Cs*
Al2O3	-0.30																							
Na2O	-0.13	0.65																						
K2O	0.34	-0.10	-0.58																					
CaO	-0.89	0.09	0.11	-0.31																				
Fe2O3	-0.66	0.13	-0.22	-0.10	0.45																			
MgO	-0.78	-0.06	-0.27	-0.31	0.61	0.60																		
MnO	-0.22	-0.02	0.03	-0.06	0.25	0.08	0.04																	
TiO2	-0.65	0.62	0.29	-0.22	0.50	0.64	0.38	-0.02																
P2O5	-0.85	0.31	0.18	-0.41	0.71	0.50	0.78	0.02	0.63															
LOI	-0.82	-0.20	-0.19	-0.19	0.85	0.43	0.75	0.27	0.17	0.63														
CO2	-0.76	-0.20	-0.05	-0.22	0.87	0.29	0.59	0.32	0.12	0.55	0.96													
Zr	0.50	0.20	0.07	0.37	-0.62	-0.28	-0.49	0.01	-0.32	-0.47	-0.52	-0.51												
Hf	0.47	0.18	0.05	0.37	-0.60	-0.22	-0.48	0.03	-0.29	-0.48	-0.48	-0.48	0.99											
Ta	0.44	0.16	-0.03	0.43	-0.57	-0.11	-0.47	0.04	-0.21	-0.53	-0.44	-0.44	0.88	0.93										
Y	0.35	-0.12	-0.21	0.33	-0.48	0.07	-0.29	0.13	-0.24	-0.46	-0.27	-0.30	0.65	0.73	0.83									
Nb	0.48	0.12	-0.06	0.45	-0.62	-0.17	-0.48	0.04	-0.30	-0.54	-0.46	-0.46	0.92	0.96	0.98	0.83								
U	-0.06	0.42	0.26	0.08	-0.13	0.15	-0.08	-0.06	0.30	0.10	-0.14	-0.16	0.61	0.66	0.65	0.50	0.60							
Th	-0.06	0.46	0.28	0.11	-0.14	0.18	-0.15	0.00	0.33	0.06	-0.16	-0.17	0.64	0.69	0.70	0.50	0.63	0.93						
Cr	-0.68	-0.15	-0.17	-0.30	0.57	0.33	0.90	0.03	0.17	0.78	0.74	0.63	-0.45	-0.45	-0.50	-0.35	-0.48	-0.10	-0.20					
Sc	-0.69	0.39	-0.04	-0.06	0.48	0.75	0.63	0.05	0.84	0.65	0.34	0.21	-0.19	-0.14	-0.04	0.02	-0.11	0.34	0.33	0.43				
V	-0.68	0.41	0.11	-0.22	0.56	0.68	0.53	-0.01	0.94	0.60	0.28	0.21	-0.48	-0.44	-0.31	-0.28	-0.41	0.13	0.14	0.32	0.87			
Ba	-0.11	0.02	-0.43	0.62	0.04	0.34	0.04	0.24	0.07	-0.07	0.14	0.07	0.21	0.25	0.33	0.35	0.31	0.12	0.20	-0.03	0.30	0.11		
Cs	0.26	0.05	-0.40	0.89	-0.27	-0.12	-0.29	-0.06	-0.19	-0.29	-0.16	-0.18	0.39	0.39	0.45	0.30	0.45	0.18	0.22	-0.25	-0.09	-0.25	0.61	
Li	-0.44	-0.11	-0.46	-0.15	0.17	0.55	0.81	-0.10	0.20	0.52	0.42	0.20	-0.16	-0.14	-0.13	0.01	-0.12	0.09	0.04	0.64	0.49	0.29	0.04	-0.10
Rb	0.24	-0.04	-0.51	0.97	-0.19	-0.06	-0.28	-0.07	-0.15	-0.35	-0.11	-0.13	0.33	0.34	0.42	0.30	0.42	0.08	0.13	-0.27	0.00	-0.16	0.63	0.90
Sr	-0.89	0.19	0.04	-0.33	0.79	0.47	0.86	0.08	0.49	0.92	0.77	0.68	-0.50	-0.50	-0.55	-0.47	-0.55	-0.02	-0.08	0.86	0.60	0.54	0.04	-0.23
Be	-0.04	0.15	-0.30	0.56	-0.13	0.10	0.07	0.14	-0.05	0.02	0.04	-0.05	0.47	0.47	0.44	0.33	0.49	0.26	0.28	0.10	0.24	-0.08	0.55	0.58
Cu	-0.14	0.19	0.09	-0.09	0.13	0.34	-0.08	-0.11	0.25	0.12	-0.03	-0.03	-0.18	-0.17	-0.18	-0.16	-0.19	-0.04	-0.02	-0.13	0.05	0.17	0.01	-0.15
Zn	0.28	-0.38	-0.55	0.36	-0.30	0.06	0.01	-0.10	-0.19	-0.25	-0.14	-0.21	0.12	0.14	0.17	0.27	0.18	-0.05	-0.03	-0.08	-0.06	-0.12	0.19	0.25
Pb	0.22	-0.21	-0.29	0.39	-0.21	-0.12	-0.08	0.05	-0.15	-0.19	-0.14	-0.15	0.15	0.16	0.15	0.23	0.17	-0.02	0.01	-0.06	-0.01	-0.12	0.23	0.23
S	0.16	-0.19	-0.06	0.05	-0.22	0.06	-0.09	-0.01	-0.12	-0.13	-0.14	-0.16	0.10	0.10	0.07	0.27	0.11	-0.09	-0.09	-0.07	-0.02	-0.11	0.08	-0.09
Cd	0.30	-0.35	-0.37	0.25	-0.28	-0.08	-0.07	-0.12	-0.21	-0.23	-0.16	-0.19	0.04	0.05	0.08	0.21	0.09	-0.04	-0.11	-0.08	-0.14	-0.16	0.02	0.17
Sb	-0.42	-0.16	-0.22	-0.10	0.31	0.27	0.56	-0.05	0.16	0.49	0.51	0.43	-0.44	-0.39	-0.26	-0.11	-0.32	0.00	-0.03	0.59	0.29	0.26	-0.08	-0.02
Tl	0.27	-0.30	-0.38	0.48	-0.16	-0.15	-0.15	-0.13	-0.23	-0.28	-0.09	-0.09	0.09	0.09	0.15	0.11	0.15	-0.12	-0.11	-0.12	-0.09	-0.16	0.23	0.45
Co	-0.86	0.23	0.04	-0.34	0.73	0.63	0.83	0.00	0.73	0.87	0.63	0.53	-0.62	-0.59	-0.52	-0.42	-0.58	0.04	-0.01	0.76	0.79	0.83	0.02	-0.30
Ni	-0.72	-0.12	-0.17	-0.30	0.60	0.37	0.91	0.03	0.22	0.81	0.75	0.63	-0.48	-0.47	-0.50	-0.36	-0.49	-0.08	-0.18	1.00	0.48	0.37	-0.01	-0.24
Mo	0.25	-0.05	0.25	-0.08	-0.18	-0.30	-0.31	0.00	-0.22	-0.31	-0.20	-0.08	0.17	0.16	0.12	0.12	0.13	0.15	-0.01	-0.21	-0.27	-0.20	-0.25	-0.11
Bi	0.06	-0.20	-0.24	0.07	-0.08	0.30	-0.05	-0.04	-0.10	-0.08	-0.03	-0.04	-0.15	-0.14	-0.12	0.01	-0.10	-0.18	-0.18	-0.03	-0.11	-0.06	0.13	-0.04
Ga	0.13	0.31	-0.30	0.61	-0.36	0.22	-0.10	-0.01	0.12	-0.18	-0.27	-0.38	0.65	0.68	0.72	0.61	0.73	0.52	0.55	-0.24	0.34	0.03	0.55	0.64
In	0.21	-0.34	-0.54	0.47	-0.24	0.24	-0.10	0.07	-0.20	-0.29	-0.10	-0.14	0.22	0.24	0.28	0.42	0.31	-0.01	0.03	-0.12	-0.01	-0.15	0.52	0.31
Sn	0.16	-0.05	-0.27	0.32	-0.17	0.09	-0.10	-0.07	0.07	-0.13	-0.18	-0.21	0.22	0.21	0.21	0.21	0.20	0.15	0.20	-0.17	0.11	0.05	0.17	0.16
W	0.26	-0.03	-0.13	0.22	-0.31	-0.04	-0.22	-0.09	-0.04	-0.27	-0.24	-0.25	0.29	0.33	0.41	0.46	0.38	0.32	0.25	-0.25	0.03	-0.03	0.08	0.13
REE (T)	0.16	0.02	-0.04	0.20	-0.26	0.01	-0.14	0.08	-0.12	-0.20	-0.14	-0.15	0.54	0.60	0.66	0.72	0.65	0.66	0.47	-0.09	0.14	-0.14	0.24	0.20

All values are different from 0 with a significance level alpha=0.05.

Table 6.2a. Pearson correlation matrix of major, trace, and rare-earth elements in rhyolite at Delbridge from whole-rock analytical data

	Li	*Rb*	*Sr*	*Be*	*Cu*	*Zn*	*Pb*	*S*	*Cd*	*Sb*	*Tl*	*Co*	*Ni*	*Mo*	*Bi*	*Ga*	*In*	*Sn*	*W*
Al2O3																			
Na2O																			
K2O																			
CaO																			
Fe2O3																			
MgO																			
MnO																			
TiO2																			
P2O5																			
LOI																			
CO2																			
Zr																			
Hf																			
Ta																			
Y																			
Nb																			
U																			
Th																			
Cr																			
Sc																			
V																			
Ba																			
Cs																			
Li																			
Rb	-0.17																		
Sr	0.52	-0.25																	
Be	0.15	0.56	0.13																
Cu	-0.05	-0.10	-0.01	-0.16															
Zn	0.25	0.24	-0.22	0.09	-0.07														
Pb	-0.02	0.25	-0.15	0.17	-0.16	0.54													
S	-0.11	-0.04	-0.15	0.18	0.06	0.18	0.43												
Cd	0.07	0.16	-0.20	0.05	-0.10	0.88	0.48	0.16											
Sb	0.53	-0.07	0.46	-0.05	-0.10	0.06	-0.03	-0.04	0.05										
Tl	-0.06	0.51	-0.22	0.05	-0.25	0.16	0.06	0.19	0.05	0.11									
Co	0.52	-0.27	0.85	-0.05	0.09	-0.18	-0.15	-0.16	-0.17	0.55	-0.22								
Ni	0.65	-0.26	0.88	0.10	-0.11	-0.09	-0.07	-0.10	-0.09	0.61	-0.13	0.80							
Mo	-0.40	-0.10	-0.31	-0.19	0.03	-0.07	0.02	0.27	0.09	-0.15	0.17	-0.27	-0.24						
Bi	0.03	0.00	-0.11	-0.06	0.49	0.06	-0.04	0.09	-0.02	-0.08	-0.08	-0.05	-0.03	-0.06					
Ga	0.21	0.62	-0.19	0.74	-0.07	0.23	0.14	0.00	0.10	-0.12	0.11	-0.17	-0.22	-0.14	-0.07				
In	0.06	0.38	-0.23	0.36	0.28	0.57	0.33	0.36	0.38	-0.11	0.15	-0.23	-0.13	-0.08	0.51	0.35			
Sn	0.10	0.27	-0.20	0.10	0.28	0.15	0.19	0.08	-0.03	-0.13	0.16	-0.11	-0.17	-0.06	0.15	0.30	0.39		
W	-0.07	0.18	-0.34	0.10	0.09	0.11	0.14	0.23	0.05	-0.01	0.25	-0.20	-0.26	0.34	0.03	0.27	0.13	0.17	
REE (T)	-0.02	0.21	-0.21	0.29	-0.13	0.03	0.07	0.05	0.13	-0.10	-0.02	-0.16	-0.10	0.37	-0.06	0.49	0.17	0.10	0.32

All values are different from 0 with a significance level alpha=0.05.

Table 6.2b. Pearson correlation matrix of major, trace, and rare-earth elements in mafic volcaniclastic rocks at Delbridge from whole-rock analytical data

	SiO2	*Al2O3*	*Na2O*	*K2O*	*CaO*	*Fe2O3*	*MgO*	*MnO*	*TiO2*	*P2O5*	*LOI*	*CO2*	*Zr*	*Hf*	*Ta*	*Y*	*Nb*	*U*	*Th*	*Cr*	*Sc*	*V*	*Ba*	*Cs*
Al2O3	0.82																							
Na2O	0.97	0.86																						
K2O	-0.56	-0.15	-0.57																					
CaO	-0.97	-0.90	-0.94	0.36																				
Fe2O3	-0.19	-0.15	-0.37	0.68	0.05																			
MgO	0.55	0.38	0.41	-0.42	-0.53	0.14																		
MnO	-0.98	-0.85	-0.96	0.41	0.98	0.11	-0.41																	
TiO2	0.66	0.91	0.65	0.22	-0.82	0.26	0.31	-0.75																
P2O5	-0.30	0.22	-0.26	0.92	0.07	0.49	-0.38	0.14	0.50															
LOI	-0.99	-0.88	-0.97	0.45	0.99	0.14	-0.53	0.99	-0.76	0.17														
CO2	-0.98	-0.90	-0.95	0.42	1.00	0.10	-0.58	0.97	-0.78	0.14	1.00													
Zr	-0.05	0.21	0.11	0.40	-0.04	-0.11	-0.81	-0.14	0.27	0.56	-0.02	0.03												
Hf	0.11	0.28	0.26	0.23	-0.17	-0.21	-0.75	-0.29	0.30	0.41	-0.16	-0.10	0.98											
Ta	-0.01	0.38	0.09	0.67	-0.16	0.22	-0.59	-0.19	0.57	0.84	-0.10	-0.08	0.89	0.83										
Y	0.20	0.62	0.32	0.51	-0.38	0.07	-0.40	-0.38	0.73	0.78	-0.32	-0.31	0.82	0.78	0.96									
Nb	0.00	0.42	0.10	0.69	-0.19	0.25	-0.53	-0.20	0.62	0.87	-0.12	-0.11	0.85	0.79	1.00	0.96								
U	0.10	0.40	0.24	0.43	-0.22	-0.04	-0.67	-0.29	0.48	0.64	-0.19	-0.15	0.97	0.96	0.95	0.92	0.93							
Th	0.05	0.28	0.17	0.44	-0.15	0.03	-0.72	-0.25	0.40	0.59	-0.12	-0.08	0.98	0.97	0.93	0.85	0.90	0.98						
Cr	0.22	0.57	0.16	0.67	-0.44	0.65	0.14	-0.34	0.85	0.80	-0.33	-0.38	0.27	0.20	0.67	0.70	0.72	0.45	0.40					
Sc	0.90	0.95	0.88	-0.24	-0.97	-0.01	0.60	-0.90	0.88	0.06	-0.95	-0.97	-0.03	0.07	0.18	0.42	0.22	0.18	0.08	0.55				
V	0.68	0.92	0.66	0.08	-0.82	0.17	0.54	-0.70	0.95	0.38	-0.76	-0.81	0.01	0.03	0.34	0.55	0.40	0.23	0.11	0.77	0.93			
Ba	-0.16	0.36	-0.12	0.86	-0.07	0.45	-0.30	0.00	0.62	0.99	0.03	0.00	0.56	0.43	0.86	0.84	0.89	0.67	0.61	0.86	0.20	0.50		
Cs	-0.37	0.01	-0.41	0.97	0.16	0.78	-0.28	0.21	0.40	0.92	0.26	0.23	0.37	0.22	0.69	0.56	0.72	0.44	0.45	0.81	-0.05	0.25	0.88	
Li	-0.83	-0.64	-0.83	0.32	0.82	0.09	-0.06	0.91	-0.59	0.12	0.83	0.78	-0.41	-0.56	-0.34	-0.43	-0.33	-0.50	-0.51	-0.23	-0.66	-0.42	0.01	0.16
Rb	-0.60	-0.19	-0.60	1.00	0.40	0.67	-0.44	0.45	0.18	0.91	0.49	0.46	0.39	0.21	0.65	0.48	0.66	0.41	0.42	0.64	-0.28	0.05	0.84	0.96
Sr	0.01	-0.31	0.05	-0.82	0.21	-0.74	0.18	0.17	-0.67	-0.87	0.11	0.13	-0.48	-0.38	-0.79	-0.72	-0.82	-0.59	-0.60	-0.92	-0.27	-0.48	-0.88	-0.92
Be	0.07	0.59	0.14	0.69	-0.30	0.31	-0.17	-0.22	0.77	0.92	-0.21	-0.24	0.55	0.46	0.85	0.91	0.89	0.70	0.60	0.88	0.43	0.68	0.96	0.75
Cu	0.50	0.20	0.51	-0.95	-0.32	-0.69	0.56	-0.32	-0.19	-0.85	-0.41	-0.40	-0.55	-0.41	-0.74	-0.54	-0.74	-0.55	-0.60	-0.61	0.28	0.03	-0.79	-0.94
Zn	0.73	0.48	0.78	-0.47	-0.66	-0.33	-0.10	-0.79	0.34	-0.29	-0.71	-0.64	0.46	0.62	0.25	0.32	0.21	0.48	0.51	-0.06	0.47	0.18	-0.20	-0.37
Pb	-0.50	-0.45	-0.32	-0.03	0.58	-0.57	-0.85	0.46	-0.60	-0.05	0.53	0.59	0.55	0.54	0.18	0.06	0.12	0.36	0.40	-0.59	-0.66	-0.71	-0.13	-0.22
S	0.43	0.08	0.50	-0.57	-0.29	-0.48	-0.32	-0.46	-0.11	-0.49	-0.36	-0.28	0.42	0.57	0.05	0.04	-0.01	0.34	0.41	-0.45	0.06	-0.27	-0.46	-0.54
Cd	-0.04	0.21	0.10	0.45	-0.06	-0.02	-0.79	-0.16	0.32	0.60	-0.03	0.02	1.00	0.97	0.92	0.83	0.88	0.98	0.99	0.34	-0.01	0.04	0.60	0.44
Sb	0.05	0.50	0.07	0.78	-0.28	0.52	-0.16	-0.21	0.77	0.93	-0.18	-0.21	0.52	0.43	0.85	0.86	0.89	0.66	0.61	0.95	0.39	0.64	0.97	0.86
Tl	-0.69	-0.20	-0.65	0.95	0.50	0.46	-0.49	0.56	0.09	0.90	0.58	0.55	0.39	0.20	0.61	0.48	0.63	0.39	0.37	0.52	-0.35	0.00	0.83	0.87
Co	0.47	0.49	0.44	0.31	-0.58	0.42	-0.17	-0.64	0.70	0.43	-0.53	-0.51	0.60	0.64	0.71	0.68	0.71	0.70	0.74	0.65	0.49	0.45	0.49	0.46
Ni	-0.49	-0.31	-0.44	0.73	0.40	0.37	-0.86	0.30	-0.04	0.63	0.44	0.47	0.78	0.68	0.75	0.52	0.71	0.70	0.79	0.27	-0.45	-0.32	0.56	0.67
Mo	0.60	0.25	0.67	-0.77	-0.43	-0.65	-0.09	-0.58	-0.04	-0.63	-0.52	-0.45	0.24	0.42	-0.11	-0.03	-0.16	0.19	0.22	-0.49	0.24	-0.11	-0.56	-0.73
Bi*	-	-	-	-	-	-	-	-	-	-	-	-	-	-	-	-	-	-	-	-	-	-	-	-
Ga	0.38	0.80	0.46	0.43	-0.57	0.13	-0.10	-0.53	0.89	0.74	-0.50	-0.51	0.61	0.59	0.84	0.95	0.87	0.77	0.68	0.82	0.65	0.78	0.82	0.53
In	0.52	0.85	0.59	0.31	-0.68	0.08	-0.07	-0.66	0.92	0.63	-0.62	-0.63	0.62	0.63	0.81	0.93	0.83	0.78	0.69	0.77	0.72	0.79	0.73	0.43
Sn	0.71	0.98	0.79	-0.07	-0.82	-0.22	0.25	-0.76	0.88	0.32	-0.79	-0.80	0.32	0.37	0.48	0.71	0.51	0.50	0.37	0.57	0.88	0.89	0.45	0.05
W	0.50	0.82	0.57	0.34	-0.66	0.11	-0.10	-0.65	0.91	0.64	-0.61	-0.60	0.64	0.65	0.83	0.94	0.85	0.80	0.72	0.78	0.69	0.77	0.74	0.46
REE (T)	-0.07	0.35	0.08	0.59	-0.08	0.02	-0.68	-0.12	0.47	0.79	-0.04	-0.01	0.94	0.87	0.97	0.94	0.96	0.97	0.93	0.52	0.10	0.25	0.80	0.57

* Bi concentrations were all below detection therefore correlation was not possible with other elements.

All values are different from 0 with a significance level alpha=0.05.

Table 6.2b. Pearson correlation matrix of major, trace, and rare-earth elements in mafic volcaniclastic rocks at Delbridge from whole-rock analytical data

	Li	*Rb*	*Sr*	*Be*	*Cu*	*Zn*	*Pb*	*S*	*Cd*	*Sb*	*Tl*	*Co*	*Ni*	*Mo*	*Bi**	*Ga*	*In*	*Sn*	*W*
Al2O3																			
Na2O																			
K2O																			
CaO																			
Fe2O3																			
MgO																			
MnO																			
TiO2																			
P2O5																			
LOI																			
CO2																			
Zr																			
Hf																			
Ta																			
Y																			
Nb																			
U																			
Th																			
Cr																			
Sc																			
V																			
Ba																			
Cs																			
Li																			
Rb	0.36																		
Sr	0.22	-0.80																	
Be	-0.15	0.67	-0.82																
Cu	-0.13	-0.95	0.85	-0.61															
Zn	-0.95	-0.50	0.02	-0.05	0.25														
Pb	0.17	0.00	0.35	-0.20	-0.08	0.11													
S	-0.72	-0.58	0.31	-0.38	0.31	0.89	0.44												
Cd	-0.43	0.44	-0.55	0.58	-0.61	0.45	0.49	0.39											
Sb	-0.18	0.75	-0.94	0.97	-0.73	-0.05	-0.30	-0.38	0.57										
Tl	0.51	0.96	-0.65	0.67	-0.85	-0.60	0.15	-0.63	0.42	0.69									
Co	-0.79	0.27	-0.75	0.53	-0.49	0.64	-0.24	0.36	0.66	0.64	0.07								
Ni	-0.04	0.73	-0.61	0.39	-0.88	0.05	0.47	0.12	0.81	0.48	0.66	0.49							
Mo	-0.71	-0.78	0.48	-0.41	0.57	0.88	0.33	0.95	0.20	-0.47	-0.79	0.21	-0.18						
Bi*	-	-	-	-	-	-	-	-	-	-	-	-	-	-					
Ga	-0.46	0.40	-0.73	0.94	-0.41	0.28	-0.22	-0.09	0.64	0.89	0.38	0.67	0.28	-0.09	-				
In	-0.61	0.27	-0.68	0.86	-0.32	0.44	-0.23	0.06	0.64	0.82	0.23	0.74	0.23	0.07	-	0.98			
Sn	-0.57	-0.10	-0.32	0.67	0.13	0.43	-0.32	0.05	0.31	0.56	-0.08	0.45	-0.22	0.21	-	0.85	0.89		
W	-0.62	0.30	-0.71	0.86	-0.36	0.45	-0.22	0.08	0.67	0.83	0.24	0.77	0.28	0.07	-	0.98	1.00	0.86	
REE (T)	-0.28	0.57	-0.65	0.80	-0.65	0.25	0.36	0.10	0.94	0.76	0.59	0.58	0.72	-0.03	-	0.80	0.76	0.47	0.78

* Bi concentrations were all below detection therefore correlation was not possible with other elements.

All values are different from 0 with a significance level alpha=0.05.

Table 6.3. Criteria used to select least-altered footwall and hanging-wall rhyolite samples

Criteria	Least-altered footwall QP rhyolite	Least-altered hanging-wall FP/QFP rhyolite
Na_2O	> 3 wt.%	5.32 wt.%
L.O.I.	< 3 wt.%	2.65 wt.%
CO_2	< 2 wt.%	1.02 wt.%
Cu	< 35 ppm	67.3 ppm
Zn	< 125 ppm	61.0 ppm
Ishikawa AI	< 0.35	0.12
CCPI	< 0.55	0.49
La_N/Yb_N	2.2 - 3.2	2.9

Notes: AI = alteration index = (K2O+MgO)/(K2O+Na2O+CaO+MgO), in wt.% (Ishikawa *et al* , 1976); CCPI = chlorite-carbonate-pyrite index = (MgO+FeO)/(MgO+FeO+Na2O+K2O), in wt.%, total Fe as FeO; L.O.I. = loss-on-ignition; N = chondrite-normalized (after McDonough and Sun, 1995). Least-altered samples were selected by comparison with typical fresh-rock compositions for high silica rhyolites elsewhere in the Abitibi subprovince. The criteria listed above are partial to the dataset in the present study; however the indicated ranges are similar to other alteration studies (e.g., Barrett et al, 1999; Koopman et al, 1999; Prior et al, 1999a, b).

Table 6.4. Immobile element concentrations and magmatic affinities of Delbridge volcanic rocks

Sample Units	Strat. Position	Lithofacies	TiO2 wt.%	Al2O3 wt.%	Zr ppm	Hf ppm	Ta ppm	Y ppm	Nb ppm	U ppm	Th ppm	Yb ppm	Lu ppm	Zr/Y ratio
RW001*	FW	Lobate QP Rhyo.	0.23	11.37	252	6.78	0.93	43.45	15.08	0.75	2.73	5.41	0.87	5.80
RW002	FW	Lobate QP Rhyo.	0.17	8.36	182	4.93	0.70	41.36	10.90	0.54	2.00	4.48	0.70	4.40
RW003	FW	Felsic Lapilli Tuff	0.23	9.87	214	5.76	0.82	52.01	13.65	0.62	2.33	5.84	0.90	4.11
RW004	FW	Felsic Lapilli Tuff	0.16	7.74	169	4.61	0.65	36.97	9.82	0.51	1.87	4.36	0.66	4.57
RW005	FW	Felsic Lapilli Tuff	0.11	5.80	119	3.18	0.44	33.61	6.93	0.36	1.31	3.61	0.55	3.54
RW006*	FW	Spherulitic QP Rhyo.	0.22	10.74	244	6.56	0.93	56.68	15.00	0.71	2.68	6.63	1.03	4.30
RW007	FW	Rhyo. Breccia	0.20	10.22	218	5.83	0.81	48.35	13.12	0.62	2.40	5.73	0.89	4.51
RW008	FW	Spherulitic QP Rhyo.	0.21	11.03	228	6.15	0.87	32.62	13.82	0.64	2.35	4.21	0.66	6.99
RW009	FW	Rhyo. Breccia	0.16	10.55	158	4.31	0.59	41.15	9.29	0.45	1.73	4.41	0.69	3.84
RW010	FW	Spherulitic QP Rhyo.	0.19	10.33	206	5.64	0.79	41.32	12.51	0.61	2.20	4.84	0.74	4.99
RW011	FW	Rhyo. Breccia	0.21	12.44	108	2.89	0.45	16.45	6.26	0.31	1.33	2.01	0.30	6.57
RW012	FW	Rhyo. Breccia	0.21	10.04	137	3.65	0.52	27.64	8.30	0.43	1.56	3.21	0.49	4.96
RW013	FW	Rhyo. Breccia	0.21	9.87	133	3.53	0.51	29.50	8.13	0.40	1.56	3.37	0.52	4.51
RW014	FW	Lobate QP Rhyo.	0.19	8.70	124	3.29	0.48	28.97	7.54	0.38	1.45	3.25	0.50	4.28
RW015	H-W	Mafic Volcaniclastic	0.82	14.61	36	0.93	0.15	10.29	2.68	0.10	0.37	1.08	0.17	3.50
RW016	H-W	Mafic Volcaniclastic	1.02	15.05	31	0.82	0.15	9.35	2.63	0.09	0.34	1.00	0.15	3.32
RW017	H-W	Mafic Volcaniclastic	1.39	20.21	43	1.11	0.21	16.48	3.96	0.15	0.51	1.48	0.22	2.61
RW018	H-W	FP Rhyo.	0.31	10.45	193	4.98	0.60	28.18	9.07	0.76	2.85	3.44	0.53	6.85
RW019	H-W	FP Rhyo.	0.46	11.44	160	4.23	0.53	27.8	8.40	0.57	2.28	3.04	0.47	5.76
RW020	H-W	FP Rhyo.	0.50	11.93	184	4.80	0.59	29.76	9.48	0.68	2.51	3.20	0.49	6.18
RW021*	H-W	FP Rhyo.	0.58	14.18	210	5.48	0.68	35.12	10.93	0.78	2.88	4.10	0.65	5.98
RW022	H-W	Mafic Volcaniclastic	1.16	19.38	27	0.77	0.13	9.50	2.17	0.08	0.27	1.06	0.16	2.84
RW023	H-W	Mafic Volcaniclastic	1.05	17.52	42	1.15	0.17	12.09	2.98	0.13	0.48	1.31	0.19	3.47
RW024	FW	Lobate QP Rhyo.	0.23	10.84	231	6.31	0.90	37.71	13.46	0.66	2.59	4.91	0.79	6.13
RW025	FW	Lobate QP Rhyo.	0.24	11.69	251	6.73	0.96	49.90	14.79	0.69	2.80	5.92	0.92	5.03
RW026*	FW	Lobate QP Rhyo.	0.23	10.51	226	6.09	0.86	51.59	13.99	0.66	2.52	5.98	0.94	4.38
RW027	FW	Spherulitic QP Rhyo.	0.20	9.16	201	5.46	0.75	46.11	12.08	0.58	2.17	5.42	0.83	4.36
RW028	FW	Spherulitic QP Rhyo.	0.19	9.18	202	5.54	0.78	49.89	12.33	0.58	2.24	5.53	0.86	4.05
RW029	FW	Rhyo. Breccia	0.21	8.97	198	5.32	0.77	50.12	11.85	0.57	2.21	5.75	0.87	3.95
RW030	FW	Rhyo. Breccia	0.21	9.29	207	5.52	0.76	48.93	12.16	0.59	2.21	5.55	0.85	4.23
RW031	FW	Spherulitic QP Rhyo.	0.18	8.62	184	4.99	0.70	49.22	11.37	0.55	2.03	5.20	0.80	3.74
RW032	FW	Felsic Lapilli Tuff	0.19	9.73	204	5.56	0.78	47.68	12.30	0.61	2.24	5.57	0.86	4.28
RW033	FW	Felsic Lapilli Tuff	0.23	10.19	218	5.89	0.83	48.85	13.49	0.64	2.41	5.69	0.88	4.46
RW034	FW	Spherulitic QP Rhyo.	0.33	11.98	192	5.14	0.69	51.34	11.71	0.56	2.09	5.37	0.85	3.74
RW035	FW	Spherulitic QP Rhyo.	0.14	7.58	152	4.05	0.58	42.01	9.14	0.46	1.68	4.31	0.66	3.62
RW036	FW	Spherulitic QP Rhyo.	0.21	10.96	216	5.93	0.86	52.94	13.31	0.92	2.46	6.28	0.98	4.08
RW037	FW	Rhyo. Breccia	0.17	10.41	171	4.62	0.63	29.97	9.88	0.50	1.86	3.66	0.56	5.71
RW038	FW	Stockwork QP Rhyo.	0.18	9.90	190	5.15	0.73	41.15	11.46	0.58	2.11	4.99	0.76	4.62
RW039	FW	Stockwork QP Rhyo.	0.23	11.26	215	5.81	0.83	45.95	13.14	0.58	2.39	5.57	0.86	4.68
RW040	FW	Stockwork QP Rhyo.	0.19	10.26	190	5.08	0.72	46.45	11.37	0.59	2.08	5.42	0.82	4.09
RW041	FW	Stockwork QP Rhyo.	0.19	9.76	187	5.00	0.72	31.97	11.33	0.52	2.08	4.06	0.63	5.85
RW042	FW	Stockwork QP Rhyo.	0.20	9.99	216	5.90	0.83	45.16	12.82	0.55	2.42	5.78	0.90	4.78
RW133	H-W	QFP Rhyo.	0.34	11.53	213	5.41	0.65	29.53	9.67	0.79	3.14	3.42	0.53	7.21
RW134	H-W	QFP Rhyo.	0.50	12.03	183	4.76	0.61	29.81	9.45	0.68	2.55	3.36	0.51	6.14

Table 6.4. Immobile element concentrations and magmatic affinities of Delbridge volcanic rocks

Sample Units	Strat. Position	Lithofacies	TiO2 wt.%	Al2O3 wt.%	Zr ppm	Hf ppm	Ta ppm	Y ppm	Nb ppm	U ppm	Th ppm	Yb ppm	Lu ppm	Zr/Y ratio
RW135	FW	QP Rhyo.	0.80	11.13	154	5.12	1.05	65.44	13.92	0.97	3.86	7.17	1.08	2.35
RW136	FW	Rhyo. Breccia	0.24	9.81	155	4.04	0.58	31.72	9.40	0.45	1.71	3.64	0.58	4.89
RW137	FW	Rhyo. Breccia	0.51	8.73	61	1.59	0.13	14.63	2.30	0.51	1.58	1.36	0.20	4.17
RW138	FW	Rhyo. Breccia	0.32	13.77	203	5.26	0.78	41.71	12.69	0.62	2.29	4.78	0.74	4.87
RW139	FW	Lobate QP Rhyo.	0.20	8.44	139	3.56	0.53	31.12	8.38	0.41	1.52	3.38	0.51	4.47
RW140	FW	Lobate QP Rhyo.	0.17	9.42	182	4.77	0.69	39.30	11.26	0.53	1.93	4.69	0.71	4.63
RW141	FW	Rhyo. Breccia	0.17	8.82	185	4.82	0.70	42.52	10.60	0.54	1.96	4.88	0.75	4.35
RW142	FW	Stockwork QP Rhyo.	0.18	9.21	202	5.30	0.77	42.94	12.20	0.57	2.14	4.77	0.71	4.70
RW143	FW	Stockwork QP Rhyo.	0.22	10.52	233	6.21	0.88	46.70	14.10	0.69	2.54	5.56	0.85	4.99
RW144	FW	Dike?	1.26	14.75	98	2.59	0.40	19.71	5.25	0.52	1.96	2.10	0.32	4.97

* Denotes least-altered samples.

Table 6.5. Mass changes for Delbridge footwall and hanging-wall rhyolites

Sample	SiO2	Al2O3	Na2O	K2O	CaO	Fe2O3	MgO	MnO	TiO2	P2O5	S	CO2	Net
Units	g/100g	g/100g	g/100g	g/100g	g/100g	g/100g	g/100g	g/100g	g/100g	g/100g	g/100g	g/100g	g/100g
Mass changes in footwall rhyolite A													
Precursor	**77.15**	**10.87**	**3.69**	**1.06**	**0.95**	**3.60**	**0.69**	**0.10**	**0.23**	**0.03**	**0.27**	**1.32**	**99.96**
RW001*	-2.64	-0.01	-0.47	0.38	0.30	-1.68	-0.40	-0.03	-0.01	0.00	0.06	0.54	-3.96
RW002	19.09	0.18	-2.23	1.40	4.68	2.27	0.58	0.11	0.00	0.01	-0.13	6.70	32.66
RW003	-8.40	0.23	-2.96	1.20	6.46	4.02	2.05	0.16	0.03	0.01	0.01	9.05	11.86
RW004	33.56	0.15	1.43	-0.26	2.47	2.41	0.05	0.08	0.00	0.01	1.76	2.96	44.61
RW005	85.76	0.86	-3.10	1.53	5.52	2.23	1.74	0.10	0.00	0.01	0.92	7.70	103.25
RW006*	-1.56	-0.28	0.57	-0.14	-0.57	0.86	-0.22	0.07	-0.01	0.00	0.18	-0.38	-1.46
RW007	10.93	0.41	-0.29	0.44	-0.42	-0.43	-0.14	-0.06	-0.01	0.00	0.98	-0.42	10.99
RW008	5.56	0.77	-1.31	0.35	-0.84	0.37	0.49	-0.05	-0.01	0.00	0.17	-1.00	4.51
RW009	33.80	5.20	1.98	-0.28	4.29	0.07	1.58	0.26	0.02	0.01	0.19	6.21	53.32
RW010	14.33	1.20	-1.21	0.01	-0.55	0.90	1.66	0.13	0.00	0.00	-0.24	-0.59	15.63
RW011	70.17	16.85	10.08	-0.59	8.57	2.35	2.94	0.16	0.24	0.06	-0.20	11.90	122.52
RW012	64.11	6.76	0.97	1.03	1.44	1.01	-0.51	0.04	0.14	0.04	-0.20	0.90	75.71
RW013	60.03	6.99	1.24	1.09	5.29	2.30	-0.36	0.15	0.15	0.06	-0.22	4.37	81.08
RW014	70.86	6.01	0.52	1.07	4.54	5.21	0.20	0.21	0.14	0.04	-0.21	6.29	94.90
RW024	0.70	0.42	-1.46	0.42	1.60	1.16	0.23	0.04	0.01	0.01	-0.19	0.90	3.85
RW025	-5.66	0.34	-0.62	0.01	0.84	0.39	0.35	-0.03	0.00	0.00	-0.26	0.24	-4.40
RW026*	4.62	0.32	-0.10	-0.27	0.27	0.94	0.68	-0.05	0.02	0.01	-0.27	-0.19	5.99
RW027	10.91	0.09	0.42	-0.53	2.45	1.85	1.61	0.29	0.01	0.01	-0.26	3.38	20.24
RW028	13.14	0.06	-0.96	0.62	2.16	0.87	0.30	0.23	0.00	0.00	0.60	3.17	20.20
RW029	15.06	0.03	-2.22	0.70	0.72	2.12	1.21	0.19	0.03	0.00	0.82	1.28	19.94
RW030	11.44	-0.07	-0.88	0.32	1.11	0.80	0.62	0.25	0.02	0.01	0.51	1.79	15.91
RW031	21.76	0.40	-3.53	0.54	0.25	7.26	1.26	0.03	0.01	0.01	0.63	0.58	29.19
RW032	13.78	0.61	0.63	-0.66	0.18	1.70	1.24	0.01	0.00	0.00	-0.19	0.17	17.48
RW033	7.87	0.38	-1.38	-0.13	-0.87	2.56	1.68	-0.04	0.03	0.01	-0.24	-0.73	9.14
RW034	13.04	4.14	1.34	-0.40	0.00	2.98	1.73	0.03	0.19	0.07	1.68	0.19	25.00
RW035	38.88	1.13	-3.29	-0.08	3.20	5.27	5.18	0.25	-0.01	0.00	-0.26	5.79	56.06
RW036	9.96	1.34	0.86	0.03	0.69	-0.68	-0.49	-0.01	0.01	0.00	-0.27	0.35	11.79
RW037	22.86	3.78	0.24	0.46	4.43	1.62	0.77	0.05	0.01	0.01	-0.22	6.54	40.56
RW038	16.11	1.67	0.44	0.12	3.20	0.57	0.13	0.16	0.00	0.00	-0.27	4.64	26.79
RW039	1.55	1.73	-0.03	0.26	2.70	0.35	-0.06	0.89	0.03	0.01	-0.20	4.28	11.52
RW040	22.84	2.12	1.72	-0.43	1.41	-1.41	-0.22	0.10	0.01	0.02	-0.27	1.80	27.70
RW041	19.71	1.69	-0.89	0.39	2.94	0.38	0.55	0.10	0.02	0.01	-0.27	4.35	28.97
RW042	10.01	0.26	-1.08	0.66	0.50	0.56	-0.13	-0.03	0.00	0.01	-0.27	0.78	11.27
RW135	16.37	6.52	0.67	0.50	6.93	10.08	3.56	0.16	1.02	0.09	-0.26	9.81	55.46
RW136	36.68	4.36	3.10	-0.36	4.76	1.62	0.75	0.08	0.15	0.04	-0.26	5.53	56.45
RW138	9.74	5.45	0.68	1.36	0.90	0.58	-0.12	0.00	0.15	0.04	-0.25	0.28	18.81
RW139	59.46	3.74	-2.54	1.69	2.18	0.47	0.24	0.02	0.12	0.04	-0.24	3.19	68.37
RW140	28.65	1.58	1.95	-0.52	1.15	-1.16	-0.21	-0.02	0.00	0.01	0.20	1.70	33.32
RW141	28.90	0.60	-3.48	0.59	-0.91	1.41	2.12	-0.04	-0.01	0.01	-0.21	-1.20	27.79
RW142	21.07	0.10	-3.46	0.77	-0.93	-0.02	1.50	-0.07	-0.01	-0.01	-0.22	-1.23	17.49
RW143	5.74	-0.01	-3.44	1.01	-0.92	-0.45	1.17	-0.07	0.00	0.00	-0.18	-1.24	1.61
Mass changes in hanging-wall rhyolite B													
Precursor	**68.11**	**14.18**	**5.32**	**0.65**	**2.7**	**5.21**	**1.53**	**0.13**	**0.58**	**0.12**	**0.005**	**1.02**	**99.56**
RW018	15.50	-2.81	0.07	0.06	-0.43	-1.79	-1.33	-0.02	-0.24	-0.05	0.00	0.88	9.82
RW019	21.14	0.83	1.37	-0.34	3.65	0.76	-0.05	0.12	0.02	0.01	0.02	4.32	31.88
RW020	6.59	-0.56	0.31	-0.15	4.11	-0.46	0.17	0.03	-0.01	-0.01	0.00	4.21	14.23
RW021*	0.00	0.00	0.00	0.00	0.00	0.00	0.00	0.00	0.00	0.00	0.00	0.00	0.00
RW133	2.95	-2.81	0.36	-0.06	-0.18	-2.16	-0.79	-0.05	-0.24	-0.06	0.00	2.81	-0.24
RW134	7.55	-0.38	-0.51	0.59	2.61	-0.71	0.13	0.02	-0.01	0.01	0.29	6.55	16.15

Notes: * Denotes least-altered samples; Because two compositionally distinct magmatic sources have been identified for footwall QP rhyolite A and hanging-wall Fs-phyric rhyolite B, mass change calculations for each type were determined separately and relative to their corresponding precursor compositions. Mass change data for individual chemical components plotted in Figure 6.15 represent the average of all samples in a given alteration assemblage (as determined by SWIR spectroscopy and petrography).

Table 6.6a. Pearson correlation matrix of major element mass transfer in footwall rhyolite at Delbridge

	SiO2	*Al2O3*	*Na2O*	*K2O*	*CaO*	*Fe2O3*	*MgO*	*MnO*	*TiO2*	*P2O5*	*S*
Al2O3	0.63										
Na2O	0.29	0.77									
K2O	0.27	-0.06	-0.53								
CaO	0.51	0.59	0.44	0.10							
Fe2O3	0.20	0.11	-0.13	0.07	0.37						
MgO	0.15	0.14	-0.10	-0.18	0.25	0.56					
MnO	0.07	0.13	0.15	-0.08	0.41	0.14	0.10				
TiO2	0.11	0.45	0.34	-0.04	0.40	0.41	0.18	0.03			
P2O5	0.42	0.71	0.53	0.01	0.49	0.35	0.05	0.11	0.77		
S	0.09	-0.14	-0.01	-0.04	-0.09	0.15	-0.02	-0.02	-0.09	0.03	
CO2	0.47	0.54	0.39	0.07	0.98	0.40	0.35	0.45	0.36	0.41	-0.07

* Calculated from absolute mass changes in footwall rhyolite 'A' (Table 6.5).
All values are different from 0 with significance level alpha=0.05.

Table 6.6b. Pearson correlation matrix of major element mass transfer in hanging-wall rhyolite at Delbridge

	SiO2	*Al2O3*	*Na2O*	*K2O*	*CaO*	*Fe2O3*	*MgO*	*MnO*	*TiO2*	*P2O5*	*S*
Al2O3	0.44										
Na2O	0.60	0.41									
K2O	-0.39	-0.13	-0.90								
CaO	0.19	0.92	0.30	-0.17							
Fe2O3	0.60	0.97	0.56	-0.30	0.88						
MgO	-0.09	0.85	0.08	0.09	0.93	0.74					
MnO	0.71	0.93	0.64	-0.37	0.80	0.99	0.62				
TiO2	0.26	0.97	0.22	0.00	0.96	0.91	0.93	0.84			
P2O5	0.33	0.97	0.19	0.07	0.92	0.91	0.89	0.85	0.99		
S	-0.19	0.32	-0.63	0.88	0.21	0.14	0.46	0.06	0.41	0.48	
CO2	-0.18	0.73	-0.18	0.44	0.71	0.56	0.90	0.45	0.81	0.82	0.77

* Calculated from absolute mass changes in hanging-wall rhyolite 'B' (Table 6.5).
All values are different from 0 with significance level alpha=0.05.

Table 6.7. Chondrite-normalized rare-earth element composition of Delbridge volcanic rocks

Sample	La	Ce	Pr	Nd	Sm	Eu	Gd	Tb	Dy	Ho	Er	Tm	Yb	Lu	La/Yb
Units	ppm	ppm	ppm	ppm	ppm	ppm	ppm	ppm	ppm	ppm	ppm	ppm	ppm	ppm	ratio
RW001*	106	93.43	84.5	74.1	55.3	34.5	38.8	32.9	30.7	30.07	32.23	31.86	33.58	35.2	3.16
RW002	68.6	64.44	62.5	59.4	59.5	37.2	40.0	33.6	31.2	28.96	29.30	27.65	27.80	28.5	2.47
RW003	68.8	64.03	59.8	57.3	57.9	38.2	46.1	41.2	38.7	36.52	37.30	35.91	36.29	36.4	1.90
RW004	62.4	55.06	49.3	43.4	36.6	26.3	29.4	27.4	26.2	24.96	26.26	25.67	27.06	26.6	2.31
RW005	50.9	44.49	40.4	35.8	30.9	19.0	26.5	25.2	24.5	23.53	23.35	22.06	22.45	22.2	2.27
RW006*	91.5	81.75	75.8	68.6	54.1	36.5	43.7	40.7	40.0	38.59	40.69	39.72	41.16	41.7	2.22
RW007	73.6	66.92	60.7	54.9	47.0	27.2	36.5	33.4	32.7	32.89	34.58	33.97	35.59	36.2	2.07
RW008	62.4	55.82	51.0	46.3	39.1	22.4	28.5	25.0	24.4	24.03	24.69	25.18	26.14	26.9	2.39
RW009	61.0	54.49	50.7	46.3	40.7	30.1	34.7	31.4	29.2	27.33	27.82	27.33	27.41	28.0	2.23
RW010	69.6	62.56	56.5	51.1	42.4	25.0	33.8	31.3	30.1	29.16	30.01	29.43	30.04	30.0	2.32
RW011	18.4	17.86	17.0	15.7	14.5	12.6	12.0	11.1	11.0	10.73	12.01	11.82	12.50	12.3	1.47
RW012	53.2	48.66	44.2	37.6	29.1	18.0	21.8	21.1	19.7	18.77	19.83	19.27	19.95	20.0	2.66
RW013	58.6	52.40	46.9	41.1	31.3	19.9	23.9	22.0	20.8	20.15	20.86	20.49	20.96	20.9	2.79
RW014	46.2	43.34	39.3	34.9	27.7	19.0	22.8	21.6	20.7	19.76	20.43	19.76	20.16	20.2	2.29
RW015	16.6	14.37	13.3	11.7	10.3	11.3	8.9	8.2	7.6	7.12	7.06	6.56	6.68	7.0	2.48
RW016	11.6	9.97	9.4	8.9	7.9	9.8	7.1	6.8	6.9	6.34	6.30	6.15	6.22	6.2	1.87
RW017	27.4	21.55	18.6	16.5	13.9	13.7	12.7	11.4	11.1	10.73	10.46	9.39	9.20	9.1	2.98
RW018	57.8	48.01	41.7	35.2	28.2	14.4	21.5	19.1	18.8	18.52	19.21	19.72	21.35	21.5	2.71
RW019	60.3	50.21	42.9	36.1	26.8	16.4	21.7	20.0	19.2	18.24	19.06	18.70	18.86	19.2	3.20
RW020	55.8	48.61	42.4	35.9	28.8	20.1	24.3	22.1	21.2	19.63	20.31	19.43	19.90	19.8	2.81
RW021*	73.0	61.44	53.4	45.2	34.3	19.6	27.7	25.4	25.0	23.74	24.89	24.41	25.47	26.4	2.87
RW022	7.6	7.11	6.7	6.8	7.2	9.3	7.2	7.1	7.0	6.68	6.78	6.36	6.55	6.5	1.15
RW023	18.3	15.58	14.2	12.7	10.8	12.6	9.7	8.9	8.7	8.28	8.45	7.81	8.14	7.8	2.25
RW024	93.8	83.61	77.7	70.5	53.5	32.1	37.6	31.1	28.8	27.45	28.58	28.46	30.52	32.0	3.07
RW025	90.0	80.36	72.6	64.7	51.8	38.4	40.9	36.8	35.0	34.29	35.57	35.26	36.75	37.2	2.45
RW026*	93.6	82.85	74.6	64.8	49.1	33.8	38.9	35.5	35.7	34.76	36.96	35.83	37.14	38.0	2.52
RW027	81.6	73.90	66.3	58.9	45.6	33.7	35.4	32.2	31.4	31.03	32.64	32.55	33.65	33.6	2.43
RW028	76.8	71.44	64.0	57.0	47.0	43.8	39.7	36.8	35.9	34.14	34.88	33.36	34.32	34.8	2.24
RW029	69.3	68.34	66.3	60.5	51.1	33.2	39.3	36.0	34.9	34.08	34.76	33.77	35.69	35.2	1.94
RW030	80.3	73.78	68.3	59.6	46.8	39.3	37.8	35.1	34.4	33.66	34.07	33.24	34.47	34.7	2.33
RW031	80.5	69.18	62.9	55.5	44.2	18.5	38.8	37.0	35.3	33.37	33.00	31.94	32.30	32.3	2.49
RW032	75.4	66.31	59.2	51.4	42.3	29.4	37.1	34.8	34.0	33.53	33.79	33.64	34.61	34.8	2.18
RW033	81.6	74.24	67.6	60.5	49.3	27.9	39.5	36.3	35.0	33.88	34.47	33.48	35.35	35.7	2.31
RW034	67.3	64.42	60.3	55.1	46.4	27.2	40.3	36.8	36.0	34.52	34.19	32.83	33.33	34.3	2.02
RW035	72.6	65.69	58.8	53.2	44.1	15.5	35.0	30.8	29.0	27.36	27.46	26.36	26.74	26.8	2.72
RW036	299	203.1	148	113	75.3	41.4	51.3	40.8	36.7	35.44	37.73	38.06	38.98	39.8	7.67
RW037	59.7	52.82	48.6	45.2	38.4	20.6	26.4	21.8	21.5	20.90	22.38	22.15	22.71	22.8	2.63
RW038	70.8	64.93	59.3	52.6	41.6	27.7	33.0	29.8	29.3	28.15	29.82	29.55	30.98	30.9	2.29
RW039	81.8	77.00	71.7	65.2	52.9	38.8	40.3	36.1	34.9	32.77	34.03	33.72	34.61	34.8	2.36
RW040	66.2	62.02	58.3	54.6	49.5	32.2	38.6	33.7	33.1	32.03	33.20	32.59	33.66	33.3	1.97
RW041	52.8	48.53	44.0	40.2	35.7	23.3	27.4	24.4	23.6	23.22	24.26	24.17	25.20	25.6	2.10
RW042	71.6	70.26	67.3	65.0	56.9	33.7	37.8	32.0	32.5	32.14	34.21	33.81	35.89	36.6	2.00
RW133	64.3	55.09	47.2	38.4	28.6	15.1	22.2	21.2	20.5	19.52	20.50	20.57	21.26	21.4	3.03
RW134	66.8	58.03	48.8	41.5	31.1	19.5	24.7	23.2	21.6	20.27	20.73	20.32	20.87	20.5	3.20
RW135	111	98.94	88.4	78.9	64.2	26.1	50.9	47.1	46.0	43.66	44.88	43.97	44.55	43.8	2.49
RW136	68.3	60.05	52.8	45.4	33.5	22.3	25.8	23.3	22.4	21.25	22.34	21.78	22.58	23.4	3.02
RW137	64.6	59.51	56.0	50.8	34.0	24.6	20.2	14.3	11.6	9.73	9.26	8.34	8.45	8.0	7.64
RW138	77.2	69.67	61.2	52.6	39.3	25.9	31.8	30.1	29.0	27.82	29.21	28.79	29.68	30.2	2.60
RW139	47.7	43.56	39.5	36.0	31.4	19.9	24.4	22.5	21.7	20.51	21.08	20.32	21.02	20.8	2.27
RW140	75.3	71.62	65.9	60.3	51.3	34.0	38.3	33.9	31.6	28.66	29.30	28.34	29.15	29.0	2.58
RW141	43.5	39.09	36.4	33.4	32.8	19.5	29.6	28.9	29.2	28.19	29.79	29.60	30.28	30.3	1.44
RW142	61.6	57.44	52.6	48.9	45.9	25.1	35.4	32.4	31.1	29.18	30.32	28.99	29.61	28.8	2.08
RW143	75.7	70.10	64.1	58.5	50.7	26.5	39.3	35.9	33.9	32.66	34.13	33.64	34.50	34.5	2.19
RW144	49.7	40.86	33.9	28.3	20.6	16.6	16.9	15.0	14.4	13.41	13.34	12.55	13.05	13.0	3.81
Chondr.**	0.237	0.613	0.0928	0.457	0.148	0.0563	0.199	0.0361	0.246	0.0546	0.16	0.0247	0.161	0.0246	1.5

* Denotes least-altered samples.

** REE data normalized to chondrite after McDonough and Sun (1995).

Table 6.8. Alteration intensity calculations of Delbridge volcanic rocks

Sample No.	Na2O	K2O	CaO	FeO	MgO	MnO	CO2	Ishikawa	CCPI	Carb.	Mn-carb.
Units	wt%	wt%	wt%	wt%	wt%	wt%	wt.%	index**	index***	index****	index*****
RW001*	3.37	1.51	1.31	1.81	0.30	0.08	1.94	27.89	30.17	0.79	0.02
RW002	1.10	1.86	4.26	4.00	0.96	0.16	6.06	34.47	62.60	0.89	0.01
RW003	0.65	2.01	6.59	6.09	2.44	0.23	9.22	38.07	76.23	0.80	0.01
RW004	3.59	0.56	2.40	3.80	0.52	0.13	3.00	15.28	50.99	0.63	0.02
RW005	0.29	1.28	3.20	2.59	1.20	0.10	4.46	41.54	70.72	0.82	0.01
RW006*	4.32	0.93	0.39	4.07	0.48	0.18	0.95	23.04	46.41	0.29	0.07
RW007	3.08	1.36	0.48	2.58	0.50	0.04	0.81	34.32	40.98	0.32	0.02
RW008	2.25	1.34	0.10	3.38	1.12	0.05	0.30	51.14	55.64	0.09	0.06
RW009	3.72	0.51	3.44	2.17	1.49	0.24	4.94	21.83	46.38	0.87	0.02
RW010	2.12	0.92	0.34	3.46	2.01	0.20	0.62	54.36	64.30	0.14	0.12
RW011	6.18	0.21	4.27	2.40	1.63	0.12	5.93	14.97	38.69	0.90	0.01
RW012	2.65	1.19	1.36	2.36	0.10	0.08	1.26	24.34	39.02	0.48	0.02
RW013	2.72	1.19	3.45	2.93	0.18	0.14	3.14	18.17	44.33	0.67	0.02
RW014	2.17	1.10	2.83	4.09	0.46	0.16	3.92	23.78	58.16	0.75	0.02
RW015	1.72	1.26	17.81	8.20	2.22	0.33	12.90	15.12	77.76	0.60	0.01
RW016	2.53	1.54	11.35	10.24	3.32	0.24	8.29	25.93	76.91	0.44	0.01
RW017	5.66	1.90	4.39	9.30	2.74	0.15	3.28	31.59	61.42	0.27	0.02
RW018	4.95	0.65	2.09	2.83	0.18	0.10	1.75	10.55	34.92	0.49	0.02
RW019	5.10	0.24	4.84	4.09	1.13	0.19	4.07	12.11	49.45	0.54	0.02
RW020	4.93	0.44	5.97	3.74	1.49	0.14	4.58	15.04	49.35	0.53	0.01
RW021*	5.32	0.65	2.70	4.69	1.53	0.13	1.02	21.37	51.02	0.15	0.05
RW022	7.15	0.23	2.60	8.29	4.45	0.13	0.79	32.43	63.32	0.07	0.06
RW023	6.64	0.52	5.77	8.18	2.34	0.13	4.00	18.73	59.50	0.33	0.01
RW024	2.14	1.42	2.45	4.11	0.88	0.14	2.13	33.38	58.37	0.39	0.03
RW025	3.20	1.12	1.87	3.74	1.08	0.08	1.62	30.26	52.75	0.33	0.02
RW026*	3.37	0.74	1.15	3.83	1.29	0.05	1.06	30.99	55.49	0.23	0.02
RW027	3.43	0.44	2.84	4.09	1.92	0.33	3.92	27.35	60.85	0.57	0.03
RW028	2.29	1.41	2.61	3.37	0.83	0.28	3.77	31.37	53.19	0.75	0.03
RW029	1.21	1.45	1.37	4.23	1.56	0.24	2.14	53.85	68.52	0.40	0.04
RW030	2.41	1.19	1.77	3.40	1.13	0.30	2.67	35.69	55.73	0.57	0.04
RW031	0.12	1.22	0.92	7.47	1.49	0.10	1.45	72.27	86.99	0.21	0.03
RW032	3.66	0.34	0.96	4.04	1.64	0.10	1.26	30.00	58.68	0.25	0.03
RW033	2.09	0.84	0.07	5.02	2.15	0.06	0.53	58.06	70.99	0.10	0.04
RW034	4.01	0.53	0.76	4.72	1.93	0.11	1.20	34.02	59.44	0.21	0.04
RW035	0.25	0.62	2.62	5.04	3.71	0.22	4.49	60.14	90.96	0.49	0.02
RW036	4.08	0.98	1.47	2.36	0.18	0.08	1.50	17.29	33.40	0.54	0.02
RW037	2.79	1.08	3.82	3.34	1.04	0.11	5.58	24.28	53.08	0.90	0.01
RW038	3.26	0.93	3.28	2.96	0.65	0.21	4.70	19.46	46.28	0.92	0.02
RW039	3.27	1.18	3.26	3.18	0.56	0.89	5.00	21.04	45.64	0.98	0.07
RW040	4.27	0.50	1.86	1.56	0.37	0.16	2.46	12.43	28.77	0.87	0.03
RW041	2.17	1.13	3.02	2.78	0.96	0.16	4.40	28.71	53.13	0.86	0.01
RW042	2.34	1.54	1.30	3.36	0.50	0.07	1.88	35.92	49.85	0.52	0.01
RW133	5.76	0.60	2.56	2.78	0.75	0.08	3.88	13.96	35.70	0.86	0.01
RW134	4.19	1.08	4.63	3.53	1.45	0.13	6.60	22.29	48.57	0.89	0.01
RW135	2.79	1.00	5.04	7.87	2.72	0.17	7.12	32.21	73.65	0.61	0.01
RW136	4.37	0.45	3.68	3.02	0.93	0.12	4.41	14.63	45.06	0.77	0.01
RW137	0.90	0.02	10.63	7.39	14.23	0.18	14.70	55.28	95.92	0.52	0.00
RW138	3.68	2.04	1.56	3.17	0.48	0.09	1.35	32.47	38.94	0.37	0.03
RW139	0.66	1.59	1.81	2.11	0.54	0.07	2.60	46.30	54.12	0.79	0.01
RW140	4.26	0.41	1.59	1.66	0.36	0.06	2.28	11.63	30.15	0.86	0.01
RW141	0.16	1.27	0.03	3.46	2.16	0.05	0.09	94.75	79.73	0.02	0.21
RW142	0.19	1.54	0.02	2.70	1.84	0.03	0.07	94.15	72.41	0.02	0.16
RW143	0.24	2.00	0.03	2.74	1.80	0.03	0.07	93.37	66.98	0.02	0.16
RW144	3.86	0.79	6.15	8.56	4.43	0.12	0.18	34.27	73.64	0.01	0.26

* Denotes least-altered samples.

** Ishikawa alteration index calculated after Ishikawa *et al* (1976).

*** Chlorite-carbonate-pyrite index, CCPI = 100 (FeO+MgO)/FeO+MgO+Na2O+K2O.

**** Carbonate index = CO2/(CaO+FeO+MgO), expressed in mole percent.

***** Mn-carbonate index = MnO/CO2, expressed in mole percent.

Table 6.9. Normative mineral abundance estimates of Delbridge volcanic rocks

Sample	Qtz	K-spar	Ab	Ms	Fe-Chl	Mg-Chl	Cc	Ank	Sid	Rt	Py	Dol	Pg	Phn	Total	Res.
Units	wt.%	wt.%	wt.%	wt.%	wt.%	wt.%	wt.%	wt.%	wt.%	wt.%	wt.%	wt.%	wt.%	wt.%	wt.%	SSQ
RW001*	53.30	8.38	16.89	0.00	0.00	0.00	0.98	2.36	1.43	0.12	0.51	0.00	16.03	0.00	100.00	0.12
RW002	58.35	10.70	0.00	0.00	0.50	0.00	3.03	8.86	3.04	0.05	0.03	0.00	15.26	0.18	100.00	0.13
RW003	45.65	0.00	0.00	0.00	4.33	0.00	2.64	18.10	0.00	0.16	0.32	0.00	11.09	17.71	100.00	0.15
RW004	55.09	0.03	27.71	0.00	0.22	0.00	2.70	2.49	2.12	0.03	2.54	0.23	2.99	3.84	100.00	0.14
RW005	71.40	0.03	0.00	0.00	0.00	0.00	1.32	8.17	0.00	0.01	0.89	0.21	6.97	11.01	100.00	0.26
RW006*	46.46	0.03	34.44	0.00	4.31	0.00	0.05	1.15	1.71	0.19	0.84	0.00	3.05	7.77	100.00	0.02
RW007	56.36	0.03	19.56	0.00	0.21	0.00	0.05	1.23	0.72	0.11	2.02	0.00	8.77	10.94	100.00	0.08
RW008	57.94	0.02	10.66	0.00	3.32	2.96	0.00	0.08	0.81	0.16	0.75	0.10	11.96	11.24	100.00	0.02
RW009	49.40	0.05	22.28	0.00	0.00	0.48	0.82	8.72	0.01	0.07	0.47	1.40	12.71	3.60	100.00	0.14
RW010	59.76	0.00	10.16	0.00	2.13	7.70	0.45	0.00	1.53	0.10	0.00	0.00	10.77	7.40	100.00	0.06
RW011	28.63	0.00	48.88	0.00	0.00	1.87	1.85	11.59	0.00	0.21	0.00	0.00	5.21	1.75	99.98	0.01
RW012	60.37	0.00	13.78	0.00	2.00	0.00	2.04	0.00	1.43	0.08	0.00	0.01	11.56	8.73	100.00	0.21
RW013	55.14	0.00	15.48	0.00	2.30	0.00	5.87	0.00	2.11	0.08	0.00	0.01	10.08	8.94	100.00	0.15
RW014	59.70	0.00	9.85	0.00	0.00	0.00	3.77	2.24	4.69	0.07	0.00	0.01	11.41	8.26	100.00	0.15
RW018	44.84	0.00	40.99	0.00	5.74	0.00	3.55	0.00	0.08	0.17	0.03	0.00	0.38	4.21	100.00	0.18
RW019	35.31	0.00	41.24	0.00	8.68	1.77	7.73	0.00	0.03	0.35	0.00	1.26	2.21	1.41	100.00	0.09
RW020	32.48	0.00	39.66	0.00	6.61	4.86	10.37	0.00	0.03	0.40	0.00	0.00	2.43	3.15	100.00	0.09
RW028	57.19	0.00	11.79	0.00	0.00	0.00	1.75	5.54	1.60	0.07	1.18	0.00	10.04	10.84	100.00	0.23
RW029	60.84	0.00	3.63	0.00	6.23	0.31	0.04	0.00	0.00	0.20	1.68	4.42	9.63	12.45	99.44	0.03
RW030	56.04	0.00	15.14	0.00	3.55	0.00	0.30	3.96	0.00	0.20	1.24	1.64	7.72	10.20	100.00	0.07
RW031	63.04	0.00	0.00	0.00	14.02	0.70	0.00	1.19	0.00	0.08	1.13	1.70	6.68	11.44	100.00	0.28
RW032	51.93	0.00	28.61	0.00	7.95	3.27	0.32	0.00	0.00	0.11	0.07	2.25	3.03	2.46	100.00	0.04
RW033	57.95	0.00	12.08	0.00	8.76	6.47	0.00	0.00	0.00	0.13	0.00	0.64	7.39	6.58	100.00	0.16
RW034	44.09	0.00	27.83	0.00	4.11	5.61	0.00	1.22	0.00	0.26	2.87	1.26	8.56	4.18	100.00	0.03
RW035	63.07	0.00	0.00	0.00	6.54	8.11	0.00	4.31	0.00	0.00	0.00	4.94	7.14	5.89	100.00	0.25
RW036	50.26	0.00	29.51	0.00	4.25	0.00	2.24	0.60	0.00	0.00	0.00	0.00	6.29	6.84	100.00	0.26
RW037	50.67	0.00	13.70	0.00	0.00	0.00	2.31	9.02	1.91	0.12	0.00	0.00	13.90	8.37	100.00	0.07
RW133	36.57	0.00	45.87	0.00	0.00	0.10	1.49	5.91	2.10	0.24	0.00	0.00	3.55	4.17	100.00	0.09
RW134	37.70	0.00	26.84	0.00	0.00	0.00	2.11	11.96	1.07	0.37	0.31	0.00	11.58	8.06	100.00	0.17
RW135	36.43	0.00	18.50	0.00	10.57	2.64	1.56	14.52	0.00	0.71	0.00	0.00	6.95	8.11	100.00	0.05
RW136	45.93	0.00	33.14	0.00	2.92	0.00	3.21	6.28	0.62	0.13	0.00	0.00	4.78	2.99	100.00	0.12
RW137	24.60	0.00	3.04	0.00	0.00	38.61	4.38	0.00	2.29	0.45	0.21	26.09	0.00	0.00	99.66	0.78
RW138	43.13	0.00	22.99	0.00	5.38	0.01	2.50	0.02	0.00	0.12	0.00	0.00	10.29	15.55	100.00	0.34
RW139	66.98	0.00	0.00	14.56	0.00	0.00	1.66	3.29	1.57	0.19	0.00	0.00	10.44	0.00	98.71	0.07
RW140	54.22	1.94	30.30	0.00	0.00	0.00	1.06	3.29	0.97	0.07	0.53	0.00	7.63	0.00	100.00	0.09
RW141	69.56	0.00	0.00	11.83	4.47	7.63	0.00	0.00	0.00	0.01	0.00	0.00	6.50	0.00	100.00	0.30
RW142	69.79	0.00	0.00	14.00	2.99	5.86	0.00	0.00	0.00	0.00	0.00	0.00	7.37	0.00	100.00	0.43
RW143	65.47	0.00	0.00	18.14	2.98	5.42	0.00	0.00	0.00	0.03	0.00	0.00	7.96	0.00	100.00	0.41

Sample	Qtz	K-spar	Ab	Ms	Fe-Chl	Mg-Chl	Cc	Ank	Sid	Rt	Py	Rh	Pg	Phn	Total	Res.
RW038	51.42	0.00	19.79	0.00	0.00	0.00	2.95	5.77	2.28	0.12	0.00	0.32	10.60	6.74	100.00	0.11
RW039	46.69	0.00	18.19	0.00	0.00	0.00	3.55	4.64	2.79	0.17	0.00	1.46	13.37	9.15	100.00	0.09
RW040	52.93	0.00	29.04	0.00	0.00	0.00	1.85	2.59	1.24	0.05	0.00	0.08	9.28	2.93	100.00	0.17
RW041	58.52	0.00	7.36	0.00	0.00	0.00	1.71	7.04	1.52	0.08	0.00	0.11	15.07	8.59	100.00	0.12
RW042	58.07	0.00	12.25	0.00	1.03	0.04	2.05	0.27	3.26	0.12	0.00	0.00	10.32	12.60	100.00	0.07

Sample	Qtz	K-spar	Ab	Ms	Fe-Chl	Mg-Chl	Cc	Ank	Ep	Ba	Py	Rt	Pg	Ph	Total	Res.
RW015	13.17	7.45	3.27	0.00	15.19	7.71	29.34	0.00	5.73	0.05	0.02	0.79	16.46	0.00	99.18	0.02
RW016	10.11	8.82	18.82	0.04	12.36	8.12	7.88	10.98	16.34	0.05	0.00	0.99	3.86	0.38	98.74	0.01
RW017	0.00	10.61	39.98	0.04	17.35	8.70	5.58	1.91	2.92	0.14	0.00	1.35	10.93	0.49	100.00	0.07
RW021*	29.06	2.88	43.67	0.02	6.06	4.52	0.00	2.20	8.57	0.00	0.00	0.51	1.47	1.04	100.00	0.05
RW022	1.42	0.53	59.16	0.00	10.31	17.38	0.04	1.80	8.19	0.00	0.12	1.06	0.00	0.00	100.00	0.16
RW023	0.89	2.93	56.05	0.00	9.05	4.96	0.00	9.14	13.51	0.02	0.77	1.03	0.00	0.00	98.35	0.01
RW024	53.85	8.15	9.07	0.00	6.23	0.47	0.00	4.74	4.56	0.00	0.00	0.17	12.77	0.00	100.00	0.04
RW025	48.96	5.83	19.30	0.00	5.58	1.83	0.00	3.53	3.44	0.00	0.00	0.15	10.76	0.63	100.00	0.06
RW026*	51.60	3.64	23.77	0.00	6.24	3.35	0.00	2.28	1.90	0.00	0.00	0.15	6.46	0.62	100.00	0.05
RW027	49.97	1.56	25.77	0.38	4.17	3.46	0.00	8.71	1.31	0.00	0.00	0.10	4.06	0.51	100.00	0.14

* Denotes least-altered samples.

NB: Normative mineral estimates based on MINSQ method after Herrmann and Berry (2002; see text for discussion).

Table 6.10. Analytical data for wallrock pyrite at Delbridge

Sample No.	Cu	Fe	Zn	Pb	Cd	Au	Ag	As	Sb	Tl	Hg	Se	Co	Ni	Te	Bi	Cr
	ppm	%	ppm	ppm	ppm	ppb	ppm	ppm	ppm	ppm	ppm	ppm	ppm	ppm	ppm	ppm	ppm
	ICP	INAA	ICP	ICP	ICP	INAA	ICP	ICP	INAA	ICP	ICP	INAA	ICP	ICP	ICP	ICP	INAA
SB001	724	34.0	9714	159	37.3	310	52.9	68.8	0.50	0.9	0.17	20	47.6	58	1.0	1.50	3
SB002	212	42.0	1819	117	9.06	94	96.8	96.0	9.0	20	0.13	5	14.0	52	0.3	0.51	0.1
SB003	230	40.8	22970	748	122	7400	310	12.4	4.9	1.0	0.54	3	26.4	12	0.3	0.30	0.4
SB004	346	39.3	969.7	101	4.62	280	45.9	226	50	10	0.12	5	39.7	37	0.4	2.80	0.2
SB005	284	40.8	386.4	98.2	2.75	100	52.4	63.0	8.4	70	0.11	2	27.8	31	0.4	0.18	0.5
SB006	196	36.5	13860	158	41.9	870	88.5	264	16	5.0	0.18	2	15.9	13	0.5	0.14	0.3
SB007	1260	42.3	4328	555	16.7	1200	140	144	7.8	0.8	0.085	2	30.5	180	1.0	1.30	0.1
SB008	782	44.8	7494	169	35.6	1400	639	106	8.1	0.5	0.20	30	28.8	31	2.0	0.75	0.1
SB010	627	38.7	5161	91.9	20.2	640	108	113	4.8	0.2	0.068	20	29.7	6.7	3.0	0.33	0.0
SB011	292	42.0	684.1	136	2.22	690	76.0	67.4	9.2	0.9	0.041	8	17.4	8.2	2.0	0.40	0.1
SB012	163	46.2	116.1	158	0.513	900	96.9	61.9	6.4	0.1	0.024	2	20.4	4.0	0.2	0.28	0.3
SB013	405	41.6	452.0	99.2	2.16	670	26.5	44.8	3.8	0.1	0.025	2	35.8	4.1	2.0	0.26	0.2
SB014	2040	39.2	481.1	112	1.95	180	99.9	56.2	4.2	0.1	0.028	50	108	3.5	2.0	1.00	0.3
SB015	793	41.3	610.5	94.1	6.05	260	59.4	19.0	6.7	0.9	0.044	2	351	190	0.5	0.74	5
SB019	475	16.6	275.8	319	3.06	540	325	591	10	2.0	0.092	2	173	210	9.0	6.20	30
SB020	1205	38.8	14280	138	69.4	1500	103	168	5.3	0.0	0.12	2	25.0	11	2.0	0.59	1
SB021	207	38.9	13250	266	44.2	960	110	68.0	5.3	0.0	0.11	2	27.4	13	0.4	0.75	2
SB022	249	40.6	12810	401	44.7	720	140	169	14	0.1	0.14	2	20.3	13	4.0	0.43	3
SB023	329	37.5	15180	458	57.6	360	116	53.2	7.9	0.0	0.097	30	24.1	6.2	5.0	0.22	2
SB024	1780	39.8	646.7	139	2.67	290	54.3	29.6	4.9	0.2	0.024	2	52.3	11	2.0	2.20	2
SB025	319	39.3	8625	148	30.8	1100	37.7	70.6	6.6	0.0	0.060	20	14.5	0.2	9.0	0.17	1
SB026	563	42.0	117.6	98.2	0.646	150	13.7	1.62	4.8	0.0	0.017	2	49.3	9.6	4.0	0.73	0.5
SB027	140	41.5	3907	105	18.6	250	10.0	51.5	4.1	0.0	0.030	40	16.3	0.9	7.0	0.40	2
SB028	597	37.6	82.19	100	2.42	120	7.49	11.3	2.8	0.0	0.018	80	20.5	4.4	4.0	0.21	0.4
SB029	1060	38.0	157.1	153	1.32	120	26.6	30.3	14	0.0	0.021	2	136	9.5	8.0	0.97	1
SB030	349	38.4	4692	154	12.2	220	81.5	25.5	4.7	0.1	0.037	2	28.5	7.9	0.1	0.38	0.1
SB085	266	25.5	148.2	159	0.484	160	151	74.0	56	10	0.023	40	35.4	3.7	0.2	1.30	0.2
SB086	293	43.8	151.0	178	0.599	410	160	73.5	8.3	10	0.024	2	39.5	9.4	0.3	1.40	0.0
SB087	668	41.8	3525	186	17.1	670	120	106	8.0	0.1	0.031	10	22.9	3.8	0.3	3.80	0.1
SB088	1050	37.9	36220	831	141	19000	236	136	9.3	0.8	0.25	2	19.1	5.0	0.3	0.78	0.5
SB090	176	34.7	69240	19000	183	8000	320	349	23	6.0	0.067	6	22.8	6.9	0.1	5.40	0.2
* Total REE																	
MAX	2040	46.2	69240	19000	183	19000	639	591	56	70	0.54	80	351	210	9.0	6.20	30
MIN	140	16.6	82.19	91.9	0.484	94	7.49	1.62	0.50	0.0	0.017	2	14.0	0.18	0.1	0.14	0.0
AVG	583	38.8	8140	827	30.1	1600	126	108	11	5.0	0.095	10	49.0	31	2.0	1.20	2

Table 6.10. Analytical data for wallrock pyrite at Delbridge

Sample No.	V	Sc	Th	Ca	Mg	Mn	Na	Ti	La	Ce	Nd	Sm	Eu	Tb	Yb	Lu	REE*
	ppm	ppm	ppm	ppm	ppm	ppm	%	ppm	ppm	ppm	ppm	ppm	ppm	ppm	ppm	ppm	ppm
	ICP	INAA	INAA	ICP	ICP	ICP	INAA	ICP	INAA	INAA	INAA	INAA	INAA	INAA	INAA	INAA	INAA
SB001	1.2	5.2	3700	6200	1130	480	0.30	79	4750	7400	3300	440	10	80	160	25	16200
SB002	1.7	2.5	1300	4700	1110	330	0.20	45	1500	2700	1300	170	5	30	62	7.5	5730
SB003	1.5	2.4	97	4500	1370	190	0.20	12	141	270	96	19	4	6	16	2.0	550
SB004	1.5	9.1	130	16000	4920	710	0.20	17	246	560	250	46	20	20	66	8.2	1220
SB005	2.3	2.1	12	2300	415	150	0.20	4.7	24.5	54	25	4.3	2	2	4.5	0.56	117
SB006	1.8	2.9	64	1300	377	90	0.50	7.9	88.7	170	81	12	1	3	8.1	1.0	365
SB007	3.0	2.7	48	7400	3000	600	0.07	5.1	77.7	150	64	11	2	4	5.3	0.89	311
SB008	2.2	1.5	6.4	180	170	120	0.04	5.2	141	310	210	27	7	5	6.8	0.81	699
SB010	1.7	2.6	1.2	100	1520	56	0.08	5.8	24.3	52	31	4.1	0.1	1	2.6	0.36	116
SB011	1.5	0.9	7.1	41	62	60	0.02	2.9	30.1	56	36	4.7	0.8	0.3	1.3	0.14	129
SB012	2.0	2.4	4.6	720	616	180	0.01	10	15.7	35	2.5	2.9	0.8	0.3	2.9	0.48	60.7
SB013	2.0	1.5	0.84	250	1180	120	0.02	190	32.0	71	47	7.6	2	1	2.0	0.35	164
SB014	1.8	1.0	1.0	40	804	61	0.01	6.3	22.9	51	34	4.7	1	0.3	0.9	0.16	115
SB015	3.6	6.8	9.5	8400	3860	560	0.30	38	59.9	150	82	12	3	0.3	3.4	0.49	309
SB019	5.2	5.0	26	12000	1250	1100	0.20	40	71.2	180	110	15	4	3	9.5	1.7	390
SB020	1.9	1.2	0.10	240	376	40	0.04	6.7	7.40	21	2.5	2.1	0.8	1	2.2	0.28	36.9
SB021	1.9	4.3	3.2	10000	2440	1300	0.10	18	38.0	84	42	10	5	2	8.3	1.1	191
SB022	1.7	4.9	30	1900	544	730	0.20	11	191	370	170	21	9	4	12	1.7	786
SB023	1.1	4.1	3.2	3400	2870	680	0.08	13	25.2	62	35	7.4	4	4	12	1.7	151
SB024	2.1	4.4	2.5	2600	1620	290	0.04	25	13.4	52	3.0	7.5	3	8	20	2.5	109
SB025	8.9	3.2	0.10	150	1340	570	0.05	12	19.7	42	16	2.8	1	1	2.6	0.36	86.0
SB026	1.7	5.7	9.4	3700	3900	1100	0.20	10	81.5	180	110	11	3	0.3	4.2	0.68	388
SB027	0.6	3.7	1.6	740	1820	980	0.06	13	47.7	100	54	6.5	1	0.3	3.4	0.50	215
SB028	0.6	3.6	7.4	87	1620	42	0.09	6.4	98.0	200	140	16	2	2.0	6.5	0.92	465
SB029	1.1	13	11	8300	9830	1500	0.08	39	445	1100	930	160	60	30	61	6.8	2840
SB030	0.5	4.0	6.9	9600	6360	1900	0.05	8.3	42.9	88	39	5.0	0.1	0.3	4.6	0.69	181
SB085	0.8	4.6	0.45	2400	707	430	0.20	8.0	30.4	81	3.5	11	6	0.3	13	2.3	147
SB086	0.8	1.9	0.72	2600	762	460	0.05	8.1	2.68	11	2.5	2.1	2	3	8.2	1.2	31.5
SB087	0.3	0.8	0.10	100	2050	610	0.05	5.6	13.3	29	13	1.9	0.7	0.3	1.5	0.26	60.5
SB088	0.3	2.0	11	140	570	97	0.05	8.2	580	1200	580	68	10	5	13	1.7	2410
SB090	0.1	0.5	0.10	34	222	120	0.05	3.4	0.918	1.5	2.5	0.21	0.1	0.3	0.10	0.13	5.71
* Total REE																	
MAX	8.9	13	3700	16000	9830	1900	0.50	190	4750	7400	3300	440	60	80	160	25	16200
MIN	0.1	0.5	0.10	34	62	40	0.01	2.9	0.918	1.5	2.5	0.21	0.1	0.3	0.10	0.13	5.71
AVG	1.8	3.6	180	3600	1900	510	0.10	21	286	510	250	36	5	7	17	2.3	1110

Table 6.11. Pearson correlation matrix for selected trace elements in wallrock pyrite at Delbridge

	Cu	*Fe*	*Zn*	*Pb*	*Cd*	*Au*	*Ag*	*As*	*Sb*	*Tl*	*Hg*	*Se*	*Co*	*Ni*	*Te*	*Bi*	*Cr*
Fe	0.04																
Zn	-0.14	-0.11															
Pb	-0.16	-0.14	0.83														
Cd	-0.10	-0.07	0.96	0.67													
Au	0.06	-0.03	0.71	0.36	0.80												
Ag	-0.02	-0.15	0.41	0.30	0.46	0.38											
As	-0.13	-0.65	0.34	0.38	0.26	0.15	0.41										
Sb	-0.23	-0.37	0.07	0.18	0.01	0.00	0.07	0.27									
Tl	-0.22	0.03	-0.09	0.01	-0.12	-0.09	-0.08	0.00	0.15								
Hg	-0.13	0.01	0.38	-0.01	0.58	0.52	0.48	0.08	-0.06	0.04							
Se	0.13	-0.12	-0.15	-0.08	-0.16	-0.18	-0.04	-0.23	0.03	-0.14	-0.20						
Co	0.28	-0.23	-0.22	-0.08	-0.23	-0.15	-0.03	0.10	-0.05	-0.09	-0.17	-0.11					
Ni	0.14	-0.36	-0.17	-0.07	-0.18	-0.12	0.16	0.45	-0.04	0.01	0.01	-0.23	0.67				
Te	0.02	-0.32	-0.20	-0.15	-0.20	-0.22	-0.11	0.19	-0.19	-0.24	-0.23	0.23	0.16	0.10			
Bi	0.05	-0.58	0.32	0.53	0.20	0.10	0.34	0.75	0.28	-0.06	-0.12	-0.17	0.22	0.38	0.08		
Cr	-0.02	-0.73	-0.11	-0.05	-0.11	-0.08	0.24	0.72	-0.05	-0.07	-0.01	-0.12	0.45	0.65	0.49	0.60	
V	0.02	-0.16	-0.22	-0.19	-0.21	-0.21	0.00	0.21	-0.14	0.00	-0.04	-0.12	0.27	0.41	0.51	0.03	0.40
Sc	0.04	-0.21	-0.29	-0.22	-0.30	-0.25	-0.32	-0.05	0.31	-0.09	-0.13	-0.11	0.44	0.20	0.38	0.03	0.17
Th	0.00	-0.12	-0.01	-0.05	0.00	-0.08	-0.11	-0.05	-0.14	0.03	0.18	0.04	-0.04	0.12	-0.14	0.01	0.02
Ca	-0.07	-0.31	-0.21	-0.15	-0.22	-0.20	-0.08	0.25	0.28	0.02	0.06	-0.34	0.41	0.54	0.03	0.30	0.40
Mg	0.12	0.03	-0.25	-0.15	-0.26	-0.21	-0.33	-0.23	0.08	-0.16	-0.22	-0.16	0.35	0.11	0.25	-0.02	-0.03
Mn	-0.15	-0.19	-0.21	-0.15	-0.24	-0.26	-0.20	0.00	0.02	-0.17	-0.23	-0.22	0.21	0.17	0.35	0.13	0.27
Na	-0.28	-0.30	-0.04	-0.12	-0.03	-0.13	-0.09	0.23	0.24	0.23	0.33	-0.17	0.26	0.32	-0.13	-0.01	0.19
Ti	-0.03	-0.06	-0.17	-0.10	-0.18	-0.12	-0.20	-0.06	-0.15	-0.08	-0.08	-0.16	0.16	0.11	0.05	-0.02	0.12
La	0.03	-0.12	0.02	-0.06	0.04	0.00	-0.10	-0.06	-0.13	0.00	0.21	0.03	-0.02	0.10	-0.11	0.01	0.01
Ce	0.04	-0.12	0.02	-0.07	0.05	0.03	-0.09	-0.06	-0.12	0.00	0.21	0.01	-0.01	0.10	-0.10	0.00	0.01
Nd	0.06	-0.12	0.01	-0.07	0.03	0.02	-0.10	-0.07	-0.12	0.00	0.19	0.01	0.02	0.10	-0.04	0.00	0.01
Sm	0.07	-0.12	-0.01	-0.08	0.01	0.00	-0.11	-0.08	-0.09	0.00	0.18	0.00	0.04	0.09	-0.02	0.00	0.01
Eu	0.15	-0.07	-0.09	-0.09	-0.09	0.00	-0.09	-0.06	0.24	-0.05	0.00	-0.12	0.23	-0.03	0.32	0.02	-0.01
Tb	0.07	-0.11	-0.04	-0.08	-0.03	-0.08	-0.13	-0.06	-0.02	0.02	0.19	-0.03	0.02	0.09	-0.03	0.04	0.00
Yb	0.04	-0.14	-0.07	-0.10	-0.05	-0.09	-0.16	-0.04	0.10	0.03	0.19	-0.03	0.02	0.09	-0.05	0.07	0.01
Lu	0.04	-0.17	-0.05	-0.09	-0.04	-0.09	-0.15	-0.03	0.07	0.01	0.18	0.00	0.02	0.10	-0.06	0.08	0.03
REE*	0.05	-0.12	0.02	-0.07	0.04	0.01	-0.10	-0.06	-0.12	0.00	0.21	0.02	0.00	0.10	-0.08	0.00	0.01

* Total REE All values are different from 0 with a significance level alpha=0.05.

Table 6.11. Pearson correlation matrix for selected trace elements in wallrock pyrite at Delbridge

	V	*Sc*	*Th*	*Ca*	*Mg*	*Mn*	*Na*	*Ti*	*La*	*Ce*	*Nd*	*Sm*	*Eu*	*Tb*	*Yb*	*Lu*
Fe																
Zn																
Pb																
Cd																
Au																
Ag																
As																
Sb																
Tl																
Hg																
Se																
Co																
Ni																
Te																
Bi																
Cr																
V																
Sc	0.05															
Th	-0.08	0.10														
Ca	0.12	0.67	0.15													
Mg	-0.07	0.80	-0.08	0.62												
Mn	0.04	0.61	-0.03	0.65	0.75											
Na	0.07	0.31	0.35	0.32	-0.01	0.03										
Ti	0.08	0.10	0.33	0.08	0.06	-0.02	0.04									
La	-0.10	0.16	0.99	0.16	-0.03	-0.01	0.34	0.33								
Ce	-0.11	0.19	0.98	0.17	0.00	0.01	0.34	0.33	1.00							
Nd	-0.12	0.27	0.96	0.19	0.09	0.05	0.32	0.34	0.98	0.99						
Sm	-0.12	0.33	0.94	0.23	0.14	0.08	0.32	0.34	0.97	0.98	1.00					
Eu	-0.12	0.80	0.08	0.39	0.70	0.39	0.05	0.12	0.17	0.22	0.33	0.40				
Tb	-0.11	0.38	0.93	0.31	0.18	0.09	0.33	0.33	0.95	0.96	0.97	0.98	0.43			
Yb	-0.12	0.45	0.89	0.39	0.22	0.12	0.36	0.31	0.91	0.93	0.94	0.95	0.45	0.99		
Lu	-0.11	0.39	0.93	0.35	0.15	0.10	0.37	0.32	0.95	0.95	0.95	0.96	0.36	0.99	0.99	
REE*	-0.11	0.21	0.98	0.18	0.02	0.02	0.33	0.33	1.00	1.00	0.99	0.99	0.24	0.96	0.93	0.96

* Total REE All values are different from 0 with a significance level alpha=0.05.

7. LITHOGEOCHEMISTRY OF THE PINKOS RHYOLITE

Table 7.1 contains major, trace, and rare earth element geochemical data for 108 rock samples collected at Pinkos (Figure 4.1) and analyzed at Geoscience Laboratories (OGS) in Sudbury, Ontario. The samples were processed at the same time as the Delbridge suite and analyzed by the same methods (i.e., XRF for major element data, ICP-MS for minor and trace element data, and infrared absorption for determination of CO_2 and total S). As at Delbridge, all iron oxide data are herein reported and manipulated as Fe_2O_3, however this does not suggest that all Fe in the system is oxidized (Fe^{3+}). Mineralogy indicates that most Fe at Pinkos occurs in its reduced (Fe^{2+}) state (e.g., carbonate, chlorite, sericite, pyrite).

Most samples are hydrothermally altered rocks. Table 7.1 classifies the samples according to four main types of alteration assemblages based on field observations, petrography, and SWIR spectroscopy (see Chapter 8). Samples of least-altered volcanic rocks have Na_2O contents in the ~3-5 wt.% range and contain minimal hydrothermal alteration products. Lithogeochemical data were analyzed to characterize the lithofacies and quantify the chemical variability caused by hydrothermal alteration and mineralization.

7.1 GEOCHEMISTRY OF DIFFERENT LITHOFACIES

QP rhyolite contains abundant silica (~68-84 wt.%), with up to nearly 80 wt.% even in fragmental facies. Both coherent and fragmental QP rhyolite have lower Al_2O_3

contents (8.5-12.5 wt.%) than mafic rocks. CaO abundance appears highly variable in all felsic facies (absent to ~3.5 wt.%) and is likely related to carbonate alteration. As expected, Fe_2O_3 (1-10 wt.%) and MgO (~0.2-6 wt.%) are less abundant in the felsic suite than in mafic rocks (14.7-16.7 wt.% Fe_2O_3 and 3.4-6.4 wt.% MgO). All but one of the felsic samples contain less than 0.26 wt.% TiO_2 and 0.03 wt.% P_2O_5. Anomalous sample RW126 is an outlier in many subsequent geochemical plots and calculations, possibly representing the basal intermediate extrusive unit. Similar to rhyolite breccia at Delbridge, fragmental rhyolite generally contains abundant CO_2 (>1 to nearly 5 wt.%). HFSE concentrations are higher in fragmental and strongly fractured facies than in coherent rhyolite. Similarly, incompatible LILE (e.g., Ba, Cs, Rb) also appear most abundant in fragmental and underlying fractured facies. Li abundance is low in fragmental rhyolite (<5 ppm Li) and much higher in coherent and fractured facies (up to ~52 ppm Li). Sr concentrations are much lower in the felsic suite than in mafic samples. Transition metal contents are generally low in all QP rhyolite facies (e.g., <5 ppm Sc and <6 ppm V). Notably, felsic rocks have more Cr than a few mafic samples. Consistent with being the least-altered rocks, basal coherent rhyolite clearly contains fewer base metals (Cu, Zn, Pb) than stringer and fragmental rhyolite. The entire felsic sample suite contains at least double the total REE content (~150-485 ppm) as mafic volcanic samples.

Mafic volcanic rocks have the lowest silica (42-53 wt.% SiO_2) and K_2O (0.02-0.2 wt.%) contents in the sample suite. This unit also has the highest Al_2O_3 (~12-14 wt.%) and CaO (~5.5-7.5 wt.%) concentrations. Elevated CaO may be due to primary pyroxene and plagioclase mineralogy and Ca-rich carbonate alteration. Mafic samples evidently

contain the greatest amount of ferromagnesian components (14.7-16.7 wt.% Fe_2O_3; 3.4-6.4 wt.% MgO). These samples also contain higher MnO (0.17-0.26 wt.%) than felsic rocks, which have as little as 0.01 wt.% MnO. The mafic unit has high TiO_2 (1.7-2 wt.%) and P_2O_5 (0.16-0.31 wt.%) relative to the felsic facies, which contain as little as 0.14 wt.% TiO_2 and 0.01 wt.% P_2O_5. Most mafic samples contain abundant CO_2 (>1.5 wt.%). As at Delbridge, mafic volcanic rocks typically have low LILE (<45 ppm Ba, <0.2 ppm Cs, <4 ppm Rb, and <0.9 ppm Be) and HFSE concentrations and high transition metal contents (up to 47 ppm Sc, >370 ppm V, >50 ppm Co, and >48 ppm Ni). Cr abundance appears bimodal (~4-8 ppm and 59-65 ppm) with the higher range corresponding to samples with >370 ppm V. Relatively high Li (>18 ppm) and Sr (~75-225 ppm) in mafic samples may be related to alteration mineralogy. Total REE concentrations are evidently lowest in the mafic unit (~40-80 ppm).

7.2 GEOCHEMISTRY OF ALTERATION AND MINERALIZATION TYPES

Similar to Delbridge, major and trace element geochemistry strongly agree with alteration and mineralization identified by field mapping and petrography.

Fe-rich carbonate and chlorite alteration is best characterized by high CO_2 and low Na_2O (mostly <3 wt.%) and MgO (mainly <2 wt.%). Up to ~4 wt.% CaO in assemblages dominated by Fe-rich alteration supports the presence of abundant Fe-bearing carbonate identified in outcrop and thin section. Similar to Delbridge, zones of intense Fe-rich carbonate alteration are generally depleted in total Fe, reflecting the destruction of Fe-sulfide in the interpreted main hydrothermal upflow (Figure 7.1a).

Abundant CO_2 (generally >1.5 wt.%; Figure 7.1b) coincident with low Fe_2O_3 in these zones supports the replacement of sulfide by CO_2-rich fluids at Pinkos. The most abundant sulfide in the footwall (wt.% S) clearly occurs outside the zone of Fe-rich carbonate alteration (Figure 7.2), further supporting field and petrographic observations of sulfide destruction in the main upflow zone. Low S concentrations typically coincide with zones of high CO_2. The Na-depletion supports the interpretation of Fe-rich alteration corresponding to the main hydrothermal upflow at Pinkos (Figure 7.3a). K_2O clearly shows negative correlation with Na_2O (Figure 7.3b), reflecting K-metasomatism associated with destruction of primary plagioclase.

High CaO (Figure 7.4a) is strongly correlated with CO_2 along the interpreted margins of the system, supporting the abundant Ca-rich carbonate identified in these zones. Similarly, high MgO (~0.5-6 wt.%; Figure 7.4b) and Al_2O_3 (~9-12 wt.%; Figure 7.5a) and relatively low CO_2 (mostly <2 wt.%) occur in zones of intense Mg-chlorite ($\pm$ epidote) and sericite alteration outside the interpreted focus of hydrothermal upflow. Li concentrations are consistently higher in these chloritized marginal zones (up to 52 ppm) and in mafic intrusive rocks (up to 40 ppm; Figure 7.5b), possibly reflecting substitution in chlorite and/or sericite. High Ba (>100 ppm; up to 1300 ppm) and Sr (up to ~60 ppm; Figure 7.6) occur in distal coherent, proximal columnar-jointed, and overlying fragmental rhyolite. Ba is mostly likely contained in sericite and Sr may be substituting for Ca in carbonate. Na_2O appears elevated in less intensely altered rocks along the margins of the system (i.e., less Na depletion). High MnO (~0.1-0.3% wt.%) corresponds to the interpreted core of hydrothermal upflow in stringers and stockwork and overlying

fragmental rhyolite (Figure 7.7a). This pattern resembles both CaO and CO_2 (cf. Figures 7.4a and 7.1b), suggesting substitution of Mn^{2+} for Ca^{2+} in Fe-bearing carbonate.

Silicification is only dominant in a broad alteration zone that occurs towards the interpreted margins of the system and effectively envelops the outline of Fe-rich alteration (Figure 7.7b). This alteration type clearly contains the most SiO_2 (~73 to >80 wt.%) at Pinkos. REE are depleted in this broad zone, possibly illustrating dilution by silica (Figure 7.8).

Unlike at Delbridge, Cu and Zn appear somewhat correlated at Pinkos. Stratigraphically, the highest Cu concentrations (~50-165 ppm) occur in fractured and stringer rhyolite facies immediately above the inferred termination of the South Bay fault and lesser in overlying fragmental rhyolite (Figure 7.9a). The most abundant Zn (>125 ppm; up to ~900 ppm) and Pb (~1.5-15 ppm) occur in fragmental rhyolite at the top of the succession and lesser in underlying fractured and stringer facies (Figures 7.9b, 7.10). Importantly, base metals (Cu, Zn, Pb) appear closely associated with zones of significant carbonate alteration.

MAJOR ELEMENT CORRELATIONS

A Pearson correlation matrix of major, trace, and rare-earth elements in the Cyprus Rhyolite at Pinkos is shown in Table 7.2a. SiO_2 is most strongly correlated with Na_2O and Al_2O_3 ($\pm$ K_2O), indicating silicification is most prominent in less altered rocks containing primary albite ($\pm$ sericite) towards the interpreted margins of hydrothermal

upflow. Negative correlation with all other major components (carbonate in particular) may reflect dilution by silica. Na-depletion and K-metasomatism mapped in the interpreted main upflow zone is confirmed by inversely related Na_2O and K_2O. Co-enrichment of CaO, MgO, Fe_2O_3, CO_2, and LOI reflects the major carbonate component and supports the presence of abundant Fe- and Mg-bearing carbonate (e.g., dolomite, ankerite) in footwall rhyolite at Pinkos. Strongly associated Fe_2O_3 and MgO also likely reflect the chlorite component. Trace MnO is strongly correlated with both CaO and CO_2, suggesting the substitution of Mn^{2+} in calcite. TiO_2 and P_2O_5 concentrations typically reflect trace rutile and phosphate. P_2O_5 and CaO are also paired in trace apatite identified by energy-dispersive spot (EDS) analysis (see Chapter 8).

A Pearson correlation matrix of major, trace, and rare-earth elements in mafic intrusive rocks is shown in Table 7.2b. Co-enrichment of SiO_2, Al_2O_3, Fe_2O_3, and MnO reflects the primary clinopyroxene and Fe-rich chlorite components identified in thin section. Unlike in rhyolite, Na_2O and K_2O are correlated, indicating a lack of Na-depletion and K-metasomatism which may suggest late emplacement of the mafic intrusive unit. Co-enrichment of CaO, MgO, and CO_2 reflects the major carbonate component and confirms the abundant Ca-rich and intermediate carbonate identified in thin section. Negative correlation between Fe_2O_3 and the carbonate component indicates Mg-rich (i.e., dolomite) compositions for the intermediate carbonate. MnO is notably unrelated to the carbonate component which contrasts with the surrounding felsic footwall and may support late emplacement of the mafic intrusive rocks. Trace rutile (TiO_2) and phosphate (P_2O_5) only appear associated with the clinopyroxene and chlorite

components in the mafic intrusive unit.

TRACE ELEMENT CORRELATIONS

Unlike at Delbridge, SiO_2 is not strongly correlated with HFSE, REE, or any other trace elements, which is atypical of felsic volcanic rocks (Table 7.2a). This poor correlation is supported by the lack of a silicified pod-like zone in the interpreted core of upflow at Pinkos. The muscovite component is reflected by strong correlation of K_2O and Al_2O_3 with HFSE, REE, Ba, Cs, Rb, Be, Tl, Ga, In, Sn, and W. Trace alkali and alkali earth metals are likely substituted for K^+ in muscovite. Co-enrichment of Li, Sc, V, Cu, Zn, and Co with MgO and Fe_2O_3 reflect the chlorite component. Correlation of Cs, Rb, Sr, Be, Pb ($\pm$ Zn), Cd, Sb, Tl, In, ($\pm$ Bi, Sn), and REE with CaO, CO_2 and LOI is characteristic of the carbonate component. Na_2O, Sr, and Eu appear associated with the albite component. Rutile (TiO_2) and phosphate (P_2O_5) components are both correlated with Sc, V, Co, and Ga. Pyrite component (Fe_2O_3, S) shows co-enrichment of Cu, Zn ($\pm$ Pb, Cd), Co, Mo, Bi, and Ga. Base metals (Cu, Zn, Pb) are only very slightly correlated with the carbonate component, supporting sulfide destruction and carbonate replacement. Cu appears most strongly associated with Fe_2O_3, MgO, MnO, Li, Zn, Pb, Cd, and Sb ($\pm$ Co, Mo, Bi). Zn appears more closely related to Fe_2O_3, MnO, CO_2, Cu, Pb, Cd, Bi, In, and Sn ($\pm$ Mo). Of the base metals, Pb is most closely related to the carbonate component (CaO, MnO, and CO_2) and W. Similar to Pb, the distributions of less abundant Cd and Sn clearly follow the same trend as Zn. Low Mo concentrations occur in the uppermost fragmental and immediately underlying columnar-jointed rhyolite facies. Similarly, Sb and Tl only appear slightly anomalous within and proximal to the

fragmental facies.

Unlike the Cyprus Rhyolite, HFSE and REE are strongly correlated with SiO_2 in the mafic unit at Pinkos (Table 7.2b). Atypical of mafic rocks, Fe_2O_3 and MgO are inversely related; however, each shows correlation with Sc and variable LILE. Fe_2O_3 appears more strongly associated to the clinopyroxene ($\pm$ chlorite) component (SiO_2, Al_2O_3, HFSE, Sr, Be, Zn, Cd, Mo, Ga, In, W, and REE) and MgO appears more closely related to the carbonate component (CaO, MnO, CO_2, Cr, V, Pb, Sb, Tl, and Sn). Similar to Fe_2O_3, rutile (TiO_2) and phosphate (P_2O_5) both show correlation with HFSE, REE, Sr, Be, Zn, Cd, Mo, Ga, In, and Sn. Notably, Cu and Pb show strong negative correlation with Zn in mafic intrusive rocks.

IDENTIFICATION OF LEAST-ALTERED RHYOLITE COMPOSITION

Similar to Delbridge, it is very unlikely that a true protolith composition for the Cyprus Rhyolite still exists at Pinkos. Instead, a least-altered composition has been estimated by comparison with typical fresh-rock compositions for high silica rhyolites elsewhere in the Abitibi subprovince and by consideration of a number of geochemical criteria listed in Table 7.3 (e.g., Barrett *et al*, 1993; Koopman *et al*, 1999; Prior *et al*, 1999a, b). All samples collected within fragmental facies were excluded as candidates due to the possibility of mixed provenance. Three samples (RW053, RW063, and RW147) were selected to represent least-altered QP rhyolite compositions at Pinkos and are identified in each of the relevant lithogeochemical tables. The average of these three analyses gives a reasonable estimation of the least-altered composition for the Cyprus

Rhyolite.

The Pinkos geochemical data were treated using the identical immobile element procedures described for Delbridge (MacLean and Kranidiotis, 1987; MacLean and Barrett, 1993). Zr, Hf, Ta, Nb, Th, Yb, and Lu all have highly correlated ($r > 0.85$) linear trends with other variables on representative x-y bivariate plots (Figure 7.11). However, Zr is chosen as the immobile element monitor component for mass balance calculations owing to its high correlation coefficients and its much greater abundance, thereby reducing the likelihood of analytical errors affecting the calculations.

Incompatible Elements

The majority of samples collected at Pinkos fall within the tholeiitic range of an incompatible-incompatible Y-Zr plot (Figure 7.12). A few samples have slightly higher Zr/Y ratios and plot within the transitional range. The cluster of six outliers with significantly lower Zr/Y ratios represents the mafic intrusive unit. These magmatic affinities are consistent with La/Yb and Zr/Yb ratios (Table 7.4). Figure 7.13a is a plot of Zr/Ti and Nb/Y immobile element ratios on the discrimination diagram of Winchester and Floyd (1977) and confirms that nearly all samples are of rhyolitic composition. One sample (RW126) collected in the basal stratigraphy plots in the rhyodacite to dacite range. The six samples that fall in the andesitic range were collected from the mafic intrusive (diorite) unit.

Compatible Elements

As at Delbridge, an immobile compatible-incompatible plot of TiO_2-Zr has been used to identify potentially discrete chemostratigraphic units at Pinkos that were initially homogeneous but subsequently altered (MacLean and Barrett, 1993; Barrett *et al*, 1993). All TiO_2-Zr data are presented in Figure 7.13b and subdivided into altered and least-altered samples. A single fractionation curve has not been estimated due to an insufficient number of samples. Only one alteration line extends from the origin, which clearly indicates a single magmatic source for the felsic sample suite. The large spread of samples along the rhyolite trend reflects the significant variation in alteration styles and intensities at Pinkos. The cluster of six outliers in the andesitic range represents the moderately porphyritic mafic intrusive (diorite) unit. The single, isolated outlier is the same rhyodacite to dacite sample (RW126) shown in Figure 7.12.

Bivariate plots of Ta vs. Zr and Nb vs. Zr (Figures 7.14a, b) confirm the consistent trend of only one alteration line produced from a single magmatic source for the felsic volcanic stratigraphy at Pinkos. Since the rocks of both tholeiitic and transitional affinities have been shown to be co-magmatic, they are grouped together and treated as a single series (Barrett *et al*, 1993). Plots of the heavy REE vs. Zr (not shown) support the relationships determined in the TiO_2-Zr plot.

Mass Gains and Losses due to Alteration

Mass balance changes at Pinkos were evaluated using the same procedures (after MacLean and Kranidiotis, 1987) as described for Delbridge. As noted above, Zr is selected as the immobile monitor for mass balance calculations at Pinkos because of its

high correlation with other immobile elements and its much greater abundance, which reduces the likelihood of analytical errors affecting calculations. Since only one compositionally distinct rhyolite has been identified, all of the samples have been treated as a single series and therefore the calculations are all relative to the same least-altered rhyolite composition. This precursor composition is presented in Table 7.5 as the calculated average of least-altered samples RW053, RW063, and RW147.

Average mass changes for individual elements in different alteration types have been plotted on a histogram in Figure 7.15. Outlier sample RW126 is excluded from the average mass changes for the Mg-chlorite assemblage due to its anomalous values and potentially separate magmatic source. Similar to Delbridge, large positive net mass changes at Pinkos are mainly the result of SiO_2 gains at Pinkos with smaller additions of Al_2O_3, K_2O, CaO, Fe_2O_3, MgO, and CO_2 associated with carbonate, chlorite, and sericite alteration. Gains of K_2O are inversely related to significant Na_2O losses, indicative of typical K-metasomatism in VMS alteration zones (Morton and Franklin, 1987). Minor CaO and CO_2 losses are only observed in the phyllosilicate-rich (Mg-chlorite, sericite) assemblage. The largest additions of CO_2 occurred in zones of Fe- and Ca-rich carbonate alteration, confirming the alteration map pattern determined from field mapping, petrography, and SWIR analytical data (see Chapter 8). Very little S has been introduced to the system with only minor additions identified in zones of Fe-carbonate and quartz-sericite alteration. Because the mass balance calculations assume a constant density, these minor S variations may simply reflect system volume changes.

Pearson correlation factors of major element mass changes in the Cyprus rhyolite at Pinkos are shown in Table 7.6. Addition of K_2O inversely related to loss of Na_2O supports K-metasomatism coincident with Na depletion in the footwall. CO_2 addition is most strongly correlated with CaO and MnO, confirming zones of abundant carbonate. Correlation of Fe_2O_3 and MnO may reflect the Fe-bearing carbonate identified in outcrop and thin section. Co-enrichment of Na_2O, K_2O, Al_2O_3, SiO_2, CaO ($\pm$ Fe_2O_3, MgO), MnO, and CO_2 in zones of Fe-rich carbonate and chlorite alteration (Figure 6.15) may support the co-precipitation of ankerite and paragonite (see Normative Alteration Mineralogy below and Chapter 8.2: Mineral Chemistry). Weakly correlated additions of CO_2 and S may confirm CO_2-rich mineralizing fluids.

Rare-Earth Elements (REE)

Chondrite-normalized rare-earth element analytical data for Pinkos are presented along with La/Yb ratios in Table 7.7. With few exceptions, the felsic samples have La/Yb ratios of ~1.4-2.7, falling in the range of tholeiitic rhyolite (MacLean and Kranidiotis, 1987). These results are consistent with Zr/Y ratios and other immobile elements plots shown previously. Mafic samples clearly exhibit flatter chondrite-normalized REE profiles than the felsic suite (Figure 7.16b).

Correlation of all rare-earth elements (Figure 7.16a) indicates that heavy REE were immobile and light REE were chemically mobile (i.e., lower Pearson coefficients). Though less evident than at Delbridge, partial mobility of the light REE in footwall rhyolite at Pinkos is demonstrated by a fan-shaped array of chondrite-normalized REE

profiles with different slopes that converge towards the heaviest REE (Figure 7.16c). This configuration of REE profiles is common in proximal alteration zones associated with VMS deposits (MacLean and Barrett, 1993).

Some Pinkos samples reveal immobility of the REE by vertical displacement of sub-parallel chondrite-normalized profiles (Figure 7.16d), which also reflects net mass changes in the system associated with alteration (Gifkins *et al*, 2005; MacLean and Barrett, 1993). Figure 7.16d displays these vertical shifts in samples representative of different alteration types compared to least-altered rhyolite samples. As at Delbridge, the REE profiles of strongly silicified samples are shifted downward due to net mass gain and dilution of REE. Upward shifts are observed in carbonatized and chloritized samples, indicating net mass loss and addition of REE.

Alteration Intensity

Alteration intensity at Pinkos was quantified using the same methods as at Delbridge, which include the Ishikawa alteration index (AI), chlorite-carbonate-pyrite index (CCPI), alteration box plot, carbonate index, and Mn-carbonate index.

At Pinkos, Ishikawa AI values range from ~10 to nearly 100, with the majority (~75%) of the samples having values less than 60 (Table 7.8). Similar to Delbridge, the highest AI values (>90) correspond to samples collected in the two offset zones containing stringer chlorite $\pm$ Fe-carbonate alteration within the interpreted hydrothermal upflow beneath the known mineralization (Figures 7.17a, 7.18a). Coupled with low AI

(~10-20) in basal and distal coherent rhyolite, this supports the dominant control of host-rock permeability on hydrothermal fluid flow at Pinkos.

CCPI values range from ~20 to 90, with the majority (~75%) of the samples having values less than 60 (Table 7.8). Consistent with the Ishikawa AI, the highest CCPI values occur mainly within the same offset zones of fracture- and stringer-controlled alteration interpreted as the focus of hydrothermal fluid flow (Figures 7.17b, 7.18b). Some relatively elevated values also occur within fragmental rhyolite at the top of the succession, confirming the importance of host-rock permeability on alteration and mineralization.

As at Delbridge, the alteration box plot is used as a discriminant for sericite-, chlorite-, and carbonate-rich altered zones at Pinkos and to distinguish between VMS hydrothermal alteration and diagenetic assemblages (Large *et al*, 2001). The least-altered footwall rhyolite samples at Pinkos plot within the box bounded by an AI of ~25 to 40 and a CCPI of ~20 to 35 (Figure 7.19). Variably altered samples are subdivided into three distinct hydrothermal fields and one diagenetic trend. Field 1 indicates intense sericite-chlorite-pyrite alteration of samples collected in zones of fracture-controlled and stringer-style alteration in the interpreted hydrothermal upflow. This trend is typical to proximal footwall alteration of VMS deposits (Large *et al*, 2001). Field 2 contains variably carbonatized and chloritized ($\pm$ sericitized) samples. Samples that plot along the chlorite-pyrite(-sericite) trend commonly occur in chlorite-dominated footwall alteration proximal to VMS deposits (Large *et al*, 2001). At Pinkos, these samples were collected

in either stringer-style alteration of coherent rhyolite or in proximal fragmental rhyolite. Fragmental rhyolite samples appear to contain abundant carbonate and sericite, a trend typical of the favourable stratigraphic host unit in a VMS system (Large *et al*, 2001). Samples that fall within Field 3 are weakly sericitized and occur along the margins of the interpreted hydrothermal system (north and south of stringer alteration) and in distal fragmental rhyolite. The few samples that plot along the diagenetic trend indicate albite and chlorite alteration typical of seawater interaction at low temperatures. These samples were collected fairly deep in the footwall, which may reflect strong drawdown of seawater in a shallow environment.

As for Delbridge, the intensity of carbonate alteration at Pinkos is estimated using molar proportions of the components CO_2, CaO, FeO, and MgO. Carbonate index values are highly variable, ranging from 0.1 to 0.92 molar units (Table 7.8). The distribution of these normalized indices indicates that the intensity of carbonate alteration is highest in fragmental rhyolite at the top of the succession and in underlying columnar-jointed rhyolite (Figure 7.20a). Carbonate intensity is clearly lowest in stringers and stockwork within the interpreted hydrothermal upflow. This is consistent with earlier observations of total CO_2 concentrations (cf. Figure 7.1b).

Conversely, weakly Mn-rich carbonate (<0.31 molar units), estimated from molar proportions of MnO to CO2, occurs mainly in the two offset stockwork zones, reflecting a strong negative correlation with estimated carbonate intensity (Figure 7.20b). The molar proportions of Mn-carbonate may represent the distribution of hydrothermal

carbonate at Pinkos, with marginal and overlying carbonate possibly resulting from a different source.

Normative Alteration Mineralogy

Mineral abundances at Pinkos were calculated from whole-rock geochemical data using the same least-squares method (Herrmann and Berry, 2002) described for the Delbridge suite. Mineral estimates of quartz, albite, white mica, chlorite, carbonate, epidote, and rutile were made for each sample and are presented in Table 7.9. As at Delbridge, multiple compositional end-members were included in the calculations for white mica, chlorite, and carbonate. The presence of different members of these series is supported by SWIR and microprobe data (see Chapter 8).

Least-altered samples occur in the interpreted margins of the hydrothermal system and have an average normative composition of ~50% quartz, 30% feldspar (~5:1 albite to K-feldspar), 10% sericite, 5% carbonate, and 2% chlorite. This correlates well with modal mineralogy identified in thin section (Table 5.1).

Quartz abundance is typically elevated in the alteration zone (up to 70 wt.%) and to a lesser extent in the quartz-sericite-chlorite assemblages. The most abundant quartz is estimated along the margins of the interpreted upflow, confirming field and petrographic observations and SWIR analytical data. Similar to the silicified core at Delbridge, silica enrichment is observed locally within the two offset stockwork zones at Pinkos. Quartz abundance is notably lower in carbonate-rich samples.

The highest normative white mica abundances (~20 to >35 wt.%) clearly occur along the interpreted margins of hydrothermal upflow and in fragmental rhyolite (Figure 7.21). Paragonite [$NaAl_2(AlSi_3)O_{10}(OH)_2$] is the dominant white mica with lesser muscovite [$KAl_2(AlSi_3O_{10})(OH)_2$] and trace phengite [$KAl_2(AlSi_3O_{10})(OH)_2$-$K(Mg,Fe^{2+})Fe^{3+}(Si_4O_{10})(OH)_2$] also present. Paragonite appears highly widespread at Pinkos and is estimated in nearly all samples (Figure 7.21) but this may reflect underestimation of primary albite. Despite less significant compositional variation than observed at Delbridge, muscovite is clearly most abundant in altered stockwork and fragmental rhyolite. The distribution of muscovite reflects the most intense Na-depletion and K-metasomatism and confirms the interpreted focus of hydrothermal fluid flow at Pinkos. Weak phengite alteration towards the margins of the system and in uppermost fragmental rhyolite reflects substitution of Mg^{2+} for Al^{3+} in potassic white micas, supporting increased MgO content in these zones (Figure 7.21).

Significant Fe-chlorite (>5 wt.%) is only estimated in the two offset zones of stringers and stockwork (Figure 7.22), reaffirming the interpreted alteration map pattern. Abundant Mg-chlorite occurs in fractured rhyolite from the stringer zone to the northwest of the map area and immediately above the inferred termination of the South Bay fault (Figure 7.22). Minor Mg-chlorite is also present with Fe-rich species in the stockwork zone to the southeast. Of interest, significant chloritization typically only occurs in samples containing little to no carbonate.

Normative carbonate occurs throughout the Cyprus Rhyolite, but is clearly most abundant in fragmental rhyolite at the top of the stratigraphy and to a lesser extent in underlying columnar-jointed and fractured rhyolite facies (Figure 7.23). The normative carbonate in the footwall is dominated by Fe-rich species (~55% ankerite and ~25% siderite) with lesser Ca(-Mg)-rich species (~10% each of calcite and dolomite). Similar to Delbridge, ankerite is widespread and appears possibly coupled with paragonite. Normative siderite appears concentrated in fragmental rhyolite and underlying proximal columnar-jointed (± stockwork) facies. The distribution of normative calcite and dolomite is essentially restricted to the interpreted margins of the system and fragmental rhyolite (Figure 7.23). This supports the interpreted zonation from higher temperature Fe-rich species in the core of the system to lower temperature Ca- and Mg-rich members distally.

Notably, significant (~10-25 wt.%) normative hedenbergite (Fe-rich calcic clinopyroxene) is estimated for all mafic samples, which reflects primary mineralogy and may explain the source for the abundant Ca-rich carbonate alteration identified in thin section.

7.3 GEOCHEMISTRY OF STRINGER AND DISSEMINATED SULFIDES

Systematic surface sampling of distal disseminated, fracture-, and matrix-controlled sulfides was conducted within an area of ~1 km^2 and at a spacing of approximately 50 to 100 m at Pinkos. Pyrite grains were selected and analyzed using identical criteria and methodologies as for Delbridge. Analytical data are summarized in Table 7.10. Again, it

should be noted that the sulfide separates were not entirely pure since some samples contain < 30-40 wt.% Fe (as opposed to 46.5 wt.% for a good pyrite analysis).

Distribution plots of selected trace elements in pyrite are shown in Figures 7.24-7.29 and a correlation matrix identifies the main groups of elements (Table 7.11).

The positive correlation of Cd with Zn in columnar-jointed and fragmental rhyolite at the top of the succession and in stringers and stockwork to the southeast (Figures 7.24b, 7.25b) is similar to other documented Archean Cu-Zn deposits (e.g., Delbridge; Hannington et al, 1999; Tables 7.10, 7.11). This shows that the pyrite being replaced at Pinkos is part of the hydrothermal system and not simply diagenetic or metamorphic in origin. Unlike at Delbridge, Pb concentrations do not appear associated with Zn and Cd (Figure 7.25a), but instead with Mn, Ag, Ni, Sb, Bi, As, and Te (Table 7.11), possibly suggesting the presence of unidentified trace arsenides and tellurides (Hannington et al, 1999). Ag may also occur in trace galena observed at Pinkos. Hg concentrations are extremely low (<0.1 ppm; up to 0.4 ppm), but strong correlation with Zn and Cd is evident (Table 7.11). Pb, Hg, Bi, and Th show minor correlations with REE. Important alkali and alkali earth metal concentrations in pyrite include Ca, Mg, and Na (up to ~4.1, 2.7, and 1.1 wt.%, respectively; Table 7.11).

The highest Cu concentrations clearly occur at the inferred termination of the South Bay Fault, in stringers and stockwork to the southeast, and in proximal columnar-jointed rhyolite (Figure 7.24a). Co-enrichment of Co, Fe, Au, Ag, As, and Se in Cu-rich samples

(~0.2 wt.%; up to 2.4 wt.%) at Pinkos is similar to that observed in the highest temperature assemblages of other volcanogenic massive sulfide deposits (Smith and Huston, 1992; Marcoux et al, 1996; Leistel et al, 1998; Hannington et al, 1999). Ag shows the strongest correlation with Cu (Table 7.11; Figure 7.26b); however its association with interpreted lower temperature trace elements (e.g., Zn, Cd) indicates that Ag concentrations in the ore fluids were not strongly temperature-dependent. Moderate correlation of Co with Cu (Table 7.11) is observed proximal to the South Bay Fault and in the stockwork zone to the southeast (Figure 7.29a), however no discrete minerals containing Co have been identified. Co concentrations appear dependent on ferromagnesian components due to co-enrichment of Sc, V, Ti ($\pm$ As), and Mg. This is supported by high Co in both strongly chloritized zones and mafic intrusive rocks (Figure 7.29a). Gold concentrations in sulfide grains are significantly lower than at Delbridge (~150 ppm and up to 0.4 wt.%; Table 7.10) and are most strongly associated with Ag, Fe, Se, and Te ($\pm$As) proximal to the South Bay Fault, in stockwork to the southeast and fragmental rhyolite at the top of the succession (Figure 7.26a). Moderate to strong correlation of Bi and Fe with As, Se, and Te may indicate the presence of unidentified trace Bi- and Fe-rich arsenides, selenides, and tellurides. Slight co-enrichments of LREE with Cu and Bi are observed (Table 7.11).

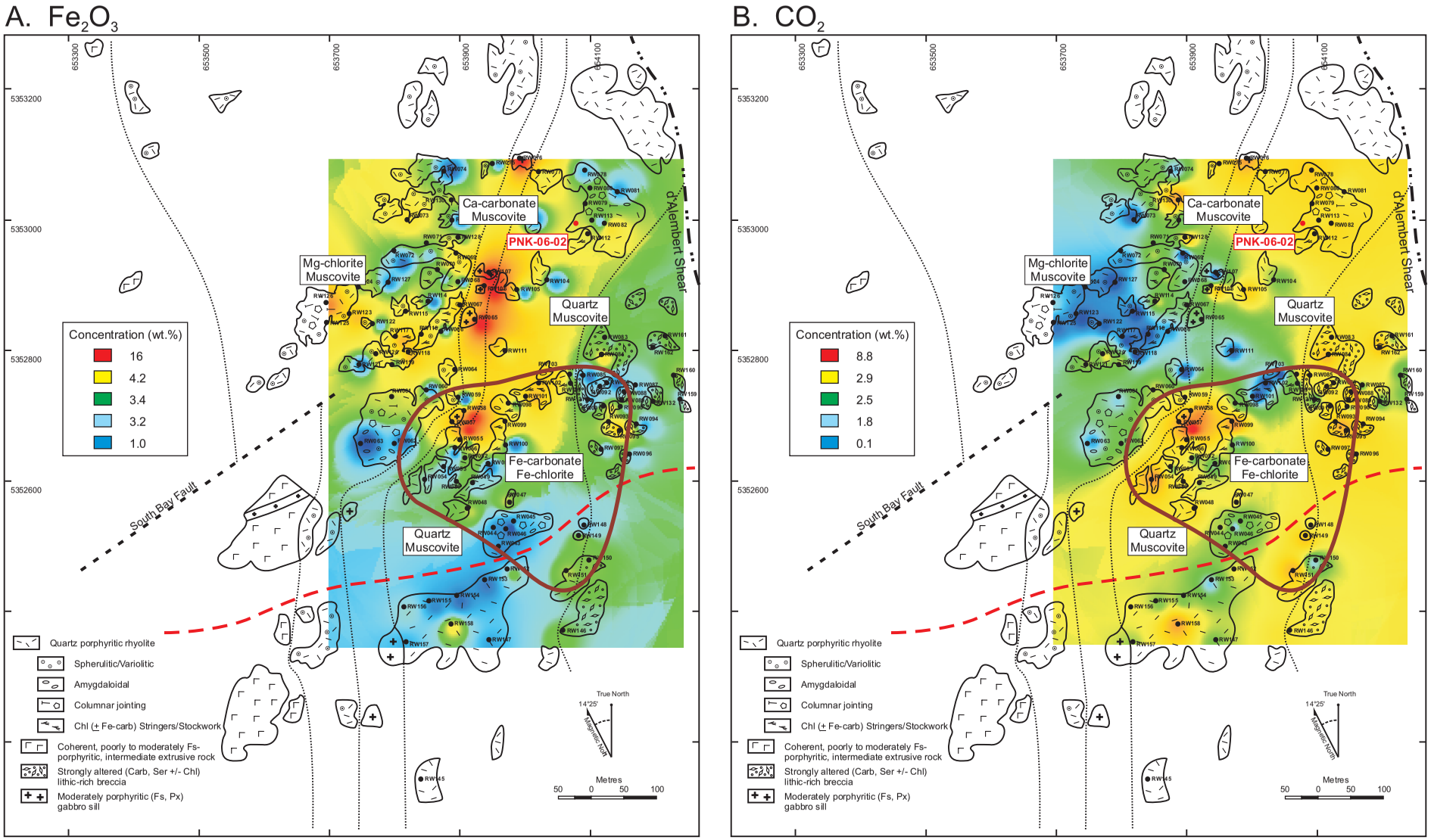

Figure 7.1. Concentrations of total Fe and CO_2 at Pinkos shown with respect to lithofacies and mapped alteration types. All plotted data are based on quantitative whole-rock geochemistry and contoured using inverse-distance weighting (IDW). a) Total Fe as Fe2O3 corresponds to mafic intrusive rocks and zones of abundant distal disseminated sulfides in stringers and stockwork above the inferred termination of the South Bay fault and in distal coherent rhyolite. Zones of intense Fe-rich carbonate alteration are overall depleted in total Fe, reflecting the destruction of Fe-sulfide in the main upflow zone. b) Abundant CO_2 to nearly clearly occurs in zones of proximal columnar-jointed rhyolite and overlying fragmental rhyolite containing low total Fe, supporting replacement of sulfide by CO_2-rich fluids at Pinkos.

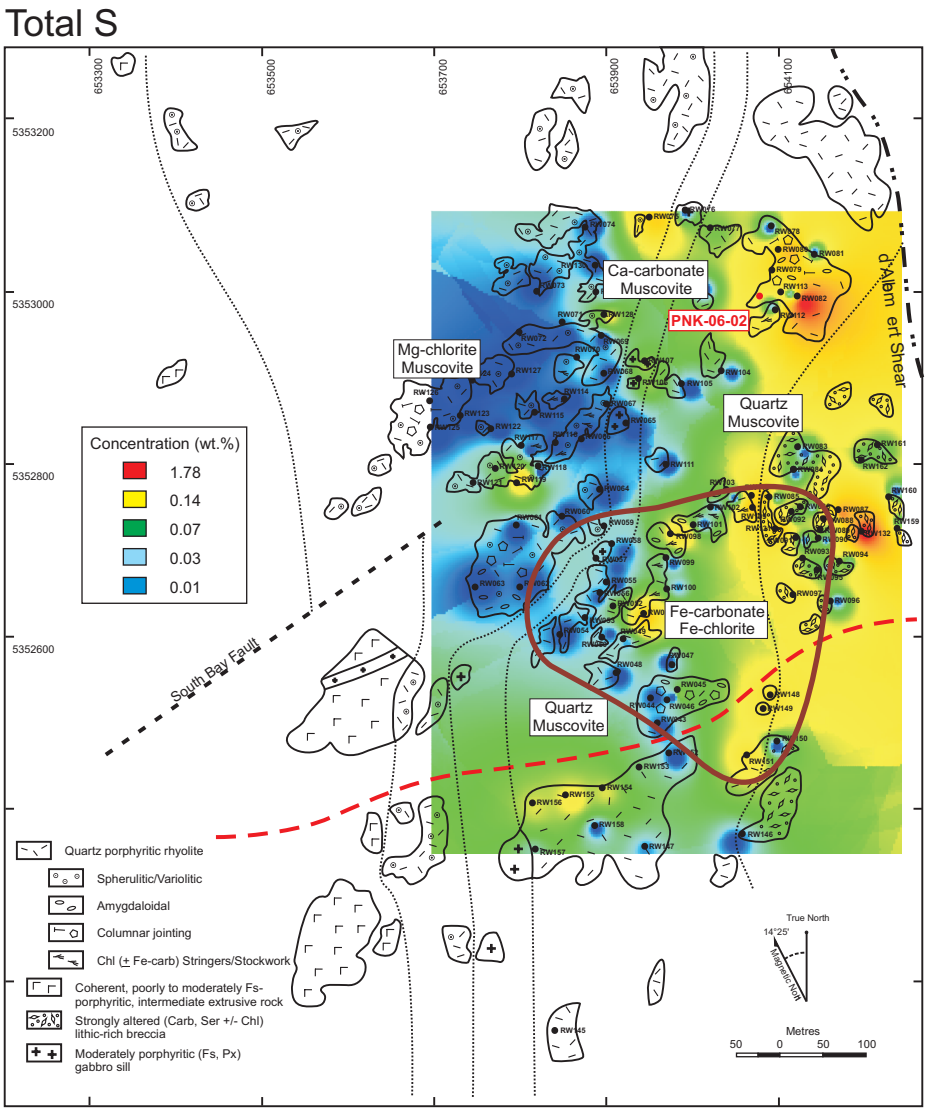

Figure 7.2. Concentrations of total S (wt.%) at Pinkos shown with respect to lithofacies and mapped alteration types. All plotted data are based on quantitative whole-rock geochemistry and contoured using inverse-distance weighting (IDW). The most abundant S (typically <0.3 wt.%) occurs in fragmental rhyolite at the top of the succession and is notably absent in stringers and stockwork, confirming field and petrographic observations of sulfide destruction. Low S concentrations coincide with zones of high CO_2 (cf. Figure 7.1b), supporting sulfide replacement by carbonate.

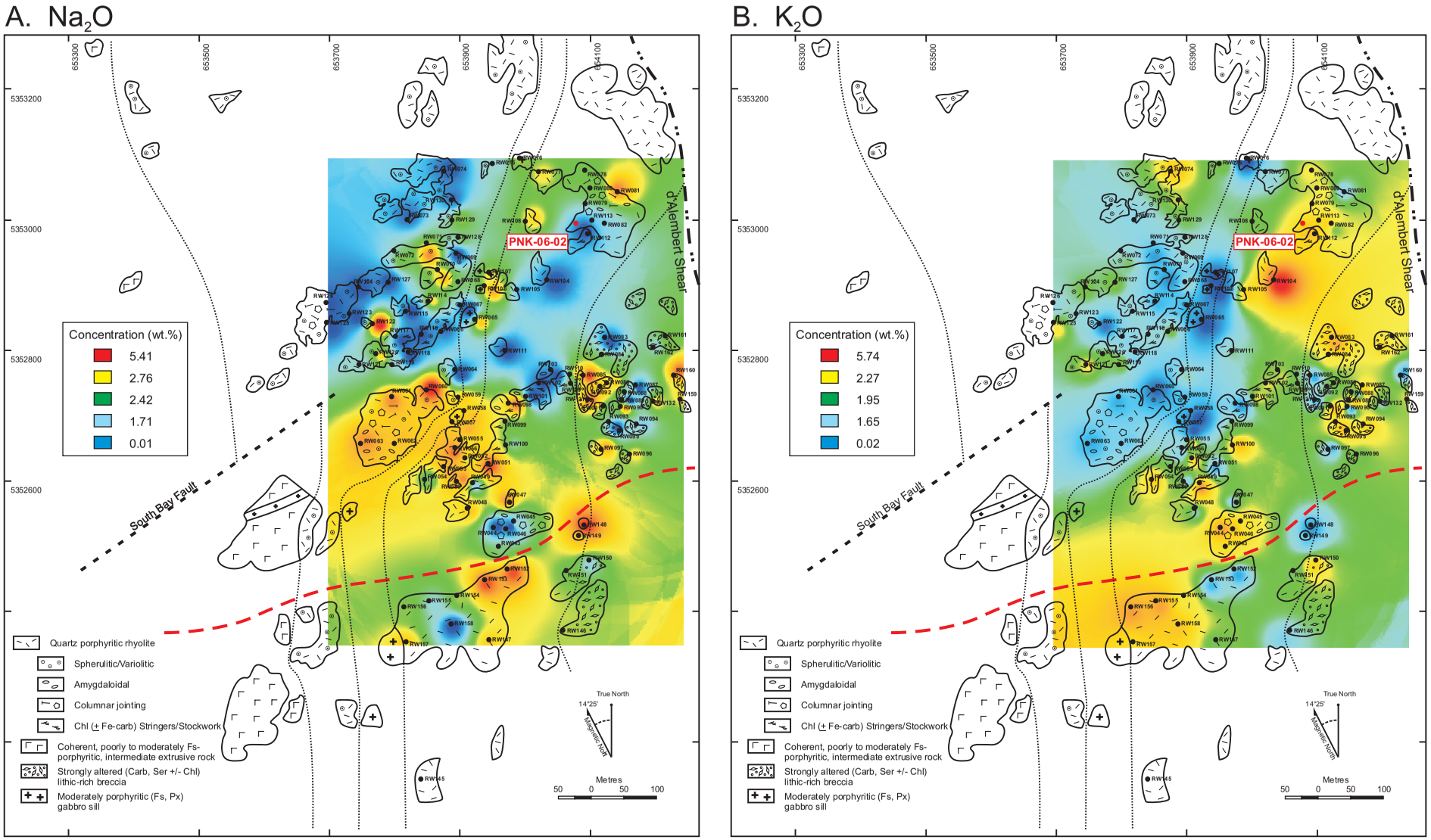

Figure 7.3. Concentrations of Na2O and K2O (wt.%) at Pinkos shown with respect to lithofacies. Plotted values are based on quantitative whole-rock geochemical data and contoured using inverse-distance weighting (IDW). a) Na_2O depletion is evident at the inferred termination of the South Bay Fault, in both zones of offset stockwork, and into overlying fragmental rhyolite. b) K_2O concentrations are inversely related to Na_2O with slight enrichment in stringers and stockwork and high K_2O in proximal columnar-jointed and fragmental rhyolite in zones of low Na_2O. Na depletion and associated K-metasomatism are characteristic vectors towards VMS-style mineralization.

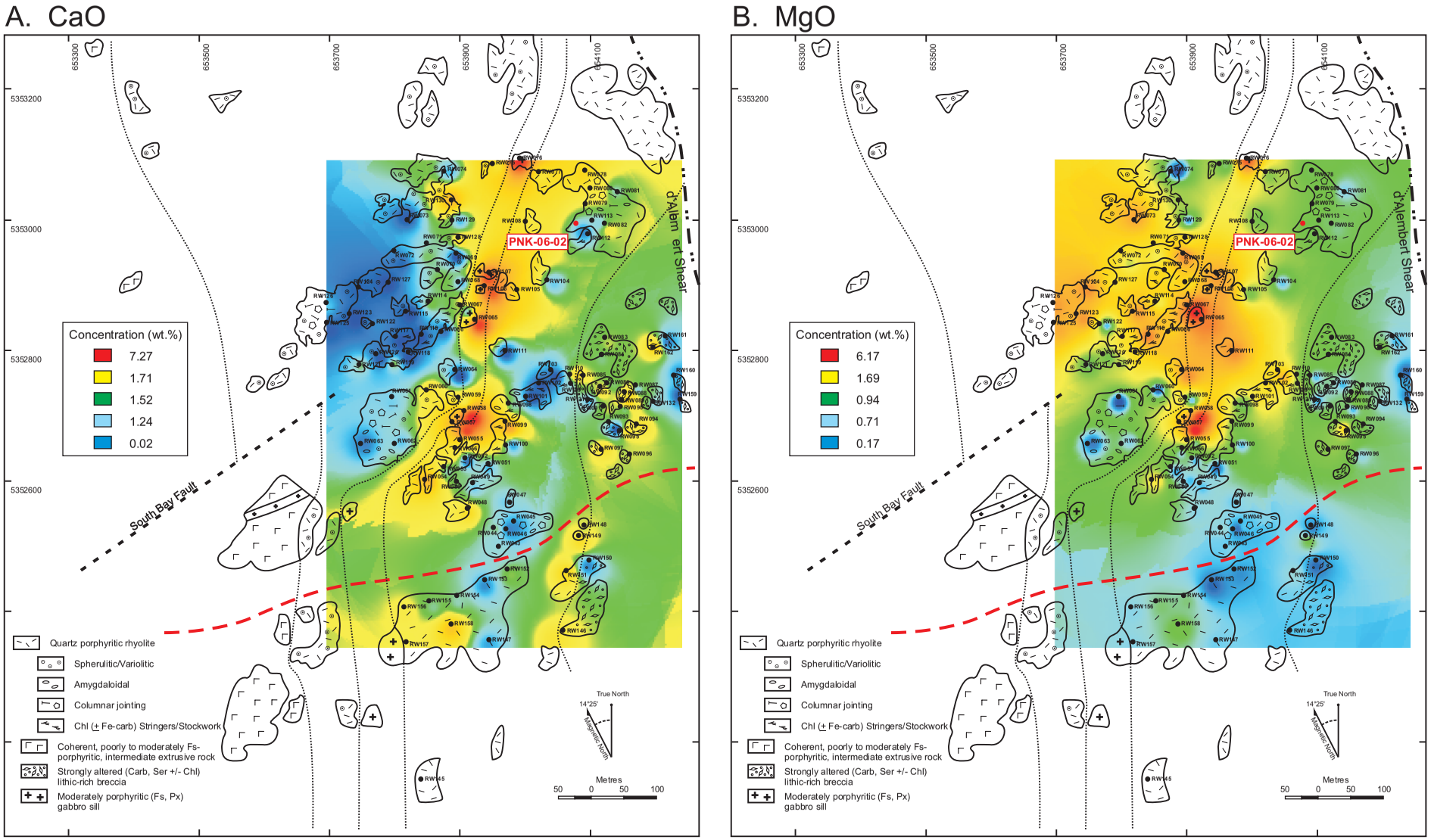

Figure 7.4. Concentrations of CaO and MgO (wt.%) at Pinkos shown with respect to lithofacies. All plotted data are based on quantitative whole-rock geochemistry and contoured using inverse-distance weighting (IDW). a) High CaO correlates with CO_2 (cf. Figure 7.1b), supporting the abundant Ca-rich carbonate identified in distal coherent QP rhyolite and in mafic intrusive rocks. b) High MgO coincides with intense Mg-rich chlorite in similar zones of distal rhyolite to the north and in mafic intrusive rocks.

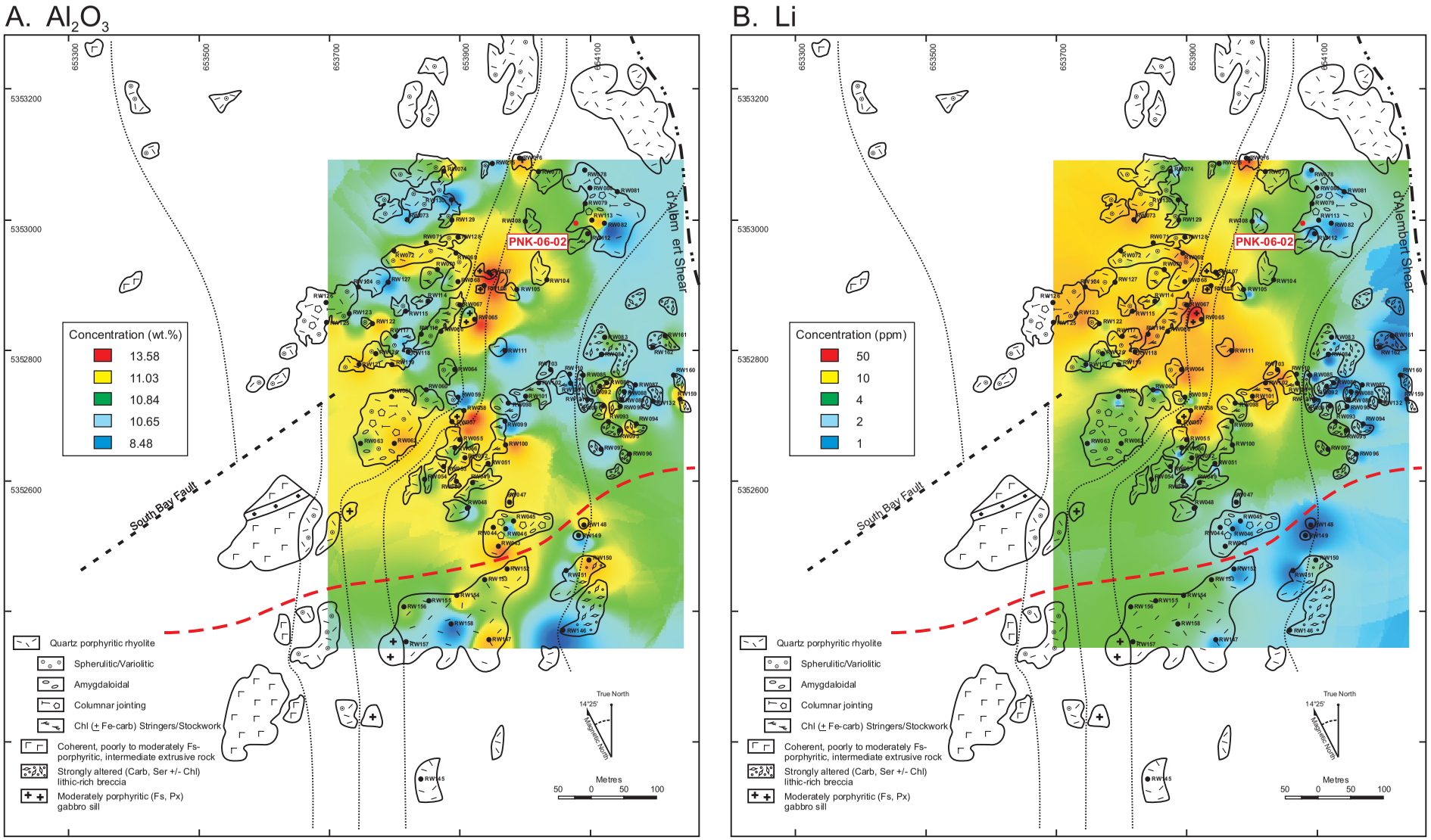

Figure 7.5. Concentrations of Al_2O_3 (wt.%) and Li (ppm) at Pinkos shown with respect to lithofacies. Plotted data are based on quantitative whole-rock geochemical analyses and contoured using inverse-distance weighting (IDW). a) High Al2O3 corresponds to zones of abundant sericite in proximal columnar-jointed and distal coherent rhyolite and chlorite in mafic intrusive rocks. b) Li concentrations clearly correlate with Al_2O_3 and MgO (cf. Figure 7.4b), suggesting substitution of Li^+ for Mg^{2+} in zones of intense chlorite alteration.

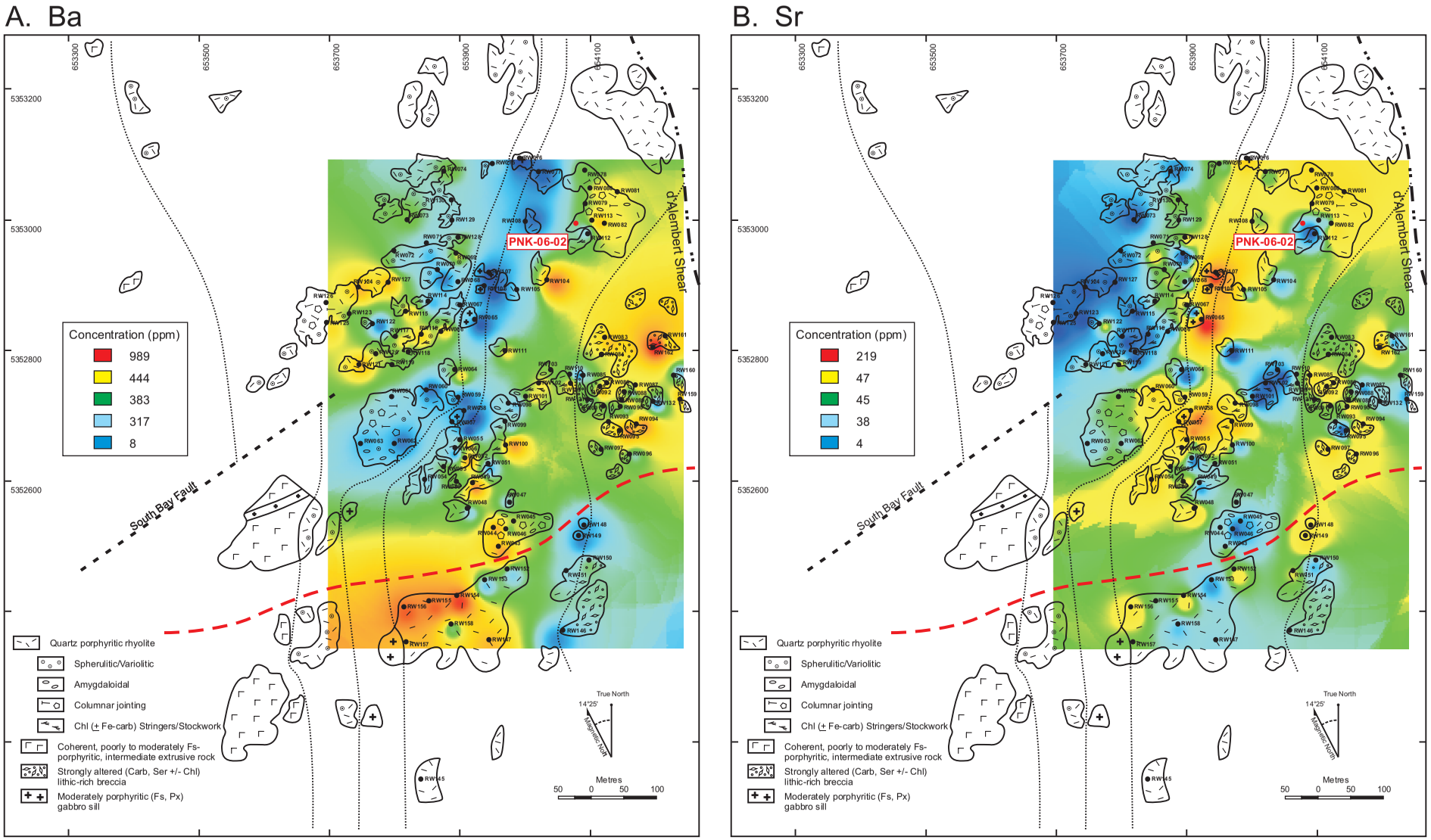

Figure 7.6. Concentrations of Ba and Sr (ppm) at Pinkos shown with respect to lithofacies. All plotted data are based on quantitative whole-rock geochemistry and contoured using inverse-distance weighting (IDW). a) High Ba concentrations (>100 ppm; up to 1300 ppm) in distal coherent, proximal columnar-jointed, and uppermost fragmental rhyolite are likely contained in sericite. Minor Sr enrichment (up to ~60 ppm) clearly mimics CaO (cf. Figure 7.4a), suggesting substitution for Ca^{2+} in Ca-rich carbonate.

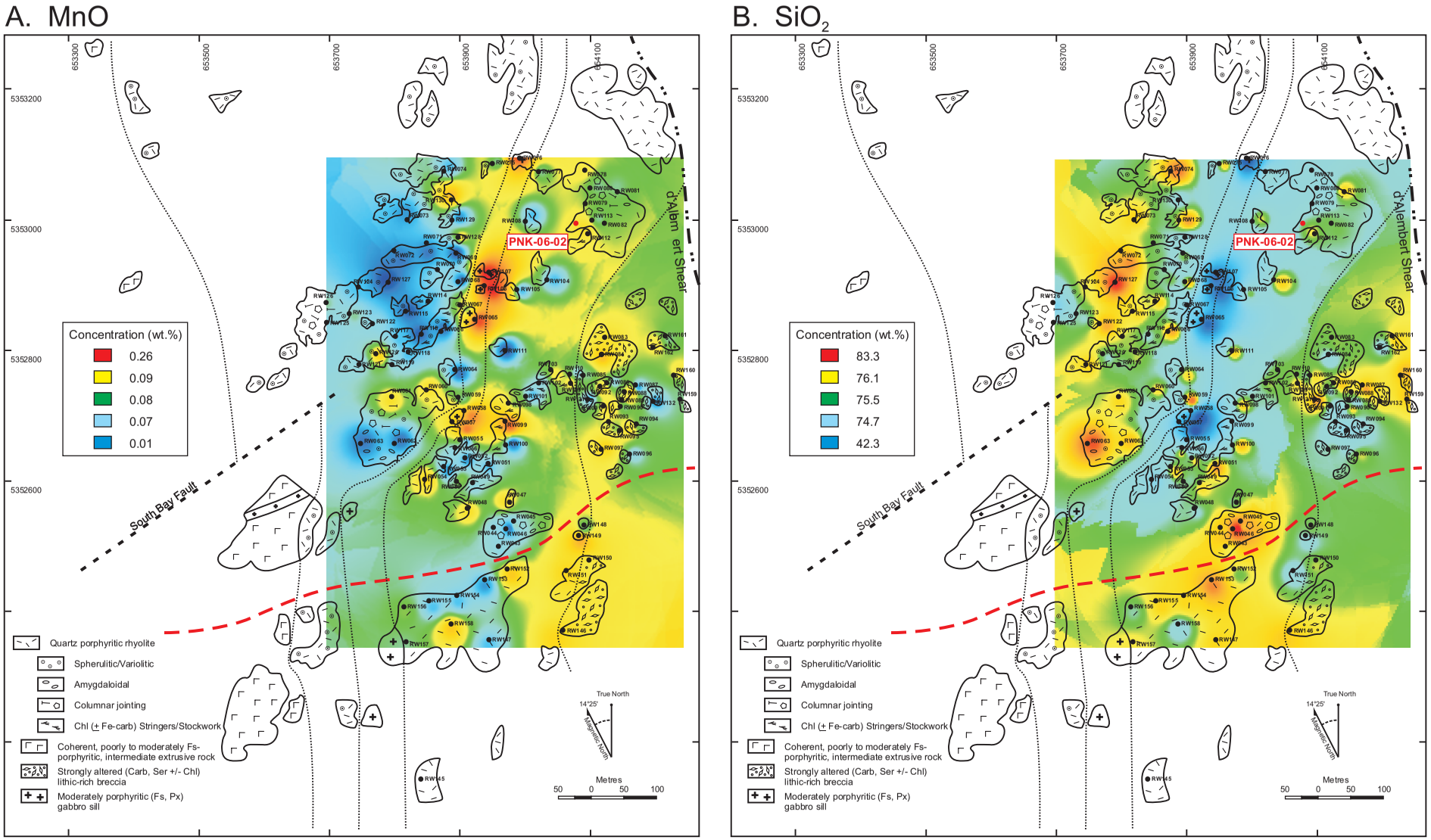

Figure 7.7. Concentrations of MnO and SiO_2 (wt.%) at Pinkos shown with respect to lithofacies. Plotted data are based on quantitative whole-rock geochemistry and contoured using inverse-distance weighting (IDW). a) High MnO corresponds to the interpreted main hydrothermal upflow in stringers and stockwork and in fragmental rhyolite. This coincides with both CaO and CO_2 patterns (cf. 7.4a and 7.1b) and suggests substitution of Mn^{2+} in carbonate. b) High SiO_2 occurs in a broad zone towards the interpreted margins of the system and effectively envelops the outline of Fe-rich carbonate (± chlorite) alteration, which supports the mapped

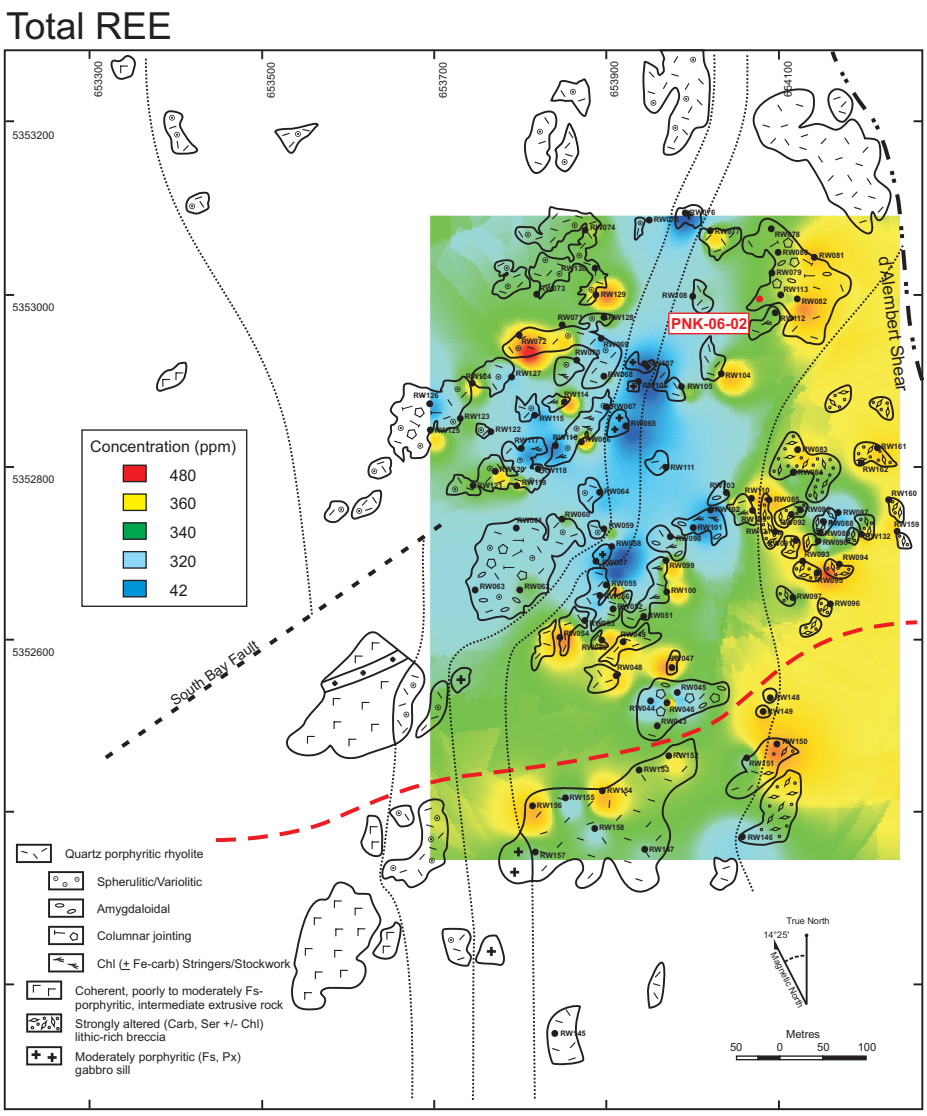

Figure 7.8. Total REE concentrations (ppm) at Pinkos shown with respect to lithofacies. Plotted data are based on quantitative whole-rock geochemistry and contoured using inverse-distance weighting (IDW). REE are most abundant in proximal columnar-jointed and overlying fragmental rhyolite. Apparent depletion in zones of intense silicification likely reflects dilution by the addition of silica.

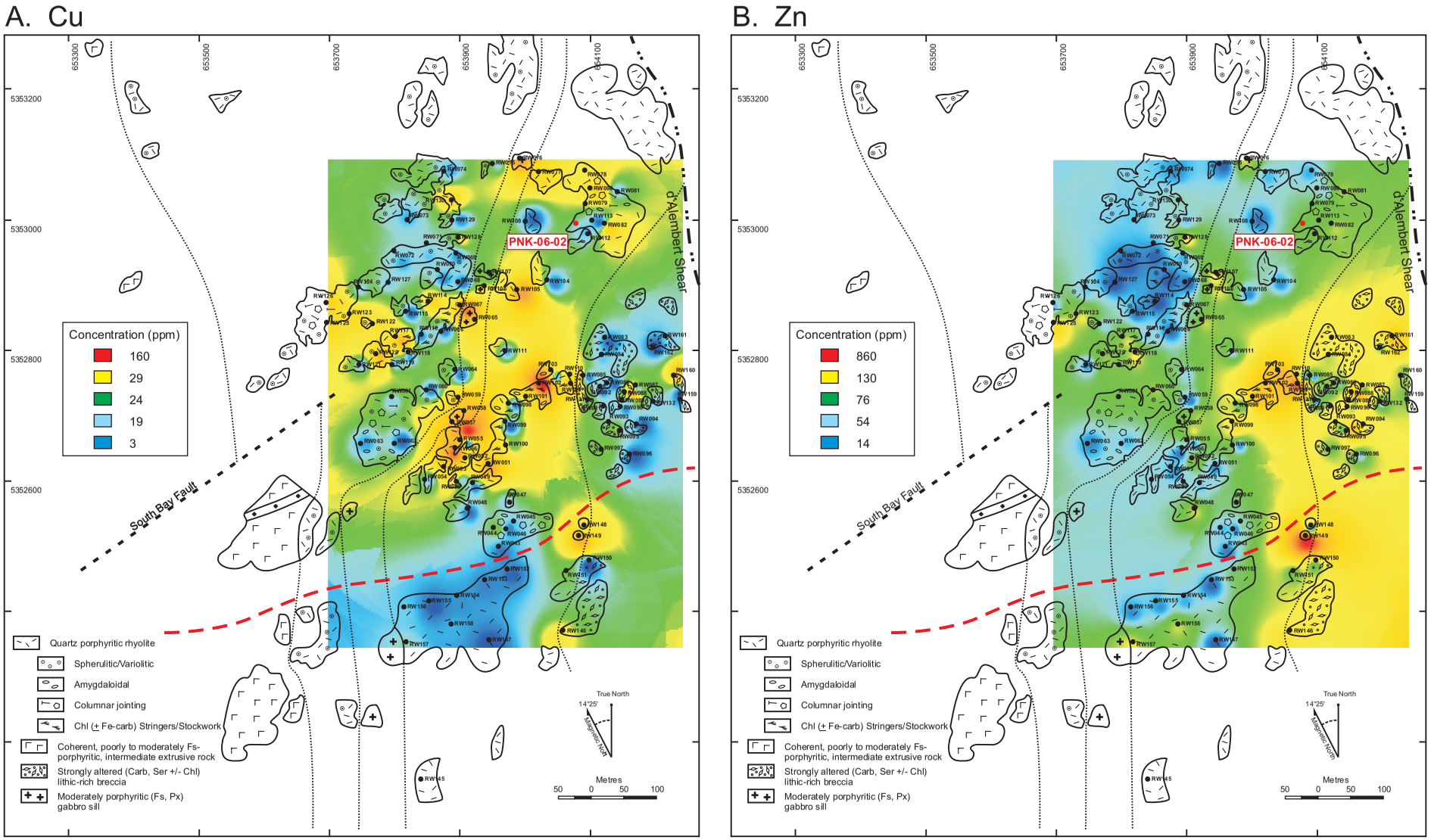

Figure 7.9. Concentrations of Cu and Zn (ppm) at Pinkos shown with respect to lithofacies. Plotted data are based on quantitative whole-rock geochemistry and contoured using inverse-distance weighting (IDW). a) The highest Cu concentrations are located in fractured and stringer rhyolite facies immediately above the inferred termination of the South Bay fault and to a lesser extent within overlying fragmental rhyolite. b) The most abundant Zn occurs stratigraphically above Cu in fragmental rhyolite with lower concentrations in underlying stringer facies.

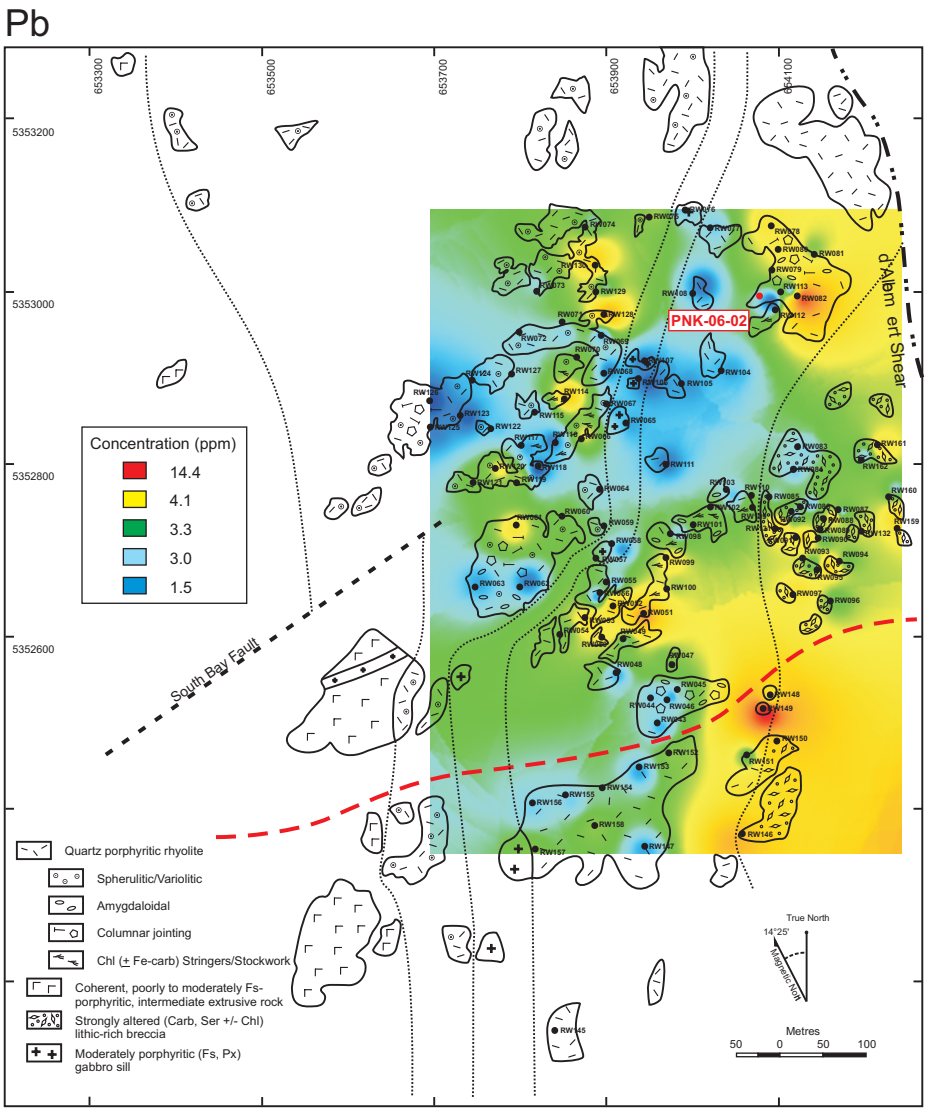

Figure 7.10. Pb concentrations (ppm) at Pinkos shown with respect to lithofacies. Plotted values are based on quantitative whole-rock geochemical data and contoured using inverse-distance weighting (IDW). Pb clearly follows the same distribution pattern as Zn (cf. Figure 7.9b) with the highest concentrations corresponding to fragmental rhyolite and underlying columnar-jointed and stringer rhyolite facies.

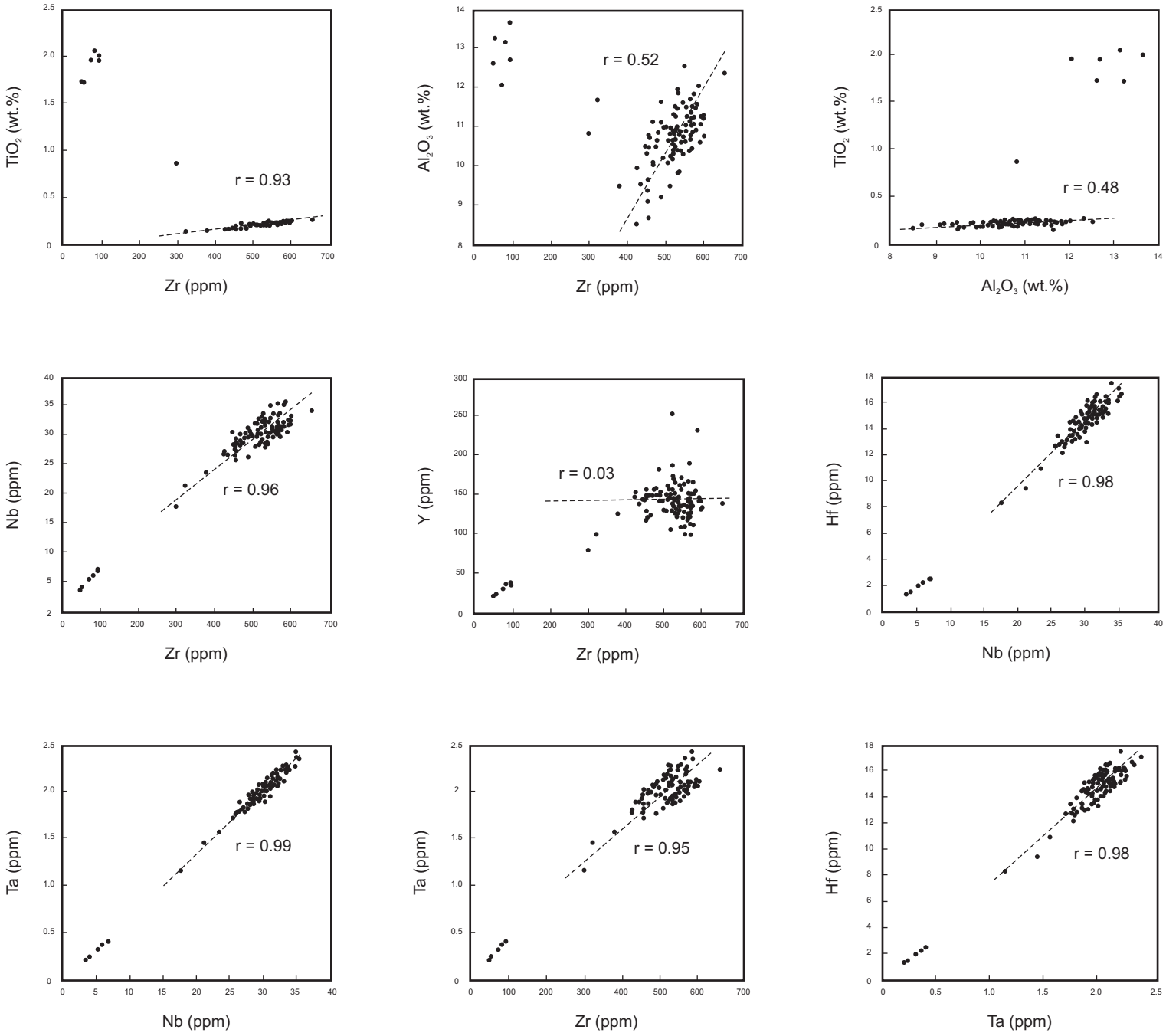

Figure 7.11. Representative x-y bivariate plots of potentially immobile elements in the Cyprus rhyolite at Delbridge. Zr is selected as the immobile monitor for mass balance calculations because it is highly correlated ($r > 0.85$) with other components. Zr abundance is also much greater than other immobile elements, which reduces the impact of analytical errors in subsequent calculations.

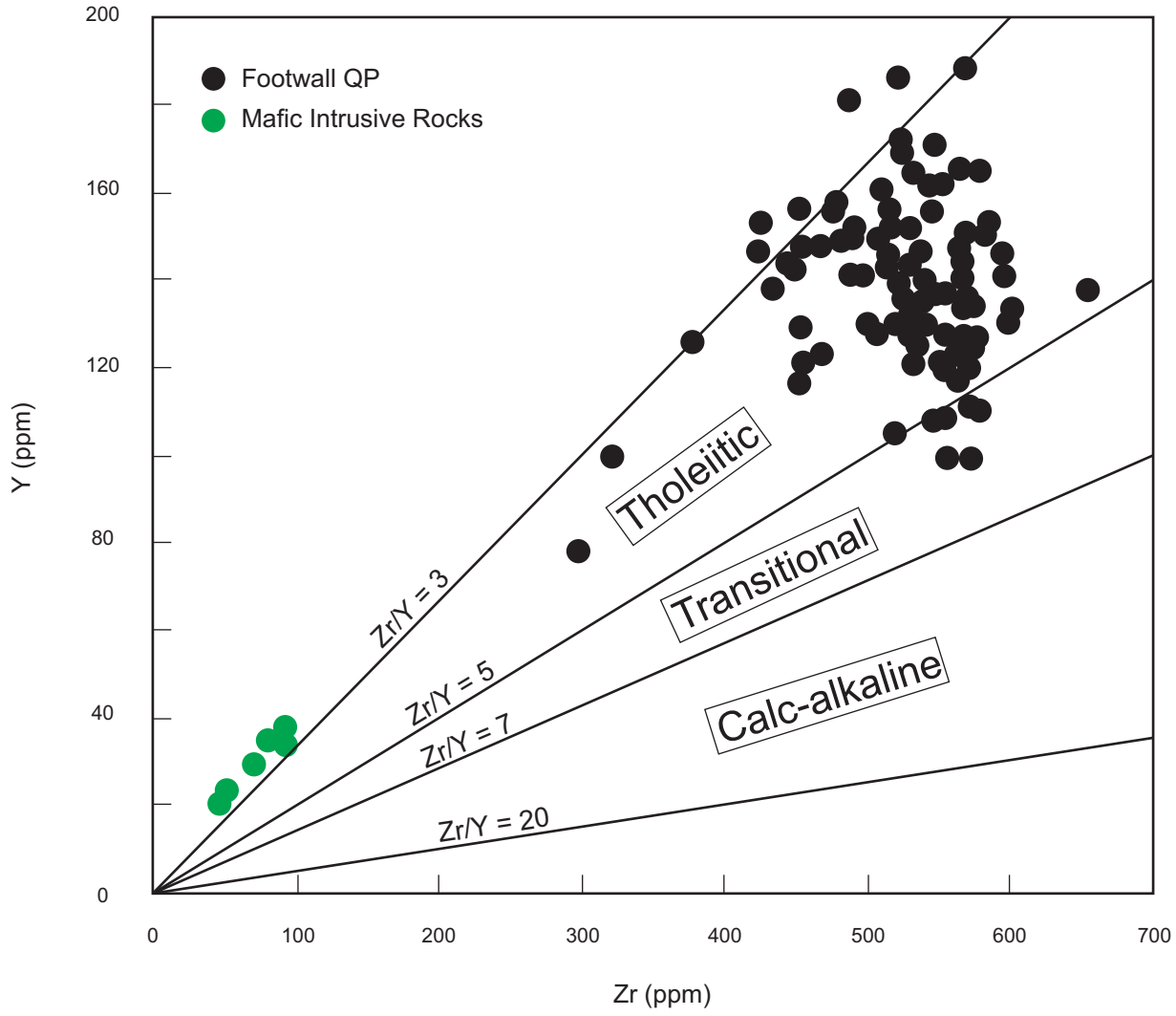

Figure 7.12. Plot of all TiO2-Zr data from Pinkos, indicating that the volcanic rocks have magmatic affinities ranging from dominantly tholeiitic to transitional.

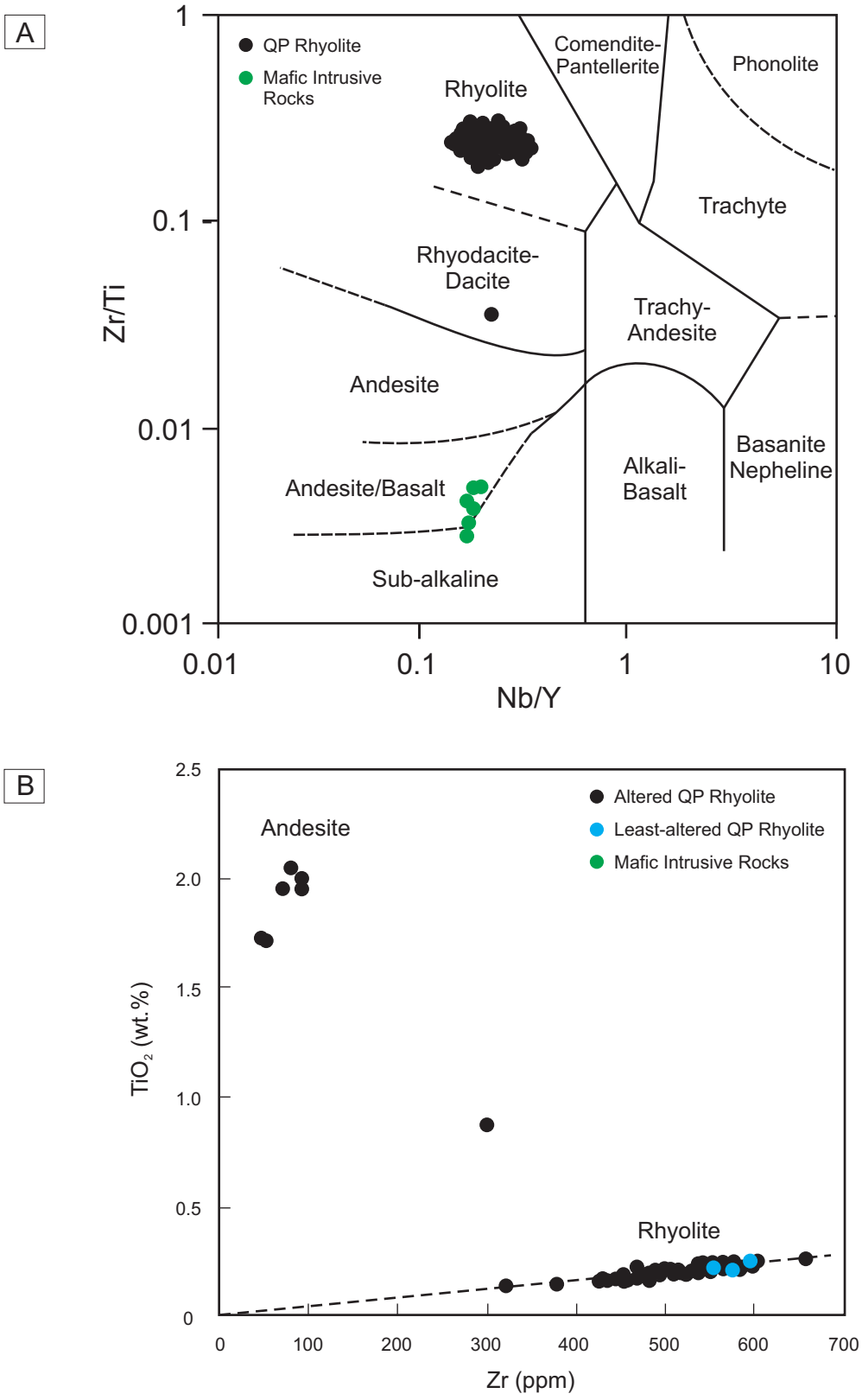

Figure 7.13. a) Zr/Ti vs. Nb/Y immobile element ratios indicate that all felsic samples are of rhyolitic composition, except for one rhyodacite to dacite sample collected in the basal stratigraphy (after Winchester and Floyd, 1977). The six samples that plot in the andesitic range were collected from the mafic dike. b) Plot of all TiO_2-Zr data, divided into altered and least-altered samples. Note only one alteration line extends from the origin, indicating a single magmatic source for all felsic samples (except one outlier) at Pinkos. The cluster of six outliers in the andesitic range represent the moderately porphyritic mafic intrusive (diorite) unit. The single, isolated outlier is the same rhyodacite to dacite sample shown in (a). A single fractionation curve has not been estimated due to an insufficient number of samples. Black dots = altered samples; blue = least-altered samples.

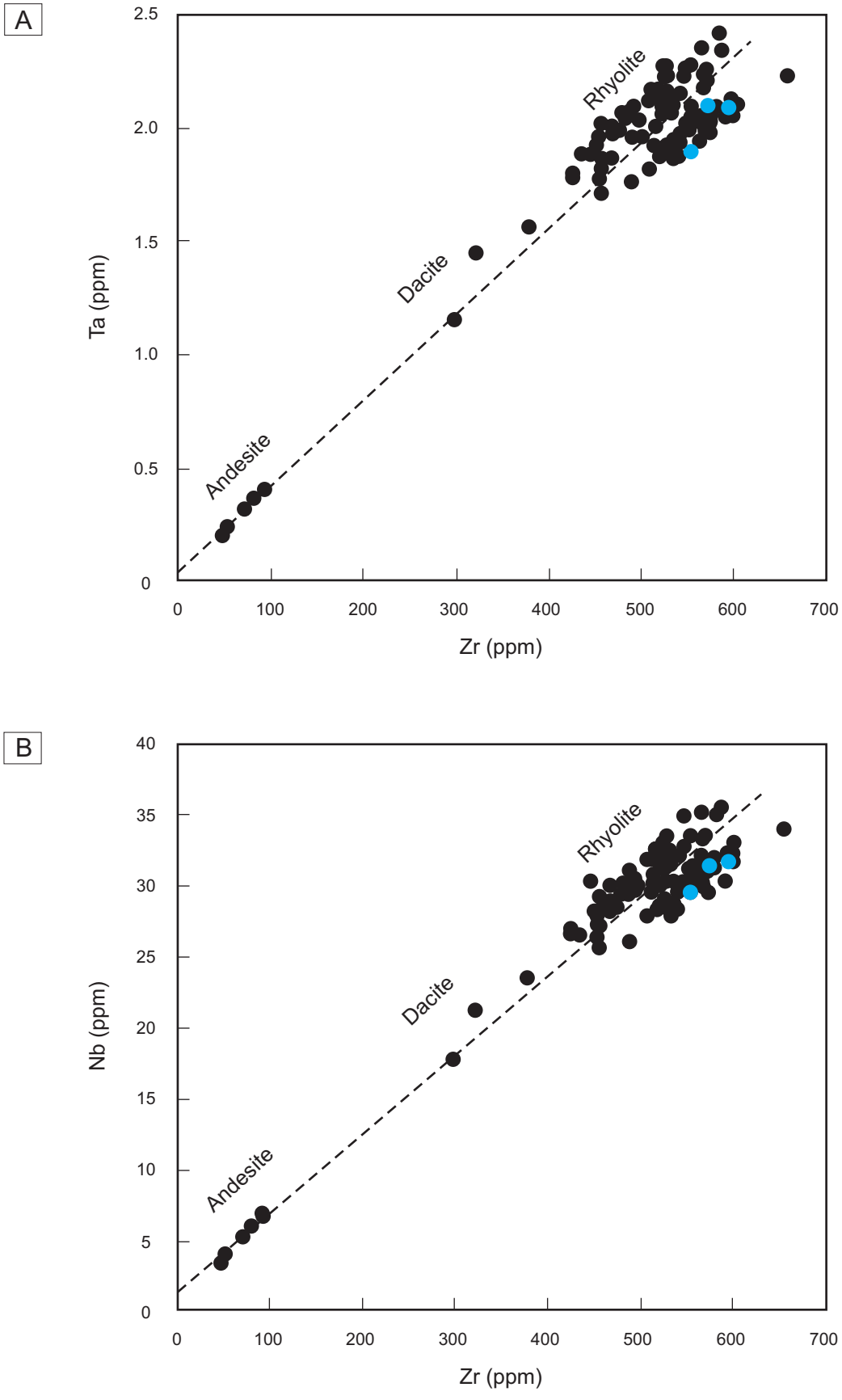

Figure 7.14. a) Plot of Ta versus Zr, indicating that the Pinkos volcanic rocks consistently display only one magmatic type. b) Plot of Nb versus Zr, again showing the presence of only one magmatic source. For both plots, black dots = altered samples; blue = least-altered samples.

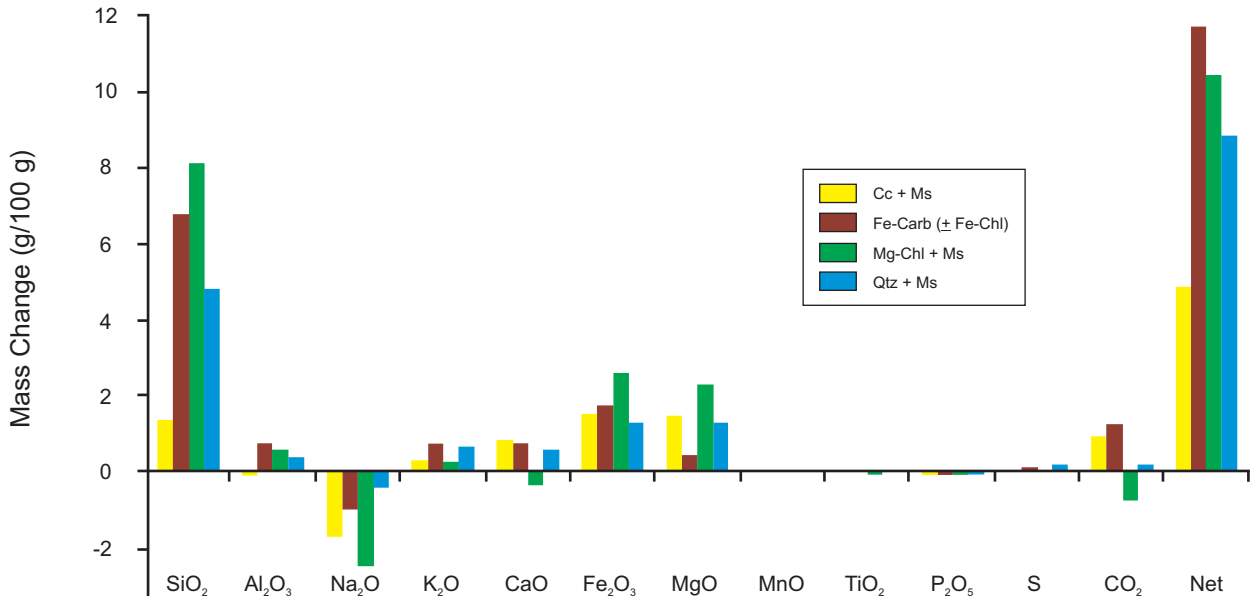

Figure 7.15. Bar graph of major component mass changes in the Pinkos footwall. Major net gains in the system are evidently the result of major additions of silica. Other important enrichments include CaO, K_2O, Fe_2O_3, MgO, and CO_2, likely caused by carbonate, chlorite, and sericite alteration. Note that losses of Na_2O are inverse to gains of K_2O, indicating typical K-metasomatism related to VMS alteration systems.

A

Pearson correlation matrix of potentially immobile elements in the Cyprus rhyolite at Pinkos

Element	La	Ce	Pr	Nd	Sm	Eu	Gd	Tb	Dy	Ho	Er	Tm	Yb	Lu
La	1													
Ce	0.981	1												
Pr	0.990	0.986	1											
Nd	0.986	0.981	0.998	1										
Sm	0.956	0.960	0.973	0.982	1									
Eu	0.656	0.691	0.658	0.665	0.695	1								
Gd	0.781	0.771	0.783	0.802	0.879	0.589	1							
Tb	0.488	0.477	0.485	0.506	0.613	0.373	0.903	1						
Dy	0.293	0.277	0.284	0.302	0.408	0.207	0.768	0.961	1					
Ho	0.174	0.154	0.161	0.175	0.270	0.080	0.651	0.893	0.978	1				
Er	0.137	0.114	0.123	0.134	0.217	0.009	0.586	0.839	0.941	0.986	1			
Tm	0.134	0.113	0.121	0.130	0.206	-0.011	0.554	0.804	0.908	0.962	0.991	1		
Yb	0.143	0.124	0.131	0.138	0.207	-0.003	0.530	0.767	0.868	0.926	0.968	0.991	1	
Lu	0.154	0.134	0.141	0.146	0.206	-0.004	0.506	0.725	0.826	0.890	0.940	0.972	0.992	1

All values are different from 0 with a significance level alpha=0.05.

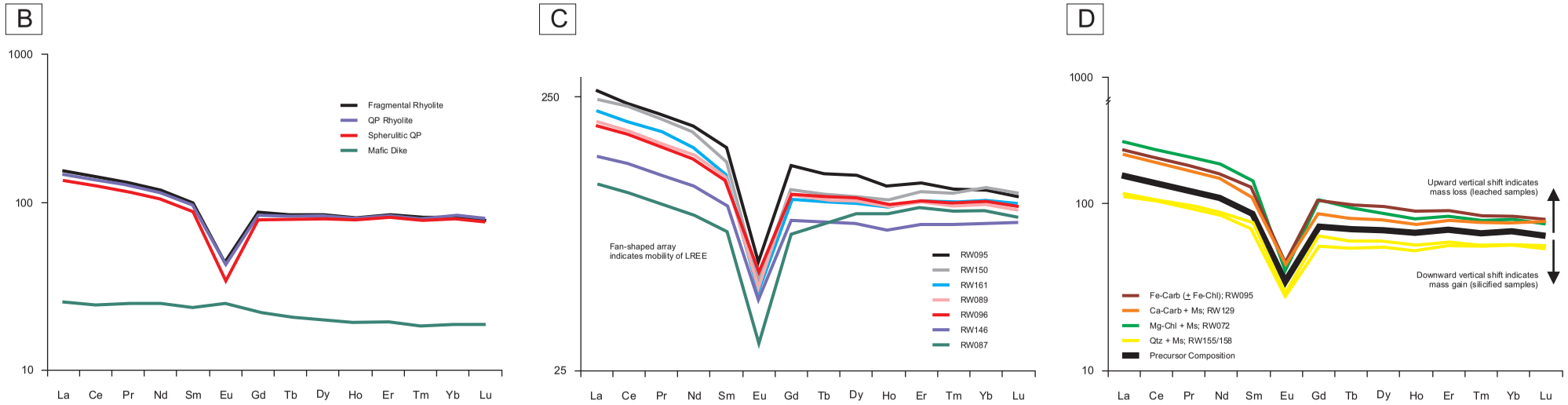

Figure 7.16. a) Pearson correlation matrix of rare-earth elements (REE) in the Pinkos volcanic rocks. Heavy REE show much stronger correlation than do light REE indicating that they behaved coherently during alteration. b) Representative REE profiles for all footwall rhyolite facies (negative Eu anomalies) and mafic extrusive volcanic samples (slightly positive Eu anomaly). c) Fan-shaped array of REE profiles for proximal altered samples indicates partial mobility of LREE, which is common immediately beneath VMS mineralization. d) Sub-parallel REE profiles are vertically displaced both upward (net mass loss) and downward (net mass gain) from an average least-altered precursor composition, depending on alteration type.

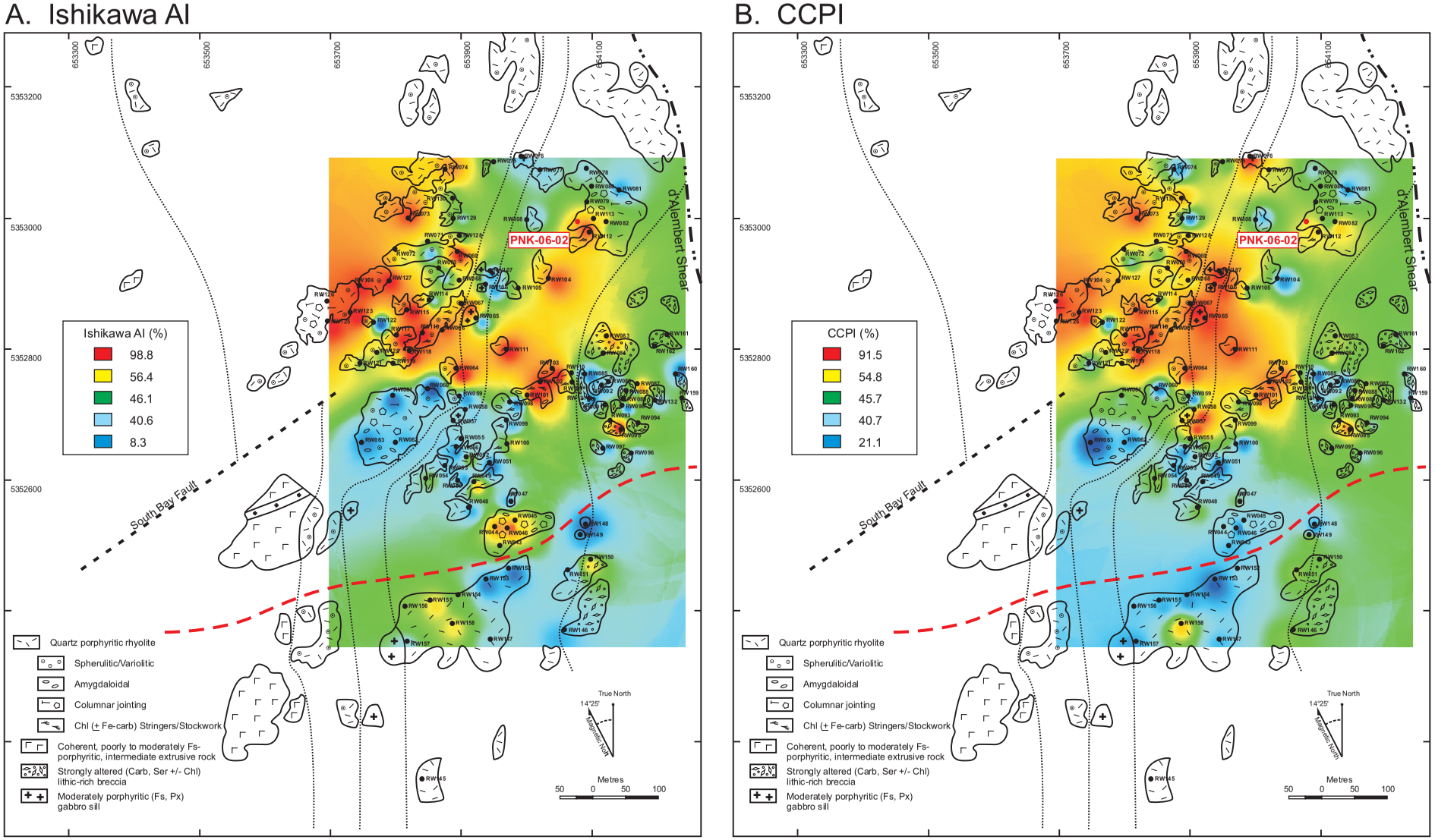

Figure 7.17. Alteration indices at Pinkos are estimated from whole-rock geochemical data and contoured using inverse-distance weighting (IDW). a) The highest Ishikawa AI values (>90) clearly occur in the two offset stockwork zones containing stringer chlorite and Fe-carbonate alteration within the interpreted hydrothermal upflow. b) Consistent with the Ishikawa AI, high CCPI values occur mainly within the offset zones of fracture-controlled alteration. These trends support host-rock permeability as the dominant control on fluid flow at Pinkos. Both AI and CCPI correlate with K_2O, reflecting the Na depletion and K-metasomatism common to VMS alteration systems.

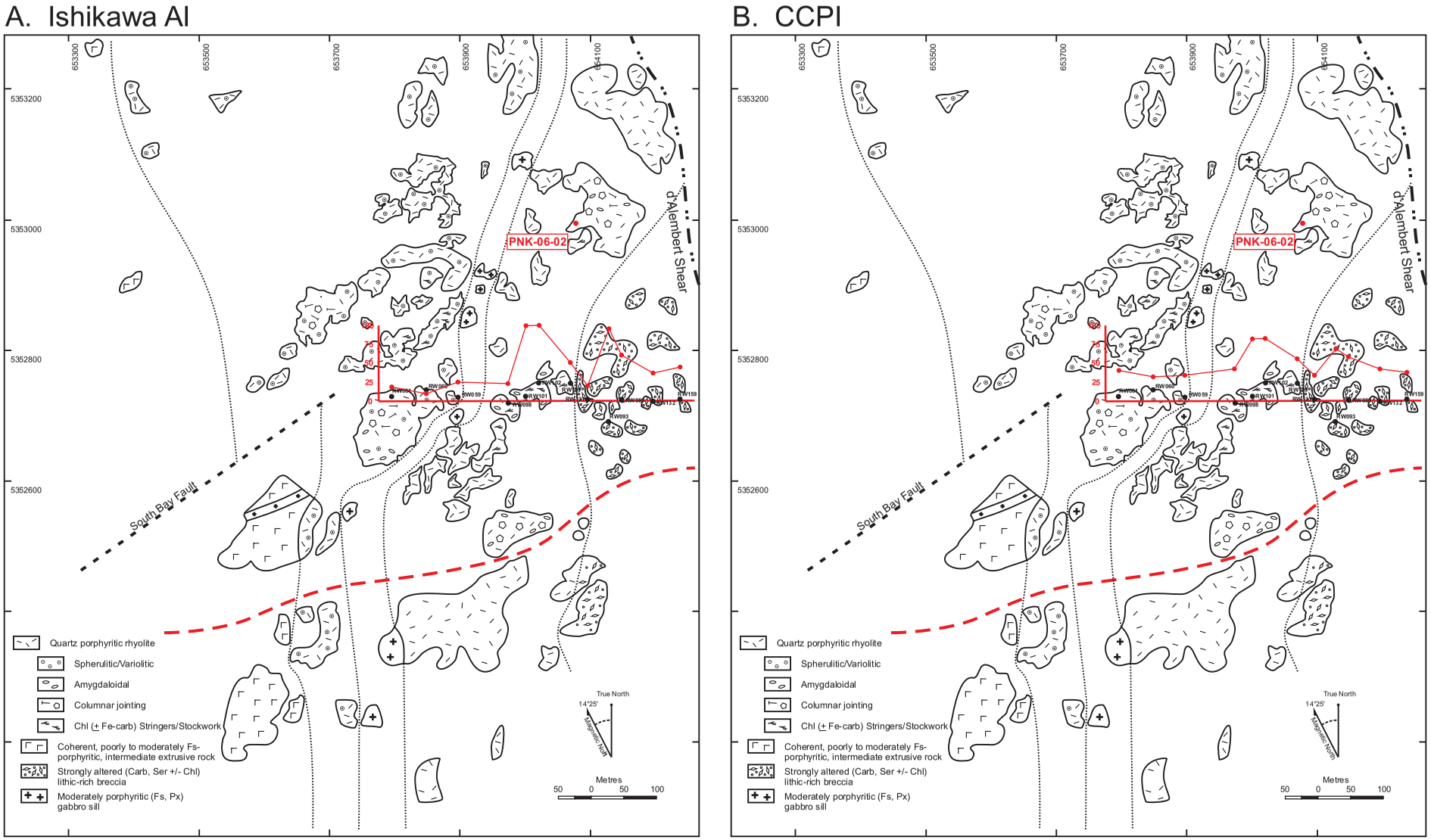

Figure 7.18. Ishikawa alteration indices (AI) and chlorite-carbonate-pyrite indices (CCPI) plotted on a traverse through the stratigraphic footwall at Pinkos. Plotted values are shown in Table 7.7. a) The highest AI values (~95-99%) clearly occur in stringers and stockwork and overlying fragmental rhyolite. Coupled with low indices (~10-20%) in basal and distal coherent rhyolite, this confirms the dominant control of host-rock permeability on alteration and mineralization. b) The same trend shown in (a) is evident for CCPI.

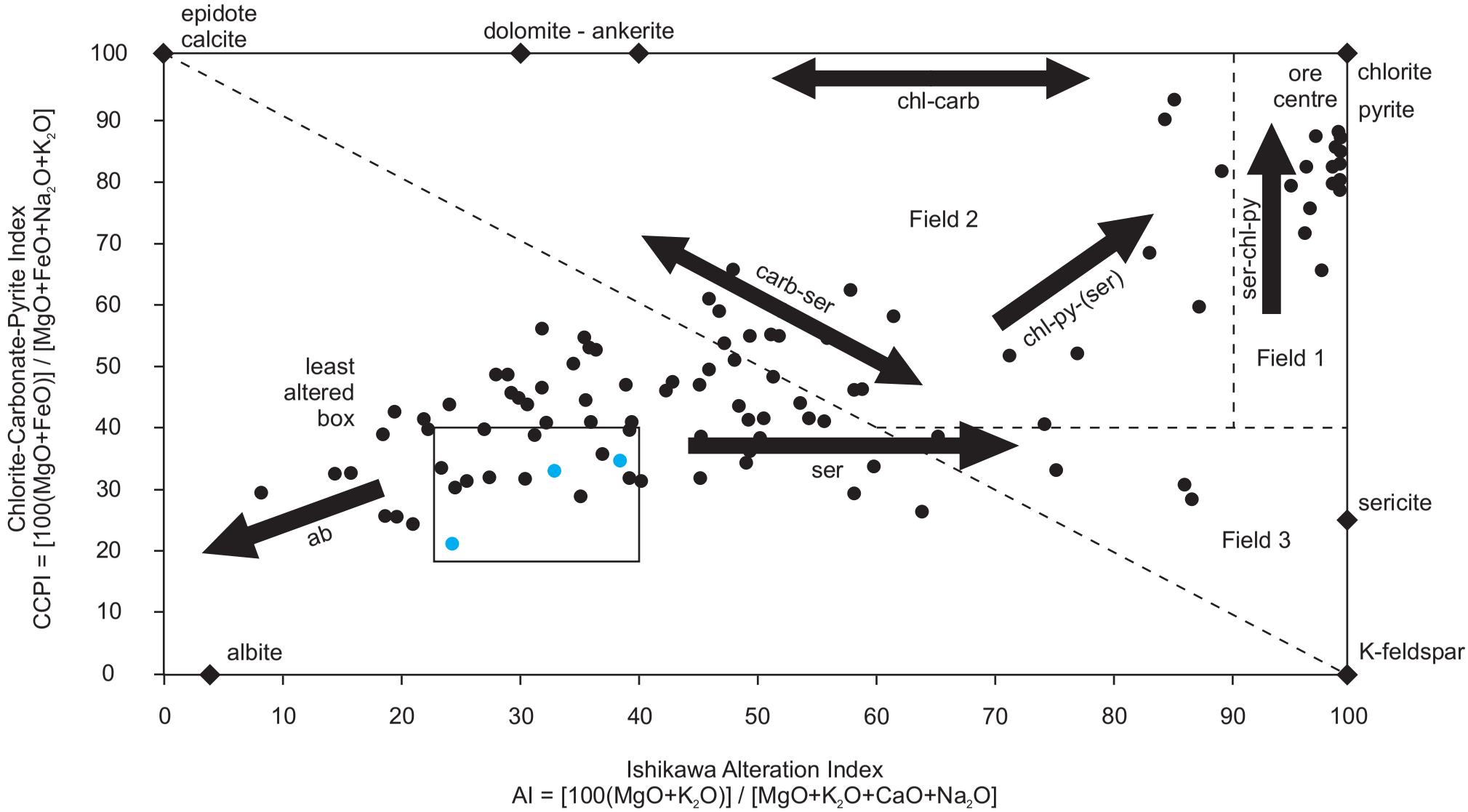

Figure 7.19. Alteration box plot for VMS-style alteration and mineralization at Pinkos. Plotted indices (AI and CCPI) are derived from whole-rock geochemical data and divided into least-altered and hydrothermal alteration fields. Variably altered samples are subdivided into three distinct hydrothermal fields and one diagenetic trend. Field 1 indicates intense sericite-chlorite-pyrite alteration of samples collected in zones of fracture-controlled and stringer-style alteration in the interpreted hydrothermal upflow. Field 2 contains variably carbonatized and chloritized (+ sericitized) samples. These samples were collected either in stringer-style altered coherent rhyolite or in proximal fragmental rhyolite. Fragmental rhyolite samples appear dominated by abundant carbonate and sericite alteration. Samples that fall within Field 3 are weakly sericitized and occur along the margins of the interpreted hydrothermal system (north and south of stringer alteration) and in distal fragmental rhyolite. The few samples that plot along the diagenetic trend indicate albite and chlorite alteration typical of seawater interaction at low temperatures. These samples were collected fairly deep in the footwall, which may reflect strong drawdown of seawater in a shallow environment. Black symbols = variably altered samples and; blue = least-altered footwall QP rhyolite compositions.

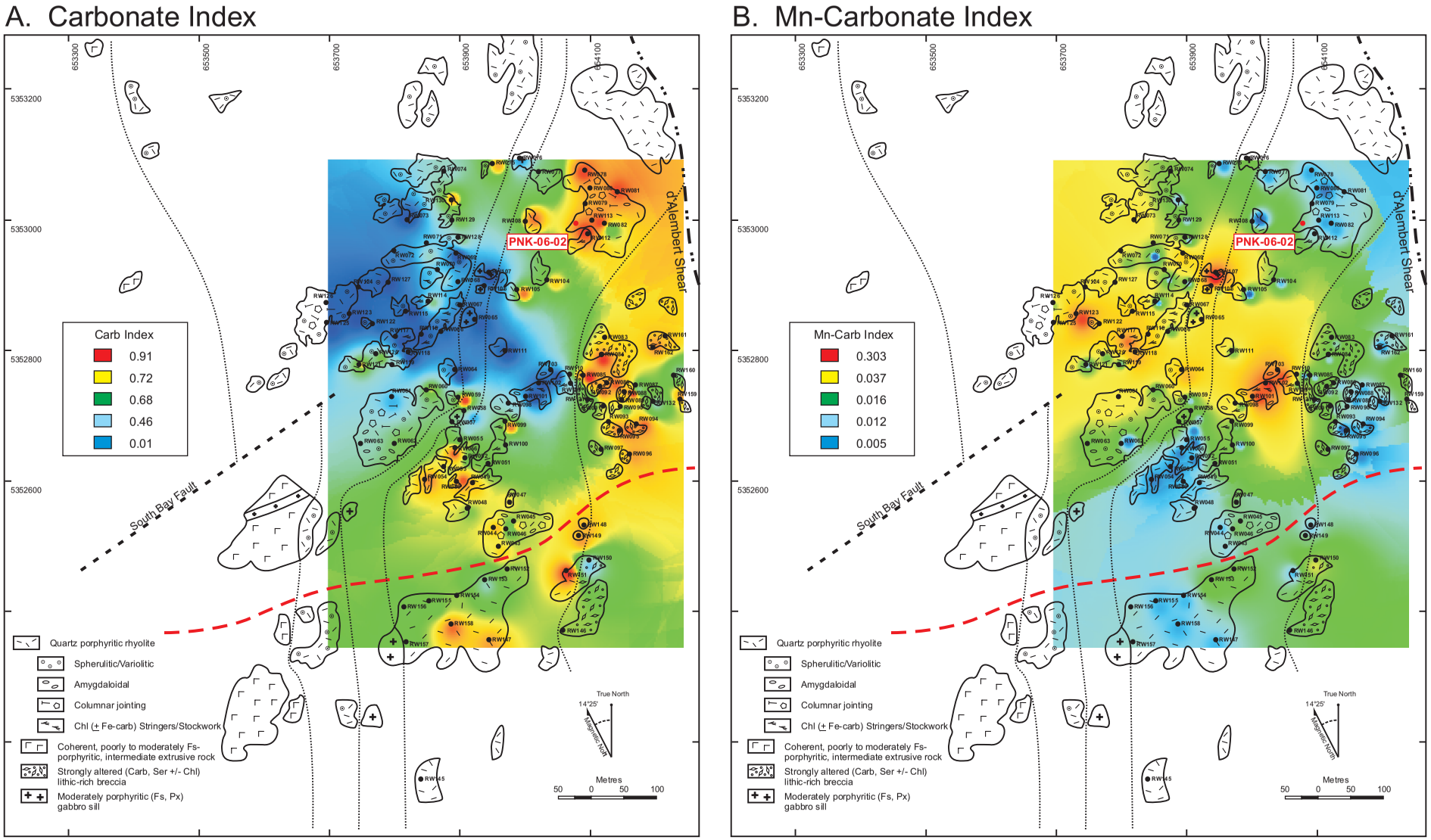

Figure 7.20. Intensity of carbonate alteration and associated Mn-substitution at Pinkos. Alteration indices are calculated from quantitative whole-rock geochemical data and contoured using inverse-distance weighting (IDW). a) Normalized carbonate indices (Carb Index = CO_2/CaO+FeO+MgO, molar proportions) indicate that the intensity of carbonate alteration is highest (up to 0.92 molar units) in fragmental rhyolite at the top of the succession and in underlying columnar-jointed rhyolite. Carbonate intensity is clearly lowest in stringers and stockwork within the interpreted hydrothermal upflow. This supports earlier observations from the variation of total CO_2 concentrations. b) Conversely, weak Mn-rich carbonate (Mn-Carb Index = MnO/CO_2, molar proportions) occurs mainly in the two offset stockwork zones, reflecting strong negative correlation relative to estimated carbonate intensity. The molar proportions of Mn-carbonate may represent the distribution of hydrothermal carbonate at Pinkos, with marginal and overlying carbonate possibly resulting from a different source.

Figure 7.21. Abundance, distribution, and compositional variation of normative sericite at Pinkos calculated using the MINSQ method (Herrmann and Berry, 2002). The highest normative white mica abundances (~20 to >35 wt.%) clearly occur along the interpreted margins of hydrothermal upflow and in fragmental rhyolite. Paragonite ($NaAl_2(Si_3Al)O_{10}(OH)_2$) is the dominant white mica with lesser muscovite ($KAl_2(AlSi_3O_{10})(OH)_2$) and trace phengite ($K(AlMg)_2(OH)_2(SiAl)_4O_{10}$) also present. Paragonite appears highly widespread at Pinkos as it is estimated in nearly every sample. Though compositional variation is less evident than at Delbridge, muscovite is more abundant in altered stockwork and fragmental rhyolite. Since depletion of Na and addition of K (metasomatism) are typically most intense in the higher temperature core of hydrothermal upflow (e.g., Delbridge), muscovite distribution effectively maps the interpreted focus of fluid flow at Pinkos. Weakly abundant phengite is evidently concentrated towards the margins of the system and in uppermost fragmental rhyolite where fluid temperatures were presumably lower due to mixing with seawater. This supports increased MgO content in these zones and reflects substitution of Mg^{2+} for Al^{3+} in potassic white micas. Compositional variation of white mica calculated in each sample is expressed as normalized percentages in pie chart format. Symbol size is a function of the total white mica estimated in a given sample and varies proportionally to the sum of all components (i.e., total white mica abundance). A symbol diameter of 1 cm represents a maximum total abundance of 38 wt.% white mica. All smaller pie charts are scaled down by square root because the area of a circle varies by the square root of its radius.

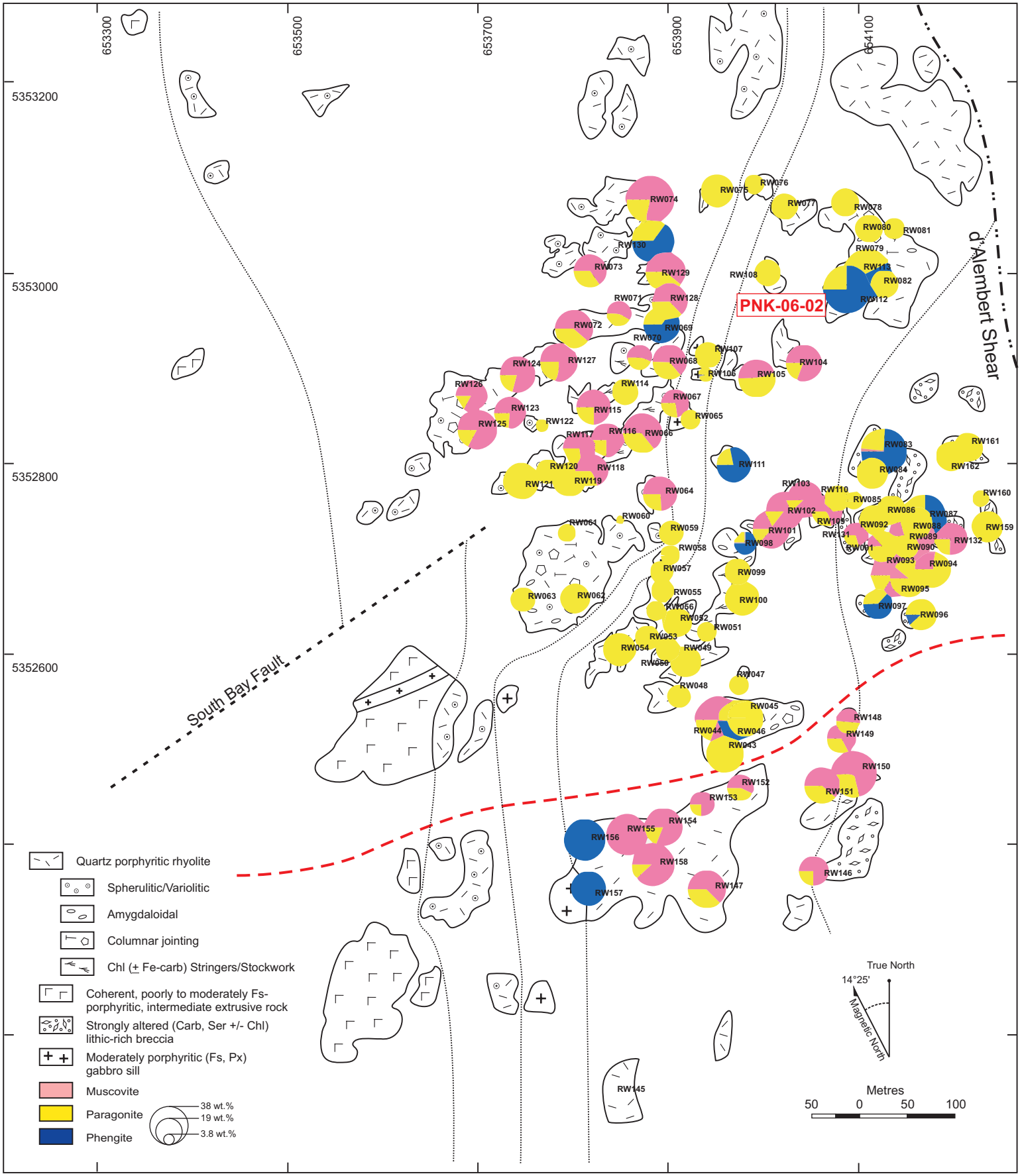
653300
653500
653700
653900
654100
5353200
5353000
5352800
5352600
d'Alembert Shear
South Bay Fault
PNK-06-02
RW074
RW075
RW076
RW077
RW078
RW080
RW081
RW130
RW079
RW073
RW129
RW113
RW082
RW108
RW112
RW071
RW128
RW072
RW069
RW070
RW107
RW068
RW104
RW124
RW127
RW106
RW105
RW126
RW114
RW067
RW123
RW115
RW065
RW125
RW122
RW117
RW116
RW066
RW083
RW161
RW084
RW162
RW111
RW120
RW118
RW121
RW119
RW064
RW103
RW110
RW085
RW160
RW102
RW086
RW087
RW061
RW060
RW109
RW092
RW088
RW159
RW059
RW101
RW131
RW089
RW132
RW058
RW098
RW091
RW090
RW057
RW093
RW094
RW099
RW055
RW063
RW062
RW100
RW095
RW056
RW097
RW096
RW052
RW051
RW053
RW054
RW049
RW050
RW047
RW048
RW045
RW148
RW044
RW046
RW149
RW043
RW150
RW152
RW151
RW153
RW154
RW155
RW156
RW158
RW146
RW157
RW147
RW145
Quartz porphyritic rhyolite
Spherulitic/Variolitic
Amygdaloidal
Columnar jointing
Chl (± Fe-carb) Stringers/Stockwork
Coherent, poorly to moderately Fs-porphyritic, intermediate extrusive rock
Strongly altered (Carb, Ser +/- Chl) lithic-rich breccia
Moderately porphyritic (Fs, Px) gabbro sill
Muscovite
Paragonite
Phengite
38 wt.%
19 wt.%
3.8 wt.%
True North
14°25'
Magnetic North
Metres
50
0
50
100

Figure 7.22. Abundance, distribution, and compositional variation of normative chlorite at Pinkos calculated using the MINSQ method (Herrmann and Berry, 2002). Abundant Fe-chlorite is fairly restricted at Pinkos with nil to trace quantities estimated in up to 60% of the samples. Major Fe-chlorite abundance (>5 wt.%) is only observed in roughly a dozen samples collected mainly from the 2 zones of stockwork alteration, interpreted as the focus of hydrothermal fluid flow. Significant Mg-chlorite occurs in ~20% of samples, the majority of which were collected in fractured rhyolite from the stringer zone to the northwest of the map area, immediately above the inferred termination of the South Bay fault. Minor Mg-rich chlorite is also mixed with Fe-rich species in the stockwork zone to the southeast. Of interest, significant chloritization is mainly observed in samples that clearly have low carbonate abundances. Compositional variation of chlorite calculated in each sample is expressed as normalized percentages in pie chart format. Symbol size is a function of the total chlorite estimated in a given sample and varies proportionally to the sum of all components (i.e., total chlorite abundance). A symbol diameter of 1 cm represents a maximum total abundance of 28 wt.% chlorite. All smaller pie charts are scaled down by square root because the area of a circle varies by the square root of its radius.

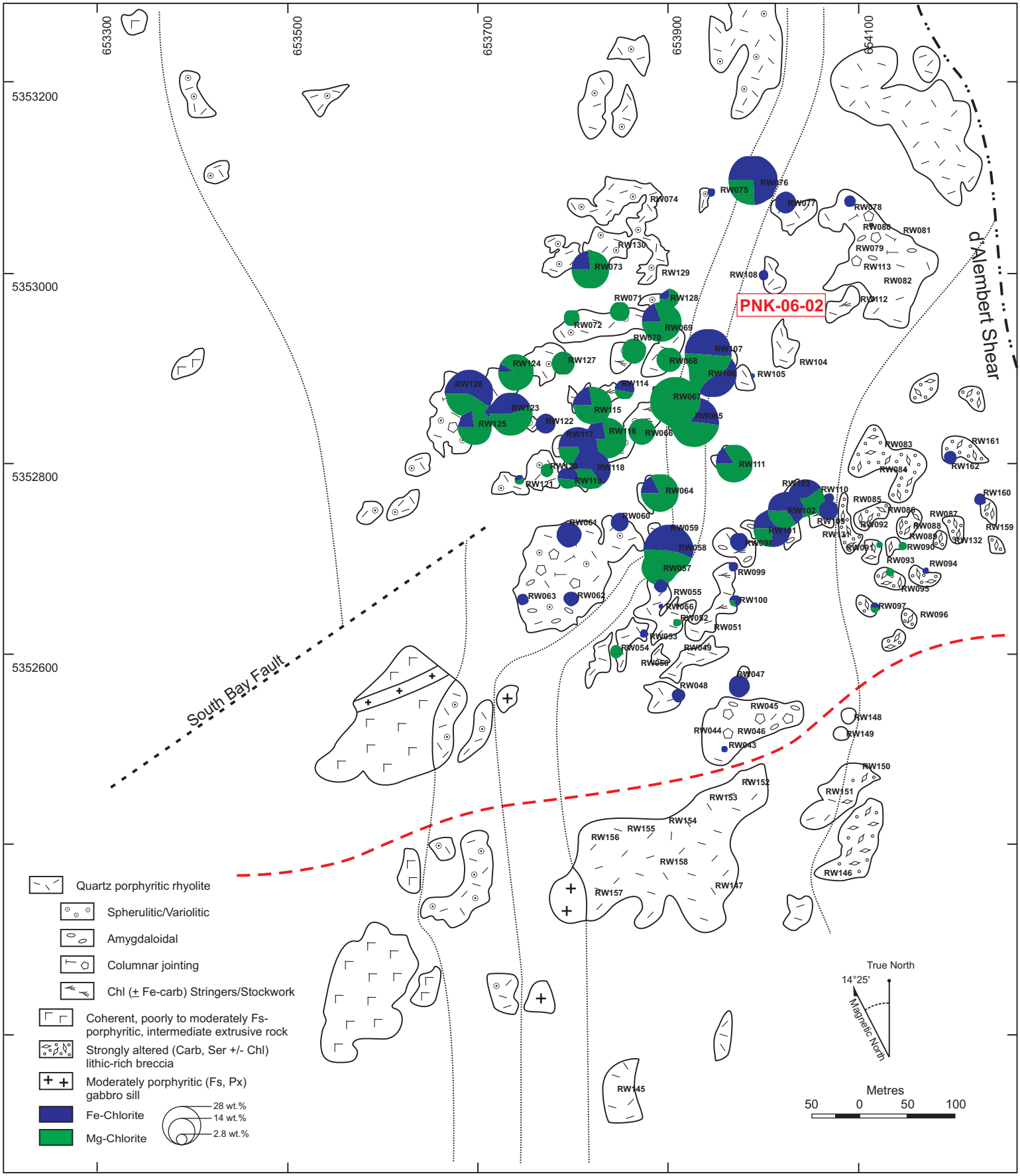

653300
653500
653700
653900
654100
5353200
5353000
5352800
5352600
PNK-06-02
d'Alembert Shear
South Bay Fault
Quartz porphyritic rhyolite
Spherulitic/Variolitic
Amygdaloidal
Columnar jointing
Chl (± Fe-carb) Stringers/Stockwork
Coherent, poorly to moderately Fs-porphyritic, intermediate extrusive rock
Strongly altered (Carb, Ser +/- Chl) lithic-rich breccia
Moderately porphyritic (Fs, Px) gabbro sill
Fe-Chlorite
Mg-Chlorite
28 wt.%
14 wt.%
2.8 wt.%
True North
14°25'
Magnetic North
Metres
50 0 50 100

Figure 7.23. Abundance, distribution, and compositional variation of normative carbonate at Pinkos calculated using the MINSQ method (Herrmann and Berry, 2002). Though background carbonate intensity is relatively strong at Pinkos (nearly 50% of the samples contain >5 wt.%), normative carbonate abundance is evidently highest in fragmental rhyolite at the top of the stratigraphy and to a lesser extent in underlying columnar-jointed and fractured rhyolite facies. Compositional variation of carbonate is dominated by Fe-rich species (~55% ankerite and ~25% siderite) with lesser Ca(-Mg)-rich species (~10% each of calcite and dolomite). Similar to Delbridge, ankerite is widespread and appears coupled with abundant paragonite precipitation. Normative siderite appears concentrated in fragmental rhyolite and underlying proximal fractured (± stockwork) facies. The distribution of more calcic carbonate (i.e., calcite and dolomite) is essentially restricted to the interpreted margins of the system and fragmental rhyolite. This supports the interpreted zonation from higher temperature Fe-rich species in the core of the system to lower temperature Ca- and Mg-rich members distally. Compositional variation of carbonate calculated in each sample is expressed as normalized percentages in pie chart format. Symbol size is a function of the total carbonate estimated in a given sample and varies proportionally to the sum of all components (i.e., total carbonate abundance). A symbol diameter of 1 cm represents a maximum total abundance of 26 wt.% carbonate. All smaller pie charts are scaled down by square root because the area of a circle varies by the square root of its radius.

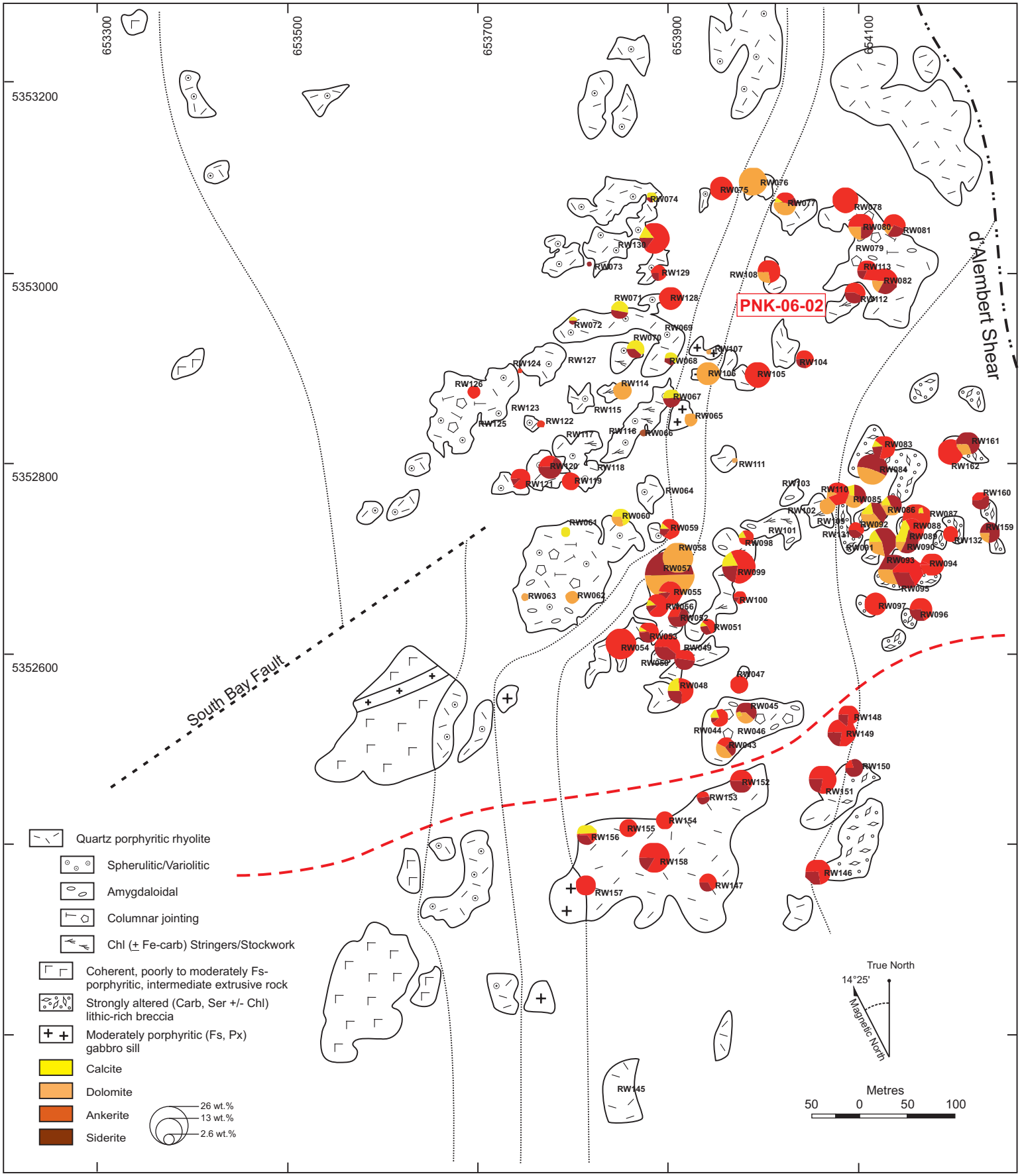
653300
653500
653700
653900
654100
5353200
5353000
5352800
5352600
PNK-06-02
d'Alembert Shear
South Bay Fault
Quartz porphyritic rhyolite
Spherulitic/Variolitic
Amygdaloidal
Columnar jointing
Chl (± Fe-carb) Stringers/Stockwork
Coherent, poorly to moderately Fs-porphyritic, intermediate extrusive rock
Strongly altered (Carb, Ser +/- Chl) lithic-rich breccia
Moderately porphyritic (Fs, Px) gabbro sill
Calcite
Dolomite
Ankerite
Siderite
26 wt.%
13 wt.%
2.6 wt.%
True North
14°25'
Magnetic North
Metres
50 0 50 100

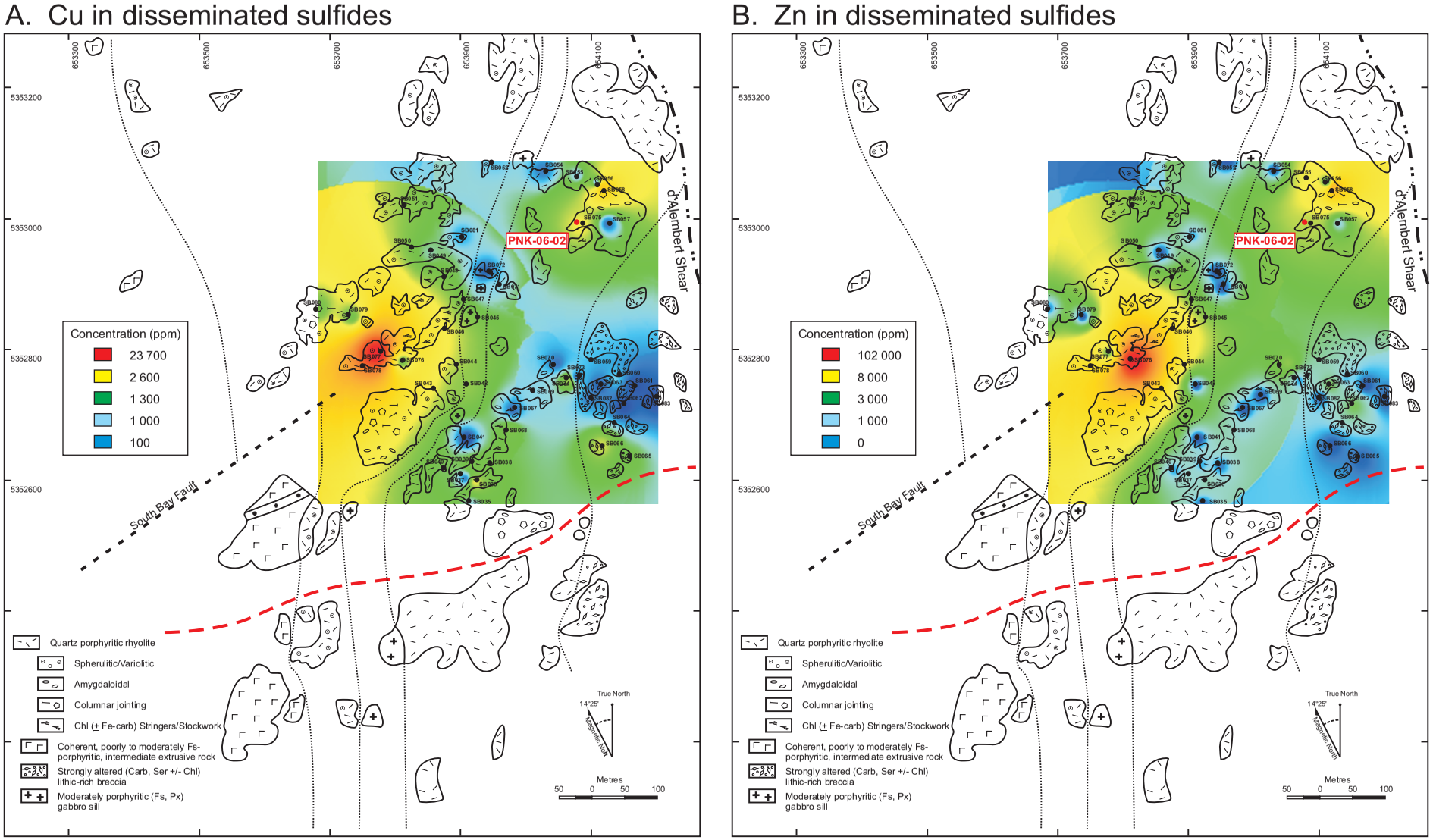

Figure 7.24. Concentrations (ppm) of Cu and Zn in disseminated and stringer sulfides at Pinkos. Plotted data are based on quantitative INAA, ICP-AES, and ICP-MS analyses and contoured using inverse-distance weighting (IDW). a) The highest Cu concentrations occur in stringers and stockwork above the inferred termination of the South Bay fault. b) High Zn clearly follows the same trend as Cu.

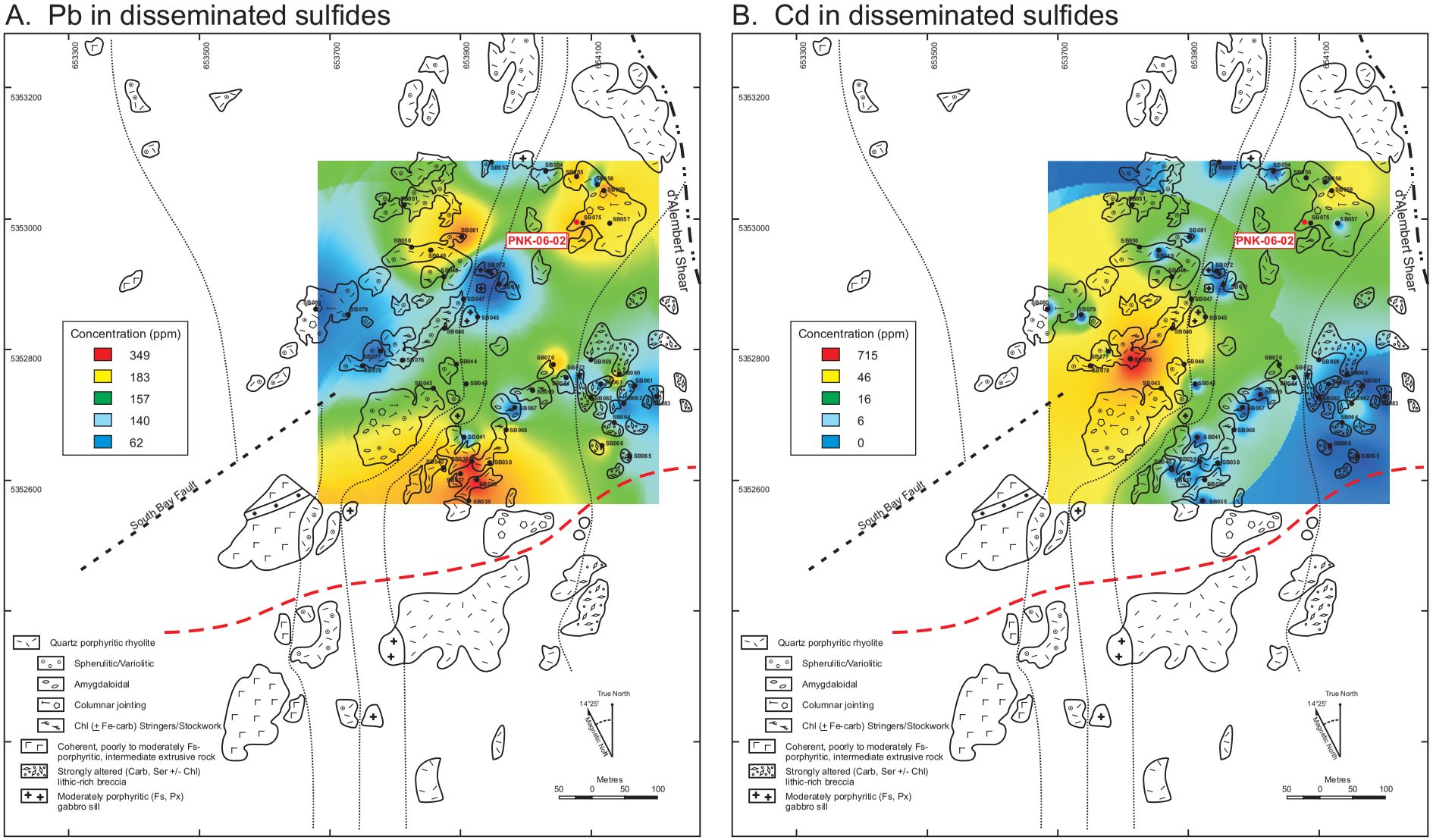

Figure 7.25. Concentrations (ppm) of Pb and Cd in disseminated and stringer sulfides at Pinkos. Plotted data are based on quantitative INAA, ICP-AES, and ICP-MS analyses and contoured using inverse-distance weighting (IDW). a) High Pb occurs in columnar-jointed and distal coherent rhyolite. b) The highest Cd concentrations clearly mimic the distribution of Zn in stringers and stockwork above the inferred termination of the South Bay fault.

A. Au in disseminated sulfides

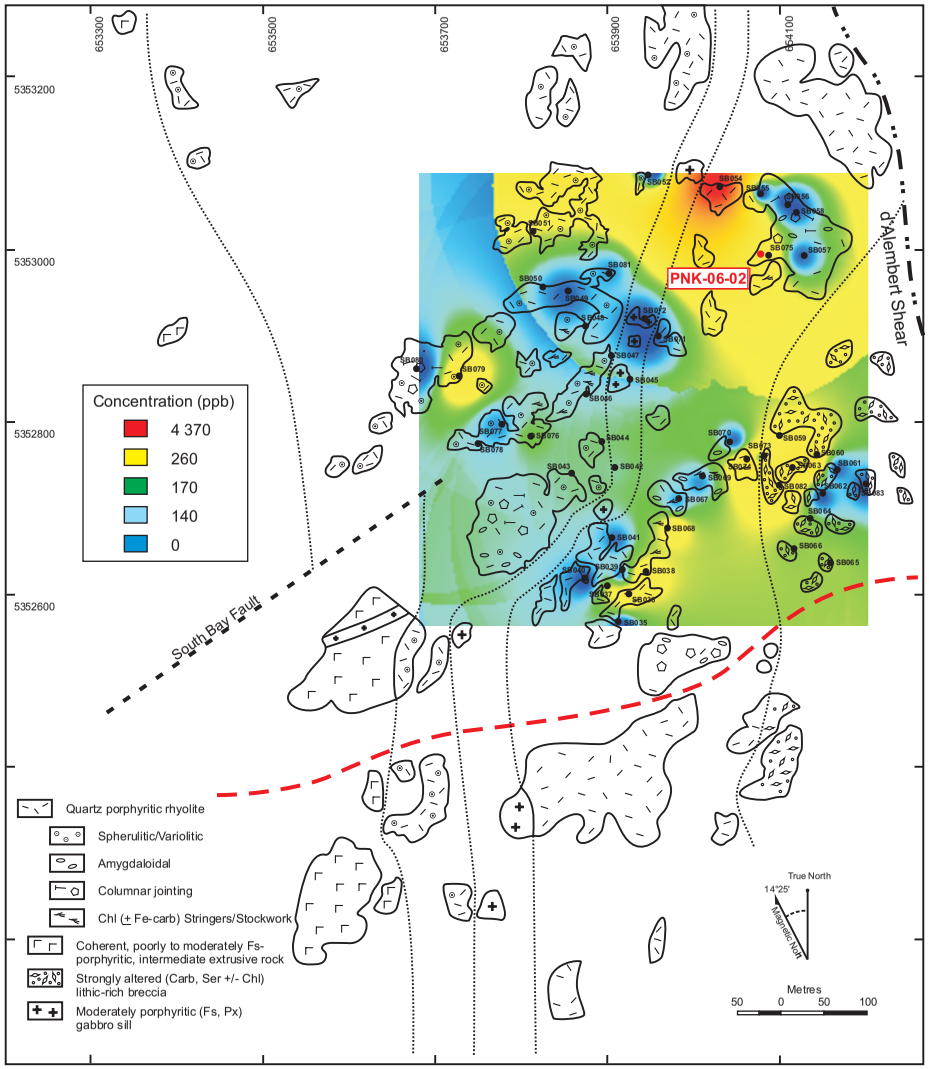

B. Ag in disseminated sulfides

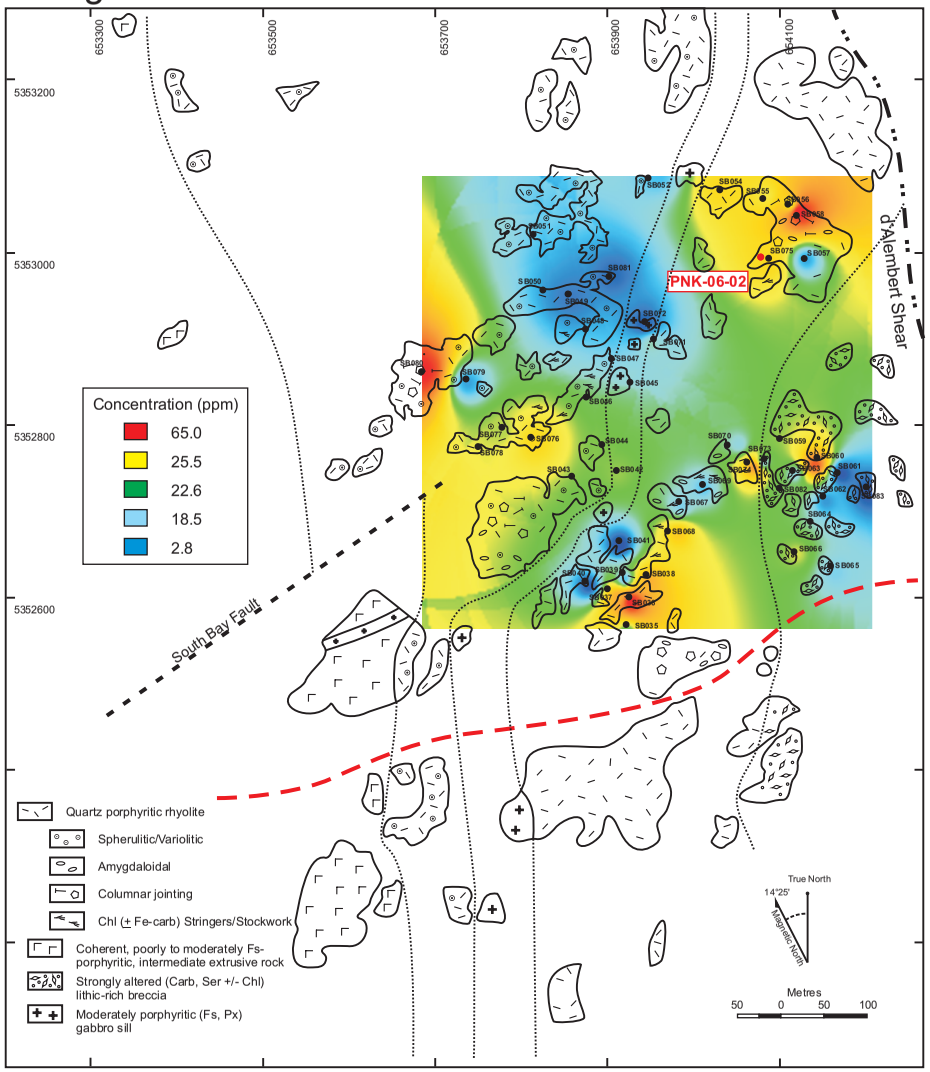

Figure 7.26. Concentrations of Au (ppb) and Ag (ppm) in disseminated and stringer sulfides at Pinkos. Plotted data are based on quantitative INAA, ICP-AES, and ICP-MS analyses and contoured using inverse-distance weighting (IDW). a) The highest Au concentrations occur in stringers and stockwork to the southeast and in fragmental and columnar-jointed rhyolite. b) High Ag clearly follows the same trend as Au.

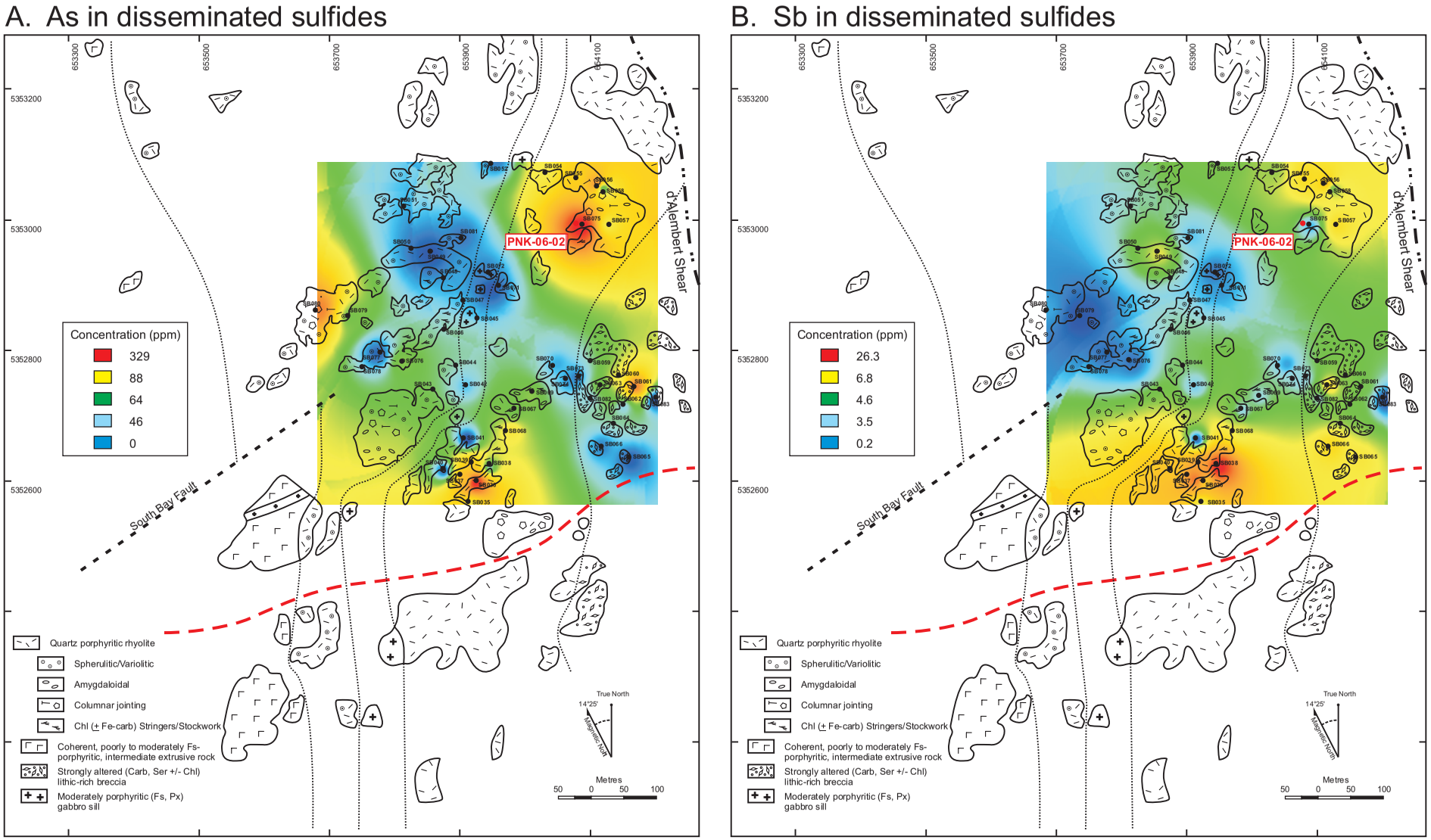

Figure 7.27. Concentrations (ppm) of As and Sb in disseminated sulfides at Pinkos. Plotted data are based on quantitative INAA, ICP-AES, and ICP-MS analyses and contoured using inverse-distance weighting (IDW). a) The most abundant As occurs in distal footwall coherent rhyolite and in fragmental rhyolite. b) Similar to As, the highest Sb values occur in distal footwall coherent (± fragmental).

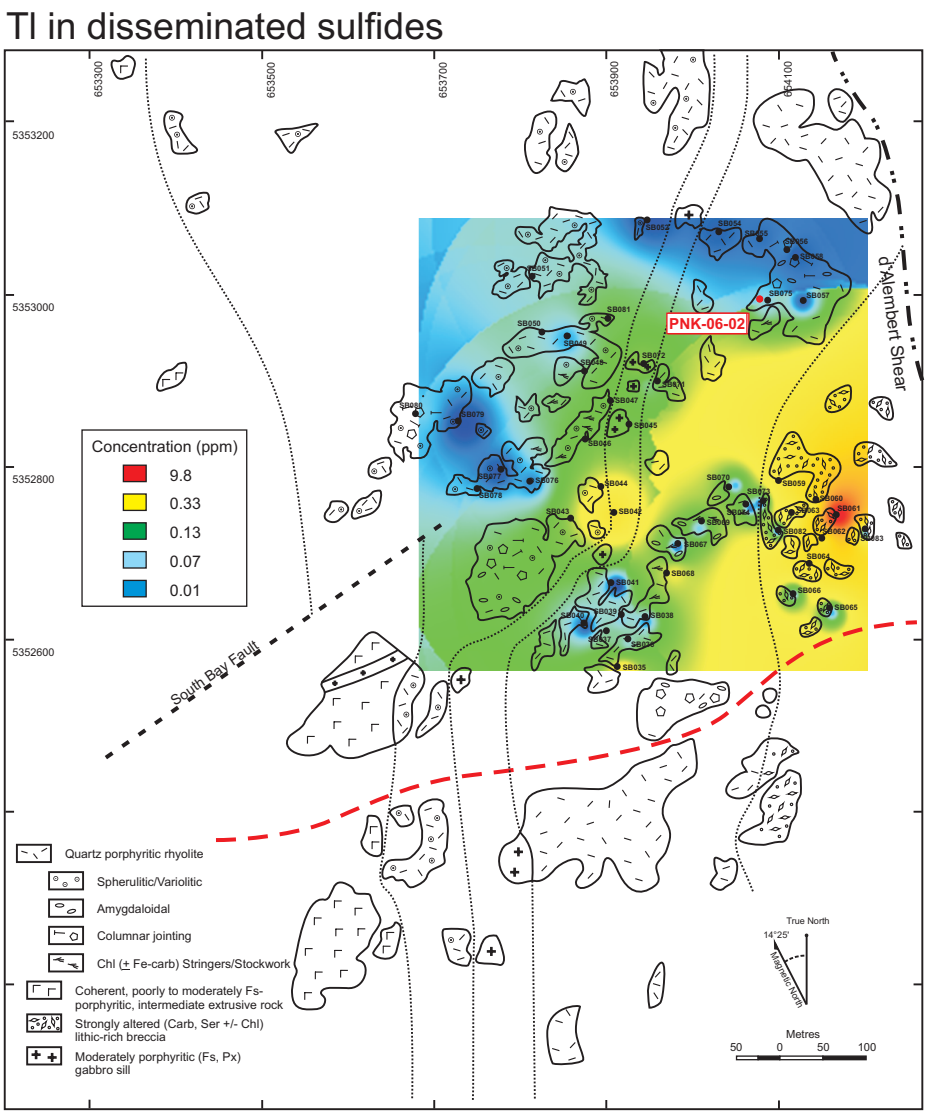

Figure 7.28. Tl concentrations (ppm) in disseminated sulfides at Pinkos. The highest Tl clearly occurs in fragmental rhyolite at the top of the succession. Plotted data are based on quantitative trace element analyses and contoured using inverse-distance weighting (IDW).

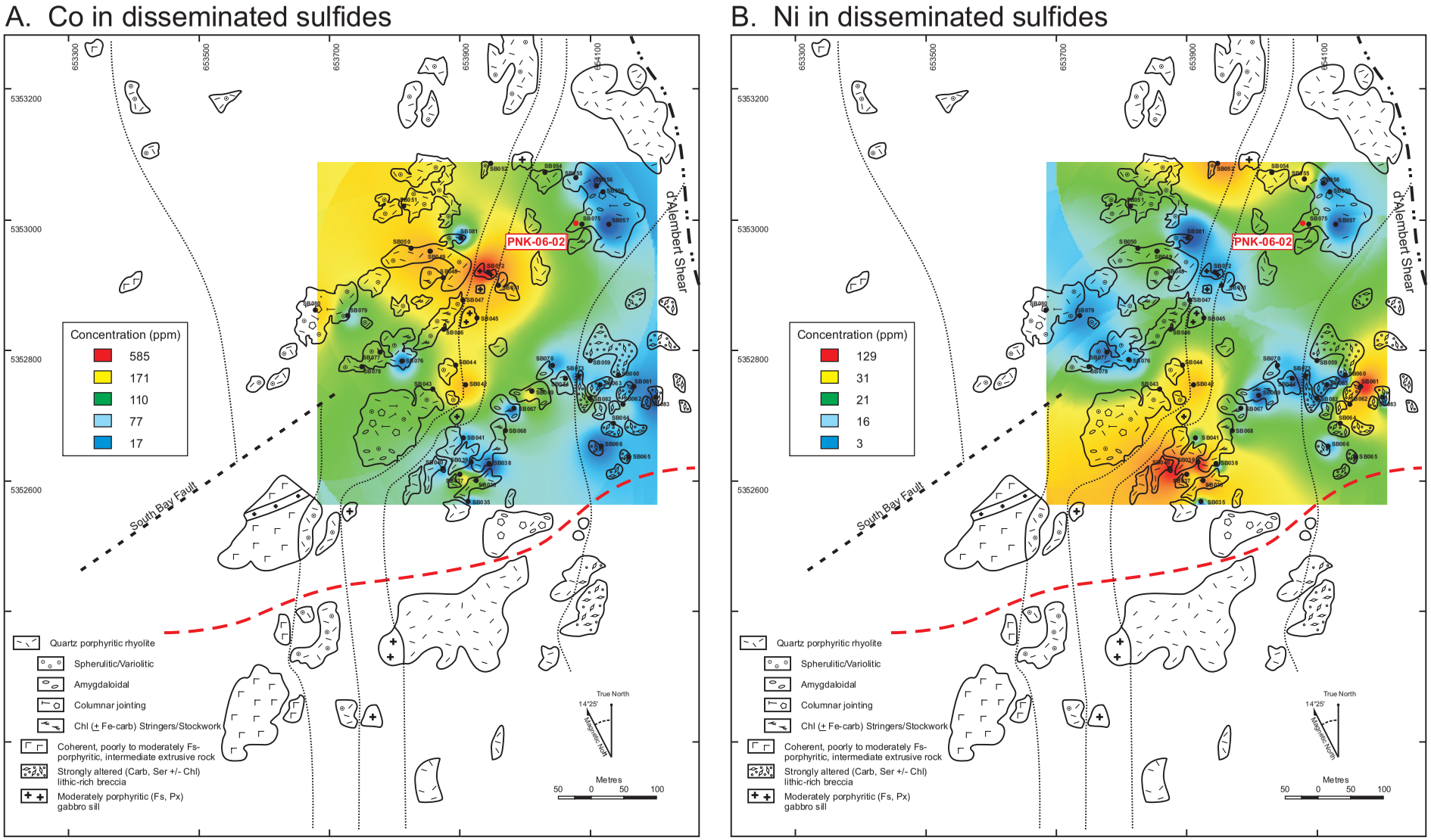

Figure 7.29. Co and Ni concentrations (ppm) in disseminated and stringer sulfides at Pinkos. Plotted data are based on quantitative INAA, ICP-AES, and ICP-MS analyses and contoured using inverse-distance weighting (IDW). a) Co is clearly highest in mafic intrusive rocks and in distal coherent rhyolite. b) The highest Ni concentrations occur in distal coherent and uppermost fragmental rhyolite.

Table 7.1a. Major element oxide data for Pinkos volcanic rocks

Sample		Alteration	SiO2	TiO2	Al2O3	Fe2O3	MnO	MgO	CaO	Na2O	K2O	P2O5	LOI	Total	CO2	S
Units	Lithofacies	Type	wt.%	wt.%	wt.%	wt.%	wt.%	wt.%	wt.%	wt.%	wt.%	wt.%	wt.%	wt.%	wt.%	wt.%
RW043	Columnar-jointed QP Rhyolite	Fe-carb	76.05	0.22	12.52	1.99	0.06	0.61	1.22	2.04	2.55	0.02	3.55	100.83	2.03	0.01
RW044	Columnar-jointed QP Rhyolite	Fe-carb	77.44	0.24	11.25	2.08	0.06	0.70	1.36	0.14	3.65	0.02	3.98	100.92	2.29	0.01
RW045	Columnar-jointed QP Rhyolite	Fe-carb	77.81	0.23	11.48	2.71	0.07	0.58	0.58	1.86	2.49	0.02	2.88	100.71	1.91	0.10
RW046	Columnar-jointed QP Rhyolite	Fe-carb	83.91	0.21	9.82	1.00	0.03	0.32	0.49	0.02	3.07	0.02	2.07	100.96	0.78	0.01
RW047	Coherent QP Rhyolite	Fe-carb	75.04	0.20	11.29	4.02	0.10	0.59	0.99	3.89	1.57	0.01	3.31	101.01	2.64	0.01
RW048	Coherent QP Rhyolite	Fe-carb	74.64	0.19	10.47	3.97	0.10	0.63	2.31	3.32	1.71	0.01	4.04	101.39	3.23	0.01
RW049	Coherent QP Rhyolite	Fe-carb	76.82	0.24	10.83	3.03	0.06	0.55	0.95	1.39	3.88	0.02	3.07	100.84	2.29	0.02
RW050	Coherent QP Rhyolite	Fe-carb	74.93	0.23	11.10	3.41	0.08	0.53	1.38	4.03	1.48	0.02	3.30	100.49	3.02	0.01
RW051	Coherent QP Rhyolite	Qtz, Ser	79.09	0.20	10.94	1.89	0.05	0.31	0.86	4.75	1.06	0.01	2.04	101.20	1.38	0.48
RW052	Coherent QP Rhyolite	Fe-carb	76.51	0.23	11.54	3.56	0.04	0.53	0.35	2.82	2.55	0.01	2.76	100.90	1.87	0.07
RW053*	Coherent QP Rhyolite	Fe-carb	77.17	0.24	11.19	2.53	0.04	0.47	1.28	3.67	1.96	0.02	2.76	101.33	2.05	0.02
RW054	Coherent QP Rhyolite	Fe-carb	69.89	0.21	10.79	3.18	0.11	1.88	3.43	2.09	2.84	0.01	6.48	100.91	5.28	0.01
RW055	Coherent QP Rhyolite	Qtz, Ser	75.40	0.22	10.73	3.14	0.05	0.67	1.64	2.99	2.33	0.01	3.33	100.51	2.66	0.01
RW056	Coherent QP Rhyolite	Fe-carb	76.34	0.25	10.74	2.06	0.06	0.67	1.96	4.39	1.40	0.02	3.27	101.16	2.88	0.01
RW057	Mafic Intrusive	Fe-carb	42.27	1.72	12.60	15.31	0.18	6.41	6.12	3.62	0.19	0.16	11.30	99.88	9.14	0.01
RW058	Mafic Intrusive	Fe-carb	44.21	1.71	13.24	14.72	0.17	5.71	7.47	3.43	0.04	0.21	8.97	99.88	5.57	0.01
RW059	Spherulitic QP Rhyolite	Fe-carb	80.57	0.19	9.36	1.66	0.07	0.52	1.75	3.22	1.19	0.01	2.88	101.42	2.51	0.03
RW060	Spherulitic QP Rhyolite	Fe-carb	76.61	0.19	10.70	2.39	0.10	0.28	2.08	5.44	0.40	0.01	2.68	100.88	2.32	0.01
RW061	Columnar-jointed QP Rhyolite	Fe-carb	77.06	0.22	11.12	3.98	0.10	0.17	0.99	4.05	1.05	0.01	2.46	101.21	0.95	0.01
RW062	Columnar-jointed QP Rhyolite	Fe-carb	77.87	0.22	11.93	1.73	0.03	0.62	0.93	3.43	1.29	0.02	2.59	100.66	1.47	0.01
RW063*	Columnar-jointed QP Rhyolite	Fe-carb	81.11	0.23	10.89	1.07	0.03	0.37	0.49	3.92	1.05	0.02	1.56	100.74	0.68	0.01
RW064	Spherulitic QP Rhyolite	Mg-Chl	76.81	0.18	10.83	4.39	0.03	3.74	0.04	0.01	1.72	0.01	3.20	100.96	0.10	0.01
RW065	Mafic Intrusive	Ca-carb, Ser	50.88	2.05	13.14	16.57	0.21	4.08	6.25	3.33	0.03	0.27	4.05	100.86	1.40	0.01
RW066	Stringers/Stockwork (NW)	Mg-Chl	78.70	0.21	10.98	2.86	0.03	2.54	0.40	0.50	1.95	0.02	2.98	101.17	0.63	0.01
RW067	Stringers/Stockwork (NW)	Ca-carb, Ser	68.35	0.24	10.58	6.55	0.08	6.11	1.21	0.01	1.01	0.02	5.49	99.65	1.55	0.01
RW068	Spherulitic QP Rhyolite	Ca-carb, Ser	77.43	0.22	11.01	2.46	0.03	2.18	0.88	2.10	1.63	0.01	3.16	101.11	1.19	0.01
RW069	Distal Spherulitic QP Rhyolite	Ca-carb, Ser	75.54	0.23	11.03	5.01	0.02	3.93	0.03	0.01	1.57	0.01	3.34	100.72	0.09	0.01
RW070	Distal Spherulitic QP Rhyolite	Ca-carb, Ser	75.36	0.19	10.64	2.94	0.06	2.12	1.53	3.53	0.78	0.01	3.73	100.89	2.27	0.03
RW071	Distal Spherulitic QP Rhyolite	Ca-carb, Ser	75.26	0.20	11.25	2.88	0.03	1.67	1.43	4.06	0.92	0.01	3.46	101.17	2.23	0.01
RW072	Distal Spherulitic QP Rhyolite	Mg-Chl	79.44	0.21	11.69	1.67	0.03	1.49	0.32	2.45	1.83	0.01	2.32	101.46	0.53	0.01
RW073	Distal Spherulitic QP Rhyolite	Ca-carb, Ser	77.19	0.18	10.02	4.97	0.04	3.37	0.15	0.42	1.44	0.01	3.24	101.03	0.31	0.01
RW074	Distal Spherulitic QP Rhyolite	Ca-carb, Ser	80.00	0.23	11.19	1.55	0.05	0.21	0.86	0.21	3.06	0.02	2.81	100.19	0.84	0.01
RW075	Distal Spherulitic QP Rhyolite	Ca-carb, Ser	76.90	0.21	10.16	2.51	0.07	0.83	2.10	1.70	1.98	0.02	4.16	100.64	3.09	0.42
RW076	Mafic Intrusive	Ca-carb, Ser	47.87	1.95	12.05	15.77	0.21	4.59	6.66	2.65	0.02	0.23	9.14	101.14	4.94	0.01
RW077	Coherent QP Rhyolite	Ca-carb, Ser	73.90	0.24	10.82	4.11	0.07	1.22	2.02	2.89	1.56	0.02	4.40	101.25	2.97	0.08
RW078	Columnar-jointed QP Rhyolite	Ca-carb, Ser	73.70	0.22	10.58	2.58	0.09	0.88	2.47	2.38	2.30	0.02	5.08	100.30	3.73	0.01
RW080	Columnar-jointed QP Rhyolite	Ca-carb, Ser	72.76	0.22	10.40	3.58	0.07	0.96	1.93	2.40	2.31	0.02	5.24	99.89	3.58	0.57
RW081	Columnar-jointed QP Rhyolite	Fe-carb	76.98	0.22	10.65	2.21	0.07	0.61	1.29	4.12	1.44	0.02	3.35	100.96	2.49	0.01
RW082	Columnar-jointed QP Rhyolite	Fe-carb	75.37	0.16	8.48	5.12	0.08	0.80	1.80	1.51	2.03	0.01	5.26	100.62	3.31	1.79
RW083	Fragmental Rhyolite	Fe-carb	75.77	0.20	10.82	3.25	0.10	0.87	1.66	0.09	3.51	0.01	4.79	101.07	3.04	0.01
RW084	Fragmental Rhyolite	Fe-carb	73.47	0.23	10.30	4.79	0.13	1.04	1.36	2.11	2.36	0.02	5.35	101.16	4.28	0.01
RW085	Fragmental Rhyolite	Fe-carb	76.74	0.23	10.88	1.66	0.07	0.53	1.76	4.88	1.00	0.03	3.22	101.00	2.65	0.02
RW086	Fragmental Rhyolite	Fe-carb	77.74	0.23	11.22	1.70	0.06	0.52	1.39	3.16	1.95	0.02	2.99	100.98	2.19	0.02
RW087	Fragmental Rhyolite	Fe-carb	79.05	0.18	10.28	2.64	0.04	0.75	1.05	0.03	2.90	0.01	3.43	100.36	1.63	0.95

Table 7.1a. Major element oxide data for Pinkos volcanic rocks

Sample Units	Lithofacies	Alteration Type	SiO2 wt.%	TiO2 wt.%	Al2O3 wt.%	Fe2O3 wt.%	MnO wt.%	MgO wt.%	CaO wt.%	Na2O wt.%	K2O wt.%	P2O5 wt.%	LOI wt.%	Total wt.%	CO2 wt.%	S wt.%
RW088	Fragmental Rhyolite	Fe-carb	76.30	0.15	9.48	3.38	0.11	0.94	2.43	1.91	1.46	0.01	5.16	101.33	4.31	0.09
RW089	Fragmental Rhyolite	Fe-carb	73.23	0.18	10.44	3.48	0.09	1.13	2.64	0.01	3.12	0.01	5.90	100.23	3.90	0.03
RW090	Fragmental Rhyolite	Fe-carb	76.76	0.18	10.76	3.04	0.07	0.50	1.33	3.93	1.01	0.01	3.16	100.75	2.17	0.01
RW091	Fragmental Rhyolite	Fe-carb	71.88	0.20	11.49	4.42	0.10	0.82	1.68	2.07	3.16	0.01	4.68	100.51	3.30	0.01
RW092	Fragmental Rhyolite	Fe-carb	74.53	0.22	11.47	2.82	0.10	0.72	2.00	3.42	1.75	0.02	3.89	100.94	3.28	0.04
RW093	Fragmental Rhyolite	Fe-carb	70.89	0.23	10.77	6.23	0.08	2.26	0.13	0.07	3.17	0.02	6.08	99.93	4.83	0.06
RW094	Fragmental Rhyolite	Fe-carb	74.77	0.23	10.77	2.31	0.07	0.83	2.14	1.36	2.77	0.02	4.44	99.71	3.25	0.04
RW095	Fragmental Rhyolite	Fe-carb	71.85	0.19	11.61	4.42	0.10	0.85	2.16	1.64	2.58	0.01	5.23	100.64	4.24	0.02
RW096	Fragmental Rhyolite	Fe-carb	76.01	0.21	10.86	2.91	0.06	0.65	1.67	2.85	1.91	0.02	3.78	100.93	2.88	0.01
RW097	Fragmental Rhyolite	Mg-Chl	75.07	0.21	10.32	2.89	0.11	1.27	2.12	3.63	1.19	0.02	3.81	100.64	3.18	0.22
RW098	Stringers/Stockwork (SE)	Mg-Chl	77.21	0.21	10.21	3.41	0.08	0.83	1.29	4.16	0.90	0.01	2.48	100.79	1.66	0.24
RW099	Stringers/Stockwork (SE)	Fe-carb	70.88	0.17	9.63	4.85	0.19	0.95	3.73	2.35	1.90	0.01	6.28	100.94	5.48	0.01
RW100	Stringers/Stockwork (SE)	Fe-carb	77.96	0.26	12.33	1.72	0.03	0.55	0.73	1.91	3.14	0.02	2.47	101.12	1.18	0.02
RW101	Stringers/Stockwork (SE)	Fe-carb	74.91	0.23	10.85	7.66	0.05	2.05	0.02	0.01	2.29	0.01	2.71	100.79	0.08	0.01
RW102	Stringers/Stockwork (SE)	Fe-carb	75.85	0.21	10.65	6.68	0.06	2.19	0.02	0.01	2.24	0.01	2.70	100.62	0.09	0.02
RW103	Stringers/Stockwork (SE)	Fe-carb	75.40	0.20	10.64	5.83	0.09	3.05	0.05	0.01	2.20	0.01	2.99	100.47	0.15	0.01
RW104	Coherent QP Rhyolite	Fe-carb	77.13	0.24	11.05	2.24	0.05	0.57	0.96	0.05	5.78	0.02	2.96	101.05	1.95	0.01
RW105	Coherent QP Rhyolite	Ca-carb, Ser	75.49	0.22	10.36	2.19	0.05	1.09	2.39	1.03	2.90	0.02	4.77	100.51	3.55	0.01
RW106	Mafic Intrusive	Ca-carb, Ser	50.76	1.95	12.69	15.83	0.25	3.38	5.46	3.74	0.03	0.31	6.23	100.63	3.69	0.10
RW107	Mafic Intrusive	Ca-carb, Ser	52.92	2.00	13.65	16.65	0.26	3.53	5.75	2.84	0.02	0.30	3.16	101.08	0.32	0.11
RW108	Coherent QP Rhyolite	Ca-carb, Ser	76.05	0.24	10.83	1.93	0.05	1.01	1.92	3.07	1.93	0.02	4.23	101.28	3.04	0.01
RW109	Stringers/Stockwork (SE)	Fe-carb	76.57	0.21	9.83	3.70	0.09	1.41	1.18	2.00	1.94	0.01	3.27	100.21	1.87	0.49
RW110	Stringers/Stockwork (SE)	Fe-carb	74.91	0.21	10.51	2.67	0.06	0.87	2.30	3.10	1.71	0.02	4.71	101.07	3.33	0.46
RW111	Coherent QP Rhyolite	Mg-Chl	77.12	0.17	9.52	4.41	0.02	3.72	0.19	0.01	1.75	0.01	3.40	100.32	0.35	0.01
RW112	Columnar-jointed QP Rhyolite	Fe-carb	76.25	0.23	10.86	4.14	0.10	0.89	0.57	0.01	3.19	0.02	4.71	100.97	3.23	0.02
RW113	Columnar-jointed QP Rhyolite	Fe-carb	75.34	0.20	11.84	2.92	0.07	0.85	1.13	1.37	2.75	0.01	4.22	100.70	2.95	0.01
RW114	Stringers/Stockwork (NW)	Mg-Chl	77.03	0.18	10.48	1.93	0.05	1.76	1.56	2.90	1.10	0.01	3.81	100.81	2.36	0.01
RW115	Stringers/Stockwork (NW)	Mg-Chl	76.83	0.22	10.46	4.62	0.02	3.51	0.02	0.01	1.65	0.01	3.15	100.50	0.08	0.01
RW116	Stringers/Stockwork (NW)	Mg-Chl	74.63	0.21	10.85	5.37	0.02	4.08	0.02	0.03	1.59	0.01	3.43	100.24	0.09	0.01
RW117	Stringers/Stockwork (NW)	Mg-Chl	75.84	0.18	10.05	8.08	0.05	2.11	0.02	0.01	1.39	0.01	2.81	100.55	0.10	0.01
RW118	Stringers/Stockwork (NW)	Mg-Chl	75.96	0.21	10.05	7.33	0.05	2.25	0.04	0.06	1.34	0.01	2.85	100.15	0.15	0.01
RW119	Spherulitic QP Rhyolite	Mg-Chl	75.03	0.24	11.49	3.51	0.06	1.38	1.48	1.71	2.07	0.02	3.80	100.79	2.26	0.30
RW120	Spherulitic QP Rhyolite	Qtz, Ser	74.69	0.21	10.96	4.64	0.11	1.00	0.18	3.05	2.00	0.02	3.58	100.44	2.52	0.05
RW121	Spherulitic QP Rhyolite	Qtz, Ser	77.20	0.22	11.67	1.92	0.06	0.79	1.39	1.71	2.36	0.02	3.53	100.87	2.20	0.03
RW122	Spherulitic QP Rhyolite	Fe-carb	78.66	0.14	11.65	2.70	0.06	0.50	0.59	5.56	0.54	0.01	1.07	101.48	0.30	0.01
RW123	Spherulitic QP Rhyolite	Mg-Chl	74.70	0.20	10.58	7.20	0.07	3.59	0.02	0.01	1.58	0.01	3.26	101.22	0.11	0.01
RW124	Spherulitic QP Rhyolite	Mg-Chl	76.05	0.20	10.64	3.86	0.05	3.72	0.27	0.02	1.98	0.01	3.35	100.15	0.50	0.01
RW125	Columnar-jointed QP Rhyolite	Mg-Chl	75.69	0.24	11.25	4.37	0.06	3.25	0.18	0.01	2.39	0.02	3.21	100.67	0.38	0.01
RW126	Columnar-jointed QP Rhyolite	Mg-Chl	68.50	0.86	10.81	10.19	0.07	3.55	0.93	0.01	1.56	0.24	4.04	100.76	0.99	0.01
RW127	Spherulitic QP Rhyolite	Mg-Chl	82.54	0.21	9.46	2.10	0.01	2.06	0.02	0.07	2.07	0.02	2.30	100.86	0.09	0.01
RW128	Distal Spherulitic QP Rhyolite	Ca-carb, Ser	72.91	0.23	11.01	3.69	0.09	2.14	2.16	2.18	1.70	0.02	4.72	100.85	3.30	0.14
RW129	Distal Spherulitic QP Rhyolite	Ca-carb, Ser	78.91	0.23	11.33	1.75	0.04	0.47	0.87	2.61	1.88	0.02	2.56	100.67	1.37	0.02
RW130	Distal Spherulitic QP Rhyolite	Ca-carb, Ser	74.28	0.20	9.19	3.99	0.13	1.33	3.34	0.47	2.20	0.02	6.17	101.32	4.96	0.01
RW131	Fragmental Rhyolite	Qtz, Ser	79.24	0.21	10.39	2.55	0.05	0.48	0.86	4.41	1.14	0.02	1.96	101.31	1.65	0.46

Table 7.1a. Major element oxide data for Pinkos volcanic rocks

Sample		Alteration	SiO2	TiO2	Al2O3	Fe2O3	MnO	MgO	CaO	Na2O	K2O	P2O5	LOI	Total	CO2	S
Units	Lithofacies	Type	wt.%	wt.%	wt.%	wt.%	wt.%	wt.%	wt.%	wt.%	wt.%	wt.%	wt.%	wt.%	wt.%	wt.%
RW132	Fragmental Rhyolite	Qtz, Ser	76.48	0.20	10.16	3.46	0.04	0.63	1.12	3.03	1.67	0.01	3.23	100.03	1.74	1.85
RW145	Coherent QP Rhyolite	Mg-Chl	80.89	0.20	11.46	1.39	0.01	0.27	0.10	1.56	2.69	0.02	1.60	100.19	0.19	0.01
RW146	Fragmental Rhyolite	Fe-carb	77.50	0.19	8.68	3.52	0.11	0.56	2.07	2.63	1.37	0.01	4.17	100.81	2.91	0.01
RW147*	Coherent QP Rhyolite	Qtz, Ser	77.12	0.22	11.82	2.31	0.05	0.59	0.74	3.19	1.87	0.02	2.87	100.80	1.98	0.02
RW148	Coherent QP Rhyolite	Fe-carb	75.28	0.23	11.49	2.71	0.07	0.40	1.66	5.04	0.86	0.02	3.30	101.06	2.52	0.26
RW149	Coherent QP Rhyolite	Fe-carb	74.20	0.17	9.92	3.72	0.14	0.93	2.22	3.35	1.26	0.01	4.59	100.51	3.83	0.21
RW150	Fragmental Rhyolite	Fe-carb	75.93	0.23	12.03	3.71	0.09	0.31	0.58	1.60	2.75	0.02	3.06	100.31	1.03	0.01
RW151	Coherent QP Rhyolite	Qtz, Ser	73.61	0.22	10.36	3.92	0.11	0.70	2.44	2.38	1.85	0.02	5.05	100.66	4.28	0.23
RW152	Coherent QP Rhyolite	Qtz, Ser	75.46	0.20	11.12	3.47	0.12	0.43	1.59	4.65	0.99	0.01	3.46	101.50	2.51	0.01
RW153	Coherent QP Rhyolite	Qtz, Ser	79.76	0.21	10.91	1.77	0.04	0.28	0.60	4.64	1.12	0.01	1.65	100.99	0.88	0.05
RW154	Coherent QP Rhyolite	Qtz, Ser	77.12	0.23	11.28	1.67	0.05	0.83	1.29	2.61	2.40	0.02	3.09	100.59	1.98	0.13
RW155	Coherent QP Rhyolite	Qtz, Ser	77.18	0.23	10.66	2.01	0.05	0.84	1.34	1.62	3.61	0.02	3.05	100.61	2.03	0.17
RW156	Coherent QP Rhyolite	Qtz, Ser	74.90	0.20	10.96	3.22	0.08	0.63	1.84	2.55	3.69	0.01	3.24	101.32	2.50	0.13
RW157	Coherent QP Rhyolite	Qtz, Ser	76.32	0.24	10.56	2.39	0.07	0.63	1.71	3.30	2.62	0.02	2.85	100.71	2.17	0.04
RW158	Coherent QP Rhyolite	Qtz, Ser	73.61	0.19	9.08	4.47	0.12	1.01	2.96	0.01	3.08	0.01	6.07	100.61	4.90	0.01
RW159	Fragmental Rhyolite	Qtz, Ser	77.72	0.23	11.59	3.13	0.07	0.40	0.20	2.94	2.22	0.02	2.77	101.29	1.83	0.05
RW160	Fragmental Rhyolite	Qtz, Ser	78.16	0.19	10.17	3.85	0.09	0.31	0.68	4.31	1.09	0.01	2.34	101.20	1.61	0.01
RW161	Fragmental Rhyolite	Qtz, Ser	77.23	0.22	10.91	3.49	0.07	0.54	0.48	2.53	2.30	0.02	3.15	100.94	2.21	0.05
RW162	Fragmental Rhyolite	Qtz, Ser	73.94	0.20	10.39	3.22	0.09	0.94	2.59	1.73	2.64	0.02	5.05	100.81	3.91	0.05

* Denotes least-altered sample suite.

Table 7.1b. Trace element concentrations of Pinkos volcanic rocks

Sample		Alteration	Zn	Cu	Pb	Ba	Cr	Sc	V	Cs	Li	Rb	Sr	Be	Cd	Sb	Tl
Units	Lithofacies	Type	ppm	ppm	ppm	ppm	ppm	ppm	ppm	ppm	ppm	ppm	ppm	ppm	ppm	ppm	ppm
RW043	Columnar-jointed QP Rhyolite	Fe-carb	27	8.00	2.5	666	15	3.7	1.0	0.856	2.4	44.1	43.1	2.21	0.007	0.14	0.065
RW044	Columnar-jointed QP Rhyolite	Fe-carb	41	25.8	2.7	610	13	3.9	0.9	1.316	2.1	59.6	38.6	2.51	0.145	0.15	0.094
RW045	Columnar-jointed QP Rhyolite	Fe-carb	64	15.6	3.1	433	19	2.8	0.8	0.896	1.6	42.2	22.7	2.59	0.053	0.20	0.073
RW046	Columnar-jointed QP Rhyolite	Fe-carb	30	8.40	2.4	392	19	3.1	1.0	0.988	1.2	47.2	10.2	2.11	0.056	0.17	0.079
RW047	Coherent QP Rhyolite	Fe-carb	65	16.8	3.4	307	16	3.4	0.9	0.562	2.0	27.3	39.8	1.57	0.080	0.17	0.041
RW048	Coherent QP Rhyolite	Fe-carb	118	7.40	2.5	291	18	3.2	1.2	0.547	2.5	30.0	56.1	2.19	0.213	0.15	0.042
RW049	Coherent QP Rhyolite	Fe-carb	44	8.70	3.1	701	27	3.9	1.1	0.879	3.5	55.9	23.4	2.26	0.007	0.15	0.085
RW050	Coherent QP Rhyolite	Fe-carb	51	16.8	4.2	372	27	3.8	1.2	0.493	1.8	26.0	48.1	2.13	0.007	0.15	0.038
RW051	Coherent QP Rhyolite	Qtz, Ser	33	77.4	8.5	213	36	2.7	1.2	0.337	1.6	19.3	36.1	1.99	0.048	0.38	0.03
RW052	Coherent QP Rhyolite	Fe-carb	92	36.9	6.0	616	21	3.6	0.4	0.911	4.2	46.7	18.2	2.41	0.052	0.17	0.058
RW053*	Coherent QP Rhyolite	Fe-carb	33	45.0	5.1	390	25	4.1	1.0	0.796	2.6	35.7	41.2	2.24	0.007	0.25	0.045
RW054	Coherent QP Rhyolite	Fe-carb	50	15.4	3.4	274	10	3.3	1.0	1.070	3.7	49.4	70.1	2.79	0.007	0.13	0.056
RW055	Coherent QP Rhyolite	Qtz, Ser	37	7.60	2.6	525	14	3.2	0.9	1.101	2.3	43.9	38.3	1.88	0.007	0.14	0.059
RW056	Coherent QP Rhyolite	Fe-carb	26	108	2.4	206	21	3.8	1.2	0.522	1.1	22.8	49.2	1.41	0.007	0.12	0.030
RW057	Mafic Intrusive	Fe-carb	126	152	3.0	44.1	59	45	370	0.176	29	3.99	129	0.34	0.084	0.34	0.008
RW058	Mafic Intrusive	Fe-carb	110	71.6	2.3	19.7	65	44	370	0.084	33	0.59	145	0.44	0.084	0.33	0.003
RW059	Spherulitic QP Rhyolite	Fe-carb	28	56.7	3.1	113	24	2.7	3.0	0.515	1.3	21.6	45.6	1.69	0.086	0.10	0.040
RW060	Spherulitic QP Rhyolite	Fe-carb	104	8.90	3.3	115	8	2.7	1.2	0.204	0.8	7.22	69.1	1.08	0.461	0.07	0.012
RW061	Columnar-jointed QP Rhyolite	Fe-carb	73	16.6	4.6	273	11	3.0	0.9	0.491	1.5	21.1	44.5	1.57	0.007	0.11	0.03
RW062	Columnar-jointed QP Rhyolite	Fe-carb	42	5.90	2.1	122	14	3.6	1.0	0.459	3.9	21.8	36.3	1.42	0.007	0.06	0.029
RW063*	Columnar-jointed QP Rhyolite	Fe-carb	32	12.0	2.4	215	21	2.7	0.9	0.447	2.7	20.9	34.1	1.53	0.007	0.09	0.026
RW064	Spherulitic QP Rhyolite	Mg-Chl	50	8.20	2.9	462	22	3.0	1.0	0.851	31	30.7	12.6	1.32	0.039	0.10	0.048
RW065	Mafic Intrusive	Ca-carb, Ser	114	35.6	2.4	43.9	6	47	290	0.076	14	0.49	225	0.69	0.077	0.30	0.003
RW066	Stringers/Stockwork (NW)	Mg-Chl	24	9.30	4.1	483	15	3.3	1.5	0.820	17	33.3	27.4	1.59	0.133	0.10	0.051
RW067	Stringers/Stockwork (NW)	Ca-carb, Ser	61	99.8	2.5	272	13	4.1	1.0	0.407	52	19.3	19.5	1.70	0.064	0.12	0.029
RW068	Spherulitic QP Rhyolite	Ca-carb, Ser	20	7.10	2.2	304	21	2.9	1.3	0.684	14	31.5	32.1	1.65	0.007	0.11	0.050
RW069	Distal Spherulitic QP Rhyolite	Ca-carb, Ser	39	10.8	2.5	435	14	3.6	0.8	0.611	33	26.9	9.50	1.11	0.007	0.13	0.041
RW070	Distal Spherulitic QP Rhyolite	Ca-carb, Ser	15	9.60	3.5	122	18	2.8	0.8	0.330	12	13.9	46.4	2.29	0.007	0.12	0.018
RW071	Distal Spherulitic QP Rhyolite	Ca-carb, Ser	21	14.7	2.8	221	18	3.2	2.0	0.444	8.9	18.1	50.1	1.46	0.007	0.14	0.025
RW072	Distal Spherulitic QP Rhyolite	Mg-Chl	16	12.2	2.8	288	16	2.3	0.4	0.678	8.5	30.4	20.5	3.26	0.007	0.11	0.043
RW073	Distal Spherulitic QP Rhyolite	Ca-carb, Ser	44	13.2	3.0	396	10	3.0	0.8	0.440	25	23.5	9.70	1.32	0.065	0.12	0.032
RW074	Distal Spherulitic QP Rhyolite	Ca-carb, Ser	33	12.8	3.1	386	6	3.6	0.4	1.235	1.7	55.1	19.1	1.96	0.086	0.15	0.098
RW075	Distal Spherulitic QP Rhyolite	Ca-carb, Ser	21	18.6	3.7	281	11	3.3	0.4	1.004	2.5	38.8	40.5	1.60	0.023	0.21	0.076
RW076	Mafic Intrusive	Ca-carb, Ser	118	78.6	2.6	8.30	8	47	350	0.053	40	0.30	73.8	0.59	0.087	0.43	0.003
RW077	Coherent QP Rhyolite	Ca-carb, Ser	41	43.2	2.7	75.5	15	4.0	2.4	0.730	7.7	26.6	41.9	1.61	0.029	0.19	0.043
RW078	Columnar-jointed QP Rhyolite	Ca-carb, Ser	39	31.6	4.6	377	17	3.8	1.0	0.794	1.4	37.3	63.6	1.95	0.020	0.33	0.051
RW080	Columnar-jointed QP Rhyolite	Ca-carb, Ser	52	49.9	4.5	459	20	3.7	0.9	0.830	1.8	39.3	67.3	1.82	0.056	0.27	0.058
RW081	Columnar-jointed QP Rhyolite	Fe-carb	105	15.7	3.6	453	25	3.4	0.9	0.601	1.5	25.5	61.4	1.72	0.223	0.36	0.034
RW082	Columnar-jointed QP Rhyolite	Fe-carb	112	49.6	11	456	21	2.8	0.4	0.737	1.1	37.0	59.8	1.69	0.260	0.40	0.051
RW083	Fragmental Rhyolite	Fe-carb	129	6.50	2.8	571	13	2.9	0.4	1.403	1.6	70.1	41.6	2.72	0.220	0.24	0.091
RW084	Fragmental Rhyolite	Fe-carb	111	14.7	2.7	429	16	3.2	0.4	0.971	0.9	48.5	45.2	2.16	0.126	0.17	0.061
RW085	Fragmental Rhyolite	Fe-carb	32	8.20	3.0	326	22	3.7	0.4	0.396	0.6	18.7	61.6	1.88	0.007	0.20	0.024
RW086	Fragmental Rhyolite	Fe-carb	56	6.70	2.7	483	24	3.4	0.8	0.797	0.7	38.0	49.2	2.07	0.047	0.18	0.052
RW087	Fragmental Rhyolite	Fe-carb	52	14.5	2.9	491	16	2.8	5.4	1.301	1.9	62.6	19.9	1.64	0.085	0.25	0.090

Table 7.1b. Trace element concentrations of Pinkos volcanic rocks

Sample Units	Lithofacies	Alteration Type	Co ppm	Ni ppm	Mo ppm	Ga ppm	In ppm	Sn ppm	W ppm
RW043	Columnar-jointed QP Rhyolite	Fe-carb	0.72	1.6	1.59	23.27	0.209	5.43	1.12
RW044	Columnar-jointed QP Rhyolite	Fe-carb	0.80	0.8	1.32	27.49	0.118	3.88	0.57
RW045	Columnar-jointed QP Rhyolite	Fe-carb	2.07	1.8	2.15	22.75	0.157	4.25	0.49
RW046	Columnar-jointed QP Rhyolite	Fe-carb	1.01	1.9	2.24	18.61	0.164	3.98	0.46
RW047	Coherent QP Rhyolite	Fe-carb	0.60	0.8	2.75	24.75	0.192	6.57	1.16
RW048	Coherent QP Rhyolite	Fe-carb	0.65	0.8	1.97	19.22	0.167	5.77	0.51
RW049	Coherent QP Rhyolite	Fe-carb	1.16	2.5	2.11	23.36	0.196	6.60	0.69
RW050	Coherent QP Rhyolite	Fe-carb	0.94	1.7	5.59	21.12	0.224	5.11	1.35
RW051	Coherent QP Rhyolite	Qtz, Ser	0.82	0.8	3.89	14.62	0.097	11.6	1.35
RW052	Coherent QP Rhyolite	Fe-carb	1.68	0.8	3.47	27.34	0.224	7.55	1.00
RW053*	Coherent QP Rhyolite	Fe-carb	1.02	1.7	2.13	21.85	0.067	6.22	0.93
RW054	Coherent QP Rhyolite	Fe-carb	1.11	2.0	1.06	23.99	0.218	7.87	0.54
RW055	Coherent QP Rhyolite	Qtz, Ser	0.93	0.8	1.58	20.26	0.195	4.28	0.48
RW056	Coherent QP Rhyolite	Fe-carb	1.21	0.8	3.81	19.61	0.025	1.68	0.72
RW057	Mafic Intrusive	Fe-carb	49.0	46	0.21	17.04	0.067	2.12	0.16
RW058	Mafic Intrusive	Fe-carb	46.7	48	0.26	17.68	0.066	1.51	0.05
RW059	Spherulitic QP Rhyolite	Fe-carb	1.48	0.8	2.89	17.16	0.139	4.99	0.41
RW060	Spherulitic QP Rhyolite	Fe-carb	0.43	0.8	0.79	14.77	0.135	5.46	0.62
RW061	Columnar-jointed QP Rhyolite	Fe-carb	0.48	0.8	1.34	17.03	0.159	6.39	0.46
RW062	Columnar-jointed QP Rhyolite	Fe-carb	0.83	0.8	1.78	20.55	0.105	3.11	0.53
RW063*	Columnar-jointed QP Rhyolite	Fe-carb	0.47	0.8	1.46	16.29	0.138	4.74	0.45
RW064	Spherulitic QP Rhyolite	Mg-Chl	10.3	0.8	1.57	18.15	0.071	2.70	0.48
RW065	Mafic Intrusive	Ca-carb, Ser	37.9	7.0	0.35	19.41	0.095	1.41	0.10
RW066	Stringers/Stockwork (NW)	Mg-Chl	7.81	0.8	2.65	15.66	0.033	2.27	0.48
RW067	Stringers/Stockwork (NW)	Ca-carb, Ser	18.8	0.8	2.23	24.93	0.068	3.35	0.53
RW068	Spherulitic QP Rhyolite	Ca-carb, Ser	6.10	0.8	1.75	18.47	0.143	4.97	0.48
RW069	Distal Spherulitic QP Rhyolite	Ca-carb, Ser	16.5	0.8	1.71	22.84	0.022	2.49	0.71
RW070	Distal Spherulitic QP Rhyolite	Ca-carb, Ser	7.33	0.8	2.98	14.86	0.078	3.27	0.32
RW071	Distal Spherulitic QP Rhyolite	Ca-carb, Ser	6.58	0.8	2.15	20.28	0.131	4.10	0.42
RW072	Distal Spherulitic QP Rhyolite	Mg-Chl	2.85	0.8	2.36	17.68	0.144	4.67	0.41
RW073	Distal Spherulitic QP Rhyolite	Ca-carb, Ser	15.3	0.8	3.16	17.72	0.025	1.89	0.36
RW074	Distal Spherulitic QP Rhyolite	Ca-carb, Ser	0.89	0.8	0.64	22.62	0.165	7.07	0.50
RW075	Distal Spherulitic QP Rhyolite	Ca-carb, Ser	3.36	2.2	2.22	20.60	0.064	3.41	0.36
RW076	Mafic Intrusive	Ca-carb, Ser	37.0	10	0.34	18.77	0.076	1.75	0.11
RW077	Coherent QP Rhyolite	Ca-carb, Ser	1.67	0.8	2.20	21.81	0.096	2.50	0.61
RW078	Columnar-jointed QP Rhyolite	Ca-carb, Ser	0.68	0.8	1.56	22.09	0.154	5.22	0.56
RW080	Columnar-jointed QP Rhyolite	Ca-carb, Ser	0.51	0.8	3.12	22.61	0.088	4.80	0.93
RW081	Columnar-jointed QP Rhyolite	Fe-carb	0.63	2.3	3.82	22.50	0.248	4.55	0.86
RW082	Columnar-jointed QP Rhyolite	Fe-carb	0.39	0.8	2.66	15.50	0.215	4.16	0.56
RW083	Fragmental Rhyolite	Fe-carb	0.65	0.8	2.92	28.29	0.243	7.32	0.49
RW084	Fragmental Rhyolite	Fe-carb	0.51	0.8	1.69	21.78	0.149	5.67	0.63
RW085	Fragmental Rhyolite	Fe-carb	0.45	0.8	2.12	19.83	0.160	3.93	0.67
RW086	Fragmental Rhyolite	Fe-carb	0.29	0.8	1.92	23.30	0.110	4.72	0.60
RW087	Fragmental Rhyolite	Fe-carb	0.64	0.8	2.45	16.96	0.128	5.93	0.45

Table 7.1b. Trace element concentrations of Pinkos volcanic rocks

Sample		Alteration	Zn	Cu	Pb	Ba	Cr	Sc	V	Cs	Li	Rb	Sr	Be	Cd	Sb	Tl
Units	Lithofacies	Type	ppm	ppm	ppm	ppm	ppm	ppm	ppm	ppm	ppm	ppm	ppm	ppm	ppm	ppm	ppm
RW088	Fragmental Rhyolite	Fe-carb	481	73.1	4.5	305	23	2.6	0.8	0.633	0.9	32.5	38.2	2.12	1.264	0.21	0.045
RW089	Fragmental Rhyolite	Fe-carb	91	15.9	4.0	474	18	2.8	0.4	1.472	2.2	71.3	47.4	2.55	0.099	0.20	0.094
RW090	Fragmental Rhyolite	Fe-carb	114	10.0	3.0	332	21	2.8	0.9	0.551	1.2	24.4	52.8	1.69	0.181	0.20	0.036
RW091	Fragmental Rhyolite	Fe-carb	140	15.4	5.3	350	16	3.0	0.4	0.982	2.8	50.0	42.3	1.76	0.095	0.24	0.059
RW092	Fragmental Rhyolite	Fe-carb	56	9.30	2.9	539	19	3.4	0.4	0.782	0.9	34.8	59.6	2.01	0.007	0.19	0.044
RW093	Fragmental Rhyolite	Fe-carb	68	26.7	3.1	499	9	3.4	0.4	1.522	3.9	69.9	8.90	1.70	0.007	0.22	0.107
RW094	Fragmental Rhyolite	Fe-carb	141	4.20	3.3	680	13	3.8	0.4	1.195	1.1	57.1	55.0	2.96	0.232	0.21	0.094
RW095	Fragmental Rhyolite	Fe-carb	320	17.0	5.5	715	13	2.9	0.9	1.207	2.0	66.1	58.1	2.43	0.678	0.21	0.090
RW096	Fragmental Rhyolite	Fe-carb	46	4.20	3.2	331	13	3.0	0.9	0.893	1.5	42.3	49.6	1.83	0.033	0.19	0.075
RW097	Fragmental Rhyolite	Mg-Chl	80	25.4	4.8	368	24	3.4	1.0	0.658	5.1	26.6	65.6	1.67	0.037	0.22	0.042
RW098	Stringers/Stockwork (SE)	Mg-Chl	75	10.4	2.9	248	14	3.2	0.4	0.654	5.6	18.8	52.3	1.16	0.019	0.14	0.025
RW099	Stringers/Stockwork (SE)	Fe-carb	177	4.80	4.5	317	22	2.8	1.0	0.710	2.4	36.9	81.3	3.12	0.609	0.16	0.046
RW100	Stringers/Stockwork (SE)	Fe-carb	34	23.8	3.8	669	22	4.0	0.4	1.056	3.7	59.3	29.3	2.41	0.007	0.22	0.074
RW101	Stringers/Stockwork (SE)	Fe-carb	328	40.3	3.4	457	15	3.4	0.8	1.021	23	40.0	5.40	1.46	0.007	0.19	0.055
RW102	Stringers/Stockwork (SE)	Fe-carb	314	164	3.2	463	13	3.3	0.4	1.006	24	41.3	6.20	1.65	0.013	0.20	0.057
RW103	Stringers/Stockwork (SE)	Fe-carb	384	12.8	2.6	388	10	3.2	0.4	1.249	31	44.6	5.40	1.80	0.159	0.20	0.059
RW104	Coherent QP Rhyolite	Fe-carb	33	9.40	2.4	737	22	4.2	0.4	1.389	3.3	76.4	29.1	2.76	0.007	0.23	0.109
RW105	Coherent QP Rhyolite	Ca-carb, Ser	32	79.9	2.3	280	11	3.7	0.4	1.154	1.1	55.2	37.5	1.40	0.007	1.11	0.071
RW106	Mafic Intrusive	Ca-carb, Ser	125	29.8	1.8	33.5	5	42	160	0.076	19	0.62	99.4	0.63	0.079	0.26	0.003
RW107	Mafic Intrusive	Ca-carb, Ser	134	23.8	2.1	24.8	4	46	160	0.063	15	0.26	182	0.87	0.102	0.33	0.003
RW108	Coherent QP Rhyolite	Ca-carb, Ser	26	5.70	2.0	95.8	8	3.7	0.9	0.853	1.6	37.7	44.4	1.39	0.022	0.18	0.046
RW109	Stringers/Stockwork (SE)	Fe-carb	628	59.8	3.4	504	7	3.4	0.4	1.229	8.9	45.6	40.5	1.83	3.549	0.19	0.055
RW110	Stringers/Stockwork (SE)	Fe-carb	31	42.4	3.1	188	13	3.4	0.8	0.745	1.4	32.3	44.5	1.57	0.059	0.21	0.044
RW111	Coherent QP Rhyolite	Mg-Chl	52	13.5	2.1	455	17	2.6	0.4	1.045	28	33.3	7.60	1.07	0.020	0.18	0.049
RW112	Columnar-jointed QP Rhyolite	Fe-carb	80	14.3	2.0	295	8	3.5	0.9	0.984	1.3	49.7	10.2	1.30	0.104	0.20	0.083
RW113	Columnar-jointed QP Rhyolite	Fe-carb	80	6.40	2.8	549	19	3.1	0.8	1.030	1.6	50.7	37.1	2.18	0.117	0.26	0.069
RW114	Stringers/Stockwork (NW)	Mg-Chl	15	47.6	5.8	219	20	2.6	1.0	0.467	7.8	21.3	42.1	1.33	0.031	0.25	0.033
RW115	Stringers/Stockwork (NW)	Mg-Chl	25	6.80	2.7	487	16	3.2	1.1	0.624	25	26.9	9.70	1.04	0.007	0.09	0.040
RW116	Stringers/Stockwork (NW)	Mg-Chl	44	9.50	2.1	525	10	3.2	0.4	0.663	33	28.9	13.0	1.53	0.007	0.11	0.047
RW117	Stringers/Stockwork (NW)	Mg-Chl	123	69.5	2.4	459	13	2.8	0.4	0.541	23	24.6	6.90	1.12	0.007	0.10	0.041
RW118	Stringers/Stockwork (NW)	Mg-Chl	135	11.8	1.8	358	19	3.3	0.8	0.502	27	23.6	11.4	1.31	0.019	0.10	0.038
RW119	Spherulitic QP Rhyolite	Mg-Chl	86	13.6	3.8	391	13	3.6	1.0	0.830	6.8	40.2	47.8	2.00	0.028	0.14	0.068
RW120	Spherulitic QP Rhyolite	Qtz, Ser	100	65.1	4.3	430	14	3.6	0.4	1.001	2.4	42.1	26.9	3.22	0.007	0.10	0.069
RW121	Spherulitic QP Rhyolite	Qtz, Ser	35	15.7	3.4	583	15	3.3	1.0	0.980	1.9	46.6	39.2	1.96	0.007	0.13	0.079
RW122	Spherulitic QP Rhyolite	Fe-carb	51	38.5	2.6	139	36	7.5	1.8	0.079	7.2	11.1	47.4	1.39	0.007	0.10	0.020
RW123	Spherulitic QP Rhyolite	Mg-Chl	127	45.0	1.8	368	19	3.2	1.5	0.539	28	27.3	4.20	3.25	0.052	0.11	0.042
RW124	Spherulitic QP Rhyolite	Mg-Chl	44	17.6	2.5	600	11	3.2	0.4	0.668	23	33.6	8.20	1.51	0.161	0.12	0.044
RW125	Columnar-jointed QP Rhyolite	Mg-Chl	212	44.0	2.1	500	13	3.7	0.8	0.819	19	42.7	7.50	2.14	0.155	0.11	0.073
RW126	Columnar-jointed QP Rhyolite	Mg-Chl	42	50.2	1.5	435	11	20	14	0.491	22	27.5	12.2	1.20	0.048	0.17	0.035
RW127	Spherulitic QP Rhyolite	Mg-Chl	14	16.0	2.9	586	14	3.5	0.4	0.683	15	35.0	8.80	1.41	0.007	0.13	0.048
RW128	Distal Spherulitic QP Rhyolite	Ca-carb, Ser	142	30.5	7.1	371	14	3.9	1.1	0.691	11	34.9	49.5	2.82	0.065	0.20	0.056
RW129	Distal Spherulitic QP Rhyolite	Ca-carb, Ser	45	10.1	3.1	281	18	3.2	0.9	0.753	3.5	38.9	38.2	2.28	0.007	0.13	0.070
RW130	Distal Spherulitic QP Rhyolite	Ca-carb, Ser	59	44.6	5.6	319	23	3.6	0.9	0.895	3.9	45.6	43.9	1.77	0.091	0.26	0.077
RW131	Fragmental Rhyolite	Qtz, Ser	30	23.6	5.0	339	24	3.3	1.3	0.532	1.0	27.0	42.9	1.56	0.007	0.27	0.034

Table 7.1b. Trace element concentrations of Pinkos volcanic rocks

Sample Units	Lithofacies	Alteration Type	Co ppm	Ni ppm	Mo ppm	Ga ppm	In ppm	Sn ppm	W ppm
RW088	Fragmental Rhyolite	Fe-carb	0.90	0.8	2.79	14.07	0.207	6.36	0.40
RW089	Fragmental Rhyolite	Fe-carb	0.59	0.8	2.60	21.36	0.177	6.11	0.49
RW090	Fragmental Rhyolite	Fe-carb	0.49	0.8	2.28	17.76	0.137	5.26	0.56
RW091	Fragmental Rhyolite	Fe-carb	0.78	0.8	1.69	24.55	0.210	6.89	0.52
RW092	Fragmental Rhyolite	Fe-carb	0.40	0.8	1.88	23.19	0.192	5.50	0.58
RW093	Fragmental Rhyolite	Fe-carb	2.05	0.8	3.42	20.81	0.096	3.80	0.68
RW094	Fragmental Rhyolite	Fe-carb	0.43	0.8	3.08	24.20	0.212	7.20	0.90
RW095	Fragmental Rhyolite	Fe-carb	0.64	0.8	2.33	22.43	0.207	6.20	0.62
RW096	Fragmental Rhyolite	Fe-carb	0.53	0.8	2.66	21.23	0.074	4.68	0.59
RW097	Fragmental Rhyolite	Mg-Chl	0.58	0.8	4.07	18.90	0.061	2.40	0.73
RW098	Stringers/Stockwork (SE)	Mg-Chl	0.81	0.8	2.37	19.35	0.069	4.07	0.54
RW099	Stringers/Stockwork (SE)	Fe-carb	0.56	0.8	4.16	17.76	0.149	5.15	0.61
RW100	Stringers/Stockwork (SE)	Fe-carb	0.74	0.8	1.91	25.30	0.210	5.99	1.75
RW101	Stringers/Stockwork (SE)	Fe-carb	0.92	0.8	2.92	23.64	0.104	5.85	1.03
RW102	Stringers/Stockwork (SE)	Fe-carb	1.63	0.8	2.63	22.35	0.163	5.65	0.79
RW103	Stringers/Stockwork (SE)	Fe-carb	0.33	0.8	1.37	23.52	0.267	6.94	0.72
RW104	Coherent QP Rhyolite	Fe-carb	0.50	5.8	3.15	24.51	0.183	6.86	0.63
RW105	Coherent QP Rhyolite	Ca-carb, Ser	1.24	0.8	0.91	22.27	0.054	2.47	0.64
RW106	Mafic Intrusive	Ca-carb, Ser	30.9	2.3	0.43	20.74	0.108	1.29	0.25
RW107	Mafic Intrusive	Ca-carb, Ser	30.5	2.3	0.55	22.43	0.123	0.91	0.16
RW108	Coherent QP Rhyolite	Ca-carb, Ser	1.18	0.8	0.83	23.00	0.041	1.90	0.46
RW109	Stringers/Stockwork (SE)	Fe-carb	0.70	0.8	1.38	20.01	0.352	6.18	0.69
RW110	Stringers/Stockwork (SE)	Fe-carb	0.98	1.6	1.41	22.94	0.076	3.15	0.46
RW111	Coherent QP Rhyolite	Mg-Chl	10.8	0.8	1.67	16.41	0.024	2.44	0.43
RW112	Columnar-jointed QP Rhyolite	Fe-carb	1.23	0.8	4.28	23.47	0.206	4.70	0.63
RW113	Columnar-jointed QP Rhyolite	Fe-carb	0.38	0.8	2.16	23.02	0.189	5.43	0.71
RW114	Stringers/Stockwork (NW)	Mg-Chl	4.21	0.8	2.39	12.10	0.032	5.74	0.36
RW115	Stringers/Stockwork (NW)	Mg-Chl	8.20	1.6	1.10	21.84	0.031	2.68	0.54
RW116	Stringers/Stockwork (NW)	Mg-Chl	13.2	0.8	1.44	21.99	0.037	2.21	0.42
RW117	Stringers/Stockwork (NW)	Mg-Chl	12.7	0.8	9.74	23.11	0.073	5.64	0.70
RW118	Stringers/Stockwork (NW)	Mg-Chl	12.4	0.8	1.43	22.45	0.044	3.01	0.58
RW119	Spherulitic QP Rhyolite	Mg-Chl	1.23	0.8	1.07	23.90	0.177	5.10	0.67
RW120	Spherulitic QP Rhyolite	Qtz, Ser	0.71	0.8	0.64	27.76	0.204	4.39	0.41
RW121	Spherulitic QP Rhyolite	Qtz, Ser	0.60	0.8	1.74	22.76	0.211	6.07	0.51
RW122	Spherulitic QP Rhyolite	Fe-carb	0.92	1.9	4.21	16.68	0.113	4.94	0.26
RW123	Spherulitic QP Rhyolite	Mg-Chl	2.56	0.8	1.81	23.73	0.087	7.49	0.55
RW124	Spherulitic QP Rhyolite	Mg-Chl	6.82	0.8	0.79	21.44	0.030	3.54	0.38
RW125	Columnar-jointed QP Rhyolite	Mg-Chl	0.70	0.8	1.46	24.87	0.121	5.61	0.60
RW126	Columnar-jointed QP Rhyolite	Mg-Chl	18.2	0.8	1.44	22.14	0.063	3.95	0.40
RW127	Spherulitic QP Rhyolite	Mg-Chl	2.97	0.8	1.37	18.99	0.031	4.56	0.59
RW128	Distal Spherulitic QP Rhyolite	Ca-carb, Ser	0.81	0.8	4.11	19.04	0.173	8.93	0.49
RW129	Distal Spherulitic QP Rhyolite	Ca-carb, Ser	2.06	4.2	1.28	23.04	0.223	8.46	0.54
RW130	Distal Spherulitic QP Rhyolite	Ca-carb, Ser	0.53	2.0	1.49	18.51	0.146	7.22	0.53
RW131	Fragmental Rhyolite	Qtz, Ser	1.33	0.8	3.61	20.88	0.108	6.28	0.58

Table 7.1b. Trace element concentrations of Pinkos volcanic rocks

Sample Units	Lithofacies	Alteration Type	Zn ppm	Cu ppm	Pb ppm	Ba ppm	Cr ppm	Sc ppm	V ppm	Cs ppm	Li ppm	Rb ppm	Sr ppm	Be ppm	Cd ppm	Sb ppm	Tl ppm
RW132	Fragmental Rhyolite	Qtz, Ser	52	15.9	4.0	211	14	3.2	2.6	0.876	2.1	34.6	34.7	1.42	0.101	0.26	0.060
RW145	Coherent QP Rhyolite	Mg-Chl	39	7.50	7.2	1298	26	3.9	1.5	0.835	4.1	76.7	11.9	2.35	0.007	0.15	0.073
RW146	Fragmental Rhyolite	Fe-carb	177	34.8	7.2	162	29	2.8	0.8	0.559	1.9	36.8	38.4	1.74	0.636	0.14	0.065
RW147*	Coherent QP Rhyolite	Qtz, Ser	22	2.90	2.4	604	40	3.7	1.3	0.684	1.5	38.1	34.5	2.14	0.007	0.10	0.057
RW148	Coherent QP Rhyolite	Fe-carb	38	34.8	4.2	190	50	4.5	1.4	0.446	0.6	18.2	52.5	2.38	0.072	0.26	0.036
RW149	Coherent QP Rhyolite	Fe-carb	886	71.0	15	147	42	2.7	1.1	0.569	1.2	24.3	56.2	1.85	2.998	0.25	0.051
RW150	Fragmental Rhyolite	Fe-carb	71	2.80	5.7	355	16	3.3	0.9	1.237	2.7	56.0	28.2	2.51	0.199	0.24	0.118
RW151	Coherent QP Rhyolite	Qtz, Ser	74	23.6	3.3	295	34	4.8	1.4	0.867	1.0	38.0	46.5	1.67	0.138	0.25	0.078
RW152	Coherent QP Rhyolite	Qtz, Ser	69	5.60	3.6	264	33	3.2	1.6	0.348	1.3	16.0	49.9	1.93	0.130	0.15	0.028
RW153	Coherent QP Rhyolite	Qtz, Ser	22	9.30	2.4	245	45	3.2	1.0	0.341	3.5	21.2	22.1	1.70	0.007	0.13	0.036
RW154	Coherent QP Rhyolite	Qtz, Ser	39	11.0	3.1	888	31	4.0	1.4	0.830	4.0	50.9	50.3	2.31	0.026	0.18	0.078
RW155	Coherent QP Rhyolite	Qtz, Ser	34	4.60	2.7	787	33	3.9	1.4	1.038	5.2	67.6	38.8	2.16	0.007	0.22	0.086
RW156	Coherent QP Rhyolite	Qtz, Ser	33	15.5	2.7	802	40	3.0	1.0	1.109	4.2	58.6	54.0	1.73	0.007	0.13	0.099
RW157	Coherent QP Rhyolite	Qtz, Ser	128	20.4	3.5	585	56	3.7	1.0	0.741	4.5	43.5	43.8	1.93	0.166	0.13	0.059
RW158	Coherent QP Rhyolite	Qtz, Ser	116	13.3	3.6	353	15	2.9	0.4	0.954	2.9	75.8	28.9	2.20	0.171	0.12	0.075
RW159	Fragmental Rhyolite	Qtz, Ser	79	5.60	5.3	529	24	3.4	1.0	1.044	1.1	46.1	24.1	2.55	0.084	0.25	0.085
RW160	Fragmental Rhyolite	Qtz, Ser	96	59.9	3.0	262	26	3.1	0.4	0.595	1.3	22.6	40.9	1.94	0.136	0.24	0.042
RW161	Fragmental Rhyolite	Qtz, Ser	304	16.0	4.7	496	201	3.2	5.6	0.973	1.0	42.3	26.1	1.76	0.714	0.27	0.073
RW162	Fragmental Rhyolite	Qtz, Ser	98	2.90	2.9	1005	21	3.1	0.4	1.216	1.0	51.9	82.4	2.30	0.133	0.19	0.075

* Denotes least-altered sample suite.

Table 7.1b. Trace element concentrations of Pinkos volcanic rocks

Sample Units	Lithofacies	Alteration Type	Co ppm	Ni ppm	Mo ppm	Ga ppm	In ppm	Sn ppm	W ppm
RW132	Fragmental Rhyolite	Qtz, Ser	0.75	0.8	3.01	19.31	0.096	6.53	0.35
RW145	Coherent QP Rhyolite	Mg-Chl	0.51	0.8	1.60	22.94	0.200	6.72	0.82
RW146	Fragmental Rhyolite	Fe-carb	0.70	2.2	1.63	16.39	0.167	4.74	0.44
RW147*	Coherent QP Rhyolite	Qtz, Ser	0.52	0.8	4.73	24.19	0.171	2.76	0.68
RW148	Coherent QP Rhyolite	Fe-carb	0.92	0.8	2.94	19.29	0.219	7.12	0.64
RW149	Coherent QP Rhyolite	Fe-carb	1.00	0.8	3.60	16.16	0.528	7.75	0.55
RW150	Fragmental Rhyolite	Fe-carb	0.57	0.8	2.99	31.23	0.162	6.26	0.57
RW151	Coherent QP Rhyolite	Qtz, Ser	0.89	0.8	1.96	23.91	0.215	5.17	0.52
RW152	Coherent QP Rhyolite	Qtz, Ser	0.58	0.8	2.85	17.36	0.143	6.13	0.79
RW153	Coherent QP Rhyolite	Qtz, Ser	1.63	0.8	2.33	18.80	0.170	4.71	0.64
RW154	Coherent QP Rhyolite	Qtz, Ser	0.59	0.8	1.38	23.70	0.063	2.23	0.72
RW155	Coherent QP Rhyolite	Qtz, Ser	0.45	0.8	4.11	22.33	0.129	4.62	0.76
RW156	Coherent QP Rhyolite	Qtz, Ser	0.79	0.8	3.05	20.55	0.150	8.05	0.42
RW157	Coherent QP Rhyolite	Qtz, Ser	0.58	0.8	4.07	19.72	0.182	6.68	0.71
RW158	Coherent QP Rhyolite	Qtz, Ser	0.81	0.8	2.51	18.70	0.177	5.36	0.42
RW159	Fragmental Rhyolite	Qtz, Ser	0.61	0.8	3.53	24.49	0.226	7.18	0.62
RW160	Fragmental Rhyolite	Qtz, Ser	0.47	0.8	2.72	22.64	0.178	6.19	0.48
RW161	Fragmental Rhyolite	Qtz, Ser	1.28	4.4	3.54	24.40	0.226	6.68	0.60
RW162	Fragmental Rhyolite	Qtz, Ser	0.66	0.8	2.78	22.28	0.218	5.57	0.57

* Denotes least-altered sample suite.

Table 7.1c. Rare-earth element composition of Pinkos volcanic rocks

Sample Units	Lithofacies	Alteration Type	La ppm	Ce ppm	Pr ppm	Nd ppm	Sm ppm	Eu ppm	Gd ppm	Tb ppm	Dy ppm	Ho ppm	Er ppm	Tm ppm	Yb ppm	Lu ppm	Total REE ppm
RW043	Columnar-jointed QP Rhyolite	Fe-carb	44.5	107	14.9	65.9	17.5	2.92	20.4	3.62	24.8	5.27	15.8	2.40	15.7	2.35	343
RW044	Columnar-jointed QP Rhyolite	Fe-carb	30.5	79.8	11.1	48.8	13.5	3.04	14.8	2.58	18.2	4.03	12.5	1.91	12.7	1.88	255
RW045	Columnar-jointed QP Rhyolite	Fe-carb	29.6	73.5	10.2	45.6	12.5	2.89	15.2	2.67	19.0	4.19	12.9	1.95	13.1	1.92	245
RW046	Columnar-jointed QP Rhyolite	Fe-carb	54.6	131	17.9	79.2	20.6	3.17	21.7	3.49	22.4	4.69	14.1	2.11	13.9	2.08	391
RW047	Coherent QP Rhyolite	Fe-carb	57.3	136	18.5	81.0	20.4	2.91	22.4	3.74	25.4	5.45	17.0	2.55	16.8	2.55	412
RW048	Coherent QP Rhyolite	Fe-carb	50.8	119	16.4	72.2	19.1	2.87	22.3	3.80	26.4	5.62	16.7	2.50	16.1	2.39	376
RW049	Coherent QP Rhyolite	Fe-carb	50.8	122	16.8	74.5	19.5	3.57	22.4	3.76	24.9	5.19	15.4	2.31	15.4	2.27	379
RW050	Coherent QP Rhyolite	Fe-carb	54.5	132	18.2	79.3	20.6	3.26	22.0	3.57	23.1	4.87	14.6	2.15	14.0	2.09	394
RW051	Coherent QP Rhyolite	Qtz, Ser	45.2	108	14.7	66.0	17.5	2.74	20.8	3.59	25.0	5.36	15.9	2.35	15.2	2.23	344
RW052	Coherent QP Rhyolite	Fe-carb	41.5	103	14.1	61.7	16.7	2.35	19.9	3.71	26.4	5.90	18.5	2.89	19.1	2.85	338
RW053*	Coherent QP Rhyolite	Fe-carb	39.5	99.6	13.7	60.6	16.3	3.07	19.2	3.58	25.1	5.39	16.2	2.44	16.0	2.37	323
RW054	Coherent QP Rhyolite	Fe-carb	52.8	124	16.8	74.5	20.3	3.27	26.8	5.27	38.4	8.47	25.1	3.61	22.5	3.27	425
RW055	Coherent QP Rhyolite	Qtz, Ser	58.2	137	19.0	83.2	21.5	3.21	24.1	4.07	27.2	5.84	17.7	2.66	17.4	2.58	424
RW056	Coherent QP Rhyolite	Fe-carb	28.2	70.7	9.8	44.0	13.1	2.70	17.4	3.31	23.4	5.06	15.2	2.24	14.7	2.16	252
RW057	Mafic Intrusive	Fe-carb	4.3	11.1	1.7	8.3	2.5	1.03	3.2	0.54	3.5	0.75	2.2	0.33	2.2	0.33	42.0
RW058	Mafic Intrusive	Fe-carb	4.7	12.3	1.9	9.5	2.9	1.21	3.7	0.63	4.2	0.88	2.6	0.37	2.4	0.37	47.7
RW059	Spherulitic QP Rhyolite	Fe-carb	48.8	116	15.8	69.8	18.1	3.09	19.5	3.35	21.6	4.49	13.4	2.01	13.2	1.88	351
RW060	Spherulitic QP Rhyolite	Fe-carb	42.8	105	14.5	64.1	17.4	2.84	20.3	3.66	24.5	5.30	16.2	2.41	15.9	2.34	337
RW061	Columnar-jointed QP Rhyolite	Fe-carb	43.0	97.2	13.2	56.7	14.3	2.21	17.5	3.43	24.7	5.49	17.0	2.55	16.5	2.41	316
RW062	Columnar-jointed QP Rhyolite	Fe-carb	42.2	104	14.3	63.0	16.8	3.03	20.2	3.75	25.6	5.52	16.9	2.53	16.7	2.48	337
RW063*	Columnar-jointed QP Rhyolite	Fe-carb	41.4	96.1	13.2	58.7	15.8	2.55	18.3	3.15	20.0	4.09	12.1	1.79	11.7	1.64	300
RW064	Spherulitic QP Rhyolite	Mg-Chl	23.6	60.6	8.7	40.0	12.2	1.24	17.2	3.50	24.7	5.55	17.1	2.61	17.0	2.48	237
RW065	Mafic Intrusive	Ca-carb, Ser	8.3	20.8	3.2	15.6	4.7	1.73	5.6	0.97	6.2	1.34	3.9	0.56	3.7	0.56	77.2
RW066	Stringers/Stockwork (NW)	Mg-Chl	51.1	129	18.7	83.6	20.9	1.62	20.7	3.49	23.0	4.82	14.7	2.19	14.4	2.13	390
RW067	Stringers/Stockwork (NW)	Ca-carb, Ser	21.7	43.5	7.1	33.3	11.7	1.30	22.7	4.68	34.3	7.58	22.6	3.16	19.1	2.69	235
RW068	Spherulitic QP Rhyolite	Ca-carb, Ser	39.6	93.6	13.4	61.5	17.5	2.52	22.3	4.27	29.7	6.55	20.1	2.97	19.2	2.79	336
RW069	Distal Spherulitic QP Rhyolite	Ca-carb, Ser	24.5	69.1	9.2	41.7	12.9	1.14	17.1	3.30	22.7	4.90	15.1	2.29	15.2	2.25	241
RW070	Distal Spherulitic QP Rhyolite	Ca-carb, Ser	38.7	93.8	12.9	58.2	16.4	2.28	20.6	3.83	25.9	5.58	17.1	2.54	16.8	2.43	317
RW071	Distal Spherulitic QP Rhyolite	Ca-carb, Ser	50.4	119	16.5	72.9	18.6	2.34	22.0	3.97	27.5	5.93	18.2	2.74	17.9	2.61	381
RW072	Distal Spherulitic QP Rhyolite	Mg-Chl	68.4	159	22.2	98.9	25.7	3.17	27.9	4.53	29.1	5.99	18.2	2.70	17.4	2.53	486
RW073	Distal Spherulitic QP Rhyolite	Ca-carb, Ser	44.3	100	15.1	66.8	17.2	1.36	19.5	3.54	24.4	5.39	16.8	2.56	16.9	2.50	336
RW074	Distal Spherulitic QP Rhyolite	Ca-carb, Ser	46.9	115	15.8	69.4	18.3	3.02	20.3	3.61	23.8	4.91	14.6	2.16	14.0	1.97	354
RW075	Distal Spherulitic QP Rhyolite	Ca-carb, Ser	40.2	98.7	13.5	59.5	15.7	2.55	17.1	2.94	19.4	4.06	12.4	1.88	12.6	1.87	302
RW076	Mafic Intrusive	Ca-carb, Ser	6.3	15.7	2.4	12.1	3.6	1.46	4.5	0.77	5.2	1.08	3.3	0.48	3.2	0.48	60.4
RW077	Coherent QP Rhyolite	Ca-carb, Ser	50.1	120	16.7	74.7	20.2	3.35	22.7	3.89	26.1	5.56	16.7	2.49	16.5	2.47	381
RW078	Columnar-jointed QP Rhyolite	Ca-carb, Ser	45.7	111	15.3	68.9	18.6	2.97	20.8	3.62	23.5	4.81	14.3	2.13	13.8	1.97	347
RW080	Columnar-jointed QP Rhyolite	Ca-carb, Ser	46.2	113	15.6	69.5	18.2	3.20	20.3	3.56	23.7	4.84	14.4	2.14	14.1	2.07	351
RW081	Columnar-jointed QP Rhyolite	Fe-carb	52.8	124	17.2	78.0	21.0	3.26	23.7	3.90	25.7	5.40	16.2	2.41	15.9	2.35	392
RW082	Columnar-jointed QP Rhyolite	Fe-carb	57.0	135	18.9	84.9	23.1	2.56	25.2	4.22	27.0	5.55	16.6	2.46	16.0	2.33	421
RW083	Fragmental Rhyolite	Fe-carb	50.2	118	16.3	72.0	19.6	2.92	23.0	4.08	27.6	5.81	17.8	2.63	17.2	2.52	380
RW084	Fragmental Rhyolite	Fe-carb	43.2	108	14.9	66.7	17.9	3.05	19.9	3.30	21.3	4.20	12.0	1.77	11.7	1.73	330
RW085	Fragmental Rhyolite	Fe-carb	52.3	122	16.6	74.4	19.9	3.42	23.6	4.19	28.6	6.10	18.9	2.84	18.9	2.83	395
RW086	Fragmental Rhyolite	Fe-carb	42.7	107	14.8	64.8	17.2	3.17	18.1	3.10	19.4	3.92	11.7	1.77	11.8	1.70	321
RW087	Fragmental Rhyolite	Fe-carb	28.7	68.7	9.4	42.4	11.9	1.75	15.8	3.15	23.1	5.10	15.7	2.36	15.5	2.24	246

Table 7.1c. Rare-earth element composition of Pinkos volcanic rocks

Sample Units	Lithofacies	Alteration Type	La ppm	Ce ppm	Pr ppm	Nd ppm	Sm ppm	Eu ppm	Gd ppm	Tb ppm	Dy ppm	Ho ppm	Er ppm	Tm ppm	Yb ppm	Lu ppm	Total REE ppm
RW088	Fragmental Rhyolite	Fe-carb	25.5	62.0	8.4	37.9	11.7	2.09	16.7	3.19	21.8	4.55	13.4	1.98	12.9	1.88	224
RW089	Fragmental Rhyolite	Fe-carb	47.8	114	15.6	70.3	18.8	2.77	21.8	3.85	25.6	5.41	16.5	2.49	16.3	2.37	364
RW090	Fragmental Rhyolite	Fe-carb	40.4	96.6	13.3	58.5	16.0	2.47	19.4	3.47	24.0	5.23	15.7	2.36	15.5	2.27	315
RW091	Fragmental Rhyolite	Fe-carb	50.9	123	16.9	74.1	20.0	2.99	23.8	4.33	29.4	6.20	19.3	2.95	19.2	2.79	395
RW092	Fragmental Rhyolite	Fe-carb	47.7	115	16.2	70.1	18.7	3.27	21.0	3.65	24.0	4.93	15.0	2.27	15.0	2.18	359
RW093	Fragmental Rhyolite	Fe-carb	50.2	120	16.4	72.1	18.8	1.82	20.8	3.61	24.7	5.27	16.1	2.44	16.1	2.37	371
RW094	Fragmental Rhyolite	Fe-carb	48.9	123	16.9	74.7	20.1	3.40	22.9	4.06	27.5	5.73	17.1	2.54	16.4	2.37	385
RW095	Fragmental Rhyolite	Fe-carb	61.9	144	20.0	88.4	23.9	3.44	27.8	4.76	31.8	6.54	19.3	2.86	18.4	2.66	456
RW096	Fragmental Rhyolite	Fe-carb	46.3	111	15.3	67.1	18.2	3.11	21.9	3.88	26.6	5.53	16.7	2.53	16.6	2.45	357
RW097	Fragmental Rhyolite	Mg-Chl	46.7	109	15.1	66.9	17.6	3.06	19.5	3.45	23.6	5.05	15.6	2.37	15.6	2.27	345
RW098	Stringers/Stockwork (SE)	Mg-Chl	43.0	98.8	13.9	61.3	16.6	2.57	20.9	3.83	27.1	5.75	17.0	2.49	16.3	2.39	332
RW099	Stringers/Stockwork (SE)	Fe-carb	52.1	121	16.6	74.4	20.5	3.06	24.7	4.29	28.4	5.74	16.8	2.51	16.4	2.41	389
RW100	Stringers/Stockwork (SE)	Fe-carb	49.9	120	16.3	72.2	19.3	3.29	22.2	3.85	25.9	5.50	16.3	2.48	16.3	2.41	376
RW101	Stringers/Stockwork (SE)	Fe-carb	12.4	31.1	4.5	20.8	9.1	1.31	17.1	3.71	26.9	5.91	18.2	2.76	18.3	2.66	175
RW102	Stringers/Stockwork (SE)	Fe-carb	10.2	25.4	3.7	17.8	8.2	1.50	16.0	3.61	27.1	6.11	19.0	2.88	18.8	2.77	163
RW103	Stringers/Stockwork (SE)	Fe-carb	47.7	109	15.9	71.3	19.3	2.53	22.0	3.93	26.2	5.56	17.4	2.69	18.1	2.67	365
RW104	Coherent QP Rhyolite	Fe-carb	54.9	125	17.4	77.0	20.3	3.17	22.7	3.85	25.9	5.55	17.1	2.54	16.6	2.42	394
RW105	Coherent QP Rhyolite	Ca-carb, Ser	49.1	116	16.0	69.1	17.9	2.66	19.5	3.42	22.6	4.69	14.4	2.13	14.3	2.10	353
RW106	Mafic Intrusive	Ca-carb, Ser	7.5	18.7	2.9	14.3	4.5	1.90	5.7	0.96	6.4	1.33	4.0	0.58	3.9	0.60	73.3
RW107	Mafic Intrusive	Ca-carb, Ser	8.4	20.6	3.1	15.5	4.6	1.98	5.8	0.98	6.5	1.39	4.1	0.59	4.0	0.61	78.2
RW108	Coherent QP Rhyolite	Ca-carb, Ser	44.1	107	14.6	63.4	17.2	2.85	19.1	3.29	21.9	4.48	13.6	2.09	13.8	2.00	329
RW109	Stringers/Stockwork (SE)	Fe-carb	50.4	117	16.5	70.9	18.0	2.49	19.8	3.38	23.0	4.73	14.2	2.13	14.1	2.11	358
RW110	Stringers/Stockwork (SE)	Fe-carb	51.3	123	16.8	73.9	19.5	3.08	24.0	4.49	31.3	6.75	20.8	3.16	21.2	3.17	402
RW111	Coherent QP Rhyolite	Mg-Chl	31.9	75.7	10.9	47.9	12.7	1.38	16.3	3.04	21.6	4.81	15.0	2.31	15.4	2.27	261
RW112	Columnar-jointed QP Rhyolite	Fe-carb	45.5	109	15.2	66.4	17.4	2.63	19.8	3.54	23.7	4.95	15.2	2.29	15.1	2.22	343
RW113	Columnar-jointed QP Rhyolite	Fe-carb	47.2	113	15.6	68.4	18.2	2.51	20.3	3.50	23.6	5.01	15.3	2.35	15.4	2.28	353
RW114	Stringers/Stockwork (NW)	Mg-Chl	57.8	130	19.0	84.5	21.0	2.19	22.0	3.67	24.7	5.19	16.0	2.42	15.9	2.32	407
RW115	Stringers/Stockwork (NW)	Mg-Chl	23.5	66.1	8.3	35.3	10.7	1.01	15.7	3.11	21.9	4.84	15.0	2.33	15.1	2.26	225
RW116	Stringers/Stockwork (NW)	Mg-Chl	8.1	21.9	3.0	14.1	6.4	0.93	15.5	3.52	26.8	6.01	18.6	2.77	18.0	2.63	148
RW117	Stringers/Stockwork (NW)	Mg-Chl	16.6	43.7	6.1	26.6	9.2	0.62	13.7	2.79	20.8	4.62	14.8	2.26	15.1	2.26	179
RW118	Stringers/Stockwork (NW)	Mg-Chl	41.9	92.2	13.8	61.4	16.1	1.14	18.5	3.24	21.8	4.67	14.2	2.16	14.2	2.09	307
RW119	Spherulitic QP Rhyolite	Mg-Chl	48.8	114	15.7	70.4	18.6	3.41	21.3	3.77	25.4	5.48	17.3	2.62	17.4	2.58	367
RW120	Spherulitic QP Rhyolite	Qtz, Ser	49.5	118	16.3	70.6	19.1	2.94	22.4	4.01	27.3	5.95	18.4	2.77	18.6	2.79	379
RW121	Spherulitic QP Rhyolite	Qtz, Ser	43.8	109	15.1	65.6	17.3	3.17	19.5	3.54	24.0	5.08	15.9	2.41	15.9	2.28	343
RW122	Spherulitic QP Rhyolite	Fe-carb	51.8	111	14.4	59.2	13.8	2.16	14.9	2.54	16.9	3.69	11.6	1.82	12.4	1.89	318
RW123	Spherulitic QP Rhyolite	Mg-Chl	38.7	115	13.1	57.8	16.3	2.01	20.5	3.77	26.4	5.80	18.2	2.75	17.9	2.58	341
RW124	Spherulitic QP Rhyolite	Mg-Chl	54.5	103	18.1	79.6	18.8	1.52	21.0	3.57	24.1	5.33	17.1	2.63	17.2	2.56	369
RW125	Columnar-jointed QP Rhyolite	Mg-Chl	50.5	118	16.8	74.4	19.4	1.88	21.8	3.76	25.6	5.45	16.8	2.49	16.2	2.43	376
RW126	Columnar-jointed QP Rhyolite	Mg-Chl	25.7	62.0	8.8	39.6	10.7	2.33	12.4	2.10	13.8	2.91	8.6	1.29	8.5	1.28	200
RW127	Spherulitic QP Rhyolite	Mg-Chl	33.0	86.5	11.3	46.7	11.6	0.95	14.1	2.78	20.8	4.85	15.7	2.37	15.6	2.32	269
RW128	Distal Spherulitic QP Rhyolite	Ca-carb, Ser	44.0	108	14.8	65.7	17.8	3.22	20.4	3.53	23.4	5.08	15.8	2.40	16.0	2.39	343
RW129	Distal Spherulitic QP Rhyolite	Ca-carb, Ser	59.0	139	18.9	84.2	21.3	3.33	23.7	4.01	26.8	5.70	17.4	2.60	17.1	2.57	426
RW130	Distal Spherulitic QP Rhyolite	Ca-carb, Ser	44.9	104	14.2	61.9	16.5	2.56	20.3	3.74	25.9	5.51	16.5	2.40	15.5	2.25	336
RW131	Fragmental Rhyolite	Qtz, Ser	49.1	116	16.2	71.0	19.0	3.26	21.8	3.84	26.0	5.59	17.4	2.60	17.1	2.48	372

Table 7.1c. Rare-earth element composition of Pinkos volcanic rocks

Sample Units	Lithofacies	Alteration Type	La ppm	Ce ppm	Pr ppm	Nd ppm	Sm ppm	Eu ppm	Gd ppm	Tb ppm	Dy ppm	Ho ppm	Er ppm	Tm ppm	Yb ppm	Lu ppm	Total REE ppm
RW132	Fragmental Rhyolite	Qtz, Ser	51.7	122	17.0	74.3	19.2	2.68	21.2	3.69	25.2	5.40	16.5	2.50	16.6	2.48	381
RW145	Coherent QP Rhyolite	Mg-Chl	38.0	96.2	13.3	58.2	16.0	2.54	18.4	3.34	23.0	5.02	15.6	2.41	16.1	2.42	310
RW146	Fragmental Rhyolite	Fe-carb	36.0	87.3	11.9	53.8	14.7	2.49	17.6	3.12	21.2	4.48	13.7	2.12	13.9	2.07	284
RW147*	Coherent QP Rhyolite	Qtz, Ser	40.7	102	14.0	62.6	17.0	2.99	20.1	3.66	24.5	5.07	15.1	2.26	14.9	2.13	326
RW148	Coherent QP Rhyolite	Fe-carb	48.1	112	15.5	68.8	18.4	2.93	21.3	3.60	24.4	5.17	15.7	2.34	15.4	2.32	356
RW149	Coherent QP Rhyolite	Fe-carb	53.6	124	17.2	75.6	20.2	3.03	23.3	3.98	26.5	5.46	16.1	2.38	15.5	2.28	389
RW150	Fragmental Rhyolite	Fe-carb	58.2	141	19.2	83.7	21.1	2.94	22.8	3.93	26.6	5.73	17.9	2.74	18.5	2.79	427
RW151	Coherent QP Rhyolite	Qtz, Ser	40.2	96.8	13.6	60.7	16.6	2.79	19.7	3.61	24.9	5.42	17.3	2.73	18.8	2.91	326
RW152	Coherent QP Rhyolite	Qtz, Ser	48.0	115	15.9	70.7	18.9	3.02	21.1	3.66	24.6	5.29	16.0	2.42	16.1	2.34	363
RW153	Coherent QP Rhyolite	Qtz, Ser	45.7	111	15.3	67.1	17.5	2.62	20.3	3.68	25.3	5.55	16.8	2.54	16.9	2.50	353
RW154	Coherent QP Rhyolite	Qtz, Ser	52.0	128	18.1	81.4	22.2	3.39	23.9	4.13	26.9	5.28	15.0	2.18	13.8	1.97	399
RW155	Coherent QP Rhyolite	Qtz, Ser	39.8	97.0	13.3	59.5	16.0	2.66	17.8	3.11	21.3	4.59	14.2	2.17	14.3	2.09	308
RW156	Coherent QP Rhyolite	Qtz, Ser	53.8	127	17.5	77.0	20.6	3.07	24.3	4.24	27.6	5.76	17.1	2.58	17.2	2.55	401
RW157	Coherent QP Rhyolite	Qtz, Ser	42.4	101	14.2	62.0	17.3	2.94	20.3	3.63	24.7	5.18	15.3	2.28	15.0	2.21	329
RW158	Coherent QP Rhyolite	Qtz, Ser	40.7	97.9	13.7	61.7	17.3	2.72	20.1	3.42	22.9	4.87	14.6	2.20	14.5	2.20	319
RW159	Fragmental Rhyolite	Qtz, Ser	48.4	117	16.0	70.3	18.9	2.77	22.8	4.21	29.5	6.34	19.1	2.86	18.5	2.74	380
RW160	Fragmental Rhyolite	Qtz, Ser	47.8	115	15.9	69.2	18.4	2.66	21.4	3.84	25.8	5.53	16.7	2.53	16.6	2.47	364
RW161	Fragmental Rhyolite	Qtz, Ser	52.6	124	17.3	74.1	18.9	2.65	21.1	3.70	25.1	5.43	16.6	2.56	16.9	2.49	383
RW162	Fragmental Rhyolite	Qtz, Ser	48.1	118	16.3	71.1	19.2	2.93	22.2	3.95	25.8	5.28	15.3	2.26	14.3	2.06	367

* Denotes least-altered sample suite.

Table 7.2a. Pearson correlation matrix of major, trace, and rare-earth elements in rhyolite from whole-rock analytical data at Pinkos

	SiO2	*Al2O3*	*Na2O*	*K2O*	*CaO*	*Fe2O3*	*MgO*	*MnO*	*TiO2*	*P2O5*	*LOI*	*CO2*	*Zr*	*Hf*	*Ta*	*Y*	*Nb*	*U*	*Th*	*Cr*	*Sc*	*V*	*Ba*	*Cs*
Al2O3	0.03																							
Na2O	0.15	0.20																						
K2O	-0.06	0.14	-0.55																					
CaO	-0.44	-0.29	0.28	0.04																				
Fe2O3	-0.60	-0.25	-0.47	-0.09	-0.23																			
MgO	-0.35	-0.16	-0.59	-0.15	-0.35	0.61																		
MnO	-0.56	-0.27	0.17	0.00	0.64	0.23	-0.23																	
TiO2	-0.28	0.16	-0.13	0.05	-0.08	0.34	0.18	-0.07																
P2O5	-0.27	0.07	-0.11	0.00	-0.02	0.33	0.15	-0.01	0.97															
LOI	-0.77	-0.34	-0.29	0.24	0.68	0.28	0.16	0.62	0.00	0.04														
CO2	-0.53	-0.22	0.21	0.19	0.86	-0.13	-0.39	0.72	-0.10	-0.05	0.80													
Zr	0.11	0.47	0.00	0.33	-0.14	-0.34	-0.10	-0.27	-0.10	-0.26	-0.13	-0.05												
Hf	0.10	0.51	0.02	0.32	-0.16	-0.32	-0.10	-0.25	-0.18	-0.35	-0.13	-0.06	0.97											
Ta	0.05	0.47	0.05	0.26	-0.17	-0.23	-0.09	-0.18	-0.32	-0.45	-0.12	-0.08	0.72	0.86										
Y	-0.32	0.06	0.00	-0.05	0.09	0.13	0.27	0.11	-0.27	-0.32	0.21	0.08	0.14	0.27	0.50									
Nb	0.11	0.49	0.06	0.28	-0.20	-0.28	-0.12	-0.23	-0.27	-0.42	-0.17	-0.10	0.80	0.90	0.96	0.41								
U	0.07	0.47	0.11	0.22	-0.13	-0.22	-0.16	-0.12	-0.42	-0.52	-0.12	-0.04	0.54	0.69	0.87	0.50	0.82							
Th	0.07	0.48	0.11	0.19	-0.19	-0.22	-0.08	-0.16	-0.42	-0.53	-0.16	-0.11	0.56	0.72	0.94	0.51	0.88	0.92						
Cr	0.12	0.03	0.23	-0.02	-0.03	-0.12	-0.21	0.03	-0.05	-0.03	-0.15	0.03	0.00	0.00	0.06	-0.06	0.08	0.09	0.07					
Sc	-0.29	0.12	-0.07	-0.03	-0.04	0.36	0.17	-0.03	0.92	0.95	-0.01	-0.10	-0.32	-0.40	-0.49	-0.31	-0.46	-0.48	-0.50	-0.02				
V	-0.17	0.02	-0.03	-0.10	-0.04	0.29	0.10	-0.05	0.78	0.82	-0.04	-0.09	-0.40	-0.45	-0.44	-0.24	-0.42	-0.47	-0.49	0.27	0.80			
Ba	0.05	0.23	-0.39	0.61	-0.20	-0.03	0.01	-0.21	0.07	0.06	-0.05	-0.11	0.25	0.24	0.19	-0.11	0.24	0.13	0.14	0.07	0.04	-0.05		
Cs	-0.13	0.07	-0.56	0.83	0.06	0.00	-0.09	0.07	-0.03	-0.06	0.35	0.24	0.28	0.30	0.32	0.02	0.31	0.24	0.24	-0.09	-0.12	-0.14	0.51	
Li	-0.19	-0.10	-0.55	-0.19	-0.51	0.62	0.94	-0.33	0.13	0.08	-0.09	-0.60	-0.07	-0.07	-0.05	0.24	-0.08	-0.11	-0.03	-0.17	0.14	0.06	0.03	-0.16
Rb	-0.09	0.09	-0.53	0.91	0.11	-0.08	-0.19	0.07	0.00	-0.02	0.32	0.28	0.25	0.25	0.22	-0.05	0.25	0.19	0.16	-0.04	-0.06	-0.10	0.66	0.88
Sr	-0.27	-0.04	0.62	-0.15	0.81	-0.39	-0.52	0.53	-0.16	-0.10	0.37	0.69	-0.05	-0.06	-0.03	0.06	-0.04	0.01	0.00	0.06	-0.11	-0.11	-0.14	-0.12
Be	-0.12	0.27	-0.01	0.41	0.20	-0.19	-0.26	0.29	-0.08	-0.10	0.19	0.29	0.30	0.36	0.39	0.18	0.39	0.44	0.37	0.03	-0.13	-0.18	0.31	0.34
Cu	-0.17	-0.26	-0.03	-0.19	0.01	0.31	0.18	0.11	0.07	0.07	0.08	-0.01	-0.12	-0.13	-0.16	0.08	-0.14	-0.11	-0.17	-0.03	0.11	0.05	-0.23	-0.14
Zn	-0.19	-0.24	-0.08	-0.04	0.08	0.29	0.04	0.42	-0.13	-0.10	0.17	0.13	-0.24	-0.21	-0.12	0.07	-0.12	-0.09	-0.12	0.16	-0.10	-0.04	-0.03	0.13
Pb	-0.05	-0.21	0.20	-0.09	0.24	-0.06	-0.25	0.31	-0.20	-0.13	0.17	0.27	-0.20	-0.15	-0.05	0.08	-0.05	0.04	-0.04	0.18	-0.16	-0.08	-0.04	-0.06
S	0.02	-0.31	0.07	-0.04	0.10	0.00	-0.14	-0.03	-0.10	-0.06	0.08	0.09	-0.13	-0.13	-0.07	0.00	-0.05	-0.03	-0.11	-0.01	-0.06	0.11	-0.07	0.05
Cd	-0.08	-0.27	0.04	-0.07	0.18	0.05	-0.06	0.35	-0.11	-0.07	0.15	0.18	-0.22	-0.22	-0.19	-0.03	-0.17	-0.15	-0.20	0.13	-0.08	-0.01	-0.06	0.07
Sb	-0.08	-0.13	0.00	0.18	0.25	-0.10	-0.19	0.08	-0.01	0.02	0.24	0.29	0.07	0.04	0.03	-0.10	0.07	0.02	-0.02	0.07	0.00	-0.02	-0.03	0.25
Tl	-0.04	0.12	-0.51	0.86	0.05	-0.09	-0.21	0.09	-0.01	-0.03	0.27	0.23	0.28	0.28	0.24	-0.06	0.25	0.23	0.17	0.02	-0.08	-0.09	0.54	0.87
Co	-0.21	-0.12	-0.42	-0.26	-0.38	0.54	0.80	-0.35	0.33	0.32	-0.02	-0.45	-0.22	-0.23	-0.24	0.08	-0.26	-0.28	-0.23	-0.13	0.33	0.29	-0.05	-0.28
Ni	0.14	0.02	-0.03	0.32	-0.01	-0.16	-0.17	-0.05	0.01	0.01	-0.08	0.03	0.11	0.07	0.02	-0.01	0.04	0.08	0.03	0.41	0.02	0.08	0.06	0.12
Mo	-0.03	-0.06	0.14	-0.06	-0.02	0.14	-0.14	0.12	-0.12	-0.08	-0.05	0.07	-0.10	-0.09	-0.07	-0.10	-0.05	0.05	-0.01	0.23	-0.06	0.00	0.02	-0.14
Bi	-0.09	-0.22	0.06	-0.12	0.10	0.11	-0.04	0.22	-0.11	-0.05	0.11	0.11	-0.23	-0.22	-0.17	0.02	-0.17	-0.11	-0.16	0.10	-0.07	-0.03	-0.12	-0.11
Ga	-0.23	0.47	-0.29	0.50	-0.19	0.16	0.01	-0.01	0.21	0.11	0.07	-0.03	0.57	0.57	0.48	0.11	0.50	0.41	0.42	-0.01	0.13	-0.05	0.40	0.49
In	-0.07	0.09	0.17	0.22	0.23	-0.13	-0.43	0.46	-0.12	-0.10	0.13	0.34	0.02	0.07	0.14	0.11	0.13	0.18	0.13	0.21	-0.11	-0.09	0.13	0.25
Sn	-0.01	0.12	0.13	0.21	0.14	-0.06	-0.36	0.30	-0.08	-0.10	-0.01	0.15	-0.02	0.07	0.22	0.17	0.19	0.30	0.24	0.18	-0.09	-0.02	0.11	0.16
W	0.00	0.34	0.12	0.14	-0.10	-0.06	-0.21	-0.05	0.04	-0.05	-0.14	-0.01	0.43	0.41	0.26	-0.04	0.31	0.19	0.18	0.07	-0.03	-0.13	0.27	0.06
REE (T)	-0.01	0.18	0.34	0.17	0.30	-0.41	-0.43	0.24	-0.20	-0.19	0.12	0.37	0.20	0.25	0.35	0.24	0.34	0.39	0.38	0.10	-0.22	-0.18	-0.01	0.15

All values are different from 0 with a significance level alpha=0.05.

Table 7.2a. Pearson correlation matrix of major, trace, and rare-earth elements in rhyolite from whole-rock analytical data at Pinkos

	Li	*Rb*	*Sr*	*Be*	*Cu*	*Zn*	*Pb*	*S*	*Cd*	*Sb*	*Tl*	*Co*	*Ni*	*Mo*	*Bi*	*Ga*	*In*	*Sn*	*W*
Al2O3																			
Na2O																			
K2O																			
CaO																			
Fe2O3																			
MgO																			
MnO																			
TiO2																			
P2O5																			
LOI																			
CO2																			
Zr																			
Hf																			
Ta																			
Y																			
Nb																			
U																			
Th																			
Cr																			
Sc																			
V																			
Ba																			
Cs																			
Li																			
Rb	-0.25																		
Sr	-0.61	-0.11																	
Be	-0.31	0.44	0.20																
Cu	0.20	-0.19	-0.11	-0.12															
Zn	0.05	0.04	0.02	0.06	0.33														
Pb	-0.27	0.01	0.27	0.15	0.22	0.45													
S	-0.17	0.00	0.15	-0.12	0.10	0.05	0.35												
Cd	-0.09	0.00	0.15	0.03	0.22	0.85	0.43	0.13											
Sb	-0.26	0.21	0.16	-0.02	0.26	0.05	0.23	0.24	0.05										
Tl	-0.26	0.90	-0.13	0.42	-0.19	0.04	0.03	0.03	0.01	0.18									
Co	0.81	-0.32	-0.47	-0.41	0.09	-0.14	-0.25	-0.14	-0.11	-0.22	-0.31								
Ni	-0.14	0.17	-0.02	0.14	-0.10	-0.03	-0.01	-0.07	-0.01	0.04	0.23	-0.10							
Mo	-0.09	-0.08	0.07	0.02	0.16	0.09	0.17	0.08	0.02	0.00	-0.04	0.00	0.02						
Bi	-0.05	-0.12	0.12	-0.06	0.24	0.61	0.69	0.23	0.58	0.10	-0.06	0.00	-0.05	0.25					
Ga	0.03	0.47	-0.18	0.34	-0.07	-0.07	-0.24	-0.20	-0.18	0.05	0.51	-0.06	0.12	-0.06	-0.19				
In	-0.42	0.27	0.27	0.42	-0.01	0.61	0.46	0.04	0.58	0.07	0.28	-0.49	0.15	0.09	0.48	0.16			
Sn	-0.31	0.23	0.14	0.44	0.06	0.29	0.41	0.09	0.19	0.08	0.25	-0.44	0.17	0.16	0.17	0.08	0.58		
W	-0.12	0.12	0.03	0.14	0.10	0.03	0.14	-0.05	-0.03	0.16	0.04	-0.22	0.00	0.23	-0.01	0.28	0.19	0.26	
REE (T)	-0.52	0.17	0.44	0.41	-0.33	-0.04	0.23	0.11	0.08	0.15	0.20	-0.48	0.15	-0.06	0.06	0.07	0.39	0.28	0.05

All values are different from 0 with a significance level alpha=0.05.

Table 7.2b. Pearson correlation matrix of major, trace, and rare-earth elements in mafic intrusive rocks from whole-rock analytical data at Pinkos

	SiO2	*Al2O3*	*Na2O*	*K2O*	*CaO*	*Fe2O3*	*MgO*	*MnO*	*TiO2*	*P2O5*	*LOI*	*CO2*	*Zr*	*Hf*	*Ta*	*Y*	*Nb*	*U*	*Th*	*Cr*	*Sc*	*V*	*Ba*	*Cs*
Al2O3	0.37																							
Na2O	-0.35	0.06																						
K2O	-0.74	-0.23	0.47																					
CaO	-0.58	-0.05	-0.17	-0.05																				
Fe2O3	0.87	0.30	-0.39	-0.40	-0.65																			
MgO	-0.97	-0.24	0.25	0.76	0.60	-0.76																		
MnO	0.90	0.24	-0.25	-0.52	-0.79	0.76	-0.92																	
TiO2	0.92	0.12	-0.43	-0.65	-0.53	0.92	-0.88	0.76																
P2O5	0.95	0.37	-0.14	-0.76	-0.57	0.70	-0.98	0.89	0.81															
LOI	-0.93	-0.65	0.23	0.66	0.46	-0.84	0.85	-0.75	-0.82	-0.88														
CO2	-0.94	-0.57	0.40	0.80	0.33	-0.80	0.87	-0.73	-0.85	-0.87	0.97													
Zr	0.98	0.26	-0.25	-0.70	-0.67	0.80	-0.99	0.94	0.89	0.97	-0.86	-0.86												
Hf	0.98	0.27	-0.24	-0.72	-0.65	0.80	-1.00	0.94	0.89	0.98	-0.87	-0.87	1.00											
Ta	0.98	0.27	-0.24	-0.72	-0.65	0.80	-1.00	0.93	0.89	0.98	-0.87	-0.87	1.00	1.00										
Y	1.00	0.33	-0.29	-0.73	-0.59	0.86	-0.98	0.89	0.93	0.96	-0.92	-0.92	0.98	0.99	0.99									
Nb	0.97	0.28	-0.20	-0.70	-0.67	0.78	-0.99	0.94	0.86	0.98	-0.86	-0.86	1.00	1.00	1.00	0.98								
U	0.98	0.20	-0.28	-0.67	-0.69	0.85	-0.98	0.94	0.92	0.95	-0.85	-0.85	0.99	0.99	0.99	0.98	0.99							
Th	0.97	0.22	-0.22	-0.71	-0.66	0.78	-1.00	0.93	0.88	0.98	-0.84	-0.84	1.00	1.00	1.00	0.98	1.00	0.99						
Cr	-0.92	0.02	0.43	0.65	0.61	-0.86	0.92	-0.85	-0.97	-0.83	0.73	0.77	-0.92	-0.92	-0.92	-0.93	-0.90	-0.95	-0.92					
Sc	0.03	-0.10	-0.71	-0.04	0.29	0.36	0.14	-0.21	0.29	-0.26	-0.06	-0.15	-0.13	-0.13	-0.12	0.00	-0.18	-0.05	-0.16	-0.16				
V	-0.83	-0.41	-0.03	0.45	0.79	-0.64	0.87	-0.95	-0.62	-0.90	0.76	0.69	-0.89	-0.89	-0.88	-0.83	-0.91	-0.86	-0.88	0.69	0.45			
Ba	-0.05	0.23	0.70	0.54	-0.46	0.22	0.10	-0.04	0.01	-0.05	-0.13	0.08	-0.04	-0.04	-0.04	-0.01	-0.03	-0.02	-0.04	0.10	-0.16	-0.12		
Cs	-0.73	-0.14	0.58	0.99	-0.05	-0.42	0.75	-0.52	-0.67	-0.72	0.61	0.77	-0.69	-0.70	-0.70	-0.72	-0.68	-0.67	-0.70	0.68	-0.13	0.41	0.62	
Li	-0.69	-0.68	-0.24	0.18	0.67	-0.73	0.61	-0.62	-0.57	-0.67	0.83	0.68	-0.65	-0.66	-0.66	-0.70	-0.67	-0.65	-0.64	0.48	0.17	0.74	-0.63	0.10
Rb	-0.72	-0.25	0.48	1.00	-0.10	-0.38	0.73	-0.48	-0.63	-0.74	0.65	0.79	-0.67	-0.69	-0.69	-0.71	-0.67	-0.64	-0.68	0.62	-0.06	0.42	0.56	0.99
Sr	0.34	0.79	0.05	-0.10	-0.05	0.50	-0.16	0.06	0.31	0.22	-0.64	-0.55	0.18	0.19	0.20	0.32	0.18	0.18	0.15	-0.09	0.31	-0.15	0.53	-0.02
Be	0.97	0.47	-0.51	-0.72	-0.48	0.87	-0.90	0.86	0.87	0.87	-0.93	-0.96	0.91	0.91	0.91	0.94	0.90	0.91	0.88	-0.85	0.17	-0.77	-0.14	-0.72
Cu	-0.90	-0.49	0.22	0.89	0.29	-0.61	0.91	-0.73	-0.76	-0.95	0.90	0.93	-0.88	-0.89	-0.90	-0.91	-0.89	-0.84	-0.88	0.73	0.15	0.75	0.16	0.84
Zn	0.37	0.18	-0.12	0.19	-0.80	0.47	-0.34	0.69	0.23	0.32	-0.28	-0.18	0.42	0.40	0.39	0.33	0.42	0.43	0.38	-0.34	-0.17	-0.65	0.16	0.15
Pb	-0.72	-0.42	-0.09	0.73	0.35	-0.30	0.81	-0.70	-0.46	-0.89	0.68	0.68	-0.78	-0.78	-0.78	-0.73	-0.81	-0.71	-0.79	0.52	0.58	0.82	0.15	0.66
S	0.67	0.40	-0.01	-0.34	-0.72	0.45	-0.72	0.89	0.40	0.76	-0.58	-0.53	0.75	0.74	0.73	0.65	0.77	0.70	0.73	-0.51	-0.53	-0.95	-0.03	-0.32
Cd	0.29	0.41	-0.64	-0.15	-0.13	0.29	-0.18	0.42	0.11	0.17	-0.28	-0.32	0.22	0.21	0.20	0.20	0.21	0.20	0.16	-0.15	0.21	-0.32	-0.42	-0.21
Sb	-0.30	-0.51	-0.76	0.02	0.47	-0.16	0.34	-0.31	-0.12	-0.47	0.44	0.27	-0.35	-0.36	-0.37	-0.34	-0.40	-0.31	-0.37	0.07	0.69	0.58	-0.67	-0.11
Tl	-0.69	-0.26	0.40	0.99	-0.11	-0.33	0.72	-0.45	-0.59	-0.74	0.64	0.77	-0.66	-0.67	-0.68	-0.69	-0.66	-0.61	-0.67	0.58	0.01	0.42	0.52	0.97
Co	-0.94	-0.16	0.34	0.71	0.65	-0.75	0.98	-0.96	-0.85	-0.94	0.78	0.80	-0.98	-0.98	-0.98	-0.94	-0.98	-0.98	-0.98	0.92	0.13	0.88	0.19	0.72
Ni	-0.94	-0.05	0.39	0.67	0.64	-0.85	0.95	-0.89	-0.96	-0.88	0.77	0.80	-0.96	-0.96	-0.96	-0.95	-0.94	-0.98	-0.96	0.99	-0.08	0.76	0.09	0.70
Mo	0.92	0.45	-0.40	-0.65	-0.60	0.75	-0.90	0.95	0.75	0.90	-0.84	-0.85	0.92	0.91	0.91	0.89	0.92	0.90	0.89	-0.79	-0.09	-0.90	-0.18	-0.65
Bi	-	-	-	-	-	-	-	-	-	-	-	-	-	-	-	-	-	-	-	-	-	-	-	-
Ga	0.93	0.47	-0.32	-0.62	-0.65	0.77	-0.91	0.96	0.75	0.92	-0.87	-0.86	0.93	0.93	0.92	0.91	0.93	0.91	0.91	-0.79	-0.14	-0.93	-0.09	-0.61
In	0.93	0.50	-0.17	-0.51	-0.75	0.81	-0.90	0.95	0.76	0.91	-0.89	-0.83	0.93	0.93	0.92	0.91	0.94	0.92	0.91	-0.78	-0.18	-0.96	0.11	-0.49
Sn	-0.86	-0.70	0.24	0.75	0.34	-0.59	0.82	-0.76	-0.61	-0.89	0.90	0.91	-0.82	-0.82	-0.82	-0.83	-0.83	-0.77	-0.80	0.59	0.19	0.82	0.15	0.70
W	0.36	-0.15	0.35	0.12	-0.91	0.31	-0.47	0.68	0.27	0.47	-0.18	-0.06	0.52	0.51	0.50	0.39	0.54	0.52	0.53	-0.43	-0.60	-0.72	0.32	0.12
REE (T)	0.99	0.36	-0.27	-0.70	-0.59	0.89	-0.96	0.85	0.94	0.94	-0.94	-0.93	0.96	0.97	0.97	1.00	0.96	0.97	0.96	-0.91	0.04	-0.80	0.07	-0.68

* Bi concentrations were all below detection therefore correlation was not possible with other elements.
All values are different from 0 with a significance level alpha=0.05.

Table 7.2b. Pearson correlation matrix of major, trace, and rare-earth elements in mafic intrusive rocks from whole-rock analytical data at Pinkos

	Li	*Rb*	*Sr*	*Be*	*Cu*	*Zn*	*Pb*	*S*	*Cd*	*Sb*	*Tl*	*Co*	*Ni*	*Mo*	*Bi*	*Ga*	*In*	*Sn*	*W*
Al2O3																			
Na2O																			
K2O																			
CaO																			
Fe2O3																			
MgO																			
MnO																			
TiO2																			
P2O5																			
LOI																			
CO2																			
Zr																			
Hf																			
Ta																			
Y																			
Nb																			
U																			
Th																			
Cr																			
Sc																			
V																			
Ba																			
Cs																			
Li																			
Rb	0.16																		
Sr	-0.72	-0.12																	
Be	-0.64	-0.71	0.40																
Cu	0.60	0.88	-0.35	-0.86															
Zn	-0.43	0.22	-0.05	0.42	-0.07														
Pb	0.50	0.72	-0.07	-0.63	0.88	-0.15													
S	-0.57	-0.31	-0.02	0.65	-0.60	0.76	-0.76												
Cd	-0.08	-0.16	0.06	0.50	-0.15	0.65	-0.08	0.50											
Sb	0.76	0.00	-0.42	-0.16	0.41	-0.13	0.59	-0.46	0.34										
Tl	0.17	0.99	-0.12	-0.66	0.88	0.27	0.75	-0.30	-0.08	0.07									
Co	0.53	0.67	-0.02	-0.89	0.83	-0.48	0.76	-0.78	-0.32	0.23	0.65								
Ni	0.53	0.64	-0.10	-0.87	0.78	-0.37	0.60	-0.59	-0.17	0.15	0.61	0.95							
Mo	-0.62	-0.63	0.20	0.95	-0.82	0.60	-0.73	0.86	0.58	-0.24	-0.59	-0.93	-0.84						
Bi	-	-	-	-	-	-	-	-	-	-	-	-	-	-					
Ga	-0.68	-0.60	0.24	0.94	-0.83	0.61	-0.75	0.87	0.52	-0.32	-0.57	-0.93	-0.84	1.00	-				
In	-0.80	-0.49	0.33	0.91	-0.80	0.64	-0.73	0.87	0.42	-0.46	-0.46	-0.90	-0.83	0.96	-	0.98			
Sn	0.66	0.75	-0.42	-0.88	0.93	-0.31	0.85	-0.75	-0.45	0.42	0.74	0.79	0.66	-0.90	-	-0.90	-0.87		
W	-0.42	0.16	-0.30	0.23	-0.17	0.72	-0.41	0.73	0.00	-0.48	0.15	-0.55	-0.47	0.44	-	0.49	0.57	-0.19	
REE (T)	-0.74	-0.68	0.41	0.93	-0.90	0.30	-0.69	0.60	0.16	-0.37	-0.66	-0.91	-0.94	0.86	-	0.88	0.90	-0.82	0.36

* Bi concentrations were all below detection therefore correlation was not possible with other elements.
All values are different from 0 with a significance level alpha=0.05.

Table 7.3. Criteria used to select least-altered footwall rhyolite samples at Pinkos

Criteria	Least-altered footwall QP rhyolite
Na_2O	> 3 wt.%
L.O.I.	< 3 wt.%
CO_2	< 2 wt.%
Cu	< 45 ppm
Zn	< 35 ppm
Ishikawa AI	< 0.40
CCPI	< 0.35
La_N/Yb_N	1.9 - 2.4

Notes: AI = alteration index = (K2O+MgO)/(K2O+Na2O+CaO+MgO), in wt.% (Ishikawa *et al*, 1976); CCPI = chlorite-carbonate-pyrite index = (MgO+FeO)/(MgO+FeO+Na2O+K2O), in wt.%, total Fe as FeO; L.O.I. = loss-on-ignition; N = chondrite-normalized (after McDonough and Sun, 1995). Least-altered samples were selected by comparison with typical fresh-rock compositions for high silica rhyolites elsewhere in the Abitibi subprovince. The criteria listed above are partial to the dataset in the present study; however the indicated ranges are similar to other alteration studies (e.g., Barrett et al, 1999; Koopman et al, 1999; Prior et al, 1999a, b).

Table 7.4. Immobile element concentrations and magmatic affinities of Pinkos volcanic rocks

Sample Units	Lithofacies	Alteration Type	TiO2 wt.%	Al2O3 wt.%	Zr ppm	Hf ppm	Ta ppm	Y ppm	Nb ppm	U ppm	Th ppm	Yb ppm	Lu ppm	Zr/Y ratio
RW043	Columnar-jointed QP Rhyolite	Fe-carb	0.22	12.52	551	15.52	1.989	136.33	30.075	1.523	5.984	15.704	2.348	4.04
RW044	Columnar-jointed QP Rhyolite	Fe-carb	0.24	11.25	557	15.67	2.075	98.71	31.358	1.606	6.168	12.681	1.88	5.64
RW045	Columnar-jointed QP Rhyolite	Fe-carb	0.23	11.48	580	15.97	2.038	109.73	31.247	1.538	5.964	13.107	1.924	5.29
RW046	Columnar-jointed QP Rhyolite	Fe-carb	0.21	9.82	535	14.48	1.864	121.24	27.856	1.369	5.328	13.899	2.076	4.41
RW047	Coherent QP Rhyolite	Fe-carb	0.2	11.29	523	15.21	2.139	144.37	31.177	1.638	6.577	16.84	2.553	3.62
RW048	Coherent QP Rhyolite	Fe-carb	0.19	10.47	476	13.79	1.987	155.1	28.408	1.48	5.989	16.099	2.385	3.07
RW049	Coherent QP Rhyolite	Fe-carb	0.24	10.83	577	15.83	2.044	133.8	30.732	1.517	6.117	15.37	2.273	4.31
RW050	Coherent QP Rhyolite	Fe-carb	0.23	11.1	564	15.55	2.04	122.3	30.634	1.448	5.83	14.021	2.089	4.61
RW051	Coherent QP Rhyolite	Qtz, Ser	0.2	10.94	497	14.57	2.038	140.5	30.072	1.567	6.093	15.176	2.227	3.54
RW052	Coherent QP Rhyolite	Fe-carb	0.23	11.54	584	17.07	2.42	150.95	35.001	1.888	7.371	19.116	2.845	3.87
RW053*	Coherent QP Rhyolite	Fe-carb	0.24	11.19	599	16.46	2.091	140.71	31.594	1.564	6.181	16.035	2.374	4.26
RW054	Coherent QP Rhyolite	Fe-carb	0.21	10.79	524	15.57	2.271	251.58	33.038	1.747	7.027	22.516	3.268	-
RW055	Coherent QP Rhyolite	Qtz, Ser	0.22	10.73	547	15.72	2.23	155.62	32.726	1.694	6.722	17.422	2.578	3.51
RW056	Coherent QP Rhyolite	Fe-carb	0.25	10.74	603	16.43	2.102	132.84	33.084	1.435	5.893	14.66	2.159	4.54
RW057	Mafic Intrusive	Fe-carb	1.72	12.6	47	1.3	0.205	19.69	3.435	0.062	0.256	2.185	0.328	2.39
RW058	Mafic Intrusive	Fe-carb	1.71	13.24	53	1.49	0.238	22.67	3.996	0.064	0.295	2.442	0.373	2.34
RW059	Spherulitic QP Rhyolite	Fe-carb	0.19	9.36	454	12.74	1.775	116.27	26.289	1.386	5.453	13.155	1.881	3.90
RW060	Spherulitic QP Rhyolite	Fe-carb	0.19	10.7	458	13.13	1.863	147.98	28.533	1.25	5.739	15.871	2.339	3.10
RW061	Columnar-jointed QP Rhyolite	Fe-carb	0.22	11.12	468	13.49	1.978	147.12	28.939	1.583	6.074	16.503	2.405	3.18
RW062	Columnar-jointed QP Rhyolite	Fe-carb	0.22	11.93	533	14.61	1.917	141.74	28.464	1.431	5.749	16.734	2.483	3.76
RW063*	Columnar-jointed QP Rhyolite	Fe-carb	0.23	10.89	555	15.06	1.894	108.11	29.561	1.384	5.789	11.723	1.636	5.13
RW064	Spherulitic QP Rhyolite	Mg-Chl	0.18	10.83	483	14.04	2.045	148.74	30.13	1.615	6.355	16.995	2.481	3.25
RW065	Mafic Intrusive	Ca-carb, Ser	2.05	13.14	81	2.22	0.362	34.41	5.95	0.115	0.45	3.74	0.555	2.35
RW066	Stringers/Stockwork (NW)	Mg-Chl	0.21	10.98	502	14.22	1.957	129.22	29.632	1.475	5.894	14.386	2.134	3.88
RW067	Stringers/Stockwork (NW)	Ca-carb, Ser	0.24	10.58	592	16.09	2.042	230.25	30.372	1.494	5.975	19.125	2.686	-
RW068	Spherulitic QP Rhyolite	Ca-carb, Ser	0.22	11.01	570	16.15	2.252	187.96	33.556	1.692	6.831	19.238	2.792	3.03
RW069	Distal Spherulitic QP Rhyolite	Ca-carb, Ser	0.23	11.03	573	15.28	1.976	132.75	29.519	1.434	5.83	15.245	2.247	4.32
RW070	Distal Spherulitic QP Rhyolite	Ca-carb, Ser	0.19	10.64	480	14.07	2.066	156.92	29.383	1.54	6.297	16.767	2.425	3.06
RW071	Distal Spherulitic QP Rhyolite	Ca-carb, Ser	0.2	11.25	526	15.24	2.225	168.72	32.115	1.63	6.923	17.875	2.605	3.12
RW072	Distal Spherulitic QP Rhyolite	Mg-Chl	0.21	11.69	566	16.43	2.353	165.19	35.218	1.833	7.202	17.425	2.532	3.43
RW073	Distal Spherulitic QP Rhyolite	Ca-carb, Ser	0.18	10.02	469	13.76	2.011	147.21	29.959	1.518	6.335	16.863	2.495	3.19
RW074	Distal Spherulitic QP Rhyolite	Ca-carb, Ser	0.23	11.19	568	16.13	2.18	124.43	31.53	1.567	6.509	13.953	1.972	4.56
RW075	Distal Spherulitic QP Rhyolite	Ca-carb, Ser	0.21	10.16	520	14.36	1.887	104.25	28.256	1.396	5.725	12.563	1.872	4.99
RW076	Mafic Intrusive	Ca-carb, Ser	1.95	12.05	72	1.96	0.316	28.81	5.185	0.101	0.4	3.162	0.481	2.50
RW077	Coherent QP Rhyolite	Ca-carb, Ser	0.24	10.82	566	15.64	2.022	146.67	30.205	1.474	5.948	16.538	2.466	3.86
RW078	Columnar-jointed QP Rhyolite	Ca-carb, Ser	0.22	10.58	553	15.23	2.089	120.55	31.189	1.517	6.144	13.801	1.974	4.59
RW080	Columnar-jointed QP Rhyolite	Ca-carb, Ser	0.22	10.4	570	15.42	2.041	119.84	30.749	1.532	6.22	14.139	2.07	4.76
RW081	Columnar-jointed QP Rhyolite	Fe-carb	0.22	10.65	567	15.4	1.998	140.29	30.489	1.451	6.01	15.88	2.347	4.04
RW082	Columnar-jointed QP Rhyolite	Fe-carb	0.16	8.48	425	12.13	1.781	146.46	26.635	1.372	5.443	15.967	2.331	2.90
RW083	Fragmental Rhyolite	Fe-carb	0.2	10.82	512	14.83	2.167	160.11	31.799	1.598	6.608	17.242	2.52	3.20
RW084	Fragmental Rhyolite	Fe-carb	0.23	10.3	548	15.15	2.014	107.35	30.369	1.375	5.981	11.743	1.725	5.10
RW085	Fragmental Rhyolite	Fe-carb	0.23	10.88	580	15.91	2.089	164.67	31.937	1.568	6.174	18.866	2.827	3.52
RW086	Fragmental Rhyolite	Fe-carb	0.23	11.22	574	15.82	2.091	98.69	30.974	1.504	6.268	11.753	1.7	5.82
RW087	Fragmental Rhyolite	Fe-carb	0.18	10.28	451	12.99	1.922	142.49	28.167	1.32	5.221	15.484	2.236	3.17

Table 7.4. Immobile element concentrations and magmatic affinities of Pinkos volcanic rocks

Sample Units	Lithofacies	Alteration Type	TiO2 wt.%	Al2O3 wt.%	Zr ppm	Hf ppm	Ta ppm	Y ppm	Nb ppm	U ppm	Th ppm	Yb ppm	Lu ppm	Zr/Y ratio
RW088	Fragmental Rhyolite	Fe-carb	0.15	9.48	379	10.92	1.566	125.27	23.46	1.233	4.62	12.85	1.877	3.03
RW089	Fragmental Rhyolite	Fe-carb	0.18	10.44	456	13.32	2.018	146.94	29.247	1.499	6.18	16.291	2.369	3.10
RW090	Fragmental Rhyolite	Fe-carb	0.18	10.76	457	12.8	1.818	146.06	27.116	1.398	5.526	15.473	2.268	3.13
RW091	Fragmental Rhyolite	Fe-carb	0.2	11.49	526	15.35	2.268	170.88	32.992	1.658	6.908	19.187	2.785	3.08
RW092	Fragmental Rhyolite	Fe-carb	0.22	11.47	555	15.24	2.028	127	30.396	1.47	6.005	15.005	2.18	4.37
RW093	Fragmental Rhyolite	Fe-carb	0.23	10.77	539	14.85	1.949	139.77	28.622	1.481	5.81	16.122	2.374	3.86
RW094	Fragmental Rhyolite	Fe-carb	0.23	10.77	567	15.96	2.176	143.86	32.126	1.624	6.428	16.447	2.368	3.94
RW095	Fragmental Rhyolite	Fe-carb	0.19	11.61	489	14.32	2.079	180.7	31.053	1.569	6.246	18.427	2.663	2.71
RW096	Fragmental Rhyolite	Fe-carb	0.21	10.86	520	14.86	2.131	154.79	30.883	1.607	6.452	16.597	2.451	3.36
RW097	Fragmental Rhyolite	Mg-Chl	0.21	10.32	523	14.41	1.898	137.93	28.628	1.406	5.622	15.59	2.274	3.79
RW098	Stringers/Stockwork (SE)	Mg-Chl	0.21	10.21	516	14.46	2.01	153.29	30.136	1.483	5.93	16.327	2.394	3.37
RW099	Stringers/Stockwork (SE)	Fe-carb	0.17	9.63	455	13.45	1.961	155.79	27.935	1.484	6.101	16.371	2.406	2.92
RW100	Stringers/Stockwork (SE)	Fe-carb	0.26	12.33	657	17.47	2.224	137.37	33.969	1.66	6.625	16.347	2.406	4.78
RW101	Stringers/Stockwork (SE)	Fe-carb	0.23	10.85	555	15.93	2.269	162.22	33.48	1.675	6.849	18.305	2.659	3.42
RW102	Stringers/Stockwork (SE)	Fe-carb	0.21	10.65	528	15.2	2.16	169.4	32.287	1.636	6.622	18.816	2.768	3.12
RW103	Stringers/Stockwork (SE)	Fe-carb	0.2	10.64	509	14.44	2.124	148.97	31.771	1.432	6.409	18.058	2.674	3.42
RW104	Coherent QP Rhyolite	Fe-carb	0.24	11.05	595	16.04	2.082	145.22	32.292	1.636	6.158	16.621	2.423	4.10
RW105	Coherent QP Rhyolite	Ca-carb, Ser	0.22	10.36	565	15.34	2.026	117.27	31.147	1.481	5.955	14.251	2.096	4.82
RW106	Mafic Intrusive	Ca-carb, Ser	1.95	12.69	92	2.49	0.404	34.45	6.912	0.127	0.518	3.928	0.603	2.67
RW107	Mafic Intrusive	Ca-carb, Ser	2	13.65	92	2.48	0.402	36.14	6.798	0.128	0.497	3.976	0.611	2.55
RW108	Coherent QP Rhyolite	Ca-carb, Ser	0.24	10.83	572	15.78	2.031	111.23	31.067	1.469	6.019	13.812	2.004	5.14
RW109	Stringers/Stockwork (SE)	Fe-carb	0.21	9.83	536	14.71	1.954	124.55	30.247	1.45	5.675	14.135	2.106	4.30
RW110	Stringers/Stockwork (SE)	Fe-carb	0.21	10.51	523	14.78	2.062	185.81	30.046	1.617	6.289	21.172	3.169	2.81
RW111	Coherent QP Rhyolite	Mg-Chl	0.17	9.52	435	12.93	1.889	137.73	26.565	1.302	5.808	15.435	2.272	3.16
RW112	Columnar-jointed QP Rhyolite	Fe-carb	0.23	10.86	542	15.07	1.966	129.1	29.654	1.457	5.883	15.061	2.224	4.20
RW113	Columnar-jointed QP Rhyolite	Fe-carb	0.2	11.84	534	15.1	2.103	131.26	32.244	1.788	6.407	15.367	2.279	4.07
RW114	Stringers/Stockwork (NW)	Mg-Chl	0.18	10.48	446	12.93	1.888	142.85	30.262	1.393	5.766	15.929	2.322	3.12
RW115	Stringers/Stockwork (NW)	Mg-Chl	0.22	10.46	527	14.53	1.923	135.07	29.09	1.308	5.604	15.129	2.255	3.90
RW116	Stringers/Stockwork (NW)	Mg-Chl	0.21	10.85	526	15.21	2.107	169.11	31.259	1.565	6.33	17.974	2.627	3.11
RW117	Stringers/Stockwork (NW)	Mg-Chl	0.18	10.05	468	13.4	1.87	122.58	28.168	1.47	5.789	15.08	2.264	3.82
RW118	Stringers/Stockwork (NW)	Mg-Chl	0.21	10.05	508	13.93	1.817	127.95	27.824	1.368	5.307	14.179	2.085	3.97
RW119	Spherulitic QP Rhyolite	Mg-Chl	0.24	11.49	572	15.78	2.061	150.17	31.126	1.564	6.166	17.408	2.582	3.81
RW120	Spherulitic QP Rhyolite	Qtz, Ser	0.21	10.96	532	15.2	2.132	164.32	32.631	1.587	6.559	18.562	2.791	3.24
RW121	Spherulitic QP Rhyolite	Qtz, Ser	0.22	11.67	565	15.76	2.051	134.31	30.225	1.459	6.06	15.906	2.283	4.21
RW122	Spherulitic QP Rhyolite	Fe-carb	0.14	11.65	322	9.41	1.445	98.98	21.231	1.481	5.762	12.42	1.889	3.25
RW123	Spherulitic QP Rhyolite	Mg-Chl	0.2	10.58	543	15.38	2.148	161.41	32.18	1.649	6.478	17.852	2.581	3.36
RW124	Spherulitic QP Rhyolite	Mg-Chl	0.2	10.64	519	14.91	2.168	150.31	31.422	1.588	6.624	17.223	2.559	3.45
RW125	Columnar-jointed QP Rhyolite	Mg-Chl	0.24	11.25	596	16.55	2.123	140.81	31.681	1.582	6.365	16.226	2.428	4.23
RW126	Columnar-jointed QP Rhyolite	Mg-Chl	0.86	10.81	299	8.28	1.151	77.6	17.682	0.73	3.064	8.514	1.284	3.85
RW127	Spherulitic QP Rhyolite	Mg-Chl	0.21	9.46	513	14.28	1.921	143.51	29.546	1.374	5.671	15.558	2.321	3.57
RW128	Distal Spherulitic QP Rhyolite	Ca-carb, Ser	0.23	11.01	555	15.33	2.047	136.27	30.636	1.628	6.178	16.044	2.387	4.07
RW129	Distal Spherulitic QP Rhyolite	Ca-carb, Ser	0.23	11.33	569	16.05	2.231	149.61	33.361	1.636	6.695	17.083	2.569	3.80
RW130	Distal Spherulitic QP Rhyolite	Ca-carb, Ser	0.2	9.19	490	13.43	1.759	148.98	25.997	1.46	5.234	15.454	2.247	3.29
RW131	Fragmental Rhyolite	Qtz, Ser	0.21	10.39	532	15.14	2.115	151.12	32.119	1.596	6.271	17.137	2.479	3.52

Table 7.4. Immobile element concentrations and magmatic affinities of Pinkos volcanic rocks

Sample Units	Lithofacies	Alteration Type	TiO2 wt.%	Al2O3 wt.%	Zr ppm	Hf ppm	Ta ppm	Y ppm	Nb ppm	U ppm	Th ppm	Yb ppm	Lu ppm	Zr/Y ratio
RW132	Fragmental Rhyolite	Qtz, Ser	0.2	10.16	518	14.88	2.134	145.18	32.613	1.669	6.365	16.604	2.482	3.57
RW145	Coherent QP Rhyolite	Mg-Chl	0.2	11.46	532	15.08	2.064	126.03	31.687	1.518	6.15	16.119	2.422	4.22
RW146	Fragmental Rhyolite	Fe-carb	0.19	8.68	457	12.7	1.716	120.29	25.622	1.292	5.144	13.912	2.074	3.80
RW147*	Coherent QP Rhyolite	Qtz, Ser	0.22	11.82	575	15.5	2.059	125.56	31.409	1.542	6.09	14.871	2.132	4.58
RW148	Coherent QP Rhyolite	Fe-carb	0.23	11.49	571	16.16	2.211	136.73	33.504	1.574	6.366	15.407	2.323	4.18
RW149	Coherent QP Rhyolite	Fe-carb	0.17	9.92	427	12.58	1.799	152.55	26.887	1.392	5.373	15.544	2.275	2.80
RW150	Fragmental Rhyolite	Fe-carb	0.23	12.03	587	16.67	2.336	152.99	35.475	1.802	7.051	18.539	2.789	3.84
RW151	Coherent QP Rhyolite	Qtz, Ser	0.22	10.36	540	14.53	1.879	145.77	28.268	1.428	5.412	18.819	2.908	3.70
RW152	Coherent QP Rhyolite	Qtz, Ser	0.2	11.12	490	14.02	1.961	141.06	29.519	1.493	5.882	16.053	2.342	3.47
RW153	Coherent QP Rhyolite	Qtz, Ser	0.21	10.91	534	15.35	2.133	144.01	31.486	1.614	6.448	16.869	2.501	3.71
RW154	Coherent QP Rhyolite	Qtz, Ser	0.23	11.28	600	16.01	2.057	130.41	32.222	1.545	6.083	13.833	1.965	4.60
RW155	Coherent QP Rhyolite	Qtz, Ser	0.23	10.66	564	15.08	1.943	118.51	31.172	1.341	5.919	14.31	2.088	4.76
RW156	Coherent QP Rhyolite	Qtz, Ser	0.2	10.96	515	14.96	2.14	155.16	30.698	1.633	6.589	17.185	2.546	3.32
RW157	Coherent QP Rhyolite	Qtz, Ser	0.24	10.56	542	15.12	1.934	135.14	29.601	1.405	5.697	14.959	2.213	4.01
RW158	Coherent QP Rhyolite	Qtz, Ser	0.19	9.08	455	13.11	1.784	128.68	27.405	1.38	5.399	14.519	2.196	3.54
RW159	Fragmental Rhyolite	Qtz, Ser	0.23	11.59	549	16.11	2.266	170.57	34.875	1.751	6.926	18.548	2.735	3.22
RW160	Fragmental Rhyolite	Qtz, Ser	0.19	10.17	493	14.39	2.095	151.76	30.472	1.586	6.447	16.629	2.469	3.25
RW161	Fragmental Rhyolite	Qtz, Ser	0.22	10.91	529	15.11	2.226	141.25	33.445	1.665	6.775	16.909	2.485	3.75
RW162	Fragmental Rhyolite	Qtz, Ser	0.2	10.39	523	14.8	2.091	129.75	31.242	1.55	6.263	14.339	2.058	4.03

* Denotes least-altered sample suite.

Table 7.5. Mass changes for Pinkos footwall rhyolite

Sample	SiO2	Al2O3	Na2O	K2O	CaO	Fe2O3	MgO	MnO	TiO2	P2O5	S	CO2	Net
Units	g/100g	g/100g	g/100g	g/100g	g/100g	g/100g	g/100g	g/100g	g/100g	g/100g	g/100g	g/100g	g/100g
Mass changes in footwall rhyolite													
Precursor	**78.47**	**11.30**	**3.59**	**1.63**	**0.84**	**1.97**	**0.48**	**0.04**	**0.23**	**0.02**	**0.02**	**1.57**	**100.15**
RW043	1.08	1.80	-1.46	1.04	0.44	0.11	0.16	0.02	0.00	0.00	-0.01	0.55	3.74
RW044	1.66	0.34	-3.45	2.15	0.57	0.18	0.25	0.02	0.02	0.00	-0.01	0.80	2.53
RW045	-1.15	0.11	-1.75	0.85	-0.26	0.72	0.10	0.03	0.00	0.00	0.08	0.33	-0.94
RW046	11.93	-0.72	-3.57	1.68	-0.31	-0.89	-0.13	-0.01	0.00	0.00	-0.01	-0.73	7.23
RW047	4.23	1.14	0.69	0.10	0.25	2.46	0.17	0.07	-0.01	-0.01	-0.01	1.34	10.43
RW048	11.91	1.38	0.43	0.44	1.96	2.84	0.29	0.08	0.00	-0.01	-0.01	2.34	21.64
RW049	-1.74	-0.48	-2.20	2.25	0.11	1.06	0.07	0.02	0.01	0.00	0.00	0.72	-0.18
RW050	-1.90	0.04	0.52	-0.11	0.57	1.51	0.06	0.04	0.01	0.00	0.00	1.52	2.27
RW051	13.25	1.39	1.91	-0.40	0.16	0.22	-0.12	0.02	0.00	-0.01	0.54	0.03	17.00
RW052	-2.96	0.09	-0.81	0.89	-0.49	1.54	0.05	0.00	0.00	-0.01	0.05	0.28	-1.38
RW053*	-4.22	-0.53	-0.06	0.26	0.39	0.46	-0.02	0.00	0.00	0.00	0.00	0.40	-3.31
RW054	-1.60	0.57	-1.29	1.50	2.94	1.53	1.59	0.08	0.00	-0.01	-0.01	4.24	9.53
RW055	0.98	0.01	-0.44	0.83	0.89	1.34	0.23	0.01	0.00	-0.01	-0.01	1.23	5.05
RW056	-5.50	-1.03	0.60	-0.29	1.04	0.00	0.16	0.02	0.01	0.00	-0.01	1.18	-3.82
RW059	23.81	0.58	0.49	-0.12	1.38	0.14	0.18	0.05	0.01	-0.01	0.02	1.62	28.17
RW060	17.94	2.16	3.25	-1.12	1.78	1.04	-0.12	0.09	0.01	-0.01	-0.01	1.35	26.35
RW061	16.43	2.39	1.39	-0.33	0.38	2.93	-0.27	0.08	0.04	-0.01	-0.01	-0.40	22.64
RW062	5.73	1.60	0.12	-0.23	0.17	-0.10	0.19	-0.01	0.01	0.00	-0.01	0.02	7.49
RW063*	5.76	0.01	0.48	-0.54	-0.33	-0.86	-0.09	-0.01	0.01	0.00	-0.01	-0.86	3.56
RW064	13.19	1.62	-3.58	0.43	-0.79	3.27	3.99	0.00	-0.02	-0.01	-0.01	-1.45	16.63
RW066	11.89	1.31	-3.02	0.61	-0.38	1.31	2.44	-0.01	0.01	0.00	-0.01	-0.85	13.31
RW067	-11.93	-1.00	-3.59	-0.64	0.34	4.41	5.47	0.04	0.00	0.00	-0.01	-0.06	-6.96
RW068	-0.18	-0.17	-1.47	0.02	0.05	0.52	1.73	-0.01	-0.01	-0.01	-0.01	-0.37	0.10
RW069	-2.49	-0.21	-3.58	-0.05	-0.81	3.07	3.48	-0.02	0.00	-0.01	-0.01	-1.48	-2.10
RW070	12.02	1.48	0.65	-0.69	1.00	1.56	2.07	0.03	0.00	-0.01	0.02	1.16	19.28
RW071	4.00	1.03	0.86	-0.62	0.73	1.19	1.35	-0.01	-0.01	-0.01	-0.01	0.87	9.36
RW072	2.42	0.60	-1.10	0.24	-0.51	-0.27	1.04	-0.01	-0.02	-0.01	-0.01	-1.03	1.35
RW073	16.39	1.01	-3.08	0.14	-0.65	4.14	3.66	0.01	-0.01	-0.01	-0.01	-1.19	20.41
RW074	2.71	0.05	-3.38	1.48	0.04	-0.40	-0.26	0.01	0.00	0.00	-0.01	-0.72	-0.48
RW075	6.76	-0.04	-1.71	0.57	1.49	0.81	0.44	0.04	0.00	0.00	0.45	1.85	10.68
RW077	-3.22	-0.28	-0.65	-0.04	1.22	2.22	0.77	0.03	0.01	0.00	0.07	1.45	1.58
RW078	-1.66	-0.27	-1.11	0.77	1.74	0.72	0.44	0.05	0.00	0.00	-0.01	2.32	2.99
RW080	-4.90	-0.78	-1.17	0.71	1.11	1.65	0.49	0.03	-0.01	0.00	0.56	2.05	-0.25
RW081	-0.22	-0.47	0.59	-0.16	0.47	0.28	0.14	0.03	-0.01	0.00	0.00	0.96	1.61
RW082	23.74	0.20	-1.55	1.13	1.60	4.97	0.61	0.07	-0.01	-0.01	2.41	2.92	36.09
RW083	6.82	0.88	-3.49	2.32	1.03	1.69	0.50	0.07	0.00	-0.01	0.00	1.85	11.67
RW084	-1.20	-0.47	-1.37	0.86	0.59	3.07	0.62	0.10	0.01	0.00	0.00	2.93	5.13
RW085	-2.21	-0.49	1.26	-0.63	0.91	-0.32	0.05	0.03	0.00	0.01	0.00	1.06	-0.33
RW086	-0.41	-0.03	-0.42	0.33	0.56	-0.26	0.05	0.02	0.00	0.00	0.01	0.63	0.46
RW087	22.55	1.84	-3.55	2.08	0.51	1.40	0.48	0.01	0.00	-0.01	1.20	0.51	27.02
RW088	37.56	3.12	-0.69	0.59	2.86	3.17	0.95	0.13	0.00	0.00	0.12	4.98	52.79
RW089	14.09	1.90	-3.59	2.32	2.50	2.43	0.95	0.07	0.00	-0.01	0.02	3.36	24.04
RW090	18.34	2.27	1.36	-0.35	0.84	1.86	0.15	0.05	0.00	-0.01	-0.01	1.17	25.67
RW091	0.29	1.29	-1.33	1.84	1.00	2.87	0.42	0.07	-0.01	-0.01	0.00	2.05	8.48
RW092	-1.07	0.61	-0.04	0.19	1.24	0.96	0.27	0.06	0.00	0.00	0.03	1.84	4.08
RW093	-2.67	0.22	-3.52	1.76	-0.70	4.69	1.94	0.05	0.02	0.00	0.05	3.59	5.43
RW094	-2.47	-0.35	-2.21	1.19	1.34	0.38	0.37	0.03	0.00	0.00	0.03	1.73	0.04
RW095	6.22	2.38	-1.66	1.41	1.71	3.24	0.53	0.08	-0.01	-0.01	0.01	3.43	17.33
RW096	5.78	0.74	-0.43	0.49	1.01	1.26	0.24	0.03	0.00	0.00	0.00	1.62	10.73
RW097	4.26	0.07	0.41	-0.32	1.50	1.21	0.92	0.08	0.00	0.00	0.23	1.93	10.31
RW098	7.77	0.10	1.05	-0.62	0.60	1.84	0.45	0.05	0.00	-0.01	0.25	0.28	11.78
RW099	11.31	0.90	-0.62	0.78	3.89	4.17	0.73	0.20	-0.01	-0.01	0.00	5.37	26.71
RW100	-10.08	-0.48	-1.92	1.13	-0.20	-0.46	0.01	-0.01	0.00	0.00	0.00	-0.53	-12.55
RW101	-0.68	-0.03	-3.59	0.75	-0.82	5.98	1.65	0.01	0.01	-0.01	0.00	-1.49	1.79
RW102	4.33	0.32	-3.59	0.82	-0.81	5.32	1.91	0.03	0.00	-0.01	0.01	-1.47	6.85
RW103	6.91	0.75	-3.59	0.86	-0.78	4.63	2.98	0.06	0.00	-0.01	-0.01	-1.40	10.40
RW104	-3.76	-0.60	-3.54	3.97	0.09	0.20	0.08	0.01	0.00	0.00	-0.01	0.32	-3.23
RW105	-1.46	-0.73	-2.54	1.33	1.60	0.26	0.64	0.01	-0.01	0.00	-0.01	2.05	1.14

Table 7.5. Mass changes for Pinkos footwall rhyolite

Sample	SiO2	Al2O3	Na2O	K2O	CaO	Fe2O3	MgO	MnO	TiO2	P2O5	S	CO2	Net
Units	g/100g	g/100g	g/100g	g/100g	g/100g	g/100g	g/100g	g/100g	g/100g	g/100g	g/100g	g/100g	g/100g
RW108	-1.84	-0.39	-0.50	0.32	1.10	-0.03	0.54	0.01	0.01	0.00	-0.01	1.49	0.71
RW109	3.87	-0.73	-1.44	0.46	0.43	2.01	1.04	0.06	0.00	-0.01	0.51	0.44	6.63
RW110	4.08	0.28	-0.18	0.26	1.70	0.97	0.48	0.03	0.00	0.00	0.49	2.10	10.22
RW111	23.71	1.31	-3.59	0.69	-0.58	3.87	4.45	-0.01	0.00	-0.01	-0.01	-1.11	28.73
RW112	2.61	0.25	-3.58	1.77	-0.23	2.43	0.47	0.07	0.01	0.00	0.01	1.86	5.67
RW113	2.85	1.48	-2.11	1.34	0.38	1.18	0.44	0.04	-0.01	-0.01	0.00	1.61	7.18
RW114	21.07	2.24	0.15	-0.21	1.18	0.52	1.80	0.02	0.00	-0.01	-0.01	1.48	28.26
RW115	5.56	0.14	-3.58	0.18	-0.81	3.08	3.36	-0.02	0.01	-0.01	-0.01	-1.48	6.41
RW116	3.30	0.59	-3.56	0.12	-0.81	3.91	3.99	-0.02	0.00	-0.01	-0.01	-1.47	6.03
RW117	14.93	1.08	-3.59	0.09	-0.81	7.98	2.12	0.02	-0.01	-0.01	0.00	-1.45	20.35
RW118	7.71	0.10	-3.53	-0.11	-0.79	6.35	2.08	0.02	0.01	-0.01	-0.01	-1.40	10.42
RW119	-2.87	0.28	-1.87	0.46	0.65	1.57	0.91	0.02	0.01	0.00	0.29	0.71	0.16
RW120	2.45	0.57	-0.29	0.54	-0.64	3.06	0.61	0.08	0.00	0.00	0.04	1.16	7.57
RW121	0.28	0.60	-1.85	0.78	0.58	-0.01	0.33	0.02	-0.01	0.00	0.02	0.67	1.42
RW122	62.32	9.55	6.36	-0.66	0.22	2.86	0.42	0.07	0.02	0.00	-0.01	-1.03	80.12
RW123	0.82	-0.07	-3.59	0.05	-0.82	5.67	3.33	0.03	-0.02	-0.01	-0.01	-1.45	3.95
RW124	5.98	0.52	-3.57	0.57	-0.54	2.32	3.65	0.02	-0.01	-0.01	-0.01	-1.01	7.91
RW125	-5.27	-0.42	-3.58	0.68	-0.66	2.26	2.67	0.02	0.00	0.00	-0.01	-1.20	-5.53
RW126	53.57	9.54	-3.58	1.38	0.96	17.67	6.37	0.09	1.43	0.44	0.00	0.34	88.20
RW127	14.26	-0.67	-3.51	0.70	-0.81	0.39	1.84	-0.03	0.01	0.00	-0.01	-1.47	10.69
RW128	-2.75	0.13	-1.33	0.14	1.41	1.86	1.75	0.05	0.01	0.00	0.13	1.86	3.25
RW129	1.46	0.18	-0.95	0.28	0.04	-0.20	0.00	0.00	0.00	0.00	0.01	-0.18	0.64
RW130	8.90	-0.49	-3.04	0.96	3.09	2.72	1.09	0.11	0.01	0.00	-0.01	4.26	17.61
RW131	7.38	-0.04	1.18	-0.39	0.10	0.79	0.04	0.01	0.00	0.00	0.48	0.22	9.77
RW132	6.63	0.00	-0.22	0.23	0.41	1.88	0.22	0.00	-0.01	-0.01	2.04	0.37	11.55
RW145	9.16	1.12	-1.90	1.29	-0.73	-0.46	-0.18	-0.03	-0.01	0.00	-0.01	-1.36	6.87
RW146	19.27	-0.35	-0.28	0.10	1.77	2.47	0.23	0.10	0.01	-0.01	0.00	2.10	25.41
RW147*	-1.17	0.55	-0.40	0.25	-0.09	0.35	0.11	0.01	-0.01	0.00	0.01	0.41	0.02
RW148	-2.48	0.30	1.49	-0.76	0.84	0.77	-0.07	0.03	0.00	0.00	0.25	0.97	1.33
RW149	21.68	2.09	0.93	0.07	2.16	3.05	0.78	0.15	0.00	-0.01	0.27	3.60	34.77
RW150	-3.92	0.51	-2.02	1.07	-0.27	1.67	-0.17	0.05	0.00	0.00	-0.01	-0.56	-3.65
RW151	0.10	-0.24	-1.05	0.35	1.77	2.21	0.27	0.08	0.00	0.00	0.23	3.00	6.71
RW152	10.29	1.78	1.88	-0.46	1.03	2.11	0.03	0.10	0.01	-0.01	-0.01	1.38	18.13
RW153	7.62	0.47	1.41	-0.42	-0.19	-0.06	-0.17	0.00	0.00	-0.01	0.04	-0.62	8.07
RW154	-4.39	-0.46	-1.09	0.68	0.40	-0.37	0.32	0.01	-0.01	0.00	0.11	0.33	-4.46
RW155	0.40	-0.41	-1.94	2.06	0.53	0.08	0.38	0.01	0.01	0.00	0.16	0.50	1.80
RW156	5.35	0.97	-0.74	2.50	1.22	1.63	0.23	0.05	-0.01	-0.01	0.13	1.23	12.56
RW157	2.69	-0.07	-0.08	1.16	0.98	0.57	0.19	0.03	0.03	0.00	0.03	0.74	6.26
RW158	14.77	0.20	-3.59	2.27	2.91	3.69	0.80	0.11	0.01	-0.01	0.00	4.64	25.82
RW159	3.12	0.87	-0.51	0.70	-0.63	1.32	-0.06	0.03	0.01	0.00	0.04	0.35	5.25
RW160	12.90	0.59	1.45	-0.35	-0.04	2.53	-0.11	0.07	-0.01	-0.01	-0.01	0.31	17.31
RW161	5.67	0.59	-0.84	0.88	-0.31	1.83	0.11	0.04	0.01	0.00	0.04	0.84	8.86
RW162	3.01	0.15	-1.69	1.28	2.02	1.58	0.56	0.06	-0.01	0.00	0.04	2.74	9.74

Notes: * Denotes least-altered sample suite; Mass change data for individual chemical components plotted in Figure 7.15 represent the average of all samples in a given alteration assemblage (as determined by SWIR spectroscopy and petrography).

Table 7.6. Pearson correlation matrix of major element mass transfer in footwall rhyolite at Pinkos

	SiO2	*Al2O3*	*Na2O*	*K2O*	*CaO*	*Fe2O3*	*MgO*	*MnO*	*TiO2*	*P2O5*	*S*
Al2O3	0.74										
Na2O	0.12	0.17									
K2O	-0.06	-0.02	-0.60								
CaO	0.13	0.03	0.27	0.07							
Fe2O3	0.37	0.43	-0.38	0.00	-0.07						
MgO	0.17	0.21	-0.56	-0.09	-0.28	0.67					
MnO	0.21	0.16	0.19	0.02	0.69	0.32	-0.12				
TiO2	0.54	0.72	-0.13	0.11	0.04	0.67	0.41	0.15			
P2O5	0.53	0.71	-0.12	0.12	0.06	0.65	0.39	0.15	0.99		
S	0.07	-0.15	0.06	-0.01	0.12	0.02	-0.13	0.00	-0.05	-0.04	
CO2	0.01	-0.04	0.19	0.21	0.87	-0.04	-0.32	0.74	-0.02	-0.01	0.12

* Calculated from absolute mass changes in footwall rhyolite 'A' (Table 7.5).

All values are different from 0 with a significance level alpha=0.05.

Table 7.7. Chondrite-normalized rare-earth element composition of Pinkos volcanic rocks

Sample	La	Ce	Pr	Nd	Sm	Eu	Gd	Tb	Dy	Ho	Er	Tm	Yb	Lu	La/Yb
Units	ppm	ppm	ppm	ppm	ppm	ppm	ppm	ppm	ppm	ppm	ppm	ppm	ppm	ppm	ratio
RW043	187.8	174.57	160.8	144.1	118.4	51.8	102.6	100.3	100.9	96.45	99.02	97.00	97.54	95.4	1.93
RW044	128.8	130.16	119.8	106.7	91.2	54.1	74.6	71.4	74.0	73.88	78.21	77.17	78.76	76.4	1.64
RW045	124.8	119.92	109.9	99.8	84.6	51.4	76.4	73.9	77.4	76.79	80.71	78.99	81.41	78.2	1.53
RW046	230.2	213.80	193.4	173.3	139.1	56.4	109.2	96.7	90.9	85.92	87.84	85.55	86.33	84.4	2.67
RW047	241.6	221.06	199.1	177.3	137.6	51.7	112.5	103.6	103.4	99.80	106.05	103.36	104.60	103.8	2.31
RW048	214.2	194.05	177.0	158.0	128.9	51.0	112.1	105.2	107.4	102.95	104.25	101.05	99.99	97.0	2.14
RW049	214.3	199.04	180.8	163.0	131.4	63.5	112.4	104.1	101.3	94.96	96.23	93.64	95.47	92.4	2.24
RW050	229.9	215.45	196.0	173.4	139.0	57.8	110.5	98.8	93.8	89.19	91.18	87.13	87.09	84.9	2.64
RW051	190.7	175.89	158.3	144.4	118.4	48.7	104.3	99.4	101.5	98.13	99.54	95.06	94.26	90.5	2.02
RW052	175.3	167.46	152.3	135.0	113.0	41.8	100.0	102.7	107.2	108.06	115.62	116.96	118.73	115.7	1.48
RW053*	166.5	162.48	147.9	132.5	109.9	54.5	96.4	99.2	102.0	98.68	101.21	98.66	99.60	96.5	1.67
RW054	222.7	202.54	181.6	163.0	137.3	58.1	134.8	146.1	156.1	155.09	156.72	146.28	139.85	132.8	1.59
RW055	245.4	223.57	205.2	182.0	145.6	57.0	121.0	112.6	110.7	106.98	110.66	107.85	108.21	104.8	2.27
RW056	119.1	115.27	105.5	96.3	88.3	48.0	87.3	91.7	95.0	92.71	94.86	90.57	91.06	87.8	1.31
RW057	18.2	18.06	17.8	18.2	17.1	18.3	15.9	14.9	14.4	13.77	13.93	13.44	13.57	13.3	1.34
RW058	20.0	20.05	20.3	20.9	19.8	21.5	18.6	17.5	16.9	16.12	16.04	15.06	15.17	15.2	1.32
RW059	206.0	189.89	170.0	152.6	122.0	55.0	98.2	92.8	87.8	82.20	83.63	81.38	81.71	76.5	2.52
RW060	180.6	170.77	155.9	140.2	117.4	50.5	102.0	101.2	99.6	96.98	101.41	97.73	98.58	95.1	1.83
RW061	181.6	158.56	142.0	124.1	96.3	39.3	88.0	95.1	100.6	100.59	106.50	103.16	102.50	97.8	1.77
RW062	177.8	169.09	153.7	137.8	113.6	53.9	101.3	103.9	104.2	101.15	105.52	102.47	103.94	100.9	1.71
RW063*	174.6	156.72	142.1	128.4	107.1	45.3	92.0	87.2	81.2	74.85	75.49	72.31	72.81	66.5	2.40
RW064	99.4	98.91	93.4	87.6	82.5	22.1	86.6	96.9	100.6	101.65	107.13	105.47	105.56	100.9	0.94
RW065	35.0	33.90	34.1	34.1	31.8	30.8	28.3	26.9	25.3	24.52	24.36	22.79	23.23	22.6	1.51
RW066	215.5	210.39	201.9	182.9	141.1	28.8	104.1	96.7	93.3	88.35	92.06	88.46	89.35	86.7	2.41
RW067	91.7	70.90	76.4	72.8	79.4	23.2	114.0	129.6	139.4	138.88	141.04	127.89	118.79	109.2	0.77
RW068	167.1	152.64	144.6	134.5	118.0	44.8	111.8	118.4	120.9	119.93	125.78	120.28	119.49	113.5	1.40
RW069	103.5	112.69	99.3	91.2	87.3	20.2	86.0	91.5	92.2	89.67	94.58	92.51	94.69	91.3	1.09
RW070	163.1	153.07	138.9	127.2	110.9	40.4	103.3	106.1	105.3	102.12	106.66	102.75	104.14	98.6	1.57
RW071	212.5	194.24	177.4	159.5	125.9	41.6	110.7	110.0	111.9	108.68	113.76	110.97	111.02	105.9	1.91
RW072	288.4	259.14	238.7	216.5	173.9	56.3	140.2	125.4	118.5	109.76	113.86	109.43	108.23	102.9	2.66
RW073	186.8	163.46	162.8	146.1	116.3	24.2	98.0	98.0	99.4	98.68	104.94	103.72	104.74	101.4	1.78
RW074	197.8	188.12	170.1	151.9	123.4	53.6	102.2	99.9	96.8	90.00	91.49	87.49	86.66	80.2	2.28
RW075	169.5	161.06	145.6	130.2	106.0	45.2	85.9	81.3	79.0	74.30	77.60	76.28	78.03	76.1	2.17
RW076	26.5	25.63	25.9	26.5	24.1	25.8	22.5	21.3	21.0	19.73	20.42	19.43	19.64	19.6	1.35
RW077	211.5	195.14	180.4	163.4	136.5	59.4	114.0	107.8	106.0	101.76	104.25	100.77	102.72	100.2	2.06
RW078	192.7	180.78	164.6	150.7	125.6	52.7	104.4	100.2	95.5	88.04	89.59	86.23	85.72	80.2	2.25
RW080	194.7	184.39	167.6	152.2	123.1	56.7	101.8	98.5	96.3	88.61	90.12	86.76	87.82	84.1	2.22
RW081	222.6	202.22	185.2	170.6	142.0	58.0	119.0	108.1	104.4	98.83	101.35	97.45	98.63	95.4	2.26
RW082	240.4	220.64	203.3	185.8	155.9	45.5	126.7	116.9	109.7	101.63	103.63	99.60	99.17	94.8	2.42
RW083	211.9	192.19	175.9	157.4	132.1	51.8	115.8	112.9	112.4	106.41	111.21	106.64	107.09	102.4	1.98
RW084	182.4	176.35	160.7	146.0	121.0	54.2	99.8	91.4	86.4	76.94	75.22	71.62	72.94	70.1	2.50
RW085	220.5	199.69	178.9	162.8	134.5	60.8	118.8	115.9	116.1	111.72	117.95	114.98	117.18	114.9	1.88
RW086	180.0	174.05	160.0	141.8	116.2	56.3	90.7	85.8	78.9	71.78	73.06	71.62	73.00	69.1	2.47
RW087	120.9	112.04	101.5	92.7	80.1	31.1	79.6	87.1	93.7	93.41	98.25	95.47	96.17	90.9	1.26
RW088	107.7	101.08	90.9	82.9	79.3	37.1	84.1	88.3	88.5	83.35	83.86	80.04	79.81	76.3	1.35
RW089	201.5	185.97	168.6	153.9	126.7	49.2	109.6	106.7	104.2	99.01	103.01	100.85	101.19	96.3	1.99
RW090	170.4	157.59	143.7	128.1	108.3	43.9	97.3	96.2	97.7	95.84	98.02	95.38	96.11	92.2	1.77
RW091	214.9	199.87	181.9	162.2	134.9	53.1	119.6	120.0	119.6	113.59	120.63	119.27	119.17	113.2	1.80
RW092	201.3	188.34	174.1	153.3	126.1	58.1	105.4	101.1	97.7	90.20	93.89	92.06	93.20	88.6	2.16
RW093	211.7	195.45	176.4	157.9	127.1	32.4	104.4	100.0	100.4	96.56	100.46	98.83	100.14	96.5	2.11
RW094	206.2	200.38	182.3	163.3	136.1	60.4	115.0	112.4	111.9	104.95	106.66	102.67	102.16	96.3	2.02
RW095	261.3	234.39	215.8	193.4	161.6	61.0	139.6	132.0	129.3	119.71	120.71	115.63	114.45	108.3	2.28
RW096	195.4	181.32	165.2	146.8	123.2	55.2	110.0	107.4	108.0	101.34	104.30	102.31	103.09	99.6	1.90
RW097	197.1	177.37	162.2	146.3	119.2	54.3	97.9	95.5	95.8	92.44	97.78	95.95	96.83	92.4	2.04
RW098	181.3	161.11	150.0	134.2	112.4	45.6	105.0	106.0	110.3	105.37	106.24	100.77	101.41	97.3	1.79
RW099	220.0	196.84	179.2	162.8	138.8	54.4	124.2	118.8	115.3	105.04	105.03	101.66	101.68	97.8	2.16
RW100	210.3	196.46	175.6	158.0	130.3	58.4	111.3	106.8	105.3	100.64	102.14	100.36	101.53	97.8	2.07
RW101	52.3	50.67	48.5	45.5	61.5	23.3	86.1	102.6	109.5	108.17	113.53	111.66	113.70	108.1	0.46
RW102	43.0	41.35	39.6	39.0	55.1	26.6	80.5	100.0	110.3	111.94	118.51	116.52	116.87	112.5	0.37
RW103	201.3	178.52	171.4	155.9	130.6	45.0	110.8	108.7	106.7	101.74	108.65	108.83	112.16	108.7	1.79
RW104	231.7	203.43	187.3	168.4	137.0	56.3	114.0	106.7	105.2	101.70	107.03	103.00	103.24	98.5	2.24

Table 7.7. Chondrite-normalized rare-earth element composition of Pinkos volcanic rocks

Sample	La	Ce	Pr	Nd	Sm	Eu	Gd	Tb	Dy	Ho	Er	Tm	Yb	Lu	La/Yb
Units	ppm	ppm	ppm	ppm	ppm	ppm	ppm	ppm	ppm	ppm	ppm	ppm	ppm	ppm	ratio
RW105	207.3	188.50	172.5	151.3	120.8	47.3	98.2	94.6	92.0	85.92	89.83	86.32	88.52	85.2	2.34
RW106	31.6	30.46	31.3	31.4	30.1	33.7	28.7	26.5	26.2	24.29	24.76	23.28	24.40	24.5	1.30
RW107	35.4	33.57	33.8	33.9	31.4	35.2	29.1	27.0	26.6	25.44	25.47	24.01	24.70	24.8	1.43
RW108	185.9	173.92	157.2	138.8	116.0	50.5	95.9	91.2	88.9	82.01	85.28	84.53	85.79	81.5	2.17
RW109	212.8	190.13	177.3	155.1	121.8	44.2	99.6	93.5	93.3	86.68	88.72	86.11	87.80	85.6	2.42
RW110	216.5	200.62	181.1	161.7	131.6	54.8	120.8	124.5	127.3	123.55	130.13	127.81	131.50	128.8	1.65
RW111	134.6	123.51	117.3	104.9	86.1	24.5	81.9	84.3	88.0	88.17	93.63	93.56	95.87	92.4	1.40
RW112	192.1	178.40	163.5	145.3	117.7	46.7	99.6	98.1	96.5	90.57	94.92	92.71	93.55	90.4	2.05
RW113	199.2	184.34	168.3	149.6	122.9	44.7	102.1	97.0	95.8	91.70	95.48	95.02	95.45	92.6	2.09
RW114	243.7	211.81	204.7	184.8	142.1	38.9	110.8	101.8	100.4	95.09	100.04	97.85	98.94	94.4	2.46
RW115	99.3	107.90	88.9	77.2	72.6	18.0	78.7	86.1	89.1	88.72	93.71	94.17	93.97	91.7	1.06
RW116	34.3	35.77	32.4	30.7	43.1	16.5	78.0	97.6	108.9	110.15	116.51	112.23	111.64	106.8	0.31
RW117	69.8	71.24	65.2	58.2	62.4	11.0	68.8	77.1	84.6	84.54	92.37	91.38	93.66	92.0	0.75
RW118	176.8	150.38	149.1	134.3	108.9	20.2	92.7	89.7	88.7	85.57	89.06	87.45	88.07	84.8	2.01
RW119	205.9	186.04	169.7	154.0	125.8	60.6	106.9	104.3	103.2	100.27	108.02	106.07	108.12	105.0	1.90
RW120	208.8	193.18	176.0	154.5	129.3	52.2	112.6	111.0	111.0	108.99	115.24	112.23	115.29	113.5	1.81
RW121	184.8	178.11	162.8	143.6	117.1	56.4	98.2	98.1	97.8	93.11	99.55	97.37	98.80	92.8	1.87
RW122	218.5	180.90	154.7	129.5	93.4	38.4	74.9	70.5	68.9	67.60	72.27	73.48	77.14	76.8	2.83
RW123	163.2	187.23	141.0	126.4	110.4	35.7	103.1	104.5	107.5	106.28	113.90	111.21	110.88	104.9	1.47
RW124	230.1	168.48	194.8	174.1	127.2	27.1	105.4	98.9	97.8	97.56	106.68	106.28	106.98	104.0	2.15
RW125	213.2	192.84	180.7	162.7	131.2	33.5	109.4	104.2	104.2	99.76	104.79	100.73	100.78	98.7	2.12
RW126	108.4	101.19	94.5	86.7	72.4	41.3	62.2	58.1	55.9	53.22	54.06	52.15	52.88	52.2	2.05
RW127	139.2	141.13	121.5	102.3	78.4	16.8	70.8	77.0	84.4	88.90	98.35	95.79	96.63	94.3	1.44
RW128	185.8	176.26	160.0	143.8	120.6	57.1	102.6	97.8	95.0	93.08	98.78	97.33	99.65	97.0	1.86
RW129	248.9	227.44	203.6	184.2	144.0	59.1	119.1	111.0	108.8	104.40	108.58	105.43	106.11	104.4	2.35
RW130	189.5	169.53	152.6	135.5	111.3	45.4	102.0	103.7	105.5	100.99	102.95	97.00	95.99	91.3	1.97
RW131	207.3	189.58	174.5	155.4	128.6	57.8	109.4	106.5	105.5	102.45	108.74	105.30	106.44	100.8	1.95
RW132	218.3	199.41	182.8	162.6	130.0	47.5	106.7	102.2	102.3	98.97	103.28	101.30	103.13	100.9	2.12
RW145	160.1	156.93	142.9	127.4	108.2	45.1	92.5	92.6	93.4	91.90	97.27	97.53	100.12	98.5	1.60
RW146	151.9	142.41	128.4	117.7	99.6	44.3	88.4	86.4	86.2	82.00	85.89	85.63	86.41	84.3	1.76
RW147*	171.7	165.77	150.4	136.9	114.9	53.1	101.0	101.5	99.5	92.78	94.35	91.54	92.37	86.7	1.86
RW148	202.9	183.05	167.3	150.6	124.3	52.0	106.8	99.8	99.1	94.67	98.42	94.82	95.70	94.4	2.12
RW149	226.1	201.79	184.8	165.4	136.5	53.8	117.3	110.4	107.8	100.04	100.33	96.19	96.55	92.5	2.34
RW150	245.5	229.20	207.0	183.1	142.3	52.3	114.4	108.9	108.2	104.87	111.67	111.05	115.15	113.4	2.13
RW151	169.5	157.88	146.8	132.8	112.0	49.5	99.1	100.1	101.4	99.21	108.09	110.32	116.89	118.2	1.45
RW152	202.4	187.44	171.6	154.8	127.5	53.6	106.0	101.3	100.1	96.89	99.86	97.85	99.71	95.2	2.03
RW153	192.7	181.84	164.4	146.8	118.0	46.6	101.8	102.0	103.0	101.59	105.11	102.63	104.78	101.7	1.84
RW154	219.2	209.46	194.9	178.2	150.3	60.3	119.9	114.5	109.2	96.78	93.76	88.26	85.92	79.9	2.55
RW155	167.9	158.16	143.3	130.2	108.4	47.2	89.2	86.1	86.7	84.10	88.48	87.85	88.88	84.9	1.89
RW156	226.9	207.65	188.3	168.4	139.4	54.5	122.1	117.3	112.2	105.53	107.09	104.62	106.74	103.5	2.13
RW157	179.1	165.14	152.9	135.7	117.1	52.2	102.2	100.6	100.3	94.95	95.52	92.35	92.91	90.0	1.93
RW158	171.6	159.64	147.5	134.9	116.7	48.4	101.0	94.6	92.9	89.18	91.40	89.03	90.18	89.3	1.90
RW159	204.2	191.34	172.4	153.8	127.5	49.2	114.4	116.6	119.9	116.06	119.24	115.67	115.20	111.2	1.77
RW160	201.8	187.32	171.1	151.5	124.1	47.3	107.6	106.5	104.8	101.25	104.44	102.47	103.29	100.4	1.95
RW161	222.1	201.55	185.9	162.1	128.0	47.1	106.0	102.5	101.9	99.36	103.90	103.68	105.02	101.0	2.11
RW162	203.1	192.95	176.0	155.5	130.0	52.0	111.8	109.5	104.8	96.78	95.58	91.30	89.06	83.7	2.28
Chondr.**	0.2	0.61	0.1	0.5	0.1	0.1	0.2	0.0	0.2	0.05	0.16	0.02	0.16	0.0	1.47

* Denotes least-altered sample suite.

** REE data normalized to chondrite after McDonough and Sun (1995).

Table 7.8. Alteration intensity calculations of Pinkos volcanic rocks

Sample No.	Na2O	K2O	CaO	FeO	MgO	MnO	CO2	Ishikawa	CCPI	Carb.	Mn-carb.
Units	wt%	wt%	wt%	wt%	wt%	wt.%	wt.%	index**	index***	index****	index*****
RW043	2.04	2.55	1.22	1.79	0.61	0.06	2.03	49.22	34.34	0.75	0.01
RW044	0.14	3.65	1.36	1.87	0.70	0.06	2.29	74.36	40.42	0.77	0.01
RW045	1.86	2.49	0.58	2.44	0.58	0.07	1.91	55.72	40.96	0.74	0.01
RW046	0.02	3.07	0.49	0.90	0.32	0.03	0.78	86.92	28.30	0.61	0.01
RW047	3.89	1.57	0.99	3.62	0.59	0.10	2.64	30.68	43.52	0.73	0.01
RW048	3.32	1.71	2.31	3.57	0.63	0.10	3.23	29.36	45.52	0.69	0.01
RW049	1.39	3.88	0.95	2.73	0.55	0.06	2.29	65.44	38.34	0.76	0.01
RW050	4.03	1.48	1.38	3.07	0.53	0.08	3.02	27.09	39.51	0.85	0.01
RW051	4.75	1.06	0.86	1.70	0.31	0.05	1.38	19.63	25.71	0.67	0.01
RW052	2.82	2.55	0.35	3.20	0.53	0.04	1.87	49.28	41.01	0.66	0.01
RW053*	3.67	1.96	1.28	2.28	0.47	0.04	2.05	32.93	32.79	0.70	0.01
RW054	2.09	2.84	3.43	2.86	1.88	0.11	5.28	46.09	49.02	0.81	0.01
RW055	2.99	2.33	1.64	2.83	0.67	0.05	2.66	39.32	39.65	0.71	0.01
RW056	4.39	1.40	1.96	1.85	0.67	0.06	2.88	24.58	30.36	0.85	0.01
RW057	3.62	0.19	6.12	13.78	6.41	0.18	9.14	40.39	84.12	0.45	0.01
RW058	3.43	0.04	7.47	13.25	5.71	0.17	5.57	34.53	84.53	0.28	0.01
RW059	3.22	1.19	1.75	1.49	0.52	0.07	2.51	25.60	31.35	0.88	0.01
RW060	5.44	0.40	2.08	2.15	0.28	0.10	2.32	8.29	29.39	0.71	0.02
RW061	4.05	1.05	0.99	3.58	0.17	0.10	0.95	19.49	42.38	0.30	0.04
RW062	3.43	1.29	0.93	1.56	0.62	0.03	1.47	30.46	31.56	0.62	0.01
RW063*	3.92	1.05	0.49	0.96	0.37	0.03	0.68	24.36	21.15	0.49	0.02
RW064	0.01	1.72	0.04	3.95	3.74	0.03	0.10	99.09	81.64	0.02	0.12
RW065	3.33	0.03	6.25	14.91	4.08	0.21	1.40	30.02	84.97	0.08	0.06
RW066	0.50	1.95	0.40	2.57	2.54	0.03	0.63	83.30	67.61	0.14	0.02
RW067	0.01	1.01	1.21	5.89	6.11	0.08	1.55	85.42	92.20	0.14	0.02
RW068	2.10	1.63	0.88	2.21	2.18	0.03	1.19	56.11	54.08	0.27	0.01
RW069	0.01	1.57	0.03	4.51	3.93	0.02	0.09	99.28	84.23	0.01	0.09
RW070	3.53	0.78	1.53	2.65	2.12	0.06	2.27	36.43	52.51	0.44	0.01
RW071	4.06	0.92	1.43	2.59	1.67	0.03	2.23	32.05	46.11	0.49	0.01
RW072	2.45	1.83	0.32	1.50	1.49	0.03	0.53	54.52	41.15	0.19	0.02
RW073	0.42	1.44	0.15	4.47	3.37	0.04	0.31	89.41	80.83	0.05	0.05
RW074	0.21	3.06	0.86	1.39	0.21	0.05	0.84	75.35	32.92	0.48	0.02
RW075	1.70	1.98	2.10	2.26	0.83	0.07	3.09	42.51	45.63	0.78	0.01
RW076	2.65	0.02	6.66	14.19	4.59	0.21	4.94	33.12	87.55	0.26	0.02
RW077	2.89	1.56	2.02	3.70	1.22	0.07	2.97	36.15	52.50	0.57	0.01
RW078	2.38	2.30	2.47	2.32	0.88	0.09	3.73	39.60	40.62	0.86	0.01
RW080	2.40	2.31	1.93	3.22	0.96	0.07	3.58	43.03	47.03	0.79	0.01
RW081	4.12	1.44	1.29	1.99	0.61	0.07	2.49	27.48	31.85	0.86	0.01
RW082	1.51	2.03	1.80	4.61	0.80	0.08	3.31	46.09	60.43	0.65	0.01
RW083	0.09	3.51	1.66	2.92	0.87	0.10	3.04	71.45	51.31	0.75	0.01
RW084	2.11	2.36	1.36	4.31	1.04	0.13	4.28	49.49	54.48	0.88	0.01
RW085	4.88	1.00	1.76	1.49	0.53	0.07	2.65	18.73	25.60	0.92	0.01
RW086	3.16	1.95	1.39	1.53	0.52	0.06	2.19	35.19	28.63	0.84	0.01
RW087	0.03	2.90	1.05	2.38	0.75	0.04	1.63	77.17	51.61	0.53	0.01
RW088	1.91	1.46	2.43	3.04	0.94	0.11	4.31	35.61	54.16	0.90	0.01
RW089	0.01	3.12	2.64	3.13	1.13	0.09	3.90	61.64	57.69	0.75	0.01
RW090	3.93	1.01	1.33	2.74	0.50	0.07	2.17	22.30	39.57	0.66	0.01
RW091	2.07	3.16	1.68	3.98	0.82	0.10	3.30	51.49	47.84	0.71	0.01
RW092	3.42	1.75	2.00	2.54	0.72	0.10	3.28	31.31	38.65	0.84	0.01
RW093	0.07	3.17	0.13	5.61	2.26	0.08	4.83	96.45	70.83	0.80	0.01
RW094	1.36	2.77	2.14	2.08	0.83	0.07	3.25	50.70	41.32	0.84	0.01
RW095	1.64	2.58	2.16	3.98	0.85	0.10	4.24	47.44	53.36	0.84	0.01
RW096	2.85	1.91	1.67	2.62	0.65	0.06	2.88	36.16	40.71	0.79	0.01
RW097	3.63	1.19	2.12	2.60	1.27	0.11	3.18	29.96	44.54	0.68	0.01
RW098	4.16	0.90	1.29	3.07	0.83	0.08	1.66	24.09	43.52	0.44	0.02
RW099	2.35	1.90	3.73	4.36	0.95	0.19	5.48	31.91	55.56	0.83	0.01
RW100	1.91	3.14	0.73	1.55	0.55	0.03	1.18	58.29	29.35	0.56	0.01
RW101	0.01	2.29	0.02	6.89	2.05	0.05	0.08	99.43	79.58	0.01	0.24
RW102	0.01	2.24	0.02	6.01	2.19	0.06	0.09	99.44	78.51	0.01	0.26
RW103	0.01	2.20	0.05	5.25	3.05	0.09	0.15	98.96	79.00	0.02	0.23
RW104	0.05	5.78	0.96	2.02	0.57	0.05	1.95	86.28	30.72	0.75	0.01

Table 7.8. Alteration intensity calculations of Pinkos volcanic rocks

Sample No.	Na2O	K2O	CaO	FeO	MgO	MnO	CO2	Ishikawa	CCPI	Carb.	Mn-carb.
Units	wt%	wt%	wt%	wt%	wt%	wt.%	wt.%	index**	index***	index****	index*****
RW105	1.03	2.90	2.39	1.97	1.09	0.05	3.55	53.85	43.78	0.83	0.01
RW106	3.74	0.03	5.46	14.24	3.38	0.25	3.69	27.04	82.38	0.22	0.03
RW107	2.84	0.02	5.75	14.98	3.53	0.26	0.32	29.24	86.62	0.02	0.31
RW108	3.07	1.93	1.92	1.74	1.01	0.05	3.04	37.07	35.46	0.83	0.01
RW109	2.00	1.94	1.18	3.33	1.41	0.09	1.87	51.30	54.60	0.42	0.02
RW110	3.10	1.71	2.30	2.40	0.87	0.06	3.33	32.33	40.49	0.79	0.01
RW111	0.01	1.75	0.19	3.97	3.72	0.02	0.35	96.56	81.42	0.05	0.02
RW112	0.01	3.19	0.57	3.73	0.89	0.10	3.23	87.55	59.05	0.87	0.01
RW113	1.37	2.75	1.13	2.63	0.85	0.07	2.95	59.02	45.77	0.86	0.01
RW114	2.90	1.10	1.56	1.74	1.76	0.05	2.36	39.07	46.64	0.56	0.01
RW115	0.01	1.65	0.02	4.16	3.51	0.02	0.08	99.42	82.20	0.01	0.10
RW116	0.03	1.59	0.02	4.83	4.08	0.02	0.09	99.13	84.62	0.01	0.09
RW117	0.01	1.39	0.02	7.27	2.11	0.05	0.10	99.29	87.05	0.01	0.19
RW118	0.06	1.34	0.04	6.60	2.25	0.05	0.15	97.29	86.34	0.02	0.13
RW119	1.71	2.07	1.48	3.16	1.38	0.06	2.26	51.96	54.56	0.49	0.01
RW120	3.05	2.00	0.18	4.18	1.00	0.11	2.52	48.15	50.61	0.66	0.02
RW121	1.71	2.36	1.39	1.73	0.79	0.06	2.20	50.40	38.22	0.73	0.01
RW122	5.56	0.54	0.59	2.43	0.50	0.06	0.30	14.46	32.44	0.12	0.08
RW123	0.01	1.58	0.02	6.48	3.59	0.07	0.11	99.52	86.40	0.01	0.24
RW124	0.02	1.98	0.27	3.47	3.72	0.05	0.50	95.16	78.24	0.08	0.04
RW125	0.01	2.39	0.18	3.93	3.25	0.06	0.38	96.74	74.95	0.06	0.06
RW126	0.01	1.56	0.93	9.17	3.55	0.07	0.99	84.53	89.04	0.10	0.03
RW127	0.07	2.07	0.02	1.89	2.06	0.01	0.09	97.87	64.86	0.03	0.04
RW128	2.18	1.70	2.16	3.32	2.14	0.09	3.30	46.94	58.46	0.54	0.01
RW129	2.61	1.88	0.87	1.57	0.47	0.04	1.37	40.31	31.29	0.63	0.01
RW130	0.47	2.20	3.34	3.59	1.33	0.13	4.96	48.09	64.82	0.79	0.01
RW131	4.41	1.14	0.86	2.29	0.48	0.05	1.65	23.51	33.33	0.63	0.01
RW132	3.03	1.67	1.12	3.11	0.63	0.04	1.74	35.66	44.33	0.50	0.01
RW146	2.63	1.37	2.07	3.17	0.56	0.11	2.91	29.11	48.24	0.70	0.01
RW147*	3.19	1.87	0.74	2.08	0.59	0.05	1.98	38.50	34.53	0.79	0.01
RW148	5.04	0.86	1.66	2.44	0.40	0.07	2.52	15.83	32.48	0.78	0.01
RW149	3.35	1.26	2.22	3.35	0.93	0.14	3.83	28.22	48.13	0.80	0.01
RW150	1.60	2.75	0.58	3.34	0.31	0.09	1.03	58.40	45.61	0.36	0.03
RW151	2.38	1.85	2.44	3.53	0.70	0.11	4.28	34.60	49.98	0.88	0.01
RW152	4.65	0.99	1.59	3.12	0.43	0.12	2.51	18.54	38.64	0.69	0.02
RW153	4.64	1.12	0.60	1.59	0.28	0.04	0.88	21.08	24.53	0.50	0.02
RW154	2.61	2.40	1.29	1.50	0.83	0.05	1.98	45.30	31.77	0.70	0.01
RW155	1.62	3.61	1.34	1.81	0.84	0.05	2.03	60.05	33.62	0.66	0.01
RW156	2.55	3.69	1.84	2.90	0.63	0.08	2.50	49.60	36.11	0.64	0.01
RW157	3.30	2.62	1.71	2.15	0.63	0.07	2.17	39.35	31.96	0.65	0.01
RW158	0.01	3.08	2.96	4.02	1.01	0.12	4.90	57.97	61.99	0.83	0.01
RW159	2.94	2.22	0.20	2.82	0.40	0.07	1.83	45.49	38.40	0.79	0.01
RW160	4.31	1.09	0.68	3.46	0.31	0.09	1.61	21.91	41.14	0.54	0.02
RW161	2.53	2.30	0.48	3.14	0.54	0.07	2.21	48.55	43.25	0.76	0.01
RW162	1.73	2.64	2.59	2.90	0.94	0.09	3.91	45.32	46.76	0.81	0.01

* Denotes least-altered samples.

** Ishikawa alteration index calculated after Ishikawa *et al* (1976).

*** Chlorite-carbonate-pyrite index, CCPI = 100 (FeO+MgO)/FeO+MgO+Na2O+K2O.

**** Carbonate index = CO2/(CaO+FeO+MgO), expressed in mole percent.

***** Mn-carbonate index = MnO/CO2, expressed in mole percent.

Table 7.9. Normative mineral abundance estimates of Pinkos volcanic rocks

Sample	Qtz	K-spar	Ab	Ms	Fe-Chl	Mg-Chl	Cc	Ank	Sid	Rt	Py	Dol	Pg	Phn	Total	Res.
Units	wt.%	wt.%	wt.%	wt.%	wt.%	wt.%	wt.%	wt.%	wt.%	wt.%	wt.%	wt.%	wt.%	wt.%	wt.%	SSQ
RW043	54.89	14.81	0.00	0.00	1.01	0.00	0.43	1.47	1.54	0.18	0.02	1.71	23.95	0.00	100.00	0.03
RW044	59.32	3.23	0.00	26.62	0.00	0.00	0.80	3.12	0.48	0.02	0.00	0.00	6.40	0.00	100.00	0.67
RW045	58.13	14.29	0.00	0.00	0.00	0.04	0.00	0.00	3.41	0.15	0.05	2.03	21.90	0.00	100.00	0.09
RW046	66.19	5.63	0.00	0.00	0.00	0.00	0.63	0.06	0.00	0.02	0.00	0.00	9.30	18.17	100.00	1.16
RW047	45.83	8.60	26.71	0.00	6.06	0.00	0.00	4.80	0.05	0.04	0.00	0.00	7.92	0.00	100.00	0.55
RW048	48.78	9.57	20.57	0.00	2.81	0.00	1.87	4.05	2.26	0.00	0.00	0.00	10.09	0.00	100.00	0.14
RW049	54.34	22.55	0.00	0.00	0.00	0.29	0.00	3.38	2.93	0.14	0.00	0.00	16.36	0.00	100.00	0.08
RW050	46.17	8.43	26.31	0.00	0.00	0.00	0.00	4.92	3.11	0.16	0.00	0.00	10.89	0.00	100.00	0.05
RW051	48.06	5.70	34.30	0.00	0.00	0.00	0.36	1.90	1.15	0.08	0.76	0.00	7.70	0.00	100.00	0.14
RW052	50.50	14.71	13.25	0.00	0.00	1.05	0.00	1.67	3.95	0.00	0.00	0.00	14.87	0.00	100.00	0.16
RW053*	48.66	11.06	23.09	0.00	1.21	0.00	0.54	3.05	1.62	0.00	0.00	0.00	10.77	0.00	100.00	0.15
RW054	50.08	16.01	0.00	0.00	0.00	2.74	0.12	11.81	0.42	0.21	0.06	0.00	18.43	0.00	99.89	0.41
RW055	48.65	13.58	18.01	0.00	2.82	0.00	0.24	5.21	0.96	0.17	0.00	0.00	10.36	0.00	100.00	0.02
RW056	45.92	7.75	31.54	0.00	0.59	0.00	0.64	5.26	0.81	0.14	0.00	0.00	7.35	0.00	100.00	0.11
RW059	58.25	6.20	18.90	0.00	0.01	0.00	0.67	4.22	0.84	0.03	0.00	0.00	10.83	0.07	100.00	0.23
RW060	42.96	1.80	44.29	0.00	4.78	0.00	3.18	0.00	0.01	0.07	0.00	1.18	1.73	0.00	100.00	0.24
RW061	47.93	5.88	29.46	0.00	8.28	0.00	1.77	0.00	0.01	0.13	0.00	0.00	6.55	0.00	100.00	0.08
RW062	52.51	7.33	17.79	0.00	3.51	0.00	0.33	0.00	0.01	0.15	0.00	2.44	15.92	0.00	100.00	0.05
RW063*	54.07	5.95	25.42	0.00	2.14	0.00	0.18	0.00	0.01	0.18	0.00	1.12	10.94	0.00	100.00	0.03
RW064	62.03	0.00	0.00	15.31	2.82	14.12	0.00	0.00	0.00	0.00	0.00	0.00	5.72	0.00	100.00	0.72
RW066	63.51	0.00	0.00	16.83	0.07	9.09	0.39	0.00	0.74	0.00	0.00	0.00	9.36	0.00	100.00	0.50
RW067	54.32	0.00	0.00	9.82	0.07	27.41	2.08	0.00	2.23	0.14	0.00	0.00	3.93	0.00	100.00	0.22
RW068	57.23	0.00	11.75	13.00	0.02	7.85	1.56	0.00	0.85	0.07	0.00	0.00	7.67	0.00	100.00	0.26
RW069	59.43	0.00	0.00	0.00	3.59	15.11	0.00	0.00	0.00	0.00	0.00	0.00	7.49	14.38	100.00	0.75
RW070	50.00	0.00	26.08	5.87	0.00	8.23	3.06	0.00	1.86	0.05	0.00	0.00	4.83	0.00	100.00	0.39
RW071	47.10	0.00	30.43	6.79	0.00	5.87	2.79	0.00	2.18	0.06	0.00	0.00	4.78	0.00	100.00	0.43
RW072	57.51	0.00	13.43	14.53	0.00	4.38	0.40	0.00	0.41	0.06	0.00	0.00	9.27	0.00	100.00	0.29
RW073	63.66	0.00	0.00	12.19	3.98	13.01	0.00	0.00	0.56	0.01	0.00	0.00	6.59	0.00	100.00	0.25
RW074	63.23	0.00	0.00	27.12	0.16	0.00	1.33	0.00	0.53	0.01	0.00	0.00	7.62	0.00	100.00	0.48
RW075	59.48	11.29	1.22	0.00	1.36	0.07	0.29	6.58	0.00	0.14	0.71	0.05	18.64	0.16	100.00	0.04
RW077	50.12	8.84	15.78	0.00	6.32	0.00	0.69	2.11	0.78	0.16	0.07	3.11	12.03	0.00	100.00	0.06
RW078	50.57	13.59	10.44	0.00	1.97	0.00	0.38	8.07	0.05	0.22	0.01	0.00	14.18	0.00	99.49	0.01
RW080	49.80	13.62	10.50	0.05	0.56	0.00	0.00	4.43	2.26	0.22	1.06	2.28	14.35	0.00	99.13	0.01
RW081	47.68	8.28	28.75	0.05	0.00	0.00	0.00	3.40	1.95	0.18	0.00	1.02	8.69	0.00	100.00	0.02
RW082	58.95	11.81	2.91	0.05	0.25	0.00	0.15	4.49	2.44	0.13	3.32	1.39	14.12	0.00	100.00	0.02
RW083	56.34	2.58	0.00	0.74	0.00	0.00	0.70	4.51	1.22	0.00	0.00	0.00	8.21	25.69	100.00	0.86
RW084	52.74	13.49	6.10	0.00	0.00	0.00	0.00	0.29	6.17	0.00	0.00	4.88	16.31	0.00	100.00	0.27
RW085	44.85	5.60	36.38	0.00	0.00	0.00	1.67	0.33	2.03	0.00	0.00	2.38	6.75	0.00	100.00	0.10
RW086	52.32	11.11	16.18	0.07	0.00	0.00	1.07	0.44	2.02	0.00	0.00	1.99	14.80	0.00	100.00	0.10
RW087	61.53	0.00	0.00	0.32	0.00	0.00	0.66	2.06	0.01	0.00	1.34	0.16	8.66	25.26	100.00	0.87
RW088	60.38	8.01	2.90	0.00	0.00	0.00	0.00	8.35	2.03	0.02	0.06	0.00	18.23	0.00	100.00	0.15
RW089	57.15	0.00	0.00	28.32	0.25	0.00	1.62	6.13	1.44	0.10	0.00	0.00	5.00	0.00	100.00	0.29
RW090	49.93	5.70	25.44	0.00	0.06	0.97	1.70	0.00	3.68	0.14	0.00	1.09	11.17	0.11	100.00	0.02
RW091	47.41	16.99	7.06	2.43	0.02	0.76	1.47	0.01	5.49	0.20	0.02	2.81	15.28	0.07	100.00	0.01
RW092	48.60	9.74	17.96	0.00	0.02	0.00	1.76	0.01	3.54	0.10	0.01	3.10	15.08	0.07	100.00	0.12
RW093	54.57	0.00	0.00	27.42	0.00	1.40	0.00	0.01	6.65	0.00	0.00	4.55	5.25	0.16	100.00	3.31
RW094	55.77	12.21	0.38	6.17	0.91	0.00	0.46	6.73	0.36	0.23	0.07	0.00	16.22	0.00	99.52	0.00
RW095	52.15	13.18	0.00	2.71	0.00	0.00	0.00	7.49	3.61	0.11	0.00	0.00	20.75	0.00	100.00	0.06
RW096	52.34	9.54	13.77	0.00	0.01	0.01	0.38	4.86	2.30	0.14	0.00	0.00	14.56	2.08	100.00	0.05
RW097	48.62	0.03	26.49	0.00	1.01	0.90	0.20	6.70	0.19	0.13	0.34	0.10	5.62	9.66	100.00	0.07
RW098	48.33	0.03	33.29	0.00	4.35	0.39	0.68	2.84	0.09	0.13	0.37	0.08	2.28	7.16	100.00	0.06
RW099	49.88	10.95	10.78	0.00	1.72	0.00	2.41	8.27	3.05	0.11	0.00	0.01	12.80	0.00	100.00	0.06
RW100	54.91	18.09	1.62	0.00	1.63	0.57	0.00	2.25	0.41	0.16	0.00	0.01	20.36	0.00	100.00	0.09
RW101	59.46	0.04	0.00	19.91	12.94	4.44	0.00	0.00	0.00	0.01	0.00	0.00	3.20	0.00	100.00	0.35
RW102	60.66	0.00	0.00	19.72	10.48	5.71	0.00	0.00	0.00	0.01	0.00	0.00	3.42	0.00	100.00	0.30
RW103	60.19	0.00	0.00	19.37	7.11	10.51	0.00	0.00	0.00	0.03	0.00	0.00	2.79	0.00	100.00	0.22
RW104	52.41	21.93	0.00	17.44	0.00	0.00	0.11	2.85	1.17	0.01	0.00	0.00	4.07	0.00	100.00	0.49
RW105	57.62	9.73	0.00	10.77	0.48	0.16	0.38	7.56	0.00	0.16	0.00	0.02	13.12	0.00	100.00	0.03
RW108	50.86	11.04	16.74	0.00	1.49	0.00	0.00	4.61	0.31	0.17	0.00	1.83	12.92	0.03	100.00	0.05
RW109	55.87	3.23	13.24	11.92	5.70	0.00	0.00	0.00	0.00	0.16	0.86	3.86	5.11	0.05	100.00	0.03
RW110	50.21	9.87	17.59	0.00	1.66	0.00	0.51	6.53	0.00	0.16	0.81	0.41	12.24	0.00	100.00	0.03

Table 7.9. Normative mineral abundance estimates of Pinkos volcanic rocks

Sample	Qtz	K-spar	Ab	Ms	Fe-Chl	Mg-Chl	Cc	Ank	Sid	Rt	Py	Dol	Pg	Phn	Total	Res.
Units	wt.%	wt.%	wt.%	wt.%	wt.%	wt.%	wt.%	wt.%	wt.%	wt.%	wt.%	wt.%	wt.%	wt.%	wt.%	SSQ
RW111	62.34	0.00	0.00	0.01	2.69	14.31	0.00	0.00	0.00	0.07	0.00	0.49	4.28	15.82	100.00	0.22
RW112	57.78	0.00	0.00	0.01	0.00	0.00	0.00	3.74	2.60	0.02	0.00	0.00	8.88	26.96	100.00	2.12
RW113	56.63	0.00	0.00	0.01	0.00	0.00	0.00	4.99	1.11	0.02	0.00	0.00	15.65	21.59	100.00	0.50
RW114	54.82	6.28	15.57	0.00	3.16	2.46	0.03	0.00	0.00	0.12	0.00	4.83	12.73	0.00	100.00	0.02
RW115	62.46	0.00	0.00	15.10	3.75	13.49	0.00	0.00	0.00	0.01	0.00	0.00	5.19	0.00	100.00	0.44
RW116	59.80	0.00	0.00	14.62	4.51	16.28	0.00	0.00	0.00	0.01	0.00	0.00	4.79	0.00	100.00	0.34
RW117	62.32	0.00	0.00	12.94	14.09	5.46	0.00	0.00	0.00	0.01	0.00	0.00	5.17	0.00	100.00	0.40
RW118	62.40	0.00	0.00	12.83	12.16	6.87	0.00	0.00	0.00	0.09	0.00	0.00	5.65	0.00	100.00	0.30
RW119	56.09	11.45	0.72	0.00	3.47	2.87	0.00	4.96	0.00	0.14	0.47	0.00	19.28	0.55	100.00	0.07
RW120	48.67	11.64	17.58	0.00	0.00	3.02	0.00	2.22	4.94	0.17	0.00	0.00	11.75	0.00	100.00	0.37
RW121	57.59	13.60	0.00	0.16	0.69	1.01	0.00	4.58	0.56	0.14	0.00	0.00	21.65	0.01	100.00	0.06
RW122	43.65	2.59	44.03	0.00	5.05	0.27	0.00	0.79	0.00	0.01	0.00	0.01	3.54	0.04	100.00	0.24
RW123	60.43	0.00	0.00	13.43	9.54	12.29	0.00	0.00	0.00	0.00	0.00	0.00	4.16	0.14	100.00	0.64
RW124	61.00	0.00	0.00	17.79	1.34	14.56	0.00	0.72	0.00	0.04	0.00	0.00	4.40	0.15	100.00	0.29
RW125	59.53	0.00	0.00	20.99	3.27	11.58	0.00	0.30	0.00	0.04	0.00	0.00	4.10	0.19	100.00	0.42
RW126	53.84	0.00	0.00	13.84	15.79	10.80	0.00	2.18	0.00	0.68	0.00	0.01	2.86	0.00	100.00	0.39
RW127	69.00	0.00	0.00	18.32	0.42	6.70	0.00	0.00	0.00	0.00	0.00	0.00	5.56	0.00	100.00	0.48
RW128	52.43	0.00	12.20	13.81	1.49	4.28	0.00	7.20	0.20	0.10	0.14	0.00	8.14	0.01	100.00	0.15
RW129	56.62	0.00	14.96	15.29	0.05	0.00	0.00	2.52	0.78	0.13	0.00	0.00	9.65	0.01	100.00	0.12
RW130	59.47	0.00	0.00	0.00	0.00	0.00	1.65	8.09	1.67	0.00	0.00	0.02	10.31	18.80	100.00	0.48
RW131	50.42	0.00	33.95	7.77	0.01	0.00	0.00	2.39	1.58	0.02	0.60	0.00	3.25	0.02	100.00	0.37
RW132	52.30	0.00	22.49	13.85	0.01	0.00	0.00	3.77	0.00	0.02	3.31	0.00	4.24	0.02	100.00	0.08
RW145	61.20	0.00	6.76	22.51	0.01	0.00	0.00	0.00	0.67	0.02	0.00	0.00	8.82	0.02	100.00	0.11
RW146	56.73	0.00	19.55	11.44	0.01	0.00	0.00	5.84	2.29	0.16	0.15	0.00	3.80	0.03	100.00	0.33
RW147*	51.92	0.00	20.26	14.63	0.01	0.00	0.00	2.95	1.47	0.06	0.00	0.00	8.67	0.03	100.00	0.25
RW148	43.28	0.00	38.51	6.04	0.01	0.00	0.00	4.85	1.47	0.12	0.41	0.00	5.28	0.03	100.00	0.23
RW149	49.83	0.00	24.57	10.35	0.01	0.00	0.00	7.54	2.04	0.12	0.35	0.00	5.16	0.03	100.00	0.07
RW150	55.27	0.00	6.99	23.63	0.01	0.00	0.00	0.90	3.35	0.21	0.12	0.00	9.48	0.03	100.00	0.24
RW151	53.33	0.00	13.45	13.99	0.01	0.00	0.00	8.04	2.20	0.08	0.05	0.00	8.76	0.09	100.00	0.44
RW152	45.22	0.00	35.28	7.15	0.01	0.00	0.00	4.24	2.84	0.08	0.05	0.00	5.04	0.09	100.00	0.31
RW153	48.72	0.00	37.05	8.73	0.01	0.00	0.00	1.26	1.38	0.11	0.05	0.00	2.60	0.09	100.00	0.13
RW154	52.56	0.00	18.60	19.81	0.00	0.00	0.00	4.24	0.00	0.13	0.09	0.00	4.41	0.15	100.00	0.09
RW155	55.11	0.00	12.07	28.22	0.00	0.00	0.00	4.23	0.00	0.09	0.09	0.00	0.00	0.20	100.00	0.34
RW156	46.80	0.05	19.49	0.00	0.00	0.00	2.71	1.04	1.98	0.00	0.00	0.00	0.00	27.92	100.00	0.57
RW157	46.77	0.03	27.21	0.00	0.00	0.00	0.00	4.83	0.35	0.01	0.06	0.00	0.00	20.73	100.00	0.39
RW158	59.50	0.05	0.00	25.74	0.00	0.00	0.00	9.47	1.98	0.01	0.00	0.00	3.25	0.00	100.00	0.69
RW159	52.87	12.52	12.72	0.00	0.00	0.00	0.00	0.00	4.01	0.00	0.00	1.20	16.68	0.00	100.00	0.27
RW160	48.87	6.02	32.16	0.00	2.29	0.00	0.00	1.91	3.01	0.10	0.00	0.00	5.66	0.00	100.00	0.08
RW161	54.23	13.17	9.79	0.00	0.00	0.00	0.00	0.00	4.50	0.13	0.00	1.96	16.22	0.00	100.00	0.12
RW162	53.39	15.40	3.65	0.00	2.80	0.00	0.00	8.83	0.06	0.15	0.06	0.00	15.65	0.00	100.00	0.04

Sample	Qtz	K-spar	Ab	Hd	Fe-Chl	Mg-Chl	Cc	Ank	Sid	Rt	Py	Dol	Pg	Phn	Total	Res.
Units	wt.%	wt.%	wt.%	wt.%	wt.%	wt.%	wt.%	wt.%	wt.%	wt.%	wt.%	wt.%	wt.%	wt.%	wt.%	SSQ
RW057	11.3	1.0	23.6	9.9	0.0	16.7	0.0	0.0	12.4	1.7	0.0	12.9	10.3	0.0	100.00	0.03
RW058	8.9	0.1	24.3	17.9	15.2	12.2	0.0	0.0	0.0	1.7	0.0	11.6	7.1	0.2	99.08	0.07
RW065	13.5	0.0	22.6	24.2	14.5	13.1	0.0	0.0	0.0	1.9	0.0	2.7	7.4	0.0	100.00	0.17
RW076	18.1	0.0	17.2	16.0	20.4	7.4	0.0	0.0	0.0	1.9	0.0	10.3	7.7	0.2	99.23	0.07
RW106	15.9	0.0	28.7	14.1	22.7	4.0	0.0	0.0	0.0	1.9	0.2	7.7	4.4	0.3	99.87	0.10
RW107	18.3	0.0	14.6	25.0	14.1	12.8	0.0	0.0	0.0	1.8	0.1	0.5	12.9	0.0	100.00	0.21

* Denotes least-altered sample suite.

NB: Normative mineral estimates based on MINSQ method after Herrmann and Berry (2002; see text for discussion).

Table 7.10. Analytical data for wallrock pyrite at Pinkos

Sample Number	Cu ppm	Fe %	Zn ppm	Pb ppm	Cd ppm	Au ppb	Ag ppm	As ppm	Sb ppm	Tl ppm	Hg ppm	Se ppm	Co ppm	Ni ppm	Te ppm	Bi ppm	Cr ppm	V ppm
	ICP	INAA	ICP	ICP	ICP	INAA	ICP	ICP	INAA	ICP	ICP	INAA	ICP	ICP	ICP	ICP	ICP	ICP
SB035	978	12.0	285.1	249	0.9	22	21.5	97.6	6.5	0.4	0.014	30	45.8	7.3	0.5	14	5.6	0.5
SB036	2530	40.7	1433	352	7.2	340	64.3	313	11	0.1	0.014	84	132	85	0.9	19	3.8	0.5
SB037	459	39.4	1054	286	2.6	270	38.9	153	18	0.1	0.018	81	179	35	1	0.97	2.1	0.8
SB038	1440	33.0	406.2	212	3.5	390	38.6	48.0	27	0.0	0.021	100	16.8	13	2	4.6	2.9	1
SB039	1400	22.6	640.6	353	2.3	73	13.9	139	15	0.1	0.020	7.0	36.9	120	0.3	1.0	420	20
SB040	1210	41.9	595.1	203	1.1	4.0	5.70	13.6	11	0.0	0.014	1.5	57.4	130	0.2	0.84	670	30
SB041	93	39.3	82.95	112	0.5	47	2.79	0.300	1.1	0.0	0.013	1.5	54.5	16	0.3	0.58	6.4	1
SB042	1870	31.2	112.7	154	1.3	150	24.0	34.2	2.8	0.8	0.025	4.5	287	56	0.9	16	66	5
SB049	1080	40.7	254.5	199	1.8	27	8.52	3.55	6.5	0.0	0.012	75	315	22	1	4.3	79	4
SB052	768	34.1	100.6	112	0.6	4.5	13.6	18.6	4.8	0.0	0.013	120	151	79	0.4	3.2	100	5
SB054	443	50.5	177.9	125	1.1	4400	30.8	88.6	5.7	0.0	0.015	140	137	32	1	2.7	5.0	0.8
SB055	878	32.7	7804	225	23	6.5	26.9	131	9.0	0.0	0.035	5.0	70.0	36	0.7	13	59.2	3
SB056	688	40.6	486.4	102	3.9	4.5	27.6	191	11	0.0	0.015	130	17.4	7.3	0.5	3.8	1.2	1
SB057	401	49.2	830.2	190	2.9	35	12.1	94.4	8.6	0.0	0.012	24	20.3	5.4	0.6	11	1.2	0.7
SB058	6970	39.7	35290	261	120	2.5	66.4	59.3	5.1	0.0	0.090	28	54.3	10	2	9.4	0.05	0.3
SB060	818	41.6	715.9	201	1.4	480	52.1	87.4	5.3	0.7	0.011	27	69.4	2.7	0.5	8.2	0.35	0.3
SB061	118	46.1	104.6	97.7	0.4	36	4.30	208	4.4	10	0.015	1.5	38.5	130	0.9	0.90	1.1	0.4
SB062	86	31.8	2432	91.9	7.2	19	11.1	41.5	4.7	1.2	0.014	1.5	80.8	52	0.3	4.9	49	0.7
SB063	257	34.4	2371	110	2.8	450	17.1	63.8	8.2	0.3	0.013	75	48.6	8.2	0.3	4.7	4.6	0.5
SB065	1300	43.8	230.9	137	0.6	220	15.6	8.35	7.7	0.0	0.010	50	57.9	19	0.4	4.6	1.4	0.2
SB066	2350	32.1	149.1	186	0.8	210	25.0	19.7	9.2	0.1	0.010	1.5	30.9	12	0.3	4.5	27	1
SB067	374	29.5	144.1	87.6	0.9	85	15.6	63.8	3.3	0.0	0.010	34	42.4	17	0.4	2.1	2.4	0.4
SB068	1540	30.0	1003	189	3.7	330	33.7	99.1	6.5	0.3	0.011	59	97.8	17	0.7	15	19	1
SB069	879	41.4	140.6	149	0.3	70	14.4	73.5	3.4	0.1	0.011	50	176	5.0	1	3.5	0.50	0.4
SB070	392	23.8	5050	220	22	38	17.3	28.3	2.1	0.0	0.054	1.5	48.4	12	0.3	9.9	40	2
SB071	877	23.7	154.0	67.3	0.8	3.5	19.3	3.79	2.0	0.1	0.010	71	247	14	0.2	0.24	16	30
SB072	291	24.1	82.11	61.5	0.5	4.0	5.53	18.5	1.3	0.2	0.017	63	590	8.7	0.4	0.35	1.5	20
SB073	412	42.7	1262	112	4.3	200	17.2	17.5	3.3	0.0	0.012	39	40.5	10	0.3	1.6	12	0.7
SB074	2030	37.8	539.7	131	5.1	550	42.2	24.8	3.2	0.0	0.012	91	86.4	5.4	0.5	13	2.3	0.7
SB075	2670	48.9	6282	232	23	330	30.9	331	2.5	0.1	0.032	90	118	25	6	7.4	1.7	0.8
SB076	1470	34.7	102500	142	720	170	31.2	71.6	1.3	0.0	0.36	16	41.8	11	0.4	19	0.16	0.4
SB077	23800	40.6	4317	82.7	27	76	24.5	10.3	1.1	0.0	0.031	3.0	139	7.6	0.3	4.9	3.2	0.5
SB079	1410	38.7	140.2	104	0.6	400	11.8	66.3	0.21	0.0	0.013	390	73.9	9.0	2	2.3	0.75	0.4
SB080	1390	17.0	483.8	77.9	1.7	6.5	62.4	214	2.2	0.1	0.015	3.5	245	16	3	5.5	0.54	90
SB081	645	41.1	667.9	273	3.1	77	6.99	15.9	2.7	0.1	0.015	64	42.1	3.5	0.3	3.3	14	0.8
SB082	442	43.7	209.6	160	0.4	470	21.2	42.4	3.5	0.0	0.013	1.5	109	8.1	0.3	3.3	9.4	0.7
SB083	116	40.0	179.3	99.5	0.8	19	3.78	4.82	0.32	0.0	0.010	1.5	25.6	9.3	0.3	0.49	0.20	0.3
*Total REE																		
MAX	23800	50.5	102500	353	720	4400	66.4	331	27	10	0.36	390	590	130	6	19	670	90
MIN	86	12.0	82.11	61.5	0.3	2.5	2.79	0.300	0.21	0.0	0.010	1.5	16.8	2.7	0.2	0.24	0.05	0.2
AVG	1750	36.1	4830	166	27	270	23.8	78.3	6.0	0.4	0.028	53	109	29	0.8	6.0	44	6

Table 7.10. Analytical data for wallrock pyrite at Pinkos

Sample Number	Sc ppm	Th ppm	Ca ppm	Mg ppm	Mn ppm	Na %	Ti ppm	Hf ppm	La ppm	Ce ppm	Nd ppm	Sm ppm	Eu ppm	Tb ppm	Yb ppm	Lu ppm	REE* ppm
	INAA	INAA	ICP	ICP	ICP	INAA	ICP	INAA	INAA	INAA	INAA	INAA	INAA	INAA	INAA	INAA	INAA
SB035	4.5	16	15820	2944	1060	0.41	154	142	75.5	245	218	48.0	15.8	18	40.1	5.49	665.6
SB036	1.9	9.7	6584	2072	691	0.02	110	82.3	73.6	209	170	46.3	13.8	16	29.2	3.87	561.1
SB037	3.6	13	6950	1569	578	0.16	48.6	118	81.7	228	157	29.2	10.3	9.0	41.0	5.93	561.4
SB038	4.7	25	21530	4702	1390	0.40	151	260	188	491	401	94.0	25.8	29	61.8	8.63	1300
SB039	13	38	24730	4599	14800	1.1	150	279	560	1300	1020	147	33.7	27	62.9	9.06	3160
SB040	2.8	13	15580	3187	25300	0.74	28.1	202	100	268	191	30.2	10.7	9.8	42.7	6.75	659.3
SB041	2.2	32	12720	2934	772	0.031	31.2	181	101	641	340	38.2	31.2	39	104	16.1	1309
SB042	2.2	6.9	9226	2264	2920	0.27	19.8	136	473	1070	651	112	24.8	14	29.9	4.59	2379
SB049	2.4	9.8	3922	2597	3150	0.92	52.5	140	102	261	164	30.8	8.06	7.7	35.0	5.41	613.8
SB052	3.2	19	16970	5484	4260	0.52	11.5	141	191	447	275	46.7	11.4	9.4	32.4	5.27	1018
SB054	3.6	8.1	5267	1820	343	0.12	43.4	166	143	355	218	39.3	9.69	0.25	31.2	5.10	801.9
SB055	2.8	15	5008	1822	1860	0.13	79.1	227	53.7	185	71.3	27.7	12.4	17	57.5	7.99	432.3
SB056	2.7	28	4724	1736	209	0.32	96.3	93.7	36.9	140	78.5	29.0	11.8	12	32.2	4.77	345.3
SB057	1.0	8.2	9025	2689	430	0.051	27.8	57.1	61.9	164	90.8	22.8	5.41	6.8	24.2	3.49	379.8
SB058	2.1	88	8200	2943	641	0.071	451	35.7	60.0	212	216	126	40.7	54	71.6	8.66	789.7
SB060	2.2	4.7	1810	580.0	241	0.10	14.3	34.7	124	280	162	40.1	10.2	8.9	23.5	3.34	652.6
SB061	0.82	2.6	1416	632.7	144	0.041	14.3	11.2	13.9	36.7	19.4	4.93	1.12	1.7	6.43	1.06	85.24
SB062	7.5	16	40820	12365	1990	0.44	28.5	217	253	612	356	70.0	16.0	12	47.9	7.98	1375
SB063	4.4	15	20140	4854	1010	0.70	102	243	162	442	296	87.5	29.3	27	57.9	8.67	1111
SB065	4.7	12	845.0	9011	1390	0.10	20.9	204	60.6	169	86.1	18.2	3.47	4.1	39.7	6.54	387.9
SB066	4.8	11	21390	9012	2270	0.63	55.6	180	317	747	478	107	30.1	36	121.8	16.1	1852
SB067	2.5	15	5786	2807	591	0.90	94.0	73.5	669	1410	858	157	27.0	16	35.7	5.12	3177
SB068	3.4	16	20560	4580	1750	0.86	220	133	828	1760	1100	199	29.1	28	50.3	7.25	4003
SB069	0.84	6.1	267.0	2677	107	0.021	24.6	71.4	134	327	185	31.7	4.52	5.5	20.3	3.36	711.4
SB070	8.2	21	14260	9613	3870	0.22	38.9	254	891	1970	1230	191	28.4	13	46.4	7.58	4377
SB071	18	0.25	19630	6963	1430	0.83	332	4.62	9.90	48.7	2.50	3.05	1.52	0.15	1.91	0.290	68.03
SB072	60	0.25	11540	2036	325	0.20	854	3.30	10.3	48.7	2.50	3.74	2.51	0.15	3.63	0.469	72.00
SB073	2.9	9.5	3574	4913	1440	0.14	46.6	97.7	141	342	254	64.5	20.3	18	37.2	5.12	881.8
SB074	10	21	6059	5204	692	0.12	163	315	146	364	278	66.7	16.5	24	77.0	11.8	983.2
SB075	3.1	7.7	3223	2906	505	0.032	19.0	230	25.4	112	44.9	18.6	7.92	14	55.4	7.91	285.7
SB076	1.6	4.7	119.6	1405	49.6	0.010	14.5	68.5	333	769	454	89.1	14.3	15	30.0	4.18	1708
SB077	1.4	6.2	3833	3104	609	0.28	47.5	112	77.8	274	287	118	35.6	36	66.2	8.66	904.2
SB079	2.1	7.2	695.6	2608	152	0.086	85.2	135	71.8	225	119	29.4	12.5	15	63.6	8.96	545.3
SB080	36	3.5	8007	26550	4490	0.010	74.7	27.1	85.1	239	165	27.5	9.83	6.6	27.5	3.73	564.0
SB081	7.9	13	9489	5567	1040	0.34	43.4	223	290	745	496	102	29.4	24	67.7	9.35	1764
SB082	2.2	8.5	4495	1853	756	0.10	26.3	98.4	276	587	393	103	29.2	27	48.7	6.63	1470
SB083	1.3	4.9	1717	741.9	172	0.043	19.1	24.6	56.2	121	70.6	14.4	2.78	3.2	12.6	2.00	283.1
*Total REE																	
MAX	60	88	40820	26550	25300	1.1	854	315	891	1970	1230	199	40.7	54.1	122	16.1	4377
MIN	0.82	0.25	119.6	580.0	49.6	0.010	11.5	3.30	9.90	36.7	2.50	3.05	1.12	0.2	1.91	0.290	68.03
AVG	6.5	14	9890	4415	2260	0.31	103	136	197	482	313	65.3	16.9	16.3	44.2	6.41	1142

Table 7.11. Pearson correlation matrix for selected trace elements in wallrock pyrite at Pinkos

	Cu	*Fe*	*Zn*	*Pb*	*Cd*	*Au*	*Ag*	*As*	*Sb*	*Tl*	*Hg*	*Se*	*Co*	*Ni*	*Te*	*Bi*	*Cr*
Fe	0.09																
Zn	0.09	0.00															
Pb	-0.05	0.00	0.04														
Cd	0.06	-0.01	0.98	-0.01													
Au	-0.07	0.33	-0.05	-0.06	-0.04												
Ag	0.20	-0.07	0.22	0.34	0.15	0.15											
As	-0.08	0.09	0.01	0.37	-0.01	0.05	0.47										
Sb	-0.12	0.00	-0.15	0.52	-0.16	0.04	0.23	0.21									
Tl	-0.09	0.15	-0.06	-0.16	-0.05	-0.06	-0.19	0.25	-0.06								
Hg	0.08	-0.04	0.99	0.03	0.99	-0.05	0.17	0.00	-0.15	-0.05							
Se	-0.10	0.18	-0.12	-0.10	-0.11	0.28	0.02	0.10	0.02	-0.15	-0.12						
Co	0.03	-0.25	-0.14	-0.24	-0.12	0.00	-0.02	-0.07	-0.23	-0.09	-0.11	0.06					
Ni	-0.10	0.04	-0.11	0.27	-0.10	-0.04	-0.15	0.29	0.28	0.49	-0.09	-0.15	-0.04				
Te	0.05	0.19	0.03	0.15	-0.02	0.10	0.36	0.63	-0.01	-0.01	0.01	0.24	0.11	-0.05			
Bi	0.08	-0.15	0.43	0.36	0.42	-0.04	0.52	0.28	-0.02	-0.12	0.44	-0.12	-0.10	-0.10	0.08		
Cr	-0.05	-0.07	-0.08	0.29	-0.07	-0.10	-0.25	-0.10	0.29	-0.06	-0.06	-0.18	-0.08	0.69	-0.16	-0.20	
V	-0.05	-0.47	-0.09	-0.18	-0.08	-0.12	0.22	0.16	-0.07	-0.07	-0.08	-0.15	0.37	0.15	0.19	-0.17	0.28
Sc	-0.10	-0.51	-0.10	-0.26	-0.09	-0.09	0.01	-0.03	-0.16	-0.08	-0.08	-0.04	0.72	-0.09	0.03	-0.20	-0.01
Th	0.12	-0.04	0.16	0.36	0.02	-0.10	0.31	-0.05	0.24	-0.15	0.08	-0.06	-0.31	0.02	0.03	0.06	0.12
Ca	-0.13	-0.49	-0.19	0.09	-0.20	-0.12	-0.13	-0.19	0.32	-0.09	-0.19	-0.19	-0.04	0.23	-0.23	-0.07	0.30
Mg	-0.04	-0.47	-0.12	-0.20	-0.12	-0.13	0.23	0.03	-0.08	-0.12	-0.11	-0.16	0.09	-0.07	0.15	-0.05	-0.02
Mn	-0.05	-0.15	-0.10	0.26	-0.09	-0.12	-0.19	-0.09	0.28	-0.09	-0.08	-0.21	-0.07	0.66	-0.13	-0.19	0.98
Na	-0.04	-0.40	-0.21	0.10	-0.19	-0.13	-0.27	-0.25	0.28	-0.13	-0.20	-0.06	0.03	0.26	-0.29	-0.21	0.49
Ti	0.03	-0.38	0.02	-0.08	-0.04	-0.09	0.10	-0.11	-0.04	-0.10	-0.02	0.07	0.60	-0.16	-0.04	-0.06	-0.07
Hf	-0.05	-0.03	-0.15	0.34	-0.14	0.13	-0.12	-0.10	0.35	-0.24	-0.12	0.07	-0.34	0.12	0.04	0.10	0.31
La	-0.11	-0.36	0.07	0.18	0.09	-0.03	-0.06	-0.16	-0.01	-0.11	0.13	-0.20	-0.17	0.03	-0.22	0.25	0.13
Ce	-0.09	-0.36	0.07	0.19	0.09	-0.03	-0.08	-0.18	-0.02	-0.14	0.13	-0.21	-0.19	0.02	-0.23	0.23	0.13
Nd	-0.02	-0.38	0.06	0.26	0.08	-0.04	-0.04	-0.17	0.05	-0.14	0.12	-0.23	-0.22	0.06	-0.23	0.22	0.19
Sm	0.23	-0.29	0.15	0.26	0.12	-0.05	0.14	-0.19	0.05	-0.18	0.17	-0.23	-0.27	-0.08	-0.20	0.29	0.07
Eu	0.38	-0.18	0.09	0.28	0.03	-0.07	0.17	-0.22	0.10	-0.24	0.07	-0.20	-0.33	-0.12	-0.16	0.14	0.06
Tb	0.43	-0.05	0.16	0.29	0.08	-0.16	0.27	-0.14	0.14	-0.21	0.10	-0.13	-0.37	-0.17	-0.03	0.17	-0.01
Yb	0.24	0.02	-0.01	0.26	-0.05	-0.02	0.08	-0.17	0.16	-0.27	-0.04	0.02	-0.40	-0.15	0.03	0.04	0.06
Lu	0.18	0.03	-0.05	0.22	-0.08	0.00	0.00	-0.20	0.14	-0.27	-0.06	0.02	-0.41	-0.12	0.00	0.02	0.09
REE*	-0.04	-0.36	0.08	0.22	0.09	-0.04	-0.05	-0.18	0.01	-0.15	0.13	-0.22	-0.22	0.03	-0.23	0.24	0.15

* Total REE All values are different from 0 with a significance level alpha=0.05.

Table 7.11. Pearson correlation matrix for selected trace elements in wallrock pyrite at Pinkos

	V	*Sc*	*Th*	*Ca*	*Mg*	*Mn*	*Na*	*Ti*	*Hf*	*La*	*Ce*	*Nd*	*Sm*	*Eu*	*Tb*	*Yb*	*Lu*
Fe																	
Zn																	
Pb																	
Cd																	
Au																	
Ag																	
As																	
Sb																	
Tl																	
Hg																	
Se																	
Co																	
Ni																	
Te																	
Bi																	
Cr																	
V																	
Sc	0.62																
Th	-0.14	-0.17															
Ca	0.13	0.18	0.21														
Mg	0.74	0.42	-0.04	0.36													
Mn	0.40	0.05	0.11	0.32	0.13												
Na	0.10	0.03	0.09	0.58	0.05	0.48											
Ti	0.18	0.74	0.24	0.17	-0.05	-0.08	0.12										
Hf	-0.22	-0.21	0.20	0.39	0.10	0.31	0.26	-0.27									
La	-0.10	-0.10	0.10	0.32	0.12	0.16	0.44	-0.11	0.29								
Ce	-0.11	-0.11	0.15	0.35	0.13	0.16	0.42	-0.12	0.35	0.99							
Nd	-0.09	-0.10	0.22	0.38	0.13	0.21	0.46	-0.10	0.38	0.98	0.99						
Sm	-0.19	-0.18	0.38	0.33	0.08	0.09	0.40	-0.02	0.32	0.88	0.88	0.92					
Eu	-0.19	-0.21	0.58	0.32	0.04	0.07	0.28	0.00	0.37	0.53	0.59	0.66	0.83				
Tb	-0.23	-0.25	0.68	0.23	-0.04	-0.01	0.12	0.08	0.31	0.22	0.29	0.36	0.60	0.89			
Yb	-0.22	-0.26	0.45	0.27	0.10	0.07	0.11	-0.15	0.62	0.18	0.27	0.30	0.41	0.70	0.80		
Lu	-0.23	-0.27	0.42	0.30	0.12	0.10	0.12	-0.20	0.69	0.20	0.30	0.32	0.39	0.66	0.74	0.99	
REE*	-0.12	-0.12	0.20	0.36	0.13	0.17	0.44	-0.11	0.37	0.99	1.00	1.00	0.91	0.65	0.35	0.31	0.33

* Total REE All values are different from 0 with a significance level alpha=0.05.

8. ALTERATION MINERALOGY AND MINERAL CHEMISTRY

8.1 SHORTWAVE INFRARED (SWIR) SPECTROSCOPY

A suite of 54 samples from Delbridge and 108 samples from Pinkos were analyzed using a portable shortwave infrared (SWIR) spectrometer. This is a relatively new field method for mapping alteration minerals in VMS environments. Recent studies by Huston et al (1997) in the Panorama district of Western Australia used SWIR to map alteration zones based on sericite/chlorite ratios. Herrmann et al (2001) used field-based SWIR spectrometry to determine compositional variations of white micas as a vector to VMS deposits in Tasmania and Queensland. Jones et al (2005) also identified previously unmapped hydrothermal alteration zones with poor mineralogical zonation around VMS deposits at Myra Falls, British Columbia, using subtle shifts in key absorption features for both sericite and chlorite. Other useful applications of SWIR to VMS alteration systems have been published by Thompson et al (1999) and Huston et al (1999).

Reflectance spectroscopy uses the energy in the visible (400-700 nm), near infrared (700-1300 nm) and shortwave infrared (1300-2500 nm) wavelength regions of the electromagnetic spectrum in order to analyze minerals (Hauff, 2005; Clark, 2004; Hunt and Ashley, 1979). SWIR spectroscopy detects the absorption of energy caused by transitions in the vibrational states of molecular bonds under a white light source. In the SWIR region, molecular changes are detected; in the visible/near-infrared (VNIR) region, variations in colour and elemental oxidation states are identifiable (Thompson et al, 1999). Absorption occurs at well-defined wavelength positions that are characteristic of the bonds (Hauff, 2005), in particular OH (hydroxyl), H_2O (water), NH_4 (ammonia), CO_3

(carbonate), SO_4 (sulfate) and cation-OH bonds (Al-OH, Mg-OH and Fe-OH) (Thompson et al, 1999). As a result, SWIR spectroscopy is useful for the identification of a wide range of mineral groups, including phyllosilicates, hydrated silicates and sulfates, carbonates and ammonium-bearing minerals (Herrmann et al, 2001; Hauff, 2005). The SWIR spectra are generally presented as plots of relative reflectivity (percentage) versus wavelength (in nm or µm) with absorption bands represented by deviations from the spectral hull (or continuum). Wavelength position, feature depth and width at half maximum all vary with the chemical composition and crystallinity of a particular mineral (Hauff, 2005; Huston et al, 1999).

Spectral measurements were obtained using an Analytical Spectral Devices (ASD) Inc. Terraspec Pro® spectroradiometer at the University of Ottawa. The spectra were collected from a set of 162 clean and dry thin section off-cuts and whole-rock geochemical pulps. Data were processed using Viewspec Pro® software and the spectral reference library in the accompanying Specmin® software, provided by Spectral International Inc.

The results of 54 spectral measurements of samples collected at Delbridge are presented in Table 5.1. Six minerals identified in the sample suite include quartz, muscovite, Ca-carbonate, Fe-carbonate, Mg-chlorite, and Fe-chlorite. Representative SWIR spectra for samples containing these minerals are shown in Figure 8.1.

Muscovite ($K_1Al_2(Si_3Al)O_{10}(F,OH)_2$) is identified by single, sharp absorption

features in the ~1400 nm region (OH and H_2O molecules) and the ~2200 nm Al-OH molecule region. Another useful indicator in well-crystallized samples is a small shoulder feature at ~2110 nm on the left limb of the sharp Al-OH absorption feature. The carbonate minerals ($X^{2+}CO_3^{2-}$) only have one major absorption feature that occurs between 2319 and 2364 nm. The dominant cation present in the carbonate species can also be identified based on the position of the ~2350 nm CO_3^{2-} absorption feature: absorption at <2350 nm indicates Ca-bearing carbonate and absorption at >2350 nm indicates Fe-bearing species. The most diagnostic feature for Fe-rich carbonate in mixtures is the positive slope of the spectral profile from ~1300 to 1900 nm. The chlorite group ($(Mg,Fe)_3(SiAl)_4O_{10}(OH)_2 \cdot (Mg,Fe)_3(OH)_6$) has several diagnostic absorption features related to the major cations present (iron, magnesium or aluminum). The dominant cation in the octahedral layer of the chlorite structure is identified based on shifts in the ~2300 nm Mg-OH absorption feature: absorption at <2340 nm indicates Mg-rich species and absorption at >2340 nm indicates Fe-bearing species. Mg-OH is also indicated by three small features in the lower wavelength regions near 1400 nm that plateau towards higher wavelengths. Aluminum substitution in the tetrahedral layer is indicated by the increasing depth of the 2250 nm feature. As for carbonate, iron in chlorite is most readily identified by a positive slope between ~1500 and 1900 nm.

For each sample, the relative abundance of the alteration minerals (major, minor, trace) was estimated based on their identification by SWIR, the relative intensity of spectral absorption features, and observations in hand specimen. Although the SWIR data cannot provide quantitative information about concentrations, relative abundances

can be readily assigned with additional information such as modal mineralogy in selected thin sections of representative assemblages.

Four well-defined alteration assemblages were identified in the SWIR spectra of the samples from Delbridge: Fe-carbonate + Fe-chlorite, Ca-carbonate + muscovite, Mg-chlorite + muscovite, and quartz + muscovite (Figure 8.1). The identified assemblages are plotted in Figure 8.2. The zone of intense Fe-carbonate alteration is clearly identified between the two interpreted syn-volcanic faults, immediately beneath the surface projection of the orebody and ~200 m into the footwall. The margins of this zone are indicated by the presence of abundant Mg-chlorite and muscovite to the north and south. The Ca-carbonate + muscovite assemblage immediately overlies the Fe-carbonate core of the hydrothermal system and extends ~200 m into the stratigraphic hanging wall (Figure 8.2). Fe-bearing chlorite is present in the mafic volcaniclastic rocks. Quartz + muscovite alteration occurs along the margins of the system and at the top of the sampled stratigraphy.

SWIR data for the samples from Pinkos are presented in Table 5.2 and plotted in Figure 8.3. Fe-carbonate and Fe-chlorite are located north of the Lamothe pit road in a zone that terminates approximately at the known mineralized horizon, diminishing towards the south within the fragmental unit. The proximity of this alteration to the South Bay Fault indicates that fluids were likely focussed along this structure and in the fractured rhyolite flows and fragmental rocks. Quartz and muscovite form a broad alteration zone that both flanks and envelopes the Fe-rich alteration. Mg-chlorite,

muscovite, and Fe-poor carbonate alteration zones are located distal to the Fe-carbonate at the margins of the system (Figure 8.3).

8.2 ALTERATION MINERAL CHEMISTRY

8.2.1 DELBRIDGE

Electron microprobe analyses of representative silicate and carbonate grains were carried out on ten carbon-coated polished thin sections from Delbridge. The results are listed in Tables 8.3-8.5. Samples from the interpreted core of hydrothermal upflow, the distal margins of the system, and the hanging wall were selected to determine possible compositional zonation for each of the analyzed minerals. Quantitative analyses were conducted in the Earth Sciences Department at Carleton University by wavelength dispersive x-ray analysis (WDX) using an automated 4 spectrometer Cameca Camebax MBX electron microprobe. The alteration minerals were analyzed using 20 kv accelerating voltage, 30 nA beam current with a focused 2 μm diameter beam, and counting times of 10-20 seconds or 40,000 accumulated counts. Digital backscattered electron (BSE) images were collected with an Electron Optic Services digital imaging system at 512 x 512 pixel resolution and a Lamont 4 element solid state BSE detector.

Muscovite

High Al (~5.7 formula ions) and moderately low Na/Na+K (~0.2 mole fraction) indicate that white micas at Delbridge tend towards aluminous compositions and mainly consist of muscovite with minor phengite and trace paragonite (Table 8.3). The analytical data are plotted on a muscovite-paragonite-celadonite ternary diagram in

Figure 8.10. The data indicate a very narrow range of muscovite compositions, similar to that previously noted by Barrett et al (1993).

Chlorite

Eight chlorite analyses are given in Table 8.4 and plotted in Figure 8.4 (after Hey, 1954). All of the analyzed chlorite has similar Si^{4+} contents (~5.0-5.3 formula ions) and nearly all plot within the ripidolite compositional field. One sample contains slightly less Si^{4+} and plots as pseudo-thuringite. All of the chlorite is Fe-rich (> 0.5 Fe/Fe+Mg), but some variation is evident between proximal and distal samples (Figure 8.4). The highest Fe/(Fe+Mg) ratios (~0.78 mole fraction) occur in stringer chlorite from the interpreted core of hydrothermal upflow and the lowest ratios (~0.55 mole fraction) in matrix chlorite collected along the margins of the system (Figure 8.5). Intermediate compositions are identified in both the hanging wall and upper footwall (Figure 8.5). Mn content is low in all analyzed samples (~0.02-0.04 formula ions).

Carbonate

Analyses of carbonate minerals are provided in Table 8.5 and plotted on a major cation ternary diagram in Figure 8.6. Consistent with SWIR spectroscopic and petrographic interpretations, calcite ($CaCO_3$) is only identified in hanging-wall ($\pm$ uppermost footwall) samples. Fe/(Fe+Mg) ratios range from 0.59-0.78 (mole fraction; Table 8.5) but total contained Fe and Mg are low. Most of the analyzed carbonate is dolomite ($CaMg(CO_3)_2$) and ferroan ankerite ($CaFe(CO_3)_2$; Figure 8.6). These ankerites are easily divided into two groups based on Fe/(Fe+Mg) mole ratios: Fe-rich ankerite

(0.60-0.73) occurs in stringers and stockwork immediately beneath mineralization and in adjacent coarse rhyolite breccia, and Mg-rich ankerite (0.31-0.51) occurs in distal QP rhyolite and felsic lapilli tuff along the interpreted margins of the system (Figure 8.7).

Three samples of carbonate in the interpreted core of hydrothermal upflow have a narrow range of high Fe/Fe+Mg (Table 8.5). Seven samples from the margins of the system and in the hanging wall have lower and more variable Fe/Fe+Mg. These heterogeneities are evident in electron backscatter as mottled textures (Figures 8.8a-d); lighter coloured zones contain more Fe than darker coloured zones (e.g., RW020; Figures 8.8a-d; Table 8.5).

Mn contents in carbonate at Delbride are in the range of 0.14-3.19 wt.% MnO (Table 8.5). Concentrations are consistently higher (1-2 wt.% MnO) between the two inferred synvolcanic faults in footwall stringers and stockwork and in the immediate hanging wall; however, the highest concentrations (> 2 wt.% MnO) occur in two isolated samples outside of this zone (Figure 8.9).

8.2.2 PINKOS

Electron microprobe analyses of representative silicate and carbonate grains were carried out on sixteen carbon-coated polished thin sections from Pinkos along with the Delbridge samples. Samples from stringers and stockwork, columnar-jointed rhyolite in the main upflow zone, and distal coherent rhyolite towards the interpreted margins of the system were selected to determine possible zonation in mineral chemistry.

Muscovite

Three muscovite analyses (Table 8.3) have low Na/(Na+K) mole ratios of 0.04 and 0.06 in both proximal (RW088) and distal (RW072, RW128) samples. Sodium content in distal samples is nearly double that of muscovite from the interpreted upflow zone, which is consistent with sodium depletion in the highest-temperature alteration associated with VMS mineralization (Franklin et al, 1981). The analytical data are plotted on a muscovite-paragonite-celadonite ternary diagram in Figure 8.10 and show the same narrow range as other well-known Archean VMS deposits in the Abitibi greenstone belt.

Chlorite

Chlorite compositions were determined in ten samples (Table 8.6) and are compared in Figure 8.11 (after Hey, 1954). All of the chlorites have similar Si^{4+} contents (~5.1-5.4 formula ions) and plot within the ripidolite compositional field (Figure 8.11). Consistent with SWIR and transmitted-light petrography, intermediate to Fe-rich chlorite (0.60-0.69 Fe/Fe+Mg) is concentrated in the stockwork zone to the southeast and Mg-rich to intermediate chlorite (0.34-0.59 Fe/Fe+Mg) in stringers to the northwest. Unlike at Delbridge, the highest Fe/Fe+Mg ratios (0.75-0.80) occur outside of the interpreted focus of hydrothermal upflow in zones of columnar-jointed rhyolite (Figure 8.12). Distal footwall chlorite shows significant variation in Fe/Fe+Mg ratios, from ~0.35-0.75. Mn content is low in all analyzed chlorites (~0.01-0.04 formula ions). Although chlorite compositions at Pinkos are similar to that of many Noranda-type VMS deposits (Figure

8.13), a trend to lower Fe/Fe+Mg ratios is evident.

Carbonate

Carbonate compositions were determined in fourteen samples (Table 8.7) and are plotted on a major cation ternary diagram in Figure 8.14. Consistent with the SWIR data and transmitted-light petrography, calcite (± calcic ankerite) is restricted to distal coherent rhyolite and stockwork in the northwest of the map area (Figure 8.15). Distal coherent footwall rhyolite contains mainly Mg-rich ankerite (0.2-0.5 Fe/Fe+Mg) and minor calcite (Figure 8.15). In columnar-jointed rhyolite, intermediate to Fe-rich ankerite (0.4-0.6 Fe/Fe+Mg) is the dominant carbonate composition with minor Mg-rich species (0.1-0.3 Fe/Fe+Mg). The highest Fe/Fe+Mg values (~0.5-0.7) occur in the stockwork zone to the southeast and in overlying fragmental rhyolite (Figure 8.15). Siderite was only identified in one fragmental rhyolite sample and analyses of two grains indicate Fe/Fe+Mg ratios in the range of 0.79-0.80.

Carbonate in the interpreted core of the hydrothermal upflow has a more homogeneous composition compared to carbonate sampled along the interpreted margins of the system. Carbonate in zones of columnar-jointed and distal coherent rhyolite is more heterogeneous in composition, which is reflected by significant mottling of lighter and darker colours in electron backscatter, representing relatively Fe-rich and Fe-poor zones, respectively (Figures 8.16a-e). Zoned carbonate was identified in several samples, with Fe contents clearly highest along grain boundaries (Figures 8.16f, g). Subhedral to euhedral siderite, only identified in one fragmental rhyolite sample (RW096), is

homogeneous and possibly included in later Fe-rich ankerite (Figure 8.16h). This may suggest more than one generation of carbonate precipitation as well as multiple sources.

Mn contents (wt.% MnO) in carbonate at Pinkos are in the range of 0.24-2.22 wt.% MnO (Table 8.7). Concentrations are consistently higher (> 1 wt.% MnO) in stringers and stockwork to the southeast and overlying fragmental rhyolite (Figure 8.17). Lower Mn contents are observed in the stockwork zone to the northwest and proximal columnar-jointed rhyolite (Figure 8.17).

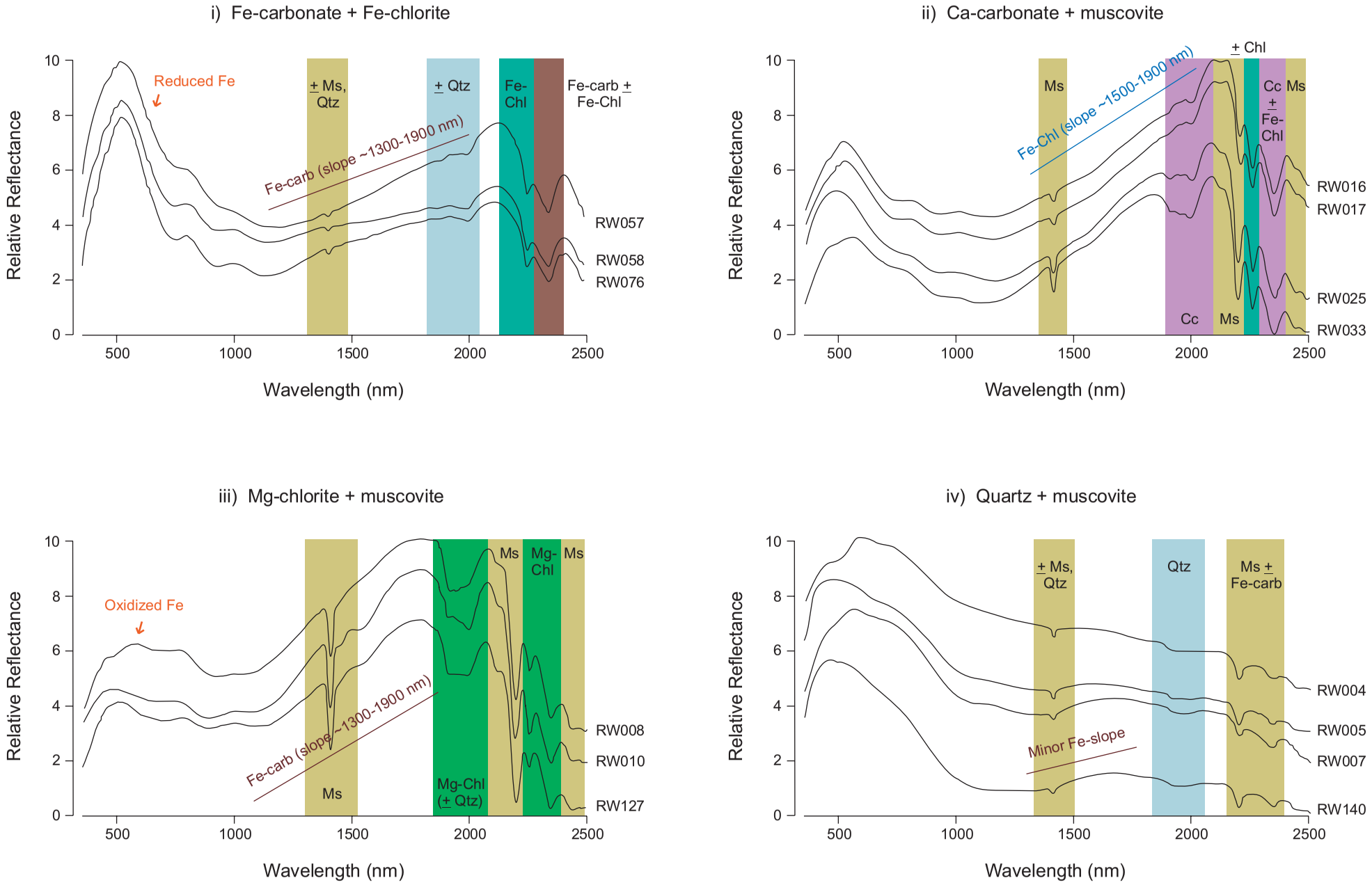

Figure 8.1. Representative short-wave infrared radiation (SWIR) spectral signatures corresponding to four well-defined alteration assemblages from the Delbridge and Pinkos study areas: (i) Fe-carbonate + Fe-chlorite; (ii) Ca-carbonate + muscovite; (iii) Mg-chlorite + muscovite; and (iv) quartz + muscovite. Mineral identification is based on characteristic absorption features: quartz is detected by broad, rounded features at <1400 nm and 1900 nm; muscovite is identified by single, sharp features at 1400 nm and 2200 nm; carbonate is manifested by a large, broad feature in the 2350 nm region (<2350 nm = Ca-rich and >2350 nm = Fe-rich); Fe-carbonate is also identified by a positive slope between 1300-1900 nm; chlorite has single, sharp features in the 2250 nm and 2350 nm regions and two minima in the 1800-2000 nm wavelength range; Mg-chlorite has three small features in the 1400 nm region that plateau towards higher wavelengths; Fe-chlorite most readily identified by a positive slope between 1500-1900 nm. Coloured bands are used in the figure to highlight the diagnostic spectral characteristics used in the identification of each mineral assemblage. (Plots modified from SpecWin, Spectral International, Inc.)

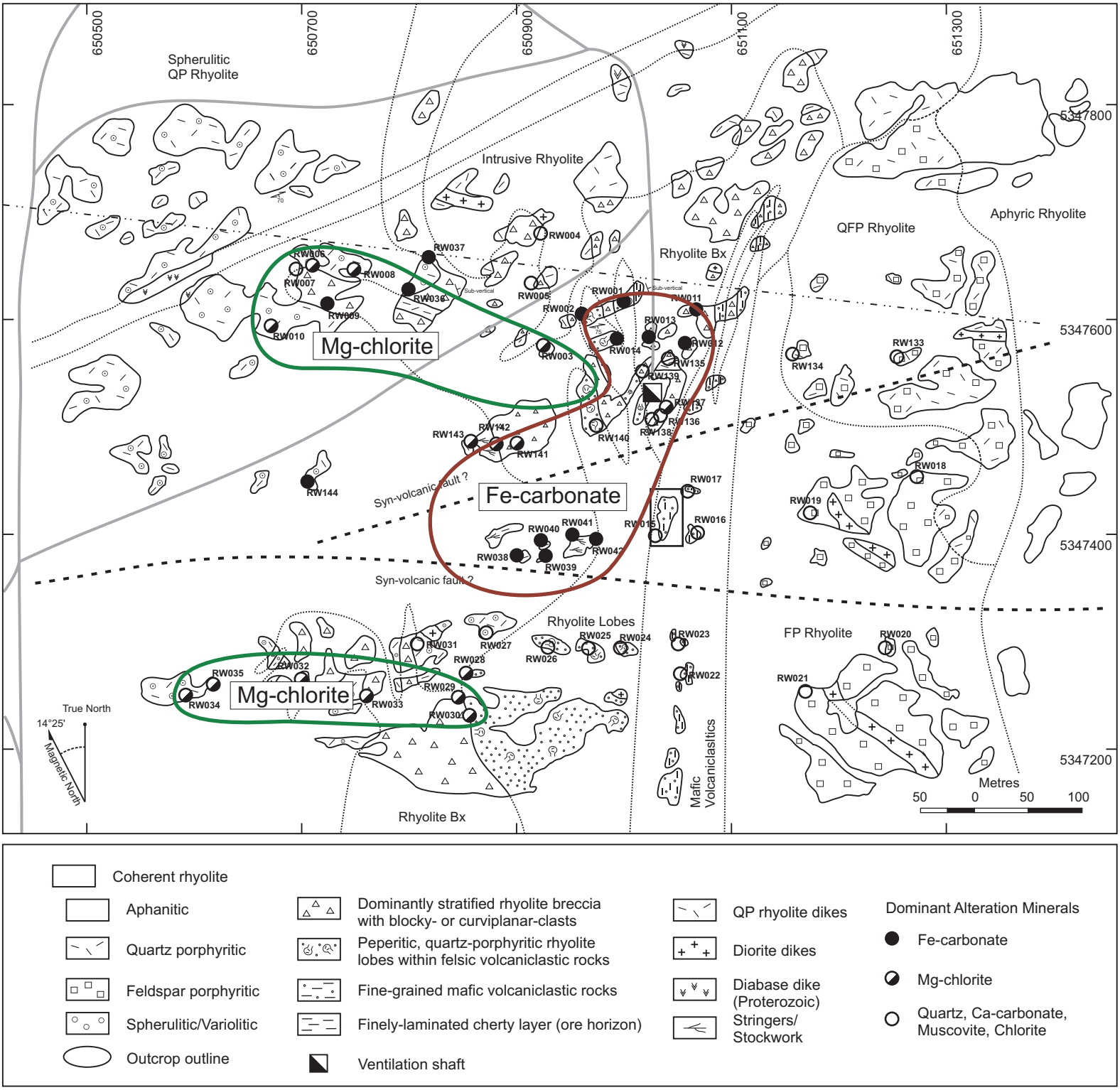

Figure 8.2. Dominant alteration minerals in the Delbridge map area identified using shortwave infrared (SWIR) spectroscopy. The main assemblages are: 1) Fe-carbonate + Fe-chlorite (red-brown); 2) Ca-carbonate + muscovite (yellow); 3) Mg-chlorite + muscovite (green); and 4) quartz + muscovite (blue). The importance of host-rock permeability as a control on alteration and mineralization is demonstrated by the infiltration of Fe-carbonate and Fe-chlorite into the adjacent coarse rhyolite breccia pile.

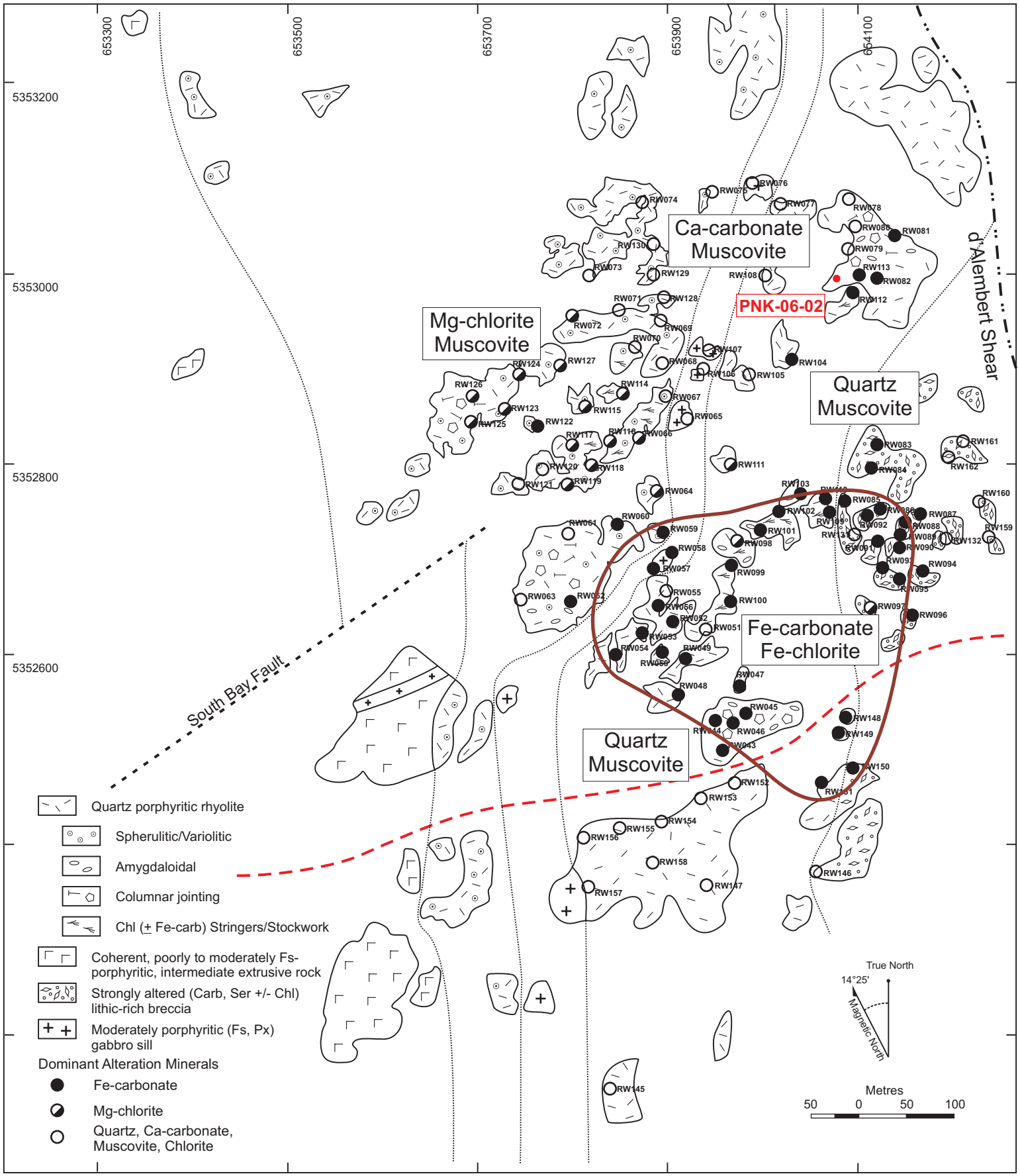

Figure 8.3. Dominant alteration minerals in the Pinkos map area identified using shortwave infrared (SWIR) spectroscopy. The major assemblages are: 1) Fe-carbonate + Fe-chlorite (red-brown); 2) Ca-carbonate + muscovite (yellow); 3) Mg-chlorite + muscovite (green); and 4) quartz + muscovite (blue). The core of the hydrothermal system is effectively along trend of the South Bay Fault. The importance of host-rock permeability as a control on alteration and mineralization is demonstrated by the occurrence of Fe-carbonate and Fe-chlorite mainly within host-rocks that are either fragmental or have high primary porosity in the form of amygdules, columnar joints, and a variety of other cooling features.

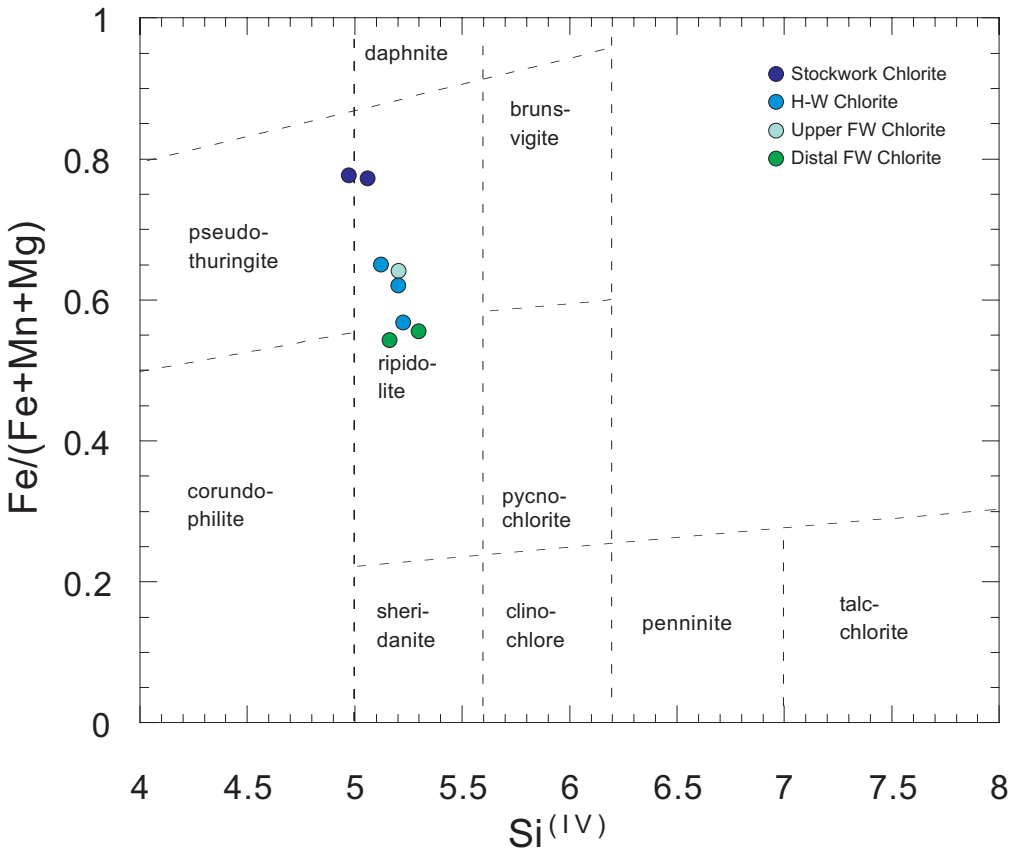

Figure 8.4. Compositional variation of chlorite at Delbridge. All of the grains show similar Si^{4+} contents (~5.0-5.3 formula ions) and nearly all plot within the ripidolite compositional field. One sample contains slightly less Si^{4+} and plots as pseudo-thuringite. Though each of the analyzed grains is relatively Fe-rich (> 0.5 Fe/Fe+Mg), compositional variation is evident between proximal and distal samples. The highest Fe/(Fe+Mg) ratios (~0.78 mole fraction) occur in stringer chlorite from the interpreted core of hydrothermal upflow and the lowest ratios (~0.55 mole fraction) in matrix chlorite collected along the margins of the system (Figure 8.5). Intermediate compositions are identified in hanging-wall and upper footwall chlorite grains (Figure 8.5). Plotted data from quantitative electron microprobe analyses are summarized in Table 8.4. The classification scheme is that of Hey (1954).

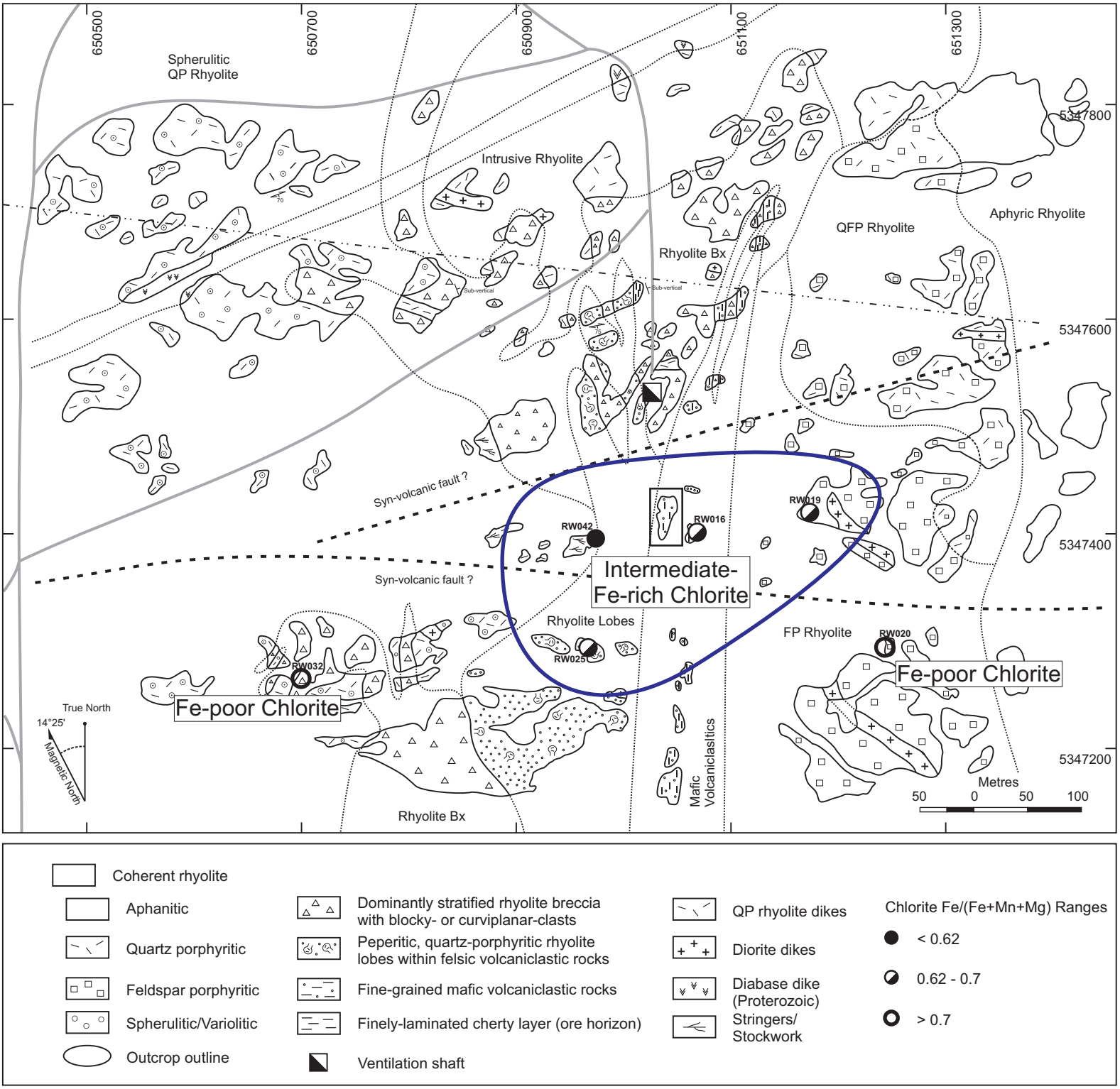

Figure 8.5. Compositional variation of chlorite at Delbridge shown with respect to lithofacies. Though nearly all analyzed grains plot within the ripidolite field of a chlorite compositional diagram (Figure 8.4; after Hey, 1954), zonation between alteration types is evident. The highest Fe/(Fe+Mg) ratios (~0.78 mole fraction) occur in stringer chlorite from the interpreted core of hydrothermal upflow and the lowest ratios (~0.55 mole fraction) in matrix chlorite collected along the margins of the system. Intermediate compositions are identified in hanging-wall and upper footwall chlorite grains. Mineral identifications based on analytical electron microprobe data (Table 8.4).

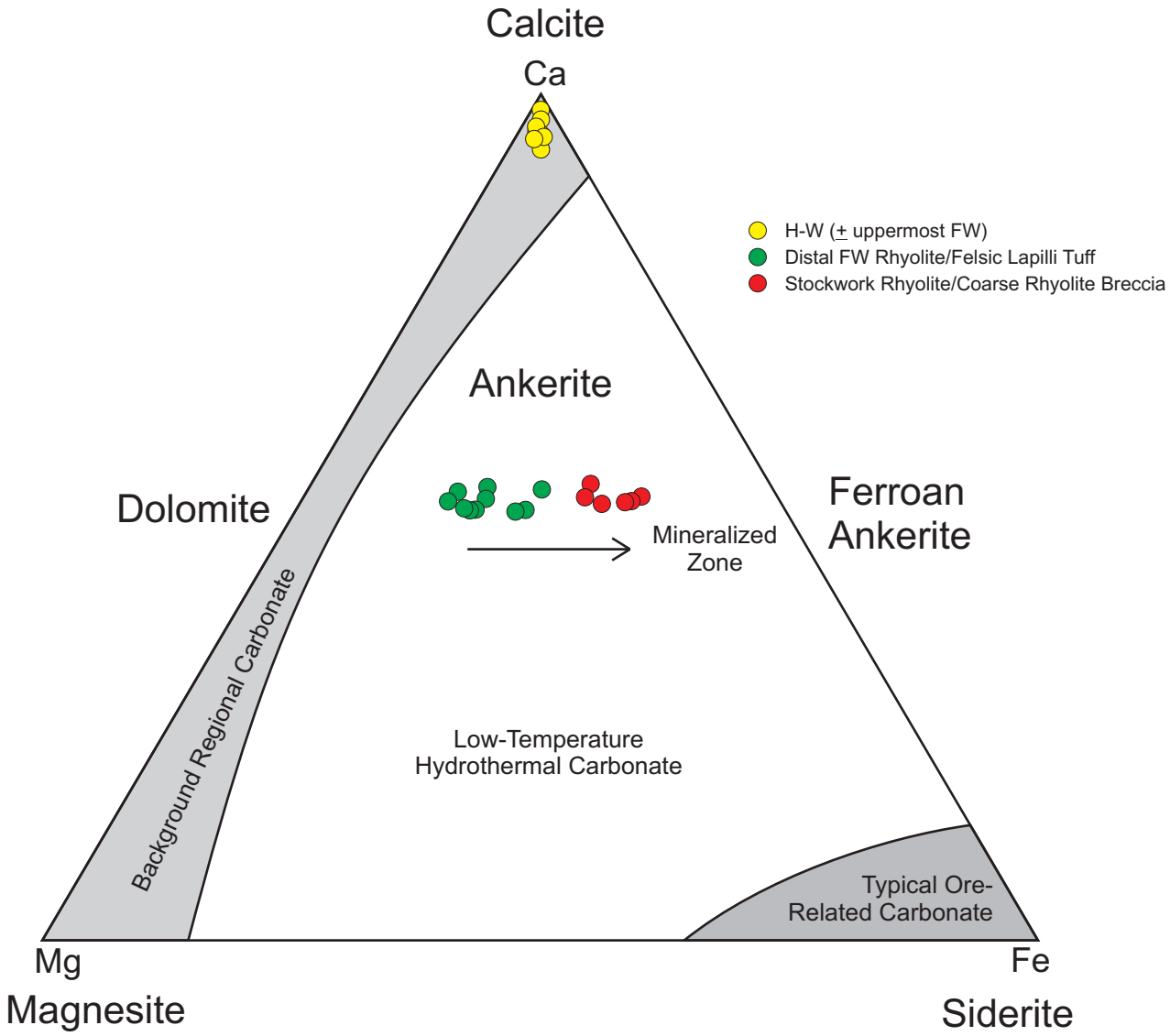

Figure 8.6. Chemical variability of carbonate at Delbridge. Calcite ($CaCO_3$) is only identified in hanging-wall (+ uppermost footwall) samples. Considerable variation of footwall carbonate along the tie-line joining dolomite ($CaMg(CO_3)_2$) and ferroan ankerite ($CaFe(CO_3)_2$) is evident. These ankerites can be divided into two groups based on Fe/(Fe+Mg) ratios: Fe-rich ankerite (0.60-0.73) occurs in stringers and stockwork immediately beneath mineralization and in adjacent coarse rhyolite breccia, and Mg-rich ankerite (0.31-0.51) occurs in distal QP rhyolite and felsic lapilli tuff along the interpreted margins of the system (Figure 8.7). Plotted data are summarized in Table 8.5.

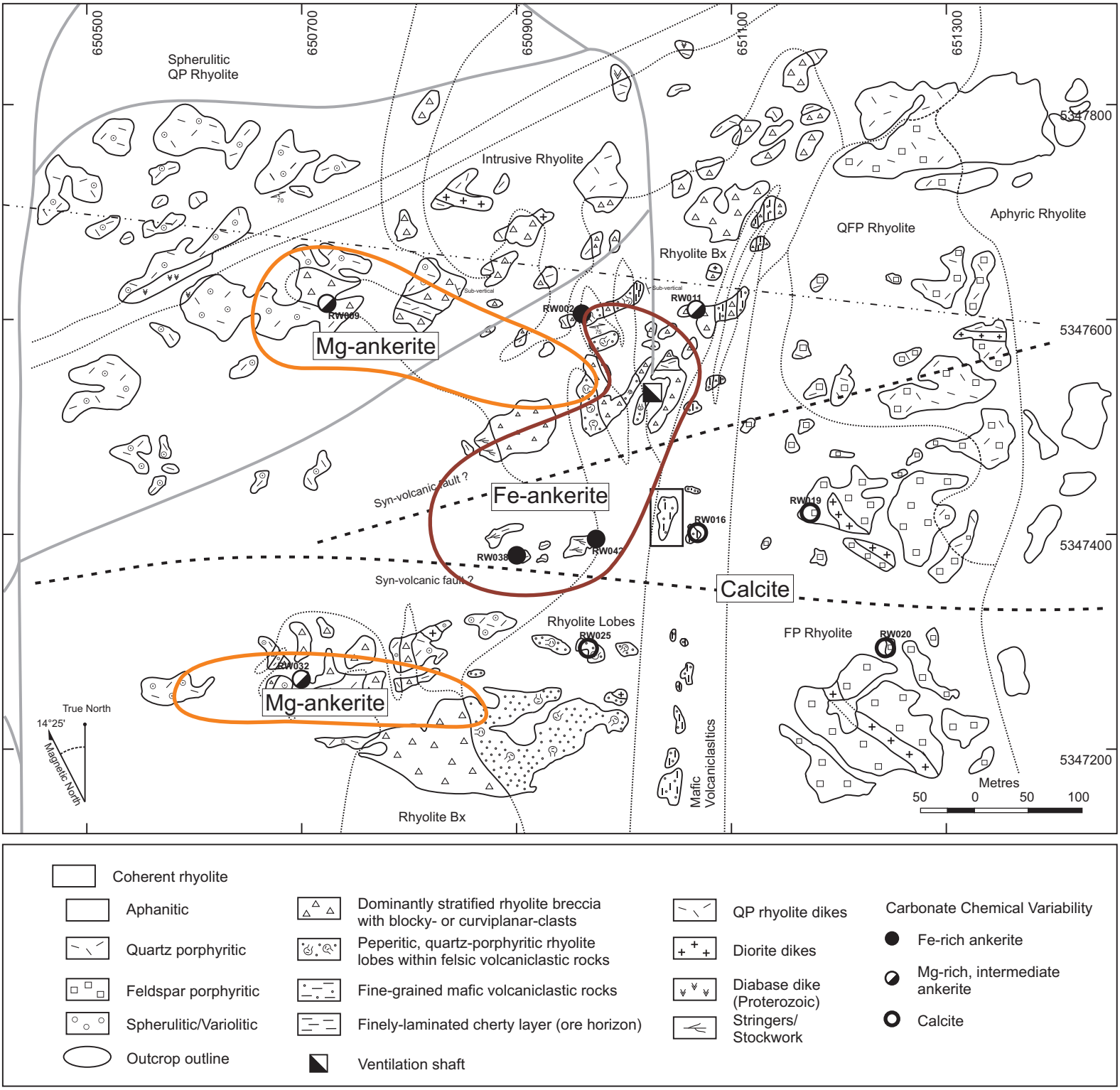

Figure 8.7. Compositional variation of dominant carbonate phases at Delbridge shown with respect to lithofacies. Calcite is only identified in hanging-wall (± uppermost footwall) samples. Calcite grains have notably high Fe/(Fe+Mg) ratios (0.59-0.78; Table 8.5). Footwall ankerite grains show considerable variation between dolomite (Mg-ankerite) and ferroan ankerite (Figure 8.6). These ankerites can be divided into two groups based on Fe/(Fe+Mg) ratios: Fe-rich ankerite (0.60-0.73) clearly occurs in stringers and stockwork immediately beneath mineralization and in adjacent coarse rhyolite breccia, and Mg-rich ankerite (0.31-0.51) occurs in distal QP rhyolite and felsic lapilli tuff along the interpreted margins of the system. Mineral identifications are based on analytical electron microprobe data (Table 8.5).

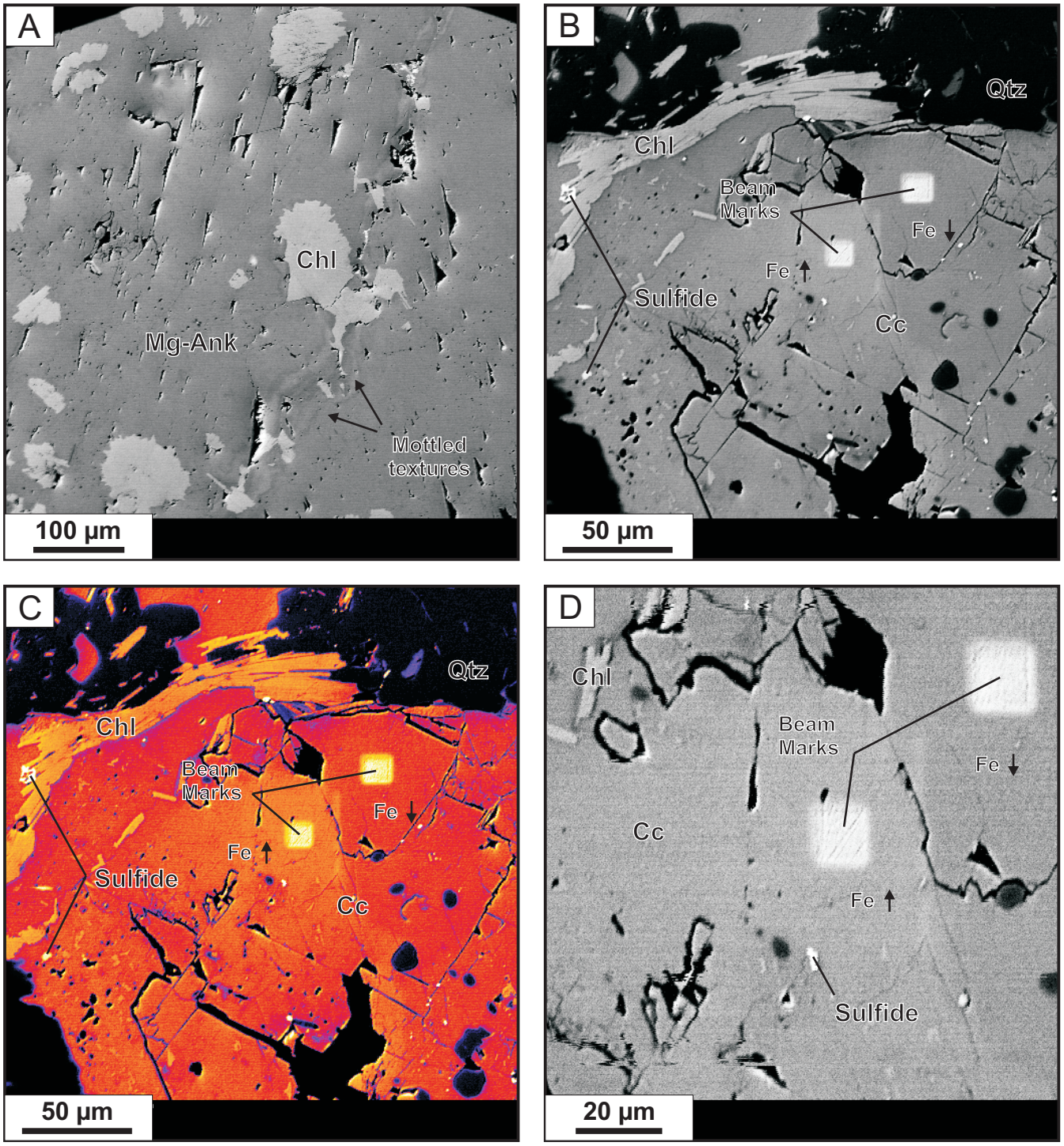

Figure 8.8. Scanning electron microscope (SEM) images of chlorite and carbonate at Delbridge. Digital back-scattered electron (BSE) images were collected with an Electron Optic Services digital imaging system at 512 x 512 pixel resolution and a Lamont 4 element solid state BSE detector. a) Bladed and radial chlorite included in Mg-ankerite. Mottled colour caused by chemical variability reflect heterogeneities in distal carbonate with lighter shades (higher backscatter) indicating increased Fe content. The mottled textures in distal samples are clearly most abundant along fracture networks and are characterized by Fe/Fe+Mg changes in the range of ~0.04-0.08 (Table 8.5) - RW032; b) Hanging-wall carbonate shows similar mottled colour; analyses of the darkest and lightest areas are in the range of ~0.05-0.09 (Table 8.5). Inclusions of chlorite and sulfide identified by spot energy-dispersive analysis (EDX) during SEM imaging support that carbonate precipitation post-dated chlorite and sulfide in the paragenetic sequence - RW020; c) The same SEM image as (b) but shown in colour to highlight contrast between Fe-rich and Fe-poor zones - RW020 and; d) A smaller-scale closeup of the same SEM image shown in (b) and (c).

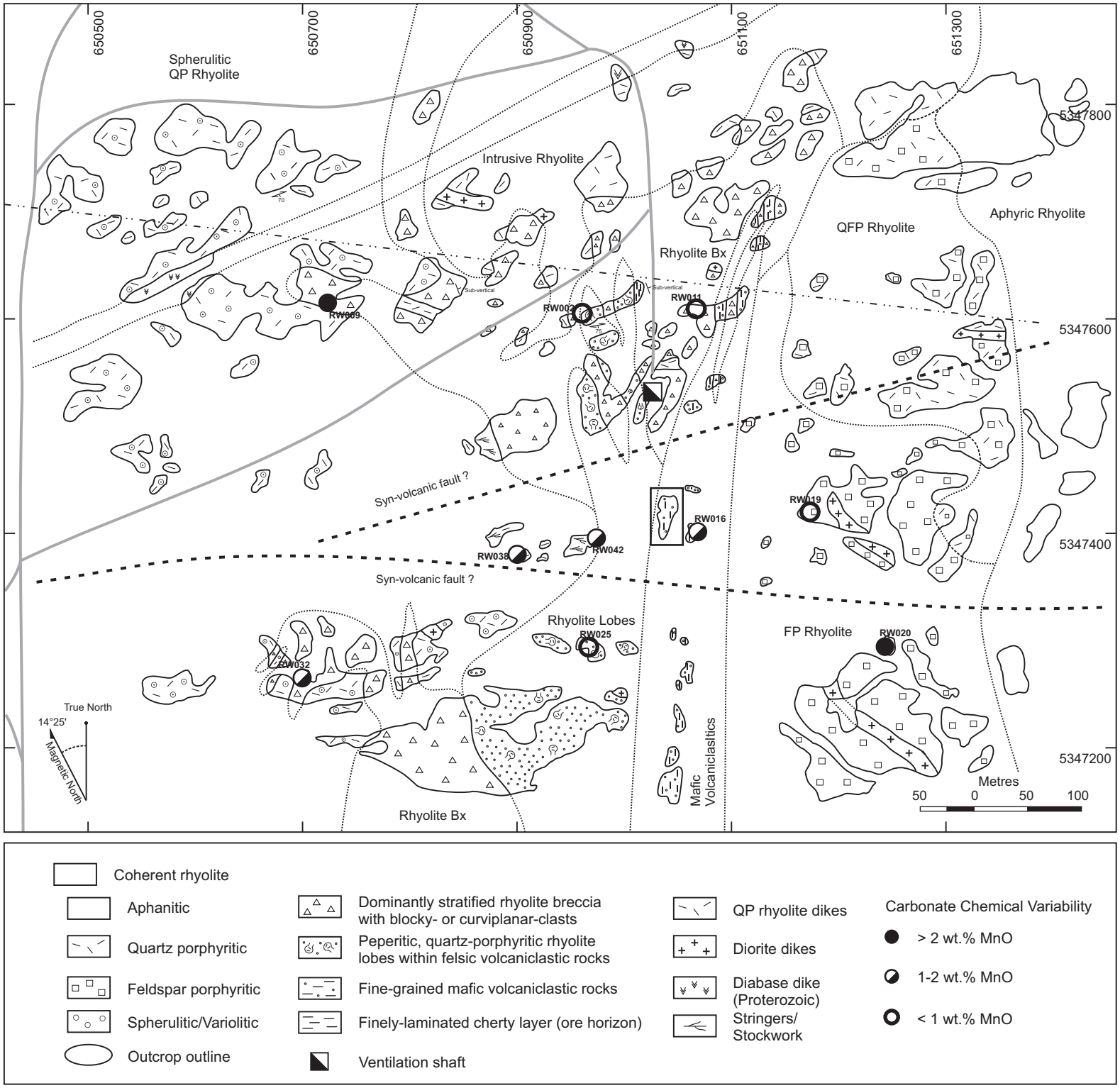

Figure 8.9. Manganese contents (wt.% MnO) in carbonate at Delbridge shown with respect to lithofacies. Mn contents are consistently higher (1-2 wt.% MnO) between the two inferred synvolcanic faults in footwall stringers and stockwork and in the immediate hanging wall; however, the highest concentrations (>2 wt.% MnO) occur in two isolated samples outside of this zone. Analytical electron microprobe data are given in Table 8.5.

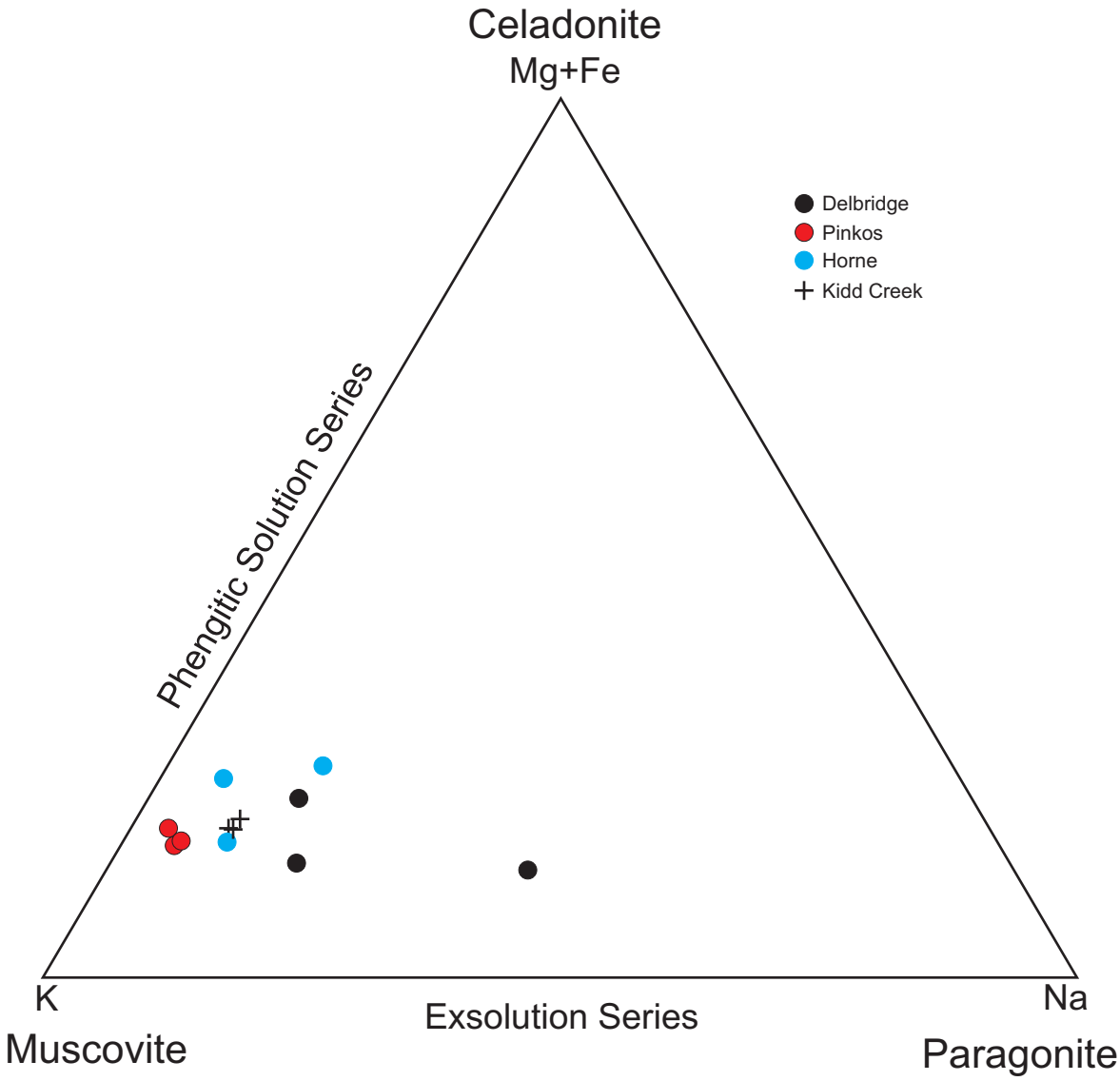

Figure 8.10. The chemical data for three analyzed white mica grains at Pinkos indicating low Na/(Na+K) values of 0.04 and 0.06 for proximal (RW088) and distal (RW072, RW128) white mica, respectively. The compositions at Pinkos are in the same range as other well-known Archean VMS deposits in the Abitibi greenstone belt (e.g., Delbridge, Horne, and Kidd Creek). The data are summarized in Table 8.3. Data for Delbridge from the present study and Barrett et al (1993), for Horne from MacLean and Hoy (1991), and for Kidd Creek from Koopman et al (1999).

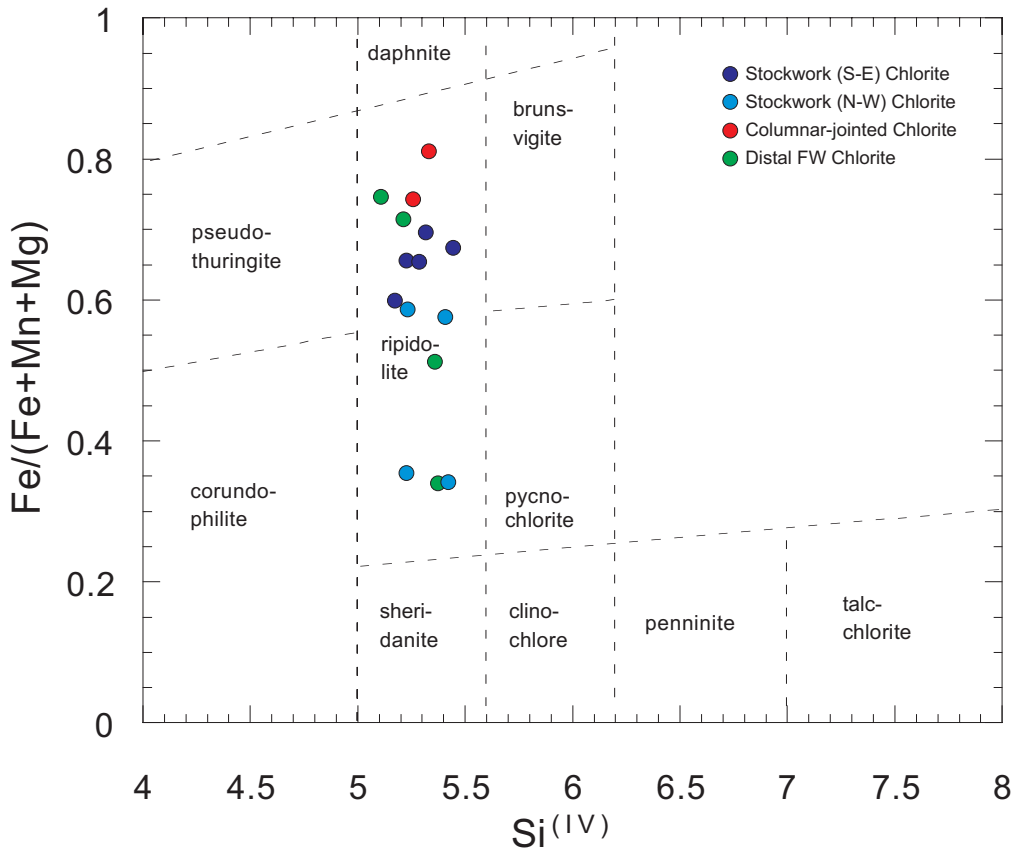

Figure 8.11. Compositional variation of chlorite at Pinkos. All of the grains have similar Si^{4+} contents (~5.1-5.4 formula ions) and plot within the ripidolite compositional field; however, chemical variability is still evident between the different alteration types. Intermediate to Fe-rich chlorite (0.60-0.69 Fe/Fe+Mg) is concentrated in the stockwork zone to the southeast and Mg-rich to intermediate chlorite (0.34-0.59 Fe/Fe+Mg) in stringers to the northwest. Unlike at Delbridge, the highest Fe/Fe+Mg values (0.75-0.80) occur outside of the interpreted focus of hydrothermal upflow in zones of columnar-jointed rhyolite (Figure 8.12). Distal footwall chlorite shows significant variation with Fe/Fe+Mg ratios ranging from ~0.35-0.75. Plotted data from quantitative electron microprobe analyses are summarized in Table 8.6. The classification scheme is that of Hey (1954).

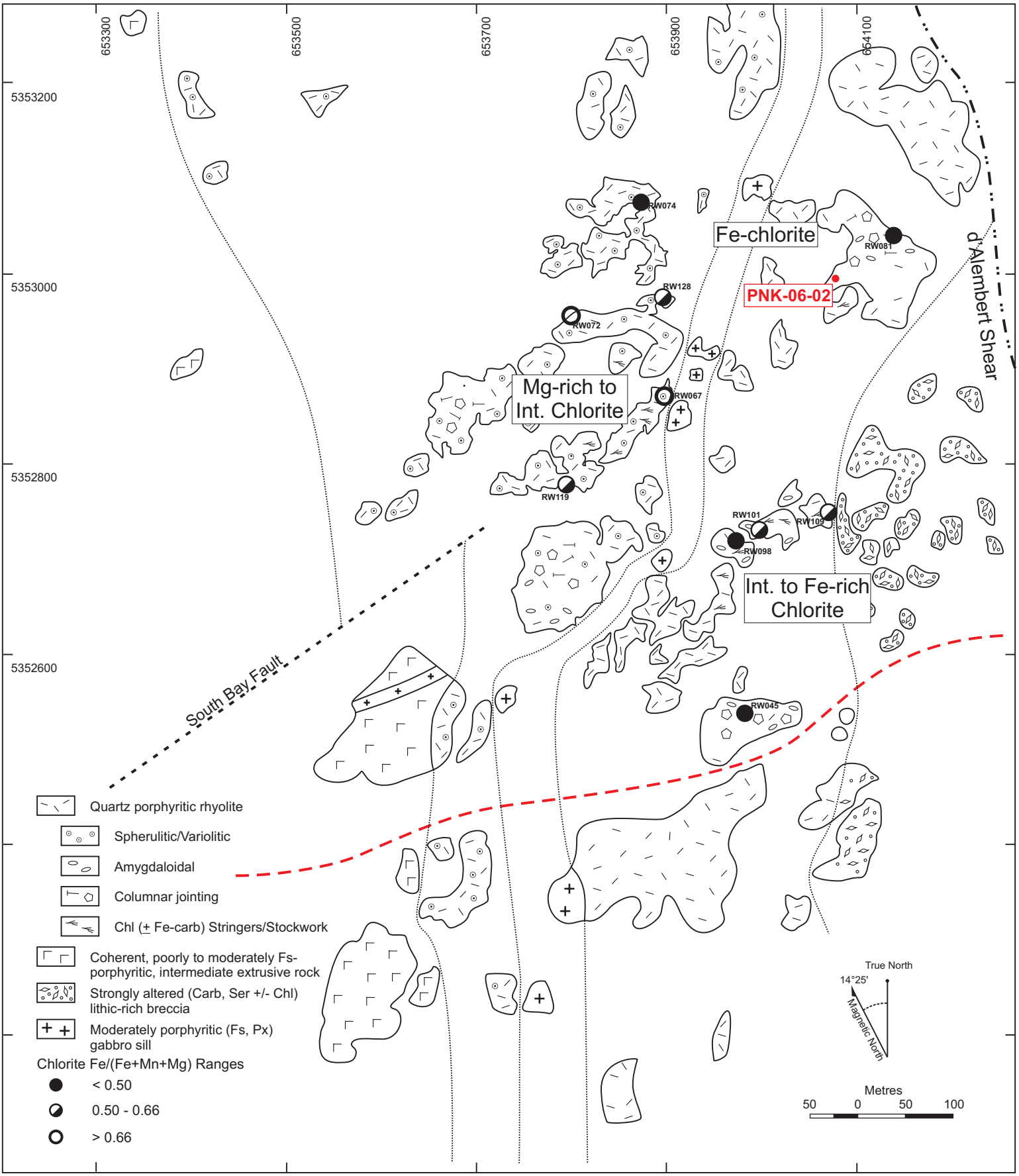

Figure 8.12. Compositional variation of chlorite at Pinkos shown with respect to lithofacies. Though all analyzed grains plot within the ripidolite field of a chlorite compositional diagram (Figure 8.11; after Hey, 1954), chemical variability between alteration types is evident. Intermediate to Fe-rich chlorite (0.60-0.69 Fe/Fe+Mg) is concentrated in the stockwork zone to the southeast and Mg-rich to intermediate chlorite (0.34-0.59 Fe/Fe+Mg) in stringers to the northwest. Unlike at Delbridge, the highest Fe/Fe+Mg values (0.75-0.80 mole fraction) occur outside of the interpreted main upflow zone of columnar-jointed rhyolite. Distal footwall chlorite shows significant variation with Fe/Fe+Mg ratios ranging from ~0.35-0.75. Mineral identifications based on analytical electron microprobe data (Table 8.6).

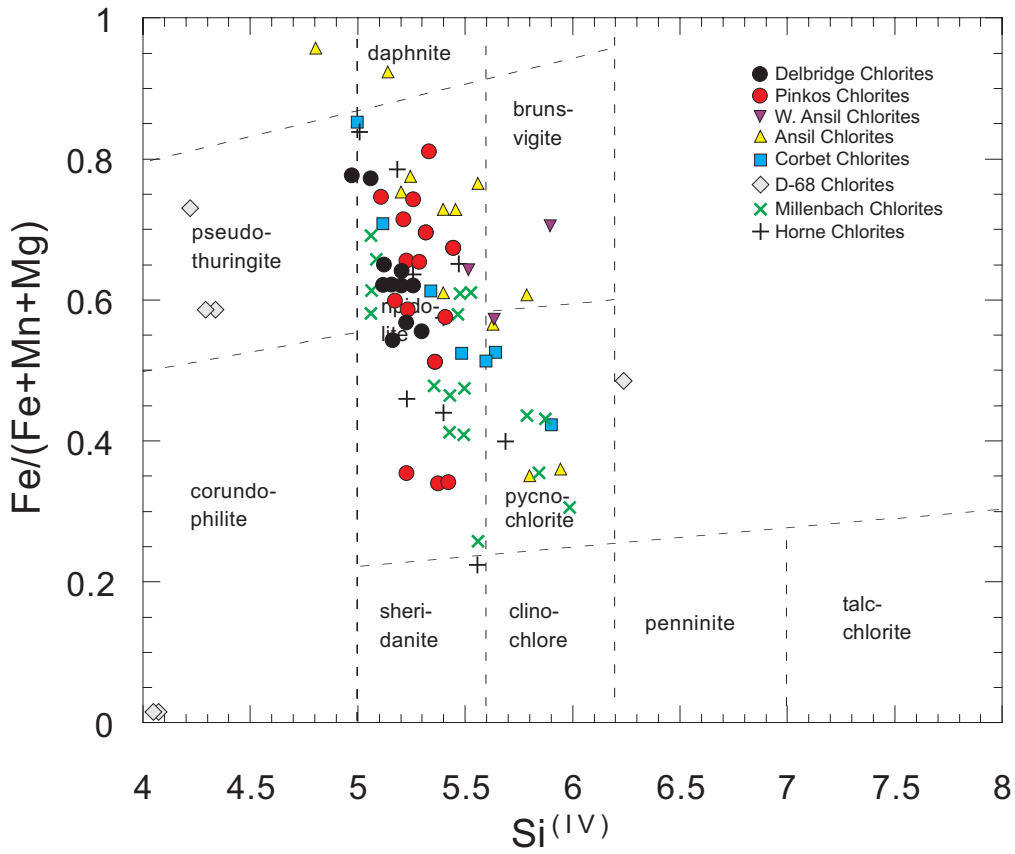

Figure 8.13. Compositional variation of chlorite at Pinkos relative to other VMS deposits of the Noranda Camp. All analyzed grains plot within the ripidolite compositional field and appear most consistent with slightly lower Fe/(Fe+Mn+Mg) ratios associated with occurrences in the upper stratigraphy of the mining camp (e.g., Delbridge). The classification scheme is that of Hey (1954). Data for Delbridge from the present study and Barrett et al (1993b), for Ansil from Barrett et al., (1991) and Galley et al, (2000), for Corbet from Barrett et al., (1993a), for D-68 from Ikingura et al, (1989), for Millenbach from Kalogeropoulos and Scott (1988), for Horne from MacLean and Hoy (1991), and for West Ansil from Boucher (2011).

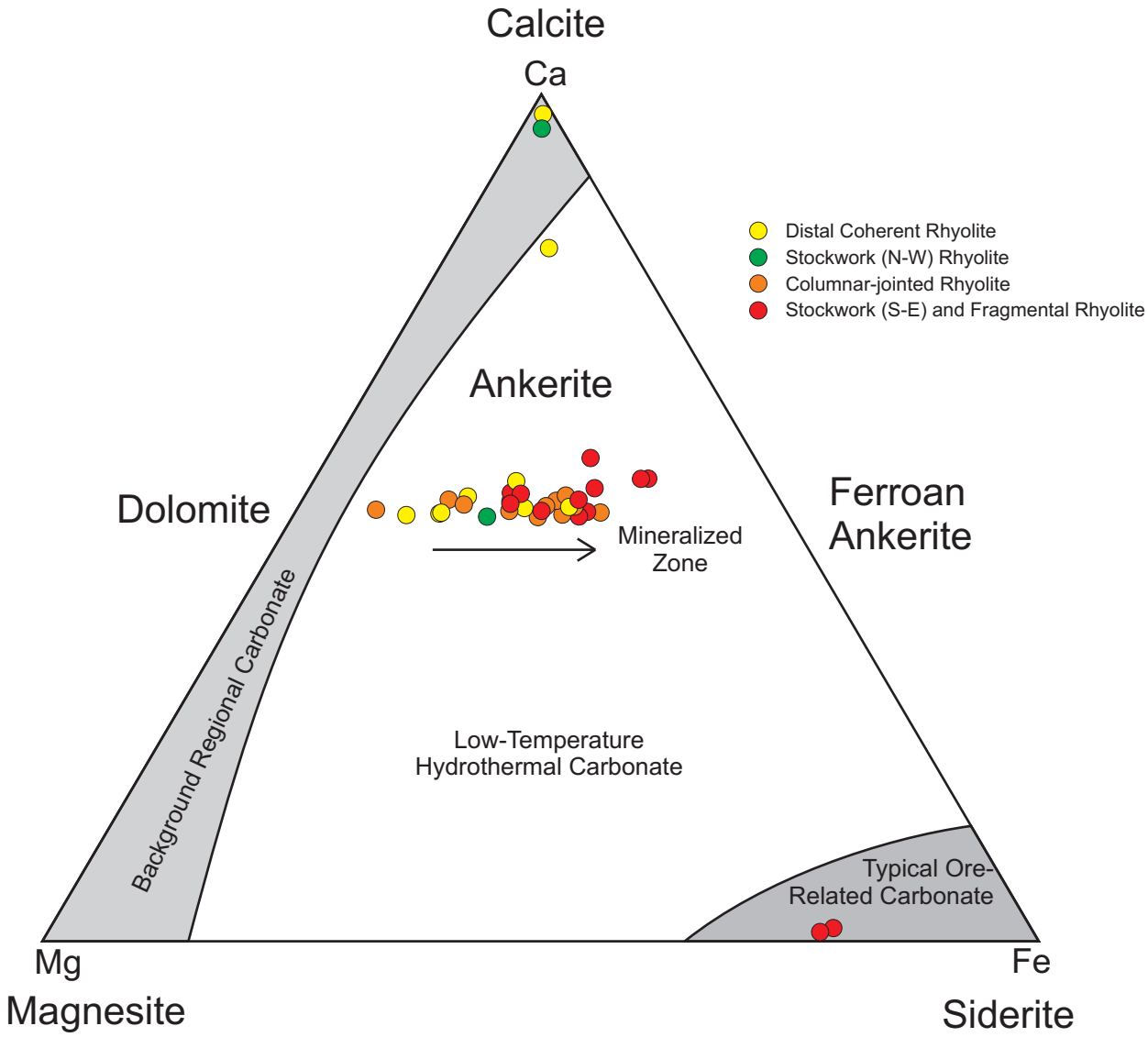

Figure 8.14. Chemical variability of carbonate at Pinkos. Calcite (± calcic ankerite; ~9 formula ions each of Mg and Fe) is effectively restricted to distal coherent rhyolite and stockwork to the northwest. Significant variation of footwall carbonate clearly occurs along the tie-line joining dolomite and ferroan ankerite. These ankerites are subdivided based on different alteration types and associated Fe/Fe+Mg ratios. Distal coherent footwall rhyolite contains mainly Mg-rich ankerite (~0.2-0.5 Fe/Fe+Mg). Intermediate to Fe-rich ankerite (~0.4-0.6 Fe/Fe+Mg) is dominant with minor Mg-rich species (~0.1-0.3 Fe/Fe+Mg) in columnar-jointed rhyolite. The highest Fe/Fe+Mg ratios (~0.5-0.7) in ankerite clearly occur in the stockwork zone to the southeast and in overlying fragmental rhyolite. Siderite (0.79-0.80 Fe/Fe+Mg) was only identified locally in fragmental rhyolite. Plotted data from quantitative electron microprobe analyses are summarized in Table 8.7. The distribution of identified carbonate phases at Pinkos are plotted in Figure 8.15.

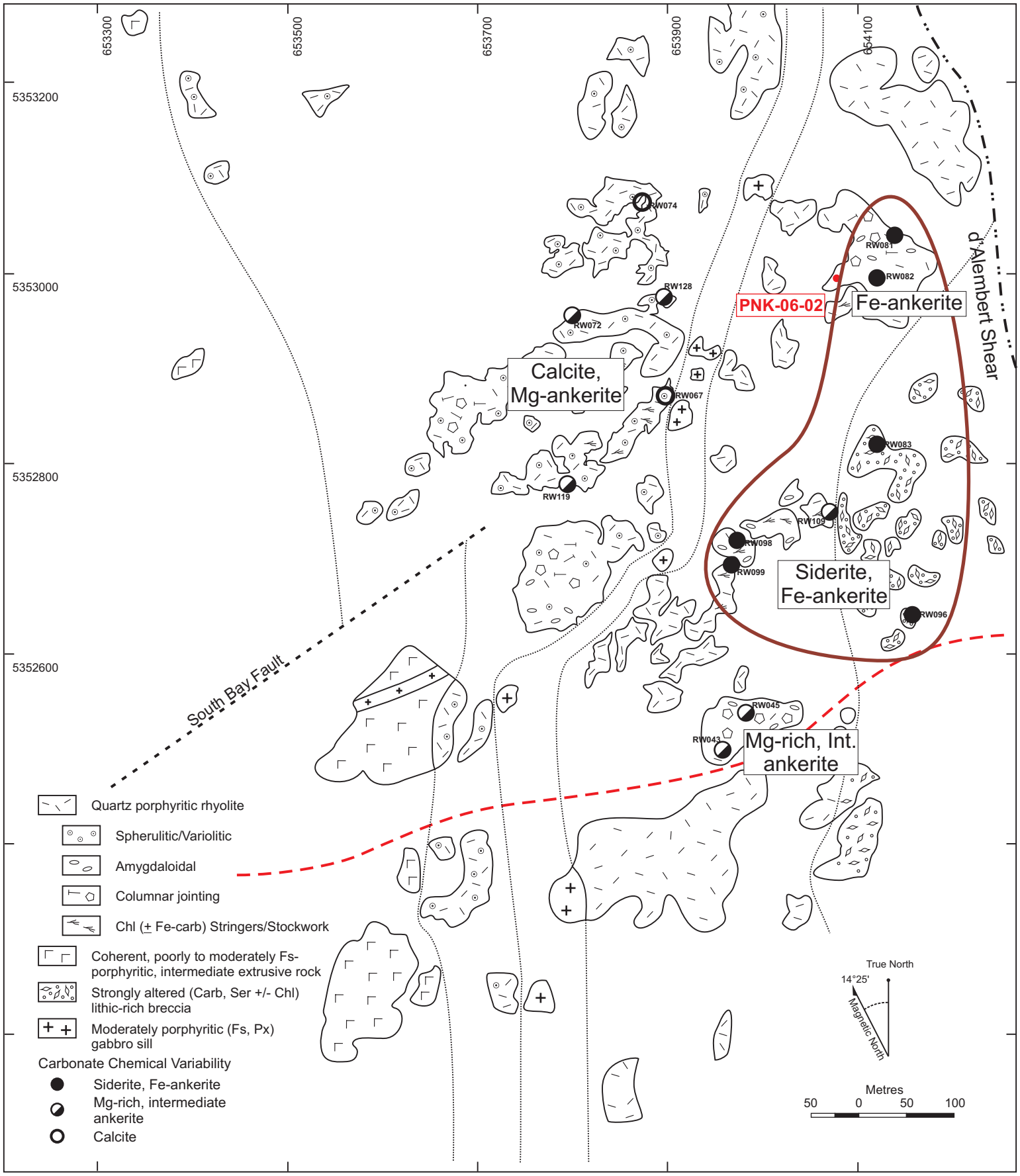

Figure 8.15. Distribution of dominant carbonate phases at Pinkos shown with respect to lithofacies. Calcite (± calcic ankerite) is effectively restricted to distal coherent rhyolite and stockwork to the northwest. Ankerite shows considerable variation between dolomite and ferroan ankerite (Figure 8.14) and can be subdivided based on different alteration types and associated Fe/Fe+Mg ratios. Distal coherent footwall rhyolite contains Mg-rich ankerite (~0.2-0.5 Fe/Fe+Mg). Intermediate to Fe-rich ankerite (~0.4-0.6 Fe/Fe+Mg) is dominant with minor Mg-rich species (~0.1-0.3) in columnar-jointed rhyolite. The highest Fe/Fe+Mg ratios (~0.5-0.7) in ankerite occur in the stockwork zone to the southeast and in overlying fragmental rhyolite. Siderite (0.79-0.80 Fe/Fe+Mg) was only identified locally in fragmental rhyolite. Mineral identifications are based on analytical electron microprobe data (Table 8.7).

Figure 8.16. Scanning electron microscope (SEM) images of carbonate at Pinkos. a) Ferroan ankerite in the interpreted core of hydrothermal upflow appears homogeneous relative to the margins of the system. Stringer carbonate shows only minor changes in Fe/Fe+Mg ratios (~0.1), which are reflected by only subtle colour changes - RW099; b) Replacement of chalcopyrite (± chlorite) by intermediate to Fe-rich ankerite in stringers and stockwork shows that carbonate precipitation post-dated chlorite and sulfide in the paragenetic sequence - RW109; c) Relatively heterogeneous carbonate in zones of proximal columnar-jointed is supported by consistently larger Fe/Fe+Mg differences in single grains (~0.1-0.5) and significant mottling of lighter (Fe-rich) and darker (Fe-poor) colours - RW043; d) Zonation and inclusions of chlorite and sphalerite in amygdaloidal columnar-jointed rhyolite support late-stage hydrothermal carbonate precipitation - RW081; e) The largest Fe/Fe+Mg difference identified in a single ankerite grain (~0.46) occurs in proximal columnar-jointed rhyolite. Zonation from Fe-poor (darker) cores to Fe-rich (lighter) rims is common - RW082; f) Strongly zoned euhedral carbonate in distal coherent rhyolite shows a highly reflective sideritic material lining grain boundaries and fine fractures - RW074; g) More highly reflective Fe-rich material (siderite) identified lining grain boundaries and fine fractures and rimming earlier alteration phases - RW074; h) Subhedral to euhedral siderite identified in fragmental rhyolite is notably homogeneous and possibly included in later Fe-rich ankerite - RW096 and; i) Heterogeneous ankerite replacing chalcopyrite in fragmental rhyolite further supports late synvolcanic carbonate precipitation after main-stage alteration and mineralization. Analytical electron microprobe data are summarized in Table 8.7.

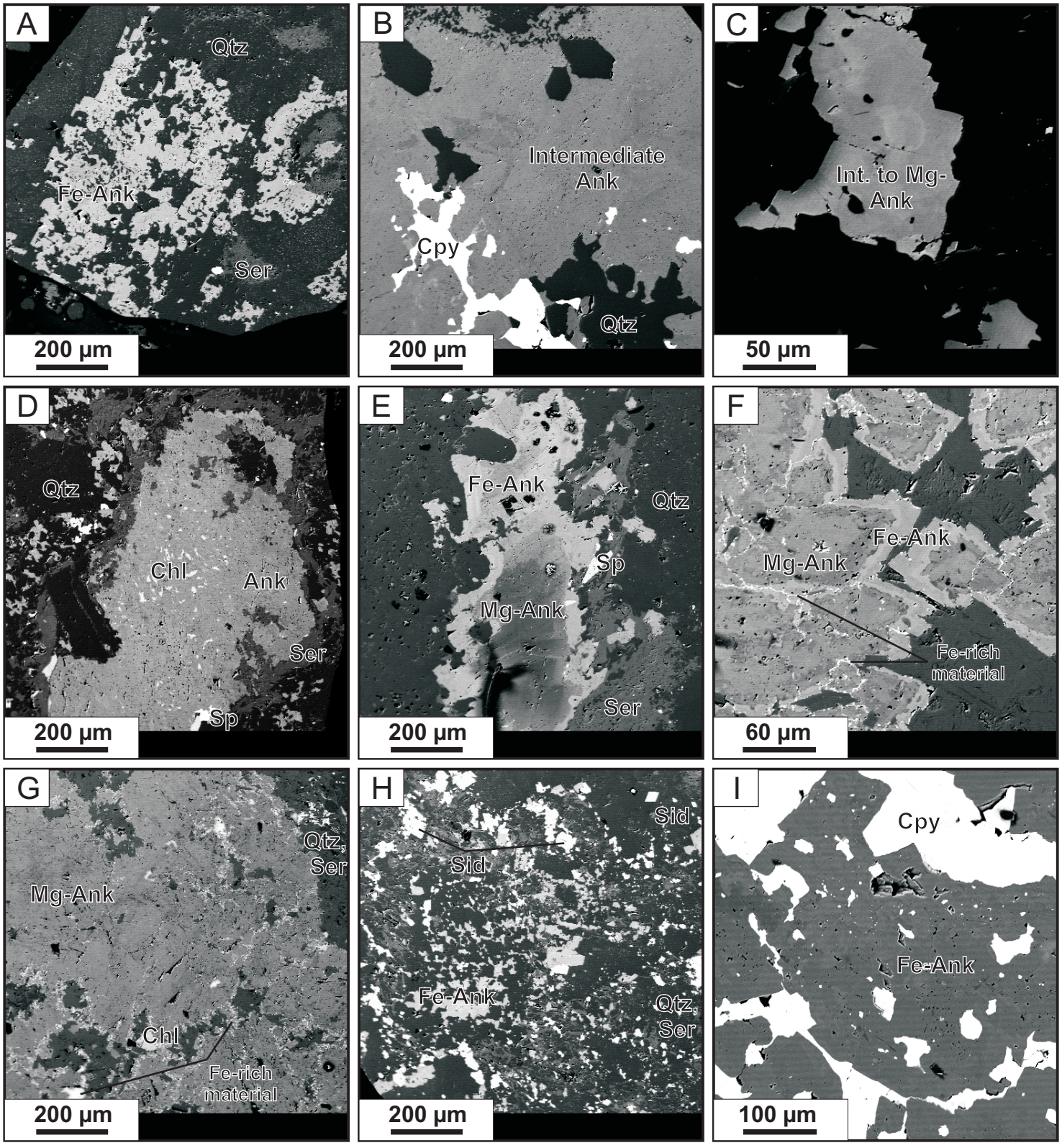
A
Qtz
Fe-Ank
Ser
200 µm
B
Intermediate Ank
Cpy
Qtz
200 µm
C
Int. to Mg-Ank
50 µm
D
Qtz
Chl
Ank
Ser
Sp
200 µm
E
Fe-Ank
Qtz
Sp
Mg-Ank
Ser
200 µm
F
Fe-Ank
Mg-Ank
Fe-rich material
60 µm
G
Qtz, Ser
Mg-Ank
Chl
Fe-rich material
200 µm
H
Sid
Sid
Fe-Ank
Qtz, Ser
200 µm
I
Cpy
Fe-Ank
100 µm

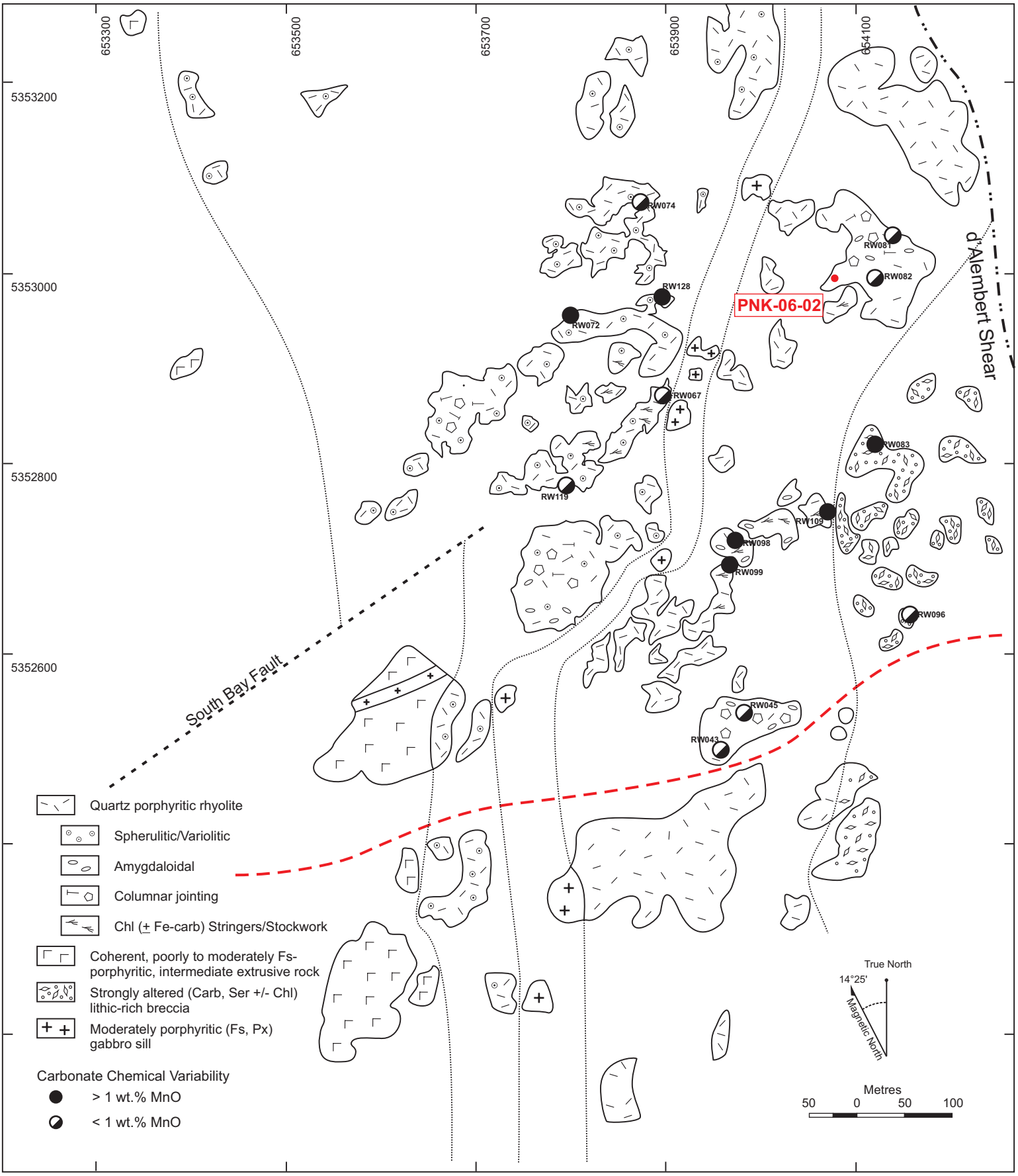

Figure 8.17. Manganese contents (wt.% MnO) in carbonate at Pinkos shown with respect to lithofacies. Mn concentrations in carbonate are consistently higher (>1 wt.% MnO) in stringers and stockwork to the southeast and overlying fragmental rhyolite. Lower Mn contents are observed in the stockwork zone to the northwest and proximal columnar-jointed rhyolite. Analytical electron microprobe data are given in Table 8.7.

Table 8.1. Dominant Alteration of Delbridge Surface Samples from Shortwave Infrared (SWIR) Analyses

	Sample	UTM NAD83 (Zn 17)				Carb		Chl		
	Number	Easting	Northing	Qtz	Ms	Ca	Fe	Mg	Fe	Lithofacies
Ca-carbonate, Muscovite	RW015	651035	5347403		◪	●			◪	Mafic volcaniclastic rocks
	RW016	651053	5347407		○	●			●	Mafic volcaniclastic rocks
	RW017	651050	5347444		○	●			●	Mafic volcaniclastic rocks
	RW019	651176	5347422	○	○	●			◪	FP rhyolite
	RW020	651245	5347294	○	◪	●			◪	FP rhyolite
	RW021	651172	5347273	○	○	○			◪	FP rhyolite
	RW022	651053	5347268		○	○			●	Mafic volcaniclastic rocks
	RW023	651054	5347304		◪	●			●	Mafic volcaniclastic rocks
	RW024	651009	5347291		◪	●			◪	Peperitic, QP rhyolite lobes
	RW025	650970	5347292		◪	●			◪	Peperitic, QP rhyolite lobes
	RW026	650931	5347292	○	◪	●			◪	Peperitic, QP rhyolite lobes
	RW027	650873	5347297	◪	◪	●			◪	Spherulitic, QP rhyolite
	RW031	650811	5347300		●	●			●	Spherulitic, QP rhyolite
	RW135	651040	5347566		●	●			●	Spherulitic, QP rhyolite
	RW136	651028	5347515		●	●			●	Rhyolite breccia
Fe-carbonate	RW001	650995	5347615	◪	●		●			Peperitic, QP rhyolite lobes
	RW002	650962	5347603	◪	●		●			Peperitic, QP rhyolite lobes
	RW009	650726	5347610	◪	◪		●			Rhyolite breccia
	RW011	651081	5347618	◪	●	○	●			Rhyolite breccia
	RW012	651056	5347585	●	●	○	●		○	Rhyolite breccia
	RW013	651029	5347581	●	●	○	●		○	Rhyolite breccia
	RW014	651006	5347582	◪	◪	○	◪		○	Rhyolite breccia
	RW036	650802	5347629	●	●		●			Spherulitic, QP rhyolite
	RW037	650802	5347641	●	●		●			Rhyolite breccia
	RW038	650900	5347383	●	●		●			Spherulitic, QP rhyolite
	RW039	650922	5347377	●	●		●		○	Spherulitic, QP rhyolite
	RW040	650922	5347389	●	●		●			Spherulitic, QP rhyolite
	RW041	650953	5347402	◪	●		●		○	Spherulitic, QP rhyolite
	RW042	650968	5347391	●	●		●		◪	Spherulitic, QP rhyolite
	RW144	650707	5347443	◪			◪	○	●	Spherulitic, QP rhyolite
Mg-chlorite	RW003	650919	5347567	◪	●		◪	●		Rhyolite breccia
	RW006	650712	5347652	◪	●		◪	●		Spherulitic, QP rhyolite
	RW008	650761	5347633	●	◪		◪	●		Spherulitic, QP rhyolite
	RW010	650677	5347584		●	○		●		Spherulitic, QP rhyolite
	RW028	650861	5347272	◪	●		○	○		Spherulitic, QP rhyolite
	RW029	650844	5347255	●	●		○	◪		Peperitic, QP rhyolite lobes
	RW030	650854	5347241	●	◪		○	◪		Peperitic, QP rhyolite lobes
	RW032	650700	5347258	●	●	◪		◪		Rhyolite breccia
	RW033	650773	5347236	●	●	○		◪		Rhyolite breccia
	RW034	650608	5347246	●	●		○	◪		Spherulitic, QP rhyolite
	RW035	650635	5347262	○	●	◪		◪		Spherulitic, QP rhyolite
	RW137	651030	5347513	○				●		Spherulitic, QP rhyolite
	RW141	650903	5347487	○	●		◪	●		Rhyolite breccia
	RW142	650883	5347487	○	●		◪	●		Spherulitic, QP rhyolite
	RW143	650864	5347487	○	●		◪	●		Spherulitic, QP rhyolite
Quartz, Muscovite	RW004	650945	5347651	●	○		●			Rhyolite breccia
	RW005	650916	5347630	●	○		●		○	Rhyolite breccia
	RW007	650703	5347644	●	○		◪	○		Rhyolite breccia
	RW018	651278	5347463	●	◪	○		◪	○	FP rhyolite
	RW133	651258	5347565	●	◪					QFP rhyolite
	RW134	651161	5347570	●	●				○	QFP rhyolite
	RW138	651031	5347517	●	●					Spherulitic, QP rhyolite
	RW139	651012	5347538	●	●		○		◪	Rhyolite breccia
	RW140	650974	5347498	●	○		●			Peperitic, QP rhyolite lobes

54 surface samples collected at Delbridge are subdivided by lithofacies and classified into well-defined alteration assemblages: 1) Fe-carbonate (+ Fe-chlorite); 2) Ca-carbonate + muscovite; 3) Mg-chlorite (+ muscovite); and 4) quartz + muscovite.

Classification is based on both depth of absorption features in SWIR spectral profiles and modal mineralogy abundances from initial petrographic analyses (● = major, >5%; ◪ = minor, 1-5%; and ○ = trace, <1%).

Table 8.2. Dominant Alteration of Pinkos Surface Samples from Shortwave Infrared (SWIR) Analyses

	Sample	UTM NAD83 (Zn 17)				Carb		Chl		
	Number	Easting	Northing	Qtz	Ms	Ca	Fe	Mg	Fe	Lithofacies
Quartz, Muscovite, Ca-carbonate	RW065	653930	5352844	◪		◪			●	Mafic dike
	RW067	653910	5352865	◪	●	○		●		Spherulitic, QP rhyolite
	RW068	653904	5352908	◪	●	◪		●		Spherulitic, QP rhyolite
	RW069	653896	5352947	◪	●	○		●		Spherulitic, QP rhyolite
	RW070	653873	5352913		●	◪		●		Spherulitic, QP rhyolite
	RW071	653852	5352948	◪	●	◪		●		Spherulitic, QP rhyolite
	RW073	653819	5353007	●	○	◪		●		Spherulitic, QP rhyolite
	RW074	653884	5353077	●	●		◪		◪	Spherulitic, QP rhyolite
	RW075	653957	5353086	●	●		◪		◪	Spherulitic, QP rhyolite
	RW076	653990	5353093	◪		◪			●	Mafic dike
	RW077	654024	5353070	●	●	◪		●		QP rhyolite (+/- spherulitic)
	RW078	654087	5353074	●	●	◪	◪		◪	QP rhyolite (+/- spherulitic)
	RW079	654091	5353028	●	●	◪	◪			QP rhyolite (+/- spherulitic)
	RW080	654112	5353047	●	●		●			QP rhyolite (+/- spherulitic)
	RW105	653995	5352891	●	●		●			QP rhyolite (+/- spherulitic)
	RW106	653949	5352894	◪		◪			●	Mafic dike
	RW107	653944	5352915	◪		◪			●	Mafic dike
	RW108	654011	5353005	●	●		●			QP rhyolite (+/- spherulitic)
	RW128	653904	5352971	◪	●		○	●		Spherulitic, QP rhyolite
	RW129	653900	5353002	●	●		○		◪	Spherulitic, QP rhyolite
	RW130	653887	5353034	●	●		○		◪	Spherulitic, QP rhyolite
Fe-carbonate	RW043	653962	5352500	●	●		◪			QP rhyolite (+/- spherulitic)
	RW044	653955	5352536	●	●		◪		○	QP rhyolite (+/- spherulitic)
	RW045	653983	5352537	●	●		◪		○	QP rhyolite (+/- spherulitic)
	RW046	653976	5352535	●	●		◪			QP rhyolite (+/- spherulitic)
	RW047	653969	5352576	●	●		●			QP rhyolite (+/- spherulitic)
	RW048	653914	5352560	●	●		●			QP rhyolite (+/- spherulitic)
	RW049	653921	5352596	●	●		◪			QP rhyolite (+/- spherulitic)
	RW050	653903	5352609	●	●		◪			QP rhyolite (+/- spherulitic)
	RW052	653912	5352637	●	●	○	◪			QP rhyolite (+/- spherulitic)
	RW053	653881	5352621	●	●	○	◪			QP rhyolite (+/- spherulitic)
	RW054	653852	5352609	●	●		●		○	QP rhyolite (+/- spherulitic)
	RW056	653890	5352649	●	●		●			QP rhyolite (+/- spherulitic)
	RW057	653911	5352683	◪			●		●	Mafic dike
	RW058	653920	5352701	◪			●		●	Mafic dike
	RW059	653906	5352730	●	●		◪		○	Spherulitic, QP rhyolite
	RW060	653854	5352746	●			◪		○	Spherulitic, QP rhyolite
	RW062	653811	5352666		●	◪	◪	○		Spherulitic, QP rhyolite
	RW081	654138	5353047	●	●		●			QP rhyolite (+/- spherulitic)
	RW082	654128	5352989	●	●		●			QP rhyolite (+/- spherulitic)
	RW083	654127	5352815	●	●		●			Fragmental, QP rhyolite
	RW084	654115	5352792	●	●		●		○	Fragmental, QP rhyolite
	RW085	654096	5352764	●	●		◪			Fragmental, QP rhyolite
	RW086	654135	5352754	●	●		◪			Fragmental, QP rhyolite
	RW087	654169	5352746	●	●		◪			Fragmental, QP rhyolite
	RW088	654161	5352741	●	○		●		○	Fragmental, QP rhyolite
	RW089	654156	5352727	●	●		●		○	Fragmental, QP rhyolite
	RW090	654151	5352716	●	●		◪			Fragmental, QP rhyolite
	RW091	654126	5352716	●	●		●			Fragmental, QP rhyolite
	RW092	654117	5352744	●	●		●		○	Fragmental, QP rhyolite
	RW093	654137	5352687	●	●		●		○	Fragmental, QP rhyolite
	RW094	654178	5352692	●	●		●			Fragmental, QP rhyolite
	RW095	654153	5352683	●	●		●			Fragmental, QP rhyolite
	RW096	654166	5352645	●	●		◪			Fragmental, QP rhyolite
	RW099	653975	5352690	●	●		◪			QP rhyolite (+/- spherulitic)
	RW100	653980	5352662	●	●		●			QP rhyolite (+/- spherulitic)
	RW101	654010	5352734	◪	○		●		●	QP rhyolite (+/- spherulitic)
	RW102	654024	5352753	◪	○		●		●	QP rhyolite (+/- spherulitic)
	RW103	654045	5352765	◪	○		●		●	QP rhyolite (+/- spherulitic)
	RW104	654044	5352907	●	●		●			QP rhyolite (+/- spherulitic)
	RW109	654068	5352753	●	●		◪	●		QP rhyolite (+/- spherulitic)
	RW110	654079	5352766	●	●				◪	QP rhyolite (+/- spherulitic)

Table 8.2. Dominant Alteration of Pinkos Surface Samples from Shortwave Infrared (SWIR) Analyses

	Sample	UTM NAD83 (Zn 17)				Carb		Chl		
	Number	Easting	Northing	Qtz	Ms	Ca	Fe	Mg	Fe	Lithofacies
	RW112	654089	5352984	●	●	○			○	QP rhyolite (+/- spherulitic)
	RW113	654110	5353000	●	●	○			○	QP rhyolite (+/- spherulitic)
	RW122	653777	5352842	◪					●	Spherulitic, QP rhyolite
	RW146	654045	5352369	●	●		●		○	Fragmental, QP rhyolite
	RW148	654090	5352534	●	○		●		◪	QP rhyolite (+/- spherulitic)
	RW149	654083	5352516	●	◪		◪		◪	QP rhyolite (+/- spherulitic)
	RW150	654096	5352479	◪	●		●		◪	Fragmental, QP rhyolite
Mg-chlorite	RW064	653900	5352768	◪	●			●		Spherulitic, QP rhyolite
	RW066	653876	5352834	◪	●	○		●		Spherulitic, QP rhyolite
	RW072	653811	5352937	●	●	◪		◪		Spherulitic, QP rhyolite
	RW097	654121	5352656	◪	●	○	◪	●		Fragmental, QP rhyolite
	RW098	653983	5352720	◪	◪	○	◪	●		QP rhyolite (+/- spherulitic)
	RW111	653971	5352801	○	●		◪	●		QP rhyolite (+/- spherulitic)
	RW114	653858	5352877	○	●		◪	●		Spherulitic, QP rhyolite
	RW115	653825	5352861	○	●		◪	●		Spherulitic, QP rhyolite
	RW116	653839	5352827	◪	◪		○	●		Spherulitic, QP rhyolite
	RW117	653810	5352818	◪	◪		○	●		Spherulitic, QP rhyolite
	RW118	653823	5352795	◪	●		○	●		Spherulitic, QP rhyolite
	RW119	653800	5352786	◪	●		○	●		Spherulitic, QP rhyolite
	RW123	653741	5352852	◪	●		○	●		Spherulitic, QP rhyolite
	RW124	653746	5352895	◪	●		○	●		Spherulitic, QP rhyolite
	RW125	653704	5352838	◪	●		○	●		Spherulitic, QP rhyolite
	RW126	653698	5352873	◪	●		○	●		Spherulitic, QP rhyolite
	RW127	653789	5352908	○	●		○	●		Spherulitic, QP rhyolite
	RW145	653841	5352141	◪	●		○	◪		QP rhyolite (+/- spherulitic)
Quartz, Muscovite	RW051	653943	5352627	●	○		●		○	QP rhyolite (+/- spherulitic)
	RW055	653912	5352664	●	○		●		○	QP rhyolite (+/- spherulitic)
	RW061	653794	5352726	●	●				○	Spherulitic, QP rhyolite
	RW063	653756	5352665	●	●				○	Spherulitic, QP rhyolite
	RW120	653778	5352794	●	●		◪			Spherulitic, QP rhyolite
	RW121	653750	5352784	●	●		◪			Spherulitic, QP rhyolite
	RW131	654098	5352728	●	●		●		○	Fragmental, QP rhyolite
	RW132	654197	5352724	●	◪					Fragmental, QP rhyolite
	RW147	653943	5352359	●	●		◪		○	QP rhyolite (+/- spherulitic)
	RW151	654063	5352467	●	●		◪		◪	QP rhyolite (+/- spherulitic)
	RW152	653978	5352465	●	●		◪			QP rhyolite (+/- spherulitic)
	RW153	653938	5352448	●	●		○		◪	QP rhyolite (+/- spherulitic)
	RW154	653898	5352424	●	●		○		◪	QP rhyolite (+/- spherulitic)
	RW155	653860	5352416	●	●		◪		○	QP rhyolite (+/- spherulitic)
	RW156	653816	5352409	●	◪		○		○	QP rhyolite (+/- spherulitic)
	RW157	653815	5352356	●	◪		○			QP rhyolite (+/- spherulitic)
	RW158	653887	5352385	◪	●		○		○	QP rhyolite (+/- spherulitic)
	RW159	654235	5352737	◪	●		◪		○	Fragmental, QP rhyolite
	RW160	654231	5352771	●	●		◪		○	Fragmental, QP rhyolite
	RW161	654215	5352819	◪	●		○		○	Fragmental, QP rhyolite
	RW162	654197	5352810	◪	●		○		○	Fragmental, QP rhyolite

108 surface samples collected at Pinkos are subdivided by lithofacies and classified into well-defined alteration assemblages: 1) Fe-carbonate (+ Fe-chlorite); 2) Ca-carbonate + muscovite + quartz; 3) Mg-chlorite (+ muscovite); and 4) quartz + muscovite.

Classification is based on both depth of absorption features in SWIR spectral profiles and modal mineralogy abundances from initial petrographic analyses (● = major, >5%; ◪ = minor, 1-5%; and ○ = trace, <1%).

Table 8.3. Microprobe analyses of selected sericite grains at Delbridge and Pinkos

Mineral			Sericite	
Property	Delbridge	Pinkos	Pinkos	Pinkos
Sample	RW011	RW072	RW088	RW128
Target	No. 2	No. 1	No. 2	No. 2
SiO2	45.76	46.62	49.77	47.84
Al2O3	35.90	34.94	37.79	36.46
FeO	2.07	1.05	1.74	1.43
MnO	0.00	0.03	0.00	0.02
MgO	0.24	0.98	0.68	0.82
CaO	0.01	0.10	0.03	0.00
Na2O	1.57	0.45	0.25	0.44
K2O	8.92	10.75	9.35	9.70
TiO2	0.10	0.12	0.08	0.11
Cr2O3	0.00	0.00	-	-
BaO	-	-	0.20	0.28
V2O3	-	-	0.02	0.00
F	-	-	0.36	0.15
Cl	-	-	0.00	0.00
Total	94.56	95.04	100.28	97.26
Formula		Based on 22 oxygens		
Si	6.122	6.217	6.227	6.201
Al	5.661	5.492	5.572	5.571
Fe	0.232	0.117	0.182	0.155
Mn	0.000	0.004	0.000	0.002
Mg	0.047	0.195	0.126	0.159
Ca	0.001	0.015	0.005	-
Na	0.407	0.116	0.062	0.110
K	1.523	1.830	1.492	1.605
Ti	0.010	0.012	0.007	0.011
Cr	0.000	0.000	-	-
Ba	-	-	0.010	0.014
V	-	-	0.002	-
F	-	-	0.142	0.063
Cl	-	-	0.001	-
Total	14.003	13.998	13.827	13.892
Fe/Fe + Mg	0.831	0.375	0.590	0.494
Na/(Na + K)	0.211	0.060	0.040	0.064

Table 8.4. Microprobe analyses of selected chlorite grains at Delbridge

Sample	Target	Mineral	SiO2	Al2O3	FeO	MnO	MgO	CaO	Na2O	K2O	TiO2	Cr2O3	Total	
RW016	No. 1	Ripidolite	23.22	21.08	30.65	0.24	10.25	0.03	0.07	0.03	0.06	0.02	85.65	
RW019	No. 3	Ripidolite	22.89	22.16	31.37	0.10	9.27	0.02	0.00	0.05	0.03	0.02	85.92	
RW020	No. 1	Ripidolite	23.59	21.42	28.18	0.20	11.82	0.04	0.00	0.02	0.03	0.00	85.30	
RW025	No. 2	Ripidolite	23.52	22.23	30.90	0.22	9.55	0.01	0.00	0.03	0.03	0.02	86.50	
RW032	No. 2	Ripidolite	24.50	22.23	27.55	0.08	12.19	0.01	0.00	0.02	0.01	0.02	86.61	
RW032	No. 3	Ripidolite	23.96	22.62	27.26	0.17	12.77	0.10	0.00	0.00	0.02	0.00	86.89	
RW042	No. 1	Pseudo-thuringite	21.52	21.92	36.42	0.06	5.71	0.23	0.00	0.03	0.06	0.03	85.97	
RW042	No. 2	Ripidolite	21.91	21.72	36.17	0.08	5.82	0.01	0.00	0.01	0.01	0.03	85.75	

Formula			Based on 28 oxygens											Fe/
			Si	Al	Fe	Mn	Mg	Ca	Na	K	Ti	Cr	Total	Fe+Mn+Mg
RW016	No. 1	Ripidolite	5.199	5.564	5.738	0.046	3.420	0.006	0.030	0.007	0.010	0.004	20.025	0.623
RW019	No. 3	Ripidolite	5.119	5.841	5.866	0.019	3.091	0.004	0.000	0.013	0.005	0.004	19.961	0.654
RW020	No. 1	Ripidolite	5.221	5.589	5.216	0.038	3.901	0.009	0.000	0.004	0.004	0.000	19.982	0.570
RW025	No. 2	Ripidolite	5.198	5.790	5.711	0.041	3.148	0.002	0.000	0.008	0.004	0.003	19.905	0.642
RW032	No. 2	Ripidolite	5.292	5.658	4.976	0.015	3.926	0.003	0.000	0.006	0.001	0.003	19.880	0.558
RW032	No. 3	Ripidolite	5.160	5.741	4.910	0.031	4.100	0.022	0.000	0.000	0.003	0.000	19.967	0.543
RW042	No. 1	Pseudo-thuringite	4.972	5.969	7.036	0.012	1.965	0.057	0.000	0.009	0.011	0.005	20.035	0.781
RW042	No. 2	Ripidolite	5.059	5.910	6.985	0.016	2.003	0.002	0.000	0.002	0.001	0.005	19.983	0.776

Table 8.5. Microprobe analyses of selected carbonate grains at Delbridge

Sample	Target	Mineral	SiO2	Al2O3	FeO	MnO	MgO	CaO	Na2O	K2O	TiO2	Cr2O3	Total
RW002	No. 1	Fe-Ankerite	0.00	0.00	22.41	0.93	5.81	27.89	0.00	0.00	0.00	0.00	57.03
RW002	No. 1	Fe-Ankerite	0.00	0.00	20.98	1.00	6.70	27.97	0.00	0.00	0.00	0.00	56.65
RW002	No. 2	Fe-Ankerite	0.00	0.00	22.48	0.93	5.83	28.20	0.00	0.00	0.00	0.00	57.44
RW009	No. 1	Mg-Ankerite	0.00	0.00	13.73	1.68	14.05	32.11	0.00	0.00	0.00	0.00	61.57
RW009	No. 1	Mg-Ankerite	0.00	0.00	14.34	1.95	13.77	32.35	0.00	0.00	0.00	0.00	62.40
RW009	No. 2	Mg-Ankerite	0.00	0.00	10.44	2.50	12.43	29.53	0.00	0.00	0.00	0.00	54.90
RW009	No. 2	Mg-Ankerite	0.00	0.00	15.93	3.19	8.62	28.39	0.00	0.00	0.00	0.00	56.13
RW011	No. 1	Mg-Ankerite	0.00	0.00	15.61	0.78	10.64	28.57	0.00	0.00	0.00	0.00	55.59
RW011	No. 2	Mg-Ankerite	0.00	0.00	16.46	0.65	10.21	28.74	0.00	0.00	0.00	0.00	56.05
RW016	No. 1	Calcite	0.00	0.00	0.46	0.63	0.07	54.39	0.00	0.00	0.00	0.00	55.56
RW016	No. 2	Calcite	0.00	0.00	0.71	1.40	0.16	54.13	0.00	0.00	0.00	0.00	56.40
RW019	No. 1	Calcite	0.00	0.00	0.91	0.82	0.35	44.88	0.00	0.00	0.00	0.00	46.97
RW019	No. 1	Calcite	0.00	0.02	1.20	0.86	0.32	53.32	0.00	0.00	0.00	0.00	55.72
RW019	No. 2	Calcite	0.00	0.00	1.46	1.05	0.40	53.99	0.00	0.00	0.00	0.00	56.90
RW020	No. 1	Calcite	0.05	0.00	1.33	2.00	0.52	52.13	0.00	0.04	0.00	0.00	56.08
RW020	No. 2	Calcite	0.05	0.00	1.00	0.98	0.29	53.74	0.00	0.04	0.00	0.02	56.12
RW020	No. 2	Calcite	0.00	0.00	2.02	3.16	0.72	50.88	0.00	0.00	0.00	0.00	56.77
RW025	No. 1	Calcite	0.00	0.00	1.47	0.96	0.42	52.93	0.00	0.00	0.00	0.00	55.77
RW025	No. 2	Calcite	0.00	0.00	1.49	0.96	0.40	53.24	0.00	0.00	0.00	0.00	56.09
RW032	No. 1	Mg-Ankerite	0.06	0.00	10.35	1.36	12.99	28.99	0.00	0.05	0.00	0.00	53.80
RW032	No. 2	Mg-Ankerite	0.02	0.00	13.02	2.05	11.29	30.61	0.00	0.01	0.00	0.01	57.01
RW032	No. 3	Mg-Ankerite	0.00	0.00	12.89	2.05	11.40	29.20	0.00	0.00	0.00	0.00	55.54
RW038	No. 1	Fe-Ankerite	0.00	0.00	22.89	1.67	5.04	27.92	0.00	0.00	0.00	0.00	57.52
RW038	No. 1	Fe-Ankerite	0.00	0.00	22.38	1.85	5.14	27.63	0.00	0.00	0.00	0.00	57.00
RW038	No. 1	Fe-Ankerite	0.00	0.00	22.71	1.65	5.09	27.81	0.00	0.00	0.00	0.00	57.25
RW038	No. 2	Fe-Ankerite	0.00	0.03	22.85	1.89	4.82	27.41	0.00	0.00	0.00	0.00	57.00
RW038	No. 2	Fe-Ankerite	0.00	0.00	22.80	1.89	5.46	27.57	0.00	0.00	0.00	0.00	57.70
RW042	No. 1	Fe-Ankerite	0.00	0.00	19.11	1.34	7.24	28.05	0.00	0.00	0.00	0.00	55.74
RW042	No. 1	Fe-Ankerite	0.00	0.00	19.45	1.61	6.70	28.99	0.00	0.00	0.00	0.00	56.76
RW042	No. 2	Apatite	0.27	0.00	0.47	0.14	0.02	54.02	0.00	0.00	0.06	0.01	55.00
RW042	No. 2	Fe-Ankerite	0.05	0.02	19.55	1.36	7.24	28.19	0.00	0.03	0.00	0.00	56.45

Formula							Based on 2 anions							Fe/
			Si	Al	Fe	Mn	Mg	Ca	Na	K	Ti	Cr	Total	Fe+Mg
RW002	No. 1	Fe-Ankerite	0.000	0.000	0.646	0.027	0.298	1.029	0.000	0.000	0.000	0.000	1.973	0.684
RW002	No. 1	Fe-Ankerite	0.000	0.000	0.601	0.029	0.342	1.027	0.000	0.000	0.000	0.000	1.971	0.637
RW002	No. 2	Fe-Ankerite	0.000	0.000	0.643	0.027	0.297	1.033	0.000	0.000	0.000	0.000	1.973	0.684
RW009	No. 1	Mg-Ankerite	0.000	0.000	0.337	0.042	0.614	1.008	0.000	0.000	0.000	0.000	1.958	0.354
RW009	No. 1	Mg-Ankerite	0.000	0.000	0.348	0.048	0.596	1.007	0.000	0.000	0.000	0.000	1.952	0.369
RW009	No. 2	Mg-Ankerite	0.000	0.000	0.286	0.069	0.607	1.037	0.000	0.000	0.000	0.000	1.931	0.320
RW009	No. 2	Mg-Ankerite	0.000	0.000	0.449	0.091	0.434	1.026	0.000	0.000	0.000	0.000	1.909	0.509
RW011	No. 1	Mg-Ankerite	0.000	0.000	0.434	0.022	0.527	1.017	0.000	0.000	0.000	0.000	1.978	0.452
RW011	No. 2	Mg-Ankerite	0.000	0.000	0.456	0.018	0.505	1.021	0.000	0.000	0.000	0.000	1.982	0.475
RW016	No. 1	Calcite	0.000	0.000	0.013	0.018	0.004	1.965	0.000	0.000	0.000	0.000	1.982	0.777
RW016	No. 2	Calcite	0.000	0.000	0.020	0.039	0.008	1.933	0.000	0.000	0.000	0.000	1.961	0.712

Table 8.5. Microprobe analyses of selected carbonate grains at Delbridge

Formula			Based on 2 anions											Fe/
			Si	Al	Fe	Mn	Mg	Ca	Na	K	Ti	Cr	Total	Fe+Mg
RW019	No. 1	Calcite	0.000	0.000	0.031	0.028	0.021	1.921	0.000	0.000	0.000	0.000	1.972	0.591
RW019	No. 1	Calcite	0.000	0.001	0.034	0.024	0.016	1.924	0.000	0.000	0.000	0.000	1.974	0.676
RW019	No. 2	Calcite	0.000	0.000	0.040	0.029	0.020	1.911	0.000	0.000	0.000	0.000	1.971	0.673
RW020	No. 1	Calcite	0.002	0.000	0.037	0.057	0.026	1.875	0.000	0.002	0.000	0.000	1.939	0.587
RW020	No. 2	Calcite	0.002	0.000	0.028	0.028	0.014	1.925	0.000	0.002	0.000	0.001	1.967	0.660
RW020	No. 2	Calcite	0.000	0.000	0.056	0.089	0.036	1.819	0.000	0.000	0.000	0.000	1.911	0.611
RW025	No. 1	Calcite	0.000	0.000	0.041	0.027	0.021	1.910	0.000	0.000	0.000	0.000	1.973	0.663
RW025	No. 2	Calcite	0.000	0.000	0.042	0.027	0.020	1.911	0.000	0.000	0.000	0.000	1.973	0.675
RW032	No. 1	Mg-Ankerite	0.002	0.000	0.287	0.038	0.641	1.029	0.000	0.002	0.000	0.000	1.957	0.309
RW032	No. 2	Mg-Ankerite	0.001	0.000	0.349	0.056	0.540	1.053	0.000	0.000	0.000	0.000	1.942	0.393
RW032	No. 3	Mg-Ankerite	0.000	0.000	0.355	0.057	0.559	1.029	0.000	0.000	0.000	0.000	1.943	0.388
RW038	No. 1	Fe-Ankerite	0.000	0.000	0.660	0.049	0.259	1.032	0.000	0.000	0.000	0.000	1.951	0.718
RW038	No. 1	Fe-Ankerite	0.000	0.000	0.650	0.055	0.266	1.029	0.000	0.000	0.000	0.000	1.945	0.709
RW038	No. 1	Fe-Ankerite	0.000	0.000	0.657	0.048	0.263	1.032	0.000	0.000	0.000	0.000	1.952	0.715
RW038	No. 2	Fe-Ankerite	0.000	0.001	0.667	0.056	0.251	1.025	0.000	0.000	0.000	0.000	1.942	0.727
RW038	No. 2	Fe-Ankerite	0.000	0.000	0.654	0.055	0.279	1.013	0.000	0.000	0.000	0.000	1.945	0.701
RW042	No. 1	Fe-Ankerite	0.000	0.000	0.552	0.039	0.372	1.037	0.000	0.000	0.000	0.000	1.961	0.597
RW042	No. 1	Fe-Ankerite	0.000	0.000	0.554	0.047	0.340	1.059	0.000	0.000	0.000	0.000	1.953	0.620
RW042	No. 2	Fe-Ankerite	0.002	0.001	0.558	0.039	0.368	1.030	0.000	0.001	0.000	0.000	1.956	0.602

Table 8.6. Microprobe analyses of selected chlorite grains at Pinkos

Sample	Target	Mineral	SiO2	Al2O3	FeO	MnO	MgO	CaO	Na2O	K2O	TiO2	Cr2O3	BaO	V2O3	F	Cl	Total
RW045	No. 2	Ripidolite	23.13	20.42	35.89	0.07	6.90	0.43	0.00	0.17	0.01	0.00	-	-	-	-	87.01
RW067	No. 1	Ripidolite	26.82	23.50	17.44	0.10	18.93	0.22	0.00	0.35	0.06	0.00	-	-	-	-	87.42
RW067	No. 3	Ripidolite	24.98	22.46	18.52	0.62	18.78	0.19	0.00	0.06	0.04	0.00	-	-	-	-	85.65
RW072	No. 2	Ripidolite	26.15	22.30	18.06	0.05	19.73	0.00	0.05	0.02	0.04	0.00	-	-	-	-	86.40
RW074	No. 2	Ripidolite	22.57	21.69	35.88	0.02	6.75	0.20	0.01	0.02	0.02	0.00	-	-	-	-	87.15
RW074	No. 3	Ripidolite	22.98	21.12	34.26	0.07	7.56	0.13	0.07	0.07	0.02	0.00	-	-	-	-	86.26
RW081	No. 3	Ripidolite	23.14	19.59	38.20	0.18	4.77	1.35	0.06	0.00	0.01	0.00	-	-	-	-	87.31
RW098	No. 4	Ripidolite	24.08	20.63	34.59	0.16	8.66	0.01	0.01	0.03	0.04	0.00	0.00	0.00	0.07	0.00	88.27
RW098	No. 6	Ripidolite	24.67	19.79	33.89	0.15	9.33	0.07	0.00	0.07	0.03	0.00	0.00	0.03	0.11	0.00	88.13
RW101	No. 1	Ripidolite	23.43	21.29	32.28	0.14	9.30	0.02	0.03	0.02	0.05	0.01	-	-	-	-	86.58
RW101	No. 1	Ripidolite	23.63	21.17	31.83	0.22	9.28	0.00	0.01	0.00	0.00	0.01	-	-	-	-	86.16
RW109	No. 2	Ripidolite	23.63	21.81	30.22	0.01	11.31	0.01	0.02	0.02	0.01	0.00	-	-	-	-	87.05
RW119	No. 2	Ripidolite	24.92	22.26	27.25	0.07	11.17	0.09	0.04	0.45	0.04	0.00	-	-	-	-	86.28
RW119	No. 1	Ripidolite	24.12	22.16	29.23	0.13	11.43	0.01	0.01	0.06	0.07	0.00	-	-	-	-	87.22
RW128	No. 5	Ripidolite	25.53	22.55	25.45	0.06	13.77	0.00	0.01	0.05	0.03	0.00	0.02	0.00	0.05	0.00	87.52

Formula			Based on 28 oxygens														Fe/
			Si	Al	Fe	Mn	Mg	Ca	Na	K	Ti	Cr	Ba	V	F	Cl	Total	Fe+Mn+Mg
RW045	No. 2	Ripidolite	5.25	5.47	6.82	0.01	2.34	0.11	0.00	0.05	0.00	0.00	-	-	-	-	20.04	0.74
RW067	No. 1	Ripidolite	5.42	5.60	2.95	0.02	5.70	0.05	0.00	0.09	0.01	0.00	-	-	-	-	19.82	0.34
RW067	No. 3	Ripidolite	5.22	5.53	3.24	0.11	5.85	0.04	0.00	0.02	0.01	0.00	-	-	-	-	20.02	0.35
RW072	No. 2	Ripidolite	5.37	5.39	3.10	0.01	6.04	0.00	0.02	0.00	0.01	0.00	-	-	-	-	19.94	0.34
RW074	No. 2	Ripidolite	5.10	5.78	6.79	0.00	2.27	0.05	0.00	0.01	0.00	0.00	-	-	-	-	20.01	0.75
RW074	No. 3	Ripidolite	5.21	5.64	6.49	0.01	2.55	0.03	0.03	0.02	0.00	0.00	-	-	-	-	19.99	0.72
RW081	No. 3	Ripidolite	5.33	5.31	7.35	0.04	1.64	0.33	0.03	0.00	0.00	0.00	-	-	-	-	20.03	0.81
RW098	No. 4	Ripidolite	5.32	5.37	6.39	0.03	2.85	0.00	0.00	0.01	0.01	-	-	0.00	0.05	-	20.02	0.69
RW098	No. 6	Ripidolite	5.44	5.14	6.24	0.03	3.06	0.02	0.00	0.02	0.00	-	-	0.00	0.08	-	20.04	0.67
RW101	No. 1	Ripidolite	5.22	5.59	6.02	0.03	3.09	0.01	0.01	0.01	0.01	0.00	-	-	-	-	19.98	0.66
RW101	No. 1	Ripidolite	5.28	5.57	5.95	0.04	3.09	0.00	0.00	0.00	0.00	0.00	-	-	-	-	19.94	0.66
RW109	No. 2	Ripidolite	5.17	5.62	5.53	0.00	3.69	0.00	0.01	0.01	0.00	0.00	-	-	-	-	20.03	0.60
RW119	No. 2	Ripidolite	5.40	5.69	4.94	0.01	3.61	0.02	0.01	0.12	0.01	0.00	-	-	-	-	19.82	0.58
RW119	No. 1	Ripidolite	5.23	5.66	5.30	0.02	3.69	0.00	0.00	0.02	0.01	0.00	-	-	-	-	19.94	0.59
RW128	No. 5	Ripidolite	5.38	5.60	4.48	0.01	4.32	0.00	0.00	0.01	0.01	-	0.00	-	0.04	-	19.85	0.51

Table 8.7. Microprobe analyses of selected carbonate grains at Pinkos

Sample	Target	Mineral	SiO2	Al2O3	FeO	MnO	MgO	CaO	Na2O	K2O	TiO2	Cr2O3	BaO	V2O3	F	Cl	Total
RW043	No. 1	Mg-Ankerite	0.00	0.00	13.77	1.04	10.73	29.88	0.00	0.00	0.00	0.00	-	-	-	-	55.42
RW043	No. 2	Mg-Ankerite	0.00	0.00	11.85	0.81	9.41	24.06	0.00	0.00	0.00	0.00	-	-	-	-	46.13
RW043	No. 2	Mg-Ankerite	0.00	0.00	12.62	0.82	8.54	23.53	0.00	0.00	0.00	0.00	-	-	-	-	45.51
RW043	No. 2	Fe-Ankerite	0.00	0.00	15.12	0.90	6.90	22.75	0.00	0.00	0.00	0.00	-	-	-	-	45.67
RW045	No. 1	Mg-Ankerite	0.00	0.00	9.88	0.62	13.62	29.99	0.00	0.00	0.00	0.00	-	-	-	-	54.10
RW045	No. 3	Mg-Ankerite	0.64	0.43	10.56	1.14	13.01	29.43	0.00	0.15	0.04	0.00	-	-	-	-	55.38
RW045	No. 3	Fe-Ankerite	0.00	0.00	18.77	0.85	8.28	28.42	0.00	0.00	0.00	0.00	-	-	-	-	56.33
RW067	No. 1	Calcite	0.00	0.00	0.88	0.65	0.63	56.40	0.00	0.00	0.00	0.00	-	-	-	-	58.56
RW072	No. 1	Mg-Ankerite	0.00	0.00	9.49	1.51	14.38	29.25	0.00	0.00	0.00	0.00	-	-	-	-	54.62
RW072	No. 3	Mg-Ankerite	0.00	0.00	7.01	1.26	16.17	29.55	0.00	0.00	0.00	0.00	-	-	-	-	53.98
RW074	No. 1	Mg-Ankerite	0.00	0.00	13.96	0.76	11.27	29.36	0.00	0.00	0.00	0.00	-	-	-	-	55.34
RW074	No. 1	Mg-Ankerite	0.00	0.00	10.78	1.05	12.74	30.17	0.00	0.00	0.00	0.00	-	-	-	-	54.74
RW074	No. 1	Fe-Ankerite	0.00	0.00	17.86	0.80	8.75	28.88	0.00	0.00	0.00	0.00	-	-	-	-	56.29
RW074	No. 1	Mg-Ankerite	0.00	0.00	16.19	0.84	9.96	27.75	0.00	0.00	0.00	0.00	-	-	-	-	54.74
RW074	No. 2	Calcite	0.00	0.00	6.24	0.85	3.67	46.84	0.00	0.00	0.00	0.00	-	-	-	-	57.60
RW074	No. 2	Calcite	0.00	0.00	0.47	0.33	0.09	56.17	0.00	0.00	0.00	0.00	-	-	-	-	57.07
RW074	No. 3	Mg-Ankerite	0.00	0.00	13.62	0.64	10.24	30.79	0.00	0.00	0.00	0.00	-	-	-	-	55.29
RW081	No. 1	Fe-Ankerite	0.00	0.00	17.73	0.80	8.63	28.78	0.00	0.00	0.00	0.00	-	-	-	-	55.94
RW081	No. 1	Fe-Ankerite	0.00	0.00	20.40	1.16	7.31	27.78	0.00	0.00	0.00	0.00	-	-	-	-	56.65
RW081	No. 2	Fe-Ankerite	0.00	0.00	17.77	0.93	8.77	28.81	0.00	0.00	0.00	0.00	-	-	-	-	56.28
RW081	No. 3	Fe-Ankerite	0.00	0.02	16.99	0.85	8.94	28.93	0.00	0.00	0.00	0.00	-	-	-	-	55.72
RW082	No. 1	Mg-Ankerite	0.41	0.36	16.28	0.56	9.02	27.47	0.03	0.41	0.03	0.02	-	-	-	-	54.58
RW082	No. 1	Fe-Ankerite	0.00	0.02	17.56	0.69	8.62	26.96	0.00	0.00	0.00	0.00	-	-	-	-	53.85
RW082	No. 1	Fe-Ankerite	0.00	0.10	4.69	0.24	17.30	30.03	0.00	0.00	0.00	0.00	-	-	-	-	52.36
RW082	No. 1	Fe-Ankerite	0.00	0.00	19.40	0.80	7.53	27.23	0.00	0.00	0.00	0.00	-	-	-	-	54.96
RW083	No. 1	Fe-Ankerite	0.00	0.00	17.39	1.09	8.12	29.88	0.00	0.00	0.00	0.00	-	-	-	-	56.48
RW083	No. 2	Fe-Ankerite	0.00	0.00	17.53	1.17	8.51	29.08	0.00	0.00	0.00	0.00	-	-	-	-	56.29
RW096	No. 1	Fe-Ankerite	0.00	0.00	19.23	0.63	8.32	27.93	0.00	0.00	0.00	0.00	-	-	-	-	56.11
RW096	No. 2	Fe-Ankerite	0.00	0.10	19.40	0.59	8.09	27.95	0.00	0.00	0.00	0.00	-	-	-	-	56.14
RW096	No. 2	Siderite	0.00	0.00	49.96	1.08	7.04	0.57	0.00	0.00	0.00	0.00	-	-	-	-	58.65
RW096	No. 2	Siderite	0.00	0.00	50.25	0.99	7.62	0.43	0.00	0.00	0.00	0.00	-	-	-	-	59.29
RW098	No. 1	Fe-Ankerite	0.23	0.08	14.84	0.33	11.09	28.48	0.02	0.00	0.03	-	0.01	0.01	0.03	0.01	55.18
RW098	No. 1	Fe-Ankerite	0.29	0.09	16.99	2.13	8.72	26.24	0.08	0.01	0.03	-	0.00	0.00	0.01	0.00	54.56
RW099	No. 1	Fe-Ankerite	0.00	0.00	17.33	1.75	6.46	31.22	0.00	0.00	0.00	0.00	-	-	-	-	56.76
RW099	No. 1	Fe-Ankerite	0.00	0.02	21.91	1.17	4.61	29.71	0.00	0.00	0.00	0.00	-	-	-	-	57.43
RW099	No. 2	Fe-Ankerite	0.00	0.00	21.21	2.22	4.84	28.62	0.00	0.00	0.00	0.00	-	-	-	-	56.89
RW109	No. 1	Mg-Ankerite	0.00	0.00	13.91	2.16	10.07	29.51	0.00	0.00	0.00	0.00	-	-	-	-	55.65
RW109	No. 3	Mg-Ankerite	0.04	0.00	15.55	1.34	10.44	29.13	0.00	0.00	0.02	0.03	-	-	-	-	56.54
RW119	No. 2	Mg-Ankerite	0.00	0.00	12.90	0.88	12.21	28.45	0.00	0.00	0.00	0.00	-	-	-	-	54.44
RW128	No. 1	Mg-Ankerite	0.12	0.02	10.35	1.02	14.46	27.75	0.00	0.00	0.01	-	0.00	0.00	0.06	0.00	53.79

Formula			Based on 2 anions														Fe/
			Si	Al	Fe	Mn	Mg	Ca	Na	K	Ti	Cr	Ba	V	F	Cl	Total	Fe+Mg
RW043	No. 1	Mg-Ankerite	0.00	0.00	0.38	0.03	0.53	1.06	0.00	0.00	0.00	0.00	-	-	-	-	1.97	0.42
RW043	No. 2	Mg-Ankerite	0.00	0.00	0.39	0.03	0.56	1.02	0.00	0.00	0.00	0.00	-	-	-	-	1.97	0.41

Table 8.7. Microprobe analyses of selected carbonate grains at Pinkos

Formula			Based on 2 anions															Fe/
			Si	Al	Fe	Mn	Mg	Ca	Na	K	Ti	Cr	Ba	V	F	Cl	Total	Fe+Mg
RW043	No. 2	Mg-Ankerite	0.00	0.00	0.43	0.03	0.52	1.02	0.00	0.00	0.00	0.00	-	-	-	-	1.97	0.45
RW043	No. 2	Fe-Ankerite	0.00	0.00	0.53	0.03	0.43	1.01	0.00	0.00	0.00	0.00	-	-	-	-	1.97	0.55
RW045	No. 1	Mg-Ankerite	0.00	0.00	0.27	0.02	0.66	1.05	0.00	0.00	0.00	0.00	-	-	-	-	1.98	0.29
RW045	No. 3	Mg-Ankerite	0.02	0.02	0.28	0.03	0.62	1.00	0.00	0.01	0.00	0.00	-	-	-	-	1.90	0.31
RW045	No. 3	Fe-Ankerite	0.00	0.00	0.53	0.02	0.42	1.03	0.00	0.00	0.00	0.00	-	-	-	-	1.98	0.56
RW067	No. 1	Calcite	0.00	0.00	0.02	0.02	0.03	1.93	0.00	0.00	0.00	0.00	-	-	-	-	1.98	0.44
RW072	No. 1	Mg-Ankerite	0.00	0.00	0.26	0.04	0.69	1.01	0.00	0.00	0.00	0.00	-	-	-	-	1.96	0.27
RW072	No. 3	Mg-Ankerite	0.00	0.00	0.19	0.03	0.77	1.01	0.00	0.00	0.00	0.00	-	-	-	-	1.97	0.20
RW074	No. 1	Mg-Ankerite	0.00	0.00	0.39	0.02	0.55	1.04	0.00	0.00	0.00	0.00	-	-	-	-	1.98	0.41
RW074	No. 1	Mg-Ankerite	0.00	0.00	0.29	0.03	0.62	1.06	0.00	0.00	0.00	0.00	-	-	-	-	1.97	0.32
RW074	No. 1	Fe-Ankerite	0.00	0.00	0.50	0.02	0.44	1.04	0.00	0.00	0.00	0.00	-	-	-	-	1.98	0.53
RW074	No. 1	Mg-Ankerite	0.00	0.00	0.46	0.02	0.50	1.01	0.00	0.00	0.00	0.00	-	-	-	-	1.98	0.48
RW074	No. 2	Calcite	0.00	0.00	0.17	0.02	0.18	1.63	0.00	0.00	0.00	0.00	-	-	-	-	1.98	0.49
RW074	No. 2	Calcite	0.00	0.00	0.01	0.01	0.00	1.97	0.00	0.00	0.00	0.00	-	-	-	-	1.99	0.74
RW074	No. 3	Mg-Ankerite	0.00	0.00	0.38	0.02	0.51	1.10	0.00	0.00	0.00	0.00	-	-	-	-	1.98	0.43
RW081	No. 1	Fe-Ankerite	0.00	0.00	0.50	0.02	0.43	1.04	0.00	0.00	0.00	0.00	-	-	-	-	1.98	0.54
RW081	No. 1	Fe-Ankerite	0.00	0.00	0.58	0.03	0.37	1.01	0.00	0.00	0.00	0.00	-	-	-	-	1.97	0.61
RW081	No. 2	Fe-Ankerite	0.00	0.00	0.50	0.03	0.44	1.04	0.00	0.00	0.00	0.00	-	-	-	-	1.97	0.53
RW081	No. 3	Fe-Ankerite	0.00	0.00	0.48	0.02	0.45	1.05	0.00	0.00	0.00	0.00	-	-	-	-	1.97	0.52
RW082	No. 1	Mg-Ankerite	0.00	0.00	0.13	0.01	0.83	1.03	0.00	0.00	0.00	0.00	-	-	-	-	1.99	0.13
RW082	No. 1	Fe-Ankerite	0.00	0.00	0.57	0.02	0.39	1.02	0.00	0.00	0.00	0.00	-	-	-	-	1.98	0.59
RW082	No. 1	Fe-Ankerite	0.01	0.01	0.46	0.02	0.46	1.00	0.00	0.02	0.00	0.00	-	-	-	-	1.92	0.50
RW082	No. 1	Fe-Ankerite	0.00	0.00	0.51	0.02	0.45	1.01	0.00	0.00	0.00	0.00	-	-	-	-	1.98	0.53
RW083	No. 1	Fe-Ankerite	0.00	0.00	0.49	0.03	0.41	1.07	0.00	0.00	0.00	0.00	-	-	-	-	1.97	0.55
RW083	No. 2	Fe-Ankerite	0.00	0.00	0.49	0.03	0.43	1.05	0.00	0.00	0.00	0.00	-	-	-	-	1.97	0.54
RW096	No. 1	Fe-Ankerite	0.00	0.00	0.55	0.02	0.42	1.02	0.00	0.00	0.00	0.00	-	-	-	-	1.98	0.56
RW096	No. 2	Fe-Ankerite	0.00	0.00	0.55	0.02	0.41	1.02	0.00	0.00	0.00	0.00	-	-	-	-	1.98	0.57
RW096	No. 2	Siderite	0.00	0.00	1.55	0.03	0.39	0.02	0.00	0.00	0.00	0.00	-	-	-	-	1.97	0.80
RW096	No. 2	Siderite	0.00	0.00	1.54	0.03	0.42	0.02	0.00	0.00	0.00	0.00	-	-	-	-	1.97	0.79
RW098	No. 1	Fe-Ankerite	0.01	0.00	0.41	0.01	0.55	1.01	0.00	-	0.00	-	0.00	0.00	0.00	0.00	1.99	0.43
RW098	No. 1	Fe-Ankerite	0.01	0.00	0.49	0.06	0.45	0.97	0.01	0.00	0.00	-	-	-	0.00	-	1.99	0.52
RW099	No. 1	Fe-Ankerite	0.00	0.00	0.49	0.05	0.33	1.13	0.00	0.00	0.00	0.00	-	-	-	-	1.95	0.60
RW099	No. 1	Fe-Ankerite	0.00	0.00	0.63	0.03	0.24	1.10	0.00	0.00	0.00	0.00	-	-	-	-	1.96	0.73
RW099	No. 2	Fe-Ankerite	0.00	0.00	0.62	0.07	0.25	1.07	0.00	0.00	0.00	0.00	-	-	-	-	1.93	0.71
RW109	No. 1	Mg-Ankerite	0.00	0.00	0.39	0.06	0.50	1.05	0.00	0.00	0.00	0.00	-	-	-	-	1.94	0.44
RW109	No. 3	Mg-Ankerite	0.00	0.00	0.43	0.04	0.51	1.02	0.00	0.00	0.00	0.00	-	-	-	-	1.96	0.46
RW119	No. 2	Mg-Ankerite	0.00	0.00	0.36	0.02	0.60	1.01	0.00	0.00	0.00	0.00	-	-	-	-	1.98	0.37
RW128	No. 1	Mg-Ankerite	0.00	0.00	0.28	0.03	0.70	0.97	-	0.00	0.00	-	-	-	0.01	-	2.00	0.29

9. SUMMARY AND CONCLUSIONS

The motivation for this study arose from the fact that anomalous Fe-carbonate alteration has been documented in some areas of the NVC, especially in the upper volcanic cycles (e.g., Cycle IV), whereas deposits of the main Noranda camp (Cycle III) typically display extensive chlorite and sericite alteration (Figure 9.1a). The past-producing Delbridge No. 2 Mine and the recently discovered subeconomic Pinkos occurrence display intense carbonate alteration in proximity to known mineralization (Figure 9.1b). Similar relationships between carbonate and sulfide mineralization were observed at both of these locations, despite different controls on hydrothermal upflow.

MAJOR CONTROLS ON ALTERATION AND MINERALIZATION

Detailed mapping of volcanic facies and alteration at Delbridge and Pinkos has shown that the dominant control on the distribution of ore-related alteration was primary porosity and permeability of the host rocks. At Delbridge, this is manifested by a variety of different alteration styles, including 1) disseminated and fracture-controlled Fe-carbonate in highly sericitized fragmental quartz-porphyritic rhyolite, 2) matrix-controlled Fe-carbonate in rhyolite breccias, 3) Fe-carbonate stringers and stockwork in close proximity to the deposit, and 4) disseminated or fracture-controlled sulfides in footwall quartz-porphyritic rhyolite along the flanks of the main upflow zone. In thin section, carbonate-filled amygdules were identified locally in spatial association with stringers and stockwork, supporting a synvolcanic origin for the carbonate. Inclusions of quartz and sericite indicate that carbonate was late in the alteration sequence. At Pinkos, the alteration styles include 1) infilling of amygdules by quartz, sericite,

chlorite (± sulfide), and Fe-carbonate, 2) infilling of well-developed polygonal columnar joints by quartz, sericite, and Fe-carbonate, and 3) matrix-controlled quartz, sericite, and Fe-carbonate in fragmental rhyolite. A clear alteration sequence is evident in the best-developed columnar joints, with early silicification and sericitization, followed by Fe-carbonate, and finally late-stage sericite. This paragenesis is supported by zoned filling of amygdules, with early quartz-sericite rims followed by later infill and replacement by chlorite (± sulfide), Fe-carbonate, and late-stage sericite.

At Delbridge, Fe-carbonate stringers and stockwork define a proximal upflow zone beneath the deposit and appear bound between two inferred synvolcanic faults. At Pinkos, the main hydrothermal upflow is defined by Fe-carbonate in stringers and proximal columnar-jointed rhyolite above the inferred termination of the South Bay fault, a major synvolcanic structure that appears to have controlled hydrothermal upflow. Sulfides are notably absent or presetn as highly corroded grains in zones of most intense Fe-carbonate alteration at both properties, suggesting replacement of early Fe-sulfides by carbonate. Whole-rock lithogeochemical plots of total CO_2 versus total S at both properties support this interpretation. In thin section, disseminated pyrite is clearly replaced by carbonate. SEM photographs indicate an abundance of corrosion pits in pyrite collected from strongly carbonatized proximal zones, possibly due to etching caused by CO_2-rich fluids. Sulfide grains from weakly altered (carbonate-poor) distal zones are not corroded.

SWIR spectroscopy readily identified four different alteration assemblages at both Delbridge and Pinkos: 1) Fe-carbonate + Fe-chlorite; 2) Ca-carbonate + muscovite; 3) Mg-

chlorite + muscovite; and 4) quartz + muscovite. Alteration maps produced from the SWIR data display similar zonation from high- to low-temperature alteration assemblages from the core to the margins of both systems, illustrating the usefulness of this technique to vector towards the high-temperature upflow zones. Zones of intense Fe-carbonate alteration at Delbridge and Pinkos are interpreted to represent the high-temperature cores of hydrothermal upflow associated with each system. Mg-chlorite and muscovite alteration occurring along the margins of these zones is interpreted to reflect infiltration of seawater that promoted the formation of Mg-, K-, and Al-rich alteration. The Ca-carbonate and muscovite assemblage is interpreted as relatively low-temperature alteration from late-stage hydrothermal fluids by analogy with muscovite alteration in the outer zones of other deposits in the Noranda camp (e.g., Cathles, 1993; Paradis et al, 1993). This alteration type occurs in the hanging wall at Delbridge and locally is found in the distal footwall at both properties.

Mass balance calculations from major element oxide data indicate similar mass gains and losses during hydrothermal alteration at both Delbridge and Pinkos. The largest CO_2 additions correspond to both Fe- and Ca-rich carbonate assemblages, consistent with field mapping, petrography, and SWIR spectral data. Net mass gains of up to nearly 50 g/100g in the Delbridge footwall reflect mainly open-space filling. Footwall carbonate in both deposits is dominated by ankerite and ferroan ankerite on a carbonate cation ternary diagram. Zonation from Fe-rich ankerite in the interpreted main upflow zones to Mg-rich ankerite ($\pm$ calcite) along the margins of the system was documented at both properties. Calcite occurs in the hanging-wall ($\pm$ distal footwall) rhyolite at Delbridge.

Distribution maps of normative carbonate estimated from bulk-rock geochemical data and the method of Herrmann and Berry (2002) show that footwall carbonate at both properties is dominated by ankerite with zonation from Fe-rich phases in the main upflow zone to Ca(-Mg)-rich members along the margins. Normative calculations confirm that calcite is the dominant carbonate phase in the hanging wall at Delbridge. Fe_2O_3 and MgO are more strongly linked to chlorite ($\pm$ pyrite) components. Plots of Na_2O and K_2O indicate Na depletion coincident with K enrichment in zones of abundant carbonate within the interpreted hydrothermal upflow at both Delbridge and Pinkos.

Commonly used alteration indices, such as the Ishikawa alteration index (AI) and CCPI, are highest in proximity to both deposits but do not reflect the mapped carbonate alteration. This is expected for AI, as it only measures the intensity of sericite and chlorite alteration associated with the breakdown of sodic plagioclase and volcanic glass. CCPI mainly reflects Mg-Fe chlorite and pyrite and also is poorly correlated with zones of abundant carbonate at Delbridge and Pinkos. The carbonate index (CO_2/CaO+FeO+MgO), a measure of the intensity of carbonate alteration, correlates well with the alteration map pattern at both Delbridge and Pinkos. The distribution of Mn also coincides with zones of abundant carbonate and substitution of Mn in the dominant carbonate species. Electron microprobe analyses of selected carbonate grains support increased Mn contents in these zones. However, a signficant amount of Mn is also contained in chlorite, confirmed by microprobe data.

COMPARISONS WITH OTHER VMS DEPOSITS

Archean Cu-Zn VMS deposits can be subdivided into two distinct groups based on their form and alteration, the Noranda- and Mattabi-types (Morton and Franklin, 1987). Noranda-type deposits (e.g., Corbet, Millenbach, Ansil) are characterized by well-defined, zoned alteration pipes in dominantly bimodal mafic and minor felsic flows (± hyaloclastites). Vertically extensive alteration that narrows with depth beneath Noranda-type deposits is typically localized between synvolcanic faults and contain zoned mineral assemblages. The inner zone is similar in width to the extent of the deposit and, unlike at Delbridge and Pinkos, contains abundant chlorite with increasing Fe content towards the core of the system (i.e., stringers and stockwork). Where intensely metamorphosed, dalmatianite (spotted anthophyllite and cordierite) textures may also be present (e.g., Amulet; Franklin, 1984). Some deposits have a silicified zone beneath the orebody (e.g., Millenbach) which may have sealed permeable units and acted as a cap rock for the hydrothermal system (Gibson et al, 1983). This may be similar to the silicified pod-like zone in stringers and stockwork at Delbridge and the silicified envelope at Pinkos. The Noranda-type deposits typically lack primary, explosively-derived fragmental rocks and contain low modal vesicle abundances (generally <5%; Morton, 1984), which is thought to be generally consistent with eruptions at water depths of greater than 500 m (Gibson et al, 1986).

In contrast, Mattabi-type deposits (e.g., Mattabi, Canadian Jamieson, Helen Siderite) are characterized by relatively broad alteration with diffuse boundaries and large, mineralogically well-defined semiconformable alteration zones in dominantly fragmental volcanic rocks (Morton and Franklin, 1987). Semiconformable alteration minerals can be grouped into two assemblage types: proximal ankerite and Fe-dolomite with Fe-chlorite and distal calcite-dolomite with

sericite and quartz (Morton and Franklin, 1987). These alteration zones are wider and less distinctly zoned than those beneath Noranda-type deposits. As at Delbridge and Pinkos, Mattabi-type alteration typically contains abundant Fe-carbonate, Fe-chlorite, sericite, and quartz. Chloritoid may also be important in greenschist facies metamorphic rocks. Alteration generally extends beyond the deposit and may grade into semiconformable alteration zones containing similar mineralogy. Siderite is typically found only in the core of the alteration zones, whereas ankerite occurs both near the deposit and in more distal semiconformable alteration (Morton and Franklin, 1987). Although siderite is lacking at Delbridge and Pinkos, similar zonation towards more Fe-rich carbonate in the main upflow zones is evident. Chlorite is also increasingly Fe-rich towards the core of hydrothermal upflow (Morton, 1984). Sericite and quartz occur throughout the pipes but intense silicification is restricted to the upper footwall. These alteration trends correspond well to the assemblages defined by SWIR and petrography in the present study. Typical alteration styles in the footwall rocks of Mattabi-type deposits include replacement of groundmass and fragments and filling of amygdules and fractures. As at Delbridge and Pinkos, amygdule contents are generally much higher (up to 50%) than in Noranda-type deposits (Morton, 1984). The dominantly volcaniclastic nature of the host rocks are interpreted to have formed from explosive hydrovolcanic eruptions in a shallow subaqueous (<500 m) and/or subaerial environment (Morton and Nebel, 1983; Groves et al, 1984). The relatively broad and gradational alteration zones are thus interpreted to reflect the primary porosity and permeability of the footwall rocks as well as more extensive hydrofracturing by the ascending mineralizing fluids under low hydrostatic pressures (Morton and Franklin, 1987). The abundance of carbonate and pervasive infilling of fragmental rocks at Delbridge has many similarities to the alteration style of Mattabi-type VMS deposits.

Comparisons can also be made to carbonate alteration associated with younger VMS districts such as the Cambrian Mount Read Volcanics (e.g., Hellyer and Rosebery) and the Cambro-Ordivician Mount Windsor subprovince (e.g., Thalanga) of eastern Australia. Similar to Noranda-type deposits, the Hellyer orebody is a single elongate massive sulfide lens overlying a well-defined pipe-like alteration zone within a relatively thick succession of intermediate to mafic volcanic (± volcaniclastic) rocks (Gemmell and Large, 1992). The Rosebery deposit consists of 16 separate ore lenses with a sheet-like morphology and occurs within a felsic-dominated sequence of volcanic sandstone, black mudstone, and rhyolitic volcaniclastic units (Large et al, 2001b). Stratabound, sericite-dominated footwall alteration zones at Rosebery are the result of diffuse fluid flow through permeable host-rocks. Thalanga is made up of several sheet-like, steeply dipping, and stratabound sulfide lenses within a single stratigraphic interval dominated by coarsely volcaniclastic facies and QP sills (Large et al, 2001b). Discordant quartz-pyrite (± chlorite) stringer zones cross-cut extensive sericite-chlorite-pyrite alteration obliquely beneath the Thalanga deposit. In all three cases, zonation from proximal chlorite ± quartz to distal sericite-rich alteration is common. In the Zn-rich stratiform deposits (e.g., Rosebery and Thalanga), disseminated to spotted carbonate (~2-20 wt.%) is commonly developed in either the chlorite or sericite-bearing zones but pervasive carbonate also occurs proximal to Zn-Pb ore. Similar to Delbridge and Pinkos, zones of abundant carbonate typically form by infill of primary porosity and stratal permeability as well as selective replacement instead of direct precipitation on the seafloor (Sharpe and Gemmell, 2001; Large et al, 2001b). The intensity of carbonate alteration has been shown to increase with proximity to ore in the Rosebery-Hercules area (Allen et al, 1998). Complex mixtures of Fe-Mn-Mg-Ca carbonate have been documented in these

deposits. Fe-dolomite, ankerite, and siderite are the common phases at Hellyer; Mn-carbonate is typical of Rosebery, and nearly pure dolomite and calcite occur with chlorite-tremolite alteration at Thalanga. As established at both Delbridge and Pinkos, Mn (Hellyer, Rosebery) and Fe (Western Tharsis) contents in hydrothermal carbonate have been shown as useful exploration vectors towards ore in some Australian VMS deposits as well. In contrast to Delbridge and Pinkos, the most intense carbonate alteration is commonly located laterally adjacent to the interpreted main upflow zones in porous volcanic units where heated seawater may have been entrained into the hydrothermal upflow (e.g., Thalanga; Herrmann and Hill, 2001).

GENETIC SIGNIFICANCE OF CARBONATE ALTERATION

The origin of abundant hydrothermal carbonate alteration associated with VMS deposits has long been a subject of debate. There are three important ways to precipitate carbonate from hydrothermal seawater: 1) heating at low temperatures, 2) increasing the pH of the solution, and 3) degassing of CO_2 where $HCO_3^- > H_2CO_3$ (Rimstidt, 1997). These changes can be brought about by entrainment of seawater into the high-temperature upflow zone or by boiling of the hydrothermal fluids. However, massive addition of CO_2 to the hydrothermal system may also require direct input from magmatic degassing.

Many studies have suggested that heating of seawater entrained into ascending hot hydrothermal fluids was the dominant mechanism for deposition of carbonate associated with VMS deposits (e.g., Mattabi: Groves, 1984; Helen Siderite: Morton and Nebel, 1984; Headway-Coulee: Osterberg et al, 1987). A number of studies in Australia also have interpreted the

precipitation of carbonate at the margins of the upflow zones to reflect more alkaline conditions developed when near-neutral hydrothermal fluids mix with entrained seawater (e.g., Hellyer and Rosebery: Large et al, 2001b). To test the possibility of seawater as the source of CO_2 for the significant carbonate alteration at Delbridge and Pinkos, mass balance data were used to estimate the amount of CO_2 added to the rocks. Using Zn production numbers from Delbridge (370 000 t of 9.6% Zn) and the concentration of Zn (5 ppm) in a typical black smoker fluid (Von Damm, 1995), the mass of fluid required to form the deposit can be estimated (7×10^9 t). Assuming a CO_2 flux of 2.3 mM (or 41 ppm) for typical seawater (Lupton et al, 2006), this mass of fluid could only produce 2.9×10^5 t CO_2 with seawater as the sole source. Carbonate alteration at Delbridge was mapped and sampled over a surface area of at least 1.6×10^5 m^2 (400 x 400 m) with an average CO_2 addition of 2.69 g/100g (or 26 900 g/t) indicated from mass balance calculations. Assuming a volume of 6.4×10^7 m^3 (400 x 400 x 400 m) and using a specific gravity of 2.7 t/m^3 for rhyolite in the Noranda camp (e.g., Ansil: Verpaelst et al, 2009), a mass of 1.7×10^8 t of altered rock containing 4.5×10^6 t CO_2 is estimated for the Delbridge footwall. Mass balance changes at Pinkos indicate an average CO_2 addition of 0.83 g/100g (or 8 300 g/t) over a similar surface area of mapped and sampled carbonate as at Delbridge. Assuming a similar volume of host-rock rhyolite, a total addition of 1.4×10^6 t CO_2 is approximated for the Pinkos footwall. These amounts of CO_2 are an order of magnitude greater than could be provided by hydrothermal seawater alone, indicating another source for the anomalous carbonate at both Delbridge and Pinkos. This finding is consistent with other studies that have suggested seawater alone cannot be the only source of CO_2 for massive carbonate alteration associated with VMS (e.g., Hellyer: Khin Zaw et al, 1996).

Boiling is well-documented in subaerial geothermal systems (Henley, 1984) and in mineralized epithermal vein deposits (Drummond and Ohmoto, 1985; Seward, 1989) but not in VMS-related systems (Large, 1992). Fluid inclusion microthermometry generally has not shown that boiling is a signficant process in VMS systems (e.g., Hellyer: Khin Zaw et al, 1996). Instead, leaching of footwall volcanic rocks by heated seawater (Ohmoto and Rye, 1974; Gemmell and Large, 1992) and magmatic degassing (Henley and Thornley, 1979; Butterfield et al, 1990; de Ronde et al, 2005) are commonly interpreted as responsible for VMS mineralization. Venting of magmatic CO_2-rich fluids has been documented in several modern submarine hydrothermal systems (e.g., JADE, mid-Okinawa Trough: Zengqian et al, 2005; Brothers, Southern Kermadec Arc: de Ronde et al, 2005). At the Brothers hydrothermal field, end-member CO_2 concentrations in the vent fluid are estimated at ~25 mM to >100 mM (Massoth et al, 2003), indicating a large subvolcanic source (de Ronde et al, 2005; Butterfield et al, 1990). Thus, a combination of recycled seawater and magmatic input of CO_2 are suggested here as the most likely source of carbonate at Delbridge and Pinkos (Figure 9.1b).

A trend towards increasingly calc-alkaline magmatic affinities in the Cycle IV felsic volcanic ($\pm$ volcaniclastic) rocks of the NVC (e.g., Barrett et al., 1992) may support a different magmatic source from the central mine sequence and account for the gas-rich nature of the hydrothermal systems at Delbridge and Pinkos. Abundant carbonate may also be linked to calc-alkaline volcanism in other Archean VMS deposits and districts (e.g., Mueller et al., 2009). Similar styles of carbonate alteration (e.g., filling of amygdules and matrix replacement) are observed in relatively calc-alkaline intermediate to felsic volcanic ($\pm$ pyroclastic) host-rocks at the outer margins of the Ben Nevis Volcanic Complex (Hannington et al, 2003; Peloquin and

Piercey, 2008). Although calcite is the dominant carbonate phase at Ben Nevis, Fe- and Mn-bearing carbonate occurs locally proximal to the subeconomic Canagau VMS occurrence (Hannington et al, 2003). Significant carbonate alteration associated with calc-alkalic host-rocks also has been reported in the Hunter Mine and at Normetal by Mueller et al (2009). Transitional to calc-alkaline magmatic affinities of host-rocks are also noted in younger VMS deposits associated with carbonate alteration in the Mount Read Volcanics (e.g., Hellyer, Gemmell and Fulton, 2001) and Mount Windsor subprovince (e.g., Thalanga, Berry et al, 1992) of eastern Australia. A clear association of carbonate alteration with regional magmatic affinity suggests that magmatic CO_2 is a major source of carbonate in these systems.

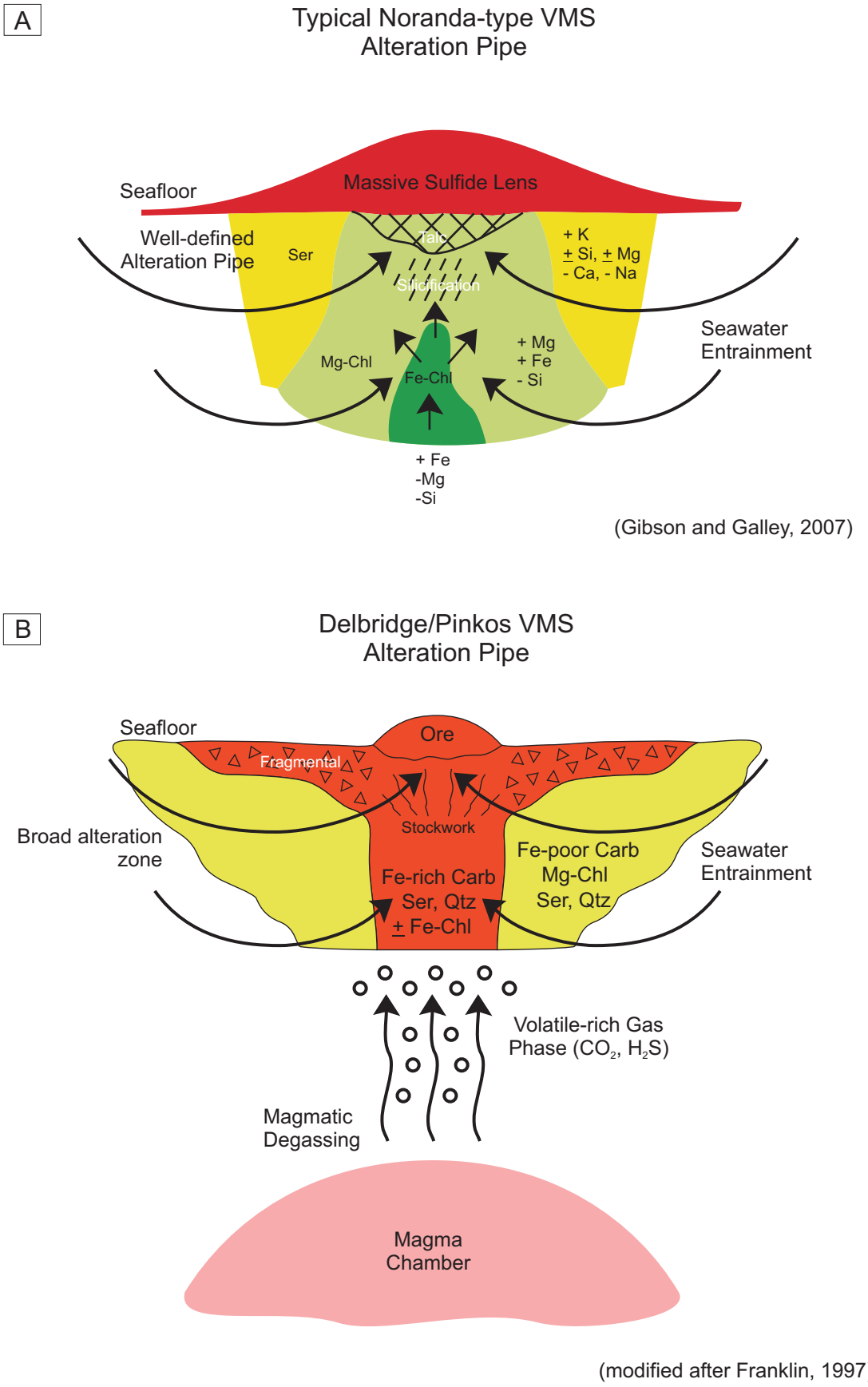

Figure 9.1. Schematic illustrations of Noranda-type versus Delbridge and Pinkos VMS deposits. a) Noranda-type deposits are characterized by a well-defined inner chlorite-rich alteration pipe with an outer sericite-rich zone that does not typically extend beyond the margins of the deposit. Schematic diagram from Gibson and Galley, 2007, and; b) The Delbridge and Pinkos deposits are interpreted as Mattabi-type as they are characterized by broad semiconformable alteration zones with inner Fe-carbonate (± Fe-chlorite) and outer Mg-chlorite and Fe-poor carbonate. The abundant hydrothermal carbonate is interpreted to have originated from a combination of heated entrained seawater and magmatic degassing of CO_2-rich volatiles.

10. REFERENCES

Alexis Minerals Corporation, 2007. Alexis – Xstrata intersects 8.1% zinc over 2.6 metres – Discovers two new massive sulphide targets in Rouyn-Noranda, Quebec; Press Release, January 9, 2007.

Allen, R.L., Gifkins, C.C., Large, R.R., and Herrmann, W., 1998. Discrimination of diagenetic, hydrothermal and metamorphic alteration: Hobart, Tasmania, University of Tasmania, CODES-Australian Mineral Industry Research Association (AMIRA) project P439, Unpublished final report, p. 93-119.

Ames, D.E., Franklin, J.M., Froese, E., 1991. Zonation of hydrothermal alteration at the San Antonio Gold Mine, Bissett, Manitoba, Canada; Economic Geology, v. 86, p. 600-619.

Aoki, A., 1999. Acid bacterial leaching of pyrite single crystals; *in* Biohydrometallurgy and the Environment Toward the Mining of the 21st Century, (ed.) R. Amils and A. Ballester; International Biohydrometallurgy Symposium, v. A, p. 119-125.

Bailey, S.W., and Lister, J.S., 1989. Structures, compositions, and X-ray diffraction identification of dioctahedral chlorites; Clays and Clay Minerals, v. 37(3), p. 193-202.

Barrett, T.J., MacLean, W.H., Cattalani, S., Hoy, L., and Riverin, G., 1991. Massive sulfide deposits of the Noranda area, Quebec, III. The Ansil Mine; Canadian Journal of Earth Sciences, v. 28, p. 1699-1730.

Barrett, T.J., Cattalani, S., Hoy, L., Riopel, J., and Lafleur, P.-J., 1992. Massive sulfide deposits of the Noranda area, Quebec: IV. The Mobrun Mine; Canadian Journal of Earth Sciences, v. 29, p. 1349-1374.

Barrett, T.J., Cattalani, L.S., and MacLean, W.H., 1993a. Volcanic lithogeochemistry and alteration at the Delbridge massive sulfide deposit, Noranda, Quebec; Journal of Geochemical Exploration, v. 48, p. 135-173.

Barrett, T.J., MacLean, W.H., and Cattalani, S., 1993b. Massive sulfide deposits of the Noranda area, Quebec, V. The Corbet Mine; Canadian Journal of Earth Sciences, v. 30, p. 1934-1954.

Barrett, T.J. and MacLean, W.H., 1994. Mass changes in hydrothermal alteration zones associated with VMS deposits of the Noranda area; Exploration and Mining Geology, v. 3, p. 131-160.

Berry, R.F., Huston, D.L., Stolz, A.J., Hill, A.P., Beams, S.D., Kuronen, U., and Taube, A., 1992. Stratigraphy, structure, and volcanic-hosted mineralization of the Mount Windsor subprovince, North Queensland, Australia; Economic Geology, v. 87, p.

739-763.

Bischoff, J.L., and Rosenbauer, R.J., 1987. Phase separation in seafloor geothermal systems: an experimental study of the effects on metal transport; American Journal of Science, v. 287, p. 953-978.

Boldy, J., 1968. Geological observations on the Delbridge massive sulfide deposit; Canadian Institute of Mining Bulletin, v. 61, p. 1045-1054.

Boldy, J., 1979. Exploration discoveries, Noranda District, Quebec; *in* Geophysics and Geochemistry in the Search for Metallic Ores, (ed.) PJ Hood; Geological Survey of Canada Economic Geology Reprint, v. 31, p. 593-604.

Boucher, S., 2007. Sulfide mineralization associated with Fe-carbonate alteration at the Delbridge and Pinkos volcanic-hosted massive sulfide deposits, Rouyn-Noranda, Quebec; B.Sc. thesis, University of Ottawa, Ottawa, Ontario, 55p.

Boucher, S., 2011. Ore petrology and alteration of the West Ansil volcanic-hosted massive sulfide deposit of the Noranda mining camp, Rouyn-Noranda, Quebec; M.Sc. thesis, University of Ottawa, Ottawa, Ontario, 174p.

Burt, D.M., 1981. Acidity-salinity diagrams – Application to greisens and porphyry deposits; Economic Geology, v. 76, p. 832-843.

Butterfield, D., Massoth, G., McDuff, R., Lupton, J., and Lilley, M., 1990. Geochemistry of hydrothermal fluids from Axial Seamount hydrothermal emissions study vent field, Juan de Fuca Ridge: Subseafloor boiling and subsequent fluid-rock interaction; Journal of Geophysical Research, v. 95, p. 12895-12992.

Cathles, L.M., 1993. Oxygen isotope alteration in the Noranda mining district, Abitibi greenstone belt, Quebec; Economic Geology, v. 88, p. 1483-1511.

Cattalani, S., MacLean, W.H., and Barrett, T.J., 1993. Géologie et géochimie du gisement Delbridge, Rouyn-Noranda; Ministère de l'Énergie et des Ressources du Québec, Report ET 91-08, 42p.

Clark, R.N., 2004. Chapter 2: Spectroscopy of rocks and minerals and principles of spectroscopy; *in* Infrared Spectroscopy in Geochemistry, Exploration Geochemistry, and Remote Sensing; (ed.) P.L. King, M.S. Ramsey, and G.A. Swayze; Short Course Series, Mineralogical Association of Canada, v. 33, p. 17-35.

Clark, R.N., King, T., Klefwa, M., Swayze, G.A., and Vergo, N., 1990. High spectral resolution reflectance spectroscopy of minerals; Journal of Geophysical Research, v. 95 (B-8), p. 12,653-12,680.

Cohen, D.R. and Ward, C.R., 1991. SEDNORM – a program to calculate a normative

mineralogy for sedimentary rocks based on chemical analyses, Computers and Geosciences, v. 17, p. 1235-1253.

Date, J., Watanabe, Y., and Saeki, Y., 1983. Zonal alteration around the Fukazawa Kuroko deposits, Akita Prefecture, northern Japan; Economic Geology Monographs, v. 5, p. 365-386.

David, J., Dion, C., Goutier, J., Roy, P., Bandyayera, D., Legault, M., and Rheaume, P., 2006. Datations U-Pb effectuées dans la Sous-province de l'Abitibi à la suite des travaux de 2004-2005: Ministère des Ressources Naturelles et de la Faune, report 2006-04, 22 p.

Dermatas, D., Chrysochoou, M., Pardali, S., and Grubb, D.G., 2007. Influence of X-ray diffraction sample preparation on quantitative mineralogy: implications for chromate waste treatment; Journal of Environmental Quality, v. 36, p. 487-497.

de Ronde, C.E.J., Hannington, M.D., Stoffers, P., Wright, I.C., Ditchburn, R.G., Reyes, A.G., Baker, E.T., Massoth, G.J., Lupton, J.E., Walker, S.L., Greene, R.R., Soong, C.W.R., Ishibashi, J., Lebon, G.T., Bray, C.J., and Resing, J.A., 2005. Evolution of a submarine magmatic-hydrothermal system: Brothers Volcano, Southern Kermadec Arc, New Zealand; Economic Geology, v. 100, p. 1097-1133.

Dimroth, E., Imreh, L., Rocheleau, M., and Goulet, N., 1982. Evolution of the south-central segment of the Archean Abitibi belt, Quebec, Part 1: stratigraphy and paleo-geographic model; Canadian Journal of Earth Sciences, v. 19, p. 1729-1758.

Donald, R., and Southam, G., 1999. Low temperature anaerobic bacterial diagenesis of ferrous monosulfide to pyrite; Geochimica et Cosmochimica Acta, v. 63, p. 2019-2023.

Drummond, S.E., and Ohmoto, H., 1985. Chemical evolution and mineral deposition in boiling hydrothermal systems; Economic Geology, v. 80, p. 126-147.

Edwards, K.J., Bach, W., McCollom, T.M., and Rogers, D.R., 2004. Neutrophilic iron-oxidizing bacteria in the ocean: Their habitats, diversity, and roles in mineral deposition, rock alteration, and biomass production in the deep-sea; Geomicrobiology Journal, v. 21, p. 393-404.

Etzel, K., Klingl, A., Huber, H., Rachel, R., Schmalz, G., Thomm, M., and Depmeier, W., 2008. Etching of {111} and {210} synthetic pyrite surfaces by two archael strains, *Metallosphaera sedula* and *Sulfolobus metallicus*; Hydrometallurgy, v. 94, p. 116-120.

Evangelou, V.P., and Huang, X., 1994. Infrared spectroscopic evidence of an iron(II)-carbonate complex on the surface of pyrite; Spectrochimica Acta, v. 50A, p. 1333-1340.

Evangelou, V.P., and Zhang, Y.L., 1995. A review: pyrite oxidation mechanisms and acid mine drainage prevention; Critical Reviews in Environmental Science and Technology, v. 25(2), p. 141-199.

Franklin, J.M., 1984. Characteristics of alteration associated with Precambrian massive sulfide deposits, *in* Morton, R.L., and Groves, D. A., eds., Volcanic rocks, hydrothermal alteration, and associated massive sulfide and gold deposits: Duluth, University of Minnesota-Duluth, Short Course notes, p. 92-105.

Franklin, J.M., 1997. Lithogeochemical and mineralogical methods for base metal and gold exploration; *in* Proceedings of Exploration 97: Fourth Decennial International Conference on Mineral Exploration, (ed.) A.G. Gubins, Exploration Geochemistry, p. 191-208.

Franklin, J.M., Sangster, D.M., and Lydon, J.W., 1981. Volcanic-associated massive sulfide deposits; *in* Economic Geology Seventy-Fifth Anniversary Volume, (ed.) B.J. Skinner; Society of Economic Geologists, p. 485-627.

Franklin, J.M., Kasarda, J., and Poulsen, K.H., 1985. Petrology and chemistry of the alteration zone of the Mattabi massive sulfide deposits; Economic Geology, v. 70, p. 63-79.

Galley, A.G., Jonasson, I.R., and Watkinson, D.H., 2000. Magnetite-rich calc-silicate alteration in relation to a synvolcanic intrusion at the Ansil volcanogenic massive sulphide deposit, Rouyn-Noranda, Quebec, Canada; Mineralium Deposita, v. 35, p. 619-637.

Galley, A.G., 2003. Composite syn-volcanic intrusions associated with Precambrian VMS-related hydrothermal systems; Mineralium Deposita, v. 38, p. 443-473.

Gemmell, J.B., and Fulton, R., 2001. Geology, genesis, and exploration implications of the footwall and hanging-wall alteration associated with Hellyer volcanic-hosted massive sulfide deposit, Tasmania, Australia; Economic Geology, v. 96, p. 1003-1035.

Gemmell, J.B., and Large, R.R., 1992. Stringer system and alteration zones underlying the Hellyer volcanic-hosted massive sulfide deposit, Tasmania, Australia; Economic Geology, v. 87, p. 620-649.

GeoLabs, 2009. Schedule of Fees and Services; Ontario Ministry of Northern Development and Mines, Ontario Geological Survey, Issue 5 (April 1), 22p., Accessible via Worldwide Web <<www.ontario.ca/geolabs>>.

Gibson, H.L., 1990. The mine sequence of the central Noranda volcanic complex: Geology, alteration, massive sulfide deposits and volcanological reconstruction; Ph.D. thesis, Carleton University, Ottawa, Ontario, 715p.

Gibson, H.L. and Watkinson, D.H., 1990. Volcanogenic massive sulfide deposits of the Noranda cauldron and shield volcano, Quebec; *in* The Northwestern Quebec Polymetallic Belt: A Summary of 60 Years of Mining Exploration, (ed.) V.P. Rive, Y. Gagon, L.M. Lulin, G. Riverin, and A. Simard; Canadian Institute of Mining and Metallurgy, Special Volume 43, p. 119-132.

Gibson, H.L. and Galley, A., 2007. Volcanogenic massive sulphide deposits of the Archean, Noranda District, Quebec; *in* Mineral Deposits of Canada: A Synthesis of Major Deposit-types, District Metallogeny, the Evolution of Geological Provinces, and Exploration Methods, (ed.) W.D. Goodfellow; Special Publication No. 5, Mineral Deposits Division, Geological Association of Canada, p. 533-552.

Gibson, H.L., Watkinson, D.H., and Comba, C.D.A., 1983. Silicification: Hydrothermal alteration in an Archean geothermal system within the Amulet Rhyolite Formation, Noranda, Quebec; Economic Geology, v. 78, p. 954-971.

Gibson, H.L., Lichtblau, A.P., Comba, C.D.A., and Watkinson, D.H., 1986. Subaqueous rhyolite flows of the central mine sequence, Noranda, Quebec (abs.): Geological Association of Canada Programs with Abstracts, v. 11, p.72.

Gifkins, C.C., Herrmann, W., and Large, R.R., 2005. Altered Volcanic Rocks: A guide to description and interpretation; Centre for Ore Deposit Research, University of Tasmania, 275p.

Giorgetti, G., Monecke, T., Kleeberg, R., and Herzig, P.M., 2003. Intermediate sodium-potassium mica in hydrothermally altered rocks of the Waterloo deposit, Australia: a combined SEM-EMP-XRD-TEM study; Contributions to Mineralogy and Petrology, v. 146, p. 159-173.

Goldie, R., 1978. Magma mixing in the Flavrian pluton, Noranda area, Quebec; Canadian Journal of Earth Sciences, v. 15, p. 132-144.

Goodwin, A.M., 1982. Archean volcanoes in southwestern Abitibi Belt, Ontario and Quebec: Form, composition, and development; Canadian Journal of Earth Sciences, v. 19, p. 1140-1155.

Goutier, J., McNicoll, V., Dion, C., Lafrance, B., Legault, M., Ross, P.S., Mercier-Langevin, P., Cheng, L.Z., de Kemp, E., and Ayer, J., 2009. L'impact du Plan Cuivre et de l'IGC-3 sur la géologie de l'Abitibi et du Groupe de Blake River; Congrès Abitibi Cuivre, Rouyn-Noranda, September 28, 2009, Proceedings Volume, p. 9-13.

Groves, D.A., 1984. Stratigraphy, lithology, and hydrothermal alteration of volcanic rocks beneath the Mattabi massive sulfide deposit, Sturgeon Lake, Ontario: Unpublished M.Sc. thesis, University of Mineesota-Duluth, 115p.

Groves, D.A., Morton, R.L., and Franklin, J.M., 1984. Stratigraphy of the footwall volcanic rocks at the Mattabi massive sulfide deposit, Sturgeon Lake, Ontario (abs.): Geological Association of Canada Program with Abstracts, v. 9, p. 69.

Hannington, M.D., Poulsen, K.H., Thompson, J.F.H., and Sillitoe, R.H., 1999. Volcanogenic gold in the massive sulfide environment; *in* Volcanic-associated Massive Deposits: Processes and Examples in Modern and Ancient Settings, (ed.) C.T. Barrie and M.D. Hannington; Society of Economic Geologists, Reviews in Economic Geology, v. 8, p. 325-356.

Hannington, M.D., Santaguida, F., Kjarsgaard, I.M., and Cathles, L.M., 2003. Regional-scale hydrothermal alteration in the Central Blake River Group, western Abitibi subprovince, Canada: implications for VMS prospectivity; Mineralium Deposita, v. 38, p.393-422.

Hannington, M.D., Gibson, H.L., and Dube, B., 2006. The metallogeny of modern submarine volcanic arcs and implications for ancient greenstone belts, *In* Program with Abstracts, annual meeting of the Geological Association of Canada and Mineralogical Association of Canada, v. 31, p. A-13.

Hardardottir, V., Brown, K.L., Fridriksson, Th., Hedenquist, J.W., Hannington, M.D., and Thorhallsson, S., 2009. Metals in deep liquid of the Rekjanes geothermal system, southwest Iceland: Implications for the composition of seafloor black smoker fluids; Geology, v. 37(12), p. 1103-1106.

Hauff, P., 2005. Applied Reflectance Spectroscopy Instruction Manual; Spectral International Inc., Colorado, v. 4.1.

Henley, R.W., 1984. Gaseous components in geothermal processes, *In* R.W. Henley, A.H. Truesdell, and P.B. Barton, Jr. (eds.); Fluid-Mineral Equilibria in Hydrothermal Systems; Reviews in Economic Geology, v. 1, p. 45-56.

Henley, R.W., and Thornley, P., 1979. Some geothermal aspects of polymetallic massive sulfide formation; Economic Geology, v. 74, p. 1600-1612.

Herrmann, W., and Hill, A.P., 2001. The origin of chlorite-tremolite-carbonate rocks associated with the Thalanga volcanic-hosted massive sulfide deposit, North Queensland, Australia; Economic Geology, v. 96, p. 1149-1173.

Herrmann, W. and Berry, R.F., 2002. MINSQ – a least-squares spreadsheet method for calculating mineral proportions from whole rock major element analyses; Geochemistry: Exploration, Environment, Analysis, v. 2, p. 361-368.

Herrmann, W., Blake, M., Doyle, M., Huston, D., Kamprad, J., Merry, N., and Pontual, S., 2001. Short wavelength infrared (SWIR) spectral analysis of hydrothermal alteration zones associated with base metal sulfide deposits at Rosebery and Western

Tharsis, Tasmania, and Highway-Reward, Queensland; Economic Geology, v. 96, p. 939-955.

Hey, M.H., 1954. A new review of the chlorites; Mineralogical Magazine, v. 30, p. 277-292.

Hillier, S., 2003. Quantitative analysis of clay and other minerals in sandstones by X-ray powder diffraction (XRPD); Special Publication of the International Association of Sedimentologists, v. 34, p. 213-251.

Hood, T.A., 1991. The kinetics of pyrite oxidation in marine systems; Ph.D. Thesis, University of Miami, 223p.

Hudak III, G.J., 1996. The physical volcanology and hydrothermal alteration associated with late caldera volcanic and volcaniclastic rocks and volcanogenic massive sulfide deposits in the Sturgeon Lake region of northwestern Ontario, Ph.D. Thesis, University of Minnesota, 463p.

Hunt, G.R. and Ashley, R.P., 1979. Spectra of altered rocks in the visible and near Infrared; Economic Geology, v. 74, p. 1613-1629.

Huston, D.L., and Large, R.R., 1989. A chemical model for the concentration of gold in volcanogenic massive sulfide deposits; Ore Geology Reviews, v. 4, p. 171-200.

Huston, D.L., Kamprad, J., and Brauhart, C., 1997. Preliminary results of PIMA analysis of the alteration zone underlying the Sulphur Springs deposit, Panorama district, Pilbara block, Western Australia; Australian Geological Survey, Organisation Record 1997/14, 36 p.

Huston, D.L., Kamprad, J., and Brauhart, C., 1999. Definition of high-temperature alteration zones with PIMA; an example from the Panorama VHMS district, central Pilbara Craton; AGSO Research Newsletter, v. 30, p. 10-12.

Ikingura, J.R., Bell, K., and Watkinson, D.H., 1989. Hydrothermal alteration and oxygen and hydrogen isotope geochemistry of the D68 Zone Cu-Zn massive sulfide deposit, Noranda district, Quebec, Canada; Mineralogy Petrology, v. 40, p. 155-172.

Ishikawa, Y., Sawaguchi, T., Iwaya, S., and Horiuchi, M., 1976. Delineation of prospecting targets for Kuroko deposits based on modes of volcanism of underlying dacite and alteration halos; Mining Geology, v. 26, p. 105-117.

Jones, S., Herrmann, W., and Gemmell, J.B., 2005. Short wavelength infrared spectral characteristics of the HW Horizon: Implications for exploration in the Myra Falls volcanic-hosted massive sulfide camp, Vancouver Island, British Columbia, Canada; Economic Geology, v. 100, p. 273-294.

Kalogeropoulos, S.I., and Scott, S.D., 1989. Mineralogy and geochemistry of an Archean

tuffaceous exhalite: The Main Contact Tuff, Millenbach Mine area, Noranda, Quebec; Canadian Journal of Earth Sciences, v. 26, p. 88-105.

Kandianis, M.T., Fouke, B.W., Johnson, R.W., Veysey, J(2nd), and Inskeep, W.P., 2008. Microbial biomass: A catalyst for $CaCO_3$ precipitation in advection-dominated transport regimes; Geological Society of America Bulletin, v. 120, p. 442-450.

Keller, L., and Murr, L.E., 1982. Acid-bacterial and ferric sulfate leaching of pyrite single crystals; Biotechnology and Bioengineering, v. 24, p. 83-96.

Kerr, D.J. and Gibson, H.L., 1993. A Comparison of the Horne volcanogenic massive sulfide deposit and intracauldron deposits of the mine sequence, Noranda, Quebec; Economic Geology, v. 88, p. 1419-1442.

Khin Zaw, Gemmell, J.B., Large, R.R., Mernagh, T.P., and Ryan, C.G., 1996. Evolution and source of ore fluids in the stringer system, Hellyer VHMS deposit, Tasmania, Australia: evidence from fluid inclusion microthermometry and geochemistry; Ore Geology Reviews 10, p. 251-278.

Kleeberg, R., 2009. State-of-the-art trends in quantitative phase analysis of geological and raw materials; Zeitschrift fur Kristallographie Suppl., v. 30, p. 47-52.

Kleeberg, R., Monecke, T., and Hillier, S., 2008. Preferred orientation of mineral grains in sample mounts for quantitative XRD measurements: How random are powder samples?; Clay and Clay Minerals, v. 56 (4), p. 404-415.

Klein, C., 2002. Mineral Science 22nd Ed., John Wiley & Sons, Inc., USA, 641 p.

Koopman, E.R., Hannington, M.D., Santiquda, E., and Cameron, B.L., 1999. Petrology and geochemistry of proximal hydrothermal alteration in the mine rhyolite at Kidd Creek; *in* The Giant Kidd Creek volcanogenic massive sulfide deposit, western Abitibi subprovince, Canada, (ed.) M.D. Hannington and C.T. Barrie; Economic Geology, Monograph 10, p. 267-296.

Kucha, H., Schroll, E., and Stumpfl, E.F., 2005. Fossil sulphate-reducing bacteria in the Bleiberg lead-zinc deposit, Austria; Mineralium Deposita, v. 40, p. 123-126.

Lafrance, B., Davis, D.W., Goutier, J., Moorhead, J., Pilote, P., Mercier-Langevin, P., Dubé, B., Galley, A., and Mueller, W.U. 2005. Nouvelles datations isotopiques dans la portion québécoise du Groupe de Blake River et des unités adjacentes; Rapports préliminaires RP 2005-01, Ministere des Ressources Naturelles et de la Faune, Québec, 15 p.

Large, R.R., 1992. Australian volcanic-hosted massive sulfide deposits: Features, styles, and genetic models; Economic Geology, v. 87, p. 549-572.

Large, R.R., Gemmell, J.B., Paulick, H., and Huston, D.L., 2001. The alteration box plot: A simple approach to understanding the relationship between alteration mineralogy and lithogeochemistry associated with volcanic-hosted massive sulfide deposits; Economic Geology, v. 96, p. 957-971.

Large, R.R., McPhie, J., Gemmell, J.B., Herrmann, W., and Davidson, G.J., 2001b. The spectrum of ore deposit types, volcanic environments, alteration halos, and related exploration vectors in submarine volcanic successions: Some examples from Australia; Economic Geology, v. 96, p. 913-938.

Larocque, A.C.L., and Hodgson, C.J., 1993. Carbonate-rich footwall alteration at the Mobrun Mine, a possible Mattabi-type VMS deposit in the Noranda Camp; Exploration Mining Geology, v. 2(2), p. 165-169.

Le Maitre, R.W., 1981. GENMIX – A generalised petrological mixing model program, Computers and Geosciences, v. 7, p. 229-247.

Lichtblau, A.P. and Dimroth, E., 1980. Stratigraphy and facies at the south margin of the Archean Noranda Caldera; *in* Current Research, Part A, Geological Survey of Canada, Paper 80-1A, p. 69-76.

Lupton, J., Butterfield, D., Lilley, M., Evans, L., Nakamura, K., Chadwick Jr., W., Resing, J., Embley, R., Olson, E., Proskurowski, G., Baker, E., de Ronde, C., Roe, K., Greene, R., Lebon, G., and Young, C., 2006. Submarine venting of liquid carbon dioxide on a Mariana Arc volcano; Geochemistry, Geophysics, Geosystems (G^3): An electronic Jounral of the Earth Sciences; v. 7(8), 20p.

MacLean, W.H. and Barrett, T.J., 1993. Lithogeochemical techniques using immobile elements; Journal of Geochemical Exploration, v. 48, p. 109-133.

MacLean, W.H., and Hoy, L.D., 1991. Geochemistry of hydrothermally altered rocks at the Horne Mine, Noranda, Quebec; Economic Geology, v. 86, p. 506-528.

MacLean, W.H. and Kranidiotis, P., 1987. Immobile elements as monitors of mass transfer in hydrothermal alteration: Phelps Dodge massive sulfide deposit, Matagami, Quebec; Economic Geology, v. 82, p. 951-962.

Massoth, G.J., de Ronde, C.E.J., Lupton, J.E., Feely, R.A., Baker, E.T., Lebon, G.T., and Maenner, S.M., 2003. Chemically rich and diverse submarine hydrothermal plumes of the southern Kermadec volcanic arc (New Zealand); Geological Society of London Special Publication, v. 219, p. 119-139.

McDonough, W.F. and Sun, S.-S., 1995. The composition of the Earth; Chemical Geology, v.120, p. 223-254.

Millero, F.J., and Izaguirre, M., 1989. Effect of ionic strength and ionic interactions on

the oxidation of Fe(II); Journal of Solution Chemistry, v. 18, p. 585-599.

Monecke, T., Gibson, H., Dubé, B., Laurin, J., Hannington, M.D., & Martin, L., 2008. Geology and volcanic setting of the Horne deposit, Rouyn-Noranda, Québec: Initial results of a new research project; Current Research, 2008-9, 16 p.

Monecke, T., Kohler, S., Kleeberg, R., Herzig, P.M., and Gemmell, J.B., 2001. Quantitative phase-analysis by the Rietveld method using X-ray powder diffraction data: Application to the study of alteration halos associated with volcanic-rock-hosted massive sulfide deposits; The Canadian Mineralogist, v. 39, p. 1617-1633.

Moore, D.M. and Reynolds, R.C., Jr., 1997. X-ray Diffraction and the Identification and Analysis of Clay Minerals, 2nd Ed., Oxford University Press, New York.

Mortensen, J.K., 1993. U-Pb geochronology of the eastern Abitibi Subprovince. Part 2: Noranda – Kirkland Lake area; Canadian Journal of Earth Science, v. 30, p. 29-41.

Mortensen, J.K., 1987. Preliminary U-Pb zircon ages for volcanic and plutonic rocks of the Noranda – Lac Abitibi area, Abitibi Subprovince, Quebec; *in* Current Research, Part A, Geological Survey of Canada, Paper 87-1A, p. 581-590.

Morton, R.L., 1984. Subaqueous volcanism, *in* Morton, R.L., and Groves, D.A., eds., Volcanic rocks, hydrothermal alteration, and associated massive sulfide and gold deposits: Duluth, University of Minnesota-Duluth, Short Course Notes, p. 15-45.

Morton, R.L., and Nebel, M.L., 1983. Physical character of Archean felsic volcanism in the vicinity of the Helen iron mine, Wawa, Ontario, Canada; Precambrian Research, v. 20, p. 39-62.

Morton, R.L., and Nebel, M.L., 1984. Hydrothermal alteration of felsic volcanic rocks at the Helen siderite deposit, Wawa, Ontario; Economic Geology, v. 79, p. 1319-1333.

Morton, J.L., and Franklin, J.M., 1987. Two-fold classification of Archean volcanic-associated massive sulfide deposits; Economic Geology, v. 82, p.1057-1063.

Mueller, W.U., Stix, J., Corcoran, P.L., and Daigneault, R., 2009. Subaqueous calderas in the Archean Abitibi greenstone belt: An overview and new ideas; Ore Geology Reviews, v. 35(1), p. 4-46.

Ndlovu, S., and Monhemius, A., 2005. The influence of crystal orientation on the bacterial dissolution of pyrite; Hydrometallurgy, v. 78, p. 187-197.

O'Dowd, 1990. Mineral deposits of Noranda, Quebec and Cobalt, Ontario; *in* The Northwestern Quebec Polymetallic Belt: Excursion Guidebook, Rouyn-Noranda, (ed.) J.R. Sullivan; p. 6-9.

Ohmoto, H., and Rye, R.O., 1974. Hydrogen and oxygen isotopic compositions of fluid inclusions in the Kuroko deposits; Economic Geology, v. 69, p. 947-953.

Osterberg, M.O., 1981. Felsic pyroclastic rocks in the vicinity of the Helen iron mine, Wawa, Ontario; Unpublished M.Sc. thesis, University of Minnesota-Duluth, 114p.

Paradis, S., Taylor, B.E., Watkinson, D.H., and Jonasson, I.R., 1993. Oxygen isotope zonation and alteration in the northern Noranda district, Quebec: Evidence for hydrothermal fluid flow; Economic Geology, v.88, p. 1512-1525.

Peloquin, A.S., and Piercey, S.J., 2008. The Ben Nevis Volcanic Complex, Ontario: Part of the late volcanic phase of the Blake River Group, Abitibi subprovince; Economic Geology, v. 103(6), p. 1219-1241.

Powell, W.G., Carmichael, D.M., and Hodgson, C.J., 1995. Conditions and timing of metamorphism in the southern Abitibi greenstone belt, Quebec; Canadian Journal of Earth Sciences, v. 32, p. 787-805.

Reysenbach, A.-L., and Shock, E., 2002. Merging genomes with geochemistry in hydrothermal ecosystems; Science, v. 296, p. 1077-1982.

Rimstidt, J.D., 1997. Chapter 10: Gangue mineral transport and deposition, *In* Geochemistry of Ore Deposits, 3rd ed., (ed.) H.L. Barnes; John Wiley & Sons, Inc., USA, 975p.

Rona, P.A., 1984. Hydrothermal mineralization at seafloor spreading centers; Earth-Science Reviews, v. 20, p. 1-104.

Rozinova, E.L., and Dubik, O.Y., 1983. Dioctahedral chlorites; Miner. Zh., v. 5, p. 14-31.

Saeki, Y. and Date, J., 1980. Computer application to the alteration data of the footwall dacite lava at the Ezuri Kuroko deposits, Akita Prefecture; Mining Geology, v. 30, p. 241-250.

Schroll, E., and Rantitsch, G., 2005. Sulfur isotope patterns in the Bleiberg deposit (Eastern Alps) and their implications for genetically affiliated lead-zinc deposits; Mineralogy and Petrology, v. 84, p. 1-18.

Seward, T.M., 1989. The hydrothermal chemistry of gold and its implications ore formation: Boiling and conduction cooling as examples; Economic Geology Monograph 6, p. 398-404.

Sharpe, R., and Gemmell, J.B., 2001. Alteration characteristics of the Archean Golden Grove Formation at the Gossan Hill deposit, Western Australia: Induration as a focusing mechanism for mineralizing hydrothermal fluids; Economic Geology, v. 96,

p. 1239-1262.

Shriver, N.A. and MacLean, W.H., 1993. Mass, volume and chemical changes in the alteration zone at the Norbec Mine, Noranda, Quebec; Mineralium Deposita, v. 28, p. 157-166.

Skirrow, R.G. and Franklin, J.M., 1994. Silicification and metal leaching in subconcordant alteration zones beneath the Chisel Lake massive sulphide deposit, Snow Lake, Manitoba; Economic Geology, v. 89, p. 31-50.

Southam, G., and Saunders, J.A., 2005. The geomicrobiology of ore deposits; Economic Geology, v. 100, p. 1067-1084.

Spence, C.D. and De Rosen-Spence, A.F., 1975. The place of sulfide mineralization in the volcanic sequence at Noranda, Quebec; Economic Geology, v. 70, p. 90-101.

Stoffers, P., Wright, I.C., and the Shipboard Scientific Party, 1999. Cruise report Sonne 135, Havre Trough-Taupo Volcanic Zone: Tectonic, magmatic and hydrothermal processes, Suva-Fiji-Wellington, New Zealand, September 9-October 15, 1998: Berichte-Reports, Institut fur Geowissenschaften, Universitat Kiel, Nr. 1, 77p.

Système d'Information Géominière du Québec (SIGÉOM), 2000. Geological Compilation Map CG-4 (1 : 20 000), NTS Map Sheet Number 32D07-200-101 (Cléricy); Ministère des Ressources naturelles et de la Faune, Accessible via Worldwide Web <<http:// www.mrnfp.gouv.qc.ca/produits-services/mines.jsp>>.

Thompson, A.J.B., Hauff, P.L., and Robitaille, J.A., 1999. Alteration mapping in exploration; application of short-wave infrared (SWIR) spectroscopy; Society of Economic Geologists Newsletter, v.39, p. 1-27.

Tuttle, J.H., Dugan, C.B., and Randles, C.I., 1969. Microbial sulfate reduction and its potential utility as an acid mine water pollution abatement procedure; Applied Microbiology, v. 17, p. 297-302.

van Ruitenbeek, F.J.A., Cudahy, T., Hale, M., and van der Meer,Freek D., 2005. Tracing fluid pathways in fossil hydrothermal systems with near-infrared spectroscopy; Geology, v. 33, p. 597-600.

Verpaelst, P., Peloquin, A.S., Erick Adam, Barnes, A.E., Ludden, J.N., Dion, D.-J., Hubert, C., Milkereit, B., and Labrie, M., 1995. Seismic reflection profiles across the "Mine Series" in the Noranda camp of the Abitibi belt, eastern Canada; Canadian Journal of Earth Sciences, v. 32, p. 167-176.

Vilks, P., 1981. Li distribution between chlorite and albite in a common vapor phase; Dissertations and Theses, Paper 3641; Available on the Worldwide Web: http://digitalcommons.mcmaster.ca/opendissertations/3641.

Von Damm, K. L., 1995. Controls on the chemistry and temporal variability of seafloor hydrothermal fluids, *In* Seafloor Hydrothermal Systems: Physical, Chemical, Biological, and Geological Interactions, (ed.) S.E. Humphris et al Geophysical Monograph Series, v. 91, p. 222–247.

Wilson, M.E., 1941. Noranda District, Quebec; Geological Survey Memoir, v. 229, 162 p.

Wright, D.T., 1999. The role of sulphate-reducing bacteria and cyanobacteria in dolomite formation in distal ephemeral lakes of the Coorong region, South Australia; Sedimentary Geology, v. 126, p. 147-157.

Wright, D.T., 2000. Benthic microbial communities and dolomite formation in marine and lacustrine environments – a new dolomite model; *in* Marine Authigenesis: From Global to Microbial, (ed.) C.R. Glenn, J. Lucas, and Prevot-Lucas, L.; Society for Sedimentary Geology (SEPM) Special Publication 66, p. 7-14.

Wright, D.T., and Oren, A., 2005. Non-photosynthetic bacteria and the formation of carbonates and evaporates through time; Geomicrobiology Journal, v. 22, p. 27-53.

Zengqian, H., Khin Zaw, Yanhe, L., Qiling, Z., Zhigang, Z., and Urabe, T., 2005. Contribution of magmatic fluid to the active hydrothermal system in the JADE field, Okinawa trough: Evidence from fluid inclusions, oxygen and helium isotopes; International Geology Review, v. 47(4), p. 420-437.

Zhang, G., Germaine, J.T., Martin, R.T., and Whittle, A.J., 2003. A simple sample-mounting method for random powder X-ray diffraction; Clays and Clay Minerals, v. 51, p. 218-225.